

Advanced methods of mathematical modeling and experimental study in oil and gas reservoirs

Edited by

Fuyong Wang, Bassem Nabawy, Evgeny Burnaev,
Xiukun Wang and Debin Kong

Published in

Frontiers in Energy Research



FRONTIERS EBOOK COPYRIGHT STATEMENT

The copyright in the text of individual articles in this ebook is the property of their respective authors or their respective institutions or funders. The copyright in graphics and images within each article may be subject to copyright of other parties. In both cases this is subject to a license granted to Frontiers.

The compilation of articles constituting this ebook is the property of Frontiers.

Each article within this ebook, and the ebook itself, are published under the most recent version of the Creative Commons CC-BY licence. The version current at the date of publication of this ebook is CC-BY 4.0. If the CC-BY licence is updated, the licence granted by Frontiers is automatically updated to the new version.

When exercising any right under the CC-BY licence, Frontiers must be attributed as the original publisher of the article or ebook, as applicable.

Authors have the responsibility of ensuring that any graphics or other materials which are the property of others may be included in the CC-BY licence, but this should be checked before relying on the CC-BY licence to reproduce those materials. Any copyright notices relating to those materials must be complied with.

Copyright and source acknowledgement notices may not be removed and must be displayed in any copy, derivative work or partial copy which includes the elements in question.

All copyright, and all rights therein, are protected by national and international copyright laws. The above represents a summary only. For further information please read Frontiers' Conditions for Website Use and Copyright Statement, and the applicable CC-BY licence.

ISSN 1664-8714
ISBN 978-2-8325-2887-7
DOI 10.3389/978-2-8325-2887-7

About Frontiers

Frontiers is more than just an open access publisher of scholarly articles: it is a pioneering approach to the world of academia, radically improving the way scholarly research is managed. The grand vision of Frontiers is a world where all people have an equal opportunity to seek, share and generate knowledge. Frontiers provides immediate and permanent online open access to all its publications, but this alone is not enough to realize our grand goals.

Frontiers journal series

The Frontiers journal series is a multi-tier and interdisciplinary set of open-access, online journals, promising a paradigm shift from the current review, selection and dissemination processes in academic publishing. All Frontiers journals are driven by researchers for researchers; therefore, they constitute a service to the scholarly community. At the same time, the *Frontiers journal series* operates on a revolutionary invention, the tiered publishing system, initially addressing specific communities of scholars, and gradually climbing up to broader public understanding, thus serving the interests of the lay society, too.

Dedication to quality

Each Frontiers article is a landmark of the highest quality, thanks to genuinely collaborative interactions between authors and review editors, who include some of the world's best academicians. Research must be certified by peers before entering a stream of knowledge that may eventually reach the public - and shape society; therefore, Frontiers only applies the most rigorous and unbiased reviews. Frontiers revolutionizes research publishing by freely delivering the most outstanding research, evaluated with no bias from both the academic and social point of view. By applying the most advanced information technologies, Frontiers is catapulting scholarly publishing into a new generation.

What are Frontiers Research Topics?

Frontiers Research Topics are very popular trademarks of the *Frontiers journals series*: they are collections of at least ten articles, all centered on a particular subject. With their unique mix of varied contributions from Original Research to Review Articles, Frontiers Research Topics unify the most influential researchers, the latest key findings and historical advances in a hot research area.

Find out more on how to host your own Frontiers Research Topic or contribute to one as an author by contacting the Frontiers editorial office: frontiersin.org/about/contact

Advanced methods of mathematical modeling and experimental study in oil and gas reservoirs

Topic editors

Fuyong Wang — China University of Petroleum, Beijing, China

Bassem Nabawy — National Research Centre, Egypt

Evgeny Burnaev — Skolkovo Institute of Science and Technology, Russia

Xiukun Wang — China University of Petroleum, Beijing, China

Debin Kong — University of Science and Technology Beijing, China

Citation

Wang, F., Nabawy, B., Burnaev, E., Wang, X., Kong, D., eds. (2023). *Advanced methods of mathematical modeling and experimental study in oil and gas reservoirs*. Lausanne: Frontiers Media SA. doi: 10.3389/978-2-8325-2887-7

Table of contents

- 05 **Multi-scale flow mechanism and water control strategy of ultra-deep multi-porosity fractured tight sandstone gas reservoirs**
Tongwen Jiang, Hedong Sun, Xiangjiao Xiao, Songbai Zhu, Weiping Ouyang and Yongliang Tang
- 23 **Formation pressure distribution and productivity prediction of fractured horizontal wells in stress sensitive reservoirs**
Wang Huzhen, Liu Tiancheng, Sun Zhuangzhuang, Wang Chunyao, Liu Zhenyu, Zhou Zhijun, Diao Changjun and Zhao Zhiming
- 32 **A Fundamental Moving Boundary Problem of 1D Commingled Preferential Darcian Flow and Non-Darcian Flow Through Dual-Layered Porous Media**
Ping Wang, Wenchao Liu, Wei Ding, Xiangwen Kong and Hailiang Fan
- 51 **Potential and challenges for the new method supercritical CO₂/H₂O mixed fluid huff-n-puff in shale oil EOR**
Lei Li, Xiaomei Zhou, Yuliang Su, Pufu Xiao, Maolei Cui and Jianyang Zheng
- 56 **Effect of retrograde condensation and stress sensitivity on properties of condensate gas reservoirs**
Nan Li, Haosen Li, Xianhong Tan, Lijun Zhang and Yuwei Liu
- 66 **Optimization of volume fracturing technology for shallow bow horizontal well in a tight sandstone oil reservoir**
Chaoli Gao, Shiqing Cheng, Mingwei Wang, Wen Wu, Zhendong Gao, Song Li and Xuangang Meng
- 81 **Differences in production decline characteristics of horizontal wells in tight gas sandstone reservoirs with different qualities: A case study of the Sulige gas field, Ordos Basin**
Minhua Cheng, Yunsheng Wei, Guang Ji, Bo Ning and Meng Zhao
- 92 **The numerical simulation study on the dynamic variation of residual oil with water drive velocity in water flooding reservoir**
Zhaobo Sun, Yingxian Liu, Hui Cai, Yue Gao and Ruizhong Jiang
- 102 **Physical modeling of development adjustment mechanism for heterogeneous thick oil reservoir**
Xu Chen, Zubo Zhang, Qingjie Liu, Linghui Sun, Hanmin Xiao, Jian Gao and Hao Kang
- 115 **Pressure transient analysis of multistage fractured horizontal wells based on detailed characterization of stimulated area**
Huzhen Wang, Tiancheng Liu, Zhuangzhuang Sun, Chunyao Wang, Yangang Zhang, Yulin Chen, Zhenyu Liu and Zhijun Zhou

- 124 **Identification method of thief zones in carbonate reservoirs based on the combination of static and dynamic data: A case study from the Cretaceous Mishrif Formation in the H oilfield, Iraq**
Ruixue Li, Hucheng Deng, Meiyan Fu, Lanxiao Hu, Xinhui Xie, Liying Zhang and Xiaobo Guo
- 138 **Characterization of pore structure and reservoir properties of tight sandstone with CTS, SEM, and HPMT: A case study of the tight oil reservoir in fuyu oil layers of Sanzhao Sag, Songliao basin, NE China**
Changhe Mu, Haojie Hua and Xiukun Wang
- 155 **Numerical simulation of in-depth profile control for dispersed particle gel in heterogeneous reservoirs**
Gang Sun, Peichao Li, Dongyuan Du, Ting Song and Detang Lu
- 168 **A pore-scale study on the dynamics of spontaneous imbibition for heterogeneous sandstone gas reservoirs**
Mingchuan Wang, Ran Wang, Shuai Yuan and Fujian Zhou
- 178 **Study on gas injection development effect of tight reservoir based on fluid occurrence state**
Liu Yishan, Zu Lin, Sheng An, Hou Yanan, Liu Yuqi, Tian Changbing, Dong Xiaohu and Lei Zhengdong



OPEN ACCESS

EDITED BY

Fuyong Wang,
China University of Petroleum, China

REVIEWED BY

Weijun Shen,
Institute of Mechanics (CAS), China
Fengyuan Zhang,
China University of Petroleum, China
Mingqiang Wei,
Southwest Petroleum University, China

*CORRESPONDENCE

Hedong Sun,
sunhed@petrochina.com.cn

SPECIALTY SECTION

This article was submitted to Advanced Clean Fuel Technologies, a section of the journal Frontiers in Energy Research

RECEIVED 24 June 2022

ACCEPTED 11 July 2022

PUBLISHED 10 August 2022

CITATION

Jiang T, Sun H, Xiao X, Zhu S, Ouyang W and Tang Y (2022), Multi-scale flow mechanism and water control strategy of ultra-deep multi-porosity fractured tight sandstone gas reservoirs. *Front. Energy Res.* 10:977439. doi: 10.3389/fenrg.2022.977439

COPYRIGHT

© 2022 Jiang, Sun, Xiao, Zhu, Ouyang and Tang. This is an open-access article distributed under the terms of the [Creative Commons Attribution License \(CC BY\)](https://creativecommons.org/licenses/by/4.0/). The use, distribution or reproduction in other forums is permitted, provided the original author(s) and the copyright owner(s) are credited and that the original publication in this journal is cited, in accordance with accepted academic practice. No use, distribution or reproduction is permitted which does not comply with these terms.

Multi-scale flow mechanism and water control strategy of ultra-deep multi-porosity fractured tight sandstone gas reservoirs

Tongwen Jiang¹, Hedong Sun^{2*}, Xiangjiao Xiao³, Songbai Zhu³, Weiping Ouyang⁴ and Yongliang Tang³

¹Science and Technology Management Department of China National Petroleum Corporation, Beijing, China, ²PetroChina Research Institute of Petroleum Exploration and Development, Beijing, China, ³PetroChina Tarim Oilfield Company, Korla, China, ⁴Changqing Downhole Technology Company, CNPC Chuanqing Drilling Engineering Co., Ltd., Xi'an, China

The Keshen gas field in the Kuqa Depression, the Tarim Basin, China, contains multiple ultra-deep fractured tight sandstone gas reservoirs with edge/bottom water, which are remarkably complex in geologic structure, with fracture systems at different scales. There is still a lack of a method for effectively describing the flow behaviors of such reservoirs. In this paper, the fracture system was characterized by classes using the actual static and dynamic data of the gas reservoirs, and the mathematical models of gas (single-phase) and gas-water two-phase flows in “pore–fracture–fault” multi-porosity discrete systems. A fracture network system was generated randomly by the Monte-Carlo method and then discretized by unstructured grid. The flow models were solved by the hybrid-unit finite element method. Taking Keshen-2/8 reservoirs as examples, four types of dynamic formation modes were built up. Performances of reservoir of the same category were systematically analyzed, which revealed the coupling of gas supply and water invasion mechanisms in different fracture systems. The gas single-phase flow was found with the characteristic of “fault–fracture gas produced successively and matrix–fracture system coupling overlaid”, while the gas-water two-phase flow showed the characteristic of “rapid water dash in fault, drained successive in fractures and matrix block divided separately”. This study reveals the development features of this unique reservoir effectively, and designs development strategies of full life cycle water control for enhancing the gas recovery. It can be expected that the recovery factor of newly commissioning reservoirs would be increased by more than 10% as compared with the Keshen-2 gas reservoir. These findings will play an important role in guiding high and stable production of Keshen gas field development in the long term.

KEYWORDS

discrete fracture network model, multi-scale, flow mechanism, water invasion, dynamic description, fractured gas reservoir

Introduction

Keshen gas field locates in the Kelasu structural belt of Kuqa Depression in Tarim Basin, China. The breakthrough of Well KS2 in August 2008 ushered in the large-scale exploration and development of the Keshen gas field. By the end of 2021, the original gas in place (OGIP) proved cumulatively reached 800 billion cubic meters (Bcm), and the annual gas production capacity exceeded 10.5 Bcm, allowing the Keshen gas field to be the main battlefield for increasing gas reserves and production in the Tarim Oilfield. With high mountains, numerous cliffs and ravines developed on the surface, and complex structures such as imbricate thrust structures and sudden structures underground, the Keshen gas field is characterized by large buried depth (5,000–8,000 m), high pressure (88–138 MPa), tight reservoir matrix (0.001–0.5 mD), multiple orders of faults, dominance of water-bearing gas reservoirs and complicated water/gas distribution.

The complex surface conditions and underground geological structures result in poor quality of seismic data. Conventional acquisition and processing technologies cannot essentially enhance the quality of data. Thus, the subsalt structures are very difficult to interpret, and the structures can hardly be confirmed. Without similar gas fields at home or abroad for reference, two stages of development tests have been carried out in Keshen-2 and Keshen-8 gas reservoirs in succession (Jiang and Sun, 2018). The Keshen-2 gas reservoir was developed using the areal well pattern and volumetric fracturing process, which is often adopted in unconventional gas reservoirs, with regard to concepts of tight gas and continuous oil and gas reservoirs. The designed production capacity was $35 \times 10^8 \text{ m}^3/\text{a}$. However, reliability evaluation was not conducted on seismic data for the development plan design and well deployment, resulting in a lot of failure and inefficient wells. Consequently, the initial production capacity was only $22 \times 10^8 \text{ m}^3/\text{a}$. At the initial stage of production, the formation pressure dropped evenly but rapidly, early two-phase flow back analysis (Zhang and Emami-Meybodi, 2020; Zhang and Emami-Meybodi, 2022) and online production rate transient analysis results shown that there was a large deviation between dynamic reserves and static reserves (Jiang et al., 2021). The actual development indexes deviated greatly from those in the designed plan, and water production was observed soon after production. The natural productivity was low, and the productivity declined rapidly after stimulation. The total absolute open flow potential of wells in the block after 3 years of production was only 30% of the initial production (Jiang and Sun, 2018). The Keshen-8 gas reservoir revealed satisfactory development performance in line with the strategy of hydrocarbon accumulation controlled by structures and production controlled by fractures (Shen et al., 2022).

Significantly different from conventional fractured gas reservoirs, the Keshen gas reservoirs have the development characteristics of great productivity differences among wells,

fast inter-well pressure responses, and quick water invasion (Wang et al., 2018; Li et al., 2022). Accordingly, for the Keshen gas reservoirs, the development strategy was defined as “centralized well placement at high positions, moderate stimulation and early drainage” (Jiang and Sun, 2018; Li et al., 2022), and it was recognized that flow occurs in the “pore–fracture–fault” triple porosity system (Wei et al., 2019). However, conventional dual-porosity (Barenblatt et al., 1960; Warren and Root, 1963; Kazemi, 1969; Dean and Lo, 1988; Kazemi and Gilman, 1993; Zeng et al., 2012) and triple-porosity models (Liu, 1981; Liu, 1983; Wu et al., 2004; Wu et al., 2018) cannot accurately characterize the flow patterns in such strongly heterogeneous reservoirs with “pores–fractures–faults”. The discrete fracture network (DFN) model (Zambrano et al., 2016; Flemisch et al., 2017; Rueda Cordero et al., 2018; Li et al., 2018; Tarhuni et al., 2021) can accurately highlight the shape, orientation and conductivity of any fractures through visual description. Although it has obvious advantages in dealing with deterministic fractured sandstone reservoirs, the DFN model is not suitable for highly randomly developed fractured reservoirs. Therefore, a multi-scale random fracture network (Sun et al., 2022) and a multi-scale discrete fracture numerical well test model were constructed by randomly generating fractures and recombining them in batches and regions for better description of reservoir dynamic characteristics. It is necessary to further identify its mechanism, so as to establish a reliable foundation for formulating rational development strategy and enhancing recovery of the gas reservoir.

Considering the highly discrete presence of fractures in the Keshen gas field, based on the idea of DFN model, this paper presents a mathematical model of gas single-phase flow in “pore–fracture–fault” triple discontinuous media (Wei et al., 2019; Sun et al., 2022) to highlight the successive gas production and coupling gas supply mechanism between matrix and fracture systems of different scales. Using the flow experimental data (Qi et al., 2021; Wang et al., 2021), a gas–water two-phase flow model is established to reveal the progressive water invasion mechanism in fractures with different scales. Depending on the flow mechanisms of different types of gas reservoirs at different stages of development, corresponding development strategies are formulated.

Flow of gas in the pore–fracture–fault multi-scale media

Physical models and assumptions

The conventional dual-porosity continuum model of fractured reservoir (Figure 1A) assumes the fractures as the flow channels and the matrix as the reservoir space. This

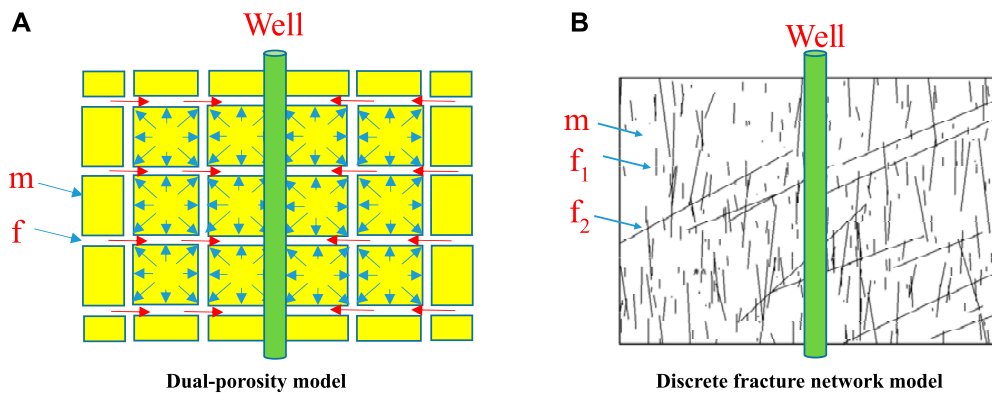


FIGURE 1
Physical models. (A) Dual-porosity model (B) Discrete fracture network model

paper considers the multi-scale discrete fracture network physical model with three porous media, i.e., faults, fractures (both natural and induced fractures) and matrix, as shown in Figure 1B.

It is assumed (Wei et al., 2019; Sun et al., 2022) that: (1) there are three kinds of porous media in the reservoir, i.e., matrix, fracture and fault, which are different in permeability on at least one order of magnitude; (2) the gas flow is single-phase flow subject to the Darcy's law; (3) the flow of fluid is one-dimensional flow in fractures and faults, and two-dimensional flow in matrix, and both fractures and faults are finitely conductive fractures with different conductivities; and (4) natural fractures and faults are randomly generated according to the probability distribution function, and the induced fractures are wing-symmetrical fractures.

Mathematical model

The governing equation of fluid flow in matrix (Sun et al., 2022) is

$$\frac{\partial^2 p_{mD}}{\partial x_D^2} + \frac{\partial^2 p_{mD}}{\partial y_D^2} = \frac{F_{mL}}{K_{mLD}} \frac{\partial p_{mD}}{\partial t_D} \quad (1)$$

The governing equation of fluid flow in faults (large fractures) is

$$\frac{\partial^2 p_{bFD}}{\partial L_D^2} = \frac{F_{bf}}{K_{bFD}} \frac{\partial p_{bFD}}{\partial t_D} \quad (2)$$

The governing equation of fluid flow in natural fractures is

$$\frac{\partial^2 p_{sFD}}{\partial l_D^2} = \frac{F_{sf}}{K_{sFD}} \frac{\partial p_{sFD}}{\partial t_D} \quad (3)$$

The governing equation of fluid flow in induced fractures is

$$\frac{\partial^2 p_D}{\partial l_D^2} = \frac{F_f}{K_{fD}} \frac{\partial p_D}{\partial t_D} \quad (4)$$

The initial condition is

$$p_D = 0 \quad (5)$$

The inner boundary condition is

$$\sum_{j=1}^N l_{jD} K_{jD} \left(\frac{\partial p_{jD}}{\partial n} \right) \bigg|_{\Gamma_{in}} = 2\pi \left(1 - C_D \frac{dp_{wD}}{dt_D} \right) \quad (6)$$

$$p_{wD} = p_{jD} - S \sum_{j=1}^N \frac{l_{jD} K_{jD}}{2\pi} \left(\frac{\partial p_{jD}}{\partial n} \right) \bigg|_{\Gamma_{in}} \quad (7)$$

The outer boundary condition is

$$\frac{\partial p_D}{\partial n} \bigg|_{\Gamma_{out}} = 0 \quad (8)$$

Dimensionless is defined as

$$\begin{aligned} p_D &= \frac{784.9Kh(\psi_i - \psi)}{Q_{sc}T}, \psi = 2 \int_{p_m}^p \frac{p}{\mu Z} dp, x_D = \frac{x}{x_f}, y_D = \frac{y}{x_f}, l_D \\ &= \frac{l}{x_f}, L_D = \frac{L}{x_f} \\ K_{sFD} &= \frac{K_{sf}}{K_m}, K_{bFD} = \frac{K_{bf}}{K_m}, K_{fD} = \frac{K_f}{K_m}, K_{mLD} = \frac{K_L}{K_m} \\ t_D &= \frac{3.6 \times 10^{-3} Kt}{\phi C_t \mu x_f^2}, C_D = \frac{0.1592C}{\phi h C_t x_f^2}, \frac{\partial p_{jD}}{\partial n} \\ &= - \left(\frac{\partial p_{jD}}{\partial x_D} \cos \theta + \frac{\partial p_{jD}}{\partial y_D} \sin \theta \right) \end{aligned}$$

where p_D is the dimensionless pressure; x_D and y_D are the dimensionless coordinate position in the reservoir; l_D is the dimensionless coordinate in the natural fracture; L_D is the dimensionless coordinate position in the fault (large fracture); K_{sFD} is the dimensionless permeability of the

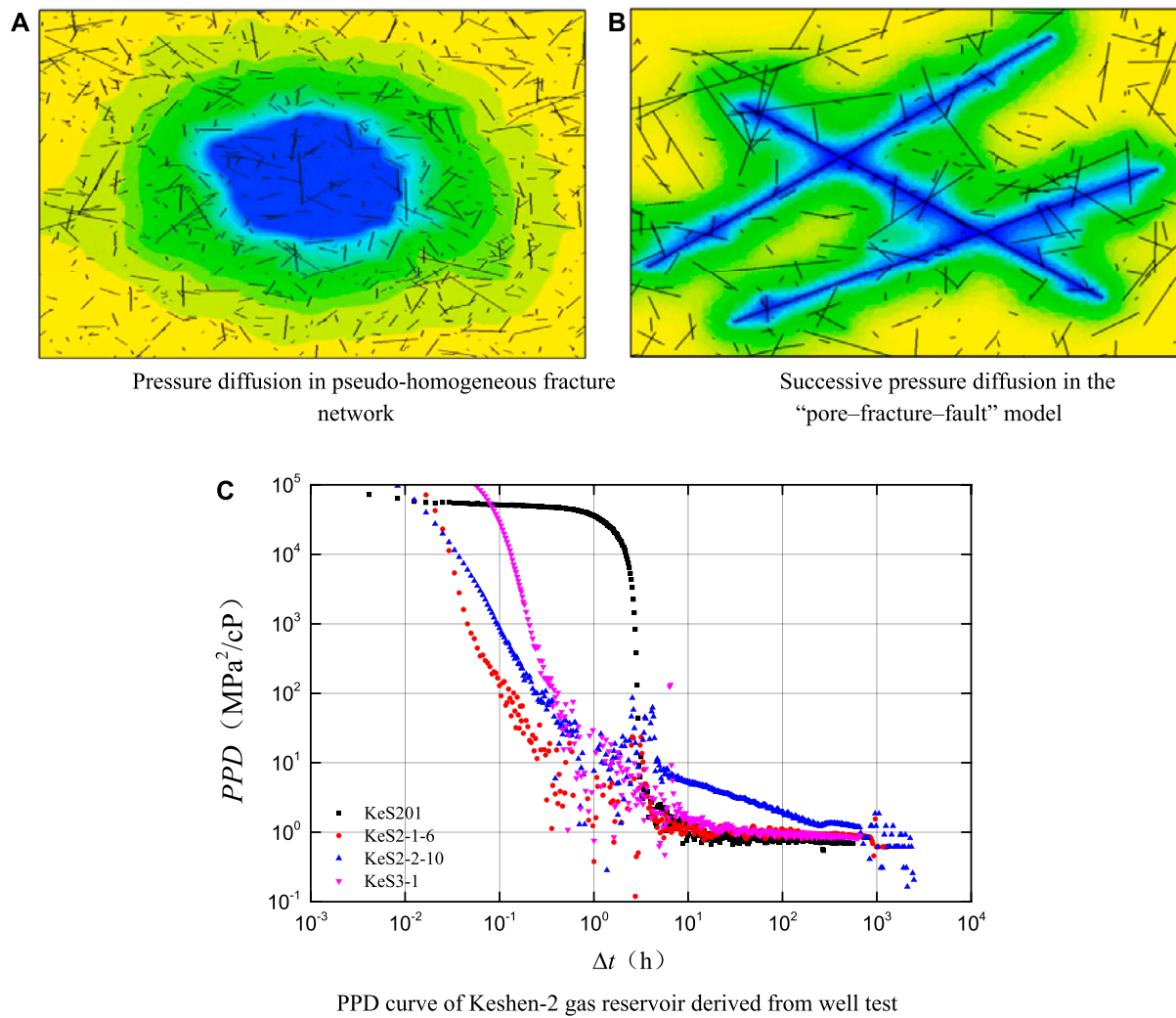


FIGURE 2

Gas supply mechanism of single-phase flow in multi-scale media. (A) Pressure diffusion in pseudo-homogeneous fracture. (B) Successive pressure diffusion in the. (C) PPD curve of Keshen-2 gas reservoir derived from well test.

natural fracture; K_{bFD} is the dimensionless permeability of faults (large fractures); K_{fD} is the dimensionless permeability of artificial fractures; K_{mLD} is the dimensionless permeability of the matrix; t_D is the dimensionless time; C_D is the dimensionless wellbore storage coefficient; x and y are the coordinate positions in reservoir, m; p is the reservoir pressure, MPa; ψ is the pseudo pressure, MPa²/(mPa·s); ϕ is the effective porosity, %; C_t is the total compressibility, MPa⁻¹; μ is the gas viscosity, mPa·s; t is the production time, h; K_m is the reservoir matrix permeability, mD; K_f is the permeability of induced fractures, mD; K_{sf} is the permeability of small fractures, mD; K_{bf} is the permeability of faults (big fractures), mD; F_f is the storativity ratio of induced fractures; F_{sf} is the storativity ratio of small fractures; F_{bf} is the storativity ratio of faults (big fractures); l is a location in the fracture, m; L is a

location in the fault, m; x_f is the half-length of the induced fracture, m; Γ_{in} is the inner boundary; q_{sc} is the gas production under standard condition, m³/d; T is the reservoir temperature, K; h is the effective thickness of reservoir, m; C is the wellbore storage factor, m³/MPa; S is the skin factor, dimensionless; N is the number of inner boundary elements, dimensionless; n indicates the external normal direction of element Γ , dimensionless; Γ_{out} is the outer boundary; Z is the gas deviation coefficient, dimensionless; subscript w indicates the bottom hole; subscript I indicates the initial state.

The unstructured grid discretization technique is used to perform Delaunay triangulation on the calculation area containing random fractures, and the hybrid element finite element method is used to solve the model (Wan et al., 2016).

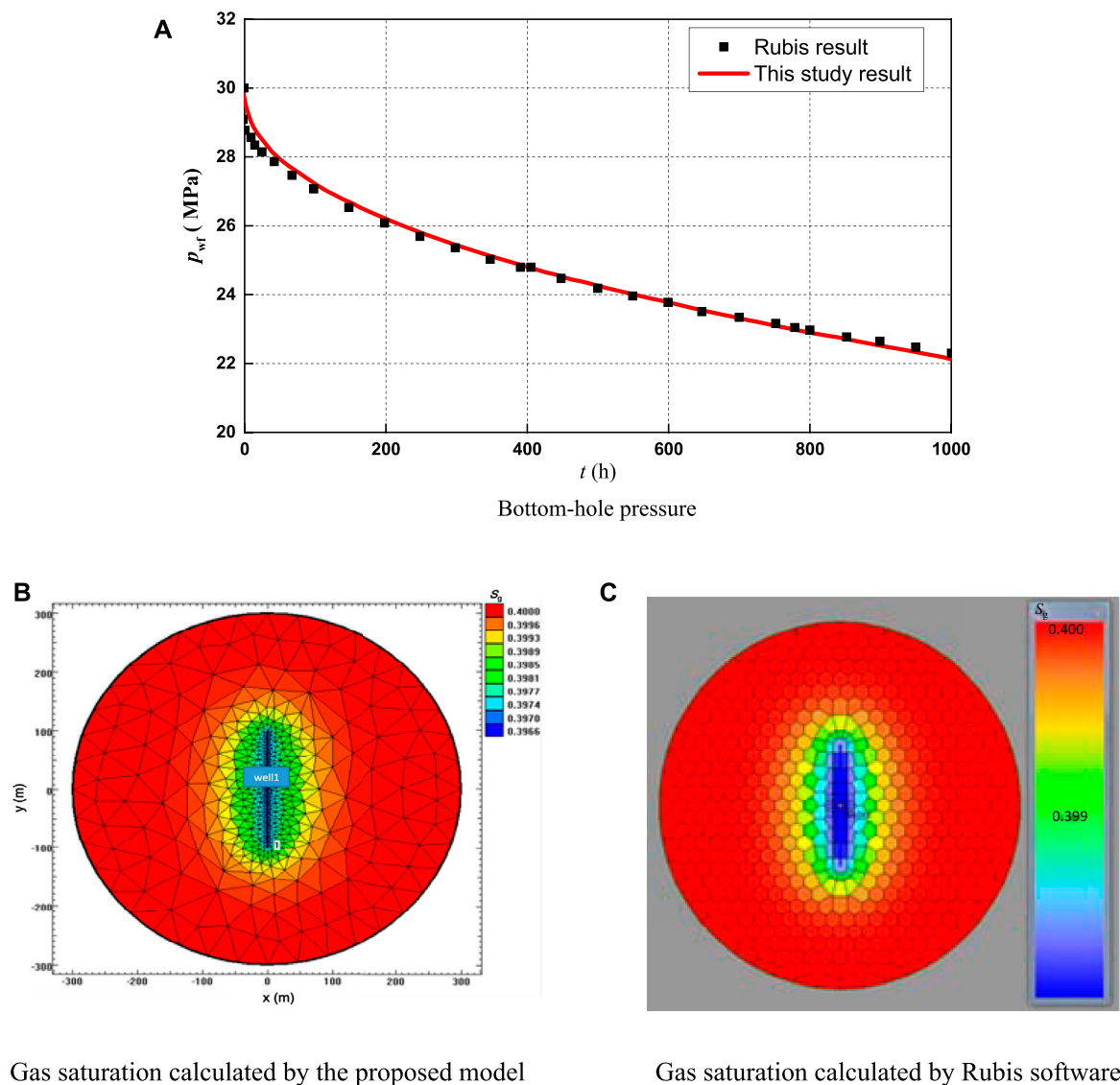


FIGURE 3
Calculation results of the proposed model and the Rubis software. (A) Bottom-hole pressure. (B) Gas saturation calculated by the proposed model. (C) Gas saturation calculated by Rubis software.

Flow mechanism

The numerical results of the above mathematical model show that different from the conventional viewpoint on the pressure gradient diffusion of the pseudo-homogeneous fracture network, there is a sudden change in pressure between adjacent media in the “pore–fracture–fault” system, and also spatial-temporal differences in gas production in different porous media. The gas single-phase flow is characterized by fault–fracture–pore gas produced successively, coupling overlaid, and synergistic gas supply. The prime pressure derivative (PPD) curve (Figure 2) (Mattar and Santo, 1992) derived from well test also shows the feature of gas supply from the matrix (the curve is usually a decline

curve, and the energy supply is reflected when the curve stops falling and flattens).

Flow of gas/water in the pore–fracture–fault multi-scale media

Assumptions

There is a gas well in the discontinuous tight gas reservoir, and there are faults, natural fractures and induced fractures around the wellbore (Wei et al., 2019; Sun et al., 2022), as

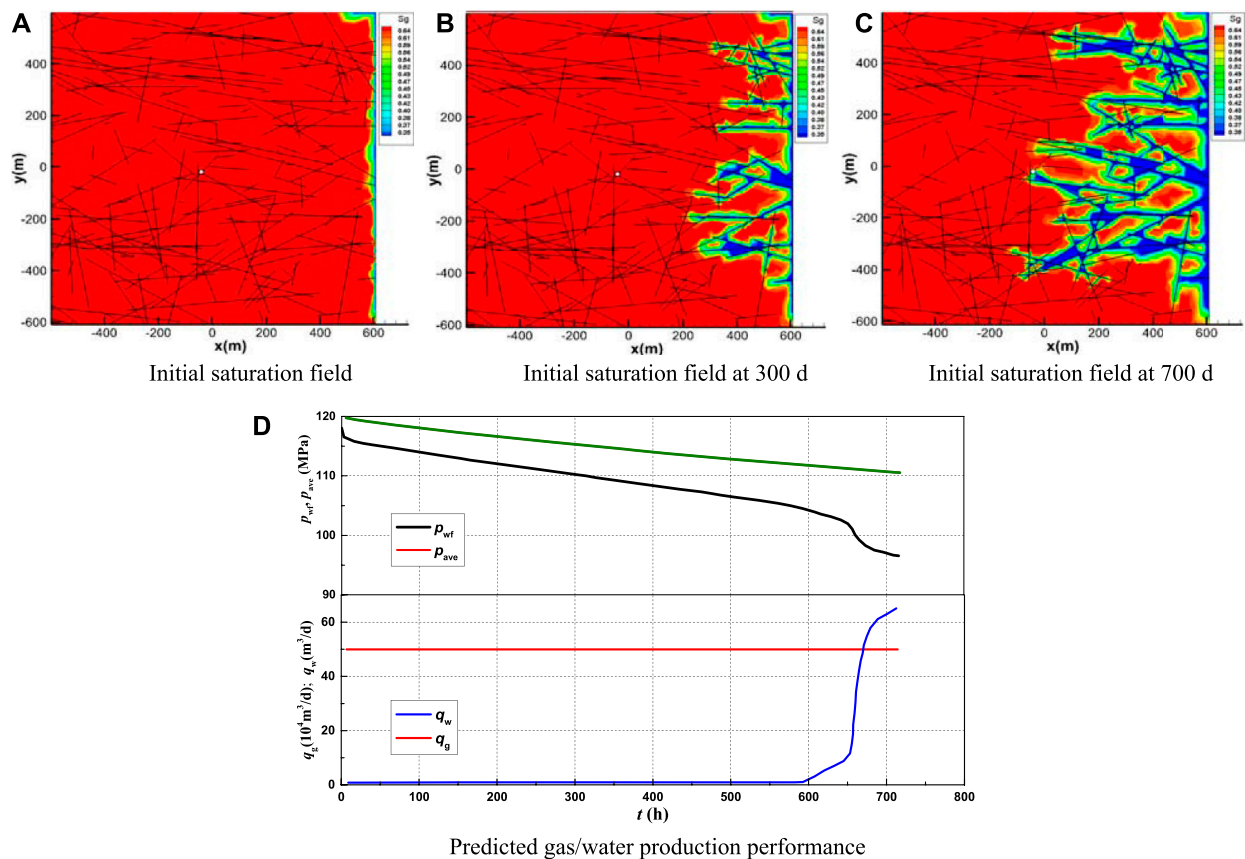


FIGURE 4

Mechanism of gas-water two-phase flow in multi-scale media (in case of edge water). (A) Initial saturation field. (B) Saturation field at 300 d. (C) Saturation field at 700 d. (D) Predicted gas/water production performance.

shown in Figure 1B. It is assumed that: (1) there are three kinds of porous media in the reservoir, i.e., matrix, fracture and fault, which are different in permeability on at least one order of magnitude; (2) the flow is gas-water two-phase flow subject to the Darcy's law, the gas slippage effect is neglected, but the impacts of capillary force is considered; (3) the flow of fluid is one-dimensional flow in fractures and faults, and two-dimensional flow in matrix, and both fractures and faults are finitely conductive fractures with different conductivities; (4) natural fractures and faults are randomly generated according to the probability distribution function, and the induced fractures are wing-symmetrical fractures; and (5) primitive water occurs in three forms: edge water, bottom water and gas/water in the same layer.

Mathematical model

The governing equation of matrix pressure (Kong, 2020; Zhang and Emami-Meybodi, 2020; Shen et al., 2022) is:

$$\nabla \cdot (\lambda_{tm} \nabla p_{wm}) + \nabla \cdot (\lambda_{gm} \nabla p_{cm}) + \lambda_{gm} C_{gm} (\nabla p_{wm})^2 = 281.46 \phi C_{tm} \frac{\partial p_{wm}}{\partial t} \quad (9)$$

The governing equation of matrix saturation is:

$$\nabla \cdot (\lambda_{wm} \nabla p_{wm}) = 281.46 \phi \frac{\partial S_{wm}}{\partial t} + 281.46 S_{wm} \phi C_{twm} \frac{\partial p_{wm}}{\partial t} \quad (10)$$

The governing equation of fracture (fault) pressure is:

$$\frac{\partial}{\partial l} \left(\lambda_{tf} \frac{\partial p_{wf}}{\partial l} \right) + \frac{\partial}{\partial l} \left(\lambda_g \frac{\partial p_{cf}}{\partial l} \right) + \lambda_g C_g \left(\frac{\partial p_{wf}}{\partial l} \right)^2 = 281.46 \phi C_t \frac{\partial p_{wf}}{\partial t} \quad (11)$$

The governing equation of fracture (fault) saturation is:

$$\frac{\partial}{\partial l} \left(\lambda_{wf} \frac{\partial p_{wf}}{\partial l} \right) = 281.46 \phi \frac{\partial S_{wf}}{\partial t} + 281.46 S_{wf} \phi C_{twf} \frac{\partial p_{wf}}{\partial t} \quad (12)$$

The initial condition is:

$$p(x, y, 0) = p_i \quad (13)$$

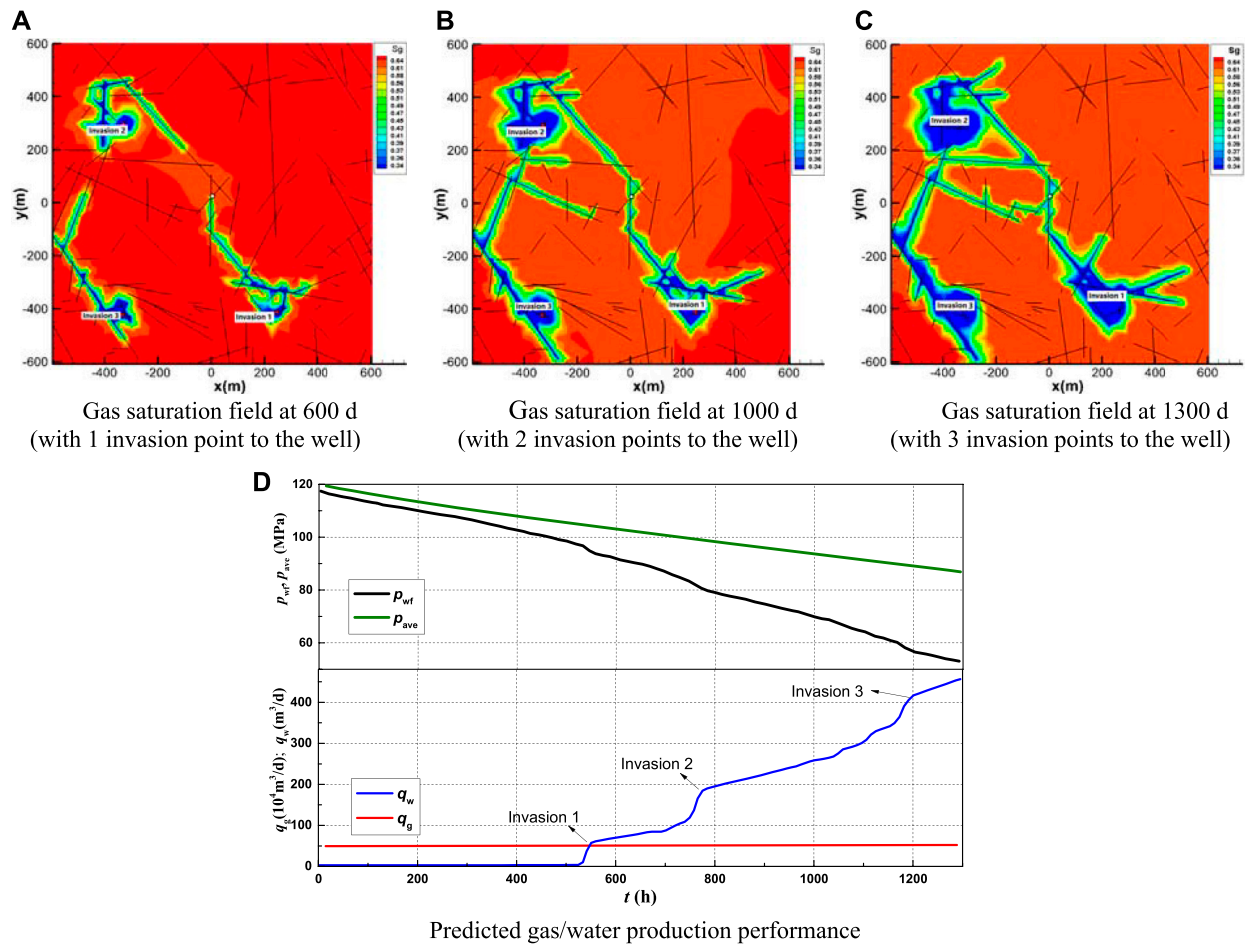


FIGURE 5

Mechanism of gas-water two-phase flow in multi-scale media (in case of bottom water). (A) Gas saturation field at 600 d (with 1 invasion point to the well). (B) Gas saturation field at 1000 d (with 2 invasion point to the well). (C) Gas saturation field at 1300 d (with 3 invasion point to the well). (D) Predicted gas/water production performance.

$$S_w(x, y, 0) = S_{wi} \quad (14)$$

The inner boundary condition is:

$$\sum_{i=1}^N w_i \frac{\partial p_{wf}}{\partial n} \Big|_{\Gamma_{in}} = \frac{11.73 q_g B_g}{\lambda_{gf} h} \quad (15)$$

The closed outer boundary is:

$$\frac{\partial p}{\partial n} \Big|_{\Gamma_{out}} = 0 \quad (16)$$

The outer boundary of edge water is:

$$p|_{\Gamma_{out}} = p_i \quad (17)$$

$$S_w(t)|_{\Gamma_{out}} = 1 - S_{gr} \quad (18)$$

The outer boundary of bottom water is:

$$p|_{\Gamma_{out}} = p_i - \Delta p_h \quad (19)$$

$$S_w(t)|_{\Gamma_{out}} = S_{w0} \quad (20)$$

where λ is the mobility, $\text{mD}/(\text{mPa}\cdot\text{s})$; p is the reservoir pressure, MPa; ϕ is the effective porosity, decimal; C_t is the total compressibility, MPa^{-1} ; C_{tw} is the sum of pore compressibility and water compressibility, MPa^{-1} ; μ is the gas viscosity, $\text{mPa}\cdot\text{s}$; t is the production time, h; S_w is the water saturation, dimensionless; S_{gr} is the residual gas saturation, dimensionless; Δp_h is the difference between bottom water pressure and original reservoir pressure at water invasion point, MPa; l is the coordinate axis of fracture governing equation, m; w_f is the fracture width, m; Γ_{in} is the inner boundary; q_g is the gas production under standard conditions, m^3/d ; h is the effective thickness of reservoir, m; Γ_{out} is the outer boundary; K is the reservoir permeability, mD; subscripts g, w, c and f indicate gas, water, capillary force and fracture or fault, respectively.

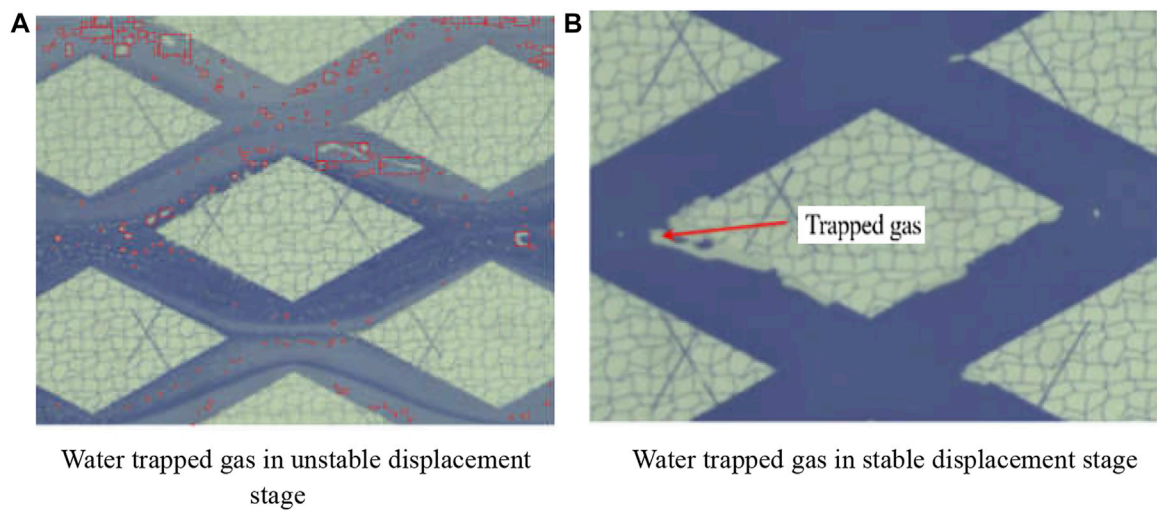


FIGURE 6

Test results for water trapped gas during displacement. (A) Water trapped gas in unstable displacement stage. (B) Water trapped gas in stable displacement stage.

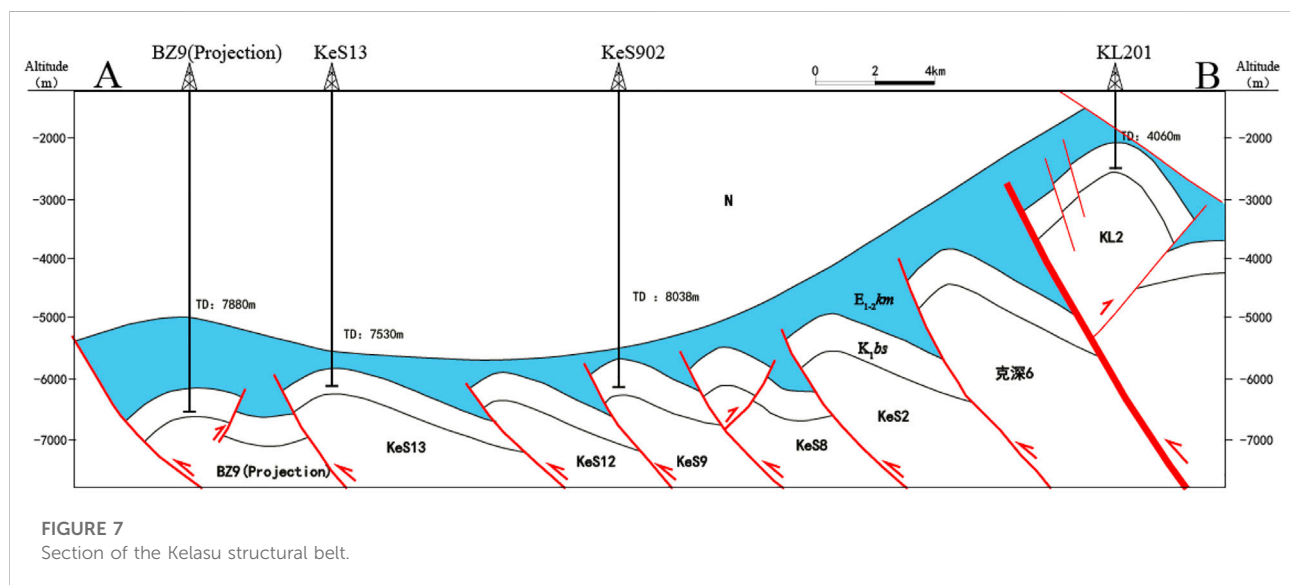


FIGURE 7

Section of the Kelasu structural belt.

In this paper, the control volume finite-element method (CVFEM) is used to solve the governing equations composed of Eqs. 9–20, with detailed procedures given in Reference (Chen et al., 2006). CVFEM is a combination of finite element method and finite volume method. It integrates the interpolation function of the former and the numerical calculation format of the latter. Without the necessity of secondary reconstruction of grid, CVFEM can directly use the finite element grids, which are more flexible and accurate, and have the feature of local conservation of finite volume.

Model validation

The proposed model and the commercial numerical simulation software are used to numerically simulate the gas-water two-phase flow in induced fractures (without considering the random natural fractures) given the same reservoir parameters and gas-water permeability curve, in order to validate that the proposed model is constructed and solved correctly. The initial pressure of the reservoir is 30MPa, the temperature is 100°C, the permeability is 0.1mD,

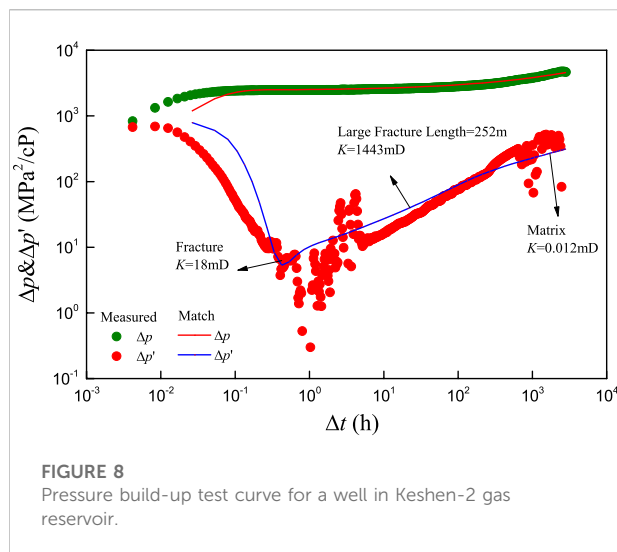
TABLE 1 Correlation of structural styles and well test modes in Keshen gas field.

Structural style Wei et al., (2020)	Well test mode	Typical block	Production performance
Compressive, highly steep fault anticline	Development of oriented fractures; Underdevelopment of fracture network	Keshen-2	High but unsteady production, with rapid water flooding
Compressive, abrupt structural anticline	Cutting-through oriented fractures; Development of fracture network	Keshen-8	High and stable production, with rapid water invasion after water production
Compressive, wide, gentle fault anticline	Pseudo-homogeneous; Well development of fracture network	Keshen-9	High and stable production after acid fracturing
Weakly compressive, wide, gentle fault anticline	Pseudo-homogeneous; Underdevelopment of fracture network	Keshen-13 (locally)	Low and stable production after acid fracturing, with significant differential pressure

the effective thickness is 10m, the porosity is 10%, the water saturation is 60%, and the gas relative density is 0.6. The half-length of the fracture is 100m, the conductivity is 100mD•m, the gas flow rate is 10000 m³/d, production time is 1000 h. [Figure 3](#) compares the calculation results of bottom-hole pressure and saturation field. It is found that the bottom-hole pressure and water production calculated by the proposed model are consistent with the results of the conventional classical model, which verifies the correctness of the proposed model and its solution.

Flow mechanism

It can be concluded from the numerical results of the mathematical model above that, in different pore–fracture–fault combinations, the characteristics of water invasion are complex and diverse, rather than the singular mode of water channeling along fault/fracture in traditional view. Generally, gas–water two-phase flow in multi-scale media is characterized by “rapid dash in fault, drained successive in fractures and matrix block divided



separately". In case of edge water, the initial pressure of the reservoir is 120MPa, the temperature is 160°C, the permeability is 0.2mD, the effective thickness is 80m, the porosity is 8%, the water saturation is 35%, and the gas relative density is 0.6. The drainage range is 1.2 km*1.2 km. There are 200 natural fractures in this area, the average fracture length is 200m, the conductivity is 10000mD-m, and the gas production is $50 \times 10^4 \text{ m}^3/\text{d}$ to simulate the production for 710 d. With the production, pressure drops gradually and the edge water approaches the producer along faults or fractures. When the water invades into the producer, the water production increases significantly, and the bottom-hole pressure decreases greatly, as shown in Figure 4.

In case of bottom water, it is assumed that there are three points at which natural fractures communicate with the bottom water around the gas well. There are 100 natural fractures in the drainage area, the average fracture length is 150m, and other parameters are consistent with the edge water conditions. With the production, the pressure drops gradually, and the water approaches the well along the fractures. When the water invades into the well, the water production increases instantaneously. As the impacts of invasion points arrive one after another, the water production increases and the bottom-hole pressure decreases in steps. The three invasion points correspond to three steps, and the time of the steps coincides with the time when the water in the saturation pressure field invades into the well, as shown Figure 5. There is a large amount of residual gas in the matrix outside the water invasion pathways.

The high-pressure lab test also shows that the displacement is faster initially when there are more fractures. After the displacement interfaces intersect in fractures, a large amount of water trapped gas is generated

in the matrix between two intersecting fractures, which reduces the instantaneous displacement efficiency. The more the intersected fractures, the easier the generation of water trapped gas. In the unstable displacement stage, migration of gases, including large gas bubbles and smaller foggy bubbles with small particle sizes, can be observed for a relatively long time. In the stable displacement stage, only a small quantity of bubbly water trapped gas is adsorbed at the interface between matrix and fracture, and a small amount of water trapped gas remains in the fracture channels, as shown in Figure 6.

Dynamic description of reservoirs in Keshen gas field

As a kind of typical fractured tight sandstone reservoirs, the Cretaceous Bashijiqike Formation reservoirs in the Keshen gas field experienced multiple phases of tectonic movements and intensive tectonic compression. Consequently, they exhibit complex patterns of fracture evolution and development, characterized by "multi-phase, multi-scale, multi-strata and multi-occurrence", as shown in Figure 7.

By using the 3D laser scanning for outcrop fracture characterization, imaging logging fracture identification under ultra-deep, high-temperature and high-pressure conditions, effectiveness evaluation and industrial CT fracture characterization, four structural patterns are identified in the Cretaceous. From north to south, the anticlines transits gradually from strongly compressive, highly steep and sudden anticlines to weakly compressive, wide, gentle and flat anticlines. Due to the difference in compressive stress during the uplift of South Tianshan Mountains, the northern belt (Keshen-2-Kela-2) is dominated by oblique extrusion deformation, with a series of basement involved thrust faults, together with multiple vertical imbricate stacks to form wedged thrust structure. The southern belt (south of Keshen-2) is dominated by horizontal shrinkage deformation, with a series of detachment faults to form detachment-thrust and abrupt structures. Fractures are different in characteristics from structural style to structural style, and the structural styles agree well with well test modes (Table 1).

Massive well test data show that the Keshen gas field has the characteristics of flow in pore-fracture-fault multi-scale media, and the permeability difference between matrix and fracture is more than 5 orders of magnitude. Figure 8 illustrates the well testing curves of typical wells. Since the existence of large fractures was not recognized in the early evaluation stage of Keshen 2 gas reservoir, the designed indexes were too optimistic. In reality, problems such as water production and sand production occurred shortly after the production.

In the past 2 years, breakthroughs in production profile technologies for gas wells with ultra-high pressure (with

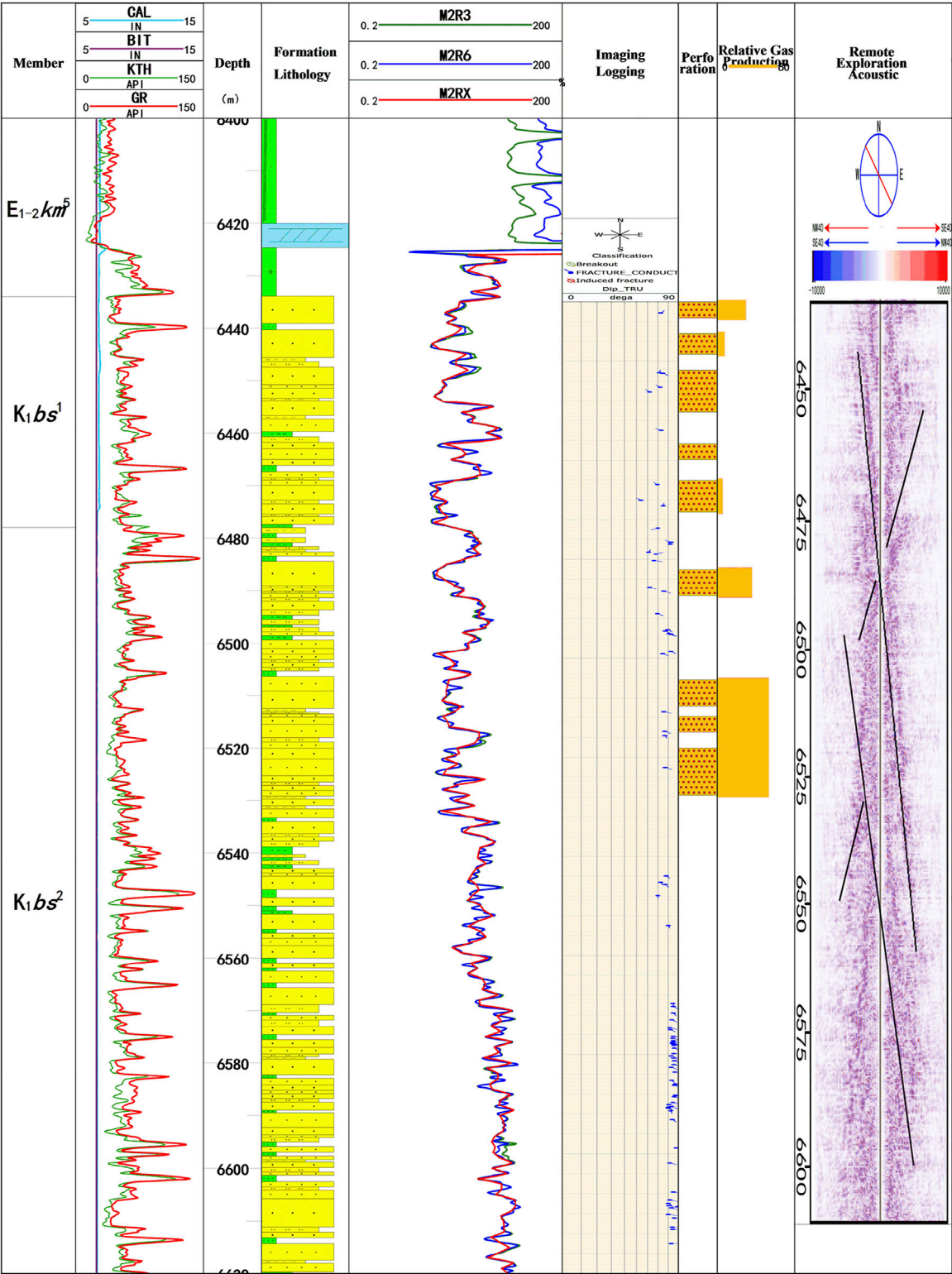


FIGURE 9
Comparison of production profile and remote exploration acoustic logging data of a well in Kelasu gas field.

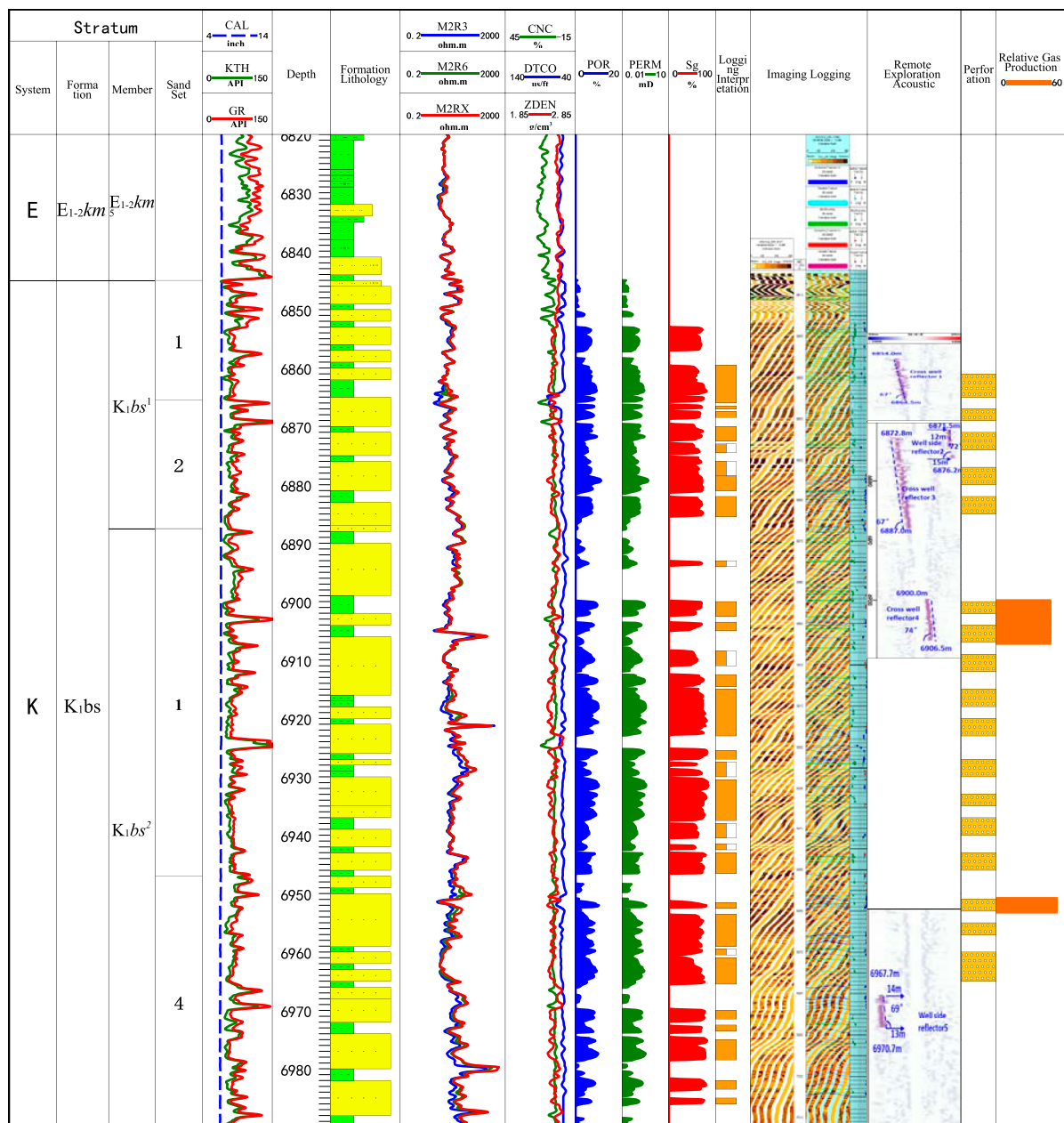


FIGURE 10

Physical properties and results of imaging logging, remote exploration acoustic logging and production profile test of Well KeS8-5.

wellhead pressure over 100 MPa) and narrow tubing and extensive application of remote acoustic logging technologies further verified the accuracy of dynamic description based on well test data. As shown in Figure 9, the remote acoustic logging data interpretation results show the existence of large fractures around a well. Production profile test further proves that both gas and water are produced from these large fractures.

Within individual gas reservoir, the overall connectivity is good, and different fracture patterns lead to varying production characteristics. According to well interference test, the inter-well interference is strong inside the gas reservoir. Due to the existence of “highway” between wells, the interference signal can reach the adjacent well, that is, 1 km away in ten some minutes, while the response time of the interference signal of two wells more than 10 km away is only 7–10 h. In the early

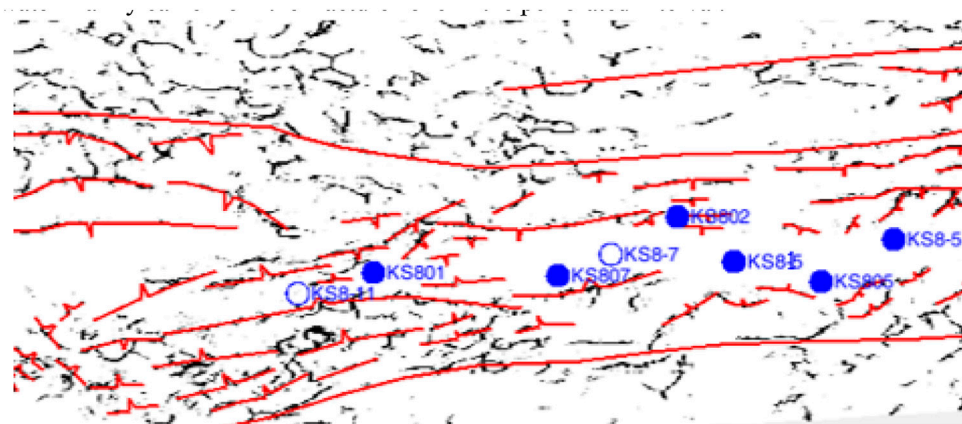


FIGURE 11
Fine fault characterization and AFE microfracture attributes in Keshen-8 gas reservoir.

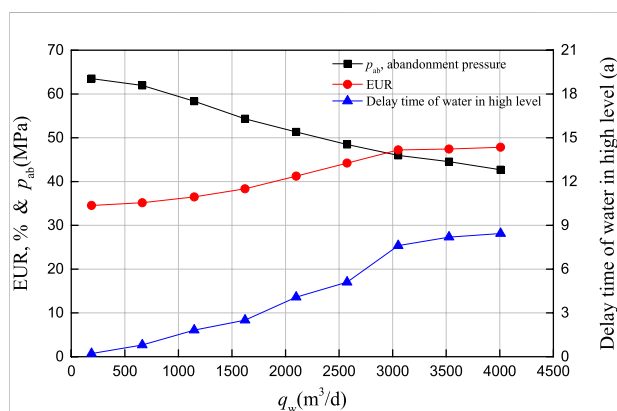


FIGURE 12
EUR and abandonment pressures at different water drainages.

development stage, the formation pressures in different parts of the gas reservoir basically keep decreasing synchronously. In the Keshen-2 gas reservoir with oriented fractures, pressure waves can sweep the entire fracture network within a short time, and formation water invades unevenly and rapidly along fault system. Matrix, fracture and fault are coupled in terms of gas supply (Figure 2B). However, the gas supply of the matrix system to the fractures is limited, leading to rapid decline of pressure and production; the gas reservoir is divided by water invasion channels after non-uniform water invasion. In addition to oriented large fractures, the Keshen-8 gas reservoir contains evenly distributed small fractures, allowing the gas wells to be highly capable of high and stable productivities. The flow behaviors of such gas reservoirs have been evidenced by the test results of Well KeS8-5. As shown in Figure 10, the remote exploration acoustic logging data show the existence of four

faults within 30 m around Well KeS8-5; the imaging logging interpretation indicates that fractures are evenly distributed vertically in Well KeS8-5; the production profile test suggests that gas is not produced evenly, but predominantly from two intervals: 6853.0–6965.0 m and 6951.0–6953.0 m. These conclusions coincide well with the results of dynamic description based on well test data.

Strategies for water control

Water invasion is the biggest challenge for maintaining the stable production at 10 Bcm in the Keshen gas field. Once water breaks through in the gas reservoir, the formation water may quickly invade the gas reservoir along the “highway” to cause “water trapped gas”, thereby reducing the production significantly. For example, the Keshen-2 gas reservoir was put into production test in April 2013, and water production was initially observed in wells at the edge in 2014. Because no continuous and effective efforts were made to drain the water timely, wells in the south, north and middle and high parts of the gas reservoir came into water production successively from May 2019. As a result, the gas production declined rapidly. The gas reservoir was divided by water with the significant feature of pressure partition, which made the gas recovery in the matrix very difficult. The Keshen-8 gas reservoir was put into production in July, 2015. Since 2020, water was produced in six wells (incl. KS8-11, KS801, and KS802) successively in the west of the gas reservoir. The formation water advanced rapidly along the large fault system (Figure 11). The logging data of the water-producing wells show that the main gas producing layers obviously correspond to the water producing layers, and the formation water mainly came from the fracture zone in the perforated interval.

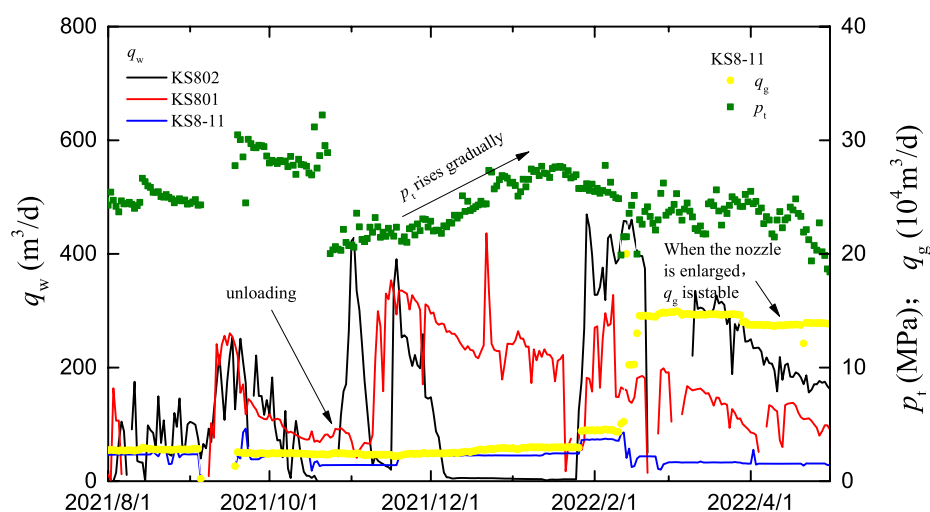


FIGURE 13

Production curve of Well KS8-11 after water drainage.

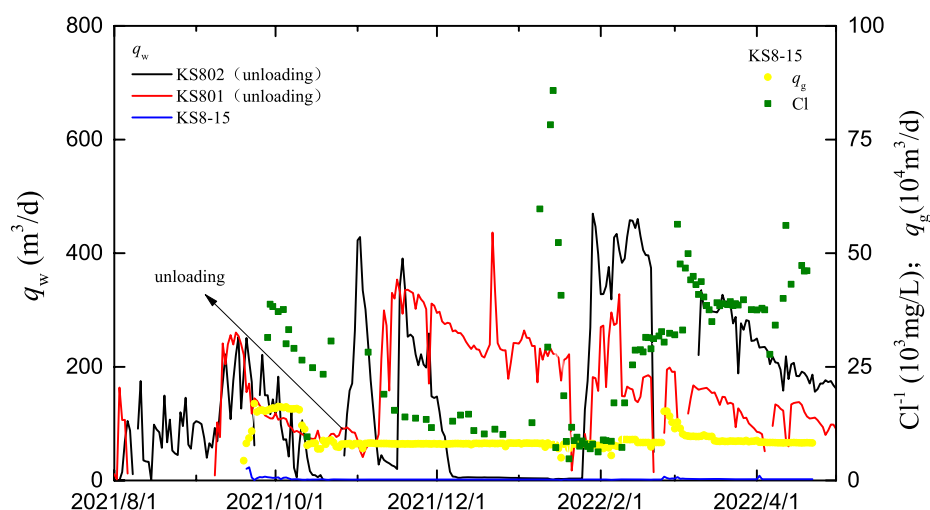


FIGURE 14

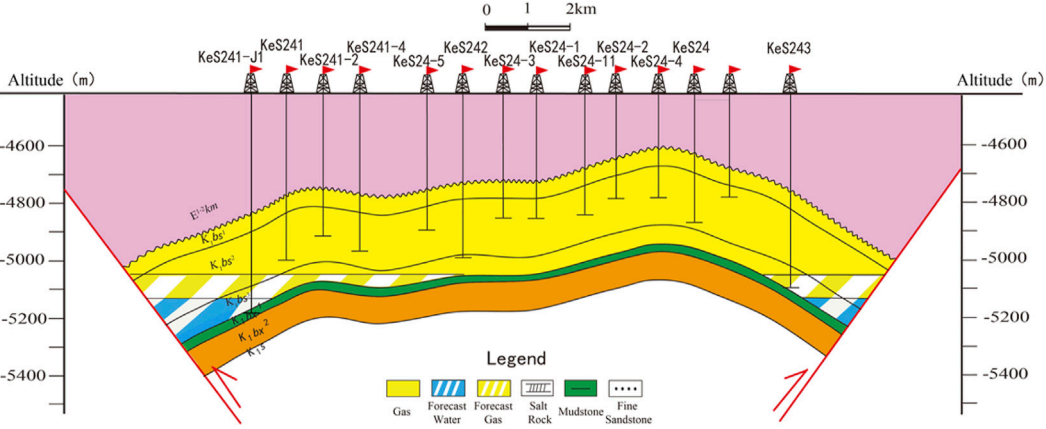
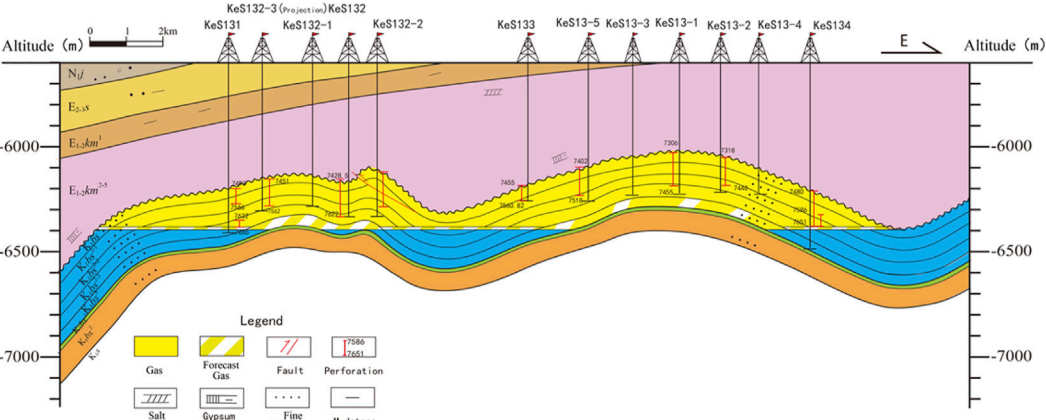
Change of chloride value in Well KS8-15.

Mechanism research and development practices have proved that the early gas recovery by water drainage has a significant impact on the enhanced gas recovery of the Keshen-8 gas reservoir. After water production, the wells at the edge of the gas reservoir were transformed to be developed by water drainage, with the designed daily water drainage of 200–4,000 m³. Figure 12 shows the prediction results of numerical simulation. Clearly, as the water drainage increases, the abandonment pressure of the gas reservoir drops, the EUR improves, and the water breakthrough time delays. This scheme exhibits the EUR enhanced by 10%, abandonment pressure reduced by 7.62 MPa and water production in structural

high delayed by 5 years compared with the schemes at the water drainage of 1000 m³ and 2800 m³.

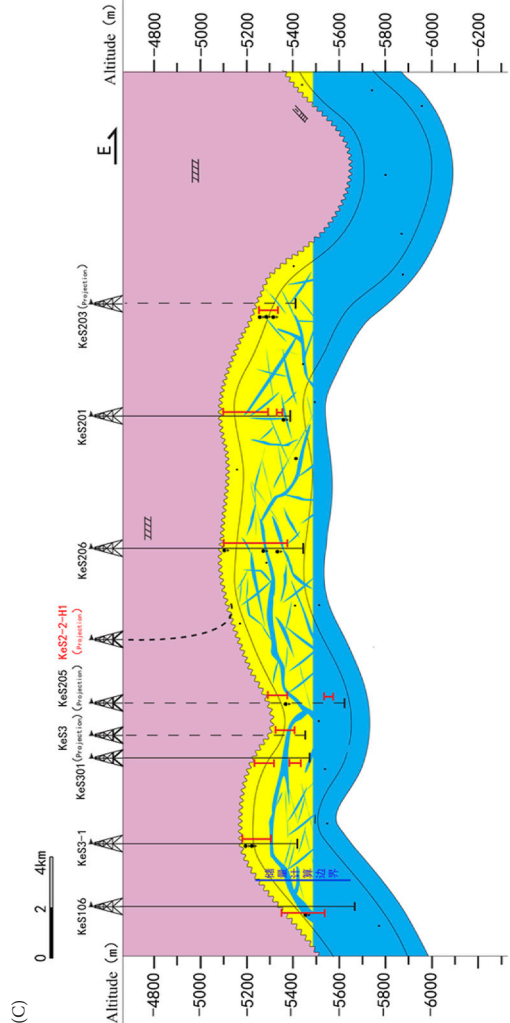
In November 2021, coiled tubing enhanced gas lift drainage was conducted in two water-producing wells, KS801 and KS802, at the structural edge of the Keshen-8 gas reservoir. After the large-scale gas-lift drainage in Well KS801, Well KS8-11 maintained stable daily gas production and slight rise of tubing pressure (from 22.5 MPa in early December 2021 to 27.79 MPa in early February 2022) while the production system was kept unchanged, indicating remarkable effects. Moreover, the water drainage capacity of the two wells

TABLE 2 Different water-control strategies for the Keshen gas fields.

Type	Gas reservoir profile	Typical block	Geological feature	Countermeasure	Recovery efficiency
Weak Water Gas Reservoir	(A) 	KeS8, 9, 24	The north and south water bodies are not developed, and the East and west water bodies can be discharged	Strong drainage Large extraction	50–60%
Strong Water Gas Reservoir	(B) 	KeS10, 13	Water bodies are developed in all directions of the gas reservoir, with poor drainage	Combination of control and drainage, Delay water invasion	40–50%

(Continued on following page)

TABLE 2 (Continued) Different water-control strategies for the Keshen gas fields.

Type	Gas reservoir profile	Typical block	Geological feature	Countermeasure	Recovery efficiency
Watered Out State of Gas Reservoir	<div><div>(C)</div></div>	Kes2	The water flooded degree of gas reservoir is high, It is difficult to use Water sealed gas	Deep potential tapping Comprehensive policy	improved by 2–4%

decreased gradually, which further indicates that the water energy is limited (Figure 13).

Enhanced gas recovery by water drainage was carried out in Wells KS802 and KS801 in the western part of the Keshen-8 gas reservoir. As a result, the chloride value in the reservoir decreased gradually until it became stabile. For example, the chloride value in Well KS8-15, 1.2 km away from Well KS802, decreased gradually from 85,772 mg/L and kept stable at 6,292–7,084 mg/L. As the intensity of water drainage reduced, the chloride value rose again rapidly (Figure 14).

The water drainage practices demonstrate that the early water drainage can cut off the “highway” for water invasion in the Keshen-8 gas reservoir. Accordingly, the water control strategies are customized for weak, strong and watered out gas reservoirs (Table 2).

Conclusion

- (1) With comprehensive consideration to morphology, orientation and conductivity of multi-scale fractures, the mathematical model for coupling gas single-phase and gas-water two-phase flows in the pore-fracture-fault system was established. It provides a new way for researches related to development mechanism of tight sandstone gas reservoirs with pores, fractures and faults.
- (2) There is a sudden change in pressure between adjacent media in the “pore-fracture-fault” system, and also spatial-temporal differences in gas production in different porous media. The mechanism of fault-fracture-pore gas produced successively, coupling overlaid, and synergistic gas supply is established, laying a foundation for enhancing the gas recovery through reservoir stimulation characterized by “moderate stimulation of low-efficiency fractures and expansion of fracture network for synergetic gas supply”.
- (3) In different pore-fracture-fault combinations, the characteristics of water invasion are complex and diverse, rather than the singular mode of water channeling along fault/fracture in traditional view. Generally, gas-water two-phase flow in multi-scale media is characterized by “rapid dash in fault, drained successive in fractures and matrix block divided separately”, laying a foundation for the water control strategy of “multi-scale complex flow field optimization for production allocation and early water drainage”.
- (4) The water drainage practices demonstrate that the early water drainage can cut off the “highway” for water invasion in the Keshen-8 gas reservoir. This scheme exhibits the EUR enhanced by 10%, abandonment pressure reduced by 7.62 MPa and water production in structural high delayed by 5 years compared with the schemes at the water drainage of 1000 m³ and 2800 m³.

Data availability statement

The original contributions presented in the study are included in the article/supplementary material, further inquiries can be directed to the corresponding author.

Author contributions

TJ, HS, and XX contributed to conception and design of the study. WO organized the model. YT performed the statistical analysis. HS, WO, and SZ wrote the first draft of the manuscript. TJ, XX, and YT wrote sections of the manuscript. All authors contributed to manuscript revision, read, and approved the submitted version.

Funding

The major science and technology project of PetroChina Co., Ltd. “Research and Application of Key Technologies for Deep & Ultra-Deep Gas Field Development in Kuqa Depression” (No. 2018E-1803).

References

- Barenblatt, G. I., Zhurav Iu, P., and Kochina, I. N. (1960). Basic concepts in the theory of seepage of homogeneous liquids in fissured rocks[J]. *PMM* 24 (5), 852–864.
- Chen, Z., Huan, G., and Ma, Y. (2006). *Computational methods for multiphase flows in porous media*[M]. Philadelphia: Society for Industrial and Applied Mathematics.
- Dean, R. H., and Lo, L. L. (1988). Simulations of naturally fractured reservoirs. *SPE Reserv. Eng.* 3 (2), 638–648. doi:10.2118/14110-pa
- Flemisch, B., Berre, I., Boon, W., Fumagalli, A., Schwenck, N., Scotti, A., et al. (2017). Benchmarks for single-phase flow in fractured porous media. *Adv. Water Resour.* 111, 239–258. doi:10.1016/j.advwatres.2017.10.036
- Jiang, T., Sun, H., Wang, H., et al. (2021). *Reserves estimation for geopressed gas reservoirs* [M]. Beijing: Petroleum Industry Press.
- Jiang, T., and Sun, X. (2018). Development of Keshen ultra-deep and ultra-high pressure gas reservoirs in the Kuqa foreland basin, Tarim Basin: Understanding points and technical countermeasures[J]. *Nat. Gas. Ind.* 38 (6), 1–9.
- Kazemi, H., and Gilman, J. R. (1993). *Multiphase flow in fractured Petroleum reservoirs*[G]. Flow and contaminant transport in fractured rock. Elsevier.
- Kazemi, H. (1969). Pressure transient analysis of naturally fractured reservoirs with uniform fracture distribution. *Soc. Petroleum Eng. J.* 9 (4), 451–462. doi:10.2118/2156-a
- Kong, X. (2020). *Advanced seepage mechanics(third edition)*[M]. Hefei, Anhui, China: University of Science and Technology of China Press.
- Li, G., Tian, J., and Duan, X. (2022). Measures and practice for improving the recovery factor of ultra-deep tight sandstone gas reservoirs: A case study of Kelasu gas field. *Tarim. Basin*[J]. *Nat. Gas. Ind.* 42 (1), 93–101.
- Liu, C. (1981). Exact solution for the compressible flow equations through a medium with triple-porosity[J]. *Appl. Math. Mech.* 2 (4), 457–462.
- Liu, C. (1983). Exact solution of unsteady axisymmetrical two-dimensional flow through triple porous media[J]. *Appl. Math. Mech.* 4 (5), 717–724.
- Li, Y., Shang, Y., and Yang, P. (2018). Modeling fracture connectivity in naturally fractured reservoirs: A case study in the yanchang formation, ordos basin, China[J]. *Fuel* 211, 789–796.
- Mattar, L., and Santo, M. (1992). How wellbore dynamics affect pressure transient analysis[J]. *JCPT* 31 (1), 32–40.
- Qi, X., Liu, S., Yu, Z., Sun, H., Chang, B., Luo, Z., et al. (2021). Interfacial dynamics of gas–water displacement in fractured porous media under high pressure. *Phys. Fluids* 33, 092003. doi:10.1063/5.0062141
- Rueda Cordero, J. A., Mejia Sanchez, E. C., and Roehl, D. (2018). Integrated discrete fracture and dual porosity - dual permeability models for fluid flow in deformable fractured media. *J. Petroleum Sci. Eng.* 175, 644–653. doi:10.1016/j.petrol.2018.12.053
- Shen, W., Ma, T., Li, X., Sun, B., Hu, Y., Xu, J., et al. (2022). Fully coupled modeling of two-phase fluid flow and geomechanics in ultra-deep natural gas reservoirs. *Phys. Fluids* 34, 043101. doi:10.1063/5.0084975
- Sun, H., Ouyang, W., Wan, Y., Zhu, S., and Tang, Y. (2022). Discrete fracture network well test analysis for naturally fractured tight sandstone gas reservoir[J]. *Nat. Gas. Ind.* 42 (7), 56–66.
- Tarhuni, M. N., Sulaiman, W. R., Jaafar, M. Z., Milad, M., and Alghol, A. M. (2021). A review of the dynamic modeling approaches for characterizing fluid flow in naturally fractured reservoirs[J]. *Energy Eng.* 118 (4), 761–795.
- Wan, Y., Liu, Y., Liu, W., Han, G., and Niu, C. (2016). A numerical approach for pressure transient analysis of a vertical well with complex fractures. *Acta Mech. Sin.* 32 (4), 640–648. doi:10.1007/s10409-016-0568-0
- Wang, F., Zeng, F., Lu, W., Hou, X., Cheng, H., Gao, J., et al. (2021). Fractal analysis of tight sandstone petrophysical properties in unconventional oil reservoirs with NMR and rate-controlled porosimetry. *Energy Fuels* 35 (5), 3753–3765. doi:10.1021/acs.energyfuels.0c03394
- Wang, Z., Sun, X., and Xiao, X. (2018). Efficient development technologies for ultra-deep, overpressured and fractured sandstone gas reservoirs: A case study of the Kelasu gas field in the Tarim Basin[J]. *Nat. Gas. Ind.* 38 (4), 87–95.
- Warren, J. E., and Root, P. J. (1963). The behavior of naturally fractured reservoirs. *Soc. Petroleum Eng. J.* 3 (3), 245–255. doi:10.2118/426-pa
- Wei, C., Zhang, C., and Dong, C. (2019). Seepage characteristics and development mechanism characterized by faults-fracture-pores“triple medium”in Keshen 2 gas reservoirs, Tarim Basin[J]. *Nat. Gas. Geosci.* 30 (12), 1684–1693.
- Wei, G., Wang, J., Zeng, L., Tang, Y., Wang, K., Liu, T., et al. (2020). Structural reworking effects and new exploration discoveries of subsalt ultra-deep reservoirs in the Kelasu tectonic zone[J]. *Nat. Gas. Ind.* 40 (1), 20–30.

Conflict of interest

TJ was employed by the Science and Technology Management Department of China National Petroleum Corporation. XX, SZ, and YT were employed by the PetroChina Tarim Oilfield Company. WO was employed by the Changqing Downhole Technology Company, CNPC Chuanqing Drilling Engineering Co., Ltd.

The remaining author declares that the research was conducted in the absence of any commercial or financial relationships that could be construed as a potential conflict of interest.

Publisher’s note

All claims expressed in this article are solely those of the authors and do not necessarily represent those of their affiliated organizations, or those of the publisher, the editors and the reviewers. Any product that may be evaluated in this article, or claim that may be made by its manufacturer, is not guaranteed or endorsed by the publisher.

Wu, Y., Cheng, L., Huang, S., Fang, S., Jia, P., and Wang, S. (2018). A semianalytical model for simulating fluid flow in naturally fractured reservoirs with nonhomogeneous vugs and fractures. *SPE J.* 24 (1), 334–348. doi:10.2118/194023-pa

Wu, Y., Liu, H., and Bodvarsson, G. S. (2004). A triple-continuum approach for modeling flow and transport processes in fractured rock. *J. Contam. Hydrology* 73 (1), 145–179. doi:10.1016/j.jconhyd.2004.01.002

Zambrano, M., Tondi, E., Korneva, I., Panza, E., Agosta, F., Janiseck, J. M., et al. (2016). Fracture properties analysis and discrete fracture network modelling of faulted tight limestones, Murge Plateau, Italy. *Italian J. Geosciences* 135 (1), 55–67. doi:10.3301/ijg.2014.42

Zeng, F., Zhao, G., and Liu, H. (2012). A new model for reservoirs with a discrete-fracture system. *J. Can. Petroleum Technol.* 51 (2), 127–136. doi:10.2118/150627-pa

Zhang, F., and Emami-Meybodi, H. (2020). A semianalytical method for two-phase flowback rate-transient analysis in shale gas reservoirs[J]. *SPE J.* 25 (4), 1599–1622.

Zhang, F., and Emami-Meybodi, H. (2022). A type-curve method for two-phase flowback analysis in hydraulically fractured hydrocarbon reservoirs. *J. Petroleum Sci. Eng.* 209, 109912. doi:10.1016/j.petrol.2021.109912



OPEN ACCESS

EDITED BY

Xiukun Wang,
China University of Petroleum, Beijing,
China

REVIEWED BY

Lei Li,
China University of Petroleum (East
China), China
Jinze Xu,
University of Calgary, Canada

*CORRESPONDENCE

Zhou Zhijun,
sygc423@163.com

SPECIALTY SECTION

This article was submitted to Advanced
Clean Fuel Technologies,
a section of the journal
Frontiers in Energy Research

RECEIVED 25 June 2022

ACCEPTED 14 July 2022

PUBLISHED 12 August 2022

CITATION

Huzhen W, Tiancheng L,
Zhuangzhuang S, Chunyao W, Zhenyu L,
Zhijun Z, Changjun D and Zhiming Z
(2022), Formation pressure distribution
and productivity prediction of fractured
horizontal wells in stress
sensitive reservoirs.
Front. Energy Res. 10:978134.
doi: 10.3389/fenrg.2022.978134

COPYRIGHT

© 2022 Huzhen, Tiancheng,
Zhuangzhuang, Chunyao, Zhenyu,
Zhijun, Changjun and Zhiming. This is an
open-access article distributed under
the terms of the [Creative Commons
Attribution License \(CC BY\)](#). The use,
distribution or reproduction in other
forums is permitted, provided the
original author(s) and the copyright
owner(s) are credited and that the
original publication in this journal is
cited, in accordance with accepted
academic practice. No use, distribution
or reproduction is permitted which does
not comply with these terms.

Formation pressure distribution and productivity prediction of fractured horizontal wells in stress sensitive reservoirs

Wang Huzhen^{1,2}, Liu Tiancheng¹, Sun Zhuangzhuang¹,
Wang Chunyao^{1,3}, Liu Zhenyu^{1,2}, Zhou Zhijun^{1,2*},
Diao Changjun⁴ and Zhao Zhiming⁵

¹Department of Petroleum Engineering, Northeast Petroleum University, Daqing, Heilongjiang, China, ²Key Laboratory of Reservoir Stimulation, CNPC, Daqing, Heilongjiang, China, ³NO. 1 Oil Production Plant PetroChina Daqing Oilfield Company, Daqing, Heilongjiang, China, ⁴Xinjiang Oilfield Company, PetroChina, Karamay, Xinjiang, China, ⁵Department of Petroleum Engineering, Panjin Vocational and Technical College, Panjin, Liaoning, China

Aiming at the problems of formation pressure distribution and productivity prediction after Horizontal Well Volume Fracturing in stress sensitive reservoirs, the methods of dynamic permeability and dynamic threshold pressure gradient are used to deal with the influence of stress sensitivity, a numerical simulation method of oil-water two-phase flow based on finite element method is established. History matching is performed on the basis of the prediction of formation pressure distribution after horizontal well volume fracturing of, which ensures high matching accuracy. Taking the ultra-low permeability sandy glutenite reservoir of Baikouquan Formation in M18 area of Aihu Oilfield as research object, the influence law of formation pressure level on productivity and stress sensitivity on formation pressure distribution is studied. Analysis of the calculation results shows that: the influence of formation pressure level on well productivity is mainly in the first year of production, and the effect of energy increasing by volume fracturing is clarified. Stress sensitivity mainly affects the middle and later stage of production. With the increase of sensitivity, the permeability loss of the formation tends to be concentrated in the low-pressure area near the artificial fracture, forming an isolation zone with high flow resistance, which make the development effect of far well zone worse.

KEYWORDS

abnormal high pressure, stress-sensitive, horizontal well, volume fracturing, pressure distribution prediction

Introduction

Generally speaking, the lower the reservoir permeability, the weaker the stress sensitivity (Li, 2005; Li, 2009; Gao et al., 2014; Dou et al., 2016; Luo et al., 2019). However, due to its special geological characteristics, abnormally high pressure and low permeability reservoirs often have higher effective stress during development, and generally show stronger stress

sensitivity. With the increase of effective stress, the loss rate of reservoir permeability gradually increases, showing greater seepage resistance, which affects the productivity of oil wells. Clarifying the influence of stress sensitivity on formation pressure distribution and productivity is of great significance for reservoir protection and design reasonable production system.

The research methods of stress sensitivity on productivity mainly include analytical method, semi analytical method, and numerical method. Analytical methods are used to establish productivity models for vertical wells (Liu et al., 2014; Shan et al., 2017; Chai et al., 2018; Zhu et al., 2018) and horizontal wells (Yang et al., 2017; Jiang et al., 2012; Ning et al., 2020; Guo and Wu 2007), most of which have to be studied for non-fractured wells. Fang et al. (2015) based on the perturbation theory and combined with the source function, established a semi-analytical method for calculating the production of fracturing horizontal wells in Laplace space, and analyzed the pressure and production dynamic curves of multi-angle and multi-stage fracturing horizontal wells in stress sensitive oil reservoirs. Numerical methods mainly use finite difference, finite volume method and finite element method. Song (2012) established the oil-water relative permeability curve under the combined effect of stress sensitivity and starting pressure on the basis of the stress sensitivity experimental results. Wang et al. (2013) established the dynamic model of threshold pressure gradient and dynamic permeability on the basis of laboratory experiments, and used the finite difference method to solve numerically. Liu et al. (2017) established a three-phase seepage mathematical model for shale oil considering the threshold pressure gradient and stress sensitivity, used the finite volume method to obtain the numerical solution, and compiled a numerical simulator. The finite element method has flexible grid division and is easy to deal with complex boundaries. It has unique advantages in the study of seepage problems in artificially fractured wells (Zhang et al., 2017; Feng et al., 2019; Su et al., 2019), and is very suitable for the development of numerical calculation programs.

The finite element-based numerical method is used to study the seepage problem of fractured wells in stress sensitive reservoirs. Innovatively establish the equivalent characterization method of stress sensitivity effect using dynamic permeability and dynamic starting pressure gradient based on the experimental data of core stress sensitivity, and improve the accuracy of history fitting of fractured horizontal wells based on the prediction of formation pressure distribution before production. In order to improve the programming efficiency, the calculation program is developed based on the Finite Element Automatic Generation System (FEPG) (Liang, 2011) of the Chinese Academy of Sciences, which can save a lot of programming work (Zhang et al., 2010; Zhang 2013; Shi et al., 2016).

Mathematical model

Basic assumptions: There is an oil-water two-phase fluid in a homogeneous reservoir, and both fluid and rock are weakly

compressible. The influence of starting pressure gradient and capillary force is considered, and the influence of gravity is ignored. The motion equation is brought into the continuity equation, the fluid densities ρ_o , ρ_w are treated as constants, and the rock state equation is considered to process the right-hand term of the equation, and the oil phase pressure equation is obtained:

$$\nabla \cdot \left[K\lambda \nabla p_o \left(1 - \frac{G}{|\nabla p_o|} \right) \right] - \nabla \cdot (K\lambda_w \nabla p_c) = \phi C_t \frac{\partial p_o}{\partial t} \quad (1)$$

Where $C_t = \frac{1}{\phi} C_f + S_w C_w + S_o C_o$, $\lambda = \frac{K_o}{\mu_o} + \frac{K_{rw}}{\mu_w}$, $\lambda_o = \frac{K_o}{\mu_o \lambda}$, $\lambda_w = \frac{K_{rw}}{\mu_w \lambda}$. Define the total seepage velocity as \mathbf{u} , then

$$\mathbf{u} = \mathbf{v}_o + \mathbf{v}_w = -K\lambda \nabla p_w \left(1 - \frac{G}{|\nabla p_w|} \right) - K\lambda_o \nabla p_c \quad (2)$$

Get:

$$\nabla p_w \left(1 - \frac{G}{|\nabla p_w|} \right) = -\frac{\mathbf{u}}{K\lambda} - \lambda_o \nabla p_c \quad (3)$$

$$\mathbf{v}_w = \lambda_w \mathbf{u} + K\lambda_o \lambda_w \nabla p_c \quad (4)$$

$$\nabla \cdot (\mathbf{v}_w) = \nabla \cdot (\lambda_w \mathbf{u}) + \nabla \cdot (K\lambda_o \lambda_w \nabla p_c) \quad (5)$$

In order to improve the calculation stability of saturation equation, the relative mobility of water phase in the first term at the right end of the above formula λ_w is implicitly treated as a function of S_w . In the second term, the capillary pressure is also implicitly treated. Expand p_c into Taylor series near S_w^{n-1} , and then take its first-order expansion and ignore the second-order small quantity, can get $\nabla p_c = \nabla p_c^{n-1} + p'_c \nabla S_w - p'_c \nabla S_w^{n-1}$, then Eq. 5 becomes:

$$\nabla \cdot (\mathbf{v}_w) = \lambda'_w \mathbf{u} \nabla S_w + K\lambda_o \lambda_w \nabla \cdot (\nabla p_c^{n-1}) + K\lambda_o \lambda_w p'_c \nabla \cdot (\nabla S_w) + K\lambda_o \lambda_w p'_c \nabla \cdot (\nabla S_w^{n-1})$$

The water phase saturation equation can be obtained:

$$\begin{aligned} & -\lambda'_w \mathbf{u} \nabla S_w - K\lambda_o \lambda_w \nabla \cdot (\nabla p_c^{n-1}) - K\lambda_o \lambda_w p'_c \nabla \cdot (\nabla S_w) \\ & - K\lambda_o \lambda_w p'_c \nabla \cdot (\nabla S_w^{n-1}) = \phi \frac{\partial (S_w)}{\partial t} \end{aligned} \quad (6)$$

Artificial fracture characterization

The traditional fracture characterization method regards the fracture as a high-permeability zone, which has certain limitations in simulating complex fractures. The mixed element finite element method is used to simulate cracks with line elements. In order to facilitate mesh division, the implicit fracture line element is adopted, that is, the division of matrix mesh element and the fracture line element are carried out at the same time, and the fracture line element is hidden in the matrix element. This fracture treatment method

needs to superimpose the stiffness of the fracture line element into the overall stiffness of the matrix, so as to improve the stiffness of the matrix element and improve the overall permeability of the matrix.

In the two-dimensional mathematical model of oil-water two-phase, artificial fractures are treated with line elements. The basic differential equations of artificial fractures have the same form as the matrix, and the dimension is one dimension lower than matrix. Due to the high fracture permeability, the threshold pressure gradient is not considered.

Oil phase pressure equation of artificial fracture:

$$\nabla \cdot (K_f \lambda \nabla p_o) - \nabla \cdot (K_f \lambda \lambda_w \nabla p_{fc}) = \phi C_t \frac{\partial p_o}{\partial t} \quad (7)$$

Water phase saturation equation of artificial fracture:

$$\begin{aligned} & -\lambda'_w \mathbf{u} \nabla S_w - K_f \lambda \lambda_o \lambda_w \nabla \cdot (\nabla p_{fc}^{n-1}) - K_f \lambda \lambda_o \lambda_w p'_{fc} \nabla \cdot (\nabla S_w) \\ & - K_f \lambda \lambda_o \lambda_w p'_{fc} \nabla \cdot (\nabla S_w^{n-1}) \\ & = \phi \frac{\partial (S_w)}{\partial t} \end{aligned} \quad (8)$$

Weak solution integral form of differential equations

Write the oil phase pressure Eq. 1 in integral form:

$$\begin{aligned} & \iint_V \nabla \cdot \left[K \lambda \nabla p_o \left(1 - \frac{G}{|\nabla p_o|} \right) \right] \delta p_o dV - \iint_V \nabla \cdot (K \lambda \lambda_w \nabla p_c) \delta p_o dV \\ & = \iint_V \phi C_t \frac{\partial p_o}{\partial t} \delta p_o dV \end{aligned} \quad (9)$$

Integral by parts of the left-hand side of Eq. 9, can get:

$$\begin{aligned} & - \iint_V K \lambda \nabla p_o \left(1 - \frac{G}{|\nabla p_o|} \right) \nabla \delta p_o dV + \int_r K \lambda \frac{\partial p_o}{\partial n} \delta p_o d\Gamma \\ & + \iint_V K \lambda \lambda_w \nabla p_c \nabla \delta p_o dV - \int_r K \lambda \lambda_w \frac{\partial p_c}{\partial n} \delta p_o d\Gamma \\ & = \iint_V \phi C_t \frac{\partial p_o}{\partial t} \delta p_o dV \end{aligned} \quad (10)$$

When the oil-water well is at a constant pressure boundary, by selecting δp appropriately, make $\delta p = 0$ on the boundary and ignore the integral along the boundary $\int_r K \lambda \frac{\partial p_o}{\partial n} \delta p_o d\Gamma$. The capillary pressure gradient is small compared to the formation pressure gradient near the bottom hole, so the boundary integral term $-\int_r K \lambda \lambda_w \frac{\partial p_c}{\partial n} \delta p_o d\Gamma$ is ignored. The weak solution integral form of the oil phase pressure equation can be obtained:

$$\begin{aligned} & - \iint_V K \lambda \nabla p_o \left(1 - \frac{G}{|\nabla p_o|} \right) \nabla \delta p_o dV + \iint_V K \lambda \lambda_w \nabla p_c \nabla \delta p_o dV \\ & = \iint_V \phi C_t \frac{\partial p_o}{\partial t} \delta p_o dV \end{aligned} \quad (11)$$

When the oil-water well is producing at a constant production rate q , and the bottom hole is the constant flow boundary, the integral term along the bottom hole boundary can be changed to $\int_r \frac{q}{A} \delta p_o d\Gamma$, can get:

$$\begin{aligned} & - \iint_V K \lambda \nabla p_o \left(1 - \frac{G}{|\nabla p_o|} \right) \nabla \delta p_o dV + \iint_V K \lambda \lambda_w \nabla p_c \nabla \delta p_o dV \\ & + \int_r \frac{q}{A} \delta p_o d\Gamma = \iint_V \phi C_t \frac{\partial p_o}{\partial t} \delta p_o dV \end{aligned} \quad (12)$$

Similarly, the weak solution integral expression of the water phase saturation equation can be obtained:

$$\begin{aligned} & - \iint_V \lambda'_w \mathbf{u} \nabla S_w \delta S_w dV + \iint_V K \lambda \lambda_o \lambda_w \nabla p_c^{n-1} \nabla \delta S_w dV \\ & + \iint_V K \lambda \lambda_o \lambda_w p'_{fc} \nabla S_w \nabla \delta S_w dV - \iint_V K \lambda \lambda_o \lambda_w p'_{fc} \nabla S_w^{n-1} \nabla \delta S_w dV \\ & = \iint_V \phi \frac{\partial (S_w)}{\partial t} \delta S_w dV \end{aligned} \quad (13)$$

The \mathbf{u} in the first term of the formula is treated explicitly, so this term does not need to be integral by parts. In the same way, the integral form of the weak solution of the fracture system can be obtained.

Algorithm

The oil phase pressure equation and the water phase saturation equation were solved by implicit pressure and explicit water saturation. The time was discretized by the Crank-Nicolson scheme. The linear equations were solved by the direct method of LDL^T decomposition. Both the water cut and the pressure gradient were solved using the least squares method.

Results and discussion

Numerical model building

Baikouquan formation in well block M18 of Aihu oil field is a low porosity, ultra-low permeability and abnormally high-pressure sandy conglomerate reservoir with a pressure coefficient of 1.63. The reservoir rocks of the Baikouquan Formation are mainly glutenite, gravel-bearing coarse sandstone and sandstone, and the pore types are mainly

residual intergranular pores, intragranular dissolved pores, matrix shrinkage pores and crushed fractures. The reservoir porosity is mainly distributed between 8 and 14%, with an average of 11.9%, and the permeability is distributed between $0.01 \times 10^{-3} \mu\text{m}^2$ and $46 \times 10^{-3} \mu\text{m}^2$, with an average of $0.5 \times 10^{-3} \mu\text{m}^2$. Crude oil has low viscosity and good fluidity. Medium water sensitivity, velocity sensitivity and strong stress sensitivity. Stress Sensitivity index $b = 0.385$ ($K = K_0 e^{-b\phi(p_0-p)}$) (Shi et al., 2016). With the natural energy development method of horizontal well + volume fracturing, the main problems faced are the large decline in the early stage and the prominent stress sensitivity problem. The fracturing construction time of each stage is 3 h, the time from the end of fracturing construction to putting into production is 10d, and the viscosity of fracturing fluid after gel breaking is 1 mPa s. Adjust the injection pressure and time of fracturing operation, and keep the total fracturing fluid volume unchanged to match the bottom hole flow pressure when it is put into production, so as to ensure the accuracy of pressure distribution prediction. A typical well in M18 well block is selected to establish a single well numerical model. The length of the horizontal section is 938 m, formation permeability is $0.5 \times 10^{-3} \mu\text{m}^2$, porosity is 0.095, reservoir thickness is 14.2 m, oil saturation is 58.6%, original formation pressure is 64 MPa, formation crude oil viscosity is 0.66 mPa s, threshold pressure gradient is 0.027 MPa/m, fracture Conductivity is $25 \mu\text{m}^2 \text{m}$, rock compressibility $1 \times 10^{-4} 1/\text{MPa}$, crude oil compressibility $18 \times 10^{-4} 1/\text{MPa}$, irreducible water saturation 26%, residual oil saturation 37.13%, water relative permeability at residual oil saturation is 12.99%.

The stress sensitive data adopts the results of laboratory experiments. When the net confining pressure is 44 MPa, the formation permeability is reduced to 20% of the initial value. In the numerical calculation, according to the net formation confining pressure value of each node, interpolate the data in stress sensitive data to obtain the formation permeability loss, and then update the formation permeability and threshold pressure gradient data of the node.

Well M1 fracturing 12 stages and 22 clusters, of which the 6th and 11th stages fracturing one cluster, and the half-length of the fractures is 55–164 m. In the M18 well block, natural fractures are not developed in the reservoir, and the rock is partially plastic and has a low brittleness value. The large stress difference between the two horizontal directions makes it difficult to achieve volume fracturing with complex artificial fracture network patterns in this area. The artificial fractures are mainly plane fractures. Building a 2D Model of Well M1.

History matching and productivity forecast

Well M1 adopts slick water + guar gum fracturing fluid, with a total fluid volume of $13,500 \text{ m}^3$. In order to improve the accuracy of history matching, simulate the fracturing fluid

injection process during fracturing construction, predict the formation pressure distribution before production under the influence of fracturing fluid energization, and use the total injected fluid volume and bottom-hole flow pressure during production to constrain Numerical calculation results.

The current production time of well M1 is 2.4 years, and the history matching is shown in Figure 1. The initial production of the well increased rapidly, and then decreased rapidly after reaching the peak. The history matching is carried out on the basis of the prediction of formation pressure distribution, which makes the matching effect in the initial stage better. When fracturing energization is not considered, the initial peak oil rate is only 60 t/d, and when fracturing energization is considered, it is 100 t/d, this is a very big difference. Therefore, if the influence of fracturing energization on the formation pressure distribution before production is not considered, history matching is difficult.

The two replacements of the nozzles caused large fluctuations in well production, and the matching effect was relatively poor in about half a year. This well lacks bottom-hole flow pressure data, which makes it difficult to accurately match production fluctuations, and can only match production trends. The cumulative oil production of well M1 in 2.4 years is 24,455 t, the cumulative oil production calculated by simulation is 24,564 t, and the fitting error is 0.45%.

The formation pressure and pressure gradient distribution of Well M1 are shown in Figure 2. At 2.4 years, the formation pressure in the simulation area of Well M1 was 35–61.23 MPa, and the permeability loss rate caused by stress sensitivity was 17.70%–2.22%.

On the basis of single well history matching, predicted cumulative oil production in 8 years is 43,187 t, and the recovery degree is 12.77%.

Influence of formation pressure level on productivity

An ideal model of a single well was established, the length of the horizontal section was 1,000 m, 24 clusters in 12 fracturing stages, and the half-length of the fractures were all 120 m, and other calculation parameters were the same as those of Well M1. Four pre-production formation pressure level schemes were established, and the average formation pressures \bar{p} within the influence range of fracturing energization during production were: 64, 66.56, 68.34, and 70.15 MPa. Among them, scheme one, 64 MPa, is the original formation pressure, which does not consider the influence of fracturing fluid on the formation pressure Scheme $\bar{p} = 66.56 \text{ MPa}$, the maximum formation pressure is 68.07 MPa, and the maximum influence range at the fracture end is 65.0 m; scheme $\bar{p} = 68.34 \text{ MPa}$, the maximum formation pressure is 71.05 MPa, and the

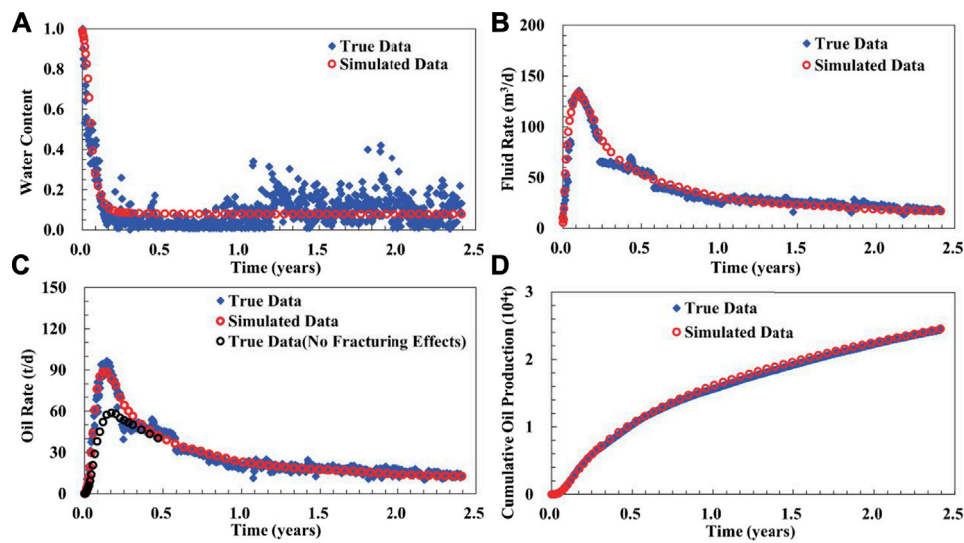


FIGURE 1
Historical matching curve of single well.(A) Water Content; (B) Fluid Rate; (C) Oil Rate; (D) Cumulative Production.

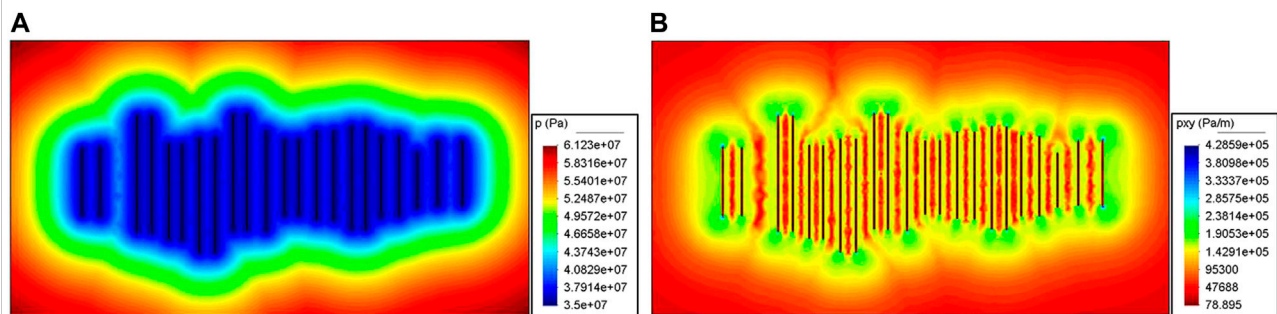


FIGURE 2
Distribution of formation pressure and pressure gradient. (A). Distribution of formation pressure, (B). Distribution of formation pressure gradient.

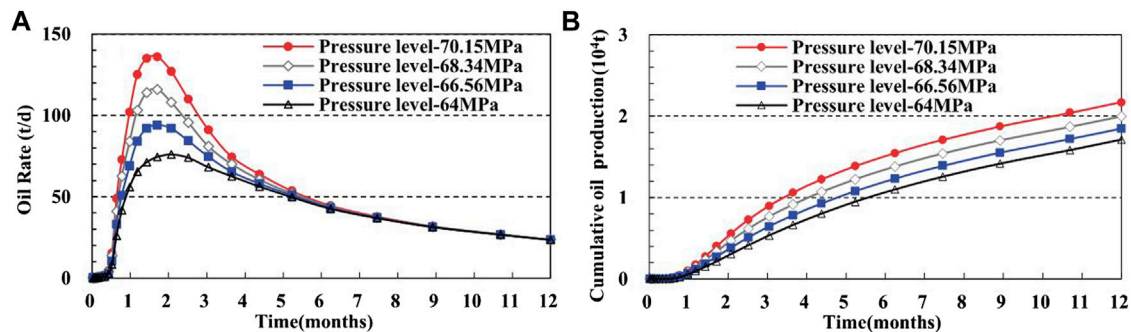


FIGURE 3
Influence of formation pressure level on initial productivity.

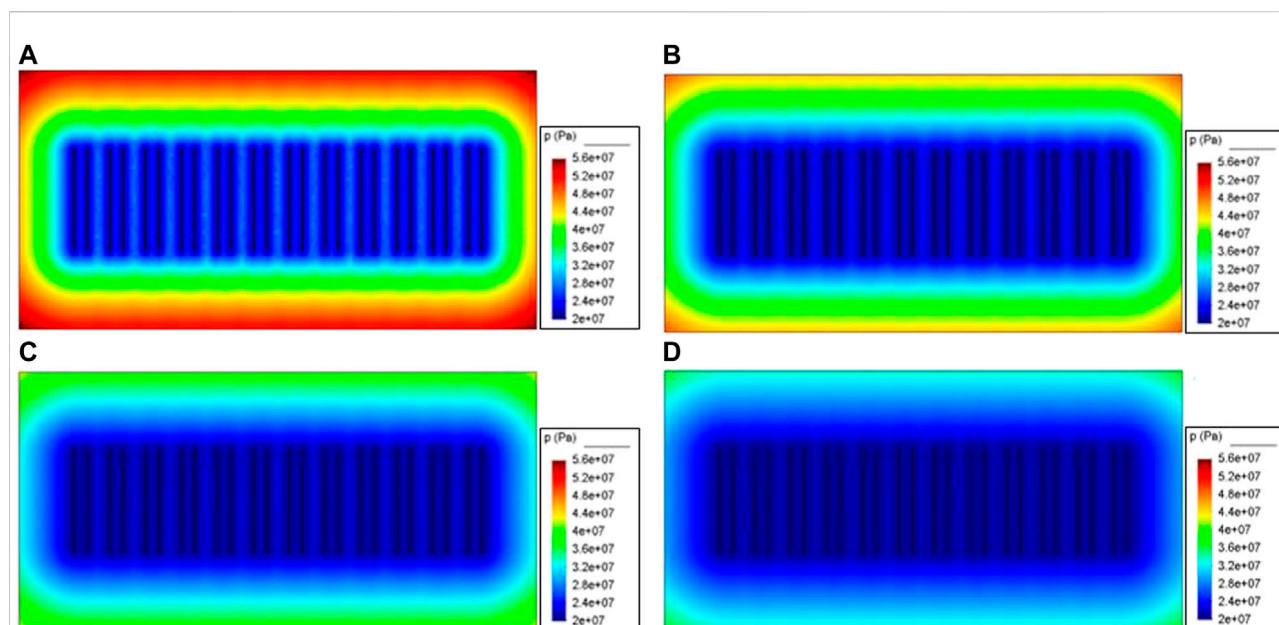


FIGURE 4

Effect of stress sensitivity on formation pressure distribution. (A) Max $K_s = 20\%$; (B) Max $K_s = 40\%$; (C) Max $K_s = 60\%$; (D) Max $K_s = 80\%$.

influence range is 78.5 m; scheme $\bar{p} = 70.15$ MPa, the maximum formation pressure. The value is 74.00 MPa, and the influence range is 85.8 m. From the one-year production performance (Figure 3), it can be seen that the impact of different formation pressure levels on the productivity of oil wells is mainly in the first half of the year. The higher the formation pressure level, the greater the peak production and the sharper the peak. Compared with not considering fracturing, the cumulative oil production of the 68.34 MPa (close to the formation pressure level of Well M1) increased by 2,421 t, an increase of 16.70%. Judging from the actual situation in the M18 well area, the average flowback rate of the fracturing fluid is low, about 12% in half a year, which makes the fracturing energy enhancement have a good oil-increasing effect.

Influence of stress sensitivity on formation pressure distribution

The bottom hole flow pressure drop is 20 MPa when the horizontal well has been in production for 8 years. Four schemes are selected for the permeability loss caused by stress sensitivity. The maximum permeability loss rates (K_s) near the bottom hole are 20%, 40%, 60%, and 80%, of which 80% scheme is close to the actual situation of well block M18. The numerical calculation model and other parameters are the same as those in the previous section, and the influence of fracturing on formation pressure is not considered. The formation pressure is taken as the original formation pressure.

Comparing the formation pressure distribution of the four stress sensitivity schemes in 8 years (Figure 4), it can be seen that the formation pressure consumed increases with the increase of stress sensitivity. The average formation pressure of the four schemes in 8 years is 35.17, 30.30, 27.40, and 25.37 MPa.

The loss of formation permeability is calculated according to the distribution of formation pressure. As the stress sensitivity increases, the difference between the maximum and minimum loss rates of the four schemes becomes larger and larger. The lowest loss rate of scheme 4 is only 26.41%, which is lower than that of scheme 2 and 3. On the one hand, the existence of stress sensitivity reduces the pore volume and reduces the reservoir permeability, which is not conducive to oil recovery. On the other hand, it is beneficial to maintain pore pressure and oil production, so stress sensitivity within a certain range may be beneficial to increase productivity (Wang et al., 2003; Li and Tu 2008). However, when the stress sensitivity is very strong, an isolation zone with lower permeability and higher fracturing gradient with high flow resistance tends to be formed near the fracture, which makes the oil production in the far-well area worse and reduces the productivity of the oil well. This situation can also be explained from the formation energy consumption, that is, the average formation pressure of scheme 4 is higher and the total pressure difference is lower. In the middle and late stages of production in the M18 well area, it is necessary to formulate a reasonable oil recovery rate and supplement formation energy to reduce the impact of stress sensitive oil wells.

Conclusion

Based on the basic principle of finite element method, a numerical method for predicting formation pressure distribution and oil well productivity of ultra-low permeability sandy conglomerate reservoir considering stress sensitivity is established. An innovative method to characterize the fracturing reformed area with permeability and threshold pressure gradient that vary with spatial location. The single well history matching is carried out on the basis of the formation pressure distribution prediction considering the influence of fracturing energy increase. In the peak yield stage, which is difficult to fit, the historical matching coincidence rate is high, and the overall historical fitting effect is good.

The fracturing energization effect in the M18 well area has a good oil-increasing effect. In view of the low fracturing fluid flowback rate, it is recommended to combine the imbibition theory to study the feasibility of oil displacement fracturing to further improve the oil recovery.

In the middle and late stages of oil well production, stress sensitivity strengthens the threshold pressure gradient and seepage resistance in the low-pressure zone near artificial fractures, so that the pressure is mainly consumed near the artificial fractures, and the production effect becomes poor. Optimizing the oil well production system, supplementing the formation energy, and reducing the influence of stress sensitivity are the key issues that need to be paid attention to in the M18 well area.

Data availability statement

The original contributions presented in the study are included in the article/supplementary material, further inquiries can be directed to the corresponding author.

References

- Chai, R. K., Liu, Y. T., Wang, J. Q., and Xin, J. (2018). Study on productivity model of oil well in low-permeability reservoirs based on two-phase threshold pressure gradient and stress sensitivity (in Chinese). *J. Xi'an Shiyou Univ. Nat. Sci. Ed.* 33 (3), 44–50. doi:10.3969/j.issn.1673-064X.2018.03.007
- Dou, H., Zhang, H., Yao, S., Zhu, D., Sun, T., Ma, S., et al. (2016). Measurement and evaluation of the stress sensitivity in tight reservoirs. *Petroleum Explor. Dev.* 43 (6), 1116–1123. doi:10.1016/s1876-3804(16)30130-6
- Fang, S. D., Cheng, L. S., Li, C. Y., Cao, R. Y., Yang, J., and He, C. G. (2015). The productivity model of multi-angled fractured horizontal well in stress-sensitive reservoir (in Chinese). *J. Northeast Petroleum Univ.* 39 (1), 87–94. doi:10.3969/j.issn.2095-4107.2015.01.011
- Feng, F. P., Lei, Y., Chen, D. F., Hu, C. Y., Wang, H. Z., and Huang, R. (2019). Parameter analysis of SRV fracturing effect of tight reservoirs based on finite element numerical simulation (in Chinese). *Reserv. Eval. Dev.* 9 (1), 29–33. doi:10.13809/j.cnki.cn32-1825/te.2019.01.006
- Gao, T., Guo, X., Liu, J. N., Li, H. T., Xie, C., and Liu, H. (2014). Stress sensitivity experiment for ultra-low permeability core (in Chinese). *Petroleum Geol. Oilfield Dev. Daqing* 33 (4), 87–90. doi:10.3969/j.issn.1000-3754.2014.04.018
- Guo, X., and Wu, Y. (2007). Influence of start-up pressure gradient and stress sensitivity on productivity of low-permeability gas reservoirs (in Chinese). *Oil Gas Geol.* 28 (4), 539–543. doi:10.11743/ogg20070417
- Jiang, R., Wang, Y. Q., Zhang, Q., Huang, P., and Xu, Z. P. (2012). A capacity formula for horizontal well in stress-sensitive reservoir considering threshold pressure gradient and quadratic pressure gradient (in Chinese). *Tuohu Oil Gas* 17 (1), 68–72.
- Li, C. L., and Tu, X. W. (2008). Two types of stress sensitivity mechanisms for reservoir rocks: being favorable for oil recovery (in Chinese). *Lithol. Reserv.* 20 (1), 111–113. doi:10.3969/j.issn.1673-8926.2008.01.019
- Li, C. L. (2005). Low permeability rocks are less sensitive to stress (in Chinese). *Oil Drill. Prod. Technol.* 27 (4), 62–63. doi:10.3969/j.issn.1000-7393.2005.04.019
- Li, C. L. (2009). Stress sensitivity influence on oil well productivity (in Chinese). *J. Southwest Petroleum Univ. Sci. Technol. Ed.* 31 (1), 170–172. doi:10.3863/j.issn.1674-5086.2009.01.041
- Liang, G. P. (2011). Finite element analysis software platform FEPG (in Chinese). *Comput. Aided Eng.* 20 (3), 92–96.

Author contributions

WH, LZ, and ZZhi contributed to conception and design of the study. DC organized the database. WH, LT, SZ, and ZZhim performed the numeral calculations and statistical analysis. WH, LT, WC, and SZ wrote sections of the manuscript. All authors contributed to manuscript revision, read, and approved the submitted version.

Funding

This work is financially supported by the Daqing guiding science and technology plan project (No. zd-2021-51).

Conflict of interest

Author WC was employed by NO. 1 Oil Production Plant PetroChina Daqing Oilfield Company. Author DC was employed by Xinjiang Oilfield Company, PetroChina.

The remaining authors declare that the research was conducted in the absence of any commercial or financial relationships that could be construed as a potential conflict of interest.

Publisher's note

All claims expressed in this article are solely those of the authors and do not necessarily represent those of their affiliated organizations, or those of the publisher, the editors and the reviewers. Any product that may be evaluated in this article, or claim that may be made by its manufacturer, is not guaranteed or endorsed by the publisher.

- Liu, F., Wang, Y. L., Chen, X. F., Yunhe, S., and Yue, W. (2014). Analysis on oil well productivity of low-permeability reservoirs with stress-sensitivity being taken into considerations (in Chinese). *Oil Gas. Geol.* 34 (1), 124–128. doi:10.11743/ogg20130117
- Liu, L. J., Yao, J., Sun, H., Bai, Y. H., Xu, B. Y., and Chen, L. (2017). The effect of threshold pressure gradient and stress sensitivity on shale oil reservoir productivity (in Chinese). *Pet. Drill. Tech.* 45 (5), 84–91. doi:10.11911/syztjs.201705015
- Luo, C., Zhou, P. G., Yang, H., and Shi, J. G. (2019). Stress sensitivity characteristics of low permeability reservoirs (in Chinese). *J. Southwest Petroleum Univ. Sci. Technol. Ed.* 41 (6), 1–7. doi:10.11885/j.issn.16745086.2019.01.21.03
- Ning, B., Xiang, Z. P., Liu, X. S., Zhijun, L., Zhonghua, C., Bocai, J., et al. (2020). Production prediction method of horizontal wells in tight gas reservoirs considering threshold pressure gradient and stress sensitivity. *J. Pet. Sci. Eng.* 187, 106750. doi:10.1016/j.petrol.2019.106750
- Shan, A. P., Shi, L. H., Kang, K., and Lu, C. (2017). A new production model of ultra-low permeability reservoirs under consideration of start-up pressure gradient and stress sensitivity effect (in Chinese). *Xinjiang Oil Gas* 13 (4), 41–46.
- Shi, W. H., Yang, T. H., Liu, H. L., and Yang, B. (2016). Non-Darcy flow model and numerical simulation for water-inrush in fractured rock mass. *Chin. J. Rock Mech. Eng.* 35 (3), 446–455. doi:10.13722/j.cnki.jrme.2015.0389
- Song, C. T. (2012). Numerical reservoir simulation considering threshold pressure gradient and stress sensitive phenomenon (in Chinese). *Sci. Technol. Eng.* 12 (25), 6319–6326.
- Su, Y. L., Lu, M. J., Li, M., Zhang, Q., Wang, W. D., and Dong, M. Z. (2019). Numerical simulation of shale oil coupled flow in multi-pore media (in Chinese). *Oil Gas. Geol.* 40 (3), 645–652+660. doi:10.11743/ogg20190319
- Wang, X. J., Zhao, Y. S., Wen, W., Chi, B., and Sun, Y. (2003). Stress sensitivity and poroperm lower limit of deliverability in the low-permeability reservoir (in Chinese). *Oil & Gas. Geol.* 24 (2), 162–165. doi:10.11743/ogg20030212
- Wang, J., Liu, H. Q., Liu, R. J., and Xu, J. (2013). Numerical simulation for low-permeability and extra-low permeability reservoirs with considering starting pressure and stress sensitivity effects (in Chinese). *J. Rock Mech. Eng.* 32, 3317–3327.
- Yang, Z. P., Yang, H., Chen, H. P., and Zhang, H. (2017). New method for evaluating rock stress sensitivity for low-permeability tight gas reservoirs. *Chem. Technol. Fuels Oils* 53 (1), 68–76. doi:10.1007/s10553-017-0782-x
- Zhang, C. L., Wang, J. Y., and Fang, G. Y. (2010). Numerical simulation of fluid flow through shale coupled with multi-field based on FEPG (in Chinese). *Drill. Fluid & Complet. Fluid* 27 (3), 69–71.
- Zhang, Q. F., Huang, Z. Q., Yao, J., Wang, Y., and Li, Y. (2017). Two-phase numerical simulation of discrete fracture model based on multiscale mixed finite element method. *Chin. Sci. Bull.* 62 (13), 1392–1401. doi:10.1360/n972016-00584
- Zhang, S. L. (2013). Numerical simulation and analysis of structural fractures based on FEPG (in Chinese). *J. Xi'an Univ. Sci. Technol.* 33 (4), 86–91+100.
- Zhu, M. Q., Wang, N. T., and Zhang, H. (2018). Influences of the start-up pressure gradient and stress sensitive effect on the productivity of the oil reservoir (in Chinese). *Petroleum Geol. Oilfield Dev. Daqing* 37 (3), 59–63. doi:10.19597/j.issn.1000-3754.201709044

Nomenclature

ϕ porosity, fraction
 ϕ_0 initial porosity, fraction
 S_o oil saturation, fraction
 S_w water saturation, fraction
 t time, s
 K permeability, m²
 K_0 initial permeability, m²
 K_{ro} oil-phase relative permeability
 K_{rw} water-phase relative permeability
 μ_o oil-phase viscosity, Pa s
 μ_w
water-phase viscosity, Pa s
 p_o oil-phase pressure, Pa
 p_0 original formation pressure, Pa
 p_w water-phase pressure, Pa
 p_c capillary pressure, Pa
 \bar{p} average formation pressure, Pa
 G threshold pressure gradient, Pa/m

C_f rock compressibility, Pa⁻¹
 C_t comprehensive compressibility, Pa⁻¹
 C_o oil-phase compressibility, Pa⁻¹
 C_w water-phase compressibility, Pa⁻¹
 λ oil-water two-phase fluidity
 λ_o oil-phase relative fluidity
 λ_w water-phase relative fluidity
 u total seepage velocity, m/s
 v_o oil-phase seepage velocity, m/s
 v_w water-phase seepage velocity, m/s
 A seepage area, m²

Superscripts and subscripts

f_o oil-phase of fracture system
 f_w water-phase of fracture system
 f_c fracture capillary pressure
 $'$ derivative
 $n-1$ previous time step



A Fundamental Moving Boundary Problem of 1D Commingled Preferential Darcian Flow and Non-Darcian Flow Through Dual-Layered Porous Media

Ping Wang^{1*}, Wenchao Liu², Wei Ding¹, Xiangwen Kong¹ and Hailiang Fan³

¹PetroChina Research Institute of Petroleum Exploration and Development, Beijing, China, ²School of Civil and Resource Engineering, University of Science and Technology Beijing, Beijing, China, ³China ZhenHuaOil Co. Ltd., Beijing, China

OPEN ACCESS

Edited by:

Fuyong Wang,
China University of Petroleum, China

Reviewed by:

Weijun Shen,
Institute of Mechanics (CAS), China
Longlong Li,
Institute of Mechanics (CAS), China
Qingwang Yuan,
Texas Tech University, United States

*Correspondence:

Ping Wang
wp2011@petrochina.com.cn

Specialty section:

This article was submitted to
Advanced Clean Fuel Technologies,
a section of the journal
Frontiers in Energy Research

Received: 11 May 2022

Accepted: 21 June 2022

Published: 29 August 2022

Citation:

Wang P, Liu W, Ding W, Kong X and Fan H (2022) A Fundamental Moving Boundary Problem of 1D Commingled Preferential Darcian Flow and Non-Darcian Flow Through Dual-Layered Porous Media.
Front. Energy Res. 10:941605.
doi: 10.3389/fenrg.2022.941605

In consideration of vertical formation heterogeneity, a basic nonlinear model of 1D commingled preferential Darcian flow and non-Darcian flow with the threshold pressure gradient (TPG) in a dual-layered formation is presented. Non-Darcian flow in consideration of the TPG happens in the low-permeability tight layer, and the Darcian kinematic equation holds in the other high-permeability layer. The similarity transformation method is applied to analytically solve the model. Moreover, the existence and uniqueness of the analytical solution are proved strictly. Through analytical solution results, some significant conclusions are obtained. The existence of the TPG in the low-permeability tight layer can intensify the preferential Darcian flow in the high-permeability layer, and the intensity of the preferential Darcian flow is very sensitive to the dimensionless layer thickness ratio. The effect of the layer permeability ratio and layer elastic storage ratio on the production sub-rate is more sensitive than that of the layer thickness ratio. In addition, it is strictly demonstrated that moving boundary conditions caused by the TPG should be incorporated into the model. When the moving boundary is neglected, the preferential Darcian flow in the high-permeability layer will be exaggerated. Eventually, solid theoretical foundations are provided here, which are very significant for solving non-Darcian seepage flow problems in engineering by numerical simulation validation and physical experiment design. Furthermore, they are very helpful for better understanding the preferential flow behavior through the high-permeability paths (such as fractures) in the water flooding development of heterogeneous low-permeability reservoirs; then, the efficient profile control technology can be further developed to improve oil recovery.

Keywords: exact analytical solution, threshold pressure gradient, heterogeneity, Darcian flow, low-velocity non-Darcian flow, moving boundary

1 INTRODUCTION

Abundant physical experiments (Bear, 1972; Prada and Civan, 1999; Dou et al., 2014; Wang et al., 2016; Hu et al., 2018; Tian et al., 2018; Wang and Cheng, 2020; Chi and Wang, 2021; Zhao et al., 2021; Yin et al., 2022) and theoretical analysis (Cai, 2014; Wang et al., 2018; Zhang et al., 2018; Zhang et al., 2019a; Ye et al., 2019) have demonstrated when the formation permeability is low, the seepage flow in

the formation will belong to the low-velocity non-Darcian flow with a threshold pressure gradient (TPG). The TPG can introduce additional formation energy consumption, which hinders the fluid flow ability through the formation. The low-velocity non-Darcian flow phenomena can be explained by the boundary layer theory and strong fluid–solid interaction (Xiong et al., 2009; Yang et al., 2016) in tiny micro-throats in low-permeability porous media. In addition, there also exists a TPG during the non-Newtonian Bingham fluid seepage flow process (Wang et al., 2006; Wang and Yu, 2011; Fusi and Farina, 2017; Bauer et al., 2019; Zhang et al., 2019b; Zhang et al., 2022). It can be explained by the existence of yield stress in the Bingham fluid. Many engineering problems relate to this non-Darcian flow behavior, such as low-permeability petroleum reservoir development, heavy oil reservoir development, water resource development, contaminant transport in porous media, and the consolidation of soils in hydrology. In fact, the resultant mathematical model is a strongly nonlinear moving boundary (MB) problem (Liu et al., 2012; Zhao et al., 2020; Jiao et al., 2021), owing to the effect of TPG. This threshold problem is really distinct from the classical Stefan MB problem (Voller et al., 2004; Olguín et al., 2007) in the heat conduction theory, although its governing equation has the same form as the heat conduction governing equation of the Stefan problem. Their main difference is that for the Stefan problem, the MB velocity is proportional to the first derivative of the potential (temperature) with respect to distance from the MB (Voller et al., 2004; Olguín et al., 2007). However, for the MB problem of the non-Darcian flow with the TPG, it has been proved theoretically that the MB velocity is proportional to the second derivative of the potential (pressure) with respect to distance from the MB (Liu et al., 2012; Liu et al., 2019a; Liu, 2019). Recently, for this type of MB problem, some exact analytical solutions (EASs) (Chen et al., 2004; Xie et al., 2010; Liu et al., 2012; Liu et al., 2019a; Liu, 2019; Zhou, 2019; Liu W. C., 2020; Liu W. C., 2020) have been presented, especially for the three basic cases of the 1D flow (Chen et al., 2004; Xie et al., 2010; Liu et al., 2012; Liu W. C., 2020; Wang et al., 2021; Zhou et al., 2021), the two-dimensional radial flow (Liu et al., 2019a; Zhou, 2019), and the three-dimensional spherical centripetal flow (Liu, 2019) in the homogenous porous media; both the existence and the uniqueness of the EASs are also strictly proved (Liu et al., 2012; Liu et al., 2019a; Liu, 2019; Liu W. C., 2020), respectively. Even more, the correctness of some numerical solutions (Yao et al., 2013; Li et al., 2016; Liu et al., 2019b) has been strictly verified by these EASs successfully, and they can also be applied to the inverse problems, such as the physical experiment design for testing the TPG.

Heterogeneity along the direction vertical to the flow (Shen and Reible, 2015; Song et al., 2015; Wu et al., 2016; Afshari et al., 2018; Gao et al., 2018; Swami et al., 2018; Li et al., 2019; Kaffel, 2019; Nijjer et al., 2019; Liu W. C., 2020; Ma et al., 2021; Shen et al., 2022), different from the heterogeneity along the flow direction (Liu et al., 2022), is a critical feature of the porous media in the real world. For example, the vertically stratified oil reservoirs (Song et al., 2015; Gao et al., 2018) with vertical permeability heterogeneity are commonly encountered in petroleum engineering, the contaminant transport (Shen et al., 2015; Swami et al., 2018) in

vertically layered formations is frequently involved in environment engineering, and the rainfall infiltration into layered soils (Wu et al., 2016; Afshari et al., 2018; Kaffel, 2019; Nijjer et al., 2019) is very common in municipal engineering. Although the research area on the mass transfer through heterogeneous porous media is very challenging due to the involvement of the nonlinear flow process and complex flow situations in the actual engineering background, abundant research on the seepage flow problems in multi-layer porous media considering the heterogeneity has been carried out in recent years. In other words, through the separation of the variable technique, Shen and Reible (2015) obtained an EAS for a 1D solute transport model, which allowed an arbitrary number of layers, and the EAS was also verified through comparing with the numerical solution. Wu et al. (2016) conducted finite-element numerical solution research on a 1D water flow model in the unsaturated dual-layered porous media, and the rainfall infiltration process under different conditions was analyzed. Afshari et al. (2018) applied direct pore-level numerical simulations to modeling the dispersion and solute transport during the pore-scale miscible displacements in the heterogeneous layered formation, and it was demonstrated that the dispersion scale dependency was mainly affected by layering configuration. Gao et al. (2018) conducted numerical simulation research on the development of low-permeability multi-layer reservoirs, and a stratified hydraulic fracturing method was put forward for oil recovery enhancement. By employing the semi-analytical solution method, Swami et al. (2018) studied the asymptotic solute transport behavior in stratified porous media and also proposed an asymptotic relation that could provide valuable information on the mass transfer coefficient during solute transport. Li et al. (2019) defined a main flow channel index to identify the type of main flow channel in heterogeneous petroleum reservoirs and put forward a quantitative classification method for the main flow channels. Through the numerical simulation method with high resolution, the permeability heterogeneity effect on the miscible displacement process in layered formation at three different flow times was analyzed by Nijjer et al. (2019). Liu W. C. (2020) focused on the exact analytical study on a generalized nonlinear MB problem of the 1D low-velocity non-Darcian flow in heterogeneous low-permeability multi-layered formation with the TPG; however, the Darcian flow is not involved in the flow behavior analysis, and the existence and the uniqueness of the EAS are not demonstrated in theory.

As far as we know, due to the strong nonlinearity, the studies on the EAS of low-velocity non-Darcian flow MB problems in heterogeneous layered formation are few at present, although they have been extensively involved in actual engineering problems (Song et al., 2015; Gao et al., 2018). In particular, the basic research topic on the preferential flow along the high-permeability porous media layer in the heterogeneous low-permeability reservoir is widely involved in the technical reservoir engineering problems for enhanced oil recovery, such as the high-permeability layer blocking by the in-depth profile control technology in the water flooding process (Zhou et al., 2017; Li et al., 2018; Zhao et al., 2018). Here, based on the concerns, considering the vertical permeability heterogeneity of porous media, a basic nonlinear model of the 1D commingled preferential Darcian flow and non-Darcian flow with the TPG in

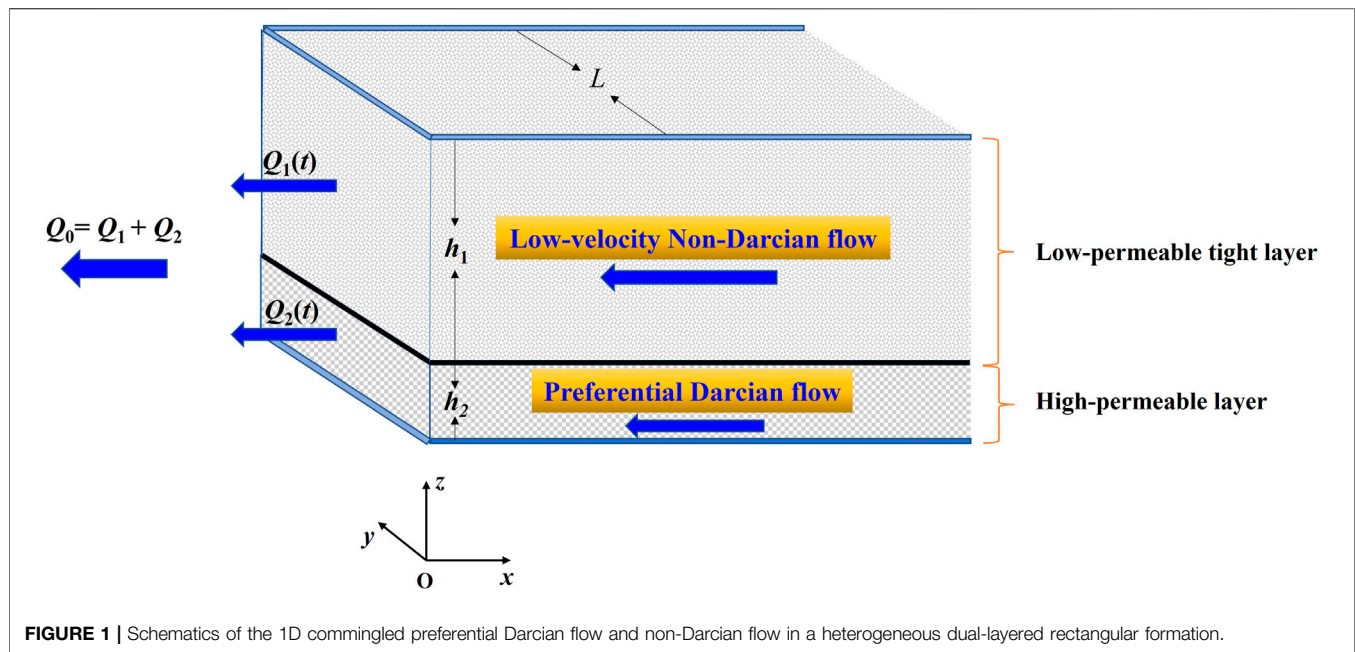


FIGURE 1 | Schematics of the 1D commingled preferential Darcian flow and non-Darcian flow in a heterogeneous dual-layered rectangular formation.

a dual-layered formation is studied. Although this commingled flow model can be considered as a partially degenerated case of the previously generalized MB model (Liu W. C., 2020), the mechanics of the high Darcian flow and non-Darcian flow happening simultaneously in each layer is first involved. For the commingled flow model, the non-Darcian flow in consideration of the TPG happens in the low-permeability tight layer (Liu et al., 2012; Dou et al., 2014), while the Darcian flow happens in the other high-permeability layer. The EAS of the nonlinear model is presented; moreover, both the existence and the uniqueness of the EAS are strictly proved. Consequently, some significant conclusions are obtained from the discussion of the EAS results.

2 MATHEMATICAL MODELING

The 1D commingled preferential Darcian flow and non-Darcian flow in a heterogeneous dual-layered rectangular formation is involved here, which is shown in **Figure 1**. The flow direction is parallel to the x coordinate. The upper tight layer (the thickness h_1 and the wideness L) has a very low permeability. The low-velocity non-Darcian flow with the TPG happens in the low-permeability tight layer (Dou et al., 2014); its kinematic equation is as follows (Liu et al., 2012; Dou et al., 2014) (**Figure 1**):

$$v_1 = \begin{cases} 0 & 0 \leq \frac{\partial p_1}{\partial x} \leq \lambda, \\ -\frac{k_1}{\mu} \cdot \left(\frac{\partial p_1}{\partial x} - \lambda \right) & \frac{\partial p_1}{\partial x} > \lambda, \end{cases} \quad (1)$$

where subscript 1 represents the low-permeability tight layer; k_1 is the tight layer permeability; λ is the TPG; v_1 is the fluid velocity; μ is the fluid viscosity; and p_1 is the pressure.

However, the lower layer (the thickness h_2 and the wideness L) has a much higher permeability, and the preferential flow in the high-permeability layer obeys Darcy's law. Darcy's law for the flow in the high-permeability layer is as follows:

$$v_2 = -\frac{k_2}{\mu} \cdot \frac{\partial p_2}{\partial x}, \quad (2)$$

where subscript 2 represents the high-permeability tight layer; k_2 is the permeability; v_2 is the fluid velocity; and p_2 is the pressure. It is worth mentioning that we assume the flow in the high-permeability layer is not fast enough to be affected by inertia and turbulence (Elkady et al., 2022), and thus, the flow obeys Darcy's law.

In addition, there exists a very thin impermeable barrier layer (nearly zero thickness) between the low-permeability tight layer and the high-permeability layer; and then, there is no cross flow (Debbabi et al., 2017) in the z direction between the two different layers. At the outlet end, i. e., $x = 0$, the variable production rate from the low-permeability tight layer is noted as $Q_1(t)$; and the variable production rate from the high-permeability layer is noted as $Q_2(t)$. Furthermore, the total production rate Q_0 keeps constant, i. e., $Q_1(t) + Q_2(t) = Q_0$. t is the time.

Some assumptions are defined for mathematical modeling. The dual-layered porous medium is infinitely long, and the low-permeability tight layer and the high-permeability layer are both homogeneous, respectively. In the isothermal environment, the single-phase fluid flows in the dual-layered porous medium. Both the porous medium and the fluid are slightly compressible. The gravity effect is not considered. Initially, the pressure in the dual-layered porous medium stays constant as p_i . Both the liquid storage

and the skin effect (Ehlig-Economides and Joseph, 1987; Liu and Wang, 1993) at the outlet end are not considered.

By applying a mathematical modeling method in the previous work (Liu W. C., 2020) for the fluid flow in multi-layered formation, a dimensionless mathematical model for the fundamental MB problem of the 1D commingled preferential Darcian flow and non-Darcian flow with the TPG in a dual-layered formation can be built. It is as follows:

$$2\alpha_1 \cdot \frac{\partial^2 U_1}{\partial X^2} = \frac{\partial U_1}{\partial T}, \quad 0 \leq X \leq \delta(T), \quad (3)$$

$$\delta(0) = 0, \quad (4)$$

$$U_1|_{T=0} = 0, \quad (5)$$

$$U_1|_{X=\delta(T)} = 0, \quad (6)$$

$$\left. \frac{\partial U_1}{\partial X} \right|_{X=\delta(T)} = -\Lambda, \quad \Lambda > 0, \quad (7)$$

$$2\alpha_2 \cdot \frac{\partial^2 U_2}{\partial X^2} = \frac{\partial U_2}{\partial T}, \quad 0 \leq X < +\infty, \quad (8)$$

$$U_2|_{T=0} = 0, \quad (9)$$

$$U_2|_{X \rightarrow \infty} = 0, \quad (10)$$

$$\beta_1 \cdot \left. \frac{\partial U_1}{\partial X} \right|_{X=0} + \beta_2 \cdot \left. \frac{\partial U_2}{\partial X} \right|_{X=0} = -(1 + \beta_1 \cdot \Lambda), \quad \Lambda > 0, \quad (11)$$

$$U_1|_{X=0} = U_2|_{X=0}, \quad (12)$$

where X is the dimensionless distance; U_1 and U_2 are the dimensionless pressures, respectively; T is dimensionless time; Λ is the dimensionless TPG; δ is the dimensionless MB distance; ω_1 and ω_2 are dimensionless layer elastic storage ratios (LESRs), respectively; H_1 and H_2 are dimensionless layer thickness ratios (LTRs); D_1 and D_2 are dimensionless layer permeability ratios (LPRs); α_1 , α_2 , β_1 , and β_2 are defined parameters; v_{w0} is the flow velocity in average.

These dimensionless variables in the model are shown as follows:

$$X = \frac{x}{L}, \quad (13)$$

$$T = \frac{k_1 + k_2}{\mu \cdot (\phi_{i1} C_{t1} + \phi_{i2} C_{t2}) \cdot L^2} t, \quad (14)$$

$$\delta = \frac{s}{L}, \quad (15)$$

$$U_1 = \frac{k_1 + k_2}{v_{w0} L \mu} (p_i - p_1), \quad (16)$$

$$U_2 = \frac{k_1 + k_2}{v_{w0} L \mu} (p_i - p_2), \quad (17)$$

$$\Lambda = \frac{(k_1 + k_2) \lambda}{v_{w0} \mu}, \quad (18)$$

$$\omega_1 = \frac{\phi_{i1} C_{t1}}{\phi_{i1} C_{t1} + \phi_{i2} C_{t2}}, \quad (19)$$

$$\omega_2 = \frac{\phi_{i2} C_{t2}}{\phi_{i1} C_{t1} + \phi_{i2} C_{t2}}, \quad (20)$$

$$H_1 = \frac{h_1}{h_1 + h_2}, \quad (21)$$

$$H_2 = \frac{h_2}{h_1 + h_2}, \quad (22)$$

$$D_1 = \frac{k_1}{k_1 + k_2}, \quad (23)$$

$$D_2 = \frac{k_2}{k_1 + k_2}, \quad (24)$$

$$\alpha_1 = \frac{D_1}{2\omega_1}, \quad (25)$$

$$\alpha_2 = \frac{D_2}{2\omega_2}, \quad (26)$$

$$\beta_1 = H_1 \cdot D_1, \quad (27)$$

$$\beta_2 = H_2 \cdot D_2, \quad (28)$$

$$v_{w0} = \frac{Q_0}{h_1 \cdot L + h_2 \cdot L}, \quad (29)$$

where ϕ_{i1} and ϕ_{i2} are the initial porosity for the two layers, respectively; C_{t1} and C_{t2} are comprehensive compressibility coefficients for the two layers, respectively; s is the distance of the transient MB; t is time; Q_0 is the constant total production rate.

3 EXACT ANALYTICAL SOLUTIONS

The model has a strong nonlinearity. It can be attributed to the existence of MB conditions, i. e., Eqs. 6, 7. However, the model can show a fully self-similarity property, which can be found by carrying out the stretching transform on the model (Ames, 1965). Then, some similarity transformations can be introduced as follows (Liu et al., 2012; Liu et al., 2019; Liu, 2019):

$$\eta = \frac{U_1}{2T^{\frac{1}{2}}}, \quad (30)$$

$$\psi = \frac{U_2}{2T^{\frac{1}{2}}}, \quad (31)$$

$$\xi = \frac{X}{2T^{\frac{1}{2}}}, \quad (32)$$

$$\theta = \frac{\delta}{2T^{\frac{1}{2}}}. \quad (33)$$

Then, through Eqs. 30–33, the mathematical model, i. e., Eqs. 3–12 can be equivalently transformed as follows:

$$\alpha_1 \cdot \frac{d^2 \eta}{d\xi^2} + \xi \cdot \frac{d\eta}{d\xi} - \eta = 0, \quad 0 \leq \xi \leq \theta, \quad (34)$$

$$\eta|_{\xi=\theta} = 0, \quad (35)$$

$$\left. \frac{d\eta}{d\xi} \right|_{\xi=\theta} = -\Lambda, \quad \Lambda > 0, \quad (36)$$

$$\alpha_2 \cdot \frac{d^2 \psi}{d\xi^2} + \xi \cdot \frac{d\psi}{d\xi} - \psi = 0, \quad 0 \leq \xi < +\infty, \quad (37)$$

$$\psi|_{\xi \rightarrow +\infty} = 0, \quad (38)$$

$$\beta_1 \cdot \left. \frac{d\eta}{d\xi} \right|_{\xi=0} + \beta_2 \cdot \left. \frac{d\psi}{d\xi} \right|_{\xi=0} = -(1 + \beta_1 \cdot \Lambda), \quad \Lambda > 0, \quad (39)$$

$$\psi|_{\xi=0} = \eta|_{\xi=0}. \quad (40)$$

Equations 34–40 belong to an ordinary differential equation system. It is linear and closed, which means it can be analytically solved with ease. By using the similar solution procedures in the previous work (Liu W. C., 2020), the EAS of the model, i. e., **Eq. 3–Eq. 12** can be deduced as follows:

$$\begin{aligned} U_1(X, T) = & -\Lambda \cdot X - \frac{\sqrt{2}}{2} \cdot \Lambda \cdot \theta \cdot \exp\left(\frac{\theta^2}{2\alpha_1}\right) \cdot \sqrt{\pi} \cdot \operatorname{erf}\left(\frac{\sqrt{2}}{2} \cdot \sqrt{\frac{\theta^2}{\alpha_1}}\right) \cdot \sqrt{\frac{X^2}{\alpha_1}} \\ & + \Lambda \cdot \theta \cdot \exp\left(\frac{\theta^2}{2\alpha_1}\right) \cdot \exp\left(-\frac{X^2}{8\alpha_1 T}\right) \cdot 2T^{\frac{1}{2}} \\ & + \frac{\sqrt{2}}{2} \cdot \Lambda \cdot \theta \cdot \exp\left(\frac{\theta^2}{2\alpha_1}\right) \cdot \sqrt{\pi} \cdot \operatorname{erf}\left(\sqrt{\frac{X^2}{8\alpha_1 T}}\right) \cdot \sqrt{\frac{X^2}{\alpha_1}}, \quad 0 \leq X \leq 2\theta \cdot T^{\frac{1}{2}}, \end{aligned} \quad (41)$$

where erf is the error function (Liu, 2019).

$$\begin{aligned} U_2(X, T) = & -\frac{\sqrt{2}}{2} \cdot \sqrt{\pi} \cdot \Lambda \cdot \theta \cdot \exp\left(\frac{\theta^2}{2\alpha_1}\right) \cdot \sqrt{\frac{1}{\alpha_2}} \cdot X \\ & + \Lambda \cdot \theta \cdot \exp\left(\frac{\theta^2}{2\alpha_1}\right) \cdot \exp\left(-\frac{X^2}{8\alpha_2 T}\right) \cdot 2T^{\frac{1}{2}} \\ & + \frac{\sqrt{2}}{2} \cdot \Lambda \cdot \theta \cdot \exp\left(\frac{\theta^2}{2\alpha_1}\right) \cdot \sqrt{\pi} \cdot \operatorname{erf}\left(\sqrt{\frac{X^2}{8\alpha_2 T}}\right) \cdot \sqrt{\frac{X^2}{\alpha_2}}, \quad 0 \leq X < +\infty, \end{aligned} \quad (42)$$

where the value of θ can be determined for any given positive value of Λ by the following equation:

$$\begin{aligned} & \sqrt{\pi} \cdot \beta_1 \cdot \Lambda \cdot \theta \cdot \exp\left(\frac{\theta^2}{2\alpha_1}\right) \cdot \operatorname{erf}\left(\frac{\sqrt{2}}{2} \cdot \sqrt{\frac{\theta^2}{\alpha_1}}\right) \cdot \sqrt{\frac{1}{\alpha_1}} \\ & + \sqrt{\pi} \cdot \beta_2 \cdot \Lambda \cdot \theta \cdot \exp\left(\frac{\theta^2}{2\alpha_1}\right) \cdot \sqrt{\frac{1}{\alpha_2}} = \sqrt{2}. \end{aligned} \quad (43)$$

However, it is necessary to prove the existence and uniqueness of the positive solution of θ through **Eq. 43**. The following is the proof process.

By **Eq. 43**, a function $f(\theta)$ is defined:

$$\begin{aligned} f(\theta) = & \sqrt{\pi} \cdot \beta_1 \cdot \Lambda \cdot \theta \cdot \exp\left(\frac{\theta^2}{2\alpha_1}\right) \cdot \operatorname{erf}\left(\frac{\sqrt{2}}{2} \cdot \sqrt{\frac{\theta^2}{\alpha_1}}\right) \cdot \sqrt{\frac{1}{\alpha_1}} \\ & + \sqrt{\pi} \cdot \beta_2 \cdot \Lambda \cdot \theta \cdot \exp\left(\frac{\theta^2}{2\alpha_1}\right) \cdot \sqrt{\frac{1}{\alpha_2}} - \sqrt{2}. \end{aligned} \quad (44)$$

From **Eq. 44**, the following equations can be obtained:

$$f(0) = -\sqrt{2}, \quad (45)$$

$$\lim_{\theta \rightarrow +\infty} f(\theta) = +\infty. \quad (46)$$

By using **Eqs. 45, 46**, it is obviously known that a positive value of θ noted as θ_1 exists, which satisfies $f(\theta_1) > 0$.

Then, the derivative of f is deduced from **Eq. 44**:

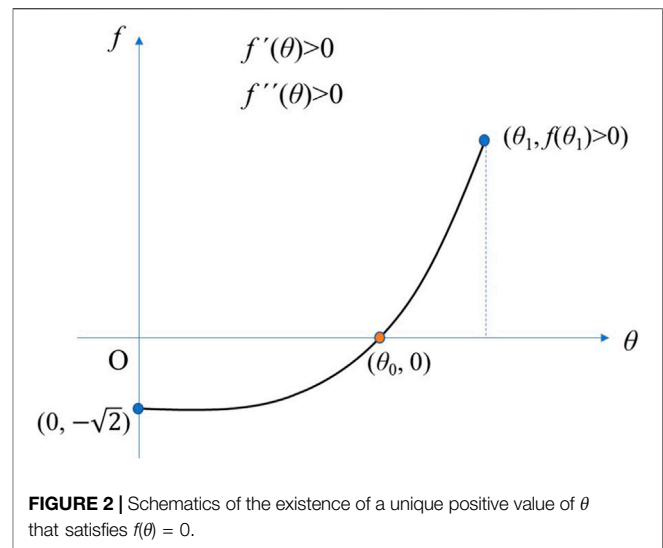


FIGURE 2 | Schematics of the existence of a unique positive value of θ that satisfies $f(\theta) = 0$.

$$\begin{aligned} f'(\theta) = & \sqrt{\pi} \cdot \beta_1 \cdot \Lambda \cdot \exp\left(\frac{\theta^2}{2\alpha_1}\right) \cdot \operatorname{erf}\left(\frac{\sqrt{2}}{2} \cdot \sqrt{\frac{\theta^2}{\alpha_1}}\right) \cdot \sqrt{\frac{1}{\alpha_1}} \\ & + \sqrt{\pi} \cdot \beta_1 \cdot \Lambda \cdot \theta^2 \cdot \exp\left(\frac{\theta^2}{2\alpha_1}\right) \cdot \operatorname{erf}\left(\frac{\sqrt{2}}{2} \cdot \sqrt{\frac{\theta^2}{\alpha_1}}\right) \cdot \sqrt{\frac{1}{\alpha_1^3}} \\ & + 2 \cdot \beta_1 \cdot \Lambda \cdot \theta^2 \cdot \exp\left(\frac{\theta^2}{2\alpha_1}\right) \cdot \exp\left(-\frac{1}{2} \cdot \frac{\theta^2}{\alpha_1}\right) \cdot \sqrt{\frac{1}{\alpha_1}} \cdot \frac{\sqrt{2}}{2} \cdot \sqrt{\frac{1}{\alpha_1}} \\ & + \sqrt{\pi} \cdot \beta_2 \cdot \Lambda \cdot \exp\left(\frac{\theta^2}{2\alpha_1}\right) \cdot \sqrt{\frac{1}{\alpha_2}} \\ & + \sqrt{\pi} \cdot \beta_2 \cdot \Lambda \cdot \theta^2 \cdot \exp\left(\frac{\theta^2}{2\alpha_1}\right) \cdot \sqrt{\frac{1}{\alpha_2}} \cdot \frac{1}{\alpha_1}. \end{aligned} \quad (47)$$

From **Eq. 47**, the following equations can be obtained as follows:

$$f'(0) = \sqrt{\pi} \cdot \beta_2 \cdot \Lambda \cdot \sqrt{\frac{1}{\alpha_2}} > 0, \quad (48)$$

$$\begin{aligned} f''(\theta) = & \sqrt{\pi} \cdot \beta_1 \cdot \Lambda \cdot \exp\left(\frac{\theta^2}{2\alpha_1}\right) \cdot \operatorname{erf}\left(\frac{\sqrt{2}}{2} \cdot \sqrt{\frac{\theta^2}{\alpha_1}}\right) \cdot \sqrt{\frac{1}{\alpha_1}} \cdot \frac{\theta}{\alpha_1} \\ & + 2 \cdot \beta_1 \cdot \Lambda \cdot \exp\left(\frac{\theta^2}{2\alpha_1}\right) \cdot \exp\left(-\frac{1}{2} \cdot \frac{\theta^2}{\alpha_1}\right) \cdot \sqrt{\frac{1}{\alpha_1}} \cdot \frac{\sqrt{2}}{2} \cdot \sqrt{\frac{1}{\alpha_1}} \\ & + 2 \cdot \sqrt{\pi} \cdot \beta_1 \cdot \Lambda \cdot \theta \cdot \exp\left(\frac{\theta^2}{2\alpha_1}\right) \cdot \operatorname{erf}\left(\frac{\sqrt{2}}{2} \cdot \sqrt{\frac{\theta^2}{\alpha_1}}\right) \cdot \sqrt{\frac{1}{\alpha_1^3}} \\ & + \sqrt{\pi} \cdot \beta_1 \cdot \Lambda \cdot \theta^3 \cdot \exp\left(\frac{\theta^2}{2\alpha_1}\right) \cdot \operatorname{erf}\left(\frac{\sqrt{2}}{2} \cdot \sqrt{\frac{\theta^2}{\alpha_1}}\right) \cdot \sqrt{\frac{1}{\alpha_1^5}} \\ & + 2 \cdot \beta_1 \cdot \Lambda \cdot \theta^2 \cdot \exp\left(\frac{\theta^2}{2\alpha_1}\right) \cdot \exp\left(-\frac{1}{2} \cdot \frac{\theta^2}{\alpha_1}\right) \cdot \sqrt{\frac{1}{\alpha_1^3}} \cdot \frac{\sqrt{2}}{2} \cdot \sqrt{\frac{1}{\alpha_1}} \\ & + 4 \cdot \beta_1 \cdot \Lambda \cdot \theta \cdot \sqrt{\frac{1}{\alpha_1}} \cdot \frac{\sqrt{2}}{2} \cdot \sqrt{\frac{1}{\alpha_1}} + \sqrt{\pi} \cdot \beta_2 \cdot \Lambda \cdot \theta \cdot \exp\left(\frac{\theta^2}{2\alpha_1}\right) \cdot \sqrt{\frac{1}{\alpha_2}} \cdot \frac{1}{\alpha_1} \\ & + 2 \cdot \sqrt{\pi} \cdot \beta_2 \cdot \Lambda \cdot \theta \cdot \exp\left(\frac{\theta^2}{2\alpha_1}\right) \cdot \sqrt{\frac{1}{\alpha_2}} \cdot \frac{1}{\alpha_1} + \sqrt{\pi} \cdot \beta_2 \cdot \Lambda \cdot \theta^3 \cdot \exp\left(\frac{\theta^2}{2\alpha_1}\right) \cdot \sqrt{\frac{1}{\alpha_2}} \cdot \frac{1}{\alpha_1^3} > 0, \quad \theta \geq 0. \end{aligned} \quad (49)$$

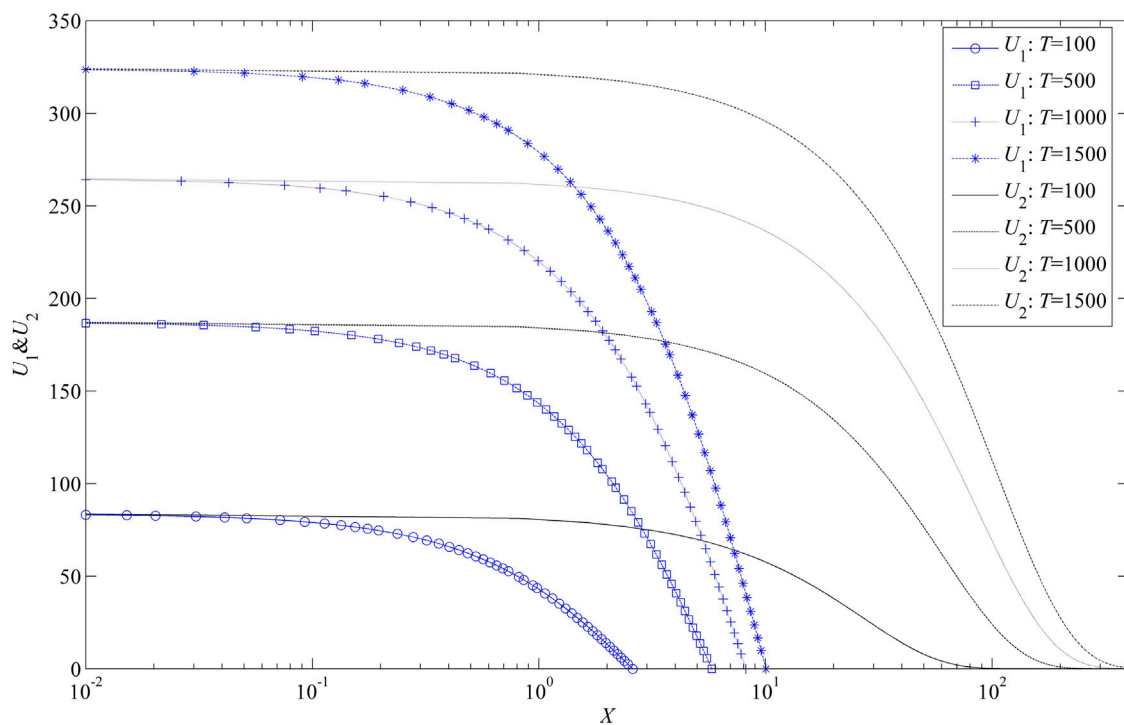


FIGURE 3 | Variation of dimensionless pressure distributions with dimensionless time.

It is indicated from **Eq. 49** that the derivative of f increases with the increment of $\theta \geq 0$. As a result, it is known from **Eq. 48** that the derivative of f is larger than zero as $\theta \geq 0$. Consequently, it is shown that f is a strictly monotonically increasing function as $\theta \geq 0$. In consideration of the strict monotonicity of f , it can be known from **Eqs. 45, 46** that there exists a unique positive value of θ noted as θ_0 that satisfies **Eq. 43** (**Figure 2**).

4 RESULTS AND DISCUSSION

In accordance with actual physical parameter values (Yao et al., 2013), the values of dimensionless variables are assigned appropriately: $D_1 = 0.03$, $D_2 = 0.97$, $H_1 = 0.9$, $H_2 = 0.1$, $\omega_1 = 0.85$, and $\omega_2 = 0.15$. From **Eqs. 25–28**, it can be calculated that $\alpha_1 = 0.0176$, $\alpha_2 = 3.2333$, $\beta_1 = 0.0270$, and $\beta_2 = 0.097$. It is worth mentioning that according to the assigned values of the dimensionless variables, thickness-weighted permeability k_{avg} for 1D flow in the whole formation (Zhang et al., 2015) can be calculated approximately as follows:

$$k_{avg} = \frac{D_1 \cdot H_1 + D_2 \cdot H_2}{H_1 + H_2} \cdot (k_1 + k_2) \quad (50)$$

$$\approx 3.97 \cdot k_1.$$

Equation 50 is based on Darcy's law, and thus, the weighted permeability must be overestimated. Therefore, it can be concluded from **Eq. 50** that this permeability on average for the dual-layered formation and the low-

permeability k_1 are on the same order of magnitude. Therefore, from the definition of the dimensionless TPG, i.e., **Eq. 18**, it can be deduced that its value for the commingled flow is much higher than the value (Liu et al., 2012; Yao et al., 2013; Liu W. C., 2020) that corresponds to the pure non-Darcian flow with the TPG in the low-permeability tight formation. It can be attributed to the reason that $k_1 + k_2$ is much higher than the low permeability k_1 , while their flow velocity v_{w0} is nearly of the same order of magnitude based on the aforementioned average permeability analysis. Here, the value of Λ is set as 20.0 appropriately. From **Eq. 43**, $\theta = 0.1297$.

The dimensionless pressure distribution change in the two different layers under different dimensionless times is shown in **Figure 3**. It is indicated from **Figure 3** that the pressure distribution curve corresponding to the Darcian flow in the high-permeability layer is much smoother than the one corresponding to the non-Darcian flow in the low-permeability tight layer. The pressure drop area in the high-permeability layer is much larger than that in the low-permeability tight layer ($U_1 > 0$). Furthermore, due to the existing TPG, there exists a large undisturbed area in the low-permeability tight layer ($U_1 = 0$); and the pressure distribution curves corresponding to the non-Darcian flow in the low-permeability tight layer with the TPG can show the characteristics of compact supports (Yao et al., 2013) (**Figure 3**).

The change of the dimensionless transient pressure at $X = 0$ with dimensionless time is shown in **Figure 4**. It is indicated from **Figure 4** that with dimensionless time increasing, the

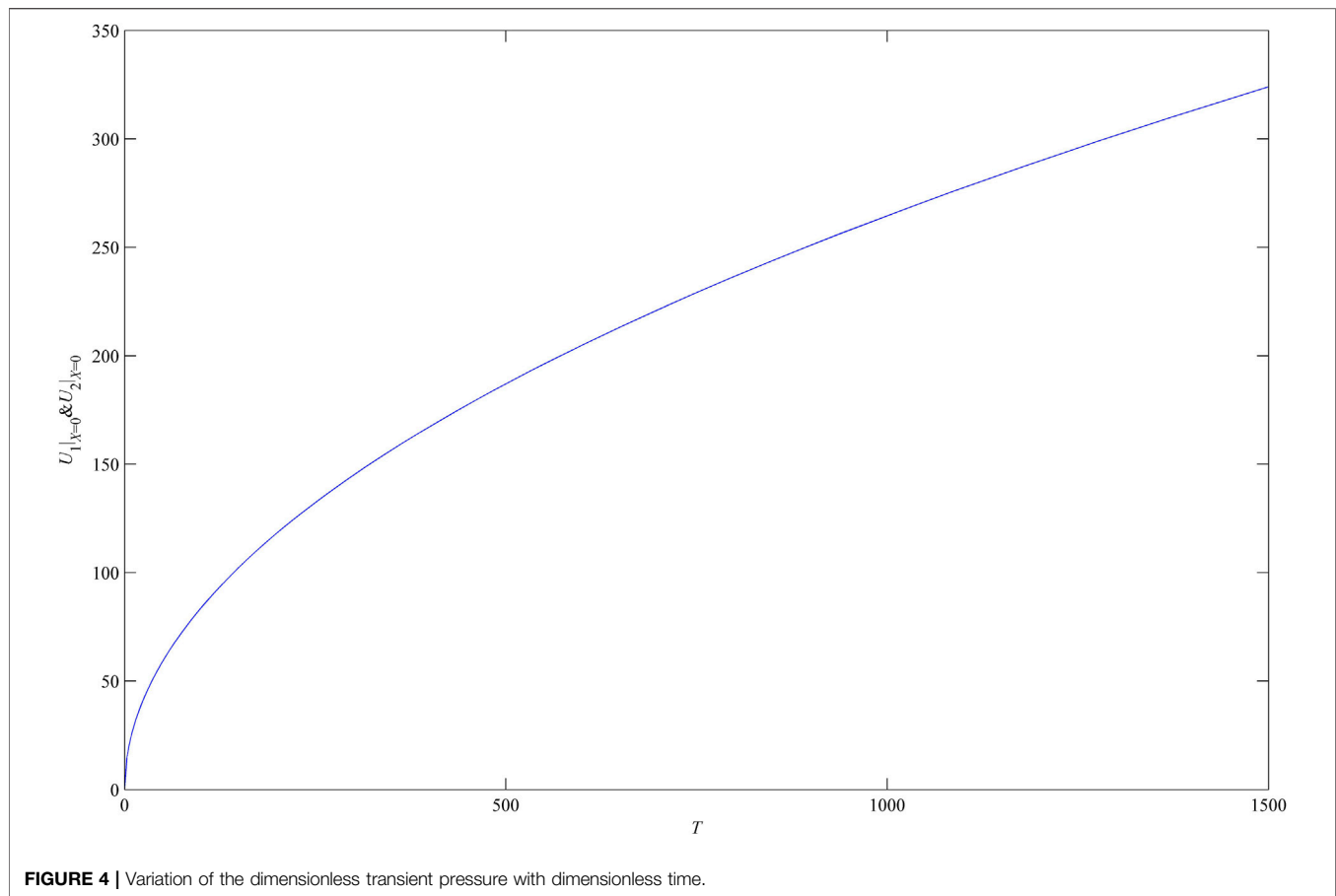


TABLE 1 | Values of θ , Q_{1D} , and Q_{2D} corresponding to Λ .

Λ	θ	Q_{1D}	Q_{2D}
25	0.1182	0.70	0.30
20	0.1297	0.72	0.28
15	0.1451	0.73	0.27
10	0.1673	0.75	0.25
0	$+\infty$	0.79	0.21

dimensionless transient pressure also increases gradually (Figure 4).

By using the model solution, from Eqs. 1, 2, and 11, the dimensionless production rate Q_{1D} from the low-permeability tight layer can be written as follows:

$$\begin{aligned}
 Q_{1D} &= -\beta_1 \cdot \left(\frac{\partial U_1}{\partial X} \right)_{X=0} + \Lambda \\
 &= \beta_1 \cdot \frac{\sqrt{2}}{2} \cdot \sqrt{\pi} \cdot \Lambda \cdot \theta \cdot \exp\left(\frac{\theta^2}{2\alpha_1}\right) \cdot \operatorname{erf}\left(\frac{\sqrt{2}}{2} \cdot \sqrt{\frac{\theta^2}{\alpha_1}}\right) \cdot \sqrt{\frac{1}{\alpha_1}}.
 \end{aligned}
 \quad (51)$$

The dimensionless production rate Q_{2D} from the high-permeability layer can be written as follows:

$$\begin{aligned}
 Q_{2D} &= -\beta_2 \cdot \left(\frac{\partial U_2}{\partial X} \right)_{X=0} \\
 &= \beta_2 \cdot \frac{\sqrt{2}}{2} \cdot \sqrt{\pi} \cdot \Lambda \cdot \theta \cdot \exp\left(\frac{\theta^2}{2\alpha_1}\right) \cdot \sqrt{\frac{1}{\alpha_2}}.
 \end{aligned}
 \quad (52a)$$

Through Eq. 43, it can be easily proven that $Q_{1D} + Q_{2D} = 1$. For this case, $Q_{1D} = 0.72$, and $Q_{2D} = 0.28$.

Next, based on the basic case, the influences of the dimensionless TPG, dimensionless LTR, LPR, and dimensionless LESR are discussed, respectively, by using the EAS results. Moreover, the necessity that the MB should be incorporated in the mathematical modeling for describing the effect of the TPG is demonstrated.

4.1 Effect of the Dimensionless Threshold Pressure Gradient

Here, the dimensionless TPG is assigned five different values, respectively: $\Lambda = 0$, $\Lambda = 10$, $\Lambda = 15$, $\Lambda = 20$, and $\Lambda = 25$. Correspondingly, by Eq. 43, θ can be calculated, as shown in Table 1. It is indicated from Table 1 that the larger dimensionless TPG corresponds to a smaller value of θ , which indicates a smaller dimensionless MB distance from Eq. 33. Figure 5A shows the influence of the dimensionless TPG on dimensionless pressure

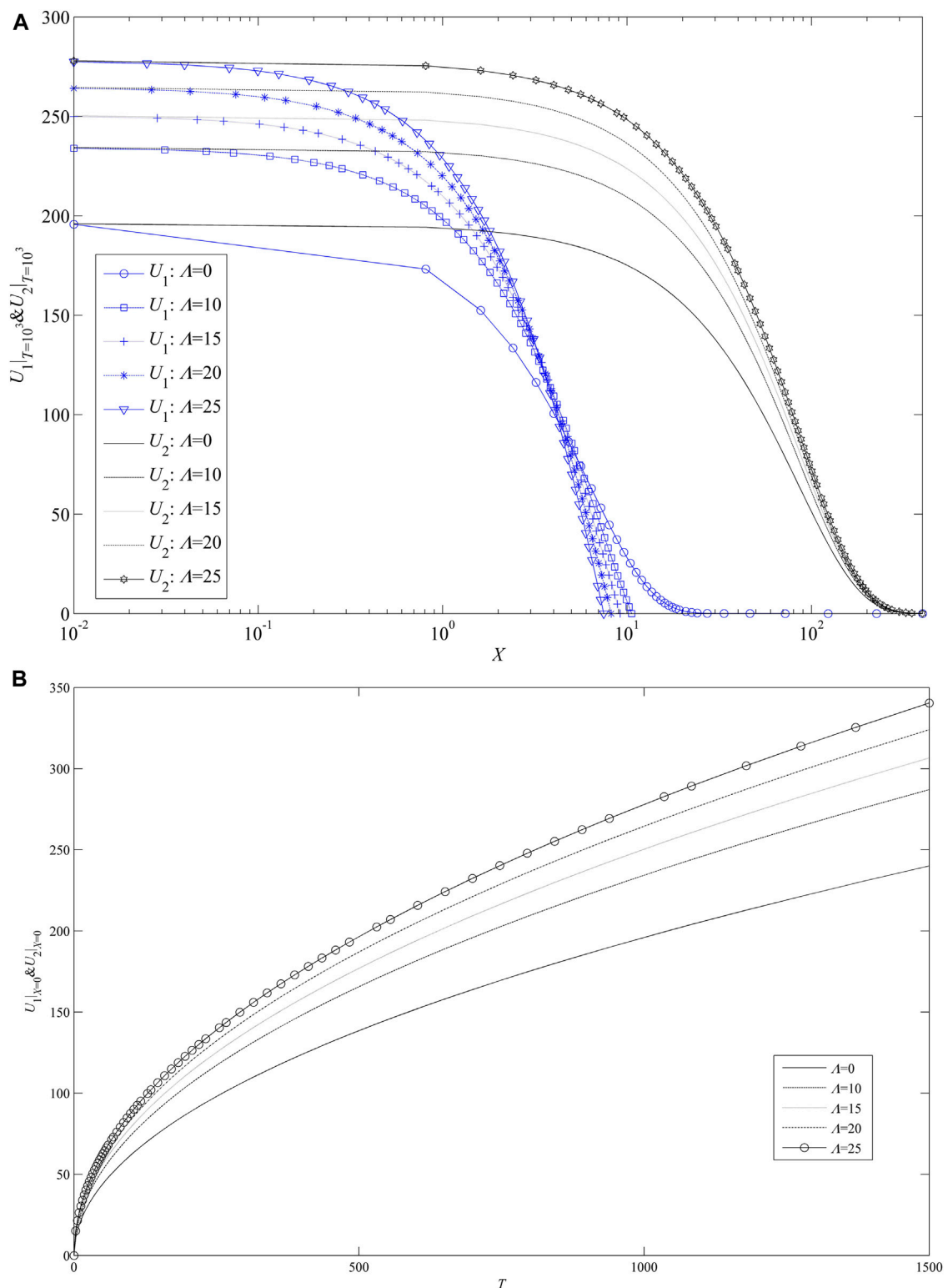


FIGURE 5 | Effect of the dimensionless TPG. **(A)** On dimensionless pressure distributions; **(B)** on dimensionless transient pressure.

distributions. It is shown from **Figure 5A** that the dimensionless TPG affects not only the pressure distribution in the low-permeability tight layer but also the pressure distribution in

the high-permeability layer. When the dimensionless distance from $X = 0$ is smaller, the influence becomes bigger. The TPG can decrease the pressure drop area in the low-permeability tight layer

TABLE 2 | The value of θ , Q1D and Q2D corresponding to Λ .

H1	θ	Q1D	Q2D
0.6	0.1019	0.26	0.74
0.8	0.1196	0.51	0.49
0.9	0.1297	0.72	0.28
0.95	0.1352	0.85	0.15

($U_1 > 0$), and it can also increase the pressure drop in the high-permeability layer (the increment of formation energy consumption). As the dimensionless TPG increases, the sensitivity of the influence declines (Figure 5A). Under different values of the dimensionless TPG, some curves of the dimensionless transient pressure are plotted in Figure 5B. It is indicated from Figure 5B that the larger dimensionless TPG corresponds to a larger dimensionless transient pressure. Furthermore, when dimensionless time is longer, the influence of the TPG increases. However, as the dimensionless TPG increases, the sensitivity of the influence declines (Figure 5B). Table 1 also shows the influence of the dimensionless TPG on production rates from each layer. From Table 1, it is concluded that with the TPG increasing, less and less production rate comes from the low-permeability tight layer, and then, more and more production rates come from the high-permeability layer when the total production rate Q_0 is constant. Therefore, the existence of TPG in the low-permeability tight layer can intensify the preferential Darcian flow in the high-permeability layer.

Physical interpretation: The larger TPG can reduce the flow ability in the low-permeability tight layer, which makes MB move more difficultly. As the total production rate is constant, the larger TPG can introduce a larger pressure drop (more energy consumption) in the layers, which also means less production rate from the low-permeability tight layer.

4.2 Effect of the Dimensionless Layer Thickness Ratio

The dimensionless LTR H_1 is assigned four different values, respectively: $H_1 = 0.6$ ($H_2 = 0.4$), $H_1 = 0.8$ ($H_2 = 0.2$), $H_1 = 0.9$ ($H_2 = 0.1$), and $H_1 = 0.95$ ($H_2 = 0.05$). Correspondingly, by Eq. 43, θ can be calculated, which is shown in Table 2. From Table 2, it is indicated that the dimensionless MB distance $2\sqrt{T} \cdot \theta$ increases as the LTR of the low-permeability tight layer H_1 increases. The influence of the LTR on pressure distributions is shown in Figure 6A. It is indicated from Figure 6A that the bigger the LTR of the low-permeability tight layer, the larger is the pressure drop (U_1 and U_2) in both the layers. Moreover, when the dimensionless distance from $X = 0$ is smaller, the influence becomes bigger (Figure 6A). Under different values of the dimensionless LTR, some curves of the dimensionless transient pressure are plotted in Figure 6B. It is indicated from Figure 6B that the larger dimensionless LTR for the low-permeability layer corresponds to a greater dimensionless transient pressure (Figure 6B). Table 2 shows the influence of the dimensionless LTR on production rates from each layer. From Table 2, it is concluded that as H_1 increases, the production rate from the low-

permeability tight layer becomes greater when the total production rate Q_0 is constant. Furthermore, the intensity of the preferential Darcian flow in the high-permeability layer is very sensitive to the LTR.

Physical interpretation: The higher value of the LTR H_1 indicates a larger thickness of the low-permeability tight layer and a smaller thickness of the high-permeability layer ($H_2 = 1.0 - H_1$). As the value of H_1 increases, due to the decrease in the average permeability of the layered porous media, more pressure drops will be generated in the layers in order to keep the production rate constant.

4.3 Effect of the Dimensionless Layer Permeability Ratio

The dimensionless LPR is assigned four different values, respectively: $D_1 = 0.01$ ($D_2 = 0.99$), $D_1 = 0.03$ ($D_2 = 0.97$), $D_1 = 0.05$ ($D_2 = 0.95$), and $D_1 = 0.1$ ($D_2 = 0.9$). Correspondingly, by Eq. (43), θ can be calculated, which is shown in Table 3. It is indicated from Table 3 that as the LPR of the low-permeability tight layer D_1 increases, the dimensionless MB distance $2\sqrt{T} \cdot \theta$ increases. Figure 7A shows the effect of the LPR on pressure distributions. From Figure 7A, it is indicated that the bigger the value of D_1 , the larger the pressure drop area in the low-permeability tight layer ($U_1 > 0$), and the smaller the pressure drop inside the pressure drop area in the low-permeability tight layer, the smaller is the pressure drop in the high-permeability layer when the LPR of the low-permeability tight layer increases. When the dimensionless distance from $X = 0$ is smaller, the influence becomes bigger (Figure 7A). Under different values of the dimensionless LPR, some curves of dimensionless transient pressure are plotted in Figure 7B. It is indicated from Figure 7B that the larger LPR for the low-permeability layer corresponds to a greater dimensionless transient pressure. Table 3 shows the influence of the LPR on production rates from each layer. From Table 3, it is concluded that as D_1 increases, the production rate from the low-permeability tight layer becomes greater, and the sensitivity of the influence of the LPR on the layer production sub-rate is not as much as that of the LTR (Figure 7B).

Physical interpretation: The higher value of D_1 directly reflects the enhancement of the flow ability in the low-permeability tight layer and, simultaneously, the reduction of the flow ability in the high-permeability layer ($D_2 = 1.0 - D_1$). Furthermore, due to the reason that the thickness of the low-permeability tight layer is nine times that of the high-permeability layer ($H_1 = 0.9$), the influence of flow ability enhancement of the low-permeability tight layer is much larger than the influence of flow ability reduction of the high-permeability layer on the flow. Therefore, as the value of D_1 increases, the pressure drop in the layers decreases, and the production rate from the low-permeability tight layer increases.

4.4 Effect of Dimensionless Layer Elastic Storage Ratios

The dimensionless LESR is assigned four different values, respectively: $\omega_1 = 0.7$ ($\omega_2 = 0.3$), $\omega_1 = 0.8$ ($\omega_2 = 0.2$), $\omega_1 =$

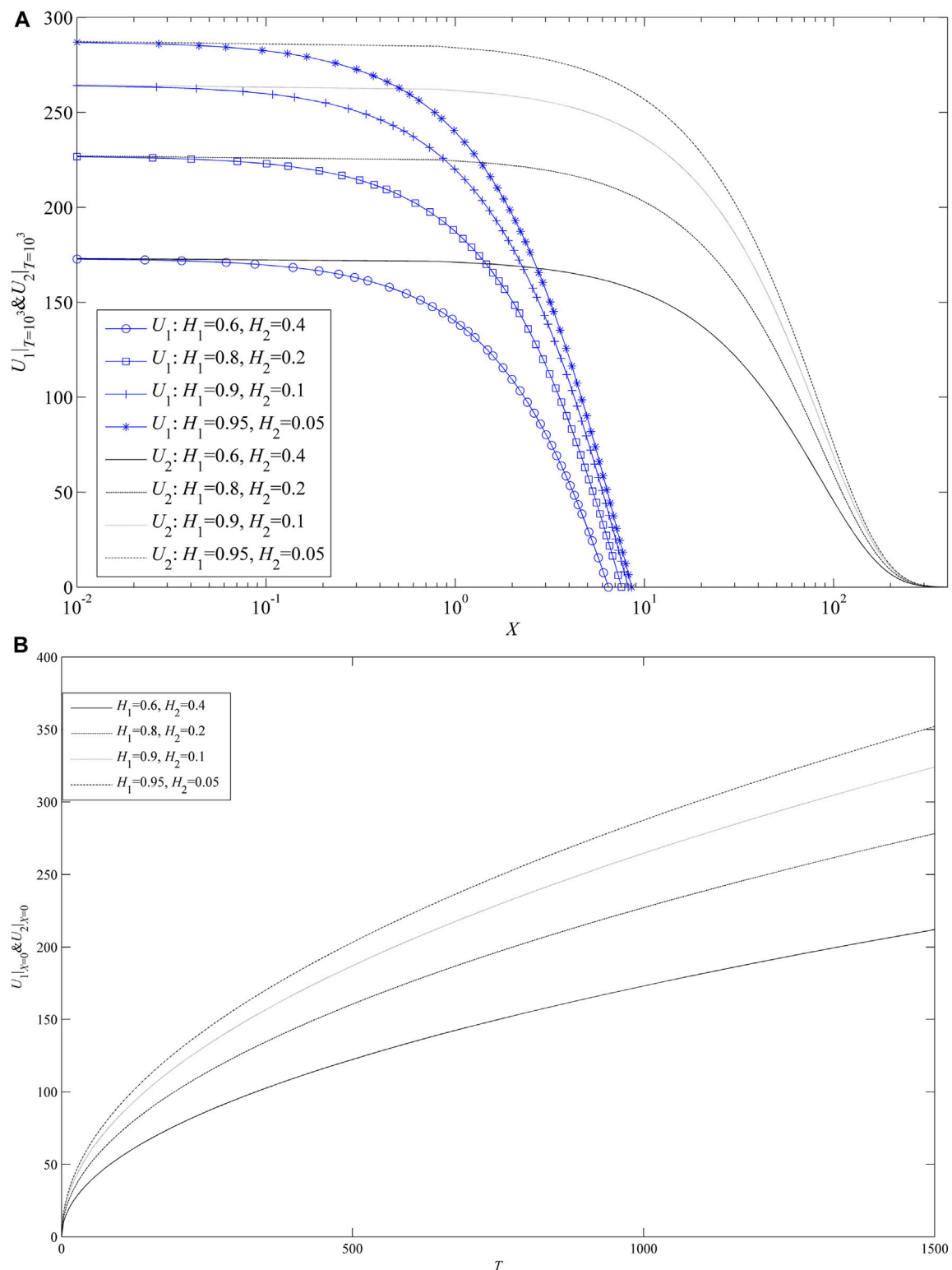


FIGURE 6 | Effect of the dimensionless LTR. **(A)** On dimensionless pressure distributions **(B)** on dimensionless transient pressure.

0.85 ($\omega_2 = 0.15$), and $\omega_1 = 0.9$ ($\omega_2 = 0.1$). Correspondingly, by Eq. 43, θ can be calculated, which is shown in Table 4. It is indicated from Table 4 that the dimensionless LESR has little

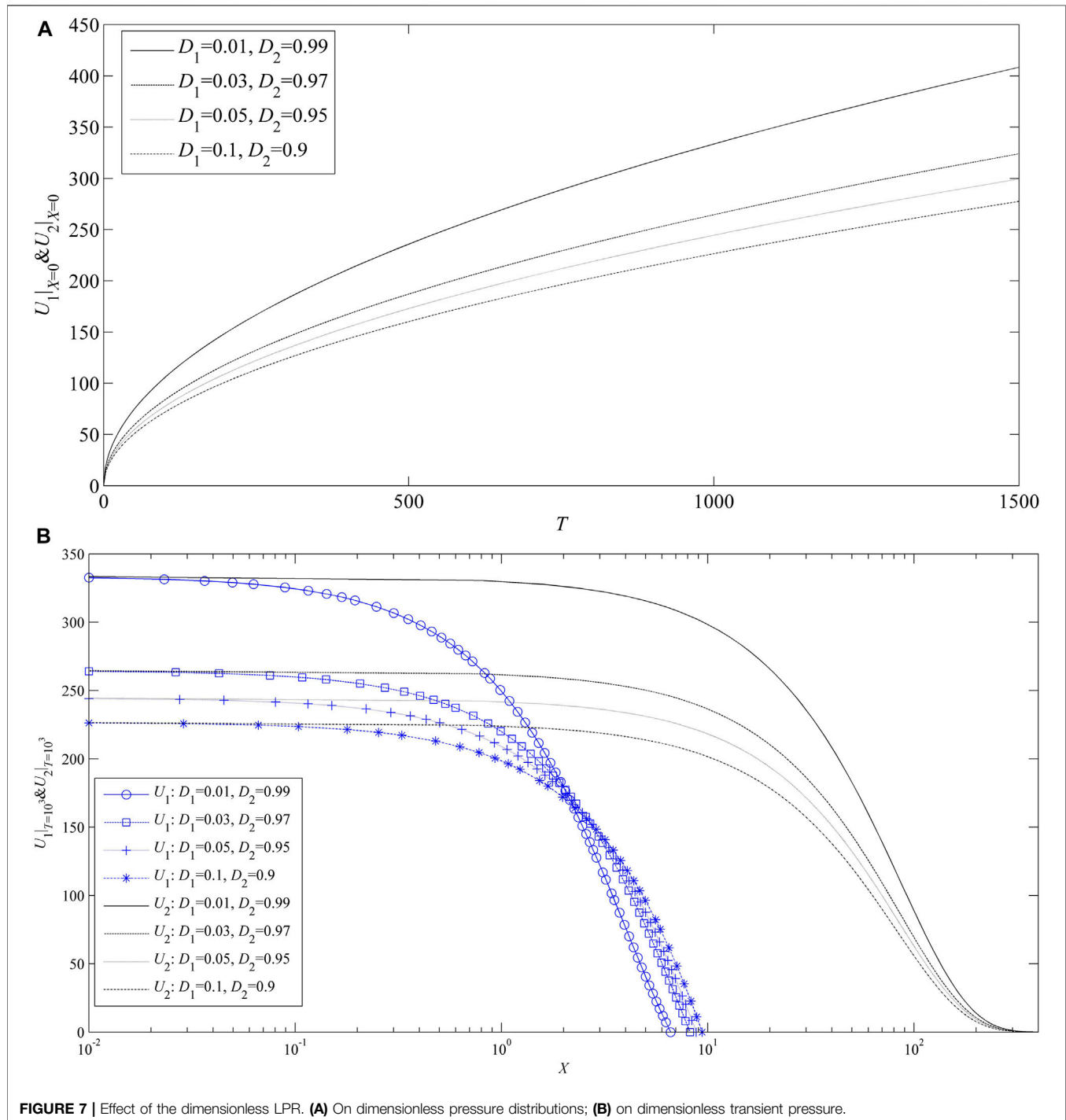
effect on θ . Figure 8A shows the effect of LESR on pressure distributions. It can be seen from Figure 8A that the LESR affects the pressure distribution of the low-permeability tight

TABLE 3 | The value of θ , Q1D and Q2D corresponding to Λ .

D1	θ	Q1D	Q2D
0.01	0.1045	0.64	0.36
0.03	0.1297	0.72	0.28
0.05	0.1391	0.74	0.26
0.1	0.1485	0.77	0.23

TABLE 4 | The value of θ , Q1D and Q2D corresponding to Λ .

$\omega 1$	θ	Q1D	Q2D
0.7	0.1344	0.61	0.39
0.8	0.1312	0.68	0.32
0.85	0.1297	0.72	0.28
0.9	0.1294	0.76	0.24

**FIGURE 7** | Effect of the dimensionless LPR. **(A)** On dimensionless pressure distributions; **(B)** on dimensionless transient pressure.

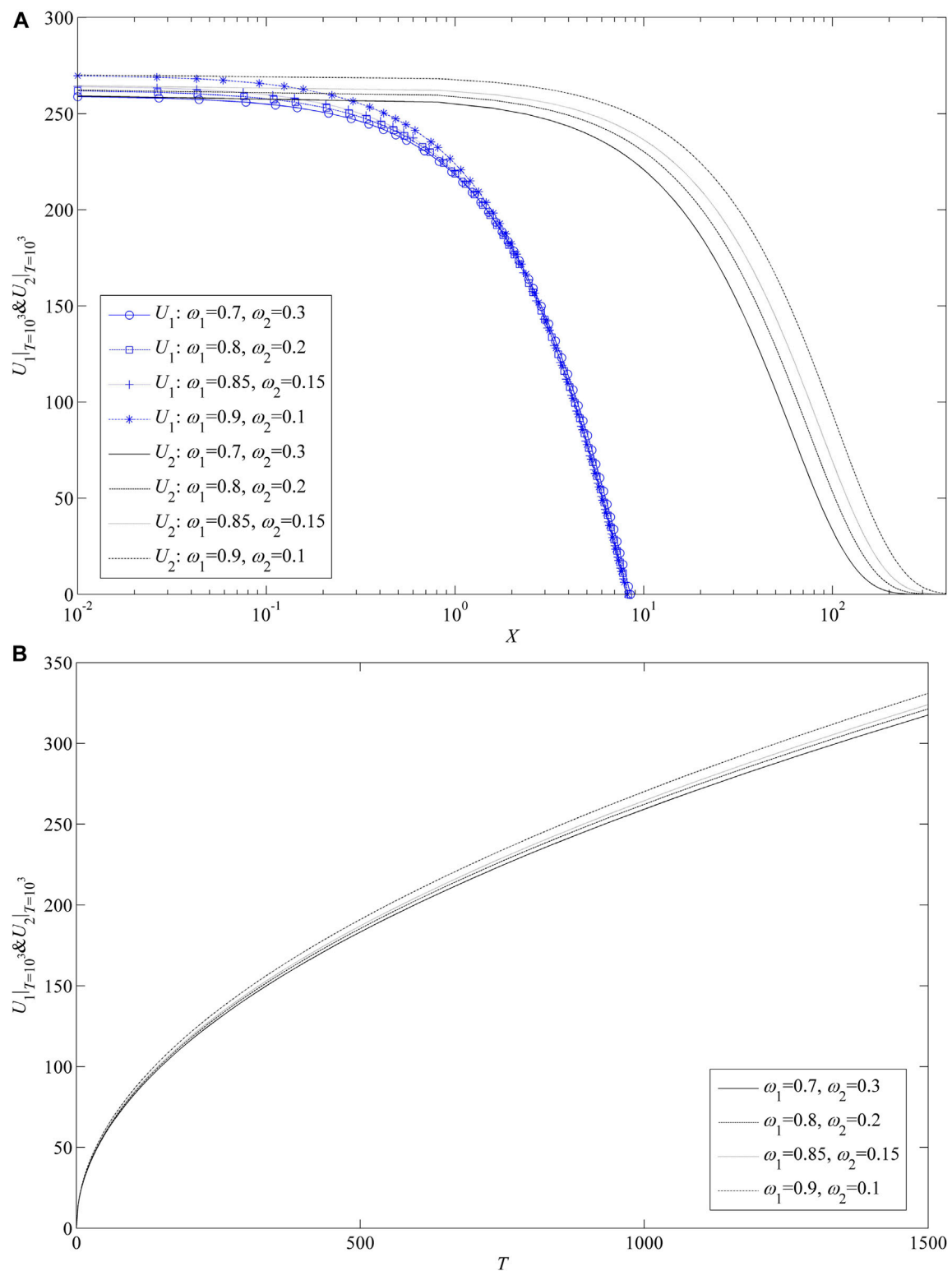


FIGURE 8 | Effect of the dimensionless LESR. **(A)** On dimensionless pressure distributions; **(B)** on dimensionless transient pressure.

layer a little. However, it has a big effect on the pressure distribution of the high-permeability layer. Furthermore, the bigger the value of ω_1 , the larger is the pressure drop in the

high-permeability tight layer. When the dimensionless distance increases, the influence of the LESR becomes bigger (**Figure 8A**). Under different values of the

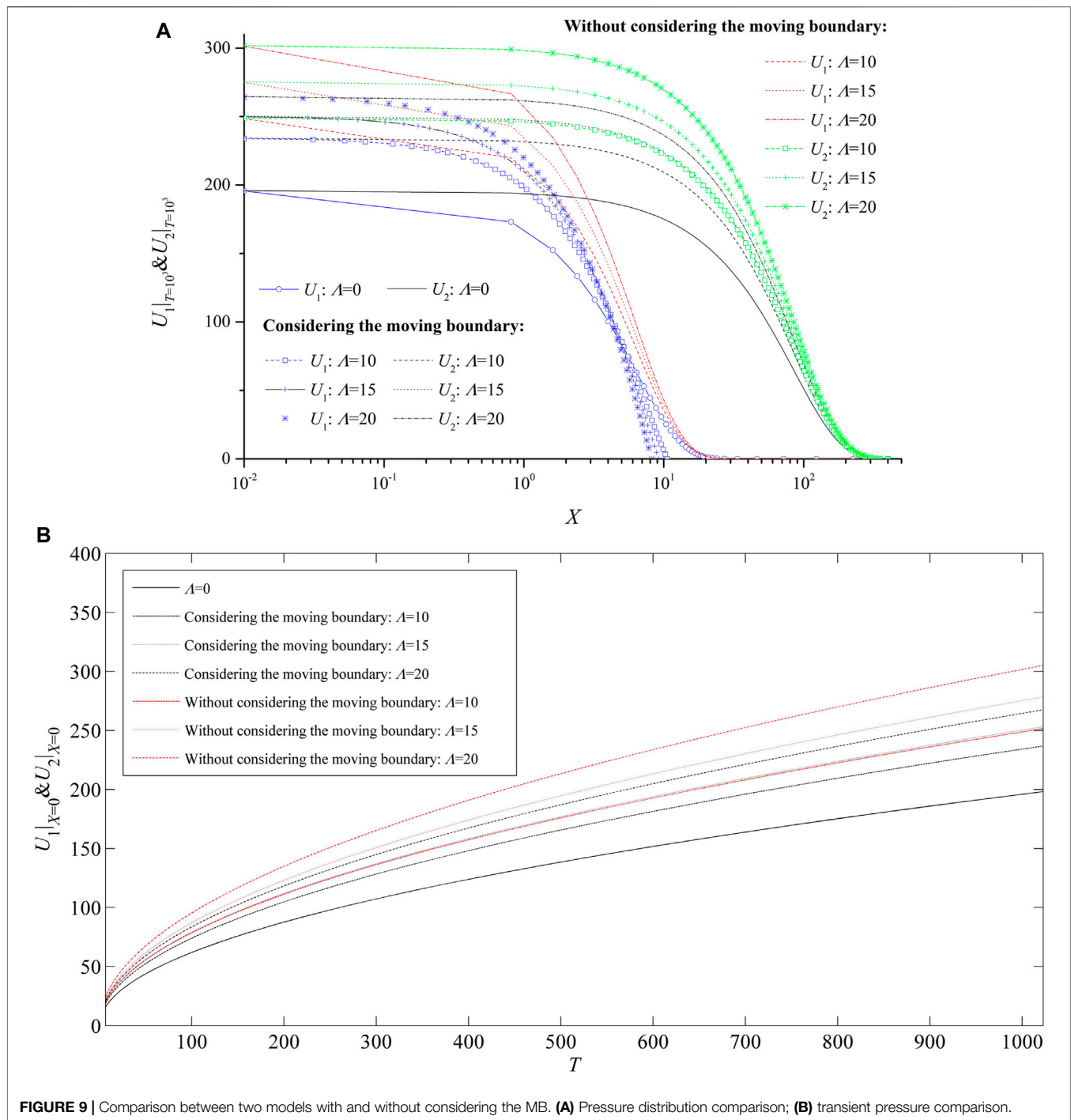


FIGURE 9 | Comparison between two models with and without considering the MB. **(A)** Pressure distribution comparison; **(B)** transient pressure comparison.

dimensionless LESR, some curves of the dimensionless transient pressure are plotted in **Figure 8B**. It is indicated from **Figure 8B** that a larger LESR for the low-permeability layer corresponds to a bigger dimensionless transient pressure. As dimensionless time increases, the influence of the LESR becomes bigger (**Figure 8B**). **Table 4** shows the influence of the LESR on production rates from each layer. From **Table 4**, it can be concluded that with ω_1 increasing, more and more production rates come from the low-

permeability tight layer. The sensitivity of the influence of the LESR on the layer production sub-rate is also not as much as that of the LTR.

Physical interpretation: The higher value of the LESR ω_1 indicates more elastic energy from porous media and fluid in the low-permeability tight layer and, simultaneously, the less elastic energy in the high-permeability layer ($\omega_2 = 1.0 - \omega_1$). When the pressure in the porous medium drops, more released elastic energy can cause more fluid to be produced. Therefore, as the

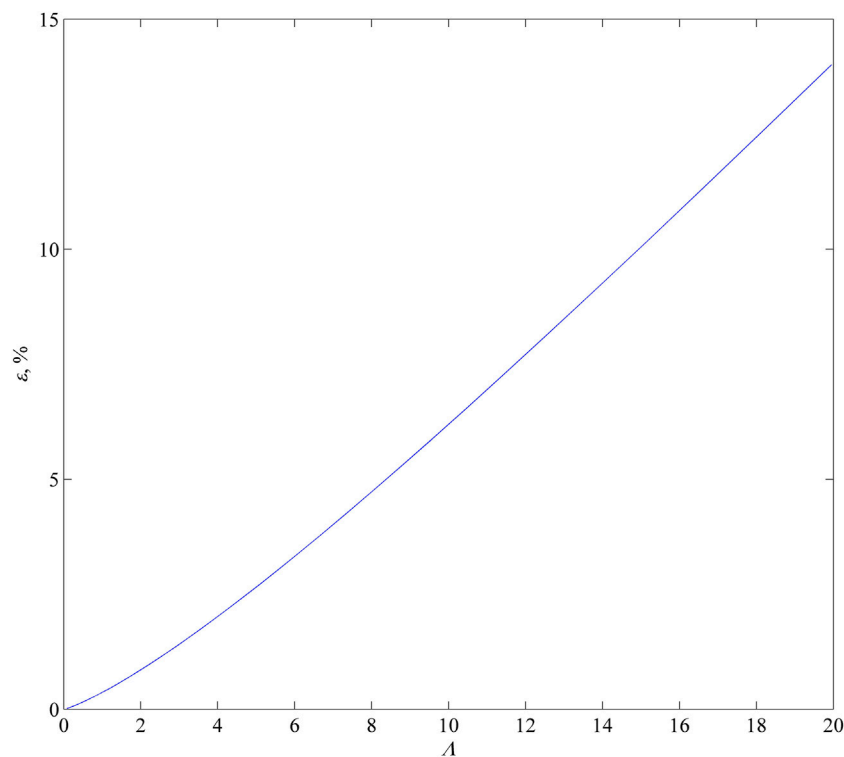


FIGURE 10 | Variation of the relative error ϵ with dimensionless TPG Λ .

TABLE 5 | Comparison of Q1D and Q2D corresponding to the two different models with and without considering the MB.

Λ	Considering MB		Neglecting MB	
	Q1D	Q2D	Q1D	Q2D
20	0.72	0.28	0.68	0.32
15	0.73	0.27	0.71	0.29
10	0.75	0.25	0.73	0.27
0	0.79	0.21	0.79	0.21

value of ω_1 increases, the production rate from the low-permeability tight layer increases, but the production rate from the high-permeability layer decreases. In addition, with ω_1 increasing, it mainly has an effect on pressure drop in the high-permeability layer.

4.5 Effect of Considering Moving Boundary Conditions or Not

MB problems usually have a strong nonlinearity. In order to linearize the mathematical models for simplifying the model computation, MB conditions that describe the effect of TPG are not always taken into account in the relevant mathematical modeling in the previously published literature (Guo et al., 2012; Zeng et al., 2018; Wu et al., 2019). The TPG effect is just described through continuity equations or inner boundary conditions. However, this kind of linearization may introduce a lot of

errors (Yao et al., 2013; Liu et al., 2019a). Here, without considering MB conditions (Guo et al., 2012; Zeng et al., 2018; Wu et al., 2019), a dimensionless mathematical model for this 1D commingle preferred Darcian flow and non-Darcian flow problem is presented, and its EAS is also presented. Please see **Appendix A** for the details of the mathematical model and its EAS process. Then, this EAS can be compared with the EAS for the model in consideration of MB conditions. As a result, the significance of considering MB conditions caused by the TPG can be demonstrated. Their dimensionless pressure distributions (U_1 and U_2) at $T = 10^3$ are compared in **Figure 9A** under different values of Λ : $\Lambda = 0$, $\Lambda = 10$, $\Lambda = 15$, and $\Lambda = 20$. It can be seen from **Figure 9A** that when MB is not incorporated, dimensionless pressures U_1 and U_2 will be overestimated largely, and the pressure distribution corresponding to the non-Darcian flow in the low-permeability tight layer with the TPG becomes much smoother, and then, the characteristics of compact supports (Yao et al., 2013) for the pressure distribution corresponding to the non-Darcian flow in the low-permeability tight layer can be lost. A larger TPG can cause larger errors. Moreover, as dimensionless distance decreases, the errors become bigger. In addition, when the MB is not taken into account in the modeling, the pressure drop area ($U_1 > 0$) in the low-permeability tight layer will be largely overestimated (**Figure 9A**). Dimensionless transient pressures are compared in **Figure 9B** under different values of Λ : $\Lambda = 0$, $\Lambda = 10$, $\Lambda = 15$, and $\Lambda = 20$. It can be seen from **Figure 9B** that when the MB is not incorporated, the dimensionless transient pressure can be

over-evaluated largely, especially when the dimensionless TPG is bigger, and errors also increase with dimensionless time. When the MB is not considered in the modeling, the relative error ε can be directly deduced through the two EASs, i. e., Eq. 41 and Eq. A9 (see Appendix B for the details) as follows (Figure 9B). The relative error affected by the dimensionless TPG Λ is directly shown in Figure 10. As Λ increases, relative error ε increases, and its increase rate also grows (Figure 10).

$$\varepsilon = \left| \frac{\beta_1 \cdot \operatorname{erf}\left(\frac{\sqrt{2}}{2} \cdot \sqrt{\frac{\theta^2}{\alpha_1}}\right) \cdot \sqrt{\frac{1}{\alpha_1}} + \beta_2 \cdot \sqrt{\frac{1}{\alpha_2}}}{\beta_1 \cdot \sqrt{\frac{1}{\alpha_1}} + \beta_2 \cdot \sqrt{\frac{1}{\alpha_2}}} \cdot (1 + \beta_1 \cdot \Lambda) - 1 \right| \times 100\%. \quad (52b)$$

Table 5 shows the effect of neglecting MB in the modeling on the dimensionless production rates from the two different layers. From Table 5, it can be concluded that as the MB caused by the TPG is neglected, the dimensionless production rate from the high-permeability layer can be overestimated. In other words, the preferential Darcian flow in the high-permeability layer can be exaggerated. A larger dimensionless TPG introduces a larger deviation. Therefore, MB conditions should be incorporated into the mathematical modeling of 1D commingled preferential Darcian flow and low-velocity non-Darcian flow problems.

5 CONCLUSION

A basic nonlinear problem of the 1D commingled preferential Darcian flow and non-Darcian flow with the TPG in a dual-layered formation is studied. The flow in a low-permeability tight layer obeys the low-velocity non-Darcy kinematic equation with the TPG, while Darcy's law holds for the flow in the high-permeability layer. Also, a nonlinear dimensionless mathematical model, incorporating MB conditions caused by the TPG, is presented. The EAS of this nonlinear model is obtained; in particular, its existence and uniqueness are both proved strictly. From the EAS results, the influences of the dimensionless TPG, dimensionless LTR, dimensionless LPR, and dimensionless LESR on pressure distribution, transient pressure, and layer production rate are discussed. It is found that the existence of the TPG in a low-permeability tight layer can intensify the preferential Darcian flow in the high-permeability layer; and the intensity of the preferential Darcian flow in the high-permeability layer is very sensitive to the LTR; however, the effect of LPR and LESR on the production sub-rate is more

sensitive than that of LTR. Furthermore, it is strictly demonstrated that MB conditions caused by the TPG should be incorporated in the model. When the MB is neglected, the preferential Darcian flow into the high-permeability layer can be exaggerated. In addition, a relative error formula for calculating transient pressure, caused by neglecting MB in the model, is provided.

All in all, in the article, the major theoretical contributions are as follows: an EAS of a fundamental MB problem of the 1D commingled preferential Darcian flow and low-velocity non-Darcian flow in a dual-layered formation is presented; its existence and uniqueness are both strictly proved; then, the commingled flow behavior is analyzed. Therefore, solid theoretical foundations are provided here, which are very significant for solving non-Darcian seepage flow problems in engineering by numerical simulation validation and physical experiment design. Finally, it is worth mentioning that in the study, an impermeable barrier layer between the two layers exists, and thus, the cross flow between the layers is not involved. However, for the situation under consideration of the cross flow, the corresponding moving boundary problem will become more challenging and interesting. It will be our future research field.

DATA AVAILABILITY STATEMENT

The original contributions presented in the study are included in the article/Supplementary Material; further inquiries can be directed to the corresponding author.

AUTHOR CONTRIBUTIONS

PW: conceptualization, writing, and editing; WL: methodology and literature survey; WD: literature survey and writing; XK: document arrangement and writing; HF: methodology and inspection.

FUNDING

This research was supported by the project (Grant Nos. FRF-TP-17-023A1) sponsored by the Fundamental Research Funds for Central Universities and CNPC Innovation Fund (Grant Nos. 2021DQ02-0901).

REFERENCES

- Afshari, S., Hejazi, S. H., and Kantzas, A. (2018). Longitudinal dispersion in heterogeneous layered porous media during stable and unstable pore-scale miscible displacements. *Adv. Water Resour.* 119, 125–141. doi:10.1016/j.advwatres.2018.06.005
- Ames, W. F. (1965). *Nonlinear partial differential equations in engineering*. New York: Academic.

- Bauer, D., Talon, L., Peysson, Y., Ly, H. B., Batôt, G., Chevalier, T., et al. (2019). Experimental and numerical determination of Darcy's law for yield stress fluids in porous media. *Phys. Rev. Fluids* 4, 063301. doi:10.1103/physrevfluids.4.063301
- Bear, J. (1972). *Dynamics of fluids in porous media*. New York: American Elsevier.
- Cai, J. (2014). A fractal approach to low velocity non-Darcy flow in a low permeability porous medium. *Chin. Phys. B* 23, 044701. doi:10.1088/1674-1056/23/4/044701
- Chen, Y. M., Tang, X. W., and Wang, J. (2004). An analytical solution of one-dimensional consolidation for soft sensitive soil ground. *Int. J. Numer. Anal. Methods Geomech.* 28, 919–930. doi:10.1002/nag.353

- Chi, J., and Wang, J. (2021). A new calculation method on the critical well spacing of CO₂ miscible flooding in ultra-low permeability reservoirs. *J. Porous Media* 24, 59–79. doi:10.1615/jpormedia.2020033488
- Debbabi, Y., Jackson, M. D., Hampson, G. J., Fitch, P. J. R., and Salinas, P. (2017). Viscous crossflow in layered porous media. *Transp. Porous Media* 117, 281–309. doi:10.1007/s11242-017-0834-z
- Dou, H., Ma, S., Zou, C., and Yao, S. (2014). Threshold pressure gradient of fluid flow through multi-porous media in low and extra-low permeability reservoirs. *Sci. China Earth Sci.* 57, 2808–2818. doi:10.1007/s11430-014-4933-1
- Ehlig-Economides, C. A., and Joseph, J. (1987). A new test for determination of individual layer properties in a multilayered reservoir. *SPE Form. Eval.* 2, 261–283. doi:10.2118/14167-PA
- Elkady, M. S., Abdelaziz, G. B., Sharshir, S. W., Mohamed, A. Y. A., Elsaid, A. M., El-Said, E. M. S., et al. (2022). Non-Darcian immiscible two-phase flow through porous materials (Darcy–Forchheimer–Brinkman Model). *Therm. Sci. Eng. Prog.* 29, 101204. doi:10.1016/j.tsep.2022.101204
- Fusi, L., and Farina, A. (2017). Peristaltic flow of a Bingham fluid in a channel. *Int. J. Non. Linear. Mech.* 97, 78–88. doi:10.1016/j.ijnonlinmec.2017.09.003
- Gao, D., Ye, J., Wang, T., Zhao, L., Pan, S., and Sun, Z. (2018). An independent fracturing water-flooding development method for shallow low-permeability thin oil layers in multi-layer sandstone reservoirs. *J. Pet. Sci. Eng.* 167, 877–889. doi:10.1016/j.petro.2018.04.049
- Guo, J., Zhang, S., Zhang, L., Qing, H., and Liu, Q. (2012). Well testing analysis for horizontal well with consideration of threshold pressure gradient in tight gas reservoirs. *J. Hydrodyn.* 24, 561–568. doi:10.1016/s1001-6058(11)60278-3
- Hu, W., Wei, Y., and Bao, J. (2018). Development of the theory and technology for low permeability reservoirs in China. *Petroleum Explor. Dev.* 45, 685–697. doi:10.1016/s1876-3804(18)30072-7
- Jiao, X. R., Jiang, S., and Liu, H. (2021). Nonlinear moving boundary model of low-permeability reservoir. *Energies* 14, 8445. doi:10.3390/en14248445
- Kaffel, A. (2019). Rigorous derivation of a new macroscopic model for modeling partially-saturated flow of a liquid in multilayered thin swelling porous media. *Int. J. Heat. Mass Transf.* 129, 1274–1286. doi:10.1016/j.ijheatmasstransfer.2018.10.058
- Li, D., Zha, W., Liu, S., Wang, L., and Lu, D. (2016). Pressure transient analysis of low permeability reservoir with pseudo threshold pressure gradient. *J. Pet. Sci. Eng.* 147, 308–316. doi:10.1016/j.petro.2016.05.036
- Li, J., Yang, H., Qiao, Y., Fan, Z., Chen, W., and Jiang, H. (2018). Laboratory evaluations of fiber-based treatment for in-depth profile control. *J. Pet. Sci. Eng.* 171, 271–288. doi:10.1016/j.petro.2018.07.060
- Li, X., Lu, D., Luo, R., Sun, Y., Shen, W., Hu, Y., et al. (2019). Quantitative criteria for identifying main flow channels in complex porous media. *Petroleum Explor. Dev.* 46, 998–1005. doi:10.1016/s1876-3804(19)60256-9
- Liu, C., and Wang, X. (1993). Transient 2D flow in layered reservoirs with crossflow. *SPE Form. Eval.* 8, 287–291. doi:10.2118/25086-PA
- Liu, W. C. (2019). Analytical study on a moving boundary problem of semispherical centripetal seepage flow of Bingham fluid with threshold pressure gradient. *Int. J. Non. Linear. Mech.* 113, 17–30. doi:10.1016/j.ijnonlinmec.2019.03.011
- Liu, W. C., Duan, Y. Y., Zhang, Q. T., Chen, Z., Yan, X. M., Sun, H. D., et al. (2022). Analytical study on a one-dimensional model coupling both Darcy flow and low-velocity non-Darcy flow with threshold pressure gradient in heterogeneous composite reservoirs. *J. Porous Media* 25, 1615.
- Liu, W. C. (2020a). Exact analytical solution of a generalized multiple moving boundary model of one-dimensional non-Darcy flow in heterogeneous multilayered low-permeability porous media with a threshold pressure gradient. *Appl. Math. Model.* 81, 931–953. doi:10.1016/j.apm.2020.01.028
- Liu, W. C. (2020b). Exact analytical solutions of non-Darcy seepage flow problems of one-dimensional Bingham fluid flow in finite long porous media with threshold pressure gradient. *J. Pet. Sci. Eng.* 184, 106475. doi:10.1016/j.petro.2019.106475
- Liu, W. C., Yao, J., Chen, Z., and Zhu, W. Y. (2019a). An exact analytical solution of moving boundary problem of radial fluid flow in an infinite low-permeability reservoir with threshold pressure gradient. *J. Pet. Sci. Eng.* 175, 9–21. doi:10.1016/j.petro.2018.12.025
- Liu, W. C., Yao, J., and Wang, Y. Y. (2012). Exact analytical solutions of moving boundary problems of one-dimensional flow in semi-infinite long porous media with threshold pressure gradient. *Int. J. Heat. Mass Transf.* 55, 6017–6022. doi:10.1016/j.ijheatmasstransfer.2012.06.012
- Liu, W. C., Zhang, Q. T., and Zhu, W. Y. (2019b). Numerical simulation of multi-stage fractured horizontal well in low-permeable oil reservoir with threshold pressure gradient with moving boundary. *J. Pet. Sci. Eng.* 178, 1112–1127. doi:10.1016/j.petro.2019.04.033
- Ma, T. R., Zhang, K. N., Shen, W. J., Guo, C. B., and Xu, H. (2021). Discontinuous and continuous Galerkin methods for compressible single-phase and two-phase flow in fractured porous media. *Adv. Water Resour.* 156, 104039. doi:10.1016/j.advwatres.2021.104039
- Nijjer, J. S., Hewitt, D. R., and Neufeld, J. A. (2019). Stable and unstable miscible displacements in layered porous media. *J. Fluid Mech.* 869, 468–499. doi:10.1017/jfm.2019.190
- Olguín, M. C., Medina, M. A., Sanziel, M. C., and Tarzia, D. A. (2007). Behavior of the solution of a stefan problem by changing thermal coefficients of the substance. *Appl. Math. Comput.* 190, 765–780. doi:10.1016/j.amc.2007.01.104
- Prada, A., and Civan, F. (1999). Modification of Darcy's law for the threshold pressure gradient. *J. Pet. Sci. Eng.* 22, 237–240. doi:10.1016/s0920-4105(98)00083-7
- Shen, W., Ma, T., Li, X., Sun, B., Hu, Y., and Xu, J. (2022). Fully coupled modeling of two-phase fluid flow and geomechanics in ultra-deep natural gas reservoirs. *Phys. Fluids* 34, 043101. doi:10.1063/5.0084975
- Shen, X., and Reible, D. (2015). An analytical solution for one-dimensional advective-dispersive solute equation in multilayered finite porous media. *Transp. Porous Media* 107, 657–666. doi:10.1007/s11242-015-0460-6
- Song, H., Cao, Y., Yu, M., Wang, Y., Killough, J. E., and Leung, J. (2015). Impact of permeability heterogeneity on production characteristics in water-bearing tight gas reservoirs with threshold pressure gradient. *J. Nat. Gas. Sci. Eng.* 22, 172–181. doi:10.1016/j.jngse.2014.11.028
- Swami, D., Sharma, P. K., Ojha, C. S. P., Guleria, A., and Sharma, A. (2018). Asymptotic behavior of mass transfer for solute transport through stratified porous medium. *Transp. Porous Media* 124, 699–721. doi:10.1007/s11242-018-1090-6
- Tian, W., Li, A., Ren, X., and Josephine, Y. (2018). The threshold pressure gradient effect in the tight sandstone gas reservoirs with high water saturation. *Fuel* 226, 221–229. doi:10.1016/j.fuel.2018.03.192
- Voller, V. R., Swenson, J. B., and Paola, C. (2004). An analytical solution for a stefan problem with variable latent heat. *Int. J. Heat. Mass Transf.* 47, 5387–5390. doi:10.1016/j.ijheatmasstransfer.2004.07.007
- Wang, F., and Cheng, H. (2020). Effect of tortuosity on the stress-dependent permeability of tight sandstones: Analytical modelling and experimentation. *Mar. Pet. Geol.* 120, 104524. doi:10.1016/j.marpetgeo.2020.104524
- Wang, F. Y., Liu, Z. C., Cai, J. C., and Gao, J. (2018). A fractal model for low-velocity non-Darcy flow in tight oil reservoirs considering boundary-layer effect. *Fractals* 26, 1850077. doi:10.1142/s0218348x18500779
- Wang, H. X., Xu, W., Zhang, Y. Y., and Sun, D. A. (2021). Simplified solution to one-dimensional consolidation with threshold gradient. *Comput. Geotech.* 131, 103943. doi:10.1016/j.compgeo.2020.103943
- Wang, S. F., and Yu, B. M. (2011). A fractal model for the starting pressure gradient for Bingham fluids in porous media embedded with fractal-like tree networks. *Int. J. Heat. Mass Transf.* 54, 4491–4494. doi:10.1016/j.ijheatmasstransfer.2011.06.031
- Wang, S. J., Huang, Y. Z., and Civan, F. (2006). Experimental and theoretical investigation of the Zaoxuan field heavy oil flow through porous media. *J. Pet. Sci. Eng.* 50, 83–101. doi:10.1016/j.petro.2005.06.015
- Wang, S., Zhu, W., Qian, X., Xu, H., and Fan, X. (2016). Study of threshold gradient for compacted clays based on effective aperture. *Environ. Earth Sci.* 75, 693. doi:10.1007/s12665-016-5502-z
- Wu, L. Z., Liu, G. G., Wang, L. C., Zhang, L. M., Li, B. E., and Li, B. (2016). Numerical analysis of 1D coupled infiltration and deformation in layered unsaturated porous medium. *Environ. Earth Sci.* 75, 761. doi:10.1007/s12665-016-5579-4
- Wu, Z., Cui, C., Trivedi, J., Ai, N., and Tang, W. (2019). Pressure analysis for volume fracturing vertical well considering low-velocity non-Darcy flow and stress sensitivity. *Geofluids* 2019, 2046061. doi:10.1155/2019/2046061
- Xie, K. H., Wang, K., Wang, Y. L., and Li, C. X. (2010). Analytical solution for one-dimensional consolidation of clayey soils with a threshold gradient. *Comput. Geotech.* 37, 487–493. doi:10.1016/j.compgeo.2010.02.001
- Xiong, W., Lei, Q., Gao, S. S., Hu, Z. M., and Xue, H. (2009). Pseudo threshold pressure gradient to flow for low permeability reservoirs. *Petroleum Explor. Dev.* 36, 232–236. doi:10.1016/s1876-3804(09)60123-3

- Yang, L., Ge, H., Shi, X., Cheng, Y., Zhang, K., Chen, H., et al. (2016). The effect of microstructure and rock mineralogy on water imbibition characteristics in tight reservoirs. *J. Nat. Gas. Sci. Eng.* 34, 1461–1471. doi:10.1016/j.jngse.2016.01.002
- Yao, J., Liu, W. C., and Chen, Z. (2013). Numerical solution of a moving boundary problem of one-dimensional flow in semi-infinite long porous media with threshold pressure gradient. *Math. Probl. Eng.* 2013, 1–7. doi:10.1155/2013/384246
- Ye, W., Wang, X., Cao, C., and Yu, W. (2019). A fractal model for threshold pressure gradient of tight oil reservoirs. *J. Pet. Sci. Eng.* 179, 427–431. doi:10.1016/j.petrol.2019.04.039
- Yin, D. T., Li, C. G., Song, S., and Liu, K. (2022). Nonlinear seepage mathematical model of fractured tight stress sensitive reservoir and its application. *Front. Energy Res.* 10, 819430. doi:10.3389/fenrg.2022.819430
- Zeng, J., Wang, X., Guo, J., Zeng, F., and Zhang, Q. (2018). Composite linear flow model for multi-fractured horizontal wells in tight sand reservoirs with the threshold pressure gradient. *J. Pet. Sci. Eng.* 165, 890–912. doi:10.1016/j.petrol.2017.12.095
- Zhang, J. G., Du, D. F., Hou, J., Lei, G. L., and Lv, A. M. (2015). *Seepage flow mechanics in oil and gas reservoirs*. Qingdao: China University of Petroleum Press.
- Zhang, Q., Liu, W., and Taleghani, A. D. (2022). Numerical study on non-Newtonian Bingham fluid flow in development of heavy oil reservoirs using radiofrequency heating method. *Energy* 239, 122385. doi:10.1016/j.energy.2021.122385
- Zhang, X., Kuang, S., Shi, Y., Wang, X., Zhu, W., Cai, Q., et al. (2019a). A new liquid transport model considering complex influencing factors for nano-to micro-sized circular tubes and porous media. *Phys. Fluids* 31, 112006. doi:10.1063/1.5126926
- Zhang, X., Shi, Y., Kuang, S., Zhu, W., Cai, Q., Wang, Y., et al. (2019b). A new liquid transport model considering complex influencing factors for nano- to micro-sized circular tubes and porous media. *Phys. Fluids* 31, 112006. doi:10.1063/1.5126926
- Zhang, X., Zhu, W., Cai, Q., Shi, Y., Wu, X., Jin, T., et al. (2018). Compressible liquid flow in nano- or micro-sized circular tubes considering wall-liquid lifshitz-van Der waals interaction. *Phys. Fluids* 30, 062002. doi:10.1063/1.5023291
- Zhao, G., You, Q., Tao, J., Gu, C., Aziz, H., Ma, L., et al. (2018). Preparation and application of a novel phenolic resin dispersed particle gel for in-depth profile control in low permeability reservoirs. *J. Pet. Sci. Eng.* 161, 703–714. doi:10.1016/j.petrol.2017.11.070
- Zhao, M. W., Cao, M. J., He, H. N., and Dai, C. L. (2020). Study on variation laws of fluid threshold pressure gradient in low permeable reservoir. *Energies* 13, 3704. doi:10.3390/en13143704
- Zhao, X., Liu, X., Yang, Z., Wang, F., Zhang, Y., Liu, G., et al. (2021). Experimental study on physical modeling of flow mechanism in volumetric fracturing of tight oil reservoir. *Phys. Fluids* 33, 107118. doi:10.1063/5.0068594
- Zhou, Y. (2019). Analytical solution for one-dimensional radial flow caused by line source in porous medium with threshold pressure gradient. *Appl. Math. Model.* 67, 151–158. doi:10.1016/j.apm.2018.10.024
- Zhou, Y., Zhang, L., and Wang, T. (2021). Analytical solution for one-dimensional non-Darcy flow with bilinear relation in porous medium caused by line source. *Appl. Math. Comput.* 392, 125674. doi:10.1016/j.amc.2020.125674
- Zhou, Z., Zhao, J., Zhou, T., and Huang, Y. (2017). Study on in-depth profile control system of low-permeability reservoir in block H of daqing oil field. *J. Pet. Sci. Eng.* 157, 1192–1196. doi:10.1016/j.petrol.2017.08.008

Conflict of Interest: HF was employed by China ZhenHuaOil Co. Ltd.

The remaining authors declare that the research was conducted in the absence of any commercial or financial relationships that could be construed as a potential conflict of interest.

Publisher's Note: All claims expressed in this article are solely those of the authors and do not necessarily represent those of their affiliated organizations, or those of the publisher, the editors, and the reviewers. Any product that may be evaluated in this article, or claim that may be made by its manufacturer, is not guaranteed or endorsed by the publisher.

Copyright © 2022 Wang, Liu, Ding, Kong and Fan. This is an open-access article distributed under the terms of the Creative Commons Attribution License (CC BY). The use, distribution or reproduction in other forums is permitted, provided the original author(s) and the copyright owner(s) are credited and that the original publication in this journal is cited, in accordance with accepted academic practice. No use, distribution or reproduction is permitted which does not comply with these terms.

APPENDIX A

As MB conditions caused by the TPG are neglected, an infinite outer boundary condition (Liu et al., 2019a; Liu, 2019; Liu W. C., 2020) has to be used instead. Then, without considering MB conditions, a dimensionless mathematical model for the 1D commingled preferential Darcian flow and non-Darcian flow in a dual-layered formation is built:

$$2\alpha_1 \cdot \frac{\partial^2 U_1}{\partial X^2} = \frac{\partial U_1}{\partial T}, \quad 0 \leq X < +\infty, \quad (\text{A1})$$

$$U_1|_{T=0} = 0, \quad (\text{A2})$$

$$U_1|_{X \rightarrow +\infty} = 0, \quad (\text{A3})$$

$$2\alpha_2 \cdot \frac{\partial^2 U_2}{\partial X^2} = \frac{\partial U_2}{\partial T}, \quad 0 \leq X < +\infty, \quad (\text{A4})$$

$$U_2|_{T=0} = 0, \quad (\text{A5})$$

$$U_2|_{X \rightarrow +\infty} = 0, \quad (\text{A6})$$

$$\beta_1 \cdot \frac{\partial U_1}{\partial X} \Big|_{X=0} + \beta_2 \cdot \frac{\partial U_2}{\partial X} \Big|_{X=0} = -(1 + \beta_1 \cdot \Lambda), \quad (\text{A7})$$

$$U_2|_{X=0} = U_1|_{X=0}. \quad (\text{A8})$$

Similarity transformations including Eqs. 30–32 can still be used here for the EAS of the self-similarity model formulated by Eqs. A1–A8. By using the similar solution procedures in the previous work (Liu W. C., 2020), the EAS of the model can be expressed as follows:

$$U_1(X, T) = \left\{ \begin{array}{l} -\sqrt{\frac{\alpha_2}{\alpha_1}} \cdot \frac{1}{\beta_1 \cdot \sqrt{\frac{\alpha_2}{\alpha_1}} + \beta_2} \cdot X + \\ \frac{1}{\beta_1 \cdot \sqrt{\frac{\alpha_2}{\alpha_1}} + \beta_2} \cdot \sqrt{\frac{2 \cdot \alpha_2}{\pi}} \cdot \exp\left(-\frac{X^2}{8\alpha_1 T}\right) \cdot 2T^{\frac{1}{2}} \\ + \frac{1}{\beta_1 \cdot \sqrt{\frac{\alpha_2}{\alpha_1}} + \beta_2} \cdot \sqrt{\alpha_2} \cdot \operatorname{erf}\left(\sqrt{\frac{X^2}{8\alpha_1 T}}\right) \cdot \sqrt{\frac{X^2}{\alpha_1}} \end{array} \right\} \cdot (1 + \beta_1 \cdot \Lambda), \quad 0 \leq X < +\infty, \quad (\text{A9})$$

$$U_2(X, T) = \left\{ \begin{array}{l} -\frac{X}{\beta_1 \cdot \sqrt{\frac{\alpha_2}{\alpha_1}} + \beta_2} + \\ \frac{1}{\beta_1 \cdot \sqrt{\frac{\alpha_2}{\alpha_1}} + \beta_2} \cdot \sqrt{\frac{2 \cdot \alpha_2}{\pi}} \cdot \exp\left(-\frac{X^2}{8\alpha_1 T}\right) \cdot 2T^{\frac{1}{2}} \\ + \frac{1}{\beta_1 \cdot \sqrt{\frac{\alpha_2}{\alpha_1}} + \beta_2} \cdot \sqrt{\alpha_2} \cdot \operatorname{erf}\left(\sqrt{\frac{X^2}{8\alpha_1 T}}\right) \cdot \sqrt{\frac{X^2}{\alpha_2}} \end{array} \right\} \cdot (1 + \beta_1 \cdot \Lambda), \quad 0 \leq X < +\infty. \quad (\text{A10})$$

APPENDIX B

From Eq. 41, we have a dimensionless transient pressure (noted as \tilde{U}):

$$\tilde{U} = U_1(0, T) = \Lambda \cdot \theta \cdot \exp\left(\frac{\theta^2}{2\alpha_1}\right) \cdot 2T^{\frac{1}{2}}. \quad (\text{B1})$$

\tilde{U} corresponds to the model in consideration of the MB caused by the TPG.

By using Eq. 43, Eq. B1 can be equivalent to the following equation:

$$\tilde{U} = \frac{\sqrt{2} \cdot 2T^{\frac{1}{2}}}{\sqrt{\pi} \cdot \beta_1 \cdot \operatorname{erf}\left(\frac{\sqrt{2}}{2} \cdot \sqrt{\frac{\theta^2}{\alpha_1}}\right) \cdot \sqrt{\frac{1}{\alpha_1}} + \sqrt{\pi} \cdot \beta_2 \cdot \sqrt{\frac{1}{\alpha_2}}}. \quad (\text{B2})$$

From Eq. A9, we have another dimensionless transient pressure (noted as \bar{U}):

$$\bar{U} = U_1(0, T) = \frac{1}{\beta_1 \cdot \sqrt{\frac{1}{\alpha_1}} + \beta_2 \cdot \sqrt{\frac{1}{\alpha_2}}} \cdot \sqrt{\frac{2}{\pi}} \cdot 2T^{\frac{1}{2}} \cdot (1 + \beta_1 \cdot \Lambda). \quad (\text{B3})$$

\bar{U} corresponds to the model without consideration of the MB caused by the TPG.

Then, when MB is not considered in the modeling, a relative error ε can be directly formulated by Eqs. B1 and B3:

$$\varepsilon = \left| \frac{\bar{U}}{\tilde{U}} - 1 \right| = \left| \frac{\beta_1 \cdot \operatorname{erf}\left(\frac{\sqrt{2}}{2} \cdot \sqrt{\frac{\theta^2}{\alpha_1}}\right) \cdot \sqrt{\frac{1}{\alpha_1}} + \beta_2 \cdot \sqrt{\frac{1}{\alpha_2}}}{\beta_1 \cdot \sqrt{\frac{1}{\alpha_1}} + \beta_2 \cdot \sqrt{\frac{1}{\alpha_2}}} \cdot (1 + \beta_1 \cdot \Lambda) - 1 \right| \times 100\%. \quad (\text{B4})$$

NOMENCLATURE

C_{t1} comprehensive compressibility coefficient of the low-permeability layer, $(0.1 \text{ MPa})^{-1}$

C_{t2} comprehensive compressibility coefficient of the high-permeability layer, $(0.1 \text{ MPa})^{-1}$

D_1 LPR of the low-permeability tight layer, dimensionless

D_2 LPR of the high-permeability layer, dimensionless

F Function defined by Eq. 44, dimensionless

h_1 thickness of the low-permeability tight layer, cm

h_2 thickness of the high-permeability layer, cm

H_1 LTR of the low-permeability tight layer, dimensionless

H_2 LTR of the high-permeability layer, dimensionless

k_1 permeability of the low-permeability tight layer, μm^2

k_2 permeability of the high-permeability layer, μm^2

k_{avg} thickness-weighted formation permeability, μm^2

L wideness of the low-permeability tight layer and high-permeability layer, cm

p_1 pressure in the low-permeability tight layer, 0.1 MPa

p_2 pressure in the high-permeability layer, 0.1 MPa

p_i initial pressure, 0.1 MPa

Q_0 total production rate, $\text{cm}^3\cdot\text{s}^{-1}$

Q_{1D} dimensionless production rate from the low-permeability tight layer, dimensionless

Q_{2D} dimensionless production rate from the high-permeability layer, dimensionless

S transient moving boundary distance, cm

t time, s

T dimensionless time, dimensionless

U_1 dimensionless pressure in the low-permeability tight layer, dimensionless

U_2 dimensionless pressure in the high-permeability layer, dimensionless

\tilde{U} dimensionless transient pressure when the moving boundary is considered in the dimensionless model, dimensionless

\bar{U} dimensionless transient pressure when the moving boundary is not considered in the dimensionless model, dimensionless

x distance, cm

X dimensionless distance, dimensionless

x, y and z coordinate axes in rectangular coordinate systems, as shown in Figure 1

α_1 and α_2 defined parameters, dimensionless

β_1 and β_2 defined parameters, dimensionless

δ dimensionless moving boundary distance, dimensionless

ε relative error, dimensionless

η, θ, ξ and ψ relevant similarity transformation variables, dimensionless

θ_0 unique positive solution of Eq. 43, dimensionless

θ_1 positive value of θ which makes $f(\theta_1) > 0$, dimensionless

λ threshold pressure gradient, 0.1 MPa cm^{-1}

Λ dimensionless threshold pressure gradient, dimensionless

μ fluid viscosity, $\text{mPa}\cdot\text{s}$

v_1 fluid velocity in the low-permeability tight layer, $\text{cm}\cdot\text{s}^{-1}$

v_2 fluid velocity in the high-permeability layer, $\text{cm}\cdot\text{s}^{-1}$

v_{w0} constant average flow velocity, $\text{cm}\cdot\text{s}^{-1}$

ϕ_{i1} initial porosity of the low-permeability tight layer, f

ϕ_{i2} initial porosity of the high-permeability layer, f

ω_1 LESR of the low-permeability tight layer, dimensionless

ω_2 LESR of the high-permeability layer, dimensionless



OPEN ACCESS

EDITED BY

Fuyong Wang,
China University of Petroleum, Beijing,
China

REVIEWED BY

Hongsheng Wang,
Virginia Tech, United States
Yue Xiao,
Research Institute of Petroleum
Exploration and Development (RIPED),
China
Jiawei Tu,
New Mexico Institute of Mining and
Technology, United States

*CORRESPONDENCE

Lei Li,
lei.li@upc.edu.cn

SPECIALTY SECTION

This article was submitted to Advanced
Clean Fuel Technologies,
a section of the journal
Frontiers in Energy Research

RECEIVED 11 September 2022

ACCEPTED 21 October 2022

PUBLISHED 03 November 2022

CITATION

Li L, Zhou X, Su Y, Xiao P, Cui M and
Zheng J (2022), Potential and
challenges for the new method
supercritical CO₂/H₂O mixed fluid huff-
n-puff in shale oil EOR.
Front. Energy Res. 10:1041851.
doi: 10.3389/fenrg.2022.1041851

COPYRIGHT

© 2022 Li, Zhou, Su, Xiao, Cui and
Zheng. This is an open-access article
distributed under the terms of the
Creative Commons Attribution License
(CC BY). The use, distribution or
reproduction in other forums is
permitted, provided the original
author(s) and the copyright owner(s) are
credited and that the original
publication in this journal is cited, in
accordance with accepted academic
practice. No use, distribution or
reproduction is permitted which does
not comply with these terms.

Potential and challenges for the new method supercritical CO₂/H₂O mixed fluid huff-n-puff in shale oil EOR

Lei Li^{1,2*}, Xiaomei Zhou^{1,2}, Yuliang Su^{1,2}, Pufu Xiao¹, Maolei Cui¹
and Jianyang Zheng²

¹State Key Laboratory of Shale Oil and Gas Enrichment Mechanisms and Effective Development, Beijing, China, ²School of Petroleum Engineering, China University of Petroleum, Qingdao, China

KEYWORDS

supercritical CO₂/H₂O, huff-n-puff technology, shale oil EOR, injection methods, organic nanopores

Introduction

The successful development of shale oil is important to ensure energy security. However, shale oil recovery is typically less than 10%. Supercritical CO₂/H₂O huff-n-puff is a potential EOR strategy for shale oil development, but it is still in the exploratory stage. Supercritical CO₂/H₂O huff-n-puff exerts the capacity of two kinds supercritical fluids, and using the same well as an injection well and a production well, which solves the problem of gas channeling in shale oil reservoir after fracturing by conventional gas drive method. This paper provides a brief overview of the advantages, potential, injection method, summarize the problems and future research directions of the new technology in shale oil development, which is of great important for the shale oil reservoir developments.

Proposal of supercritical CO₂/H₂O huff-n-puff in shale oil reservoirs development

Shale oil is a promising energy source with great potential for development. Shale oil storages in mud shale matrix pores, micro-fractures and thin interlayers of non-source rocks in the occurrence state of free state and dissolved or absorbed state in organic kerogen (Feng et al., 2020; Xu et al., 2022). These characteristics lead to the poor development effect. The movable reserves of shale oil are generally less than 10% under the fracturing conditions of horizontal wells with existing technologies (Hoffman, 2018; Jia et al., 2019). As the low porosity and low permeability, high clay content are key characteristics of shale oil, conventional water injection development is not suitable for shale oil development because of its difficulties in injection, small sweep volume and serious water sensitivity. As the most widely used gas displacement agent, supercritical fluid CO₂ has the potential to develop shale oil efficiently. Compared with CH₄ and N₂, CO₂ is more easily miscible with crude oil, increasing the flow capacity of oil and thus improving oil recovery by 5%–25% (He et al., 2022; Jin et al., 2017; Sheng, 2015).

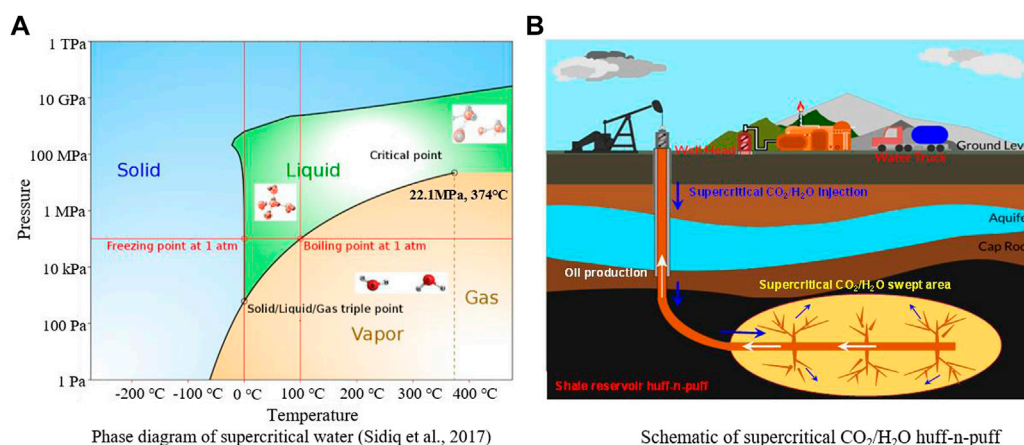


FIGURE 1

Supercritical CO₂/H₂O huff-n-puff in shale oil reservoirs. (A) Phase diagram of supercritical water; (B) Schematic of supercritical CO₂/H₂O huff-n-puff.

Supercritical H₂O is a fluid with better performance than supercritical CO₂, with higher dissolving capacity, increasing solvent diffusion coefficient ability and better reactivity, which can improve sweep coefficient and oil washing efficiency in the process of oil displacement (Walther and Woodland, 1993; Schaef and McGrail, 2004; Li et al., 2020). Meanwhile, the better dissolving capacity and diffusion performance are beneficial for entering nanopores of organic matter, which has the potential to exploit the adsorption and dissolution oil (Weingärtner and Franck, 2005; Caniaz and Erkey, 2014; Zheng et al., 2020). Therefore, the use of supercritical CO₂/H₂O mixed fluid to improve shale oil recovery is considered to be a promising technology.

Status of supercritical CO₂ huff-n-puff in shale oil reservoirs development

In the past few years, supercritical fluid has been applied in many fields as solvent or reaction medium due to its unique properties. Under supercritical conditions, by controlling the pressure, the reaction environment can be manipulated, which can increase the solubility of supercritical fluid in crude oil, enhance the interphase mass transfer ability, and improve the oil stripping effect and oil displacement efficiency. At present, a large number of experiments and numerical simulation studies have been carried out to improve shale oil recovery by supercritical CO₂ (ScCO₂) huff-n-puff. Gamadi et al., (2013), Gamadi et al., (2014) found in laboratory core-scale experiments that the use of nitrogen or CO₂ huff-n-puff at different injection pressures can increase shale core recovery by approximately 10%–50%. And the effect of enhanced oil

recovery relies on injection pressure, huff-n-puff cycles, core size, soaking time and gas injection rate, etc., (Hoffman, 2012; Song and Yang, 2013; Yu and Sheng, 2015; Yu et al., 2016; Zhang, 2016; Li et al., 2017).

Core-scale macroscopic experiments in laboratories have proved that ScCO₂ huff-n-puff is an effective method to improve shale oil recovery. Field tests of ScCO₂ huff-n-puff EOR were carried out in Bakken formation and Eagle Ford in North America. They all reported this method is effective in some extent. However, the ultimate recovery factor of different types of shale rock samples fluctuates greatly after multiple cycles of huff-n-puff. For most shale oil reservoirs, the minimum miscible pressure (MMP) of CO₂ and crude oil is higher than the formation pressure, thus it could not achieve the miscible state, resulting in unsatisfied displacement effect.

The advantages of supercritical H₂O injection fluid

Compared with ScCO₂, the properties of supercritical H₂O (ScH₂O) are more advantageous. As shown in Figure 1A (Sidiq et al., 2017), the condition of ScH₂O is that the temperature and pressure exceed the critical point (22.1 MPa, 374 °C), at which time the gas-liquid interface disappears and most of the hydrogen bonds are distorted or broken (Zhao et al., 2019). Because of the absence of surface tension, ScH₂O can enter micropores and nanopores more easily. And in the vicinity of the critical point, the fluid density increases sharply with the increase of pressure, so that the supercritical fluid has a higher density, which is close to the value of liquid. Water exhibits properties closer to non-polar organic compounds and becomes a good solvent for non-polar substances. It can dissolve many solid or high boiling

substances and form a homogeneous phase with organic substances (Adschiri et al., 2011). This feature creates conditions for supercritical water extraction of crude oil.

The viscosity of supercritical water is only one-tenth of that of normal water. The low viscosity makes ScH_2O and solute molecules have higher mobility, and solute molecules can easily diffuse in ScH_2O (Guo et al., 2015; Zheng et al., 2020). Supercritical fluid can not only be used as reaction medium in chemical reaction, but also directly participate in reaction. Supercritical fluid can change the phase behavior, diffusion rate and solvation effect, homogenize the reaction mixture and increase the diffusion coefficient (Heltai et al., 2002; Yang et al., 2019; Chen et al., 2020), thus controlling the phase separation process and the distribution of products. When ScH_2O is used as the reaction medium, its specific physical and chemical properties will affect the progress of the reaction. For example, at 400°C and 35 MPa, the ion product increases to 7 times that of the normal state, which is conducive to the formation of hydrogen bonds. This property can promote the conversion of organic kerogen in shale reservoir and drive oil out of organic matter (Akiya and Savage, 2002; Fauvel et al., 2003).

Therefore, the high dissolving ability, wide diffusivity and strong reactivity of ScH_2O can improve the sweep coefficient and displacement efficiency, thereby improving the oil recovery. The flow characteristics of ScH_2O in the flow process have an important impact on oil recovery, and the heat transfer process from wellbore to formation is an important factor to be considered in the energy utilization process (Nian et al., 2016; Phuoc et al., 2019; Gao et al., 2021). Because of its higher temperature, better cracking rate and larger heating area, ScH_2O flooding shows better effect than hot water flooding and steam flooding (Sun et al., 2018). And in heavy oil production, the operational parameters for supercritical water injection are slightly influencing the reservoir performance, and the influence is negligible as long as a minimum miscible pressure is achieved (Nie, 2021; Ma et al., 2022). As an organic solvent, ScH_2O provides a homogeneous environment for the recovery and thermal cracking of heavy oil. In addition, the properties of ScH_2O can be adjusted over a wide range of temperatures and pressures, which can not only reduce the viscosity of crude oil as a heat carrier, but also eliminate seepage resistance and carbon loss in thermal recovery as a solvent (Zhao et al., 2018).

Status of supercritical $\text{CO}_2/\text{H}_2\text{O}$ huff-n-puff in enhancing oil recovery

ScCO_2 and ScH_2O have great potential for shale oil development. The characteristics of strong mass transfer rate to crude oil, efficient extraction capacity, wide source, easy access of ScCO_2 , combined with the properties of ScH_2O , supercritical $\text{CO}_2/\text{H}_2\text{O}$ mixed fluid huff-n-puff can give full play to their

respective advantages. In the process of supercritical $\text{CO}_2/\text{H}_2\text{O}$ mixed fluid injection as shown in Figure 1B, the interaction of ScCO_2 and ScH_2O under supercritical conditions (Deleau et al., 2022), the influence of mixed fluid on pore permeability structure (Liu et al., 2020; Zhou et al., 2020) and mechanical properties (Zhou et al., 2019), the interaction of supercritical $\text{CO}_2/\text{H}_2\text{O}$ -shale and its influence on shale adsorption characteristics (Yang et al., 2022) and so on, all play important roles in enhancing oil recovery.

Injection methods of supercritical $\text{CO}_2/\text{H}_2\text{O}$ huff-n-puff

Supercritical $\text{CO}_2/\text{H}_2\text{O}$ huff-n-puff can be divided into two methods: one is injecting supercritical fluid from the surface; the other one is to inject liquid $\text{CO}_2/\text{H}_2\text{O}$ from the surface and heated in the bottom of the wellbore to achieve supercritical conditions (Fakher and Imqam, 2020; Gao et al., 2022; Ren et al., 2023). For method one, the percolation heat transfer of supercritical fluid in wellbore and reservoir is very complicated, and it is difficult to maintain the high-temperature and high-pressure (HTHP) environment of ScH_2O during transportation. In addition, the mixed fluid is corrosive to the pipe string, so special attention should be paid to the HTHP resistance and corrosion resistance of pipelines in the process of preparation, storage, transportation and injection, which needs advance technology and high requirements for material. For method two, as *in situ* combustion, electromagnetic heating or microwave heating and other formation heat treatment to improve oil and gas recovery is more and more popular in recent years, these treatment methods can be used to achieve the supercritical temperature of CO_2 and H_2O . Thus, the complex heat transfer problems and stringent pipeline material requirements of supercritical fluid injection from wellbore to the reservoir can be solved. In this way, method two is more feasible.

The research direction of supercritical $\text{CO}_2/\text{H}_2\text{O}$ huff-n-puff for shale oil development

Novel laboratory experiments should be designed to study the feasibility of supercritical $\text{CO}_2/\text{H}_2\text{O}$ huff-n-puff in shale oil recovery. 1) The pore structure and mineral composition before and after the interaction of supercritical $\text{CO}_2/\text{H}_2\text{O}$ can be studied by combining nuclear magnetic resonance technology, mercury injection method and scanning electron microscopy test. 2) The interaction between supercritical $\text{CO}_2/\text{H}_2\text{O}$ and crude oil can be obtained by means of HTHP PVT test. 3) Core scale supercritical $\text{CO}_2/\text{H}_2\text{O}$ huff-n-puff experiments need to be applied to evaluate the EOR performance and the optimization of operation

parameters. 4) The biggest limitation of the existing experimental equipment is that it cannot meet the HTHP conditions of ScH_2O , and the materials of the experimental equipment should be resistant to HTHP as well as corrosion. Nickel-based alloys have excellent strength and corrosion resistance and can be used for pipeline transportation and ScH_2O storage. Therefore, experimental equipment made of nickel-based alloy can be used for indoor HTHP experiments to study the effects of temperature, pressure and injection parameters on the huff and huff effects of supercritical $\text{CO}_2/\text{H}_2\text{O}$ mixed fluid. 5) It is necessary to design microscopic experiments and combined with molecular simulation technology to explore the competitive adsorption, dissolution, diffusion and displacement processes in microscopic pores during the huff-n-huff process of supercritical $\text{CO}_2/\text{H}_2\text{O}$ mixed fluid, and quantitatively characterize the mobilization mechanism of crude oil in organic matter and inorganic matter.

Conclusion

In conclusion, the mixed fluid of supercritical $\text{CO}_2/\text{H}_2\text{O}$ huff-n-puff can give full play to their respective advantages and have great potential for shale oil development. The main challenges of this approach are summarized in detailed below:

- 1) Whether the supercritical condition of $\text{CO}_2/\text{H}_2\text{O}$ can be achieved under shale reservoir conditions is the focus of research. Some formation heat treatment methods such as electromagnetic heating can be combined to meet the supercritical state of $\text{CO}_2/\text{H}_2\text{O}$.
- 2) The interaction between supercritical $\text{CO}_2/\text{H}_2\text{O}$ and shale reservoir is very important for clarifying the mechanism of supercritical $\text{CO}_2/\text{H}_2\text{O}$ huff-n-huff to improve shale oil recovery. The next step is to quantitatively characterize the effects of the two fluids on rocks and pores by means of various experimental studies.
- 3) Laboratory core scale experiment is an important method to verify the feasibility of supercritical $\text{CO}_2/\text{H}_2\text{O}$ mixed fluid huff-n-huff to improve shale oil recovery. Materials should be selected to make experimental apparatus suitable for test conditions.
- 4) Organic nanopores are developed in shale reservoirs. The next research direction is to determine the quantitative characterization methods of dissolution, displacement, diffusion, competitive adsorption and other processes in microscopic pores in the process of huff-n-huff, and to clarify the influence of supercritical $\text{CO}_2/\text{H}_2\text{O}$ mixed fluid on organic matter.

Author contributions

In this article, LL: performed the experiments and wrote the draft. XZ: Literature review, Investigation. YS: Supervision, Investigation. MC: Writing-Reviewing and Editing; PX: contributed to the interpretation and discussion of results; JZ: Literature review, wrote the draft.

Acknowledgments

The authors would like to acknowledge financial support from the National Natural Science Foundation of China (No.51904324), Open Fund (G5800-20-ZS-KFGY017) of State Key Laboratory of Shale Oil and Gas Enrichment Mechanisms and Effective Development.

Conflict of interest

The authors declare that the research was conducted in the absence of any commercial or financial relationships that could be construed as a potential conflict of interest.

Publisher's note

All claims expressed in this article are solely those of the authors and do not necessarily represent those of their affiliated organizations, or those of the publisher, the editors and the reviewers. Any product that may be evaluated in this article, or claim that may be made by its manufacturer, is not guaranteed or endorsed by the publisher.

References

- Adschiri, T., Lee, Y. W., Goto, M., and Takami, S. (2011). Green materials synthesis with supercritical water. *Green Chem.* 13 (6), 1380–1390. doi:10.1039/c1gc15158d
- Akiya, N., and Savage, P. E. (2002). Roles of water for chemical reactions in high-temperature water. *Chem. Rev.* 102 (8), 2725–2750. doi:10.1021/cr000668w
- Caniaz, R. O., and Erkey, C. (2014). Process intensification for heavy oil upgrading using supercritical water. *Chem. Eng. Res. Des.* 92 (10), 1845–1863. doi:10.1016/j.cherd.2014.06.007
- Chen, L., Liu, D., Zhang, H., and Li, Q. (2020). Theoretical investigations on heat transfer to $\text{H}_2\text{O}/\text{CO}_2$ mixtures in supercritical region. *Sci. China Technol. Sci.* 63 (6), 1018–1024. doi:10.1007/s11431-019-1515-3
- Deleau, T., Letourneau, J. J., Camy, S., Aubin, J., and Espitalier, F. (2022). Determination of mass transfer coefficients in high-pressure $\text{CO}_2\text{-H}_2\text{O}$ flows in microcapillaries using a colorimetric method. *Chem. Eng. Sci.* 248, 117161. doi:10.1016/j.ces.2021.117161
- Fakher, S., and Imqam, A. (2020). Application of carbon dioxide injection in shale oil reservoirs for increasing oil recovery and carbon dioxide storage. *Fuel* 265, 116944. doi:10.1016/j.fuel.2019.116944

- Fauvel, E., Jousset-Dubien, C., Pomier, E., Guichardon, P., Charbit, G., Charbit, F., et al. (2003). Modeling of a porous reactor for supercritical water oxidation by a residence time distribution study. *Ind. Eng. Chem. Res.* 42 (10), 2122–2130. doi:10.1021/ie0207616
- Feng, Q., Xu, S., Xing, X., Zhang, W., and Wang, S. (2020). Advances and challenges in shale oil development: A critical review. *Adv. Geo-Energy Res.* 4 (4), 406–418. doi:10.46690/ager.2020.04.06
- Gamadi, T. D., Sheng, J. J., Soliman, M. Y., Menouar, H., Watson, M. C., and Emadibaladehi, H. (2014). "An experimental study of cyclic CO₂ injection to improve shale oil recovery," in Presented at SPE Improved Oil Recovery Symposium, Tulsa, 12–16 April. SPE-169142-MS. doi:10.2118/169142-ms
- Gao, J., Yao, Y., Wang, D., and Tong, H. (2021). A comprehensive model for simulating supercritical-water flow in a vertical heavy-oil well. *SPE J.* 26 (06), 4051–4066. doi:10.2118/205496-pa
- Gao, Y., Wan, T., Dong, Y., and Li, Y. (2022). Numerical and experimental investigation of production performance of *in-situ* conversion of shale oil by air injection. *Energy Rep.* 8, 1099–1112. doi:10.1016/j.egyr.2022.08.174
- Guo, L., Jin, H., and Lu, Y. (2015). Supercritical water gasification research and development in China. *J. Supercrit. Fluids* 96, 144–150. doi:10.1016/j.supflu.2014.09.023
- He, L., Jiaping, T., Siwei, M., Dongxu, L., Gang, C., and Yang, G. (2022). Application and prospects of CO₂ enhanced oil recovery technology in shale oil reservoir. *China Pet. explor.* 27 (1), 127. doi:10.3969/j.issn.1672-7703.2022.01.012
- Heltai, G., Fehér, B., Percsich, K., Barabás, B., and Fekete, I. (2002). Application of sequential extraction with supercritical CO₂, subcritical H₂O, and an H₂O/CO₂ mixture for estimation of environmentally mobile heavy metal fractions in sediments. *Anal. Bioanal. Chem.* 373 (8), 863–866. doi:10.1007/s00216-002-1388-6
- Hoffman, B. T. (2012). "Comparison of various gases for enhanced recovery from shale oil reservoirs," in SPE 154329, presented at SPE improved oil recovery symposium, Tulsa, OK; April 14–18. doi:10.2118/154329-ms
- Hoffman, B. T. (2018). "Huff-N-Puff gas injection pilot projects in the Eagle Ford," in Presented at the SPE Canada Unconventional Resources Conference, 13–14 March, Calgary, Alberta, Canada. SPE-189816-MS. doi:10.2118/189816-ms
- Jia, B., Tsau, J.-S., and Barati, R. (2019). A review of the current progress of CO₂ injection EOR and carbon storage in shale oil reservoirs. *Fuel* 236, 404–427. doi:10.1016/j.fuel.2018.08.103
- Jin, L., Hawthorne, S., Sorensen, J., Pekot, L., Kurz, B., Smith, S., et al. (2017). Advancing CO₂ enhanced oil recovery and storage in unconventional oil play—experimental studies on bakken shales. *Appl. Energy* 208, 171–183. doi:10.1016/j.apenergy.2017.10.054
- Li, G., Lu, Y., and Glarborg, P. (2020). Development of a detailed kinetic model for hydrogen oxidation in supercritical H₂O/CO₂ mixtures. *Energy fuels.* 34 (12), 15379–15388. doi:10.1021/acs.energyfuels.0c01914
- Li, L., Zhang, Y., and Sheng, J. J. (2017). Effect of the injection pressure on enhancing oil recovery in shale cores during the CO₂ huff-n-puff process when it is above and below the minimum miscibility pressure. *Energy fuels.* 31 (4), 3856–3867. doi:10.1021/acs.energyfuels.7b00031
- Liu, H., Zhu, Z., Patrick, W., Liu, J., Lei, H., and Zhang, L. (2020). Pore-scale numerical simulation of supercritical CO₂ migration in porous and fractured media saturated with water. *Adv. Geo-Energy Res.* 4 (4), 419–434. doi:10.46690/ager.2020.04.07
- Ma, H., Yang, Y., and Chen, Z. (2022). Numerical simulation of bitumen recovery via supercritical water injection with *in-situ* upgrading. *Fuel* 313, 122708. doi:10.1016/j.fuel.2021.122708
- Nian, Y.-L., Cheng, W.-L., Wang, C.-L., and Han, B.-B. (2016). Analysis for formation thermal properties of water injection well from temperature data. *Int. J. Therm. Sci.* 101, 158–168. doi:10.1016/j.ijthermalsci.2015.11.001
- Nie, B. (2021). A comprehensive model for simulating supercritical water flow in a vertical heavy oil well with parallel double tubes. *J. Pet. Sci. Eng.* 205, 108790. doi:10.1016/j.petrol.2021.108790
- Phuoc, T. X., Massoudi, M., Wang, P., and McKoy, M. L. (2019). Heat losses associated with the upward flow of air, water, CO₂ in geothermal production wells. *Int. J. Heat. Mass Transf.* 132, 249–258. doi:10.1016/j.ijheatmasstransfer.2018.11.168
- Ren, D., Wang, X., Kou, Z., Wang, S., Wang, H., Wang, X., et al. (2023). Feasibility evaluation of CO₂ EOR and storage in tight oil reservoirs: A demonstration project in the ordos basin. *Fuel* 331, 125652. doi:10.1016/j.fuel.2022.125652
- Schaefer, H. T., and McGrail, B. P. (2005). Direct measurements of pH and dissolved CO₂ in H₂O-CO₂ brine mixtures to supercritical conditions. *Greenh. Gas. Control Technol.* 7, 2169–2173. doi:10.1016/B978-008044704-9/50294-9
- Sheng, J. J. (2015). Enhanced oil recovery in shale reservoirs by gas injection. *J. Nat. Gas. Sci. Eng.* 22, 252–259. doi:10.1016/j.jngse.2014.12.002
- Sidiq, H., Amin, R., and Kennaird, T. (2017). The study of relative permeability and residual gas saturation at high pressures and high temperatures. *Adv. Geo-Energ. Res.* 1 (1), 64–68. doi:10.26804/ager.2017.01.06
- Song, C., and Yang, D. (2013). "Performance evaluation of CO₂ huff-n-puff processes in tight oil formations," in SPE Unconventional Resources Conference Canada. doi:10.2118/167217-ms
- Sun, F., Yao, Y., Li, G., and Li, X. (2018). Numerical simulation of supercritical-water flow in concentric-dual-tubing wells. *SPE J.* 23, 2188–2201. doi:10.2118/191363-pa
- Walther, J. V., and Woodland, A. B. (1993). Experimental determination and interpretation of the solubility of the assemblage microcline, muscovite, and quartz in supercritical H₂O. *Geochimica cosmochimica acta* 57 (11), 2431–2437. doi:10.1016/0016-7037(93)90407-N
- Weingärtner, H., and Franck, E. U. (2005). Supercritical water as a solvent. *Angew. Chem. Int. Ed.* 44 (18), 2672–2692. doi:10.1002/anie.200462468
- Xu, Y., Lun, Z., Pan, Z., Wang, H., Zhou, X., Zhao, C., et al. (2022). Occurrence space and state of shale oil: A review. *J. Pet. Sci. Eng.* 2022, 110183. doi:10.1016/j.petrol.2022.110183
- Yang, K., Zhou, J., Xian, X., Jiang, Y., Zhang, C., Lu, Z., et al. (2022). Gas adsorption characteristics changes in shale after supercritical CO₂-water exposure at different pressures and temperatures. *Fuel* 310, 122260. doi:10.1016/j.fuel.2021.122260
- Yang, X., Duan, C., Xu, J., Liu, Y., and Cao, B. (2019). A numerical study on the thermal conductivity of H₂O/CO₂/H₂ mixtures in supercritical regions of water for coal supercritical water gasification system. *Int. J. Heat Mass Transf.* 135, 413–424. doi:10.1016/j.ijheatmasstransfer.2019.01.146
- Yu, Y., Li, L., and Sheng, J. J. (2016). "Further discuss the roles of soaking time and pressure depletion rate in gas huff-n-puff process in fractured liquid-rich shale reservoirs," in SPE-181471-MS paper presented in at the SPE Annual Technical Conference and Exhibition held in Dubai, UAE, 26–28 September 2016. doi:10.2118/181471-ms
- Yu, Y., and Sheng, J. J. (2015). "An experimental investigation of the effect of pressure depletion rate on oil recovery from shale cores by cyclic N₂ injection," in SPE 178494 in SPE Unconventional Resources Technology Conference Held in San Antonio, Texas, 20–22 July. doi:10.2118/178494-ms
- Zhang, K. (2016). "Experimental and numerical investigation of oil recovery from Bakken formation by miscible CO₂ injection," in Paper SPE 184486 presented at the SPE international Student Paper Contest at the SPE Annual Technical Conference and Exhibition held in Dubai, UAE, 26–28 September 2016. doi:10.2118/184486-stu
- Zhao, Q., Guo, L., Huang, Z., Chen, L., Jin, H., and Wang, Y. (2018). Experimental investigation on enhanced oil recovery of extra heavy oil by supercritical water flooding. *Energy fuels.* 32 (2), 1685–1692. doi:10.1021/acs.energyfuels.7b03839
- Zhao, Q., Guo, L., Wang, Y., Jin, H., Chen, L., and Huang, Z. (2019). Enhanced oil recovery and *in situ* upgrading of heavy oil by supercritical water injection. *Energy fuels.* 34, 360–367. doi:10.1021/acs.energyfuels.9b03946
- Zheng, H., Yu, T., Qu, C., Li, W., and Wang, Y. (2020). Basic characteristics and application progress of supercritical water. *IOP Conf. Ser. Earth Environ. Sci.* 555, 012036. doi:10.1088/1755-1315/555/1/012036
- Zhou, J., Yang, K., Tian, S., Zhou, L., Xian, X., Jiang, Y., et al. (2019). CO₂-water-shale interaction induced shale microstructural alteration. *Fuel* 263, 116642. doi:10.1016/j.fuel.2019.116642
- Zhou, J., Yang, K., Zhou, L., Jiang, Y., Xian, X., Zhang, C., et al. (2020). Microstructure and mechanical properties alterations in shale treated via CO₂/CO₂-water exposure. *J. Pet. Sci. Eng.* 196, 108088. doi:10.1016/j.petrol.2020.108088



OPEN ACCESS

EDITED BY

Fuyong Wang,
China University of Petroleum, Beijing,
China

REVIEWED BY

Hu Guo,
China University of Petroleum, Beijing,
China
Youwei He,
Southwest Petroleum University, China

*CORRESPONDENCE

Yuwei Liu,
782343312@qq.com

SPECIALTY SECTION

This article was submitted to Advanced
Clean Fuel Technologies,
a section of the journal
Frontiers in Energy Research

RECEIVED 24 October 2022

ACCEPTED 23 November 2022

PUBLISHED 03 January 2023

CITATION

Li N, Li H, Tan X, Zhang L and Liu Y
(2023), Effect of retrograde
condensation and stress sensitivity on
properties of condensate gas reservoirs.
Front. Energy Res. 10:1078755.
doi: 10.3389/fenrg.2022.1078755

COPYRIGHT

© 2023 Li, Li, Tan, Zhang and Liu. This is
an open-access article distributed
under the terms of the [Creative
Commons Attribution License \(CC BY\)](#).
The use, distribution or reproduction in
other forums is permitted, provided the
original author(s) and the copyright
owner(s) are credited and that the
original publication in this journal is
cited, in accordance with accepted
academic practice. No use, distribution
or reproduction is permitted which does
not comply with these terms.

Effect of retrograde condensation and stress sensitivity on properties of condensate gas reservoirs

Nan Li¹, Haosen Li², Xianhong Tan¹, Lijun Zhang¹ and
Yuwei Liu^{2*}

¹CNOOC Research Institute Co. Ltd., Beijing, China, ²School of Civil and Resource Engineering,
University of Science and Technology, Beijing, China

In the production process of low permeability condensate gas reservoir, the reverse condensate action and stress sensitivity will lead to the decrease of reservoir permeability and gas well productivity. However, there are few studies on the effect of retrograde condensation and stress sensitivity on permeability. In this study, the stress-sensitive experiments using the method with constant confining pressure but variable inner pressure were carried out on three cores from the BZ gas field in southwestern Bohai Sea. The test result that use the nitrogen as the experimental fluid represent the effect of core skeleton damage on reservoir permeability during formation pressure drop, and the test result that use the condensate gas as the experimental fluid represent the effect of core skeleton damage and retrograde condensation on reservoir permeability. The results reveal that when the formation pressure drops to the dew point pressure, retrograde condensation damage is the main cause of permeability decline. And the effects of core skeleton damage will increase as the formation pressure drops and exceed the retrograde condensation damage when the net stress is greater 7 MPa. When the net stress reaches 20 MPa, the core skeleton damage accounts for more than 90% of the total damage. Furthermore, the gas well production was calculated considering stress sensitivity and retrograde condensation based on the experimental results, the result shows that gas well production decreases by 97.65% when retrograde condensation is considered. This study can provide a reference for quantitative evaluation of the retrograde condensation and stress sensitivity in the production process of condensate gas reservoir.

KEYWORDS

condensate reservoirs, stress sensitivity, retrograde condensation damage, production calculation, gas well

Introduction

In recent decades, the development of unconventional reservoirs, including condensate reservoirs, has attracted increasing attention as the global demand for oil and gas has increased. Among different gas reservoirs, the condensate gas reservoir is special and complex. Due to the existence of condensate and retrograde condensate in a certain temperature and pressure range, gas and condensate can be produced simultaneously in the process of gas reservoir exploitation, which has extremely high economic value (Chen, 2016; Hekmatzadeh and Gerami, 2018). Condensate gas reservoirs are important for improving the efficiency of the oil industry in China and the world because of their rich oil and gas reserves (Xu et al., 2017; Yang et al., 2021).

For conventional oil and gas reservoirs, the reservoir pressure continuously decreases during the development process while the overlying pressure remains unchanged, leading to increasing net stress in the reservoir. As a result, the structural deformation of the core occurs, resulting in changes in core porosity, permeability, and other parameters (Settari et al., 1989; Buchsteiner et al., 1994). This phenomenon is called the stress-sensitive effect. According to Davies and Davies, 2001, stress sensitivity is caused by particle slip motion, particle deformation, and particle fracturing in the core. Geertsma, 1957 argued that the decrease in overlying pressure could cause an increase in core pore volume. Tian et al. (2015) conducted stress-sensitive experiments by changing the back pressure. The results suggested that the inner compressive stress caused by back pressure variation acts directly on the skeleton particles of rock pores. Jiao et al. (2011) carried out the stress-sensitive experiments using the method with constant internal pressure but variable peripheral pressure. The result shows that the process of rock deformation could be divided into two phases, namely the microcrack closure phase and the rock compression phase. For condensate reservoirs, Bentsen, 1998 found that when the internal pressure of the reservoir drops below the dew point pressure of condensate gas, retrograde condensation occurs. Some scholars found that when retrograde condensation occurs, a part of condensate oil is attached to the surface of the larger pores of the reservoir rocks in the form of a liquid film, reducing the gas-phase permeation channels, and the other part of condensate oil is in the form of liquid droplets at the smaller pore throats, blocking the originally connected flow channels and causing the effective permeability of the gas phase to decrease. Zhu et al. (2007) found that the condensate oil is easy to accumulate in the small pores in the pore and on the surface of rock particles, and the condensate oil gradually evolves to form slug after aggregation. Song and Li, 2005 analyzed the mechanism of the phenomena of the streaming

along the pore-wall with condensate oil. The streaming along the pore-wall with condensate oil can be divided into three layers: adsorbed oil, bound oil and outer oil. In addition, more retrograde condensation leads to more pore space occupied by condensate oil before the saturation reaches the critical point. The higher decrease rate of gas effective permeability eventually causes a decrease in the recovery of condensate (Barnum et al., 1995; Liu et al., 2001; Shi et al., 2006; Zhu and Huang, 1992). Fevang and Whitson, 1997 and Mott, 2003 found that when bottom flow pressure drops below the dew point, an area of high condensate saturation forms near the wellbore, resulting in reduced gas permeability. Zhang et al. (2020) carried out the experimental test of pollution damage of retrograde condensate. The result show that the retrograde condensate pollution will lead to a significant reduction of gas permeability and when the formation pressure drops to 7 MPa, the gas permeability is only 1/6 of that in the early stage of development. Wang et al. (2018) found that condensate gas reservoirs during natural development have persistent condensate blockage, and the core permeability decreases with decreasing pressure. Several experimental studies have been conducted on the retrograde condensation damage of gas reservoirs (Feng et al., 2020; Li et al., 2004; Tong et al., 2004) However, the influence of retrograde condensation and stress sensitivity on reservoir permeability and its changing pattern during pressure changes need to be explored.

In this study, nitrogen and condensate gas were used as experimental fluids to conduct the stress-sensitive experiments on cores of three permeabilities. The percentages of core skeleton damage and retrograde condensation damage during the rise of net stress are determined based on the experimental results. The influence of the two types of damage on the decrease of permeability and the change law are analyzed, and the



FIGURE 1
The core samples.

TABLE 1 Core parameters.

Core number	Permeability (mD)	Porosity (%)	Diameter (mm)	Length (mm)
BZ-1	0.52	1.76	25.26	49.92
BZ-2	2.14	7.34	25.33	26.95
BZ-3	3.32	9.32	25.59	31.89

TABLE 2 Analysis of shale mineral composition.

Core number	Mineral composition (%)							
	Plagioclase	Potassium feldspar	Quartz	Calcite	Siderite	Ankerite	Biotite	Phlogopite
BZ-1	42	17	20	4	1	3	13	0
BZ-2act	39	16	23	4	2	2	0	14
BZ-3	36	15	29	2	1	2	0	15

TABLE 3 The component of the condensate gas.

Component	Moore content (%)	Component	Moore content (%)	Component	Moore content (%)
N ₂	0.41	iC ₄	0.464	C ₇	0.525
CO ₂	8.733	nC ₄	0.886	C ₈	0.956
C ₁	71.318	iC ₅	0.319	C ₉	1.049
C ₂	6.057	nC ₅	0.382	C ₁₀	0.837
C ₃	2.519	C ₆	0.76	C ₁₁₊	4.787

equation of gas well production is established considering stress sensitivity and retrograde condensation. This study aims to analyze the influence of retrograde condensation and stress sensitivity and summarize the change law of core skeleton damage and retrograde condensation damage on reservoir permeability in the production process.

Experimental samples and methods

Core parameter

The core samples (Figure 1) used in the experiment were taken from the BZ gas field in southwestern Bohai Sea, the largest metamorphic buried hill condensate gas field in the Bohai Sea. BZ gas field is characterized by diverse reservoir types, extremely high condensate content, and great stress sensitivity. The buried depth is 3,400~5,600 m, the formation temperature is

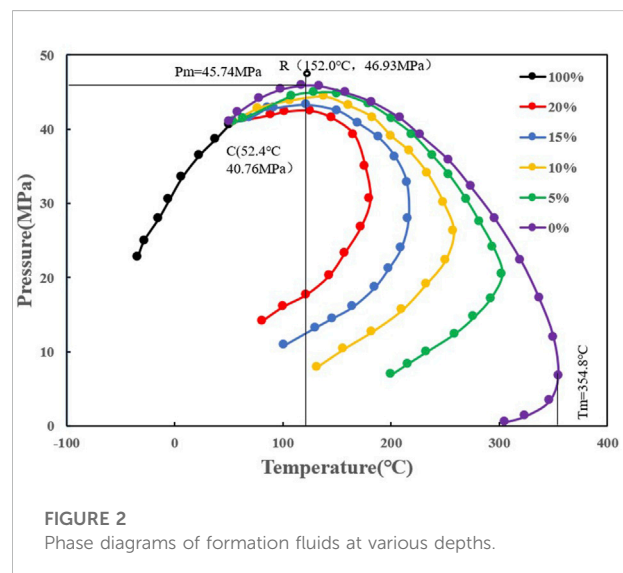
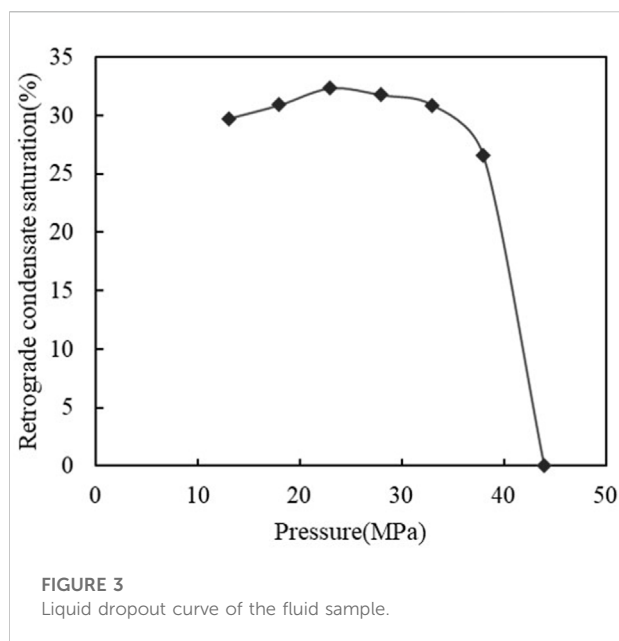


FIGURE 2
Phase diagrams of formation fluids at various depths.



158.4~198°C, the condensate content is 711~751 g/m³, the porosity is 8.7% and the permeability is 0.3~4 mD. The basic parameters of each core are shown in Table 1. Moreover, the mineral composition of core samples was tested, and the test results are listed in Table 2.

Condensate gas parameters

The condensate gas used in the experiments was prepared based on PVT data from the gas field. The fluid composition distribution, fluid phase, and condensate gas precipitation are shown in Table 3; Figures 2, 3, respectively. Data in Figure 2 was experimentally obtained with collected oil and gas samples in the PVT cylinder, reflecting the percentage of oil and gas in the mixture under certain temperature and pressure conditions. It can be found that the critical temperature of the field is 52.4°C, the critical condensation temperature is 384.8°C, and the formation temperature is 152°C. The critical pressure is 40.76 MPa, the critical condensate pressure is 45.74, and the formation pressure is 46.93 MPa. Figure 3 shows the variation of condensate saturation with pressure in a constant volume decay experiment of the formation fluid. It can be seen that the dew point pressure of this gas field is 43.97 MPa, and the condensate saturation is maximum at 23 MPa, which is 32.31%.

Experimental principles and methods

Rock stress-sensitive experiments can be divided into two types: one with variable confining pressure and constant inner

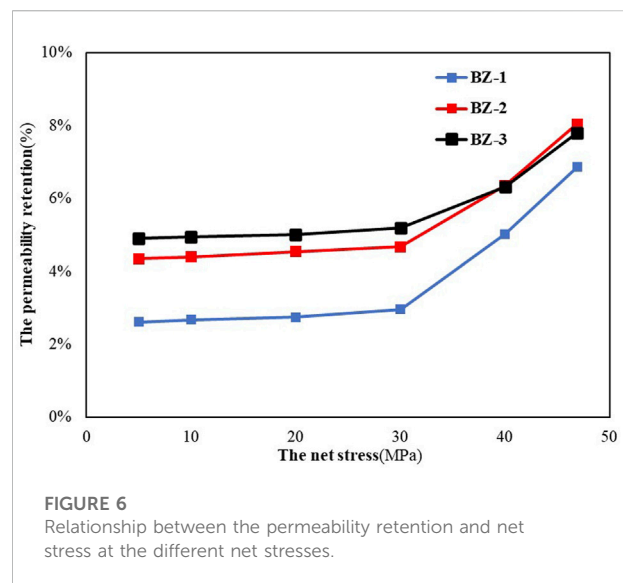
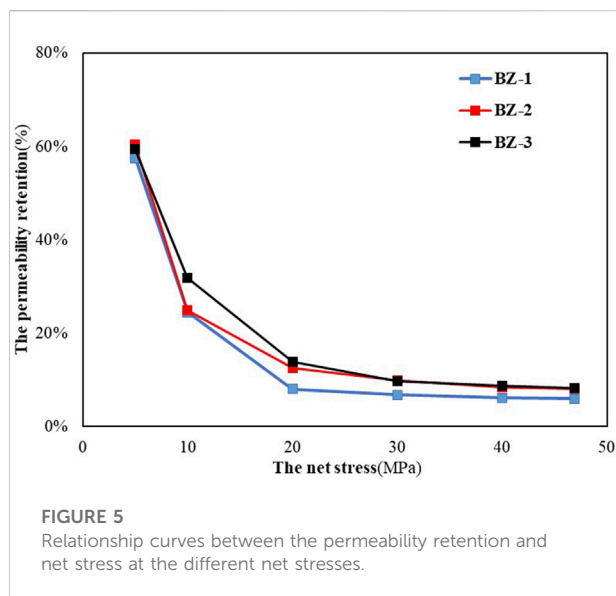
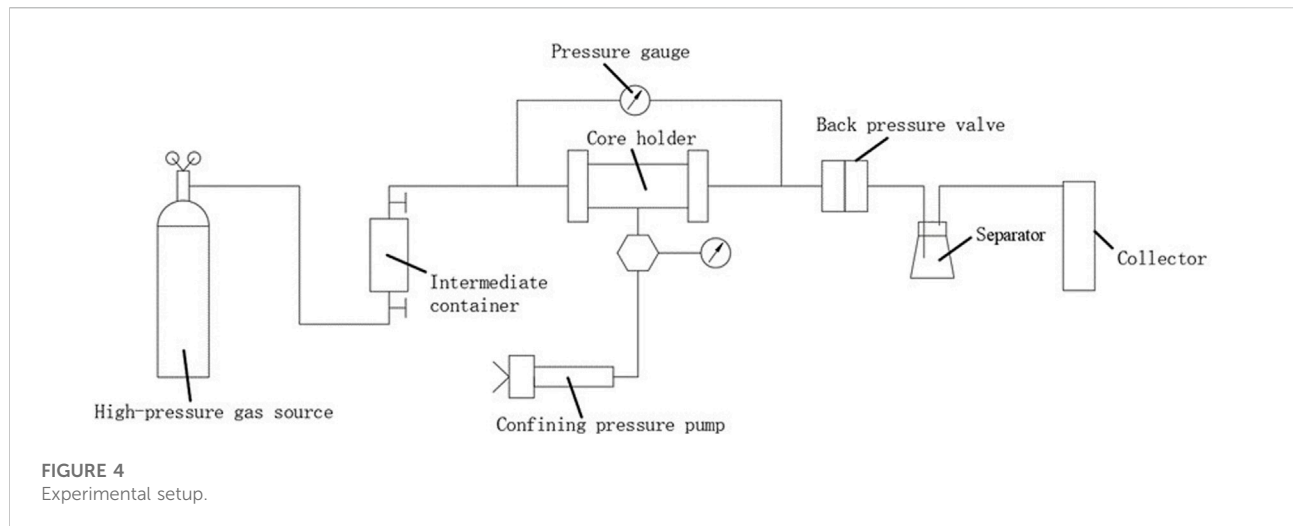
pressure, and the other with constant confining pressure and variable inner pressure. Considering that the overburden pressure of the reservoir does not change during the actual exploitation and the internal pressure gradually decreases with the production, the measurement method of fixed circumferential pressure and variable internal pressure is more consistent with the practical production (Guo et al., 2007). In this study, the stress sensitivity experiment method of constant confining pressure and variable inner pressure was adopted. The confining pressure of the core gripper was kept unchanged, and the back pressure was gradually decreased to change the net stress of the core, thus altering the core permeability. Finally, the stress sensitivity of the core was obtained by calculating the core permeability at each pressure point. The experimental setup is shown in Figure 4. The main experimental devices include an injection pump, a core holder, a confining pressure pump, an intermediate container, a differential pressure gauge, a back pressure valve, and a separator. In addition, the maximum working pressure of the injection pump is 150 MPa, and the working pressure range of the core holder, the confining pressure pump, the intermediate container and the back pressure value is 0–70 MPa.

The stress-sensitive experiments were divided into two groups. Nitrogen was used as the experimental fluid in the first group of stress-sensitive experiments, and condensate gas was used in the second group. In order to facilitate the control of the experimental group and match the actual situation, the experimental process only simulated the stress sensitivity during the rise of the net stress. The specific operation steps are as follows: 1) The experimental equipment is connected, and the dried core is loaded into the gripper and heated to the actual formation temperature. 2) The initial confining pressure is 3 MPa. The inlet pressure and the back pressure are equal and slowly increased with the confining pressure at a step of 2 MPa and an interval of 30 min until the confining pressure rose to 50 MPa. The inlet pressure and back pressure rise to the original formation pressure. 3) The confining pressure and inlet pressure are kept constant, and the back pressure value is reduced step by step according to the setback pressure point. The permeability under each back pressure point is measured when the gas seepage is stable. 4) After measuring all the set pressure points, the source valve is closed to end the experiment.

The experimental results

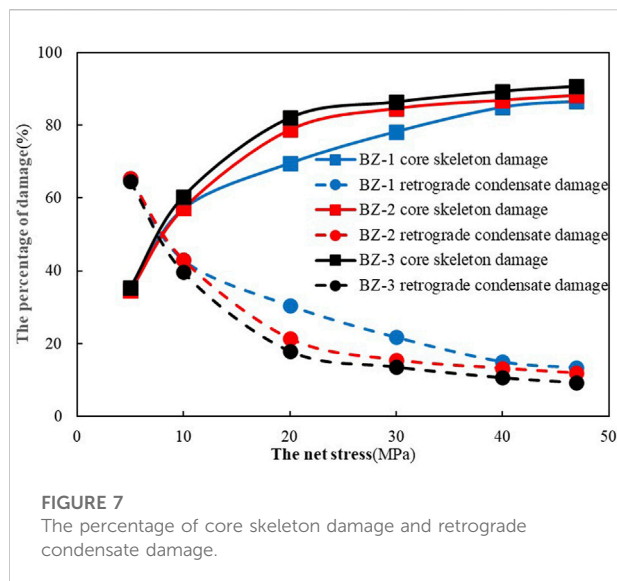
Stress sensitivity of cores with nitrogen as the flow medium

The stress-sensitive test results of the three cores are shown in Figure 5. The permeability retention rate



(i.e., the ratio of permeability to initial permeability after core deformation) is basically the same for the three cores at different net stresses. It can be seen that the permeability rate gradually decreases with the increase of the net stress. When the net stress increases from 2.5 MPa to 20 MPa, the permeability decreases rapidly, and the permeability retention rate of all three cores decreases to less than 20%. As the net stress increases from 20 MPa to 45 MPa, the decreasing of permeability slows down, and the permeability retention rate of the three cores decreases by about 10%. Finally, the permeability retention of all three cores decreases to less than 10%. When the net stress is 45 MPa, the permeability retention rate is 6.89% for BZ-1, 9.26% for BZ-2, and 9.41% for BZ-3. When the net stress is

less than 20 MPa, the permeability significantly decreases with the rise of effective force. When the net stress is greater than 20 MPa, the decrease of permeability slows down, indicating that at the initial stage of net stress increase, the core is compressed, the internal structure is deformed and destroyed, and the change of permeability is significant. When the net stress increases to 20 MPa, the variation degree of the core structure stabilizes, and the permeability retention rate remains unchanged. Because the mineral composition of cores from the same formation is basically the same, the deformation ability and degree of different permeability cores are similar, and the variation curves at different permeability show the same trend.



Stress sensitivity of cores with condensate gas as the flow medium

The stress-sensitive test results of the three cores are shown in Figure 6. When the net stress increases, the permeability decreases rapidly, and the permeability retention rate of all three cores decreases to less than 10%. When the net differential pressure increases from 30 MPa, the permeability retention rate also increases. When the net stress reaches 45 MPa, the permeability retention rate of all three cores decreases to less than 10% (6.85% for core BZ-1, 8.04% for core BZ-2, and 7.8% for core BZ-3). When the net stress increases to 5 MPa, the permeability retention rate rapidly decreases to less than 10%. According to Figure 3, the pressure drops below the dew point pressure of 43.97 MPa when the net stress increases to 5 MPa. At this time, retrograde condensation occurs, and the saturation of condensate oil rapidly increases. After the formation pressure drops by 3 MPa, the oil saturation in the core reaches about 30%, causing pore throat blockage. This situation keeps aggravating and leads to a rapid drop in permeability. When the net differential pressure reaches 30 MPa, the permeate retention rate increases with the increase of the net differential pressure. When the net stress reaches 20 MPa, the pore throat blockage decreases, and the permeate rate increases.

Core skeleton damage and retrograde condensation damage discrimination

The experimental fluid used in the first group was nitrogen, and the stress-sensitive damage factor in the experiment can be considered as only core skeleton damage. In the second group,

condensate gas was used as the experimental fluid. During the experiment, retrograde condensation occurs in the core with the change of the net stress, producing condensate oil. The factors causing the decrease in permeability can be regarded as a combination of core skeleton damage and retrograde condensation damage. By comparing the damage at the same permeability level in the two sets of experiments, the percentage of the total damage caused by retrograde condensation damage and core skeleton damage can be obtained:

$$D_{st} = \frac{100\% - D_a}{100\% - D_b} \times 100\% \quad (1)$$

where D_{st} is the percentage of damage caused by the core skeleton (%); D_a is the permeability retention rate under experimental nitrogen conditions (%); D_b is the permeability retention rate under experimental conditions of condensate gas (%).

$$D_{con} = 100\% - D_{st} \quad (2)$$

where D_{con} is the percentage of damage caused by condensate (%).

According to Eqs. 1, 2, the percentage of retrograde condensation damage and core skeleton damage of the three cores were obtained, as shown in Figure 7. It can be seen that the damage percentage change of the three cores shows the same trend. When the net stress is 5 MPa, the percentage of retrograde condensation damage is greater than that of core skeleton damage. However, as the net stress increases, the percentage of retrograde condensation damage gradually decreases, and the core skeleton damage gradually increases. Finally, the percentage of core skeleton damage exceeds 90%, while the percentage of retrograde condensation damage is less than 10%. With a smaller core permeability, the percentage of core skeleton damage is smaller, and the percentage of retrograde condensation damage is larger.

According to the variation curve, retrograde condensation damage and core skeleton damage can be divided into three stages (Figure 8). Stage 1 occurs before the net differential pressure reaches 7 MPa. At this stage, the pressure drops below the dew point, and some component phases in the condensate gas become condensate oil, rapidly occupying the core pore throat. However, the core skeleton is not broken. The retrograde condensation damage is the main factor leading to the decrease in permeability. Stage 2 is between 7 MPa and 20 MPa. The oil saturation of the core stabilizes at about 30%, while the degree of deformation and damage of the core structure increases, resulting in a higher percentage of core skeletal damage than the percentage of retrograde condensation damage. In stage 3, the percentage of each damage stabilizes after 20 MPa. After 20 MPa, the core skeleton damage accounts for about 90% of the net pressure drop and tends to be stable. Therefore, the core skeleton damage can be considered the main cause of the permeability drop, while the proportion of reverse retrograde condensation damage is smaller.

According to the experimental results, the impact of retrograde condensate and stress sensitivity on the permeability of the reservoir during production can be divided into five stages: 1) The initial stage: In this state, the formation pressure is greater than the dew point pressure, there is only condensate gas in the core, and the core skeleton does not change; 2) The leading stage of retrograde condensate: When the formation pressure drops to the dew point pressure, the condensate gas condensate phenomenon occurs, condensate oil occupies the core pore throat, resulting in a rapid decline in core permeability, and the core skeleton is not broken; 3) Joint action stage: when the formation pressure drops between 5 and 7 MPa, the core skeleton begins to be broken. At this stage, the retrograde condensation damage and core skeleton damage jointly lead to the decrease of reservoir permeability; 4) The leading stage of core skeleton damage: when the formation pressure drops to 7 MPa, the degree of deformation and damage of the core structure increases, while the condensate content in the core remains unchanged, and core skeleton damage is the main reason for the decrease of permeability; 5) Final stage: After the formation pressure drops by 20 MPa, the degree of deformation and damage of the core structure is maximum and condensate oil content remain unchanged, and the permeability remains stable.

The impact of condensation on capacity

The experimental results can be used to fit the equation for calculating gas well production. Moreover, gas well production under different bottom flow pressures can be obtained to evaluate the degree of condensation damage.

Penetration rate calculation formula

Permeability calculation requires the consideration of stress sensitivity and condensate oil. The variation of condensate saturation is related to the variation of formation pressure. By fitting the condensate saturation and pressure curves to Figure 3, the following equation can be obtained:

$$S_w(p) = a \cdot p^4 + b \cdot p^3 + c \cdot p^2 + d \cdot p + e \quad (3)$$

where $S_w(p)$ is the condensate oil content saturation (%); p is the formation pressure (MPa); a , b , c , d , and e are the coefficients.

Based on the results of stress-sensitive experiments with condensate gas as the experimental fluid and Eq. 1, the equation for calculating the permeability is fitted considering the stress-sensitive case where the phase occurs in condensate gas:

$$k = a \cdot S_w(p) + b \cdot k_0 e^{c \cdot (p_e - p_0)} \quad (4)$$

TABLE 4 Calculated parameters.

Reservoir temperature (K)	452.15
Reservoir pressure (MPa)	45.7
The radius of the well (m)	0.1
The thickness of the reservoir (m)	67.2
Fluid viscosity (mPa·s)	0.067
Gas compression coefficient	0.9
Reservoir permeability (mD)	0.7

where k is permeability (mD); k_0 is the initial permeability (mD); p_e is the initial pressure (MPa); p_0 is the test pressure (MPa); a , b , and c are the coefficients.

Calculation of gas well production

To facilitate the modeling and solution requirements, the following assumptions need to be made: 1) Rocks and stratigraphic fluids are compressible, and the compression coefficient is constant; 2) Percolation of gases in the reservoir obeys Darcy's law; 3) The effects of capillary forces and gravity on seepage is neglected; 4) No change in temperature of the reservoir; 5) The strata are homogeneous and isotropic. Under stable production conditions, the production equation for gas wells can be expressed as follows:

$$Q_{sc} = \frac{Z_{sc} T_{sc}}{Z T p_{sc}} \frac{2\pi r h p k}{\mu} \frac{dp}{dr} \quad (5)$$

where Q_{sc} is the gas well production (m^3/d); Z_{sc} is the gas compression coefficient under standard conditions; T_{sc} is the gas temperature at standard conditions, (K); Z is the gas compression coefficient of the reservoir; T is the reservoir temperature (K); p_{sc} is the reservoir pressure (MPa); r is the radius of the well (m); h is the thickness of the reservoir (m); p is the bottom flow pressure (MPa); k is the reservoir permeability (mD); μ is the fluid viscosity (mPa·s).

By substituting Eq. 4 into the gas production equation and integrating, the gas production equation considering stress sensitivity and condensate gas phase is obtained:

$$Q_{sc} = \frac{2\pi Z_{sc} T_{sc} h}{T p_{sc} \mu Z \ln \frac{r_e}{r_w}} (p_e^2 - p_{wf}^2) [a \cdot S_w(p) + b \cdot k_0 e^{c \cdot (p_e - p)}] \quad (6)$$

Gas well production calculation

Based on the actual reservoir conditions, the parameters are given in Table 4, and the gas well production is calculated for different bottom flow pressures with and without retrograde condensation.

The calculated results are shown in Figure 9. It can be seen that the production increases as the bottom flow pressure

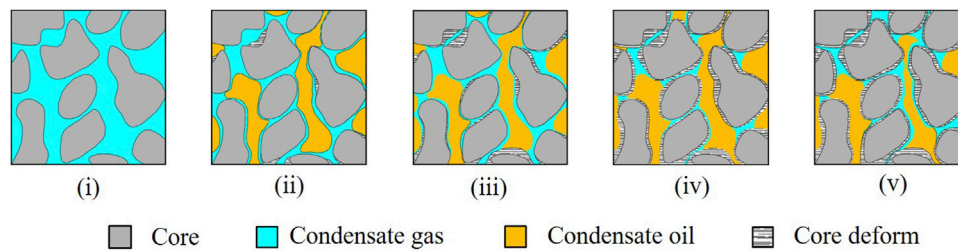


FIGURE 8

Five stages of the impact of retrograde condensate and stress sensitivity on the permeability of the reservoir during production: (i) The initial stage; (ii) The leading stage of retrograde condensate; (iii) The joint action stage; (iv) The leading stage of core skeleton damage; (v) The final stage.

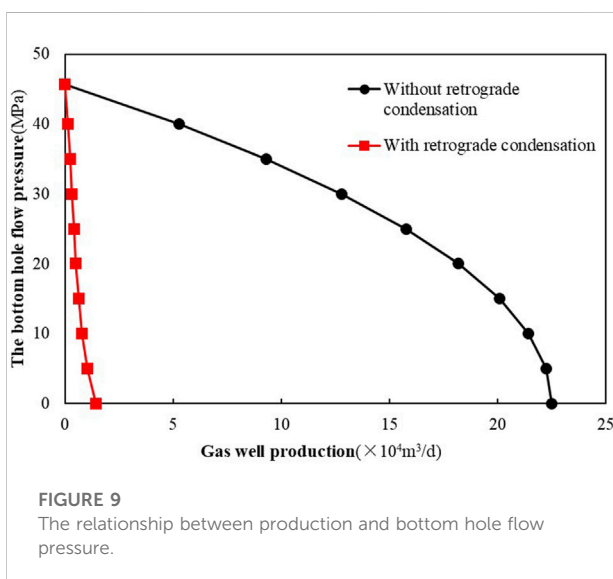


FIGURE 9

The relationship between production and bottom hole flow pressure.

decreases. When the flow pressure at the bottom of the well is 0 MPa, the gas well production without retrograde condensation decreases by 97.65%, suggesting that the precipitation of condensate gas seriously affects gas well production. However, this equation is a steady-state production equation, and the calculation process does not consider the impact of production time on capacity, which has certain limitations.

Conclusion

In this study, the change of retrograde condensate damage and core skeleton damage during pressure drop was analyzed through the stress-sensitive experiment with nitrogen and condensate gas as the experimental fluid. According to the experimental results, the calculation formula of gas well production considering the phase change of condensate gas was derived. The following conclusions were made:

- (1) The results of stress-sensitive experiments using nitrogen as the experimental fluid show that when the net stress is less than 20 MPa, the core structure is deformed and damaged, resulting in a decrease in permeability. When the net stress exceeds 20 MPa, the structural damage and permeability change tend to be stable. The results of stress-sensitive experiments using condensate gas as the experimental fluid show that after the net stress increases to 5 MPa, the condensate gas undergoes a phase change, and condensate oil rapidly occupies the pore throat, resulting in a rapid decrease in rock permeability. When the net stress reaches 20 MPa, the condensate saturation decreases, the pore throat blockage slows down, and the permeability increases.
- (2) The discrimination between core skeleton damage and retrograde condensation damage indicates that the damage can be divided into three stages. At Stage 1 (the net stress is less than 7 MPa), the core skeleton damage accounts for about 35%, and the retrograde condensation damage accounts for about 65%. At Stage 2 (the net stress is greater than 7 MPa and less than 20 MPa), the percentage of core skeleton damage gradually increases from 35% to 70%–80%, and the percentage of retrograde condensation damage decreases to 20%–30%. At Stage 3 (the net stress is greater than 20 MPa), two kinds of damage tend to stabilize, in which the core skeleton damage accounts for about 90%, and the percentage of retrograde condensation damage is about 10%.
- (3) Because core skeleton damage and retrograde condensate damage have different sensitivity to pressure changes, the main damage of each stage is different. After the pressure drops below the dew point, part of the component phase in the condensate gas becomes condensate oil, the core skeleton does not break the ring to a large extent, suggesting that retrograde condensation damage is the main factor contributing to the decrease in permeability in stage 1. At stage 2, the degree of phase transformation of condensate gas stabilizes, while the degree of deformation and damage to the core structure increases. The percentage of core skeleton damage starts to increase and exceeds the percentage of retrograde condensation damage. At stage 3, the

deformation and failure degree of the core skeleton stabilize when the net stress reaches 20 MPa, with little change in the percentage of both types of damage.

- (4) According to the experimental results, the equation considering stress sensitivity and condensate gas phase transformation is obtained to calculate gas well production. The calculation results show that the production decreases by 97.65% when the phase transformation is considered. The phase transformation of condensate gas seriously affects the exploitation of condensate gas reservoirs, leading to a significant decrease in production.

Data availability statement

The raw data supporting the conclusion of this article will be made available by the authors, without undue reservation.

Author contributions

NL, XT, and LZ contributed to conception and design of the study. HL and YL performed the numeral calculations and statistical analysis. NL, XT, LZ, HL, and YL wrote sections of the manuscript. All authors contributed to manuscript revision, read, and approved the submitted version.

References

- Barnum, R. S., Brinkman, F. P., Richardson, T. W., and Spillette, A. G. (1995). Gas condensate reservoir behaviour: Productivity and recovery reduction due to condensation. *Spe Tech. Conf. Exhib.* 32 (3), 451–456. doi:10.2118/30767-MS
- Bentsen, R. G. (1998). Effect of momentum transfer between fluid phases on effective mobility. *J. Pet. Sci. Eng.* 21 (1-2), 27–42. doi:10.1016/S0920-4105(98)00035-7
- Buchsteiner, H., Warpinski, N. R., and Economides, M. J. (1994). Stress-induced permeability reduction in fissured reservoirs. *SPE* 265113. doi:10.2118/265113-MS
- Chen, C. (2016). Multiscale imaging, modeling, and principal component analysis of gas transport in shale reservoirs. *Fuel* 182, 761–770. doi:10.1016/j.fuel.2016.06.020
- Davies, J. P., and Davies, D. (2001). Stress-dependent permeability: characterization and modeling. *SPE J.* 6, 224–235. 56813. doi:10.2118/71750-PA
- Feng, Q., Deng, B., Yang, Y., Jia, J., Peng, X., and Yuan, J. (2020). Evaluations and removing methods of the retrograde condensate damage of the gas condensate reservoirs in the tight sandstone. *Petroleum Geol. Oilfield Dev. Daqing* 39 (02), 139–146. doi:10.19597/J.ISSN.1000-3754.201905014
- Fevang, Ø., and Whitson, C. H. (1997). Modeling gas-condensate well deliverability. *SPE Reserv. Eng.* 1997 (04), 221–230. doi:10.2118/30714-PA
- Geertsma, J. (1957). The effect of fluid pressure decline on volumetric changes of porous rocks. *Trans. AIME* 210, 331–340. doi:10.2118/728-g
- Guo, P., Xu, Y., Chen, Z., Jiang, Y., and Pang, Y. (2007). New ideas obtained from laboratory study of flowing mechanisms in low-permeability reservoirs. *Nat. Gas. Ind.* 2007 (07), 86–88+140–141. doi:10.3321/j.issn:1000-0976.2007.07.025
- Hekmatzadeh, M., and Gerami, S. (2018). A new fast approach for well production prediction in gas-condensate reservoirs. *J. Petroleum Sci. Eng.* 160, 47–59. doi:10.1016/j.petrol.2017.10.032
- Jiao, C., He, S., and Xie, Q. (2011). An experimental study on stress-dependent sensitivity of ultra-low permeability sandstone reservoirs. *Acta Pet. Sin.* 32 (03), 489–494. doi:10.7623/syxb201103018
- Li, J., Li, X., Tong, M., Cheng, S., and Kang, X. (2004). Study on a new method for liquid phase transformation of condensate gas in porous media. *Petroleum Explor. Dev.* 2004 (06), 101–103. doi:10.3321/j.issn:1000-0747.2004.06.027
- Liu, Y., Yuan, S., Song, W., Li, B., and Wang, J. (2001). Mechanism study of condensate influencing on productivity. *Petroleum Explor. Dev.* 2001 (01), 54–56+12–4+3. doi:10.3321/j.issn:1000-0747.2001.01.018
- Mott, R. (2003). Engineering calculations of gas-condensate-well productivity. *SPE Reserv. Eval. Eng.* 6 (5), 298–306. doi:10.2118/86298-PA
- Settari, A., Kry, P. R., and Yee, C. T. (1989). Coupling of fluid flow and soil behaviour to model injection into uncemented oil sands. *J. Can. Petroleum Technol.* 28 (1). doi:10.2118/89-01-08
- Shi, D., Li, X., and Liu, Y. (2006). Deliverability equation study of gas condensate well considering phase change. *Oil Drill. Prod. Technol.* 2006 (04), 68–70+85–86. doi:10.3969/j.issn.1000-7393.2006.04.021
- Song, Y., and Li, Z. (2005). To analyze the mechanism of the phenomena of the streaming along the pore-wall with condensate oil. *Nat. Gas. Geosci.* 2005 (02), 214–215. doi:10.3321/j.issn:1000-0976.2005.09.030
- Tian, W., Zhu, W., Zhu, H. Y., Zhang, X. L., Wang, R. M., and Yong, L. I. (2015). Study on testing method of back-pressure sensitivity evaluation. *Nat. Gas. Geosci.* 26 (2), 377–383. doi:10.11764/j.issn.1672-1926.2015.02.0377

Funding

This work was supported by the CNOOC Group Major Project (Grant No. KJGG 2022-0700 and Grant No. YXKYZX 07 2021). The authors declare that the funder was not involved in the study design, collection, analysis, interpretation of data, the writing of this article, or the decision to submit it for publication.

Conflict of interest

NL, XT, and LZ were employed by CNOOC Research Institute Co. Ltd.

The remaining authors declare that the research was conducted in the absence of any commercial or financial relationships that could be construed as a potential conflict of interest.

Publisher's note

All claims expressed in this article are solely those of the authors and do not necessarily represent those of their affiliated organizations, or those of the publisher, the editors and the reviewers. Any product that may be evaluated in this article, or claim that may be made by its manufacturer, is not guaranteed or endorsed by the publisher.

- Tong, M., Li, X., Hu, Y., Wang, J., and Li, J. (2004). Experimental study on influence of porous media on phase behavior of gas condensate. *J. Xi'an Shiyu Univ. Sci. Ed.* 2004 (05), 61–64. doi:10.3321/j.issn:1000-5870.2004.05.013
- Wang, Z., Zhu, S., Zhou, W., Liu, H., Hu, Y., Guo, P., et al. (2018). Experimental research of condensate blockage and mitigating effect of gas injection. *Petroleum* 4 (3), 292–299. doi:10.1016/j.petlm.2018.03.008
- Xu, C., Zou, H., Yang, Y., Yong, D., Yang, S., Luo, B., et al. (2017). Status and prospects of exploration and exploitation of the deep oil and gas resources onshore China. *Nat. Gas. Geosci.* 28 (8), 1139–1153. doi:10.11764/j.issn.1672-1926.2017.07.014
- Yang, X., Tian, J., Wang, Q., Li, Y., Yang, H., Tang, Y., et al. (2021). Geological understanding and favorable exploration fields of ultra-deep formations in Tarim Basin. *China Pet. Explor.* 26, 17–28. doi:10.3969/j.issn.1672-7703.2021.04.002
- Zhang, C., Song, X., and Tang, Y. (2020). Experimental study on retrograde condensate damage of Longfengshan extra-low porosity and extra-low permeability condensate gas reservoir. *J. Xi'an Shiyu Univ. Sci. Ed.* 35 (02), 50–53+97. CNKI: SUN:XASY.0.2020-02-009.
- Zhu, W., and Huang, Y. (1992). A description of microscopic flowing mechanisms of a gas-liquid condensate through porous media. *Petroleum Explor. Dev.* 1992 (01), 45–48+108-109. CNKI:SUN:SKYK.0.1992-01-006.
- Zhu, W., Liu, X., and Shi, Z. (2007). Porous flow mechanism of multiphase complex flow of condensate gas reservoirs with wax deposition. *Acta Pet. Sin.* 2007 (02), 87–89+93. doi:10.3969/j.issn.1672-1926.2006.03.002



OPEN ACCESS

EDITED BY

Debin Kong,
University of Science and Technology
Beijing, China

REVIEWED BY

Jinze Xu,
University of Calgary, Canada
Wenhui Song,
China University of Petroleum,
Huadong, China

*CORRESPONDENCE

Mingwei Wang,
201999010137@swpu.edu.cn

SPECIALTY SECTION

This article was submitted to Advanced
Clean Fuel Technologies,
a section of the journal
Frontiers in Energy Research

RECEIVED 23 June 2022

ACCEPTED 07 September 2022

PUBLISHED 05 January 2023

CITATION

Gao C, Cheng S, Wang M, Wu W, Gao Z,
Li S and Meng X (2023), Optimization of
volume fracturing technology for
shallow bow horizontal well in a tight
sandstone oil reservoir.
Front. Energy Res. 10:976240.
doi: 10.3389/fenrg.2022.976240

COPYRIGHT

© 2023 Gao, Cheng, Wang, Wu, Gao, Li
and Meng. This is an open-access article
distributed under the terms of the
[Creative Commons Attribution License](#)
(CC BY). The use, distribution or
reproduction in other forums is
permitted, provided the original
author(s) and the copyright owner(s) are
credited and that the original
publication in this journal is cited, in
accordance with accepted academic
practice. No use, distribution or
reproduction is permitted which does
not comply with these terms.

Optimization of volume fracturing technology for shallow bow horizontal well in a tight sandstone oil reservoir

Chaoli Gao^{1,2}, Shiqing Cheng¹, Mingwei Wang^{3*}, Wen Wu⁴,
Zhendong Gao⁵, Song Li⁶ and Xuangang Meng⁵

¹State Key Laboratory of Petroleum Resources and Prospecting, China University of Petroleum, Beijing, China, ²Exploration and Development Technology Research Institute, Yanchang Oil Field Co., LTD., Yanan, China, ³School of Oil and Natural Gas Engineering, Southwest Petroleum University, Chengdu, China, ⁴Southwest Oil and Gas Field Company of CNPC Chengdu, Chengdu, China, ⁵Technology and Information Management Department of Yanchang Oilfield Co., Ltd., Yanan, China, ⁶Engineering Research Institute of PetroChina Southwest Oil and Gasfield Company, Chengdu, China

The physical property of Chang 6 reservoir in Yanchang oilfield is poor, and the heterogeneity is strong. Multistage fracturing of horizontal wells is easy to form only one large horizontal fracture, but it is difficult to control the fracture height and length. The new mining method of “bow horizontal well + multistage horizontal joint” can effectively increase the multistage horizontal joint’s spatial position, which improves the drainage area and stimulation efficiency of oil wells. Due to the reservoir’s low permeability and strong heterogeneity, the single well mode of “bow horizontal well + multistage horizontal fracture” cannot effectively produce Chang 6 reservoir. To improve the production degree of the g 6 reservoir, the fracture model is established using equivalent conductivity and the multigrid method. The pressure response functions of horizontal wells and volume fracturing horizontal wells are established by using the source function, and the relationship between reservoir permeability and starting pressure gradient in the block is calculated. On this basis, the reservoir productivity equation of the block is established, which provides a basis for optimizing the fracturing design parameters of horizontal wells. It is proposed that the flow unit should be considered in the design of fracturing parameters of horizontal fractures, the number of fractures should comprehensively consider whether the fractures can make each flow unit be used, and have large controlled reserves, and the scale of fracturing should comprehensively consider the output and cost. The fracture network model is established by using equivalent conductivity and multi-grid method, and the volume fracturing design parameters of horizontal wells are optimized, considering the seepage characteristics of the flow unit. The fracturing design parameters of the horizontal section are further defined, which provides a theoretical basis for the efficient development of shallow tight reservoirs.

KEYWORDS

Chang 6 reservoir, sandstone formation, volume fracturing, bow horizontal well, horizontal fracture

1 Introduction

With the development of the global economy, the exploration and development process of oil and gas resources continues to expand, and a tight sandstone reservoir has been proven to be a main force in the world energy supply (Li et al., 2018; Xu et al., 2019a). A tight sandstone reservoir is typically classified as a reservoir with permeability less than 0.1 mD, which is not economically producible for a long history (Kazemi, 1982; Li et al., 2019). Qilicun oilfield, which is a typical tight sandstone reservoir, is located in the southeast of the Yishan slope in the Ordos Basin of China. The main oil layer for development is Chang 6 oil layer. The buried depth of this layer is shallow, and the reservoir is thin-layer interactive deposition, but the physical property is poor and the heterogeneity is strong. According to the statistics of existing core analysis reports in the study area, the reservoir porosity distribution is close to the normal distribution, with the main distribution range of 8.1%–10.1% and the average porosity of 9.4%; The permeability gradient is large, ranging from 0.02 to 8.8 mD, and the average permeability is 1.1 mD, tight sandstones exhibit the characteristics of small pore size and low porosity. Especially, for deep tight gas sandstone reservoirs, their pore sizes range from nanometers to micrometers after compaction and solidification for a long time, some scholars have carried out experimental and simulation research on the influence of rock microstructure on gas transmission in tight reservoirs (Meng et al., 2014; Du et al., 2015; Xu et al., 2018; Zhang et al., 2018; Xu et al., 2019b). In recent years, horizontal wells have been widely used in the development of unconventional reservoirs. Horizontal wells combined with multi-stage hydraulic fracturing technology are the main technical means for efficient development of low-permeability and tight reservoirs, which can greatly increase the production of single wells and improve the overall economic benefits of the oilfield (Xiong et al., 2012; Wang et al., 2014; Su et al., 2018a; Su et al., 2018b; Jiang et al., 2018; Su et al., 2020; Zhang et al., 2020). Generally, the direction of the minimum principal stress in the reservoir is horizontal, so the pressure fractures are vertically developed. Multi-stage fracturing in a horizontal well has proven to be effective for the development of unconventional shale resources (Mutalik and Gibson, 2008; King, 2010; Wellhoefer et al., 2014). Long horizontal wells combined with multi-stage fracturing can effectively increase the contact area between the oil well and the reservoir (Zhang et al., 2004; Weng et al., 2011; Chang, 2013; Li et al., 2013; Yang et al., 2014; Westwood et al., 2017; Zhang et al., 2018).

With this technique, large amounts of fracturing fluid are sequentially injected into different stages to simultaneously initiate multiple perforation clusters within one stage, creating dozens of hydraulic fractures (HFs) along the horizontal segment to maximize access to productive zones (Yew and Weng, 2015). However, monitoring during fracturing has found that the actual stimulated volume is much smaller than that interpreted via microseismic mapping (Xu et al., 2016), implying that considerable areas between two fractures may not be effectively stimulated. Xiong et al. (2020) developed the small cluster and stage spacings to further increase the area of fracture surfaces in reservoirs. Dohmen et al. (2014) and Somanchi et al. (2017) believed that strong stress interference among multiple fractures under such a tight spacing can induce nonuniform simultaneous growth (or asymmetrical growth of subsequent fractures, which may considerably undermine the stimulation performance. Zhang et al. (2021) proposed a novel experimental process to model the simultaneous and sequential propagation of multiple closely spaced fractures, and rock splitting and 3D reconstruction technology were used to characterize HF geometries. They investigated the effects of the number of clusters per stage, stage spacing, and net pressure in the previously created fractures on the propagation geometries. Thus, the interference mechanism among multiple closely-spaced fractures in the simultaneous and sequential propagation of multi-stage fracturing should be clarified to improve the effectiveness of fracturing.

HanYi Wang (2016) presented a fully coupled hydraulic fracture propagation model based on the Extended Finite Element Method (XFEM), Cohesive Zone Method (CZM), and Mohr-Coulomb theory of plasticity, which investigated the interference and coalescence of fluid-driven hydraulic fractures that initiated from horizontal wells (Wang, 2016). Hillerborg et al. (1976) introduced the concept of fracture energy into the cohesive crack model and proposed several tractions–displacement relationships. Based on this conception, Mokryakov (2011) proposed an analytical solution for hydraulic fracture with Barenblatt's cohesive tip zone, the results demonstrate that the derived solutions from the cohesive tip zone model can fit the pressure log much more accurately than LEFM for the case of fracturing soft rock. Wang et al. (2016) developed a cohesive poro-elastoplastic hydraulic fracture model for both brittle and ductile rocks. Their work indicates that plastic damage during fracturing execution can lead to higher propagation pressure and shorter and wider fracture geometry. Lecampion et al. (2015) (Brice and Jean, 2015) developed a numerical model for the initiation and growth of an array of parallel radial hydraulic fractures, and the solution accounts for fracture growth, coupling between elastic deformation and fluid

flow in the fractures, elastic stress interactions between fractures and fluid flow in the wellbore.

Bunger et al. (2011) proposed that production forecasting analysis is used by assuming straight-lined fractures to optimize spacing and staging between fractures, but in reality, fractures tend to propagate in a complex manner when they are closely spaced or where preexisting fractures exist. El Rabba (1989) studied that simultaneous fracturing of closely spaced clusters may cause fracture interferences such that some of the fractures stop in between, and some may not even initiate due to the stress shadow effects. Thus, the design of efficient systems can benefit from hydraulic fracture simulations that couple fluid flow to fracture deformation and fracture mechanics principles. The numerical method that can accurately model 2D or 3D fracture propagation can help to understand and improve the fracturing process. The growth of multiple simultaneous fractures assuming no fluid flow inside the fractures has been studied, and simulated the sequential fracturing has been treated with no explicit fluid. Some studies (Rafiee et al., 2012) have utilized stress analysis to suggest a modification to the zipper fracturing to improve the SRV based on heuristic arguments of complexity. However, more rigorous modeling is needed to better understand the problem and to help improve the design. Sesetty and Ahmad (2015) presented a fully coupled DD-based fracturing model, which considered different boundary conditions to simulate the effect of previously created fractures as pressurized (during the flow back is restricted) and propped (proppant filled fracture).

The burial depth of Chang 6 reservoir in the study block is shallow, mostly less than 1000 m, the sand layer thickness is generally less than 12 m, and the interlayer between different sand layers is widely distributed. The direction of the minimum principal stress in the reservoir is vertical, hydraulic fracturing is easy to produce horizontal fractures, and the difference in the principal horizontal stress in the reservoir is small. The reservoir thickness is small, and the development effect of vertical wells is poor. However, for horizontal wells, multi-stage fracturing is easy to form only a large horizontal fracture, and it is difficult to control the fracture height and length, resulting in formation channeling during fracturing, ranging from poor stimulation effect of staged fracturing to scrapping of the whole well. Therefore, the Yanchang oilfield has formed a new production model of “bow horizontal well + multi-level horizontal fracture,” which effectively increases the spatial position of multi-level horizontal fracture, and improves the drainage area and stimulation efficiency of oil wells (Yi et al., 2013; Xiong et al., 2014; Zhang et al., 2015). Due to the low permeability and strong heterogeneity of the reservoir, the single well method of “bow horizontal well + multistage horizontal fracture” cannot effectively produce Chang 6 reservoir. To further improve the production degree of the Chang 6 reservoir.

Firstly, based on the reservoir characteristics of Chang 6, the distribution function of reservoir *in-situ* stress and formation pressure after the fracturing of horizontal wells is established, and

the relationship between reservoir permeability and starting pressure gradient in the block is calculated. On this basis, the reservoir productivity equation of the block is established, which provides a basis for optimizing the fracturing design parameters of horizontal wells. It is proposed that the flow unit should be considered in the design of fracturing parameters of horizontal fractures, the number of fractures should comprehensively consider whether the fractures can make each flow unit be used, and have large controlled reserves, and the scale of fracturing should comprehensively consider the output and cost; The seepage mathematical model of multi-layer fracturing horizontal fracture bow horizontal well can be regarded as the combination of multiple horizontal fracture flow units. The fracture network model is established by using the equivalent conductivity and multi-grid densification method, and the volume fracturing design parameters of horizontal wells are optimized, considering the seepage characteristics of the flow unit. The fracturing design parameters of the horizontal section are further defined, which provides a theoretical basis for the efficient development of shallow tight reservoirs.

2 Reservoir characteristics

Lithological characteristics: the lithology of Chang 6 reservoir is mainly gray fine-grained arkose, and the mineral composition is mainly feldspar 52% and quartz 22%. The structural characteristics of the reservoir are that the sandstone particles are well sorted and directionally arranged. Another characteristic is that the diagenesis is strong. The sandstone has experienced diagenetic epigenesis such as compaction, pressure dissolution, antigenic mineral filling, dissolution, metasomatic, and clay mineral transformation and recrystallization, and has evolved into a tight sandstone reservoir with ultra-low porosity and ultra-low permeability.

Reservoir physical properties: According to the statistical results of core analysis data, the maximum porosity of the Chang 6 reservoir is 15.12%, the minimum is 1.52%, and the average is 8.39%; the maximum permeability is 7.79 mD minimum 0.01 mD, with an average of 0.54 mD. In Chang 6 reservoir, Chang 6-1 reservoir has the highest porosity and permeability, and the average value of Chang 6-2 and Chang 6-3 porosity and permeability is close. Pore structure characteristics: the main reservoir spaces of Chang 6 reservoir include intergranular pores, intergranular dissolved pores (mainly laumontite dissolved pores), etc. The pore throat types mainly include large pore fine throat type, small pore fine throat type, and small pore micro throat type (large pore: The average pore diameter is greater than 50 μm . Fine throat: average throat radius 0.2–1.0 μm , microlarynx: the average throat radius is less than 0.2 μm), various reservoir types are controlled by sedimentation and diagenesis, and their distribution in Chang 6 oil-bearing formation is very uneven.

TABLE 1 Test results of rock mechanical parameters in Zhengzhuang block.

Test sample no.	Horizon	Well depth/m	Temperature/ °C	Pore pressure/ MPa	confining pressure/ MPa	Poisson's ratio	Modulus of elasticity/MPa	Differential stress/MPa
1	Chang 6 ₁	382.65	20	3.06	5.85	0.341	19,417.8	136.1
2	Chang 6 ₁	404.17–404.32	20	3.23	6.21	0.372	13,967.2	106.7
3	Chang 6 ₁	405.39–405.69	20	3.24	6.23	0.377	16,171.2	117.3
4	长6 ₂	629.56–629.86	20	5.04	7.34	0.374	14,323.5	120.1
5	长6 ₃	472.5–472.8	20	3.78	7.24	0.397	13,752.7	100.6

3 Volume fracturing analysis of bow horizontal well

3.1 Rock mechanics parameter test

The rock mechanical parameters of Chang 6 reservoir in Zhengzhuang block of Qilicun oilfield in China are tested experimentally. The test conditions are shown in Table 1. The experimental results show that the rock in the Chang 6 section has high compressive strength (102.8–135.2 MPa), showing the elastic characteristics of the outgoing line, and the strain range is 0.9%–1.2%. The elastic modulus of rock is 13,752.7–19,417.8, and the Poisson's ratio is 0.341–0.397.

3.2 Calculation of *in-situ* stress profile of the reservoir

There are usually two methods to obtain *in-situ* stress data, one is an *in-situ* stress test, and the other is through calculation. The *in-situ* stress test is a direct means to obtain *in-situ* stress data. Its precision is high, but the test cost is high, and the measurement data is limited. The key to *in-situ* stress calculation is to establish a mechanical mathematical model suitable for the reservoir geological model and make full use of a large amount of information provided by logging data to conveniently and quickly obtain *in-situ* stress profiles continuously distributed along with the depth.

In situ stress is a very important basic parameter for fracture pressure calculation and fracturing optimization design. Here, a three-dimensional *in-situ* stress model is adopted. For the determination of vertical stress, the commonly used mode of vertical stress equal to overburden pressure is adopted. Overburden pressure is the pressure generated by the total weight of rock and pore fluid. It is usually expressed in the form of equivalent density, which is called the pressure gradient of overlying strata, and its change curve with depth is called the pressure gradient curve or profile of overlying strata. The pressure gradient of overlying strata mainly depends on the variation of rock

mass density with well depth. The pressure gradient of the overlying strata is different in different areas.

The formula for calculating overburden pressure using density logging data is as follows.

$$\sigma_v = 10^{-6} \int_0^H \rho(h) \cdot g \cdot dh \quad (1)$$

Where: σ_v is the vertical stress at well depth h , MPa; $\rho(h)$ is the density of overlying rock mass varying with depth, kg/m³; h is the well depth, m.

The horizontal principal stress is related to the formation pore pressure, the skeleton stress, and the tectonic stress in two directions on the horizontal plane. It is assumed that the rock is a homogeneous and isotropic linear elastomer and that there is no relative displacement between the stratum and the stratum in the process of sedimentation and later geological tectonic movement, and the strains in both horizontal directions of all strata are constant. From the generalized Hooke's Law:

$$\sigma_{hmin} - \alpha p_p = \frac{\mu}{1 - \mu} (\sigma_v - \alpha p_p) + K_h \frac{EH}{1 + \mu} \quad (2)$$

$$\sigma_{hmax} - \alpha p_p = \frac{\mu}{1 - \mu} (\sigma_v - \alpha p_p) + K_H \frac{EH}{1 + \mu} \quad (3)$$

σ_{hmax} is the maximum horizontal principal stress, MPa. σ_{hmin} is the minimum horizontal principal stress, MPa. α is the effective stress coefficient; p_p is pore pressure, MPa. K_h , K_H is the construction coefficient in the direction of minimum and maximum stress, constant in the same fault block, m⁻¹.

According to the above calculation method and logging data, the stress of the Chang 6 production interval is shown in Table 2, 3. The calculation results show that the stress difference of the Chang 6 production interval in the study block is less than 2 MPa, the stress difference of the reservoir interval is small, and the probability of longitudinal fracture penetration is large. During the fracturing process of horizontal wells, artificial fractures are easy to penetrate the layer vertically, which improves the reservoir reconstruction volume.

The *in-situ* stress direction of the Chang 6 reservoir in the study block is 70° to the northeast. The direction of the maximum horizontal principal stress matches the extension direction of the

TABLE 2 Basic parameters of horizontal stress of production interlayer.

Horizon	Well no.	Medium deep reservoir(m)	Type	Thickness (m)	Minimum horizontal stress (MPa)
Chang 6	Guo A	661.5	Upper compartment	5.1	16.01
			Pay zone	8.7	16.52
			Lower compartment	6.2	17.33
	Guo B	576.7	Upper compartment	8.3	15.92
			Pay zone	12.4	16.16
			Lower compartment	11.7	17.53

TABLE 3 Calculation of starting pressure gradient of Chang 6 reservoir.

Well no.	1	2	3	Average
Horizontal starting pressure gradient (MPa)/m	0.01867	0.01503	0.01397	0.01693
Vertical starting pressure gradient (MPa)/m	0.15472	0.12517	0.18036	0.15143



FIGURE 1

Development diagram of arch well with multiple horizontal fractures.

artificial fracture. The volume of the volume fracturing reservoir is large. To solve the problem of easy formation channeling during fracturing and vertically connect different flow units, and improve the reservoir production degree. The arch well design is adopted in the study block. The well has a certain curvature when extending in the horizontal direction, and multiple horizontal fractures can be pressed out during fracturing. This can avoid the phenomenon that horizontal wells are prone to channeling during fracturing, and can drill through different flow units, which is conducive to improving production (Figure 1).

The horizontal fractures produced after the fracturing of bow-shaped horizontal wells are mostly circular and elliptical. Because the calculation of the elliptical fracture model is very complex, rectangular fractures are used in this paper. The rectangular model is approximately equal to the circular or elliptical fracture model in terms of parameters such as fluid flow and pressure distribution.

Multilayer fracturing horizontal fracture - when a horizontal fracture is produced by the fracturing of a bow horizontal well. Assuming that the length of the horizontal well is $2L$, the horizontal well is along the X axis, which divides the fracture

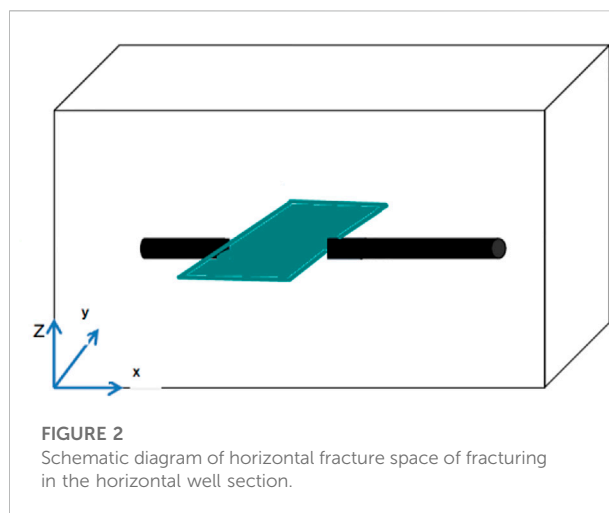


FIGURE 2

Schematic diagram of horizontal fracture space of fracturing in the horizontal well section.

plane into two. The fracture passes through the shaft of the near horizontal well, and x_f , y_f and z_f is long along the X direction, Y direction and Z direction (Figure 2).

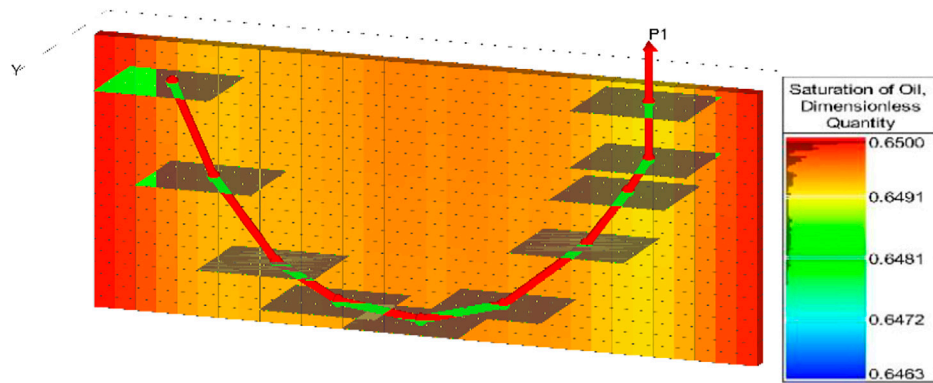


FIGURE 3
Simulation of bow horizontal well with horizontal fractures.

Assuming that the reservoir thickness is h , the formation compressibility coefficient is unchanged, and the fluid is a slightly compressible fluid with constant viscosity and compressibility coefficient, ignoring the influence of the gravity field. The near horizontal well section has infinite conductivity, that is, there is no pressure drop in the near horizontal well section. The simplified physical model of horizontal fracture near the horizontal well is shown in Figure 3.

3.3 Demonstration of horizontal well pattern and well spacing

3.3.1 Formation pressure distribution of horizontal well

According to Lord Kelvin's point source solution (Kelvin, 1884), the instantaneous point source function of a homogeneous reservoir is:

$$\bar{y} = \exp(-\rho_D \sqrt{u}) / 4\pi\rho_D \quad (4)$$

According to the superposition of countless isomorphic point sources corresponding to the top bottom closed reservoir vertically, the basic solution of the instantaneous point source of the top bottom closed reservoir is:

$$\bar{y} = \frac{1}{4\pi} \sum_{n=-\infty}^{+\infty} \left\{ \frac{\exp\left(-\sqrt{u} \sqrt{R_D^2 + (Z_D - Z'_D - 2nZ_{eD})^2}\right)}{\sqrt{R_D^2 + (Z_D - Z'_D - 2nZ_{eD})^2}} + \frac{\exp\left(-\sqrt{u} \sqrt{R_D^2 + (Z_D - Z'_D + 2nZ_{eD})^2}\right)}{\sqrt{R_D^2 + (Z_D - Z'_D + 2nZ_{eD})^2}} \right\} \quad (5)$$

Using the properties of the series function, Poisson superposition formula, Laplace transform, and other methods,

the basic solution of an instantaneous point source in the top bottom closed reservoir can be abbreviated as:

$$\bar{y} = \frac{1}{2\pi Z_{eD}} \left[K_0(R_D \sqrt{u}) + 2 \sum_{n=1}^{\infty} K_0\left(R_D \sqrt{u + \frac{n^2 \pi^2}{Z_{eD}^2}}\right) \cos\left(n\pi \frac{Z_D}{Z_{eD}}\right) \cos\left(n\pi \frac{Z'_D}{Z_{eD}}\right) \right] \quad (6)$$

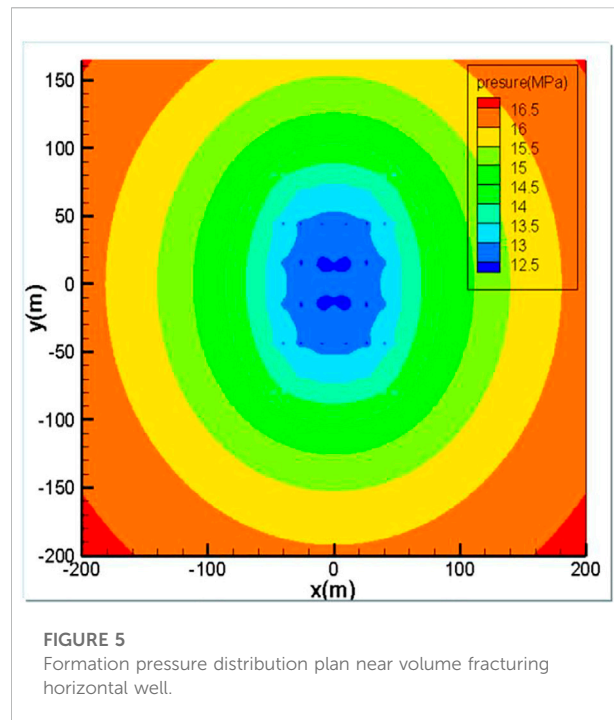
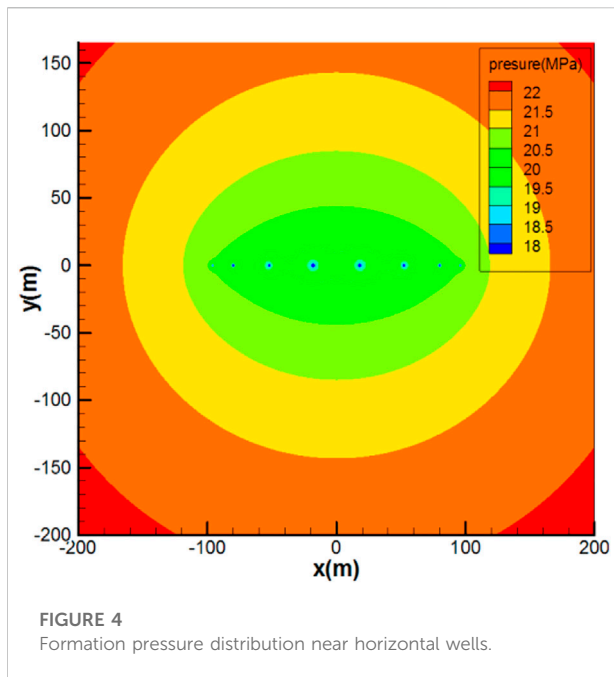
By integrating the basic solution along the wellbore direction, the corresponding mathematical model of the bottom hole pressure response can be obtained. For a vertical well, assuming that the length of the vertical well is $2L_h$, and q represents the fluid flow in the wellbore, the bottom hole pressure response function of a vertical well in a homogeneous reservoir can be obtained by integrating the basic solution of the instantaneous point source along the Z direction. Define dimensionless pressure function is $P_D(x_D, y_D, z_D, t_D) = \frac{2\pi K h}{q\mu} (P_i - P(x, y, z, t))$, then the Laplace solution of dimensionless bottom hole pressure response of vertical wells in the top bottom closed reservoirs is:

$$\bar{P}_D = \frac{1}{2u} \int_{-1}^1 K_0\left(\sqrt{u} \sqrt{x_D^2 + y_D^2}\right) d\alpha \quad (7)$$

Suppose that the oil well bore produces at a constant flow rate, and the well is located at the center of the fracture $(0, 0, Z_e/2)$, the length of fracture is $2L_f$, and the height of fracture is h , $l = L_f$, integrate the fundamental solution of a point source, then the Laplace solution of the bottom hole pressure response function with a vertical fracture model is:

$$\bar{P}_D(x_D, y_D) = \frac{1}{2u} \int_{-1}^1 K_0\left(\sqrt{u} \sqrt{(x_D - \alpha)^2 + y_D^2}\right) d\alpha \quad (8)$$

Derivation of Lord Kelvin point source solution (King, 2010; Chang, 2013; Wellhoefer et al., 2014), using the series function



properly, Poisson superposition formula, Laplace transform, and other methods to simplify, the basic solution of the instantaneous source function of the top-bottom top-bottom reservoir is:

$$\bar{p} = \frac{1}{2\pi Z_{eD}} \left[K_0(R_D \sqrt{u}) + 2 \sum_{n=1}^{\infty} K_0 \left(R_D \sqrt{u + \frac{n^2 \pi^2}{Z_{eD}^2}} \right) \cos \left(n\pi \frac{Z_D}{Z_{eD}} \right) \cos \left(n\pi \frac{Z'_D}{Z_{eD}} \right) \right] \quad (9)$$

Assuming the length of the horizontal well is $2L_H$, fluid flows in or out through a line source, The line source is parallel to the X axis, and the center of the horizontal well (X_W, Y_W, Z_W) is the integration in the axial direction from $X_W - L_h$ to $X_W + L_h$, then the pressure response function of horizontal well in corresponded ding formation can be obtained. The Laplace solution of formation pressure response function of the horizontal well is:

$$\begin{aligned} \bar{p}_D = & \frac{1}{2u} \int_{-1}^1 K_0 \left(\sqrt{(x_D - \alpha)^2 + y_D^2} \sqrt{u} \right) d\alpha \\ & + \frac{1}{u} \sum_{n=1}^{\infty} \cos(n\pi z_D) \cos(n\pi z_{wD}) \\ & \int_{-1}^1 K_0 \left(\sqrt{(x_D - \alpha)^2 + y_D^2} \sqrt{u + \frac{n^2 \pi^2}{Z_{eD}^2}} \right) d\alpha \end{aligned} \quad (10)$$

The Laplace solution of the bottom hole pressure response function of the volume fracturing horizontal well can be obtained by integrating the formation pressure calculation formula of the horizontal well in the Y direction:

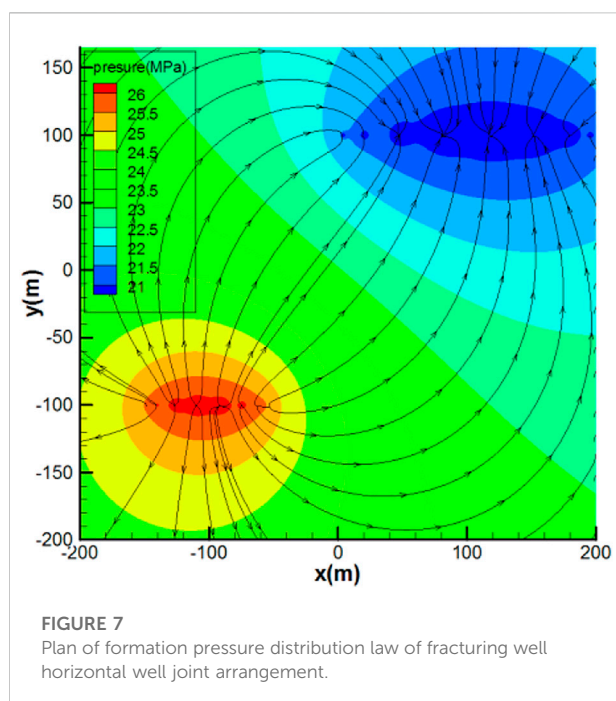
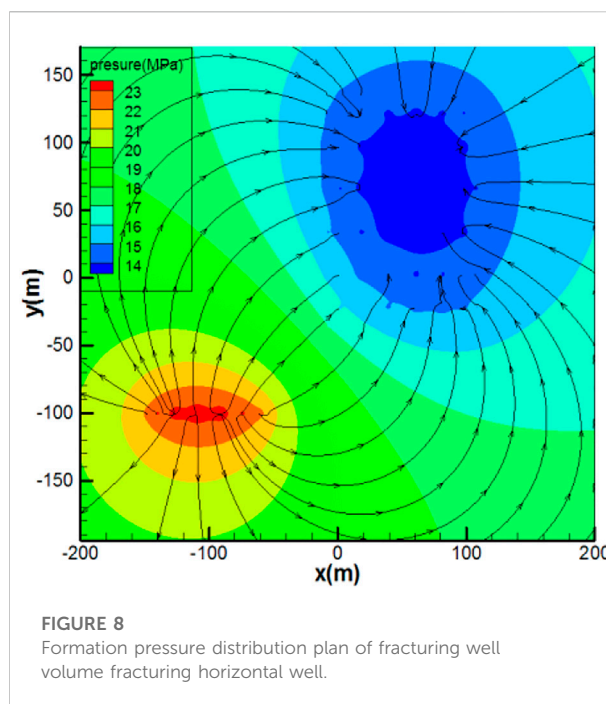
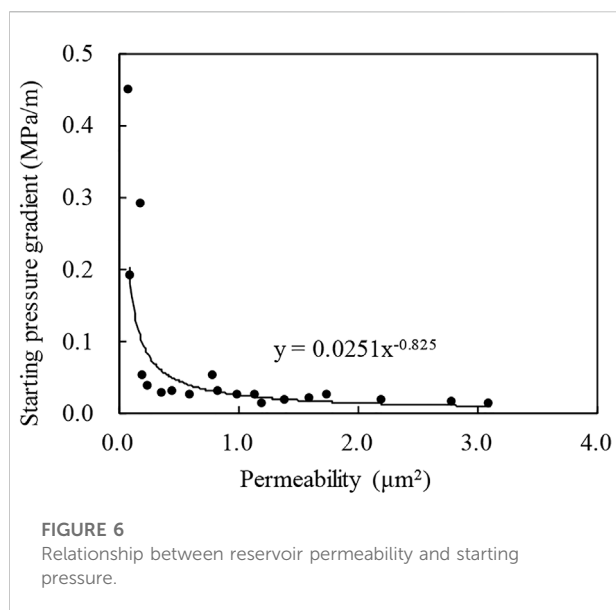
$$\begin{aligned} \bar{p}_D = & \frac{1}{2u\sqrt{u}} \left[\pi - \frac{1 - K_{i2}(2\sqrt{u})}{\sqrt{u}} \right] + \frac{1}{u} \sum_{n=1}^{\infty} \frac{\cos n\pi z_D \cos n\pi z_{wD}}{\sqrt{u + n^2 \pi^2 L_D^2}} \\ & \left[\pi - \frac{1 - K_{i2} \left(2\sqrt{u + n^2 \pi^2 L_D^2} \right)}{\sqrt{u + n^2 \pi^2 L_D^2}} \right] \end{aligned} \quad (11)$$

The bottom hole pressure response function calculation model of the horizontal well in the top-bottom top-bottom reservoir is established, and the infinite formation pressure distribution plan is defined, as is shown in Figure 4. The formation pressure of the horizontal well is elliptical in the near well zone and radial in the far well zone. The pressure drop mainly occurs within 50 m from the bottom of the well. The formation pressure of the fractured horizontal well is elliptical in the near well zone and radial in the far well zone, as is shown in Figure 5. The effective displacement pressure system of horizontal well and volume fracturing well is demonstrated by using the formation pressure calculation formula of horizontal well and volume fracturing well, combined with the potential superposition theory.

3.3.2 Formation pressure distribution

Formation fluid can flow only when the pressure gradient is greater than a certain critical value, and this critical value can flow. This critical value is called starting pressure gradient, and this effect is called the low-speed non-Darcy effect.

The velocity equation considering the starting pressure gradient is:



$$\frac{dP}{dr} = 0.0251K^{-0.825} \quad (12)$$

In combination with the relationship between starting pressure gradient and permeability, according to the formation pressure distribution functions of fractured well, horizontal well, and volume fractured horizontal well, and using the potential superposition theory, the formation pressure distribution calculation functions of the fractured well horizontal well (Figure 7) and fractured well volume fractured horizontal well (Figure 8) are compiled. The horizontal pressure distribution maps of a vertical well horizontal well, fracturing well horizontal well, and fracturing well volume fracturing horizontal well are drawn, and the relationship between different well spacing and start-up pressure gradient is obtained. Combined with the existing relationship between start-up pressure gradient and permeability in the work area, reasonable well spacing under different well types and different permeability is obtained. The starting pressure gradient in the work area is 0.05 mPa/m, the limit well spacing between fracturing and mental well is determined to be 150 m, and the limit well spacing between fracturing and volume fracturing horizontal well is determined to be 190 m.

$$v = \begin{cases} 0 & |\nabla P| < \lambda \\ -\frac{k}{\mu} \nabla P \left[1 - \frac{\lambda}{|\nabla P|} \right] & |\nabla P| > \lambda \end{cases}$$

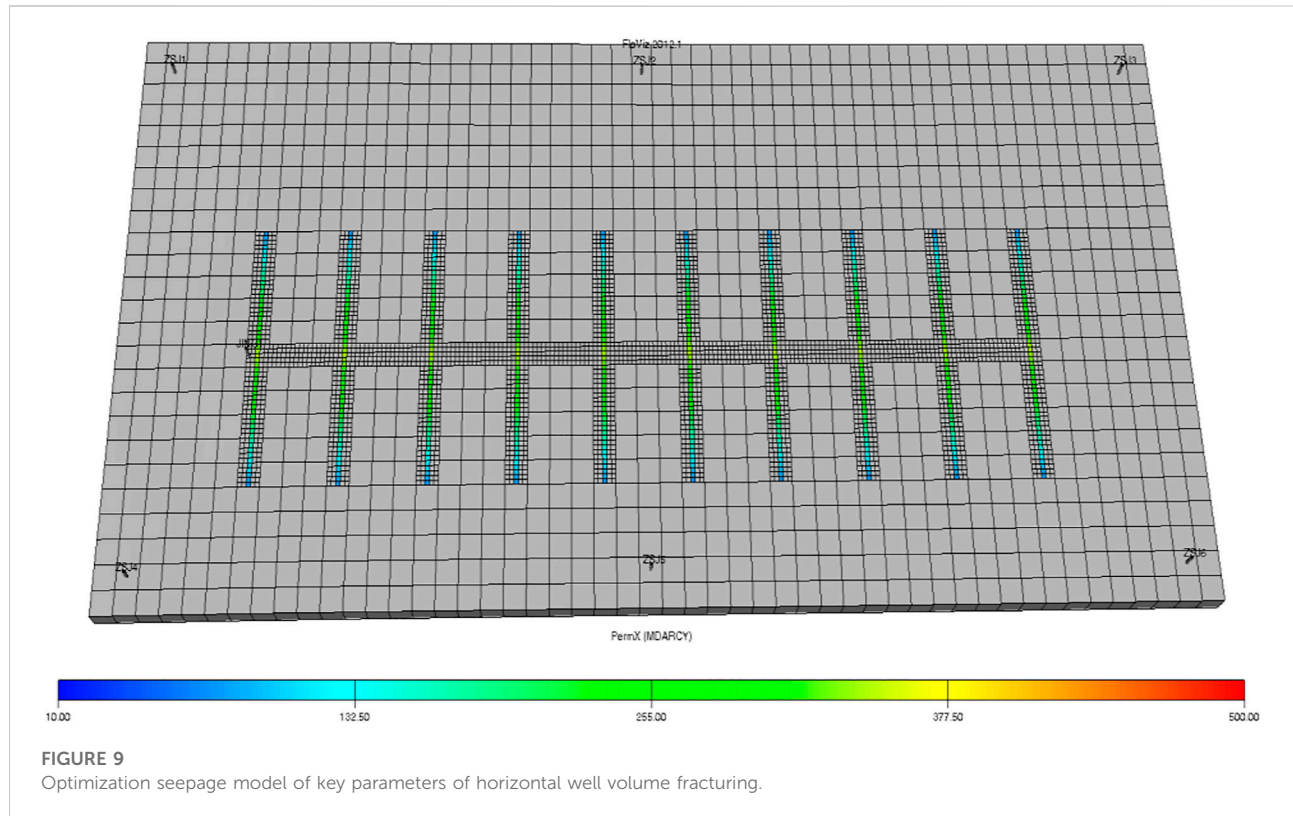
Calculation of starting pressure gradient in low and extra low permeability reservoirs is as follows in Figure 6. The relationship between starting pressure gradient and permeability in the work area is:

4 Optimization of key parameters for volume fracturing of horizontal wells

The fracture network model is established by using the equivalent conductivity and multigrid encryption method. At the same time, the small-scale fracture network simulation

TABLE 4 Hydraulic fracture location data of bow horizontal well.

Fracture no.	1	2	3	4	5	6	7	8	9	10
Vertical depth, m	480.80	482.37	484.38	486.14	487.23	480.38	482.35	485.73	487.93	476.39



method of “main fracture + SRV regional permeability” can be used to study the conductivity matching between secondary fractures, branch fractures, and main fractures.

4.1 Numerical simulation model of volume fracturing in horizontal well

During the development of a fractured horizontal fracture reservoir, there exists a three-phase fluid flow of oil, gas, and water. Fractures can be the main channel of fluid flow, and the reservoir matrix is the main reservoir space of formation fluid. It is assumed that the model meets the following conditions:

1) The pore zone and pressure fracture zone occupy different space areas; 2) Considering the oil, gas, and water phases, the percolation of each phase obeys Darcy’s law; 3) Rock micro compressibility and homogeneity; 4) The water component has no mass transfer effect with the oil phase; 5) Considering the

influence of gravity and capillary force; 6) The compression crack is horizontal, and the crack closure effect is considered.

The fracture network model is established by using equivalent conductivity and a multi-grimulti-gradation method. According to the characteristics of Chang 6 reservoir in Qilicun oilfield of China and well layout (Table 5). Uniform step size is adopted on the plane, and the mesh step size is 30 m × 30 m. The grid direction is East-West to ensure that the artificial crack is parallel to the grid direction. In consideration of the approximate treatment requirements of artificial fractures and horizontal shafts, the local artificial fractures and static areas are densified. The approximate width of artificial fractures is 1 m, and the conductivity of hydraulic fractures is 0.2 Dm.

Combined with the pore permeability and saturation parameters of the reservoir, select the reservoir location with high permeability, high porosity, and high oil saturation in the flow unit for fracturing. Refer to the data divided by the previous flow unit, and select the location with the best physical properties in the flow unit for fracturing. The specific location is shown in Table 4.

TABLE 5 Setting of simulation parameters.

Physical parameters	Parameter value	Physical parameters	Parameter value
Reservoir top depth/m	500	Porosity/%	9.4
Reservoir thickness/m	12	Permeability/mD	0.9
Formation pressure/MPa	4.95	Crude oil density/g/cm ³	0.83
Formation crude oil density/(g/cm ³)	0.83	Formation water viscosity/(mpa·s)	1
Formation crude oil viscosity/(mpa·s)	4.30	Compressibility coefficient of formation water/MPa ⁻¹	0.00005
Crude oil volume factor	1.035	Compressibility of crude oil/MPa ⁻¹	0.0002

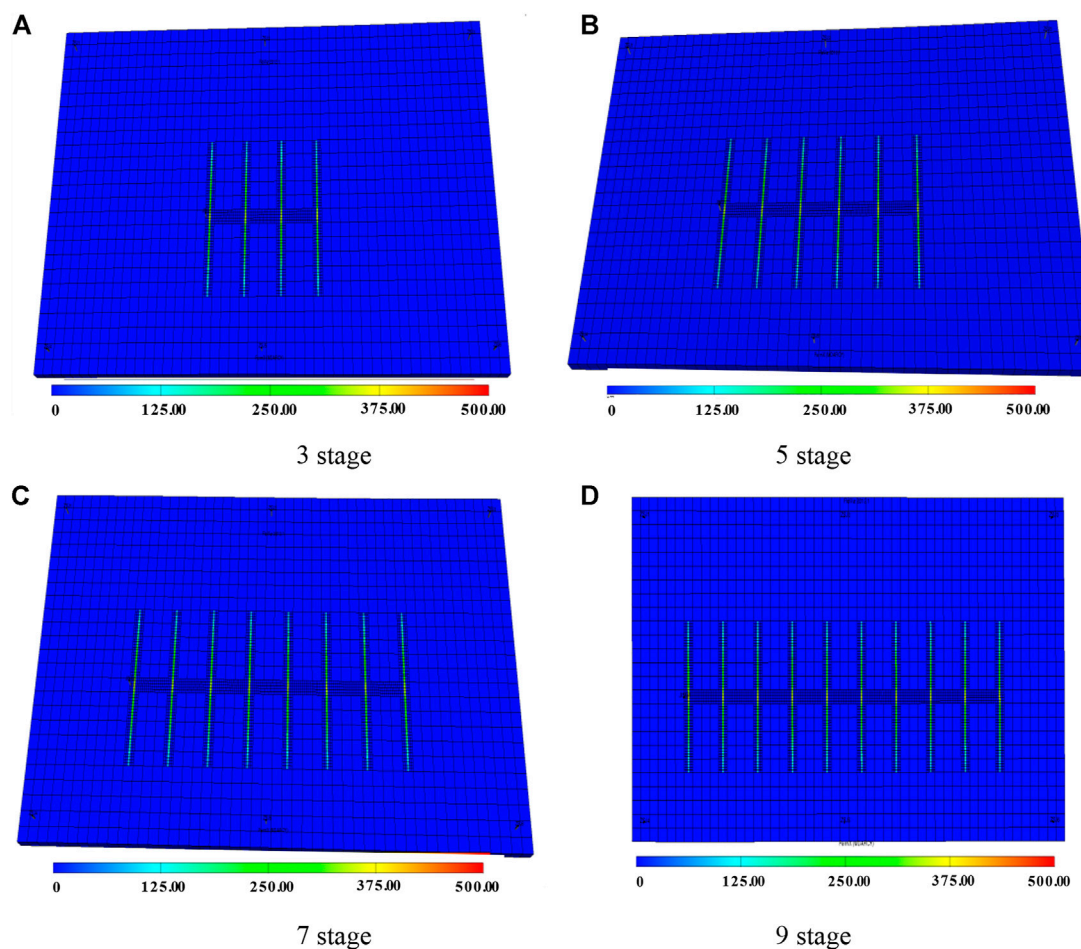
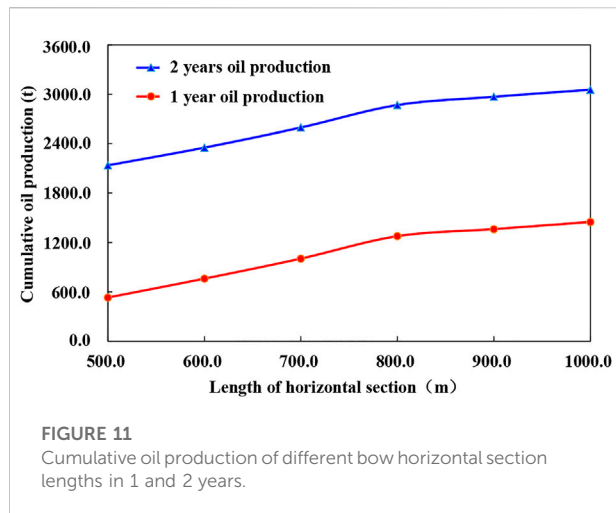


FIGURE 10
Influence of different horizontal well length on reservoir seepage field.

4.2 Calculation of oil well productivity

Assuming that a horizontal well is deployed in the center of a homogeneous circular formation with equal thickness, the fluid flow from the boundary to the wellbore in the formation will no

longer be radial flow like a vertical well but will show more complex fluid flow characteristics. Ignoring the influence of capillary pressure, gravity, and elastic expansion, under the condition of steady flow, different calculation formulas are derived by [Renand and Dupuy \(1991\)](#),

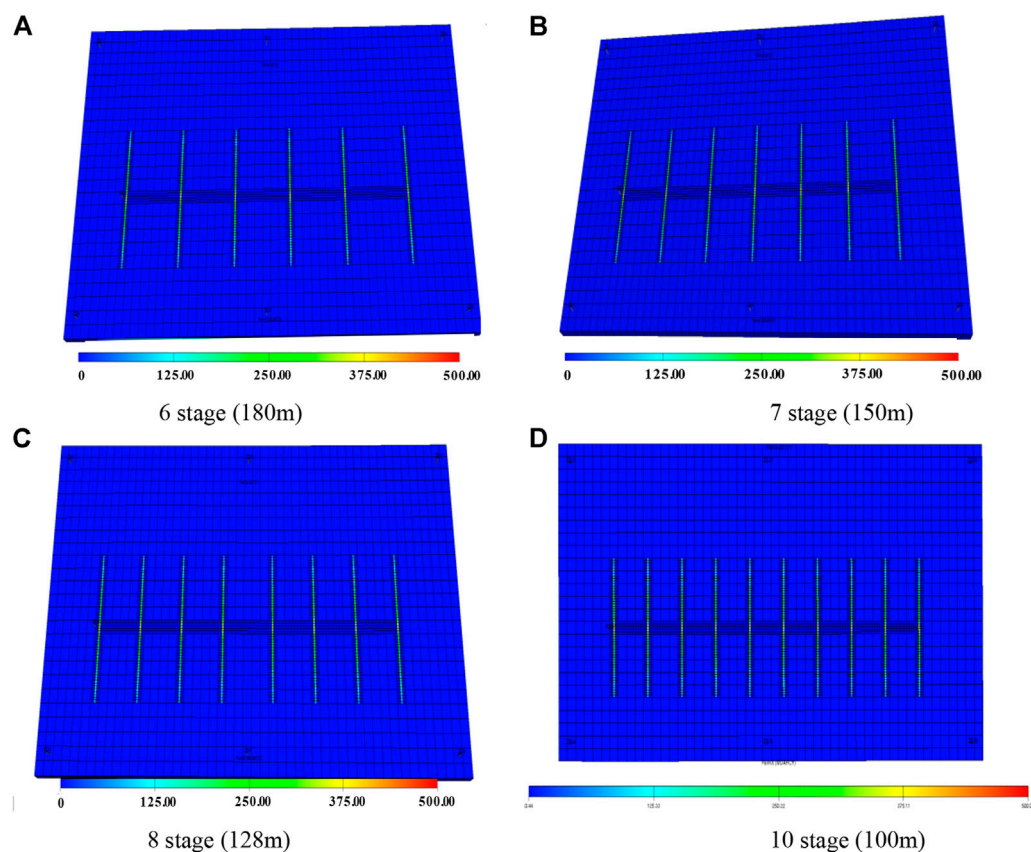


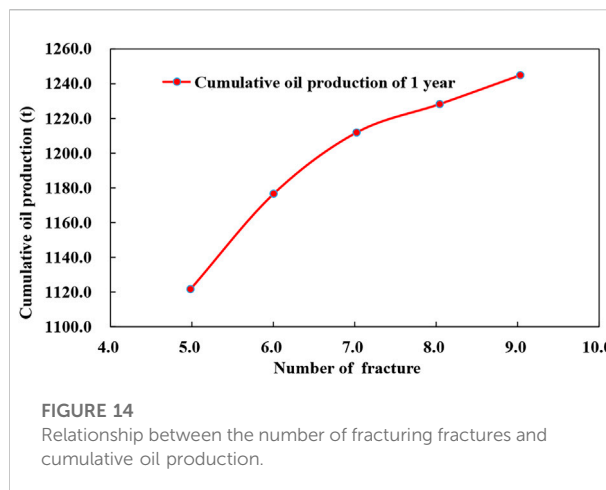
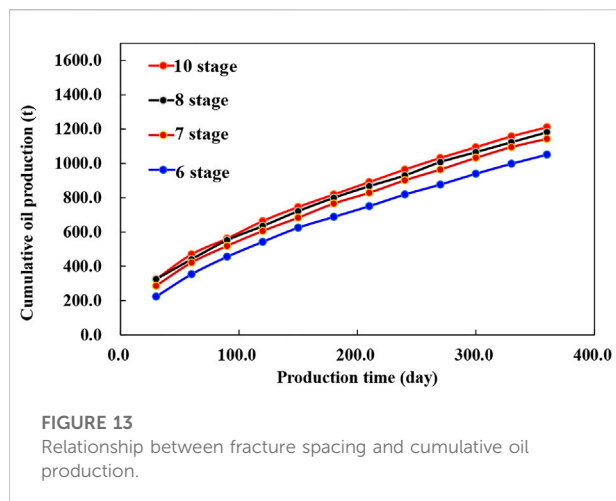
$$q = \frac{2\pi kh(p_e - p_{wf})}{\mu \left(\ln \frac{d + \sqrt{d^2 - 0.25L^2}}{0.05L} + \frac{h}{L} \ln \frac{h}{2\pi r_w} \right)} \quad (13)$$

$$d = \frac{L}{2} \sqrt{\frac{1}{2} + \sqrt{\left(\frac{2r_e}{L}\right)^4 + \frac{1}{4}}}$$

Where, q is well production, m^3/ks ; K is permeability, mD ; h is the reservoir thickness, m ; p_e is supply boundary pressure, MPa ; p_{wf} is the bottom hole pressure, MPa ; μ is the viscosity of oil, $\text{mPa}\cdot\text{s}$; L is the length of horizontal section, m ; r_w is bottom hole radius, m ; r_e is the ellipsoid oil drain radius, m .

Taking the distribution of reservoir seepage field in a fractured horizontal well as an example, as is shown in Figure 9. According to the geological characteristics of the study area and the well layout mode, the uniform step size is adopted on the plane, and the grid step size is $30 \text{ m} \times 30 \text{ m}$, the grid direction is east-west, ensuring that the artificial cracks are parallel to the grid direction. The reservoir thickness is 10 m , the production pressure difference is 2.7 MPa , the viscosity is $4.29 \text{ mPa}\cdot\text{s}$, the horizontal section length is 650 m , the oil drainage radius is 150 m , the well diameter is 0.065 m , a is 960 m , the volume factor is 1.05 after the production is stable, it is 6.0 t/d , and 6.5 t/d is calculated according to the improved formula.





4.3 Optimization of fracture parameters for volume fracturing of horizontal wells

To study the optimal matching of hydraulic fractures, the physical parameters required by the model are set according to the physical properties of the reservoir in the block, and the numerical simulation of oil well productivity under different lengths, segments, and half, length of fractures of horizontal wells is carried out.

4.3.1 Length of horizontal section

The reservoir seepage field model of horizontal well after staged fracturing is obtained by numerical simulation, the pure blue represents the original permeability of the reservoir, the gradual red color represents the increase of reservoir permeability caused by fracturing, and the red represents the optimal conductivity after fracturing. The length of the horizontal well is an important factor affecting the productivity of the oil well. The Four situations are designed, i.e., the length of the horizontal well is 300, 500, 700, and 900 m, respectively, and the fracturing segments of horizontal wells are 3, 5, 7, and 9, respectively, as is shown in Figure 10. Eclipse is used to simulate the above schemes.

The continuous production of horizontal wells is predicted for 1 year. The prediction results show that with the increase in the length of horizontal wells, the cumulative production of oil wells gradually increases. When the length of the horizontal well exceeds 900 m, the increment of production will decrease. Therefore, the optimal length of a horizontal well in this area is recommended to be 900 m.

It can be seen from Figure 11 that the cumulative oil production in 1 and 2 years increases with the increase of horizontal section length of bow shaped well, but it is not a simple linear relationship. At first, the cumulative oil production increases rapidly with the increase of horizontal section length of

bow shaped well, and then slowly decreases. When the length of arcuate well exceeds 900 m, the cumulative oil production curve has an obvious inflection point. Considering that the increase of the length of the water horizontal section will help to improve the productivity, but the drilling and completion cost will rise accordingly, so there is an optimal value, and the optimal value in this study is 900 m.

4.3.2 Spacing of hydraulic fractures

The optimization of the distance between the staged fracturing of horizontal wells is the key to the success of the staged fracturing of horizontal wells. Assuming that the length of the horizontal well is 900 m, four modes of fracturing 6, 7, 8, and 10 are designed respectively, and the numerical simulation models of the above four modes are established by using eclipse numerical simulation software (Figure 12).

It can be seen from the simulation results that the number of fractures in horizontal wells affects the final production effect of horizontal wells. With the increase in fracture interval, the cumulative oil production of the oil well increases. However, due to the limited well control range of horizontal wells, when the fracture density increases to a certain value, the production increment will decrease, and too small the fracture spacing will produce serious inter-fracture interference.

According to the simulation results (Figures 13, 14), at first, the cumulative oil production of bow type wells increases with the increase of production time and the number of fractures, but when the number of fractures increases to 8, the cumulative oil production appears an inflection point, and the increase is obviously slower. The reason is that after the fracture spacing becomes smaller, the mutual interference increases, which reduces the output of a single fracture. The increase of fracturing fracture will lead to the increase of fracturing process cost, so the number of fractures has an optimal value. Therefore, it is suggested that the optimal fracture interval of horizontal wells is 120–130 m/interval, which

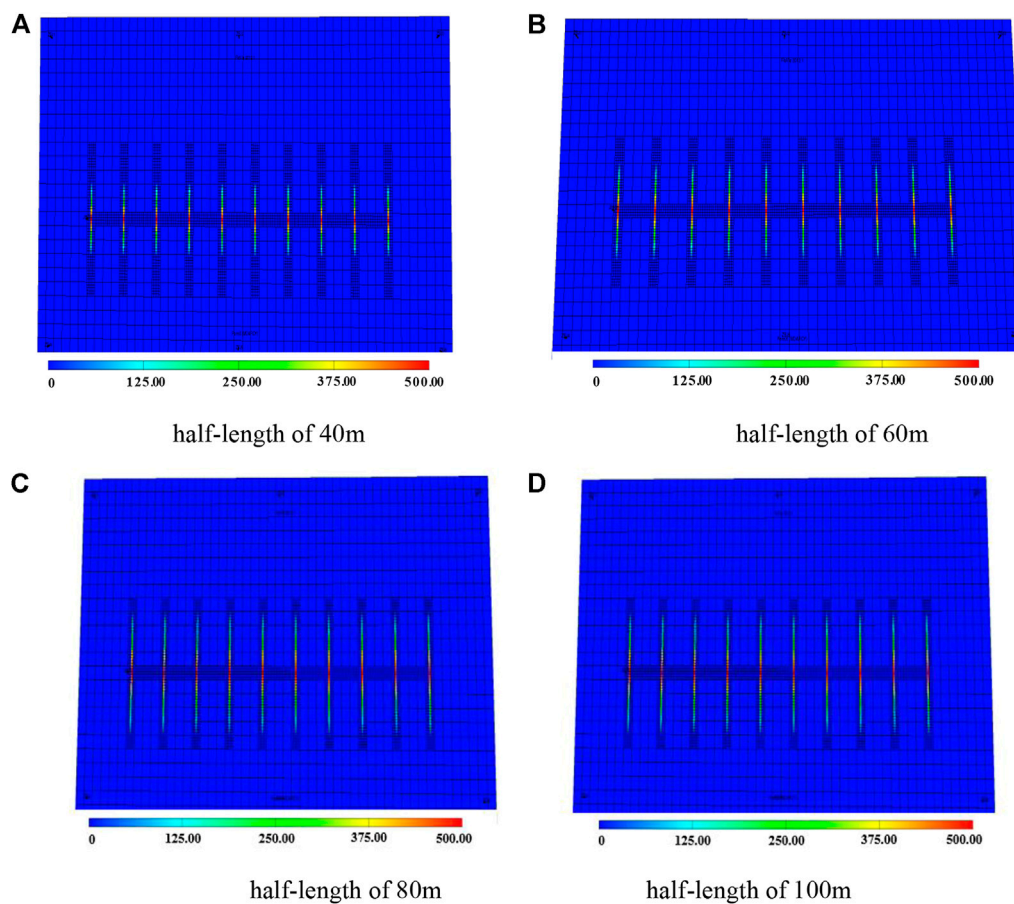


FIGURE 15
Influence of different fracture half-lengths on reservoir seepage field.

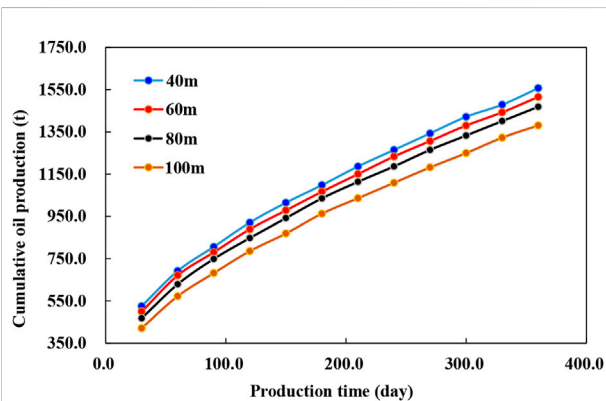


FIGURE 16
The cumulative production of bow shaped horizontal well with half lengths of horizontal fracture.

means that the optimal number of fracturing fractures in horizontal well is 8.

4.3.3 Half-length of hydraulic fractures

Fracture half-length is a key parameter for volume fracturing of horizontal wells. The shorter the fracture half-length, the lower the fracture penetration ratio and the lower the multiple ratios of horizontal wells; The longer the half-length of the fracture, the higher the fracture penetration ratio, and the higher the multiple production ratio of the horizontal well, but the greater the possibility of water channeling in the water injection well. Therefore, using eclipse numerical simulation software, the fracture half-length optimization schemes with fracture half-length of 40, 60, 80, and 100 m are simulated (Figure 15). The longer the half-length of the fracture, the higher the production multiplier ratio of the horizontal well, which is more beneficial to

the production of the oil well. However, the longer the half-length of the fracture, the greater the penetration ratio, and the easier the water channeling of the horizontal well, resulting in violent water flooding. The prediction results show that when the effective half-length of the horizontal well fracture reaches 90 m, the cumulative oil production of the horizontal well is the highest. It is suggested that the half-length of staged fracturing fracture of a horizontal well is 80–90 m.

It can be seen from the analysis in Figure 16 that the cumulative production of the bow shaped horizontal well with multiple horizontal fractures increases with the increase of the fracture half length, but when the fracture half-length is 80m, the increase of the cumulative oil production curve narrows. At the same time, considering the fracturing cost, there is an optimal value. The half-length of the crack is preferably 80 m.

5 Conclusion

- 1) The rock mechanics test shows that the horizontal principal stress difference is small, the rock brittleness index is high, and the transverse sweep width of the joint network is large. The artificial fracture is matched with the horizontal wellbore, and the probability of longitudinal fracture penetration is large. Therefore, large-scale network fracture fracturing in horizontal wells is feasible.
- 2) The pressure response functions of horizontal well and volume fracturing horizontal well are established by using the point source function. Combined with the pressure superposition principle, the formation pressure plane distribution and flow line diagrams of fracturing horizontal well is drawn.
- 3) The distribution function of reservoir *in-situ* stress and formation pressure is established, and the relationship between reservoir permeability and starting pressure gradient in the block is calculated. The reservoir productivity equation of the block is established, which provides a basis for optimizing the fracturing design parameters of horizontal wells. It is proposed that the flow unit should be considered in the design of fracturing parameters of horizontal fractures, the number of fractures should be comprehensively considered whether the fractures can make each flow unit used. The seepage mathematical model of multi-layer fracturing horizontal fracture bow horizontal well can be regarded as the combination of multiple horizontal fracture flow units.
- 4) The fracture network model is established by using equivalent conductivity and multi-grid method, and the volume fracturing design parameters of horizontal wells are optimized, considering the seepage characteristics of the flow unit. The simulation results show that the optimal length of the horizontal well is 800 m, the optimal fracture interval is 120 m/segment, and the optimal half-length of fracture is 80–90 m, which can improve the reservoir development effect.

Data availability statement

The raw data supporting the conclusion of this article will be made available by the authors, without undue reservation.

Author contributions

We confirm that the manuscript has been read and approved by all named authors and that there are no other persons who satisfied the criteria for authorship but are not listed. We further confirm that the order of authors listed in the manuscript has been approved by all of us. We understand that MW is the sole contact for the Editorial process. MW is responsible for communicating with the other authors about progress, submissions of revisions, and final approval of proofs. CG and MW: Conceptualization Formal analysis, Writing an original draft, Project administration, funding acquisition. SC: Software, Methodology, writing original draft, Writing-review, editing. WW, XM, SL, and ZG: Project administration, Formal analysis, Data curation.

Funding

This work was supported by the support of the National Natural Science Foundation of China: Study on dynamic characteristics of methane/carbon dioxide in shale heterogeneous reservoir under multi-field coupling (Program No. 41772150).

Conflict of interest

CG was employed by Yanchang Oil Field Co., LTD. WW was employed by Southwest Oil and Gas Field Company of CNPC Chengdu. ZG and XM were employed by Technology and Information Management Department of Yanchang Oilfield Co., Ltd. SL was employed by Engineering Research Institute of PetroChina Southwest Oil and Gasfield Company

The remaining authors declare that the research was conducted in the absence of any commercial or financial relationships that could be construed as a potential conflict of interest.

Publisher's note

All claims expressed in this article are solely those of the authors and do not necessarily represent those of their affiliated organizations, or those of the publisher, the editors and the reviewers. Any product that may be evaluated in this article, or claim that may be made by its manufacturer, is not guaranteed or endorsed by the publisher.

References

- Brice, L., and Jean, D. (2015). Simultaneous initiation and growth of multiple radial hydraulic fractures from a horizontal wellbore. *J. Mech. Phys. Solids* 82, 235–258. doi:10.1016/j.jmps.2015.05.010
- Bunger, A. P., Zhang, X., and Jeffery, R. G. (2011). “Parameters affecting the interaction among closely spaced hydraulic fractures,” in *SPE 140426, SPE hydraulic fracturing technology conference and exhibition* (Woodlands, TX, USA, 24–26).
- Chang, X. (2013). Fracture propagation in shallow tight reservoirs of Fuxian Block. *Pet. Drill. Tech.* 41, 109–113. (In Chinese).
- Dohmen, T., Zhang, J., and Blangy, J. P. (2014). “Measurement and analysis of 3D stress shadowing related to the spacing of hydraulic fracturing in unconventional reservoirs,” in *SPE annual technical conference and exhibition*, Amsterdam, Netherlands, October 2014.
- Du, G. C., Hu, S. Q., Shi, L. H., Wei, F., et al. (2015). Reservoir characteristics and pore evolution of Chang 6 oil reservoir set in Qilicun Oilfield. *Lithol. Reserv.* 27, 51–57. (In Chinese).
- El Rabba, W. (1989). “Experimental study of hydraulic fracture geometry initiated from horizontal wells,” in *SPE annual technical conference and exhibition*. San Antonio, TX, USA.
- Hillerborg, A., Modeer, M., and Petersson, P. E. (1976). Analysis of crack formation and crack growth in concrete by means of fracture mechanics and finite elements. *Cem. Concr. Res.* 6 (6), 773–781. doi:10.1016/0008-8846(76)90007-7
- Jiang, T. X., Wang, H. T., Bian, X. B., Li, H., Liu, J., Wu, C., et al. (2018). Volume fracturing technology for horizontal well and its application. *Lithol. Reserv.* 30, 1–11. (In Chinese).
- Kazemi, H. (1982). Low-permeability gas sands. *J. Petroleum Technol.* 34 (10), 2229–2232. doi:10.2118/11330-PA
- Kelvin, L. (1884). *Mathematical and physical papers*. London: Cambridge University Press.
- King, G. E. (2010). “Thirty years of gas shale fracturing: What have we learned?,” in *SPE annual technical conference and exhibition*, Florence, Italy, September 2010.
- Li, Y., He, Q., Yao, C., Zhang, Y., Wang, X., et al. (2013). Discussion on fracture morphology of shallow layer fracturing in the south of Ordos basin. *Petroleum Geol. Eng.* 27, 105–107. (In Chinese).
- Li, K., Chen, G., Li, W., Wu, X., Tan, J., and Qu, J. (2018). Characterization of marine-terrestrial transitional Taiyuan formation shale reservoirs in Hedong coal field, China. *Adv. Geo-Energy Res.* 2 (1), 72–85. doi:10.26804/ager.2018.01.07
- Li, C., Singh, H., and Cai, J. (2019). Spontaneous imbibition in shale: A review of recent advances. *Capillarity* 2 (2), 17–32. doi:10.26804/capi.2019.02.01
- Meng, X. G., Yuan, Y. J., and Dai, X. X. (2014). Characteristics of Chang 6 reservoir in Y49 region, Qilicun oilfield. *Liaoning Chem. Ind.* 43, 791–793. (In Chinese).
- Mokryakov, V. (2011). Analytical solution for propagation of hydraulic fracture with Barenblatt's cohesive tip zone. *Int. J. Fract.* 169, 159–168. doi:10.1007/s10704-011-9591-0
- Mutalik, P. N., and Gibson, B. (2008). “Case history of sequential and simultaneous fracturing of the Barnett shale in parker county,” in *SPE annual technical conference and exhibition*, Denver, Colorado, September 2008.
- Rafiee, M., Soliman, M. Y., and Pirayesh, E. (2012). “Hydraulic fracturing design and optimization: A modification to zipper frac,” in *SPE 159786, presented at the SPE eastern regional meeting* (Kentucky, USA).
- Renand, G., and Dupuy, J. M. (1991). Formation damage effects on horizontal well flow efficiency. *JPT* 7, 786–789.
- Sesetty, V., and Ahmad, G. (2015). A numerical study of sequential and simultaneous hydraulic fracturing in single and multi-lateral horizontal wells. *J. Petroleum Sci. Eng.* 132, 65–76. doi:10.1016/j.petrol.2015.04.020
- Somanchi, K., Brewer, J., and Reynolds, A. (2017). “Extreme limited entry design improves distribution efficiency in plug-n-perf completions: Insights from fiber-optic diagnostics,” in *SPE hydraulic fracturing technology conference and exhibition*.
- Su, H., Lwi, Z., Zhang, D., Li, J., Ju, B., and Zhang, Z. (2018). Volume fracturing parameters optimization of horizontal well in tight reservoir. *Lithol. Reserv.* 30, 140–148. (In Chinese).
- Su, G., Han, Q., Ma, X., and Wang, L. (2018). Study and application of the stimulated reservoir volume fracture technology in dense gasfield. *Petrochem. Ind. Appl.* 37, 74–76. (In Chinese).
- Su, Y., Wang, B., Xu, N., Zhang, Z., Liu, Y., and Hou, J. (2020). Discussion on energy storage fracturing technology of Chang X tight reservoir in block A of Dingbian area. *Petrochem. Ind. Appl.* 39, 62–65. (In Chinese).
- Wang, H., Marongiu-Porcu, M., and Economides, M. J. (2016). Poroelastic and poroplastic modeling of hydraulic fracturing in brittle and ductile formations. Paper SPE 168600-PA. *SPE Production & Operations* 31 (1), 47–59.
- Wang, H. (2016). Numerical investigation of fracture spacing and sequencing effects on multiple hydraulic fracture interference and coalescence in brittle and ductile reservoir rocks. England: Eng. Fract. Mech. 157, 107–124. doi:10.1016/j.engfracmech.2016.02.025
- Wang, X. J., Tang, H., She, L., Zou, G., Zhou, J., Li, X., et al. (2014). Optimization of fracture parameters of horizontal well in low permeability reservoir. *Lithol. Reserv.* 26, 129–132. (In Chinese).
- Wellhoefer, B. J., Eis, A., and Gullickson, G. W. (2014). “Does a multi-entry, multi-stage fracturing sleeve system improve production in Bakken Shale wells over other completion methods?,” in *SPE/CSUR unconventional resources conference*.
- Weng, X., Kresse, O., Cohen, C. E., Wu, R., and Gu, H. (2011). Modeling of hydraulic fracture network propagation in a naturally fractured formation. *SPE Prod. Operations* 26 (4), 368–380. doi:10.2118/140253-pa
- Westwood, R. F., Toon, S. M., Styles, P., and Cassidy, N. J. (2017). Horizontal respect distance for hydraulic fracturing in the vicinity of existing faults in deep geological reservoirs: A review and modelling study. *Geomech. Geophys. Geo. Energy. Ge. Resour.* 3, 379–391. doi:10.1007/s40948-017-0065-3
- Xiong, J., Wang, S. P., and Guo, P. (2012). Study on the production-increasing law of the horizontally fractured wells in low-permeability reservoirs. *Special Oil Gas Reservoirs* 19, 101–103. (In Chinese).
- Xiong, Y., Zhang, L., Zhao, Y., and Liu, Q. (2014). Pressure transient analysis of hydraulic fractured vertical well in stress-sensitive shale gas reservoirs. *Sci. Technol. Eng.* 14, 221–225.
- Xiong, H. J., Liu, S. X., Feng, F., Liu, S. A., and Yue, K. M. (2020). Optimizing fracturing design and well spacing with complex-fracture and reservoir simulations: A permian basin case study. *SPE Prod. Operations* 35 (04), 0703–0718. doi:10.2118/194367-pa
- Xu, Y., Chen, M., Wu, Q., Li, D. Q., Yang, N. Y., Weng, D. W., et al. (2016). Stress interference calculation model and its application in volume stimulation of horizontal wells. *Petroleum Explor. Dev.* 43 (5), 849–856. doi:10.1016/s1876-3804(16)30101-x
- Xu, J., Wu, K., Li, R., Li, Z., Jing, L., Xu, Q., et al. (2018). Real gas transport in shale matrix with fractal structures. *Fuel* 219, 353–363. doi:10.1016/j.fuel.2018.01.114
- Xu, J., Chen, Z., Wu, K., Li, R., Liu, X., and Zhan, J. (2019). On the flow regime model for fast estimation of tight sandstone gas apparent permeability in high-pressure reservoirs. *Energy Sources, Part A Recovery, Util. Environ. Eff.*, 1–12. doi:10.1080/15567036.2019.1687625
- Xu, J., Wu, K., Li, R., Li, Z., Li, J., Xu, Q., et al. (2019). Nano-scale pore size distribution effects on gas production from fractal shale rocks. *Fractals* 27 (8), 1950142. doi:10.1142/S0218348X19501421
- Yang, H., Liang, X., He, H., Wang, D., Wang, J., et al. (2014). Study on the hydraulic fracture morphology in Yanchang oilfield. *J. Chongqing Inst. Sci. Technol.* 16, 9–11. (In Chinese).
- Yew, C. H., and Weng, X. W. (2015). in *Chapter eight- stress shadow* (Boston: Gulf Professional Publishing), 177–195.
- Yi, X. Y., Zhang, Z., Li, C. Y., Li, D. C., and Wang, S. B. (2013). “Well, test interpretation method of horizontal well in stress-sensitive gas reservoir,”. *Applied mechanics and materials* (Trans Tech Publications, Ltd), 295–298, 3183–3191.
- Zhang, S., Wen, Q., Wang, F., Zhang, G., et al. (2004). Optimization design of integral fracturing parameters for a four-spot well pattern with horizontal fractures. *Acta Pet. Sin.* 25 (1), 74–78. (In Chinese).
- Zhang, R., Li, L., Qi, L., and Luo, Y. (2015). Vertical well network fracturing technique policy argument in zhaoyuannan oilfield. *Sci. Technol. Eng.* 15, 29–35. (In Chinese).
- Zhang, H., Meng, X. G., Shao, C. J., Dai, X., Yu, H., Li, X., et al. (2018). Forming mechanism and monitoring of horizontal hydraulic fracture: a case from Qilicun oilfield. *Lithol. Reserv.* 30, 138–145. (In Chinese).
- Zhang, Y., Yan, Y., Liu, L., Gao, Y., and Zhao, S. (2020). Exploration and practice of extending the stage fracturing technology of horizontal wells in Yanchang oilfield. *J. Yanan Univ. Nat. Sci. Ed.* 39, 57–60. (In Chinese).
- Zhang, Z., Zhang, S., Zou, Y., Ma, X., Ning, L., and Liu, L. (2021). Experimental investigation into simultaneous and sequential propagation of multiple closely spaced fractures in a horizontal well. *J. Petroleum Sci. Eng.* 202, 108531. doi:10.1016/j.petrol.2021.108531



OPEN ACCESS

EDITED BY

Fuyong Wang,
China University of Petroleum, China

REVIEWED BY

Zhonghu Wu,
Guizhou University, China
Shuai Gao,
Northeast Petroleum University, China

*CORRESPONDENCE

Meng Zhao,
mengzhao@petrochina.com.cn

SPECIALTY SECTION

This article was submitted to Advanced
Clean Fuel Technologies,
a section of the journal
Frontiers in Energy Research

RECEIVED 25 May 2022

ACCEPTED 31 October 2022

PUBLISHED 06 January 2023

CITATION

Cheng M, Wei Y, Ji G, Ning B and Zhao M
(2023), Differences in production
decline characteristics of horizontal
wells in tight gas sandstone reservoirs
with different qualities: A case study of
the Sulige gas field, Ordos Basin.
Front. Energy Res. 10:952454.
doi: 10.3389/fenrg.2022.952454

COPYRIGHT

© 2023 Cheng, Wei, Ji, Ning and Zhao.
This is an open-access article
distributed under the terms of the
[Creative Commons Attribution License](#)
(CC BY). The use, distribution or
reproduction in other forums is
permitted, provided the original
author(s) and the copyright owner(s) are
credited and that the original
publication in this journal is cited, in
accordance with accepted academic
practice. No use, distribution or
reproduction is permitted which does
not comply with these terms.

Differences in production decline characteristics of horizontal wells in tight gas sandstone reservoirs with different qualities: A case study of the Sulige gas field, Ordos Basin

Minhua Cheng, Yunsheng Wei, Guang Ji, Bo Ning and
Meng Zhao*

Research Institute of Petroleum Exploration and Development (RIPED), Beijing, China

Development of horizontal wells is one of the important means to improve the well production of the tight gas reservoir and realize the effective development of tight gas. Based on abundant static and dynamic data of a large number of horizontal wells that have been put into operation, structure characteristics of a tight reservoir carried out, detailed geologic analysis of the effective reservoir drilled by horizontal wells, and development dynamic analysis, three effective reservoir lateral distribution modes of the block concentrated development mode, medium layer, and thin layer superimposed mode and thin layer isolated model mode are proposed and their adaptability to the horizontal well deployment is evaluated. The drilled reservoir is divided into three types: high-quality reservoir, suboptimal reservoir, and poor reservoir, and the quantitative classification standard is established. On this basis, the decline rule and the difference of horizontal well drilling in different quality reservoirs are discussed, and the quantitative evaluation standard of the horizontal well development effect is established. The initial decline rates of the three types of horizontal wells are 32.9%, 35%, and 40%, and the estimate ultimate recoveries (EURs) of three types of horizontal wells are 89 million cm³, 68 million cm³, and 31 million cm³, respectively. The results of this study provide technical support for the optimal deployment of new horizontal wells in the Sulige gas field and a reference for the development of horizontal wells in the same types of gas reservoirs.

KEYWORDS

tight sandstone gas reservoir, reservoir quality, horizontal well, decreasing characteristics, Ordos Basin

Introduction

The use of horizontal wells was originally proposed in 1928 and has been widely implemented in many countries since the 1980s. Currently, the United States and Canada are the two major countries with a large number of horizontal wells and a high technological level. Compared with vertical wells, horizontal wells can expand the seepage area in a fixed reservoir area, reduce the size of the drilling footage, and reduce material costs while ensuring production. This is currently one of the most effective means of increasing single well production and reducing the number of wells. The development and application of horizontal wells have greatly benefited the large-scale development of tight oil, tight gas, and shale gas.

Horizontal wells have been successfully used in the development of tight gas sandstone reservoirs around the world. Tight gas reservoirs are mainly sand bar-coastal plains and delta sedimentary systems, such as the Dakota and Pictured Cliffs gas reservoirs in the San Juan Basin. These reservoirs have a large effective thickness, stable effective reservoir distribution, and good connectivity and continuity. Moreover, the amount of fluvial sediment is relatively small. In comparison, the tight gas sandstone reservoirs in China are mostly fluvial sediment systems. For example, in the Sulige gas field in the Ordos Basin, the effective sandstone bodies are distributed in a lenticular form and are connected horizontally. Moreover, the sand body thickness is small (He et al., 2004; Jia et al., 2007). Due to the complex geological conditions and the limitations of horizontal well technology, the horizontal well development in the Sulige gas field underwent four stages: preliminary exploration (before 2010), scale production (2010–2013), rapid development (2014–2016), and stable development (2017 to present). With an increasing understanding of the geological conditions and the development of horizontal well technology, the overall development of horizontal wells has gradually improved. However, due to differences in the strata, reservoir quality, and structural characteristics of the different blocks, the results of the horizontal well implementation vary greatly. Under the situation where in the development of the gas field enrichment areas is prioritized, the quality of the remaining areas gradually decreases, and the outcome of horizontal well drilling needs to be further evaluated (Zhang et al., 2013; Lu et al., 2015; Guang et al., 2019).

Based on the static and dynamic data for a large number of horizontal wells that have been put into production, in this study, we focused on the detailed geological characteristics of the horizontal wells and the dynamic and static parameters in order to analyze the declining characteristics and differences in the horizontal wells in different reservoirs. Then, quantitative identification and classification standards were established,

thereby providing technical support for the scale production and efficient development of the Sulige gas field and providing a reference for the development of horizontal wells in the same types of gas reservoirs in China.

Study area

The Sulige gas field is located in the middle section of the northern part of the Ordos Basin, with an exploration area of $5 \times 10^4 \text{ km}^2$ and a superimposed gas-bearing area of about $4 \times 10^4 \text{ km}^2$. The main gas-bearing strata are located in the Upper Paleozoic Permian He 8 member of the Shihezi Formation and the Shan 1 member of the Shanxi Formation (Well patterning filling strategy to, 2018; He et al., 2022) (Table 1). The proven reserves (including almost proven reserves) in the area are $4 \times 10^{12} \text{ m}^3$, the reservoir permeability ranges from 0.01 to 2.0 mD, and the porosity ranges from 2% to 14%. The area is a large-scale tight gas sandstone reservoir, and it currently has the largest scale natural gas reserves and the highest annual output in China.

Basic geological characteristics

Sedimentary facies

The Sulige gas field is 250 km long and 200 km wide (Li and Peng, 2007; Wen et al., 2007). The He 8 member of the Upper Paleozoic Lower Shihezi Formation is a gentle-slope braided river delta deposit, with a 0.2–1.0 km single-stage channel. The river channel has undergone repeated horizontal migration and vertical stacking, forming a large contiguous sandstone reservoir that is hundreds of kilometers long. The Shan 1 member of the Shanxi Formation is a low-curvature meandering river delta deposit. The channel and swamps are alternately distributed. The channel sand body extends for hundreds of kilometers. The single-stage channel width is 0.1–1.0 km, which is superimposed and extended on the plane.

A large amount of core analysis data has revealed that only the coarse facies such as coarse sandstone and gravel-bearing coarse sandstone in the gas field form effective reservoirs (Cheng et al., 2021). The coarse facies are mainly distributed in the core and the lower part of the channel filling microfacies, accounting for 35%–40% of the total thickness of the sandstone. The coarse facies in the core account for 25%–30%, and the coarse facies in the lower channel account for 10%.

Reservoir characteristics

The main strata in the gas field, i.e., the He 8 and Shan 1 members, have similar sandstone compositions. The types of

TABLE 1 Formation development situation of the Sulige gas field, Ordos gas field, and Ordos Basin.

Strata		Indication layer			
Triassic		Liujiagou formation			
Permian	Upper Permian	Shiqianfeng formation P _{3q}			
	Middle Permian	Upper Shihezi formation	He ₁	P _{2sh1}	—K1: top of the upper Shihezi, purple-red mudstone, high gamma.
			He ₂	P _{2sh2}	
			He ₃	P _{2sh3}	
			He ₄	P _{2sh4}	
		Lower Shihezi formation	He ₅	P _{2x5}	—K2: top of the lower Shihezi, peach shale, high gamma.
			He ₆	P _{2x6}	
			He ₇	P _{2x7}	
			He ₈	P _{2x8}	
	Lower Permian	Shanxi formation	Shan ₁	P _{1s1}	—K3: Above the sandstone at the bottom of the lower Shihezi, purple mudstone, high gamma.
			Shan ₂	P _{1s2}	
		Taiyuan formation	Tai ₁	P _{1t1}	
			Tai ₂	P _{1t2}	
Carboniferous	Upper	Benxi formation		C _{2b}	Stable distribution of No. 8 coal at the top.
Ordovician	Lower	Majiagou formation		O _{1m}	

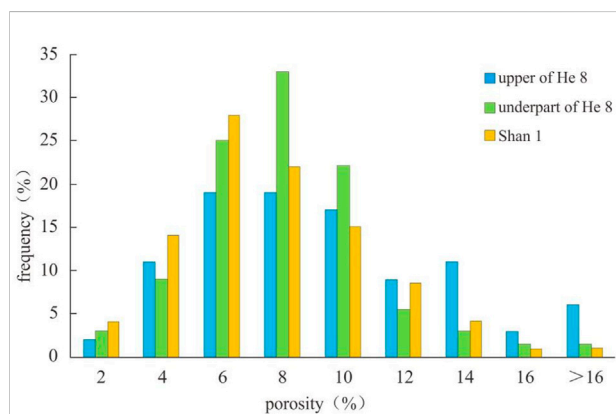


FIGURE 1

Reservoir porosity distribution histogram for the Sulige gas field.

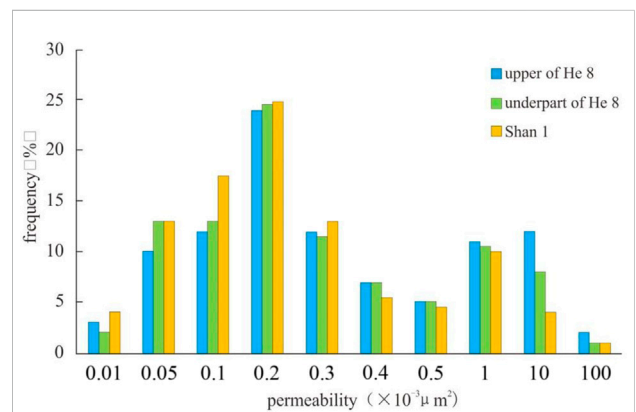
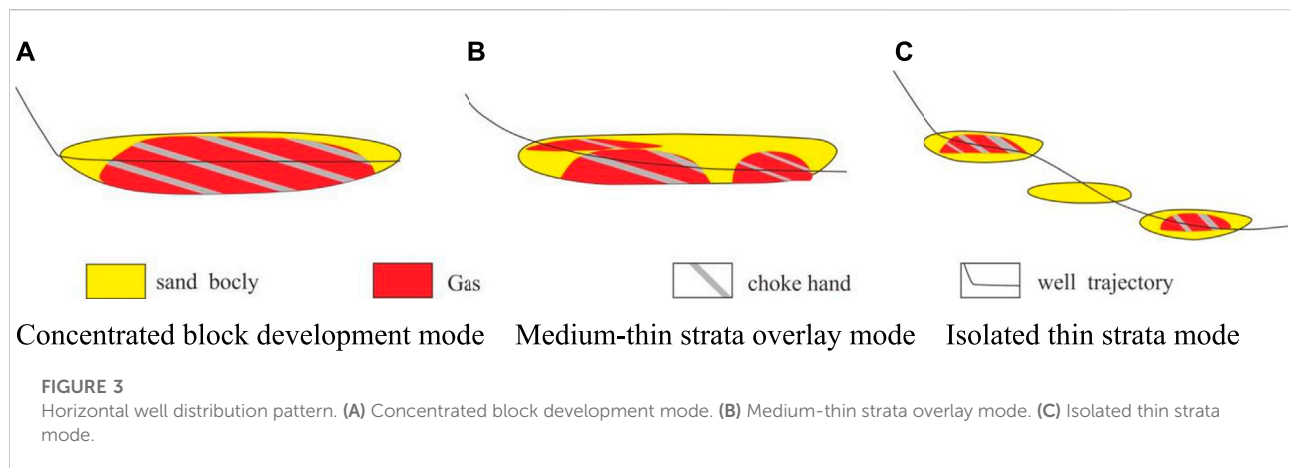


FIGURE 2

Reservoir permeability distribution histogram for the Sulige gas field.

sandstone are mainly lithic quartz sandstone and quartz sandstone, with a small amount of lithic sandstone (Zeng et al., 2022). The sandstone has a large grain size (0.2–1 mm) and is mainly composed of coarse sandstone, medium-coarse sandstone, and a small amount of gravel-bearing coarse sandstone and medium-fine sandstone. The reservoir has typical physical

properties, i.e., low porosity and low permeability. The average porosity is 7.45% (range: 4%–12%) (Figure 1). The permeability exhibits a double peak characteristic (Figure 2), with primary and secondary peaks at $0.2 \times 10^{-3} \mu\text{m}^2$ and $1 \times 10^{-3} \mu\text{m}^2$, respectively. Generally, the physical properties of the He 8 member are better than those of the Shan 1 member (Fu et al., 2008).



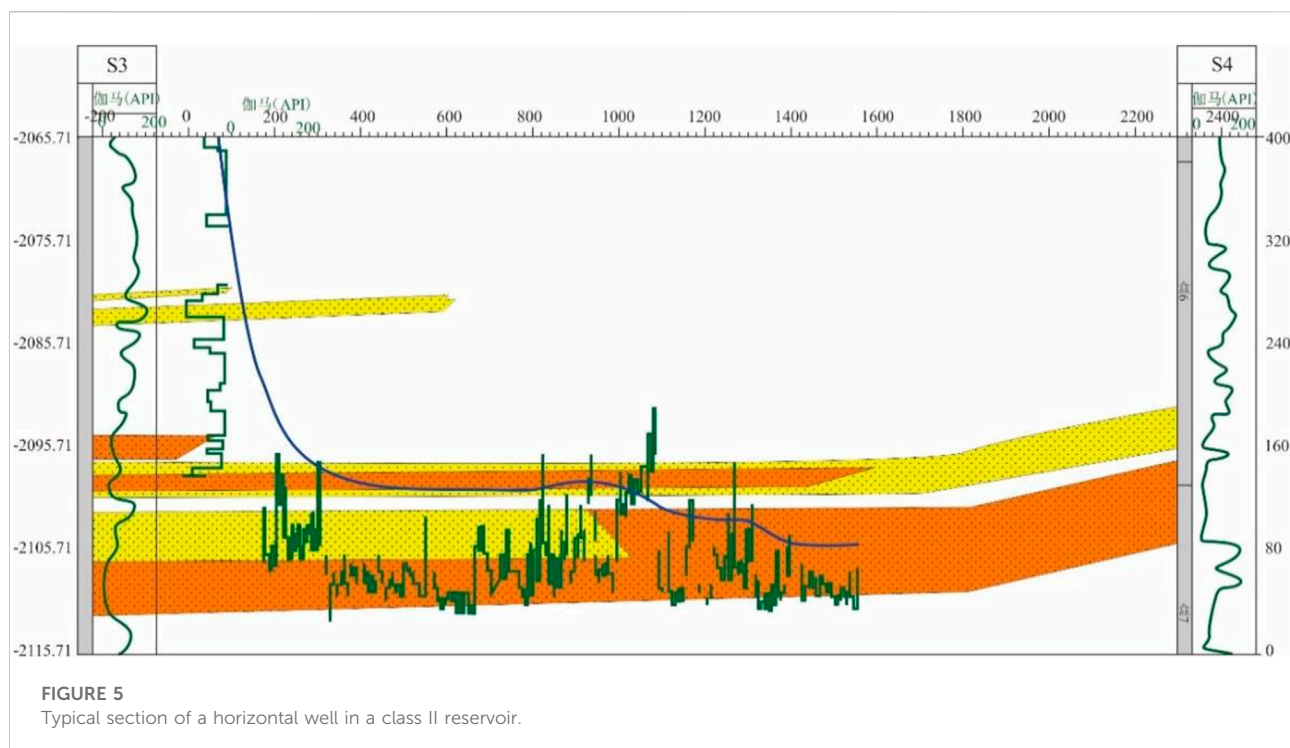
Fine characterization of the reservoir spatial structure and development of the classification standard

Due to the obvious zonal characteristics of the spatial development of braided river systems, there are large differences in the spatial structural characteristics of the different zones. The differences not only affect the quality of the reservoir but also the dynamic indicators of the gas wells, such as the open flow, decline rate, dynamic reserves, and control range. Based on the analysis of the effective reservoirs in a large number of horizontal wells, the factors influencing the reservoir quality were identified, and a reservoir quality classification

standard was formulated to provide a reference for analyzing the suitability of the horizontal well development.

Reservoir structure modes

Based on the spatial distribution of the structural characteristics of the tight gas reservoirs, the well trajectory of the effective reservoirs, and the dynamic response, three horizontal reservoir distribution modes were established: the concentrated block development mode, the medium-thin strata overlay mode, and the isolated thin strata mode (Figure 3).



Characterization of the reservoir structure

The concentrated block development mode is mainly distributed in the main part of the superimposition zone of the braided river system, and it has the best hydrodynamic conditions. As can be seen from the typical section shown in Figure 4, the effective sand body of a single-stratum block with a large thickness has good horizontal continuity, the distribution of the geological reserves is relatively concentrated, the main stratum is prominent, and the lithology is pure medium-coarse sandstone. The effective sand body drilling success rate of this structural mode was 63.6% on average.

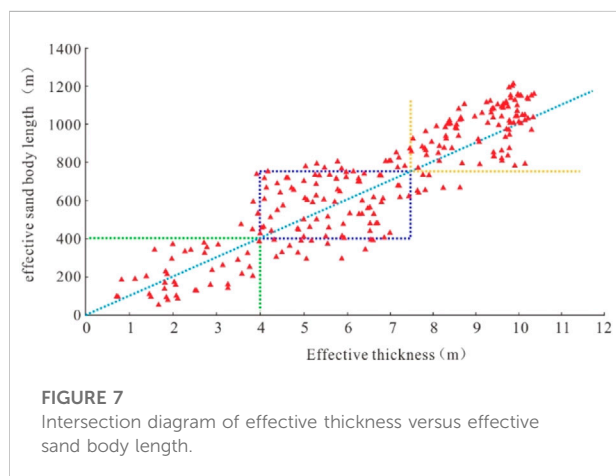
The medium-thin strata overlay mode is mainly distributed in the lateral wings and the transition zone of the braided river system. The hydrodynamic conditions of these facies were fairly good. As can be seen from the typical section shown in Figure 5, the superimposition thickness of the sandstone is about 10 m. There are a number of effective sand bodies with varying thicknesses, and the horizontal continuity is good. The sandstone is finer than that of the block strata mode, and there is obvious sand–shale interbedding. The effective sand body drilling success rate was 50%–60% on average.

The isolated thin strata mode is mainly distributed between the braided river systems. This facies had the weakest hydrodynamic conditions. There are obvious channel stages, and the horizontal continuity is poor. As can be seen from Figure 6, there is obvious sand–shale interbedding, and the effective sand bodies are thin and isolated. The grain size is fine, and the shale content is high. The effective sand body drilling success rate was less than 40%.

Reservoir quality classification standard

Based on the spatial distribution of the structural characteristics of a large number of single horizontal wells and the dynamic and static indicators (Figures 7, 8), the reservoirs were classified into three types: high-quality reservoirs (Type I), sub-optimal reservoirs (Type II), and poor-quality reservoirs (Type III). The details of the classification standard are presented in Table 2.

Based on the reservoir quality classification standard, the dynamic and static indicators of the horizontal distribution patterns of the three types of reservoirs are significantly different, and there are also significant differences in terms of the adaptability of the horizontal wells. As the gas field development progressed, the high-energy superimposed channel zone located in the main part of the superimposition zone of the braided river system has been fully exploited, and the development has gradually shifted to the lateral wings and the transition zone of the river channel (Wang and Wang, 2014). The engineering practice of drilling horizontal wells has revealed that the fractured horizontal wells in the Sulige gas field generally do not have an obvious stable production period. The output of these wells was high but declined rapidly in the early stage of production, and the production was low with a slow decline in the late stages. However, there were large differences in the production and decline characteristics of the horizontal wells drilled in the different quality reservoirs. Through research on the decline characteristics and differences of the different quality

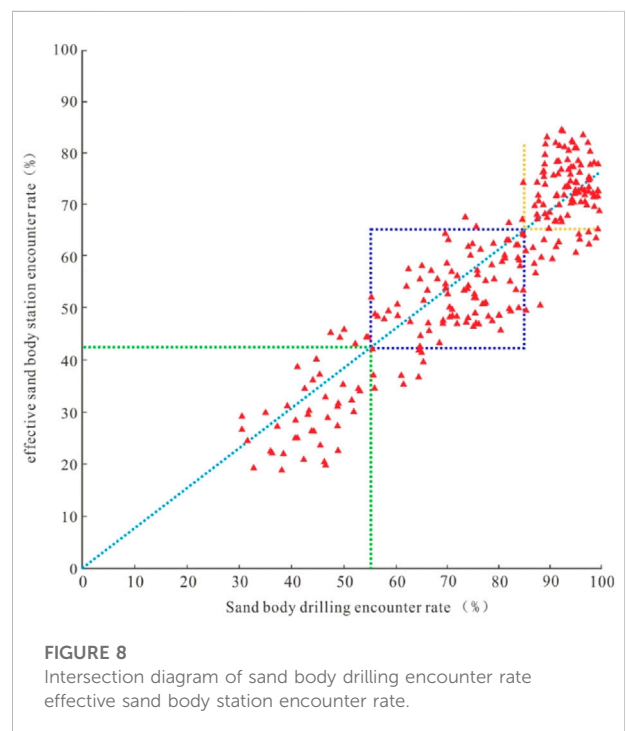


reservoirs, a quantitative classification standard was established to help predict the production of new horizontal wells.

Differences in the production decline characteristics of horizontal wells in different quality reservoirs

Horizontal well seepage characteristics

Due to the poor physical properties and strong heterogeneity of the tight gas sandstone reservoirs, staged fracturing needed to be conducted after the completion of the horizontal wells in order



to achieve high productivity and well-controlled reserves (Zeng et al., 2022). After staged fracturing of the horizontal wells, a composite reservoir was formed, which was composed of a high-permeability fracture reformed zone in the near-well area and a

TABLE 2 Classification standard for effective reservoir quality in horizontal wells drilled in the Sulige gas field.

Reservoir quality	Horizontal distribution type of reservoir	Horizontal well trajectory type	Number of samples	Effective sand body length	Sand body penetration rate	Effective sand body penetration rate	Effective thickness
			(Wells)	(m)	(%)	(%)	(m)
Type I	Massive thick connection	Single layer horizontal	116	≥750	≥85	≥65	≥7.5
Type II	Thin-splicing with local connection	Single layer horizontal/high inclination	121	500–750	60–85	45–65	4–7.5
Type III	Thin dispensation and isolation	Step type	39	<500	<60	<45	<4

tight non-reformed zone in the far-well area (Clarkson, 2013). Figure 9 shows several flow conditions experienced by the staged fracturing horizontal well from the initiation of the production to become stabilized in the later stages. In the early stage of production, the formation fluid in contact with the fracture surface started to provide gas to the fractures, and the gas entered the well after it entered the fractures. Overall, this was a bilinear flow (BLF). As the flow in the fractures became quasi-stable, the pressure reduction everywhere in the fractures was the same, and the formation fluid steadily provided gas to the fractures, presenting a formation linear flow (FLF). As the pressure spread within the formation, each single fracture entered the formation radial flow (FRF) stage, and the fractures did not interfere with each other. When the interference became strong, the space between the fractures showed the characteristics of quasi-stable production in general and entered the second linear flow (SLF) stage. As the pressure continued to spread, the overall flow pattern of the horizontal well was similar to a single wide well; that is, the second radial flow (SRF) stage. The fracturing horizontal well reached a relatively stable state at this time. When the production reached the mid-to-late stage, the discharge range reached the well-control flow boundary, entering the last quasi-stable stage, and the rate of production decline gradually decreased (Cheng et al., 2021; PALACIO J CBLASINGAME, 2003) (Figure 7).

In this study, ARPS (Arps, 1945) decline curve analysis was used to study the production decline characteristics of the horizontal wells in the tight gas sandstone reservoirs. It is a simple method and only requires limited actual development data. However, the results of this method are only accurate after the gas well flow has entered the boundary control stage. Therefore, the key to the success of the ARPS analysis is to determine when the horizontal well has reached the pseudo-steady state stage.

According to the studies of Huo et al. (Huo, 2013) and the current development status of the Sulige gas field (reservoir permeability: 0.01–0.2 mD, average reservoir porosity: 8%), it was concluded that it takes less than 900 days to reach the

pseudo-steady state stage. Therefore, in this study, the horizontal wells with a production time of more than 3 years were selected for ARPS decline curve analysis.

Production decline characteristics of horizontal wells

The development of horizontal wells in the Sulige gas field has lasted for over a decade, during which thousands of horizontal wells have been put into production. In this study, 685 horizontal wells were selected to analyze the production decline characteristics and differences of the horizontal wells in the different quality reservoirs. The inclusion criteria were as follows: 1) the production time was greater than 900 days; 2) the rate of well operation was >85%; and 3) the pressure drop was less than 0.02 Ma/d.

As can be seen from Figures 10, 11, the gas wells with various reservoir qualities had their respective productivity levels, and with a reasonable range of pressure drop, the gas well had continuous production capacity. The production volumes and pressures of the different wells exhibit similar trends. Specifically, the decline was rapid in the first year, and then, it gradually slowed down in the subsequent years. However, the decline characteristics of the gas wells in the different reservoirs were different.

Differences in the decline characteristics of horizontal wells in different quality reservoirs

The model established based on the ARPS production decline theory and the curve fitting method are currently used to analyze the decline characteristics of tight gas sandstone reservoirs. Production decline can be divided into three types: exponential decline, hyperbolic decline, and harmonic decline

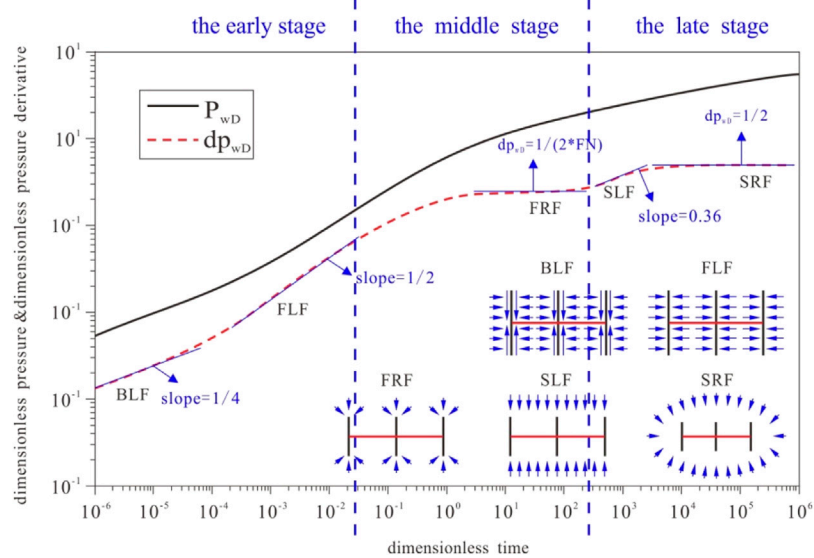


FIGURE 9
Schematic diagram of the formation pressure wave propagation for a multifractured horizontal well.

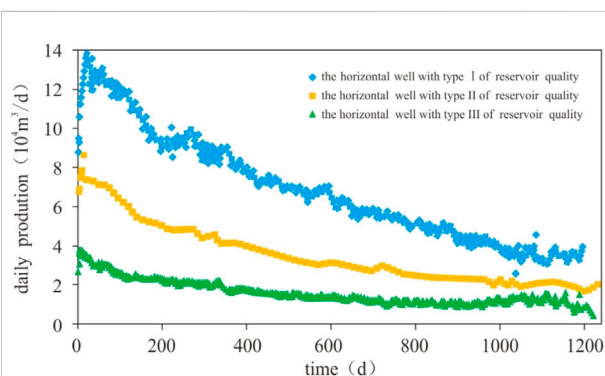


FIGURE 10
Comparison of production of horizontal wells with three types of reservoir qualities.

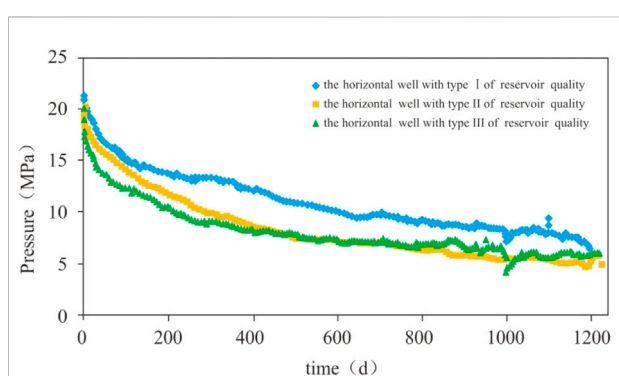


FIGURE 11
Comparison of horizontal well pressure for three types of reservoir qualities.

(Arps, 1945). The relationship between the production and decline rate is as follows:

$$\frac{Q}{q_i} = \left(\frac{D}{D_i} \right)^{1/n} \quad (1)$$

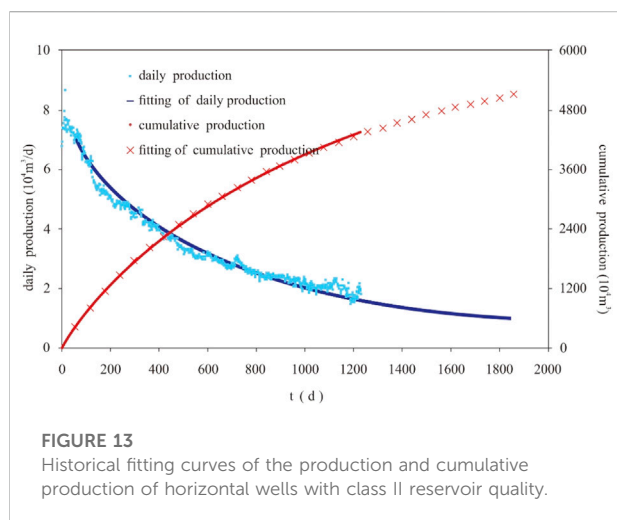
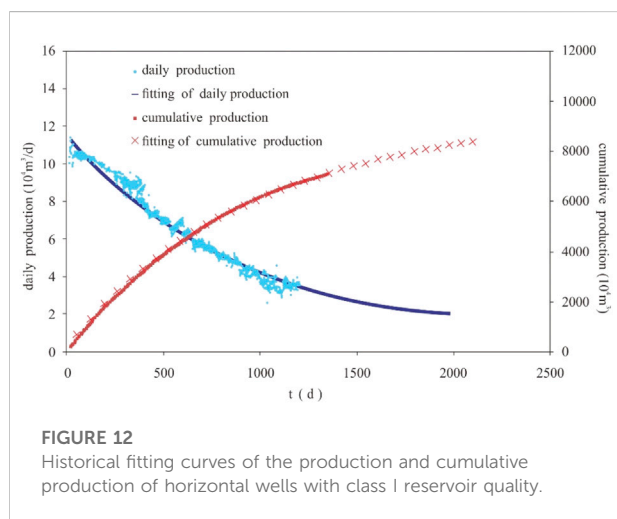
where $D = -(1/Q) \cdot (dQ/dt)$ and q is the production at any time in the declining stage ($10^4 \text{ m}^3/\text{month}$ or $10^8 \text{ m}^3/\text{a}$). q_i is the initial production in the decline stage ($10^4 \text{ m}^3/\text{month}$ or $10^8 \text{ m}^3/\text{aaa0}$); D_i is the initial instantaneous rate of decline when the decline begins ($1/\text{month}$ or $1/\text{a}$); D is the instantaneous decline rate ($1/\text{month}$ or $1/\text{a}$); and n is the decline index. In the above equation, $n = 1$ indicates harmonic decline, $n = 0$ indicates exponential decline, and $0 < n <$

1 indicates hyperbolic decline. The smaller the value of n , the faster the decline occurs.

In actual field operations, due to unstable working conditions and large changes in the production difference of gas wells (Ilk et al., 2010), if the actual production curve was used to calculate the rate of decline, there would be noise and even negative values (Pratikno et al., 2003). Therefore, the production decline formula was used to fit the curve. The fitted curve is smooth, and the rate of decline calculated based on the fitted curve is more accurate (Figures 12–14).

It can be seen from Figure 15 that the production volumes of all three types of reservoirs began to decline after the horizontal wells were put into production, and there was no stable

production stage. In the early stage of production decline, there was a difference between the different reservoirs in terms of the initial decline rate in Stage A, which was mainly caused by the differences in reserves near the well and around the fractures. Moreover, there were differences in the predicted well life and the cumulative gas production. The gas wells in Type I reservoirs had a production life of 18 years, and those in Type II and Type III reservoirs had a production life of 15 years. The main reasons for this difference were the increase in the pressure difference, the pressure decrease in the near-well zone, and the difference in the reserves of the surrounding reservoirs. In the late stage of production, the decline rate gradually decreased and became stable, leading to stable and low production for a long period of time.



Development of quantitative identification and classification standards

Based on the above decline characteristics and the differences in the horizontal wells drilled in the different quality reservoirs, a set of quantitative identification and evaluation criteria for the decline parameters of the horizontal wells in the Sulige gas field was established (Table 3). A quantitative classification standard was developed for the initial production rate, the initial annual decline rate, the average annual decline rate, the production life of the gas well, and the final estimated ultimate recovery (EUR). This standard can be used to systematically analyze and evaluate the horizontal wells in the tight gas sandstone

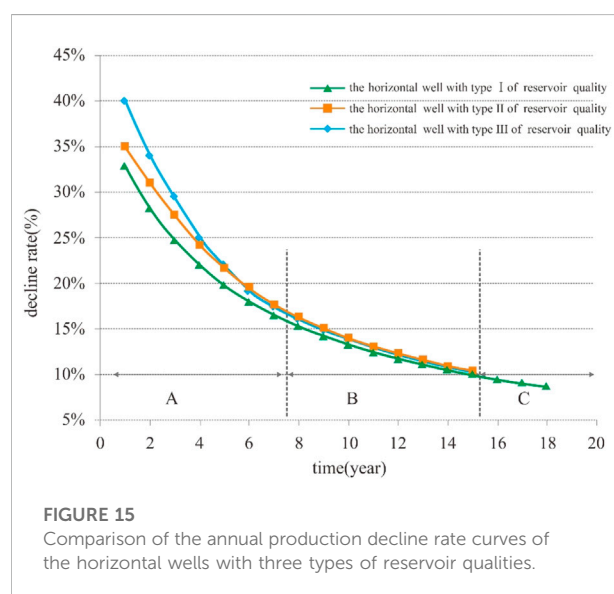
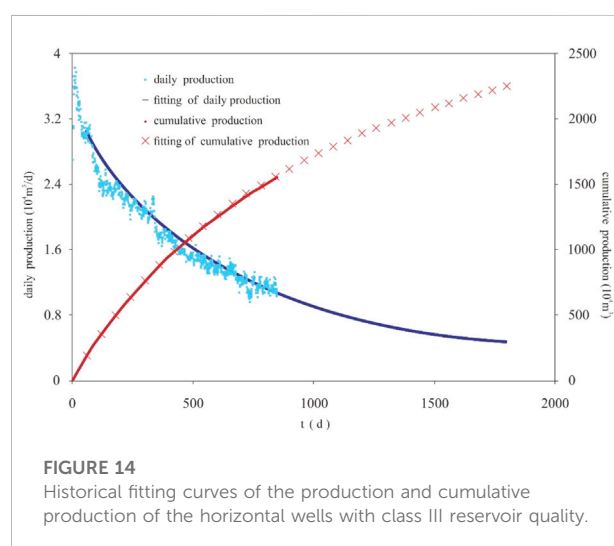


TABLE 3 Quantitative evaluation of the decline of the characteristic parameters of horizontal wells with different reservoir qualities.

Reservoir quality	Initial production in the declining stage	Initial annual decline rate	Late-stage decline rate	Average annual decline rate in the first 3 years	Gas well life	Cumulative production
	(10 ⁴ m ³ /day)	(%)	(%)	(%)	(years)	(10 ⁴ m ³)
Type I	12.3	32.9	9.1	18	18	8900
Type II	7.8	35	10.8	15	15	6800
Type III	3.7	40	10.9	14	14	3100

reservoirs in the Sulige gas field, and it can also be used to predict the development of new horizontal wells.

Conclusions

- 1) Based on the spatial structural characteristics of tight gas reservoirs, the well trajectory of effective reservoirs, and the dynamic responses, three horizontal reservoir distribution modes were defined: the concentrated block development mode, medium-thin strata overlay mode, and isolated thin strata mode.
- 2) Based on the spatial distribution of the structural characteristics of a large number of single horizontal wells and the dynamic and static indicators, the reservoirs were classified into three types: high-quality reservoirs (Type I), sub-optimal reservoirs (Type II), and poor-quality reservoirs (Type III).
- 3) In view of the long time required for seepage to reach the boundary in tight gas sandstone reservoirs, based on the seepage theory, it was determined that it takes less than 3 years for the horizontal wells in the Sulige gas field to reach the pseudo-steady seepage stage.
- 4) Horizontal wells in the different quality reservoirs that were stable in terms of production and had a production time of more than 3 years were selected for analysis. The differences in the production decline characteristics of the wells were analyzed, and a quantitative classification standard for the characteristic decline parameters was established. This quantitative standard can be used to predict the development potential of new horizontal wells and guide the effective development of similar gas fields.
- 5) At present, the decline rate of the horizontal wells in use is high at the initial stage and gradually decreases in the middle and later stages. The decline rate of the gas well is closely related to the gas production rate. Especially for the tight sandstone gas reservoir, the flow in the well control area includes two aspects: the flow from the fracture network stimulation area to the wellbore and the flow from the matrix area to the fracture network stimulation area. In the

later stage, the flow resistance in the matrix area is much greater than that in the fracture network area, and the gas supply capacity is limited, which cannot guarantee the stability of high production. Therefore, the higher gas production rate in the initial stage will cause a large decline rate. Therefore, the production pressure difference should be properly controlled, and the gas production rate and the decline of gas wells should be reduced to maintain the stable production of gas wells.

Data availability statement

The datasets presented in this article are not readily available because this research participants did not agree for their data to be shared publicly. Requests to access the datasets should be directed to chengmh2011@petrochina.com.cn.

Author contributions

MC: research on gas reservoir engineering and economic evaluation, writing the article. MZ: research on gas reservoir engineering and economic evaluation, writing the article.

Funding

This thesis was funded by the National Science and Technology (No. 2016ZX05047) and the science and technology project of PetroChina Company Limited (2021DJ-1704). The funder was not involved in the study design, collection, analysis, interpretation of data, the writing of this article, or the decision to submit it for publication.

Conflict of interest

The authors declare that the research was conducted in the absence of any commercial or financial relationships that could be construed as a potential conflict of interest.

Publisher's note

All claims expressed in this article are solely those of the authors and do not necessarily represent those of their affiliated

organizations, or those of the publisher, the editors, and the reviewers. Any product that may be evaluated in this article, or claim that may be made by its manufacturer, is not guaranteed or endorsed by the publisher.

References

- Arps, J. J. (1945). Analysis of decline curves. *Trans. AIME* 160 (1), 228–247. doi:10.2118/945228-g
- Cheng, Minhua, Wen, Xue, Zhao, Meng, Wang, Guoting, Ning, Bo, Ji, Guang, et al. (2021). Production data analysis and practical applications in the Sulige tight gas reservoir, Ordos Basin, China[J]. *Geofluid*, 2021. 5549725. doi:10.1155/2021/5549725
- Clarkson, C. R. Production data analysis of unconventional gas wells: Review of theory and best practice. *International J. Coal Geology*, 2013, 101–120.109–110, doi:10.1016/j.coal.2013.01.002
- Fu, Jinhua, Wei, Xinshan, and Ren, Junfeng (2008). Distribution and Genesis of large-scale upper paleozoic lithologic gas reservoirs on yi-shaan slope. *Petroleum Explor. Dev.* 35 (6), 664–691. doi:10.1016/s1876-3804(09)60099-9
- Guang, J. L., Jia, Ailin, Meng, Dewei, et al. (2019). Technical strategies for effective development and gas recovery enhancement of a large tight gas field: A case study of Sulige gas field, Ordos Basin NW China[J]. *Petroleum Explor. Dev.* 46, 602–611. doi:10.1016/S1876-3804(19)60043-1
- He, Dongbo, Guang, J. L., and Jiang, Qianfeng, (2022). Differential development technological measures for high-water-cut tight sandstone gas reservoirs in Western area of Sulige Gas Field[J]. *Nat. Gas. Ind.* 42 (1), 73–82. doi:10.3787/j.issn.1000-0976.2022.01.007
- He, Dongbo, Jia, Ailin, Tian, Changbing, et al. (2004). Diagenesis and Genesis of effective sandstone reservoirs in the Sulige gas field[J]. *Petroleum Explor. Dev.* 31 (3), 69–71. doi:10.1016/j.ijmst.2012.04.005
- Huo, Xiaoyu (2013). *Productivity evaluation and prediction methods of fractured horizontal wells in tight sandstone gas reservoir*. Beijing: China University of petroleum, 9–10.
- Ilk, D., Anderson, D. M., Stotts, G. W., Mattar, L., and Blasingame, T. (2010). Production data analysis—challenges, pitfalls, diagnostics. *SPE Reserv. Eval. Eng.* 13 (3), 538–552. doi:10.2118/102048-pa
- Jia, Ailin, Tang, Junwei, and He, Dongbo, (2007). Geological modeling for sandstones reservoirs with low permeability and strong heterogeneity in Sulige gas field[J]. *China Pet. Explor.* 12 (1), 12–16.
- Li, Haiyan, and Peng, Shimi (2007). Characteristics of diagenetic reservoir facies of low permeability reservoir in Sulige gas field[J]. *Acta Pet. Sin.* 28 (3), 100–104.
- Lu, Tao, Liu, Yanxia, and Wu, Lichao, (2015). Challenges to and counter measures for the production stabilization of tight sand-stone gas reservoirs of the Sulige gas field, Ordos Basin[J]. *Nat. Gas. Ind.* 35 (6), 43–52. doi:10.1016/j.ngib.2015.09.005
- Palacio J Cand Blasingame, T. (2003) A Decline-curve analysis using type curves-analysis of gas well production data" *Decline Curve Analysis Using Type Curves*.32 doi:10.2118/4629-PA
- Pratikno, H., Rushing, J. A., and Blasingame, T. A. (2003). "Decline curve analysis using type curves—fractured wells," in *SPE annual technical conference and exhibition* (Denver, Colorado, 53–55.
- Wang, L., and Wang, X. (2014). Type curves analysis for asymmetrically fractured Wells. *J. Energy Resour. Technol.* 136 (2), 1–9. doi:10.1115/1.4025712
- Well patterning filling strategy to enhance oil recovery of giant low permeability tight gasfield:a case study of Sulige gasfield, Ordos Basin[J].*Acta pet. sin.* , 2018, 39(7):802–813. doi:10.7623/SYXB201807007
- Wen, Huaguo, Zheng, Rongcai, Gao, Hongcan, et al. (2007). Sedimen-tary facies of the 8th member of lower Shihezi Formation in Su 6 area, Sulige gas field[J]. *Acta Sedimentol. Sin.* 25 (1), 90–98.
- Zeng, Lianbo, Gong, Lei, Guan, Cong, Zhang, Benjian, Wang, Qiqi, Qi, Zeng, et al. (2022). Natural fractures and their contribution to tight gas conglomerate reservoirs: A case study in the northwestern sichuan basin, China. *J. Petroleum Sci. Eng.* 210, 110028. doi:10.1016/j.petrol.2021.110028
- Zhang, Minglu, Fan, Youhong, and He, Guanghuai, (2013). Latest progression development technologies for low-permeability gas reser-voirs in the Changing Gas Zone[J]. *Nat. Gas. Ind.* 33 (8), 1–7. doi:10.1016/j.ngib.2018.11.002



OPEN ACCESS

EDITED BY

Xiukun Wang,
China University of Petroleum, China

REVIEWED BY

Shuyang Liu,
China University of Petroleum (East
China), China
Junrong Liu,
China University of Petroleum, China

*CORRESPONDENCE

Zhaobo Sun,
xisover@126.com

SPECIALTY SECTION

This article was submitted to Advanced
Clean Fuel Technologies,
a section of the journal
Frontiers in Energy Research

RECEIVED 24 June 2022

ACCEPTED 29 August 2022

PUBLISHED 06 January 2023

CITATION

Sun Z, Liu Y, Cai H, Gao Y and Jiang R
(2023), The numerical simulation study
on the dynamic variation of residual oil
with water drive velocity in water
flooding reservoir.
Front. Energy Res. 10:977109.
doi: 10.3389/fenrg.2022.977109

COPYRIGHT

© 2023 Sun, Liu, Cai, Gao and Jiang. This
is an open-access article distributed
under the terms of the [Creative
Commons Attribution License \(CC BY\)](#).
The use, distribution or reproduction in
other forums is permitted, provided the
original author(s) and the copyright
owner(s) are credited and that the
original publication in this journal is
cited, in accordance with accepted
academic practice. No use, distribution
or reproduction is permitted which does
not comply with these terms.

The numerical simulation study on the dynamic variation of residual oil with water drive velocity in water flooding reservoir

Zhaobo Sun^{1*}, Yingxian Liu², Hui Cai², Yue Gao² and
Ruizhong Jiang³

¹CNOOC International Limited, Beijing, China, ²Tianjin Branch of CNOOC Ltd., Tianjin, China, ³School of Petroleum Engineering, China University of Petroleum (East China), Qingdao, China

The results of core displacement experiments show that increasing the water drive velocity when it is bigger than the limit value can effectively reduce the residual oil saturation and improve the oil displacement efficiency under the same PV. However, the existing commercial simulators (Eclipse, CMG et al.) cannot simulate the effect of water velocity on the relative permeability curve in the process of numerical simulation.

In this article, capillary number (Ca), defined as the dimensionless ratio of viscous force to capillary force, is used to characterize the relationship between water drive velocity and residual oil. Second, a new Boltzmann (BG) equation is proposed to match the nonlinear relationship between C_a and residual oil. The BG equation is a continuous function, which is very beneficial to the stability of numerical calculation. Finally, a new reservoir numerical simulator is established which captures the dynamic variation of residual oil saturation with water drive velocity in a water flooding reservoir based on the black oil model. The new simulator was verified by comparing it with the commercial reservoir simulator ECLIPSE and experimental data. The simulation results show that compared with the common model, the model considering the dynamic variation of residual oil saturation with water drive velocity reduced the residual oil saturation near the main flow line after enhanced injection rate. The oil phase flow capacity in the model is enhanced, the water cut is decreased, and the oil recovery rate is higher. The history matching of the S oilfield in Bohai Bay is achieved with the new simulator, and the history matching accuracy is obviously higher than that of Eclipse. The findings of this study can help with a better understanding of the distribution law and flow law of remaining oil in the high water cut stage of the reservoir and have good theory and application value for water flooding offshore oilfields.

KEYWORDS

numerical simulation, water flooding reservoirs, capillary number, relative permeability, residual oil

Introduction

Deeply understanding the seepage law of oil, gas, and water in reservoir porous media and the time-varying law of rock porous is the basis for improving the accuracy of reservoir numerical simulators, which has been widely studied by scholars in recent years (Xu et al., 2012; Jiang et al., 2018; Shen et al., 2019; Sun et al., 2019; Rios et al., 2020; Qiao, 2021).

Cui and Ma (Cui et al., 2014; Ma et al., 2019) found through experiments that long-term water flooding will lead to the change of the pore throat structure of an unconsolidated sandstone reservoir and promote the formation of large pores. Zhang et al. (1997) found that with the progress of water injection development, the pore throat dimensions, relative permeability, and wettability of rocks have changed. Xu et al. (2015) and Xu et al. (2016) carried out experimental research on the change of relative permeability after waterflooding. He found that long-term waterflooding will reduce the residual oil saturation, increase the irreducible water saturation, increase the relative permeability of the water phase under the residual oil saturation, and move the iso-osmotic point to the right. Ju et al.'s (2005) research shows that in the process of oilfield water drive development, with the increase of water cut, the content of light components in crude oil decreases, resulting in the increase of crude oil viscosity to three times the initial state. Based on the microscopic grid and numerical simulation technology, Hou et al. (2016) proposed a new simulation method, which can consider the changes of porosity, permeability, and relative permeability with time in the process of water drive. A comprehensive reservoir simulation technique based on time-varying petro-physical parameters characterized by effective displacement flux was proposed by Zhao et al. (2022).

The water cut of the oil field has been rising after a long period of water flooding development. Enhancing liquid for oil increment is an effective way to sustain stable production and improve recovery factors in the mid-late life of reservoirs developed by water flooding (Feng et al., 2013; Liu et al., 2017; Sun et al., 2020). Many scholars have found that increasing the displacement pressure difference can improve the oil displacement efficiency through microscopic displacement experiments by CT and microfluidic technology (Zhang et al., 2017; Zhu et al., 2017; Liu et al., 2021; Tan et al., 2022). After long-term water flooding, most of the remaining oil in the rock pore space exists in five forms such as cluster-shaped, pore surface film-like, slit-like, cube corner-shaped, and intergranular adsorption-like (Li et al., 2014; Gao et al., 2020). Without changing the water drive velocity, it is difficult to drive

the residual oil by high PV displacement alone, but as the water drive velocity increases, the residual oil keeps decreasing and is driven out by water (Li et al., 2006). In addition, the results of core displacement experiments show that increasing the water drive velocity when it is bigger than a limit value can effectively reduce the residual oil saturation and improve the oil displacement efficiency under the same PV (Ji et al., 2012).

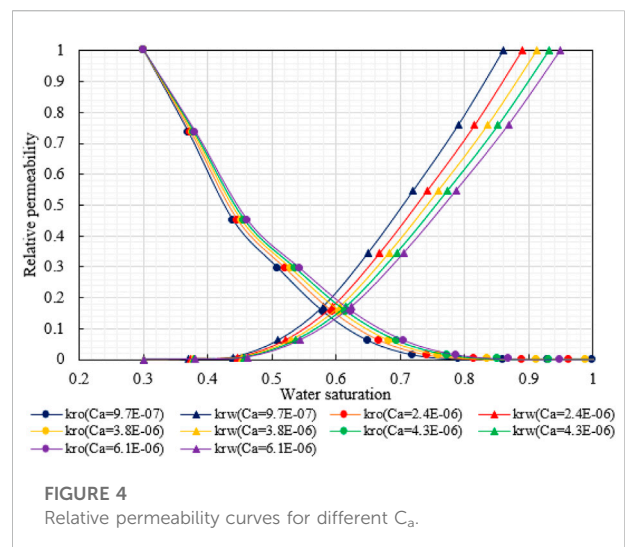
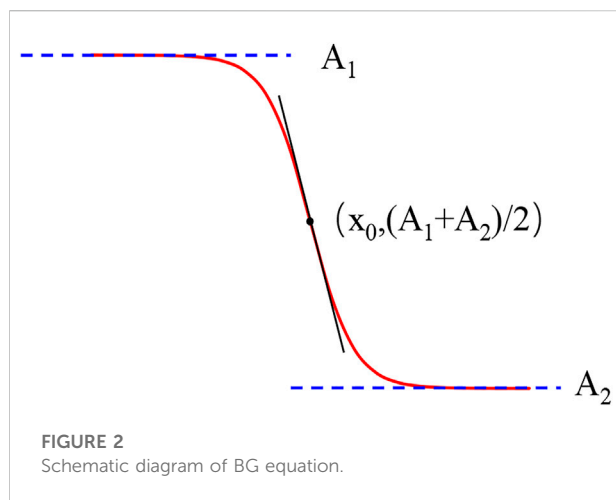
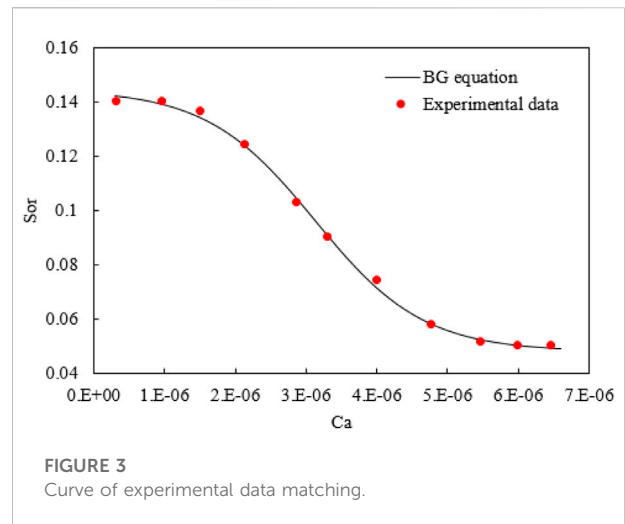
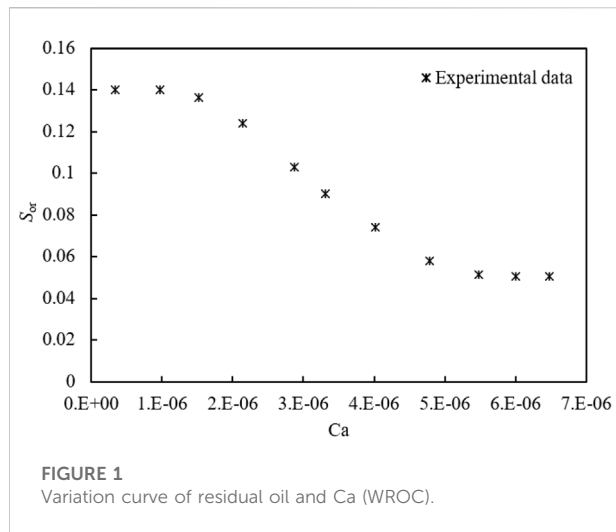
However, all commercial reservoir numerical simulators (Eclipse, CMG et al.) do not consider the mechanism that the increase in water drive velocity leads to the decrease of residual oil (Ning et al., 2019). Therefore, reservoir numerical simulators frequently encounter the problem of large errors in history matching, especially in the mid-late life of reservoirs developed. This study aims to propose a novel method to characterize the mechanism of the dynamic variation of residual oil with water drive velocity. In this article, we propose a new BG equation to match the variation of residual oil saturation with the C_a , and then develop a new numerical simulator. In addition, compared with the Eclipse, we analyzed the differences in the distribution of residual oil saturation and oil saturation in the numerical model under different liquid production rates and further presented how the new method contributes to accurate history matching in S Oilfield.

Matching of experimental results and BG equations

In order to explain the mechanism of the phenomenon, increasing the water drive velocity when it is bigger than the limit value can effectively reduce the residual oil saturation and improve the oil displacement efficiency under the same PV. We introduce the C_a as shown in Eq. 1, which is defined as the ratio of viscous force to capillary force. Changing the displacement conditions, such as increasing the water drive velocity, can effectively increase the C_a , which is conducive to increasing the contribution of the viscous force of the injected water in the displacement process.

$$C_a = \frac{v_w \mu_w}{\sigma} \quad (1)$$

In order to better quantitatively describe the variation law of residual oil saturation with the water drive velocity, we have drawn the variation curve of residual oil and C_a , as shown in Figure 1. When the C_a is small ($Ca < 1.51 \times 10^{-6}$ in Figure 1), there is little change in residual oil saturation, which is a repellent region dominated by capillary forces. As the value of the C_a increases, an inflection point appears in Figure 1, which indicates the transition from a predominantly capillary force to a



predominantly viscous force. This transition zone occurs when C_a is in the range of $1.51 \times 10^{-6} \sim 5.48 \times 10^{-6}$. In this transition zone, the residual oil saturation decreases rapidly with the increase of C_a . However, when the C_a is large ($C_a > 5.48 \times 10^{-6}$ in Figure 1), the residual oil saturation in the rock has been reduced to the limit value and cannot be further reduced, and increasing the water drive velocity cannot further change the residual oil saturation.

In order to show more precisely the relationship between the C_a and the residual oil saturation, the residual oil saturation decreases nonlinearly with the increase of the C_a . A new nonlinear equation (BG equation) is proposed in this article, as shown in Eq. 2. The functional schematic of the BG equation is shown in Figure 2.

$$y = \frac{A_2 - A_1}{1 + e^{(x-x_0)/dx}} + A_1. \quad (2)$$

From the variation of Eq. 2, we obtain Eq. 3, which is the matching equation of residual oil saturation and the C_a .

$$S_{or} = \frac{S_{or\max} - S_{or\min}}{1 + e^{(C_a - C_{a0})/dC_a}} + S_{or\min}. \quad (3)$$

In the curve matching process, $S_{or\max}$, $S_{or\min}$, and C_{a0} can be obtained directly from the curve and only need to adjust the value of dC_a to complete the curve matching as shown in Figure 3. The BG equation accurately matches the nonlinear variation law of residual oil saturation and the C_a and can realize the continuous change of residual oil saturation in the numerical simulation process.

After obtaining the residual oil saturation under different C_a according to Eq. 3, the oil–water relative permeability curve

under different C_a can be calculated according to Eqs 4–6, as shown in Figure 4.

$$S_{wn} = \frac{S_w - S_{wc}}{1 - S_{wc} - S_{or}}, \quad (4)$$

$$k_{rwn} = \frac{k_{rw}}{k_{rw}(S_{or})}, \quad (5)$$

$$k_{ron} = \frac{k_{ro}}{k_{ro}(S_{wc})}. \quad (6)$$

Simulator development

Methodology

Seepage equation

Oil phase:

$$\nabla \cdot \left[\frac{kk_{ro}(C_a)}{B_o \mu_o} \nabla (p_o - \rho_o g D) \right] + q_{vo} = \frac{\partial}{\partial t} \left(\frac{\phi S_o}{B_o} \right). \quad (7)$$

Water phase:

$$\nabla \cdot \left[\frac{kk_{rw}}{B_w \mu_w} \nabla (p_w - \rho_w g D) \right] + q_{vw} = \frac{\partial}{\partial t} \left(\frac{\phi S_w}{B_w} \right). \quad (8)$$

Gas phase:

$$\begin{aligned} & \nabla \cdot \left[\frac{kk_{rg}}{B_g \mu_g} \nabla (p_g - \rho_g g D) \right] + \nabla \cdot \left[\frac{R_{so} k k_{ro}}{B_o \mu_o} \nabla (p_o - \rho_o g D) \right] + \\ & \nabla \cdot \left[\frac{R_{sw} k k_{rw}}{B_w \mu_w} \nabla (p_w - \rho_w g D) \right] + q_{vg} = \frac{\partial}{\partial t} \left[\phi \left(\frac{R_{so} S_o}{B_o} + \frac{R_{sw} S_w}{B_w} + \frac{R_{sg} S_g}{B_g} \right) \right]. \end{aligned} \quad (9)$$

Auxiliary equation

$$s_o + s_w + s_g = 1, \quad (10)$$

$$p_{cow} = p_o - p_w, \quad (11)$$

$$p_{cog} = p_g - p_o. \quad (12)$$

Initial condition

Initial pressure:

$$p_l(x, y, z)|_{t=0} = p^0(x, y, z). \quad (13)$$

Initial saturation:

$$S_l(x, y, z)|_{t=0} = S^0(x, y, z). \quad (14)$$

Outer boundary condition

$$\frac{\partial p}{\partial n} \Big|_G = 0. \quad (15)$$

Inner boundary condition

Constant production rate:

$$Q_l(x, y, z, t) \Big|_{x=x_w, y=y_w, z=z_w} = Q_l(t). \quad (16)$$

Constant bottom hole flowing pressure:

$$p(x, y, z, t) \Big|_{x=x_w, y=y_w, z=z_w} = p_{wf}(t). \quad (17)$$

The mathematical model is differentially discretized using the finite difference method to establish a fully implicit numerical model of the oil, gas, and water phases with the following procedure:

$$\Delta \left[T_o^{(u+1)} \Delta \phi_o^{(u+1)} \right] + Q_{vo}^{(u+1)} = \frac{V_b}{\Delta t} \left[\left(\frac{\phi S_o}{B_o} \right)^{(u)} - \left(\frac{\phi S_o}{B_o} \right)^n + \delta \left(\frac{\phi S_o}{B_o} \right) \right] \quad (18)$$

$$\Delta \left[T_w^{(u+1)} \Delta \phi_o^{(u+1)} \right] + Q_{vw}^{(u+1)} = \frac{V_b}{\Delta t} \left[\left(\frac{\phi S_w}{B_w} \right)^{(u)} - \left(\frac{\phi S_w}{B_w} \right)^n + \delta \left(\frac{\phi S_w}{B_w} \right) \right] \quad (19)$$

$$\begin{aligned} & \Delta \left[T_o^{(u+1)} T_{so}^{(u+1)} \Delta \phi_o^{(u+1)} \right] + \Delta \left[T_w^{(u+1)} T_{sw}^{(u+1)} \Delta \phi_w^{(u+1)} \right] \\ & + \Delta \left[T_g^{(u+1)} \Delta \phi_g^{(u+1)} \right] + Q_{vg}^{(u+1)} \\ & = \frac{V_b}{\Delta t} \left\{ \left[\phi \left(\frac{S_g}{B_g} + \frac{R_{so} S_o}{B_o} + \frac{R_{sw} S_w}{B_w} \right) \right]^{(u)} - \left[\phi \left(\frac{S_g}{B_g} + \frac{R_{so} S_o}{B_o} + \frac{R_{sw} S_w}{B_w} \right) \right]^n \right. \\ & \quad \left. + \delta \left[\phi \left(\frac{S_g}{B_g} + \frac{R_{so} S_o}{B_o} + \frac{R_{sw} S_w}{B_w} \right) \right] \right\} \end{aligned} \quad (20)$$

$$Q_{vo} = V_b q_{vo}, \quad (21)$$

$$Q_{vw} = V_b q_{vw}, \quad (22)$$

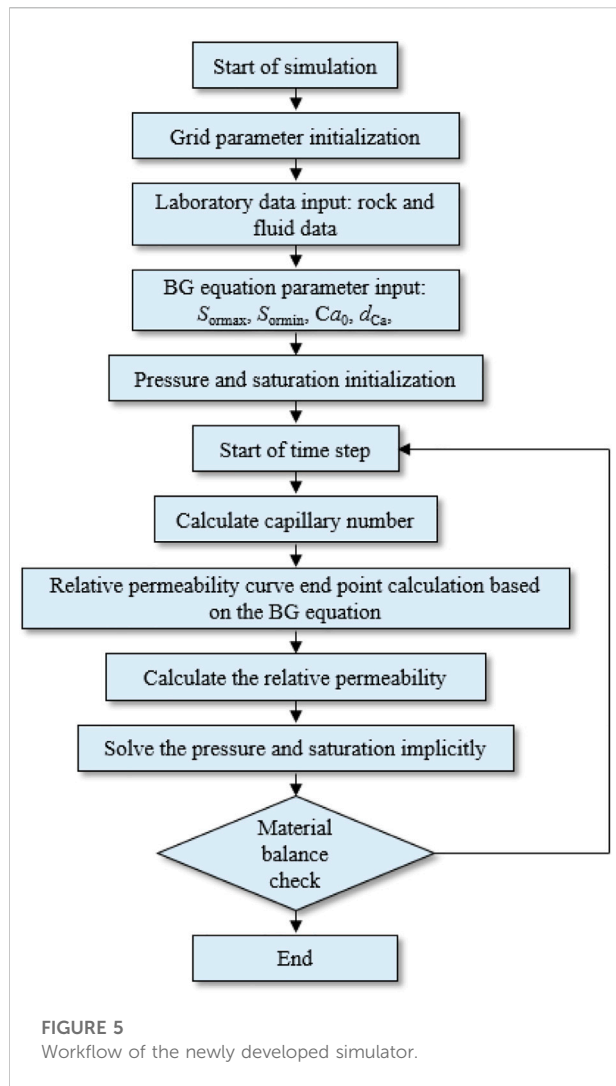
$$Q_{vg} = V_b q_{vg}, \quad (23)$$

$$T_l = \frac{kk_{rl} A}{B_l \mu_l L}, \quad (24)$$

$$\Phi_l = p_l - \rho_l g D. \quad (25)$$

Workflow of the newly developed simulator

Based on the established mathematical model, a new simulator is developed. The workflow of the overall solution procedure and the calculation of parameters are shown in Figure 5. At the end of each time step, the C_a of each grid is



calculated. Then, the residual oil saturation of each grid is calculated by the BG equation, a new relative permeability curve is recalculated, and finally, the conductivity of each grid is corrected. The code of the framework is programmed in Fortran 90.

Simulator validation

In order to verify the accuracy of the new simulator, a conceptual numerical model was established using the basic parameters of the S reservoir in Bohai Bay, which are shown in Table 1. The water injection rate of the water injection well is 400 m³/d, and the daily fluid production rate of the oil production well is 400 m³/d. The simulation lasted for 40 years. In the verification stage, the new simulator developed in this article did not consider the change in residual oil saturation with the C_a . Finally, the simulation

TABLE 1 Basic parameters of the conceptual model.

Parameter	Value
Permeability	1,500*1,500*150 mD
Porosity	0.32
Oil viscosity	60 mPa s
Crude oil volume factor	1.13
Grid number	20*20*10
Dimension of reservoir	30 m*30 m*5 m
Water viscosity	0.49 mPa s
Oil density	840 kg/m ³

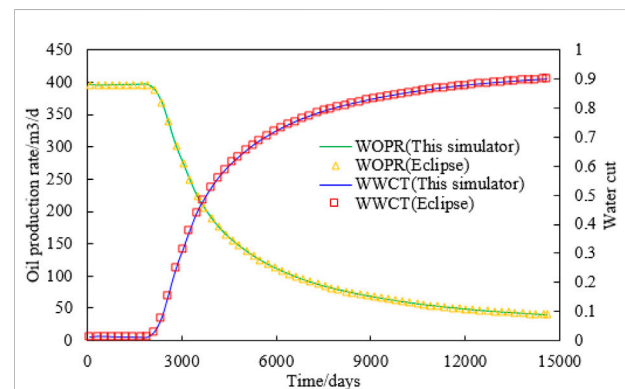


FIGURE 6
Simulation results of the new simulator and Eclipse.

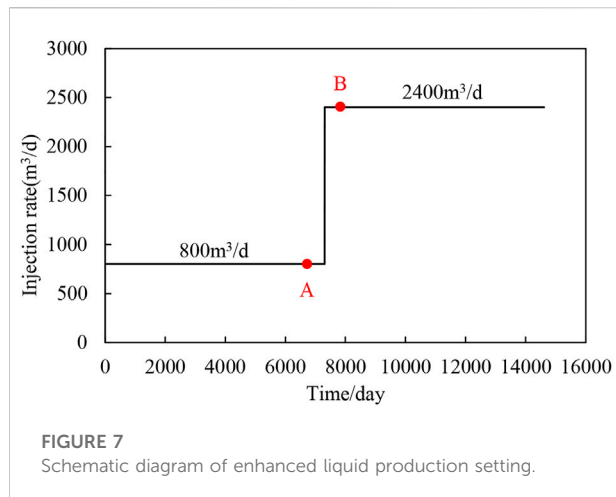
results were compared with those of the commercial simulator (Eclipse).

In Figure 6, the new simulator (without considering the residual oil variation) is in full agreement with the simulation results of Eclipse, and the error is controlled within 0.2%. Therefore, the new simulator is accurate and effective.

Results and discussion

To study the effect of different water velocities on the oil saturation distribution of the numerical model, the water injection rate of the injection well increased from 800 m³/d to three times the original rate to 2,400 m³/d at 7,500 days of the simulation, and the oil well also increased the fluid production rate according to the principle of balance between injection and production, as shown in Figure 7.

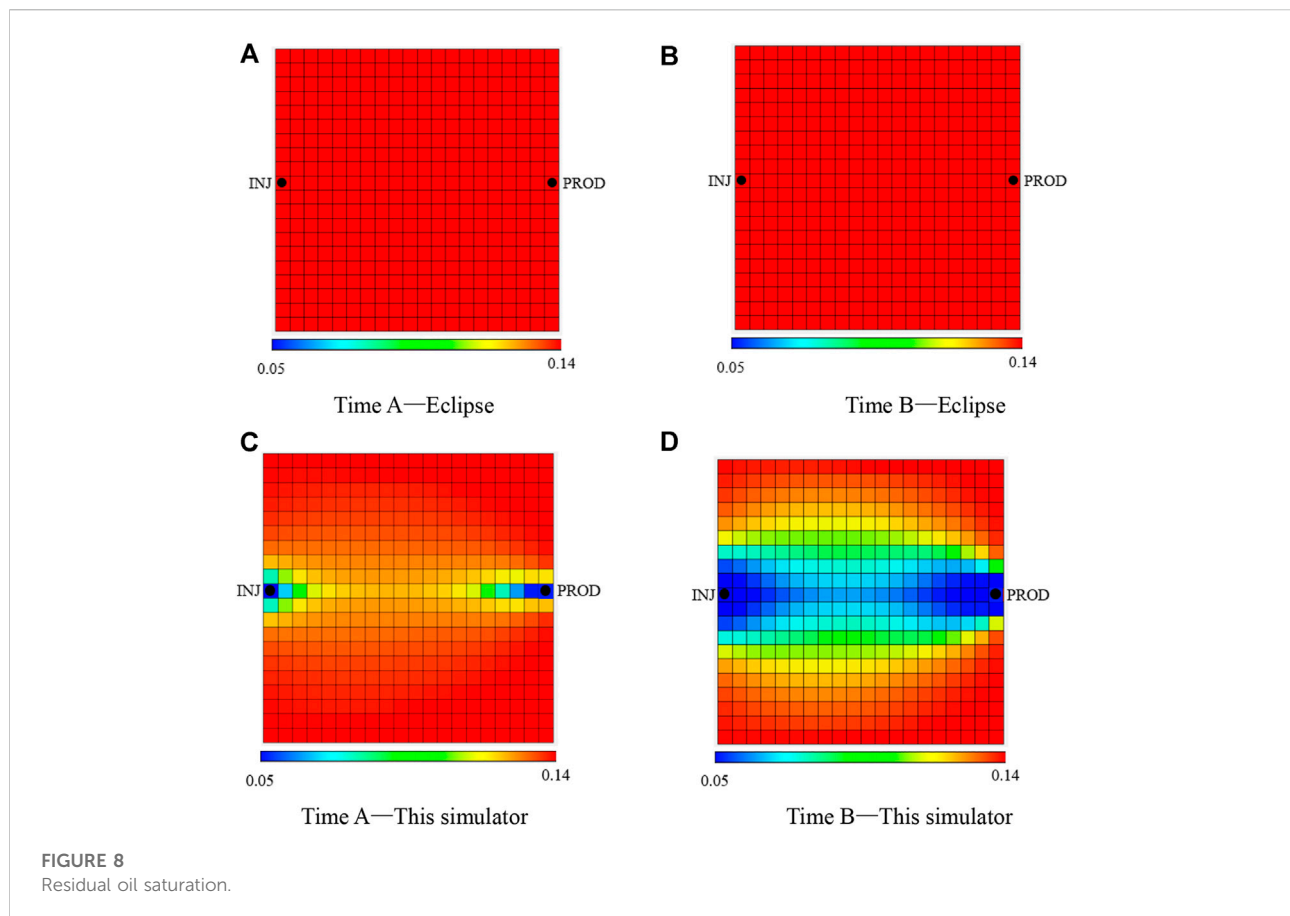
The numerical simulation results of the new simulator and Eclipse were compared in 3D Grid, and the basic parameters of the reservoir numerical model are exactly the same. The residual oil saturation of the reservoir model was intercepted at the time A



(before enhanced liquid production) and at the time B (after enhanced liquid production) as shown in Figure 8. As shown in Figures 8A and B, Eclipse cannot realize the change in residual oil

saturation, so its residual oil saturation is unchanged after enhanced liquid production. In Figures 8C and D, the new simulator considers the dynamic change of residual oil saturation with water drive velocity. Before enhanced liquid production, the water drive velocity can only change the residual oil saturation of the grid near the well, as shown in Figure 8C. After enhanced liquid production, the residual oil saturation of the grid near the main flow line decreases under the effect of high-speed flushing of the injected water, as shown in Figure 8D. Furthermore, the decrease in residual oil saturation also improves the displacement efficiency, and that is why the oil saturation near the injection well in Figure 9A is much lower than that in Figure 9B because more oil can be displaced by the high-speed injected water.

Before enhanced liquid production, the water drive velocity of most grids in the model is low and has not reached the limit that can change the residual oil. Therefore, the oil production rate and water cut of the new simulator did not differ significantly from the Eclipse, as shown in Figure 10. After enhanced liquid production, as shown in Figure 11. The water cut of the new simulator decreases and forms a concave after enhanced liquid



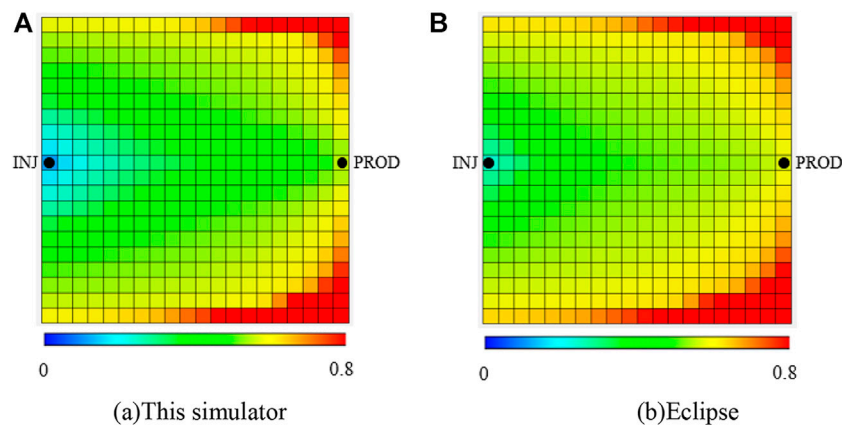


FIGURE 9
Oil saturation at the end of development.

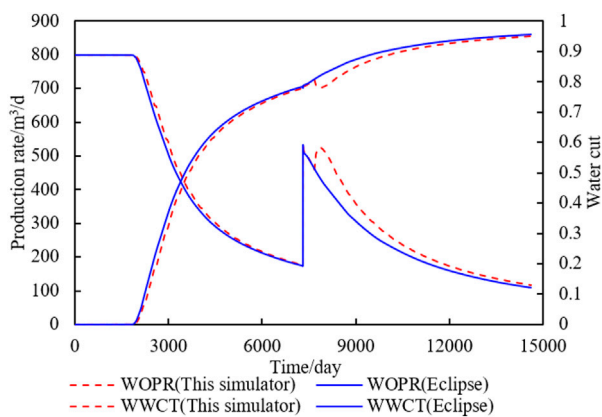


FIGURE 10
Comparison curves of oil production rate and water cut of different simulators.

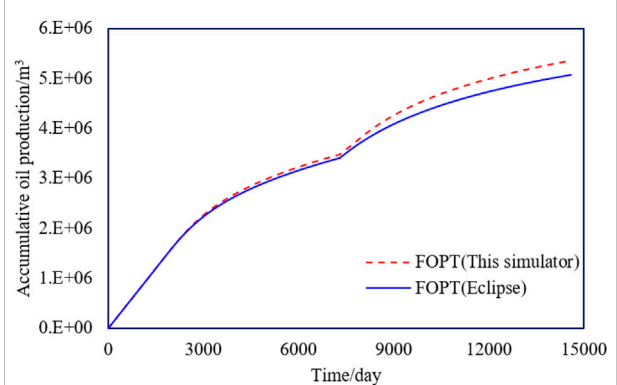


FIGURE 11
Comparison curve of cumulative oil production of different simulators.

production. The reason for the abovementioned phenomenon is that the new simulator considers the influence of water drive velocity on residual oil saturation. After enhanced liquid production, the water drive velocity of the model increases, and more oil is displaced by water.

Field application

The S oilfield is located in Bohai Bay, China. The porosity is mainly distributed between 27.0 and 35.8%, with an average of 32.0% and a median of 32.6%. The permeability ranges from 100.0 mD to 12,000.0 mD, with an average of 2,815.0 mD and a median of 2,195.0 mD. It is an extra-high porosity, extra-high

permeability reservoir. After two well network encryptions and multiple rounds of fluid extraction in the reservoir, the tracer test data indicate that the water drive rate has reached 2–3 times that of the initial development stage, entering the stage of high water cut and high fluid production.

The new simulator is applied to the S oilfield to verify if the realization of the dynamic variation of residual oil with water drive velocity will get better simulation results. The parameters of the BG equation in the new simulator were optimized with reference to the results of the core displacement experiments in the S reservoir. Eclipse and the new simulator are used for the history match of the S reservoir numerical model, respectively, where the model parameters in both simulators were the same except that the new simulator considered the mechanism of residual oil variation with water drive velocity. As shown in

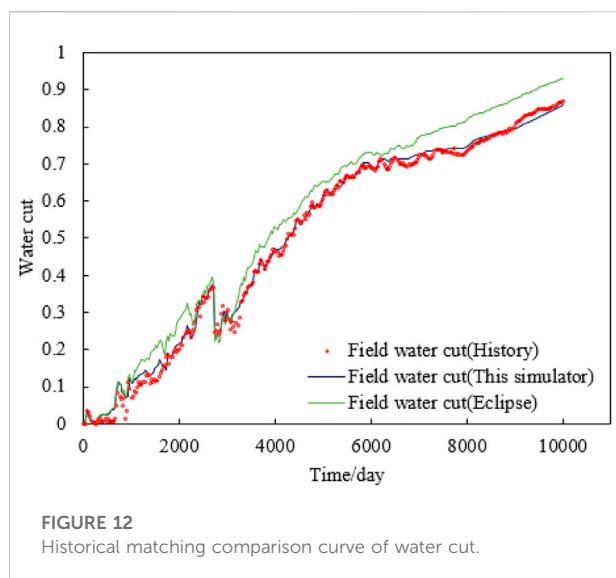


Figure 12, in the early stage of development, the water drive velocity is small, and the results of both simulators are similar; in the later stages of development, the large water drive velocity leads to residual oil decline, so the water cut of the new simulator is more consistent with the historical data, while the water cut of the Eclipse is significantly higher than the historical data. In summary, compared with the traditional numerical simulator (Eclipse), the new simulator has a higher accuracy of historical matching, and the simulation results are more compounded with the actual situation. The overall accuracy of historical matching is improved by 24% compared with Eclipse.

Summary and conclusion

For waterflooding reservoirs, increasing water drive velocity can significantly reduce residual oil saturation. This mechanism of dynamic variation of residual oil saturation with water drive velocity will significantly impact the fluid flow in the reservoir and the development performance of the oilfield. However, all commercial reservoir numerical simulators (Eclipse, CMG et al.) have not considered this mechanism. In this article, a novel method based on the C_a and BG equation is proposed to describe the nonlinear variation of residual oil with water drive velocity. A new reservoir numerical simulator is developed and validated against Eclipse. Compared to the existing studies, the new study simulates the effect of water velocity on the relative permeability curve in the process of numerical simulation for

the first time. The novel method and new reservoir numerical simulator are implemented for the history matching of S oilfield, and the new simulator has a higher accuracy of historical matching which is improved by 24% compared with Eclipse.

Data availability statement

The raw data supporting the conclusion of this article will be made available by the authors, without undue reservation.

Author contributions

Study conception and design: ZS; methodology: ZS and MK; experimental and data collection: HC; simulation study: ZS, YG; analysis of results: ZS; writing the manuscript: All authors. All authors reviewed the results and approved the final version of the manuscript.

Funding

This research was funded by the Major Scientific and Technological Projects of CNOOC (Grant numbers: KJGG 2022-0904).

Conflict of interest

ZS was employed by the company CNOOC International Limited; YL, HC, and YG were employed by the Tianjin Branch of CNOOC Ltd; RJ was employed by the China University of Petroleum (East China).

The remaining author declares that the research was conducted in the absence of any commercial or financial relationships that could be construed as a potential conflict of interest.

Publisher's note

All claims expressed in this article are solely those of the authors and do not necessarily represent those of their affiliated organizations, or those of the publisher, the editors, and the reviewers. Any product that may be evaluated in this article, or claim that may be made by its manufacturer, is not guaranteed or endorsed by the publisher.

References

- Cui, C., Li, K., Yang, Y., Huang, Y., and Cao, Q. (2014). Identification and quantitative description of large pore path in unconsolidated sandstone reservoir during the ultra-high water-cut stage. *J. Petroleum Sci. Eng.* 122, 10–17. doi:10.1016/j.petrol.2014.08.009
- Feng, Q., Wang, S., and Bai, J. (2013). Numerical simulation of development effect of enhanced liquid production in heterogeneous reservoirs. *Petroleum Geol. Recovery Effic.* 20 (3), 49–52. doi:10.13673/j.cnki.cn37-1359/te.2013.03.014
- Gao, W., Li, Y., He, S., Pan, D., Liu, M., and Guan, C. (2020). Classification method of occurrence mode of remaining oil based on fluorescence thin sections. *Acta Pet. Sin.* 41 (11), 1406–1415. doi:10.7623/syxb202011010
- Hou, J., Zhang, Y., Wang, D., and Zhou, K. (2016). Numerical simulation of reservoir parameters' synergetic time-variability on development rules. *J. Pet. Explor. Prod. Technol.* 6 (4), 641–652. doi:10.1007/s13202-015-0208-4
- Ji, S., Tian, C., Shi, C., Ye, J., Zhang, Z., and Fu, X. (2012). New understanding on water-oil displacement efficiency in a high water-cut stage. *Petroleum Explor. Dev.* 39 (3), 362–370. doi:10.1016/s1876-3804(12)60052-4
- Jiang, R., Zhang, W., Zhao, P., Jiang, Y., Cai, M., Tao, Z., et al. (2018). Characterization of the reservoir property time-variation based on 'surface flux' and simulator development. *Fuel* 234 (15), 924–933. doi:10.1016/j.fuel.2018.06.136
- Ju, B., Fan, T., and Zhang, J. (2005). Oil viscosity variation and its effects on production performance in water drive reservoir. *Pet. Explor* 33 (1), 99–102.
- Li, Y. Q., Li, J., Ding, S., and Sun, X. (2014). Characterization of remaining oil after polymer flooding by laser scanning confocal fluorescence microscopy. *J. Dispersion Sci. Technol.* 35 (7), 898–906. doi:10.1080/01932691.2013.802243
- Li, Z., He, S., Yang, W., and Men, C. (2006). Physical simulation experiment of water driving by micro-model and fractal features of residual oil distribution. *J. China Univ. Petroleum (Edition Nat. Sci.)* 3, 67–71.
- Liu, C., Zhang, J., Zhou, W., and Wang, K. (2017). Dynamic calculation method for liquid production increase potential of offshore oilfield at high water cut stage. *Petroleum Geol. Recovery Effic.* 24 (4), 110–115. doi:10.13673/j.cnki.cn37-1359/te.2017.04.009
- Liu, X., Ren, D., Dong, F., Nan, J., and Zhou, R. (2021). Quantitative study of residual oil distribution during water flooding through digital core analysis. *Geofluids* 1, 1–8. doi:10.1155/2021/6619440
- Ma, K., Cai, H., and Sun, Z. (2019). Nuclear magnetic resonance-based experiment on the effects of displacement velocity and multiple on the pore throat characteristics and recovery factor of unconsolidated sandstone reservoirs. *China Offshore Oil Gas* 6, 86–91.
- Ning, Y., Zhang, K., He, S., Chen, T., Wang, H., and Qin, G. (2019). Numerical modeling of gas transport in shales to estimate rock and fluid properties based on multiscale digital rocks. *Energy Procedia* 158, 6093–6098. doi:10.1016/j.egypro.2019.01.505
- Qiao, X. (2021). Status analysis and development of reservoir numerical simulation technology. *IOP Conf. Ser. Earth Environ. Sci.* 631 (1), 012052. doi:10.1088/1755-1315/631/1/012052
- Rios, V. S., Avansi, G. D., and Schiozer, D. J. (2020). Practical workflow to improve numerical performance in time-consuming reservoir simulation models using submodels and shorter period of time. *J. Petroleum Sci. Eng.* 195, 107547. doi:10.1016/j.petrol.2020.107547
- Shen, L., Cui, T., Liu, H., Zhu, Z., Zhong, H., Chen, Z., et al. (2019). "Numerical simulation of two-phase flow in naturally fractured reservoirs using dual porosity method on parallel computers: Numerical simulation of two-phase flow in naturally fractured reservoirs," in Proceeding International Conference on High Performance Computing in Asia-Pacific Region, New York, 14 January 2019 (Guangzhou, Peoples R China: Acm), 91–100. doi:10.1145/3293320.3293322
- Sun, K., Liu, H., Wang, Y., Ge, L., Gao, J., and Du, W. (2020). Novel method for inverted five-spot reservoir simulation at high water-cut stage based on time-varying relative permeability curves. *ACS Omega* 5 (7), 13312–13323. doi:10.1021/acsomega.0c01388
- Sun, Z., Li, Y., Ma, K., Xu, J., Zhang, G., Jiang, R., et al. (2019). "A novel method to characterise time-variation of reservoir properties: Experimental study, simulator development and its application in Bohai Bay oilfield," in Proceeding SPE/IATMI Asia Pacific Oil & Gas Conference and Exhibition, Bali, Indonesia, October 29–31, 2019. Bali, Indonesia: society of petroleum engineers). doi:10.2118/196261-MS
- Tan, J., Cai, H., Li, Y. L., Liu, C., Miao, F., and Liu, C. (2022). Physical simulation of residual oil displacement production in offshore strong bottom water reservoir. *J. Pet. Explor. Prod. Technol.* 12, 521–546. doi:10.1007/s13202-021-01297-w
- Xu, J., Guo, C., Jiang, R., and Wei, M. (2016). Study on relative permeability characteristics affected by displacement pressure gradient: Experimental study and numerical simulation. *Fuel* 163, 314–323. doi:10.1016/j.fuel.2015.09.049
- Xu, J., Guo, C., Wei, M., and Jiang, R. (2015). Impact of parameters' time variation on waterflooding reservoir performance. *J. Petroleum Sci. Eng.* 126, 181–189. doi:10.1016/j.petrol.2014.11.032
- Xu, X., Tian, S., Xu, T., Xu, T., and Su, Y. (2012). The equivalent numerical simulation of fractured-vuggy carbonate reservoir. *Appl. Mech. Mater.* Trans Tech Publications Ltd. 110, 3327–3331. doi:10.4028/www.scientific.net/AMM.110-116.3327
- Zhang, H., Liu, Q., Li, F., and Lu, Y. (1997). Variations of petrophysical parameters after sandstone reservoirs watered out in Daqing oilfield. *SPE Adv. Technol. Ser.* 5 (1), 128–139. doi:10.2118/30844-pa
- Zhang, X., Zhao, L., Wang, J., Chen, L., and Yue, X. (2017). "Residual oil distribution of heterogeneous reservoir at different water drive velocity," in Proceedings of the International Field Exploration and Development Conference, Singapore, 12 July 2018 (Springer), 326–332. doi:10.1007/978-981-10-7562-5-29
- Zhao, P., Shen, Z., Cai, M., Zhang, J., Jiang, R., Zhao, M., et al. (2022). A comprehensive reservoir simulation technique based on time-varying petrophysical parameters characterized by effective displacement flux. *J. China Univ. Petroleum (Edition Nat. Sci.)* 46 (1), 89–96.
- Zhu, G., Yao, J., Zhang, L., Sun, H., and Zhang, K. (2017). Pore-scale investigation of residual oil distributions and formation mechanisms at the extra-high water-cut stage. *Chin. Sci. Bull.* 62 (22), 2553–2563. doi:10.1360/n972017-00392

Nomenclature

C_a capillary number, dimensionless

ν_o, ν_g, ν_w velocity of oil, gas, and water, m/s

μ_o, μ_g, μ_w viscosity of oil, gas, and water, mPa·s

σ interfacial tension, mN/m

S_{or} residual oil saturation, dimensionless

$S_{or\max}$ maximum residual oil saturation, dimensionless

$S_{or\min}$ minimum residual oil saturation, dimensionless

C_{a0}, dC_a BG equation matching value, dimensionless

S_{wn} normalized water saturation, dimensionless

S_o, S_g, S_w saturation of oil gas and water, dimensionless

S_{wc} irreducible water saturation, dimensionless

k_{rwn} normalized water relative permeability, dimensionless

k_{ro}, k_{rg}, k_{rw} relative permeability of oil, gas, and water, dimensionless

q_{vo}, q_{vg}, q_{vw} Volume flow rate of oil gas and water, m³/s

p_{cow} capillary force between oil and water, Pa

p_{cog} capillary force between oil and gas, Pa

n time steps

x_w, y_w, z_w location coordinates of the well

p_{wf} bottom hole flowing pressure, Pa

u number of iterations

V_b mesh block volume

δ The difference between the u+1 and u parameter iterations at the n+1 time step.



OPEN ACCESS

EDITED BY

Xiukun Wang,
China University of Petroleum, Beijing,
China

REVIEWED BY

Liwu Jiang,
University of Regina, Canada
Yi Ding,
Southwest Petroleum University, China

*CORRESPONDENCE

Hao Kang,
✉ haokang@hebtu.edu.cn

SPECIALTY SECTION

This article was submitted to Advanced
Clean Fuel Technologies,
a section of the journal
Frontiers in Energy Research

RECEIVED 10 November 2022

ACCEPTED 27 December 2022

PUBLISHED 09 January 2023

CITATION

Chen X, Zhang Z, Liu Q, Sun L, Xiao H,
Gao J and Kang H (2023), Physical
modeling of development adjustment
mechanism for heterogeneous thick
oil reservoir.
Front. Energy Res. 10:1094697.
doi: 10.3389/fenrg.2022.1094697

COPYRIGHT

© 2023 Chen, Zhang, Liu, Sun, Xiao, Gao
and Kang. This is an open-access article
distributed under the terms of the [Creative
Commons Attribution License \(CC BY\)](#).
The use, distribution or reproduction in
other forums is permitted, provided the
original author(s) and the copyright
owner(s) are credited and that the original
publication in this journal is cited, in
accordance with accepted academic
practice. No use, distribution or
reproduction is permitted which does not
comply with these terms.

Physical modeling of development adjustment mechanism for heterogeneous thick oil reservoir

Xu Chen^{1,2}, Zubo Zhang^{1,2}, Qingjie Liu^{1,2}, Linghui Sun^{1,2},
Hanmin Xiao^{1,2}, Jian Gao^{1,2} and Hao Kang^{3*}

¹State Key Laboratory of Enhanced Oil Recovery, PetroChina, Beijing, China, ²Research Institute of Petroleum Exploration and Development, PetroChina, Beijing, China, ³College of Engineering, Polytechnic Institute, Hebei Normal University, Shijiazhuang, China

With the gradually deep development of oil field, the remaining oil in reservoir become more scattered, to exploit them within the high water-cut pay become extremely difficult. Based on the characteristics of extremely high water-cut reservoir, three large scale physical models with different injection-production well patterns are designed. Through the analysis of oil production rate and the data of Computed Tomography (CT) scanning, the change law of fluid content within the core are obtained; The new calculation method of sweep efficiency for waterflooding within non-homogeneous models are set up in accordance with the CT number at different waterflooding stages. Furthermore, the development results of different plans are compared with each other, both injection and production with horizontal wells at low-permeability formation have the best recovery, because the displacement fluid can reach the places in reservoir where conventional waterflooding cannot. Therefore, this well pattern is the optimum plan for the positive rhythm model in this experiment, and the development strategy optimization is realized for high water-cut thick oil formation.

KEYWORDS

non-homogeneous, development adjustment, high water-cut, physical modeling, computerized tomography

1 Introduction

With the increase of the world's population, human demand for fossil energy such as oil and gas has been increasing (Tang, 2022; Wang et al., 2022). However, due to the impact of the epidemic and geopolitical factors, oil and gas companies are facing a series of challenges, such as large fluctuations in oil prices, increasingly complex exploration environment, continuous increase in environmental regulation and increasing exploitation costs (Cao and Liu, 2021; Dang et al., 2022; Dou et al., 2022; Li et al., 2022). Therefore, how to continuously improve oil recovery has always been of great significance to oil and gas companies (Chen, 2021; Wang et al., 2021).

Reservoir heterogeneity is one of the important factors affecting oilfield development, which not only reduces vertical sweep efficiency of the reservoir, but also has a greater impact on the oil displacement efficiency in the water injection layer system, and reduces the ultimate recovery (Tang et al., 2006; Li et al., 2018; He et al., 2021). For example, in the typical case of Daqing Lasaxing Oilfield, 100% of the main oil layers with thickness larger than 1 m have water breakthrough, and the remaining oil is mainly distributed in the water washing layer with 74.4% of the remaining geological reserves, and 45.7% of the remaining geological reserves are controlled by the oil layers with thickness larger than 2 m. The "in-layer contradiction" of thick oil reservoirs has become the main contradiction in the high water cut stage (Wu et al., 2014; Du

et al., 2019; Shi and Wu, 2019). Understanding reservoir heterogeneity and remaining oil distribution is the basis of improving oilfield development effect. Seismic, logging and other means can be used to depict the geological model of the reservoir scale and characterize its macroscopic heterogeneity, which lays a solid foundation for the water injection development of the oilfield. Taking the Badaowan Formation reservoir in the Chong-18 well block of Fengcheng Oilfield as an example, He et al. established a geological model of combined facies types and combined facies. Then the sequential Gaussian algorithm is used to establish the reservoir property model, and the reliability of the model is verified. The study can provide reference for reservoir dynamic management and numerical simulation (He et al., 2017). Wen et al. proposed 14 main parameters affecting reservoir heterogeneity and established a three-dimensional reservoir comprehensive index model. Then the model is applied to the reservoir characterization of gas reservoir in Su 53 block, and useful results are obtained (Wen and Sun, 2011). In the study of the heterogeneity of the fan-delta reservoir in the Tan-Lu fault zone, Huang et al. synthesized a variety of modeling methods and theories, and established its sedimentary microfacies model, physical parameter model, fractal geometric model, etc. Furthermore, the advantages and disadvantages of various models are compared (Huang et al., 2005). However, with the deepening of development, the distribution of remaining oil tends to be scattered, and the understanding of reservoir micro-heterogeneity needs to be strengthened. How to excavate the remaining oil in the water layer will be an unavoidable problem for continuous improvement of oil recovery (Zhang et al., 2008; Li et al., 2010; Liu et al., 2015). In order to improve the recovery factor of low permeability reservoir in high water cut stage, Hou et al. carried out the core displacement experimental study in the laboratory and obtained the mechanism of deep profile control to improve the recovery factor (Hou et al., 2020). Lin et al. used the parallel core water drive technology to obtain the main reasons for the low efficiency of water injection development in the late stage of high water cut. This study provides a reasonable basis for the formulation of development measures in the later stage of high water cut (Lin and Zhang, 2010). Zhao et al. confirmed that cyclic water injection can improve the development effect of heterogeneous sandstone reservoirs through indoor physical simulation experiments, which provides experimental basis for technical decision-making of oilfield development (Zhao et al., 2019). Zhuge used the strip heterogeneous simulation microscopic model to carry out the experimental study of water flooding, and defined the microscopic oil displacement mechanism for improving the water flooding effect in high water cut period (Zhuge, 2010). Guo combined laboratory oil-water phase permeability and nuclear magnetic resonance (NMR) to study the percolation characteristics of reservoirs in high water cut stage, and studied the percolation characteristics of reservoirs in high water cut stage from a microscopic point of view, which is of great significance to the adjustment of old oilfield plans (Guo, 2022). Zhou et al. obtained the influencing factors of remaining oil distribution in the process of water flooding through the analysis of nuclear magnetic resonance imaging core micro-displacement experiment (Zhou et al., 2021). Wu et al. carried out T2 spectrum test and slice imaging detection on each stage of Bailey core high multiple water flooding experiment by using nuclear magnetic resonance instrument, and obtained the

specific correlation between oil displacement efficiency and injection multiple (Wu et al., 2019). Based on the established three-dimensional physical model and combined with nuclear magnetic resonance, Xiao et al. defined the remaining oil producing mechanism under the dominant channel. Specific strategies for remaining oil recovery are proposed (Xiao et al., 2017).

As early as the 1980s, Computed Tomography (CT) scanning technology has been applied to the study of oil and gas reservoirs in China, and has gradually become an important tool for studying the characteristics of formation rocks. In the displacement experiment, CT scanning technology can be used to dynamically observe the fluid seepage process and saturation distribution characteristics in the core during different displacement processes without changing the experimental device as well as the external shape and internal structure of the core. Gao et al. uses CT scanner to scan the core displacement process axially to obtain the oil saturation and oil displacement characteristic curve of each section. By comparing with the measured oil saturation obtained by the displacement method, it is found that the CT method has higher accuracy (Gao et al., 2009); Cao found that CT scanning is an intuitive and effective technology to study remaining oil through CT scanning of water flooding, polymer flooding and subsequent water flooding experiments, and comparing the remaining oil distribution during the experiment according to the scanning results, which can quantitatively depict the distribution of remaining oil in different displacement processes and at different displacement times (Cao, 2015; Cao and Liu, 2015); By comparing the water saturation distribution obtained by the oil-water metering method and the X-ray scanning method in the water-flooding CT scanning experiment, Sun et al. found that CT scanning can not only obtain the dynamic change of the water-flooding front and the real-time water saturation distribution, but also more accurately describe the distribution of water saturation at different sections (Sun et al., 2017). Compared with the oil saturation measured by oil-water measurement method and displacement experiment method, the CT scanning method has higher accuracy and can make up for the shortcomings of the first two methods. Although the application of CT scanning technology to study the distribution of remaining oil in the core has been relatively mature, there is still room of improvement for the application of CT scanning displacement experiment into large-scale physical models. In this experiment, the calculation method of sweep efficiency is built and the application scope of CT scanning is enlarged in the study of oil field development. According to the reservoir characteristics of ultra-high water cut stage, three large-scale physical models with different types of injection-production wells are designed to simulate oil displacement experiments, study the oil-water distribution and seepage characteristics of each model in the process of water flooding, analyze the development effect of different injection-production schemes, and finally realize the optimization of development strategy for thick reservoirs in high water cut stage.

2 Experimental system

A physical modelling experimental device based on CT scanning system is established to study the mechanism of

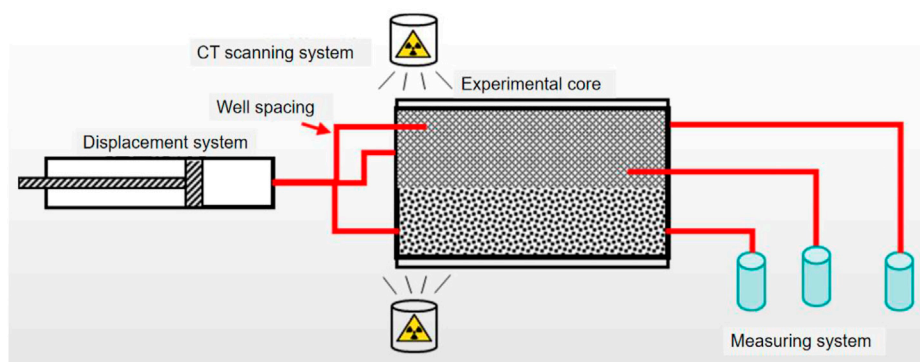


FIGURE 1

Schematic diagram of physical modelling platform for mechanism study on development adjustment strategy of heterogeneous thick reservoir.

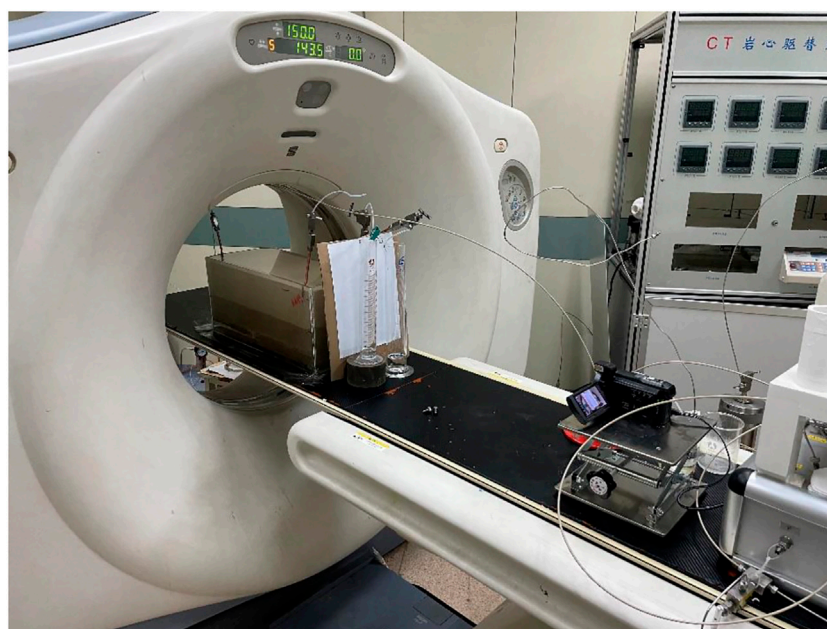


FIGURE 2

Physical modelling platform for mechanism study on development adjustment strategy of heterogeneous thick reservoir.

development adjustment strategy for heterogeneous thick reservoir. Its schematic diagram is shown in Figure 1. It is mainly composed of CT scanning system, displacement system, experimental core and measurement system. The core is designed by layering, embedded in the well pipe according to the experimental requirements, and covered by epoxy resin material, which can be used for CT scanning and can be measured by layer. The experimental flow setup and the large-scale physical model are shown in Figures 2, 3.

3 Experimental method

In this study, three groups of water flooding experiments with positive rhythmic intraformational heterogeneity were carried out to

analyze the water flooding recovery percent and oil-water movement law of the positive rhythmic intraformational heterogeneity model under different water injection schemes.

As shown in Figure 3, from top to bottom, the models are SZ1, SZ2 and SZ3 respectively. The physical experimental model is a positive rhythm heterogeneous core of epoxy resin material with different well spacing schemes. Experimental oil used is the mixed oil of 15# white oil with aviation kerosene. At temperature 23 °C, its viscosity is 11.93 mPa s and its density is .8292 g/cm³ 10% content NaBr saline is used as formation water in the experiment. Parameters and schemes of models are shown in Table 1.

Firstly, the basic parameters of each model, such as porosity and permeability, were measured. The permeability is as shown in Figure 3 and the porosity for each model is 25%. The model, simulated oil and 10% NaBr saline were scanned by CT. The core is then evacuated to

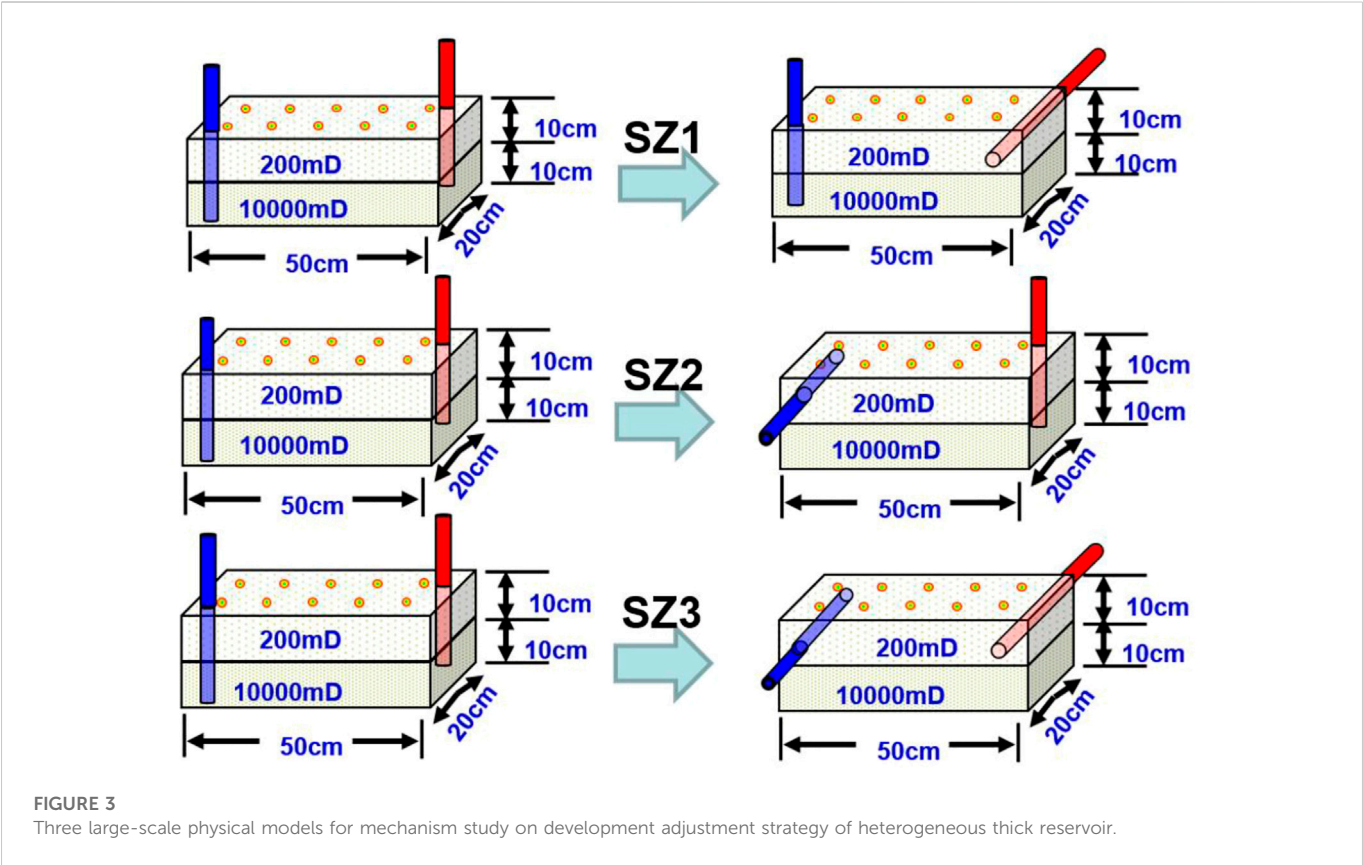


FIGURE 3
Three large-scale physical models for mechanism study on development adjustment strategy of heterogeneous thick reservoir.

TABLE 1 Basic data of heterogeneity models in positive rhythm layer.

Model	Dimension	Permeability ratio between two layers	Early-stage water injection scheme	Late-stage water injection scheme
SZ1	Length (50 cm) Width (20 cm) Height (20 cm)	50	Injection/production by vertical wells until water cut reaches 95%	Production by horizontal well from the low permeability layer
SZ2				Injection by horizontal well from the low permeability layer
SZ3				Injection and production by horizontal well from the low permeability layer

saturate the simulated oil, and the saturated wet model is CT scanned. In the first stage, 10% NaBr saline is used for displacement at the rate of 6 ml/min, and the amount of oil and water produced at the outlet is measured separately (stratified measurement method). In the early stage of water flooding, CT is used to scan once every 25 min, and in the late stage of water flooding, the time interval of CT scanning is increased. At the end of the experiment, the software was used to analyze the CT scanning data and calculate the sweep efficiency and water saturation of the model at each scanning time.

For the calculation of sweep efficiency, there are actually three steps. First of all, through the oil and water production and CT scanning data, the digital core analysis software is used to analyze and obtain the internal fluid changes in models. Secondly, according to the distribution characteristics of oil and water in models of the experiment, the change of CT number in each stage of water flooding is calculated on the basis of establishing the data matrix and visual image of oil and water distribution. Finally, the

water flooding sweep efficiency of the heterogeneous model is calculated.

4 Results and discussion

4.1 Overall injection-production displacement effect of vertical and horizontal wells

Through the online CT scanning of the water flooding process of the heterogeneous model, the oil-water distribution of three groups of positive rhythm heterogeneous models at each water injection stage can be obtained.

In the process of water flooding experiment, after the injection and production of vertical wells, the injection and production of horizontal wells were used, and the water cut of the produced fluid decreased in the three groups of positive rhythm models, the total recovery degree

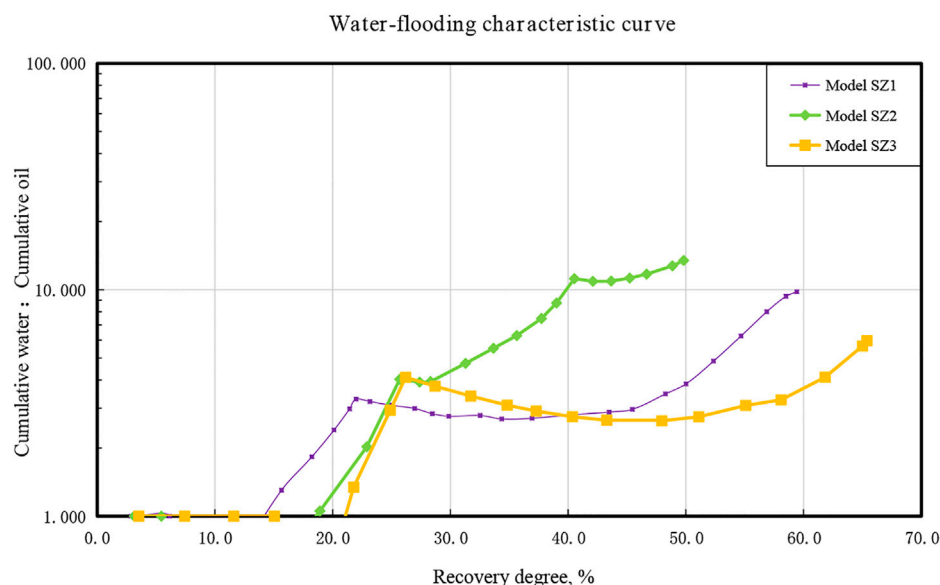


FIGURE 4
Water-flooding characteristic curve of positive rhythm model.

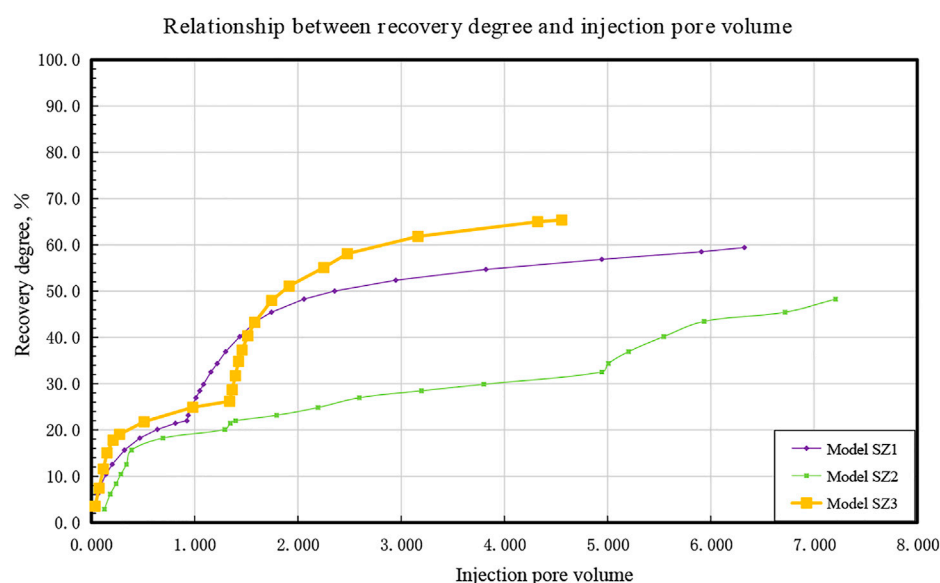


FIGURE 5
Relation between recovery and injection pore volume.

was further improved, and the upwarping water flooding characteristic curve turned downward, as shown in Figure 4, Figures 5, 6. It shows that in the high water cut stage, the above measures can effectively improve the oil displacement efficiency and improve the recovery percent of the reservoir. Specifically, Figure 4 is about the water-flooding characteristic curves of different positive rhythm models SZ1, SZ2, and SZ3. Figure 5 is about the relation between recovery degree and injection pore volume of different models SZ1, SZ2, and SZ3. Figure 6 is about the relation between water cut and injection pore volume of different models SZ1, SZ2, and SZ3.

4.2 Overall water saturation distribution in conventional water flooding stage by vertical wells

As shown in Figures 7, 8, in the injection-production stage of the vertical well, due to the permeability difference, the displacement fluid first enters the lower part of the high permeability layer, forming a dominant channel for water flow. The displacement fluid entering the middle part of the low permeability layer and the middle and upper part of the high

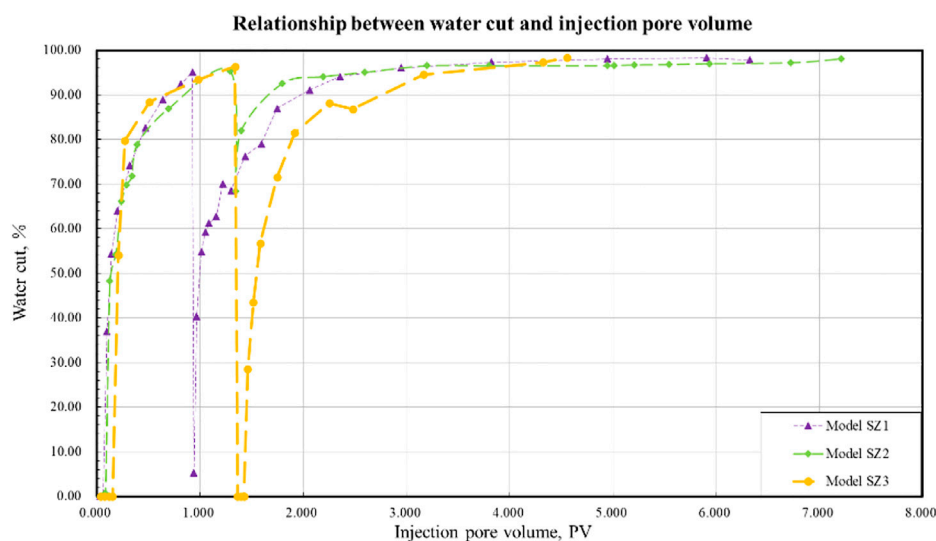


FIGURE 6
Relation between water cut and injection pore volume.

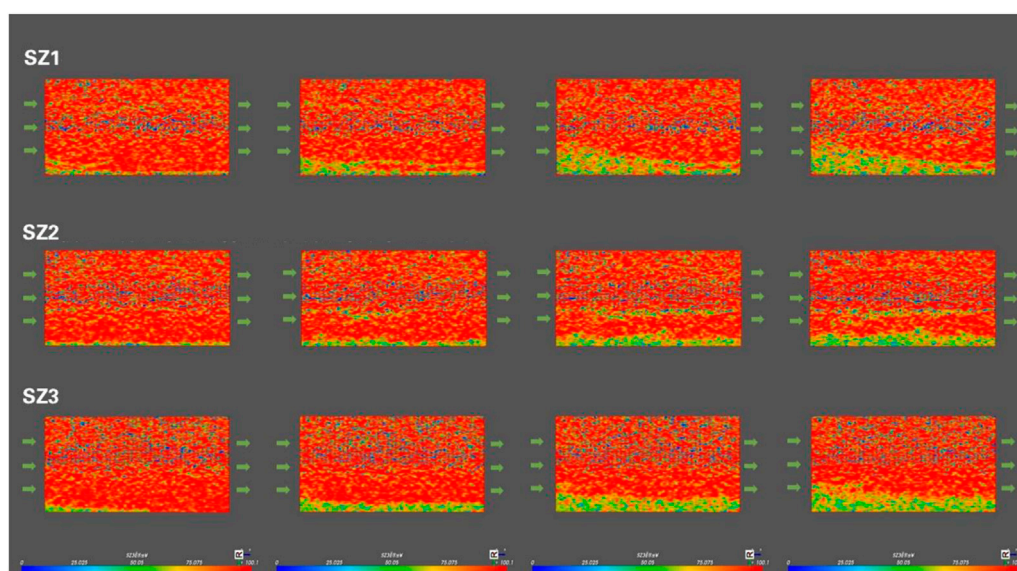


FIGURE 7
Oil saturation distribution of 3 groups of positive rhythm models (central slice).

permeability layer become less, and the two parts have a low degree of production, resulting in a low degree of recovery.

4.3 Water saturation distribution of each layer at production stage by horizontal well in SZ1 model

As shown in Figure 9, the recovery percent of the SZ1 model is 22% at the injection and production stage by vertical wells. It is switched to the mode of injection by vertical well and production by horizontal well in the low permeability layer at the later stage. At this time, a large amount of

displacement fluid enters the high permeability layer through the vertical well, and gradually moves up into the low permeability layer in the flow process, and finally flows into the horizontal well in the low permeability layer. The water saturation in the near wellbore area of the horizontal well increases significantly. In this process, the oil in the middle and upper part of the high permeability layer is swept by the displacement liquid and enters the horizontal well in the low permeability layer, while the oil in the lower and rear part of the low permeability layer is also produced, and the final recovery degree reaches 59.4%.

In terms of sweep efficiency, when the final recovery degree reaches 59.4%, the sweep efficiency of low permeable layer in SZ1 model increases from 25.1% to 42.3% in the conventional water flooding stage, with an

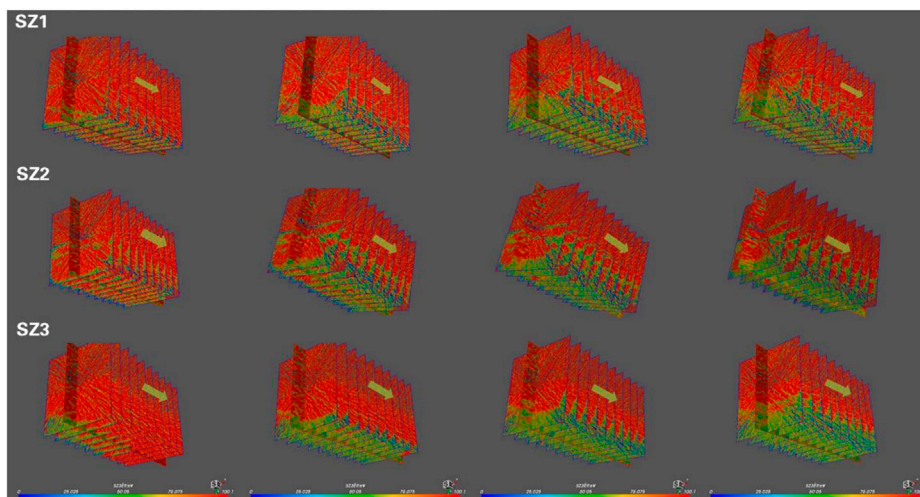


FIGURE 8
Oil saturation distribution of three groups of positive rhythm models (3D).

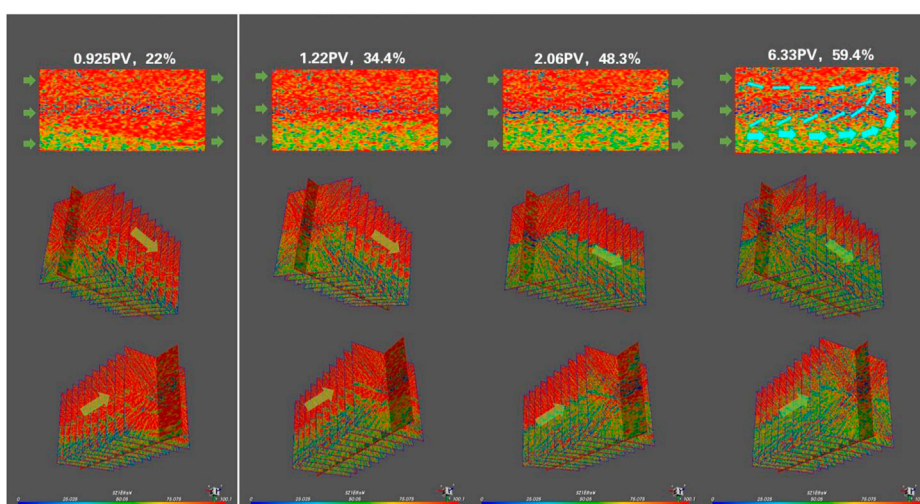


FIGURE 9
Oil saturation distribution in SZ1 model.

increase of 17.2%. The sweep efficiency of high permeable layer in SZ1 model increases from 51.2% to 83.3%, with an increase of 32.1%. It can be seen that the vertical well injection and horizontal well recovery scheme in low permeability layer can obviously improve the sweep efficiency of high permeability layer, and the recovery percent is mainly contributed by high permeability layer, and also has a certain improvement effect on low permeability layer.

4.4 Water saturation distribution of each layer at injection stage by horizontal well in SZ2 model

As shown in Figure 10, the recovery percent of the SZ2 model is 25.7% at the injection and production stage of the vertical wells, and it

is switched to the horizontal well injection and vertical well production mode in the low permeability layer at the later stage. The horizontal well increases the vertical sweep range, and the displacement fluid flows through the upper part of the low permeability layer or through the front part of the low permeability layer to the upper part of the high permeability layer, and the producing degree of these positions is obviously improved, while the lower part of low permeability layer has little change. The final recovery percent is 49.8%.

The sweep efficiency can also reflect the flow of the displacement fluid. When the final recovery of 49.8% is reached, the sweep efficiency of SZ2 model increases from 22.2% during the conventional water flooding stage to 43.3% in the low permeable layer with an increase of 21.1%. The sweep efficiency increases from 53.6% to 65% in the high permeable layer with an increase of 11.4%. This also shows that the scheme of horizontal well injection and vertical well production in low

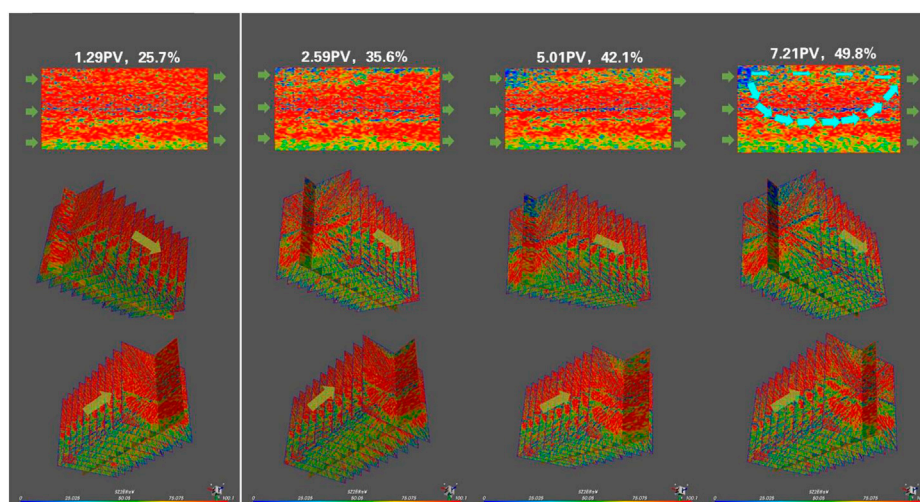


FIGURE 10
Oil saturation distribution in SZ2 model.

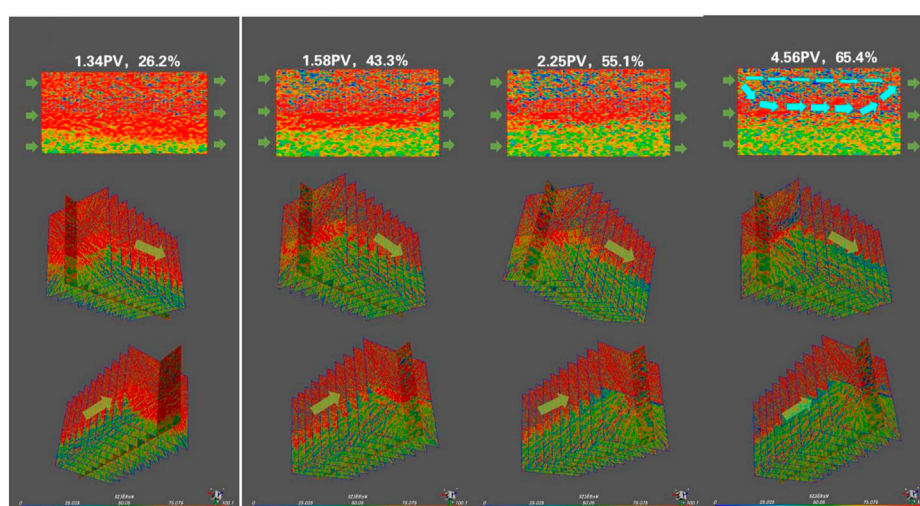


FIGURE 11
Oil saturation distribution in SZ3 model.

permeability layers mainly improves the sweep efficiency of low permeability layers, and has little effect on the sweep efficiency of high permeability layers, and the overall recovery percent of the model is mainly contributed by the low permeability layer.

4.5 Water saturation distribution of each layer at injection/production stage by horizontal well in SZ3 model

As shown in Figure 11, the recovery percent of the SZ3 model is 26.2% at the conventional injection and production stage of the vertical wells, and it is switched to the horizontal well injection and horizontal well production mode in the low permeability layer at the

later stage. Because the injection and production horizontal wells are located in the low permeability layer, more displacement fluid keeps flowing in the low permeability layer and enters the middle and upper part of the high permeability layer at the same time, and the recovery degree of the high and low permeability layers is obviously improved. When the ultimate recovery of 65.4% is reached, the sweep efficiency of SZ3 model increases from 23% to 41.4% in the low permeable layer and from 56.8% to 88.6% in the high permeable layer, with an increase of 18.4% and 31.8%, respectively. It shows that the effect of horizontal well injection and horizontal well production in low permeability layer is similar to that of vertical well injection and horizontal well production in low permeability layer, and the improvement of sweep efficiency in high permeability layer is obvious, and it also has a certain improvement effect on low permeability layer.

Advanced methods of mathematical modeling and experimental study in oil and gas reservoirs

Topic editors

Fuyong Wang — China University of Petroleum, Beijing, China

Bassem Nabawy — National Research Centre, Egypt

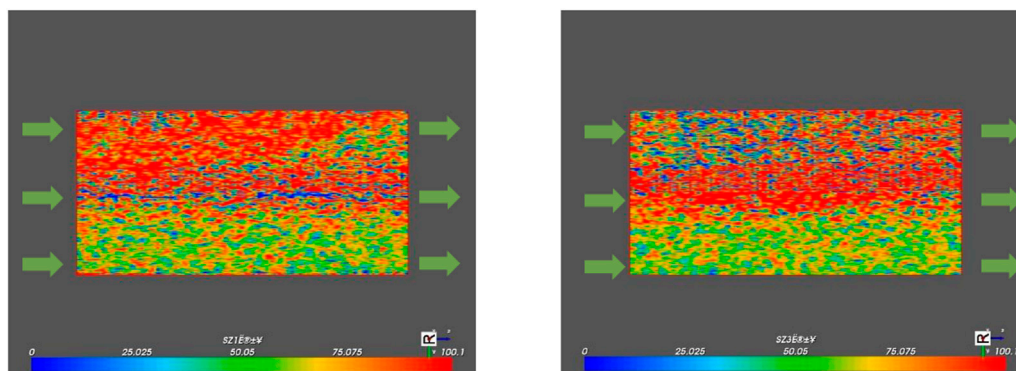
Evgeny Burnaev — Skolkovo Institute of Science and Technology, Russia

Xiukun Wang — China University of Petroleum, Beijing, China

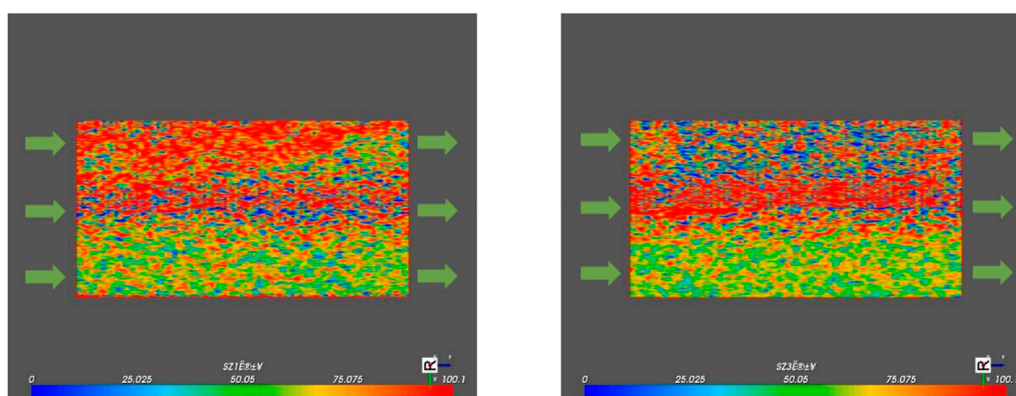
Debin Kong — University of Science and Technology Beijing, China

Citation

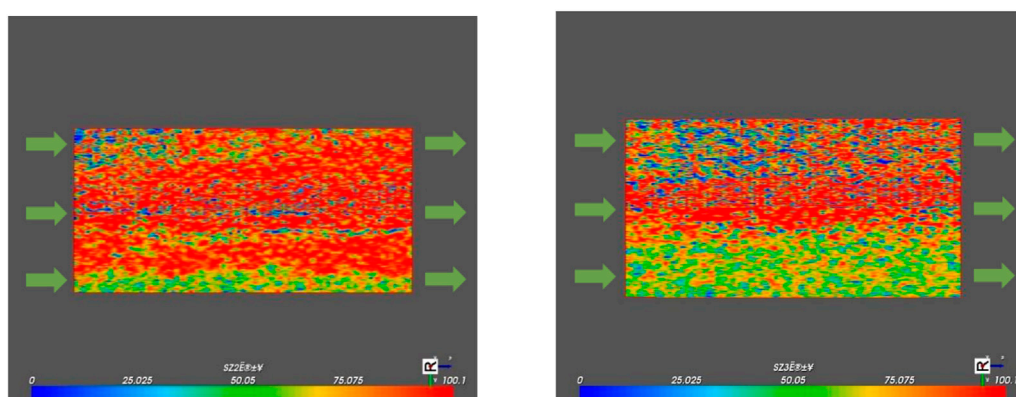
Wang, F., Nabawy, B., Burnaev, E., Wang, X., Kong, D., eds. (2023). *Advanced methods of mathematical modeling and experimental study in oil and gas reservoirs*. Lausanne: Frontiers Media SA. doi: 10.3389/978-2-8325-2887-7

**FIGURE 12**

Distribution of oil-water saturation in SZ1 (left image) and SZ3 (right image) model respectively.

**FIGURE 13**

Final oil-water saturation distribution of SZ1 (left image) and SZ3 (right image) model respectively.

**FIGURE 14**

Distribution of oil-water saturation in SZ2 (left image) and SZ3 (right image) model respectively.

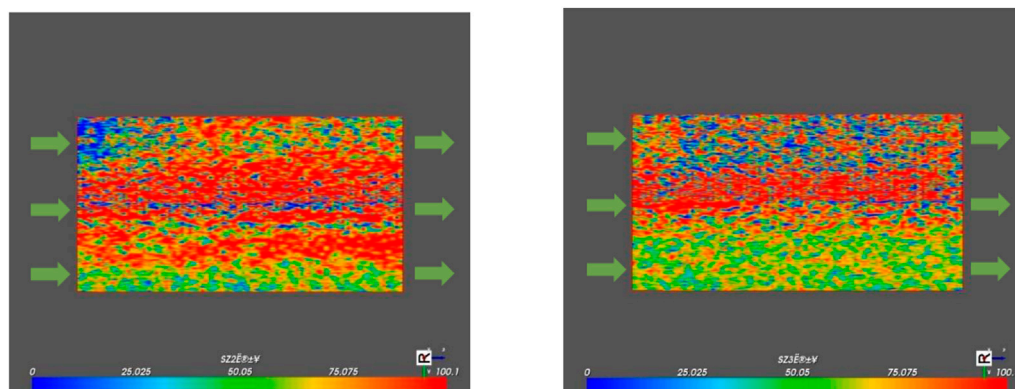


FIGURE 15

Final oil-water saturation distribution of SZ2 (left image) and SZ3 (right image) model respectively.

4.6 Effect comparison of three models

The experimental data of recovery percent and sweep efficiency concerning the three models are shown in Table 2. Through the comparison of SZ1 model and SZ3 model, as shown in Figure 12, in the injection and production stage of horizontal wells, under the condition of retaining vertical wells for oil production in low permeability layers, the displacement volume is about 1 pore volume (PV). Comparing SZ1 (vertical well injection, horizontal well production) with SZ3 (horizontal well injection, horizontal well production), the recovery degree of SZ1 is 48.3%, which is 26.3% higher than that before taking potential stimulating measures. The recovery percent of SZ3 is 55.1%, increased by 28.9% than before. The sweep efficiency of SZ1 in high and low permeable layers are increased by 31.1% and 2.1% respectively. Compared with the sweep efficiency of SZ3 in high and low permeable layers which are increased by 27.5% and 12.7% respectively, the sweep effect of SZ1 scheme on low permeable layer is poor, while that of high permeable layer is slightly better. The difference is due to the different flow channels of the two models. The horizontal well in SZ3 makes all the displacement fluid injected into the low-permeability layer, and the sweep range near the injection end of the low-permeability layer is larger, so the sweep efficiency of the low-permeability layers is greatly improved, while the displacement fluid in SZ1 model enters the high-permeability layers in large quantities, so the sweep efficiency of the high-permeability layers is greatly improved.

Continue to close the vertical wells for oil production in low permeability layers until the overall water cut reaches 98%. The final recovery degree of SZ1 (vertical well injection and horizontal well production) is 59.4%, which is 37.4% higher than that before potential stimulating measures are taken. The final recovery degree of SZ3 (horizontal well injection and horizontal well production) is 65.4%, which is 39.2% higher than that before potential stimulating measures are taken. The final increase rates of sweep efficiency of high and low permeable layers in SZ1 are 32.1% and 17.2% respectively, while the final increase rates of sweep efficiency of high and low permeable layers in SZ3 are 31.8% and 18.4% respectively. It can be seen that there is little difference

between the two schemes, the sweep efficiency in high permeable layer of SZ1 is slightly better than that in SZ3, and the sweep efficiency in low permeable layer of SZ3 is slightly better than that in SZ1. On the whole, the results in SZ3 is slightly better than that in SZ1. As the vertical well in the low permeability layer is closed, the sweep efficiency of the SZ1 low permeability layer is further significantly improved, and the gap between the two schemes is finally leveled (as shown in Figure 13).

As shown in Figure 14, by comparing the SZ2 model with the SZ3 model, it is found that in the case of retaining the vertical wells with high and low permeability layers in SZ2 and retaining the vertical wells of low permeability layer in SZ3, comparisons are firstly made when the displacement volume in SZ2 is 1.3 PV, and the displacement volume in SZ3 is 0.9 PV. The recovery percent of SZ2 is 35.6%, which is 9.9% higher than that before potential stimulating measures are taken, and the recovery percent of SZ3 is 55.1%, which is 28.9% higher. The increase of sweep efficiency in SZ2 high and low permeability layers is 2.5% and 8.6% respectively, which is much lower than that in SZ3 high and low permeability layers by 27.5% and 12.7%. The reason is that in the SZ2 model, although the horizontal well injection can improve the sweep efficiency of the low permeability layer, a large amount of displacement fluid enters the vertical well through the water flow channel at the lower part of the high permeability layer, and the ineffective circulation is more serious, so the recovery degree is less improved. The overall recovery percent of reserves of SZ2 is only 40.5% even when the water cut of high-permeability vertical wells is 98%.

With the experiment going on, the vertical oil well in high permeability layer is closed for model SZ2, and the vertical oil well in low permeability layer is closed for model SZ3. After that, continue to displace the oil until the total water cut of the produced fluid reached 98%. The final recovery degree of SZ2 (horizontal well injection, vertical well production) was 49.8%, which was 24.1% higher than that before potential stimulating measures were taken, and 39.2% lower than that of SZ3. The final increase of sweep efficiency in SZ2 high permeability layer is 11.4%, which is also much lower than 31.8% of SZ3. The final increase of sweep efficiency in SZ2 low permeability layer is 21.1%, which is slightly higher than 18.4% of SZ3. In general,

the recovery degree of SZ3 model is significantly higher than that of SZ2 model, and the horizontal well production scheme is still better than the vertical well production scheme (Figure 15).

Therefore, based on the analysis of the displacement experiment results of three groups of positive rhythm heterogeneous models with different water injection schemes, it can be seen that the recovery of horizontal well injection-production scheme is the best, the recovery of vertical well injection and horizontal well production scheme is in the middle and the recovery of horizontal well injection and vertical well production scheme is the smallest. Reasonable utilization of horizontal well injection-production program can change the internal flow channel of displacement fluid in the ultra-high water cut stage reservoir, improve the sweep efficiency in different layers, reduce the inefficient and ineffective circulation, and further improve the recovery of the reservoir.

5 Conclusion

By analyzing the heterogeneous water flooding experiment and according to the variation of CT number in each waterflooding stage, a new method for calculating the waterflooding sweep efficiency of heterogeneous model is established. According to the reservoir characteristics of ultra-high water cut stage, the physical simulation platform and experimental method for the study of the development adjustment strategy of the heterogeneous thick oil reservoir are established. Experiments show that the mode where the horizontal well is used for water injection and oil production in the low permeability layer, which can most effectively make the displacement fluid enter the position that cannot be swept by the conventional water flooding in the reservoir, and the recovery percent is most obviously improved. Therefore, the positive rhythm model is the best solution for this experiment. Although the two schemes of horizontal well and vertical well (model SZ1 and SZ2) can optimize the flow of displacement fluid to a certain extent, they are limited by the small area of vertical well in the horizontal direction, which is easy to generate dead angle for displacement. At the same time, displacement fluid crossing different layers leads to the fast generation of dominant channels for water flows in high permeability layers, so the effect is not as good as that of model SZ3 (injection and production with horizontal wells at the same time). Through large-scale physical modelling experiment, the mechanism of development adjustment strategy for heterogeneous thick reservoir is recognized, the oil-water distribution law and seepage characteristics of different strategies in the process of water flooding are revealed, the development effect is evaluated, and the development strategy of thick reservoir in high water cut stage is optimized.

References

- Cao, D., and Liu, S. (2021). The lagging response of U.S. Shale oil production to international oil price change —phenomena, causes and future prospects. *Int. Pet. Econ.* 29 (12), 24–33. doi:10.3969/j.issn.1004-7298.2021.12.004
- Cao, Y., and Liu, X. M. (2015). Application CT scanning technology analysis micro-flooding experiments and the residual oil. *Comput. Tomogr. Theory Appl.* 24 (1), 47–52. doi:10.1007/s12020-014-0354-3

Data availability statement

The original contributions presented in the study are included in the article/supplementary material, further inquiries can be directed to the corresponding author.

Author contributions

All authors listed have made a substantial, direct, and intellectual contribution to the work and approved it for publication.

Funding

This work is supported by Science and Technology Management Department of PetroChina with funding grant number 2019B-1207 and is also supported by the Open Fund of State Key Laboratory of Enhanced Oil Recovery, PetroChina with funding grant number 2022-KFKT-29 and RIPED-2022-JS-2156.

Acknowledgments

The authors acknowledge the contributions of Hebei Normal University, State Key Laboratory of Enhanced Oil Recovery and Research Institute of Petroleum Exploration and Development, PetroChina that aided the efforts of the authors.

Conflict of interest

Authors XC, ZZ, QL, LS, HX, and JG were employed by PetroChina.

The remaining authors declare that the research was conducted in the absence of any commercial or financial relationships that could be construed as a potential conflict of interest.

The authors declare this study received funding from State Key Laboratory of Enhanced Oil Recovery, PetroChina. The funder had the following involvement with the study: study design, data analysis and preparation of the manuscript.

Publisher's note

All claims expressed in this article are solely those of the authors and do not necessarily represent those of their affiliated organizations, or those of the publisher, the editors and the reviewers. Any product that may be evaluated in this article, or claim that may be made by its manufacturer, is not guaranteed or endorsed by the publisher.

Cao, Y. (2015). Study of microscopic flooding process using CT scanning technique. *Sci. Technol. Eng.* 15 (6), 64–68, 77. doi:10.3969/j.issn.1671-1815.2015.06.013

Chen, X. (2021). Digital management transformation of distributed CO₂-EOR project: Exploration and practice. *Reserv. Eval. Dev.* 11 (4), 635–642, 658. doi:10.13809/j.cnki.cn32-1825/te.2021.04.021

- Dang, L., He, J., Liu, M., Huang, M., and Kong, B. (2022). Innovative development of laboratory in oil and gas companies: An example from PetroChina Southwest Oil & Gasfield Company. *Nat. Gas. Res. Technol. Econ.* 16 (3), 71–77. doi:10.3969/j.issn.2095-1132.2022.03.011
- Dou, L., Wen, Z., Wang, J., Wang, Z., He, Z., Liu, X., et al. (2022). Analysis of the world oil and gas exploration situation in 2021. *Pet. Explor. Dev.* 49 (5), 1195–1209. doi:10.1016/s1876-3804(22)60343-4
- Du, Q., Song, B., Zhu, L., Jiang, Y., and Zhao, G. (2019). Challenges and countermeasures of the waterflooding development for Lasaxing Oilfields during extra-high watercut period. *Pet. Geol. Oilfield Dev. Daqing* 38 (5), 189–194. doi:10.19597/j.issn.1000-3754.201907004
- Gao, J., Han, D., Wang, J., Wu, K., and Liu, L. (2009). Application of CT scanning image technique to study of oil saturation distribution in core displacement test. *Xinjiang Pet. Geol.* 30 (2), 269–271.
- Guo, X. (2022). The application of relative permeability with NMR on percolation characteristics in high water cut period—taking minghuazhen reservoir of sealed coring wells in D oilfield. *Petrochem. Ind. Technol.* 29 (1), 172156–172173. doi:10.3969/j.issn.1006-0235.2022.01.078
- He, W., Yang, T., Fei, L., Huang, X., Bao, H., and Yang, Y. (2017). 3D geological modeling for heterogeneous glutenite reservoir with viscous oil: A case of Jurassic Badaowan formation reservoir in Zhong 18 well block in Fengcheng oilfield. *Complex Hydrocarb. Reserv.* 10 (1), 21–26. doi:10.16181/j.cnki.fzyqc.2017.01.004
- He, Z., Guo, Y., Guo, B., Wang, Y., and Bai, H. (2021). Heterogeneity of yan 91 reservoir in yang 66 wellblock of jing'an oilfield, ordos basin. *J. Xi'an Shiyou Univ. Nat. Sci.* 36 (1), 37–44. doi:10.3969/j.issn.1673-064X.2021.01.005
- Hou, S., Wang, Y., Rao, Z., and Zhang, C. (2020). Experimental study on deep profile control and oil displacement mechanism of high water cut reservoir. *Sci. Technol. Eng.* 20 (32), 13163–13167. doi:10.3969/j.issn.1671-1815.2020.32.012
- Huang, J., Peng, S., and Huang, J. (2005). Application of stochastic simulation of reservoir parameters on heterogeneity in fan delta reservoir. *Pet. Explor. Dev.* 32 (6), 52–55. doi:10.3321/j.issn:1000-0747.2005.06.012
- Li, H., Wang, C., Zhang, Y., Xu, J., Zheng, H., Zhang, E., et al. (2022). Safety and environmental risks and control measures in the oil and gas production for oilfield in beach-shallow sea. *Environ. Prot. Oil Gas. Fields* 32 (3), 58–62. doi:10.3969/j.issn.1005-3158.2022.03.012
- Li, J., Liu, Y., Gao, Y., Cheng, B., Meng, F., and Xu, H. (2018). Effects of microscopic pore structure heterogeneity on the distribution and morphology of remaining oil. *Pet. Explor. Dev.* 45 (6), 1112–1122. doi:10.1016/s1876-3804(18)30114-9
- Li, M., Gao, J., Zhang, L., and Wang, K. (2010). The influence of medium heterogeneity on the residual oil of reservoirs in the period of high water content and high dispersion. *Prog. Geophys* 25 (1), 85–89. doi:10.3969/j.issn.1004-2903.2010.01.014
- Lin, Y., and Zhang, J. (2010). Laboratory experiment on flow characteristics of heterogeneous reservoir at late stage of high water cut. *Pet. Geol. Oilfield Dev. Daqing* 29 (5), 90–95. doi:10.3969/j.issn.1000-3754.2010.05.018
- Liu, B., Zhang, Y., Zhang, W., and Deng, J. (2015). The vertical heterogeneity affecting of residual oil distribution in heavy oil reservoir. *Sci. Technol. Eng.* 15 (26), 161–164. doi:10.3969/j.issn.1671-1815.2015.26.028
- Shi, C., and Wu, X. (2019). Development modes and evolution trend of Lasaxing Oilfields. *Pet. Geol. Oilfield Dev. Daqing* 38 (5), 45–50. doi:10.19597/j.issn.1000-3754.201907084
- Sun, L., Wang, Z., and Pan, Y. (2017). Comparison of X-CT scanning technique and Berkeley-Villewater water-flooding theory fluid saturation distribution. *Sci. Technol. Eng.* 17 (32), 87–92. doi:10.3969/j.issn.1671-1815.2017.32.014
- Tang, J., Jia, A., He, D., Wang, W., Fan, L., Bai, Q., et al. (2006). Development technologies for the Sulige gas field with low permeability and strong heterogeneity. *Pet. Explor. Dev.* 33 (1), 107–110. doi:10.3321/j.issn:1000-0747.2006.01.025
- Tang, J. (2022). The energy writing in the anthropocene-on margaret Atwood's MaddAddam trilogy. *J. China Univ. Pet. Soc. Sci.* 38 (3), 39–45. doi:10.13216/j.cnki.upcjess.2022.03.0006
- Wang, B., Wu, Y., Liu, P., and Chen, S. (2022). Regional heterogeneity governing renewable energy development—from the perspective of industrial chain of production, transportation and consumption. *J. Beijing Inst. Technol. Soc. Sci.* 24 (1), 39–50. doi:10.15918/j.jbitss1009-3370.2022.5679
- Wang, G., Wang, F., Zhao, B., Sun, G., Meng, Q., Wang, Y., et al. (2021). Exploration and development situation and development strategy of Daqing Oilfield Company. *China Pet. explor.* 26 (1), 55–73. doi:10.3969/j.issn.1672-7703.2021.01.005
- Wen, H., and Sun, N. (2011). A new quantitative description method of gas reservoir heterogeneity. *Spec. Oil Gas. Reserv.* 18 (1), 51–53. doi:10.3969/j.issn.1006-6535.2011.01.013
- Wu, X., Wang, B., Liang, X., and Hao, Q. (2014). Produced recoveries of Lasaxing Oilfields at extra-high watercut period. *Pet. Geol. Oilfield Dev. Daqing* 33 (6), 52–56. doi:10.3969/j.issn.1000-3754.2014.06.010
- Wu, Y., Wang, C., Kan, L., Ao, W., Tian, J., Fu, Y., et al. (2019). Study on the characteristics of high multiple water drive by NMR. *Petrochem. Ind. Appl.* 38 (12), 15–19, 35. doi:10.3969/j.issn.1673-5285.2019.12.005
- Xiao, K., Mu, L., Jiang, H., Shen, J., and Zhang, P. (2017). Mechanisms of remaining oil production by plugging dominant flowing path and the application and strategies. *Oil Gas Geol.* 38 (6), 1180–1186. doi:10.11743/ogg20170619
- Zhang, Z., Shen, X., Jones, B. H., Xu, B., Herr, J. C., and Strauss, J. F., 3rd (2008). Phosphorylation of mouse sperm axoneme central apparatus protein SPAG16L by a testis-specific kinase, TSSK2. *Inn. Mong. Petrochem. Ind.* 34 (8), 75–83. doi:10.1095/biolreprod.107.066308
- Zhao, J., Weng, D., Chen, P., Zheng, J., Zhang, Q., and Hu, X. (2019). Experimental study on the cyclic water flooding of heterogeneous reservoir in a high water cut stage. *Appl. Sci. Technol.* 46 (6), 92–95. doi:10.11991/yykj.201611016
- Zhou, Z., Zhang, F., Liu, B., and Liu, J. (2021). Microscopic residual oil seepage mechanism and pore throat producing characteristics in high water-cut reservoirs. *Xinjiang Geol.* 39 (2), 275–279. doi:10.3969/j.issn.1000-8845.2021.02.012
- Zhuge, Z. (2010). Study on the microscopic water displacing oil mechanism experiment of high water-cut oil field. *Petrochem. Ind. Appl.* 29 (11), 27–29. doi:10.3969/j.issn.1673-5285.2010.11.008



OPEN ACCESS

EDITED BY

Xiukun Wang,
China University of Petroleum, Beijing,
China

REVIEWED BY

Xiangwen Kong,
Research Institute of Petroleum
Exploration and Development (RIPED),
China
Wenlong Jia,
Southwest Petroleum University, China
Qiusi Zhang,
Liaoning Petrochemical University,
China

*CORRESPONDENCE

Huzhen Wang,
wanghuzhen@nepu.edu.cn
Chunyao Wang,
wcy1370467@163.com

SPECIALTY SECTION

This article was submitted to Advanced
Clean Fuel Technologies,
a section of the journal
Frontiers in Energy Research

RECEIVED 05 July 2022

ACCEPTED 08 August 2022

PUBLISHED 09 January 2023

CITATION

Wang H, Liu T, Sun Z, Wang C, Zhang Y,
Chen Y, Liu Z and Zhou Z (2023),
Pressure transient analysis of multistage
fractured horizontal wells based on
detailed characterization of
stimulated area.
Front. Energy Res. 10:987098.
doi: 10.3389/fenrg.2022.987098

COPYRIGHT

© 2023 Wang, Liu, Sun, Wang, Zhang,
Chen, Liu and Zhou. This is an open-
access article distributed under the
terms of the [Creative Commons
Attribution License \(CC BY\)](#). The use,
distribution or reproduction in other
forums is permitted, provided the
original author(s) and the copyright
owner(s) are credited and that the
original publication in this journal is
cited, in accordance with accepted
academic practice. No use, distribution
or reproduction is permitted which does
not comply with these terms.

Pressure transient analysis of multistage fractured horizontal wells based on detailed characterization of stimulated area

Huzhen Wang^{1,2*}, Tiancheng Liu¹, Zhuangzhuang Sun¹,
Chunyao Wang^{1,3*}, Yangang Zhang³, Yulin Chen³, Zhenyu Liu^{1,2}
and Zhijun Zhou^{1,2}

¹Department of Petroleum Engineering, Northeast Petroleum University, Daqing, China, ²Key Laboratory of Reservoir Stimulation, China National Petroleum Corporation, Daqing, China, ³Daqing Oilfield Co., Ltd., Daqing, China

In ultralow permeability tight oil reservoirs, the fracturing scale of multistage fractured horizontal wells (MFHWs) is relatively large, and the artificial fracture system is generally more complex. Analytical and semi-analytical methods are difficult to characterize the stimulated area in detail, which includes main fractures, branch fractures, and microfractures. Numerical methods have unique advantages in studying such problems. The mathematical model of oil–water two-phase seepage is established by the finite element method, the permeability and pseudo threshold pressure gradient that vary with spatial position are proposed to characterize the stimulated area except the main fracture. A single well numerical model was established to study the influence of the width and permeability of the stimulated area on the pressure response. The analysis shows that the transient pressure response of MFHW is controlled by main fracture conductivity. Main fractures have high conductivity can better communicate the stimulated area, and MFHW can be better developed.

KEYWORDS

numerical well test, pressure transient analysis, multistage fractured horizontal wells, stimulated area, finite element method

Introduction

In recent years, the application of horizontal well volume fracturing technology has made important breakthroughs in the development of unconventional oil and gas reservoirs. Core flooding studies show that low-velocity non-Darcy flow exists in tight reservoir development. It is generally believed that non-Darcy flow has three flow states: no flow part, non-linear flow part, and linear flow part. The no flow part is when the pressure gradient is less than the threshold pressure gradient (TPG), the fluid does not flow. The flow rate under low-pressure gradient is very small, and it is difficult to

measure directly. Many scholars believe that TPG does not exist, and the non-linear flow part should start from zero pressure gradient (Wang et al., 2017). The intersection point of the linear flow section extension with the X-axis (pressure gradient) at high pressure gradients is called the pseudo threshold pressure gradient (PTPG). PTPG is easy to obtain, and the processing in the mathematical model is relatively simple. The non-Darcy flow is treated as two parts: no flow and linear flow. When detailed data on non-linear flow are not available, non-Darcy flow can be approximated by PTPG. Prada and Civan (1999) studied non-Darcy flow phenomena using salt water and analyzed the effect of permeability and fluid viscosity on PTPG. In practical application, it was found that the PTPG value estimated by the experiment was very large, and the same problem was found in similar experiments (Zeng et al., 2010).

After volume fracturing of horizontal wells, a large number of branch fractures and microfractures are formed. Regardless of the analytical method or the numerical method, the characterization of the main fracture and the stimulated area is an important work in well test analysis. The trilinear-flow model presented by Brown, the whole drainage area is decomposed into three contiguous flow regions: outer reservoir, inner reservoir, and hydraulic fractures (Brown et al., 2011). Stalgorova and Mattar (2012a) developed an enhanced fracture region model with a higher permeability region near each hydraulic fracture and unstimulated region in the bulk of the space between fractures. A more advanced five-region model that encompasses both the existing trilinear-flow model and previous enhanced fracture region model further represented (Stalgorova and Mattar, 2012b). Fuentes-Cruz presented an induced permeability field within SRV to improve the continuous assumption of linear-composite permeability model and extended to the dual porosity idealization model (Fuentes-Cruz et al., 2014a; Fuentes-Cruz et al., 2014b). Many scholars conventional multiple hydraulic fractured horizontal (MFH) well into a composite model to describe the stimulated reservoir volume (SRV). Simplify the SRV into a circle (Zhao et al., 2014; Hu et al., 2021), rectangular shape (Wang et al., 2016; Li et al., 2021), irregular shape (Chen et al., 2018, 2021; Zhang and Yang, 2021), and ellipse shape (Wang and Sheng, 2017). Some scholars use embedded discrete fracture model (EDFM) (Xu et al., 2017; He et al., 2022) and discrete fracture model (DFM) (Liu et al., 2020) to treat MFHW, considering the complexity of fractures and not considering the stimulated area near the fractures.

In summary, ultralow permeability tight oil reservoirs have large fracturing scale and complex artificial fractures. The analytical and semi-analytical methods generally do not consider the stimulated area, or consider stimulated area

with a single permeability. The numerical methods generally divide the stimulated area into multiple areas, each area has different properties, and the characterization of stimulated area is not detailed enough. For this problem, the parameters of the stimulated area are characterized by using the formation permeability and the starting pressure gradient that change with the spatial position. The finite element numerical method was used to build the mathematical model.

Mathematical model

Seepage differential equation

Basic assumption: there is oil–water two-phase fluid in homogeneous anisotropic reservoir, and both fluid and rock are weakly compressible, ignoring the influence of gravity. Several vertical fractures are fractured along the horizontal well pressure, and the fractures run through the entire reservoir.

The two-dimensional oil-phase pressure differential equation of the matrix system considering the threshold pressure gradient is:

$$\nabla \cdot \left[K \lambda \nabla p_o \left(1 - \frac{G}{|\nabla p_o|} \right) \right] - \nabla \cdot (K \lambda \lambda_w \nabla p_c) = \phi C_t \frac{\partial p_o}{\partial t} \quad (1)$$

where $C_t = C_f + S_w C_w + S_o C_o$, $\lambda = \frac{K_{ro}}{\mu_o} + \frac{K_{rw}}{\mu_w}$, $\lambda_o = \frac{K_{ro}}{\mu_o \lambda}$, and $\lambda_w = \frac{K_{rw}}{\mu_w \lambda}$

The water-phase saturation equation (ρ_w treated as constant):

$$\begin{aligned} & -\lambda'_w \mathbf{v}_t \nabla S_w - K \lambda \lambda_o \lambda_w \nabla \cdot (\nabla p_c^n) - K \lambda \lambda_o \lambda_w p'_c \nabla \cdot (\nabla S_w) \\ & - K \lambda \lambda_o \lambda_w p'_c \nabla \cdot (\nabla S_w^n) \\ & = \phi \frac{\partial (S_w)}{\partial t} \end{aligned} \quad (2)$$

A mixed element discrete fracture model is used to characterize artificial fractures, ignoring the flow in the fracture perpendicular to the direction of the fracture, and the flow in the fracture is simplified to one dimension, which is described by line elements. The effect of threshold pressure gradient is not considered in the fracture. Then the equations of oil-phase pressure and water-phase saturation in the artificial fracture system are:

$$\nabla \cdot \left(K_f \lambda \frac{\partial p_{fo}}{\partial x} \right) - \nabla \cdot \left(K_f \lambda \lambda_w \frac{\partial p_{fc}}{\partial x} \right) = \phi C_t \frac{\partial p_{fo}}{\partial t} \quad (3)$$

$$\begin{aligned} & -\lambda'_w \mathbf{v}_t \frac{\partial S_w}{\partial x} - K_f \lambda \lambda_o \lambda_w \nabla \cdot \left(\frac{\partial p_{fc}^n}{\partial x} \right) - K_f \lambda \lambda_o \lambda_w p'_{fc} \nabla \cdot \left(\frac{\partial S_w}{\partial x} \right) \\ & - K_f \lambda \lambda_o \lambda_w p'_{fc} \nabla \cdot \left(\frac{\partial S_w^n}{\partial x} \right) \\ & = \phi \frac{\partial (S_w)}{\partial t} \end{aligned} \quad (4)$$

Inner boundary well model

Assuming that the fracturing horizontal well only has production at the fracture, and the sum of the production of all fractures is equal to the production of the horizontal well, the intersection of the artificial fracture and the horizontal well is treated as the inner boundary.

When considering the effects of wellbore storage coefficient and skin factor, the pressure at the inner boundary node is taken as the wellface pressure p_{wb} . According to the definition of the skin coefficient, when the wellbore friction is not considered, the pressure at each inner boundary node is equal to the bottom hole flowing pressure p_{wf} , and the additional pressure drop Δp_s caused by the skin effect should also be equal at each inner boundary node. The relationship between bottom hole flowing pressure p_{wf} and wellface pressure p_{wb} , sand face flow rate q_b :

$$p_{wb} - p_{wf} = \Delta p_s = \frac{q_b \mu}{2\pi K h} S. \quad (5)$$

According to the definition of the wellbore storage coefficient, the relationship between the sand face flow rate q_b and the well flow rate q at the node is obtained:

$$q_b = qB - C \frac{(p_{wf}^n - p_{wb})}{\Delta t}. \quad (6)$$

In Eq. 5, let $F_n = \frac{\mu S}{2\pi K h}$, then:

$$p_{wf} = p_{wb} - q_b \cdot F_n. \quad (7)$$

Combining Eqs. 6, 7:

$$q_b = \frac{\Delta t q B - C p_{wf}^n}{CF_n + \Delta t} + \frac{C}{CF_n + \Delta t} p_{wb}. \quad (8)$$

The aforementioned formula is the bottom hole production expression of the inner boundary node, considering the influence of well storage coefficient and skin factor.

Weak solution integral form of differential equations

Equation 1 applies the principle of virtual displacement (δp is the virtual displacement of pressure) to obtain the equivalent integral form:

$$\begin{aligned} & \iint_V \nabla \cdot \left[K \lambda \nabla p_o \left(1 - \frac{G}{|\nabla p_o|} \right) \right] \delta p_o dV - \iint_V \nabla \cdot (K \lambda_w \nabla p_c) \delta p_o dV \\ &= \iint_V \phi C_t \frac{\partial p_o}{\partial t} \delta p_o dV. \end{aligned} \quad (9)$$

Partial integration at the left end of the aforementioned formula can obtain:

$$\begin{aligned} & - \iint_V K \lambda \nabla p_o \left(1 - \frac{G}{|\nabla p_o|} \right) \nabla \delta p_o dV + \int_{\Gamma} K \lambda \frac{\partial p_o}{\partial n} \delta p_o d\Gamma \\ &+ \iint_V K \lambda_w \nabla p_c \nabla \delta p_o dV - \int_{\Gamma} K \lambda_w \frac{\partial p_c}{\partial n} \delta p_o d\Gamma \\ &= \iint_V \phi C_t \frac{\partial p_o}{\partial t} \delta p_o dV. \end{aligned} \quad (10)$$

where $\frac{\partial}{\partial n} = n_x \frac{\partial}{\partial x} + n_y \frac{\partial}{\partial y}$, n_x, n_y , is the component of the unit vector in the normal direction outside the boundary.

The fixed production of a horizontal well, the integral along the bottom hole boundary $\int_{\Gamma} K \lambda \frac{\partial p_o}{\partial n} \delta p_o d\Gamma$ can be expressed as

$$\int_{\Gamma} K \lambda A \frac{\partial p_o}{\partial n} \frac{1}{A} \delta p_o d\Gamma = \int_{\Gamma} \frac{q_b}{A} \delta p_o d\Gamma \quad (A \text{ is the bottom seepage area}).$$

Substitute Eq. 8, p_{wf}^n is the bottom hole flow pressure in the previous step for display processing, and the wellface pressure p_{wb} is regarded as an unknown, then the weak integral form of the basic differential equation in constant flow production can be obtained:

$$\begin{aligned} & - \iint_V K \lambda \nabla p_o \left(1 - \frac{G}{|\nabla p_o|} \right) \nabla \delta p_o dV + \int_{\Gamma} \frac{\Delta t q B - C p_{wf}^n}{CF_n + \Delta t} \delta p_o d\Gamma \\ &+ \int_{\Gamma} \frac{C}{CF_n + \Delta t} p_{wb} \delta p_o d\Gamma + \iint_V K \lambda_w \nabla p_c \nabla \delta p_o dV \\ &= \iint_V \phi C_t \frac{\partial p_o}{\partial t} \delta p_o dV. \end{aligned} \quad (11)$$

In the same way, the weak solution integral form of the water-phase saturation equation can be obtained:

$$\begin{aligned} & - \iint_V \lambda'_w \nabla S_w \nabla \delta S_w dV + \iint_V K \lambda_o \lambda_w \nabla p_c^{n-1} \nabla \delta S_w dV \\ &+ \iint_V K \lambda_o \lambda_w p_c' \nabla S_w \nabla \delta S_w dV - \iint_V K \lambda_o \lambda_w p_c' \nabla S_w^n \nabla \delta S_w dV \\ &= \iint_V \phi \frac{\partial S_w}{\partial t} \delta S_w dV. \end{aligned} \quad (12)$$

The total seepage velocity v_t in the aforementioned formula is treated explicitly.

The weak solution integral form of the fracture system can be obtained, which will not be repeated here.

Algorithm

The oil-phase pressure equation and the water-phase saturation equation were solved by implicit pressure and explicit water saturation. The time was discretized by the Crank–Nicolson scheme. The linear equations were solved by the direct method of LDL^T decomposition. Both the water cut

TABLE 1 Basic parameters of the reservoir, well, and fracture.

Types	Parameter	Value	Unit
Reservoir	Initial pressure	40	MPa
	Thickness of formation	33	m
	Oil viscosity	10	mPa·s
	Permeability of matrix	0.043	$10^{-3}\mu\text{m}^2$
	Porosity of matrix	0.1099	—
	Rock compressibility	0.45	10^{-4} 1/MPa
	Oil compressibility	12.1	10^{-4} 1/MPa
	Water compressibility	4.5	10^{-4} 1/MPa
	Initial water saturation	0.15	—
	Oil volume factor	1.293	—
Fracture	Conductivity of fracture	0.02, 0.1, and 0.5	$10^{-3}\mu\text{m}^2\cdot\text{m}$
	Number of stage	15	—
	Half length of fracture	60–190	m
	Average half length of fracture	125	m
Well	Well length	1,305	m
	Production rate	20	m^3/day
	Wellbore storage coefficient	1	m^3/MPa

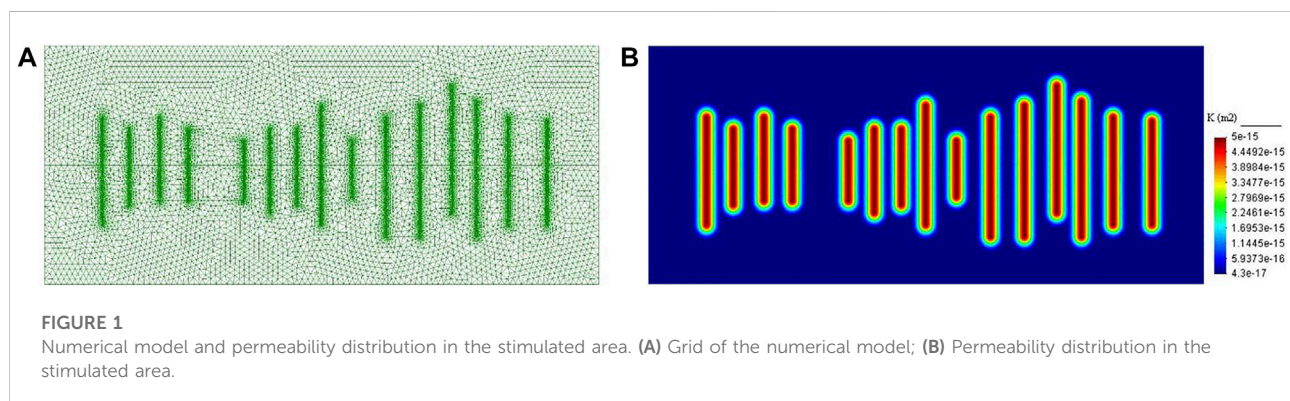
permeability. The basic parameters of reservoirs, wells, and fractures are shown in Table 1.

Characteristics of relative permeability curve: irreducible water saturation 0.15, residual oil saturation 0.422, and relative permeability of water-phase at residual oil saturation is 0.272.

Numerical model and parameter characterization of stimulated area

Take a MFHW in a homogeneous tight oil reservoir, the outer boundary is closed. The single well numerical model is established as shown in Figure 1A. The size of the simulation area is $1500\text{ m} \times 600\text{ m}$. The matrix is meshed with arbitrary triangular elements, and the fractures are meshed with 2-node line elements. The mesh size of the fracture line element is 1 m, the maximum mesh size of the matrix is about 25 m, the total number of nodes is 25011, and total number of triangular elements is 49740.

It is assumed that the position in the formation with the same vertical distance from the fracture surface has the same



and the pressure gradient were solved using the least squares method.

Numerical model building

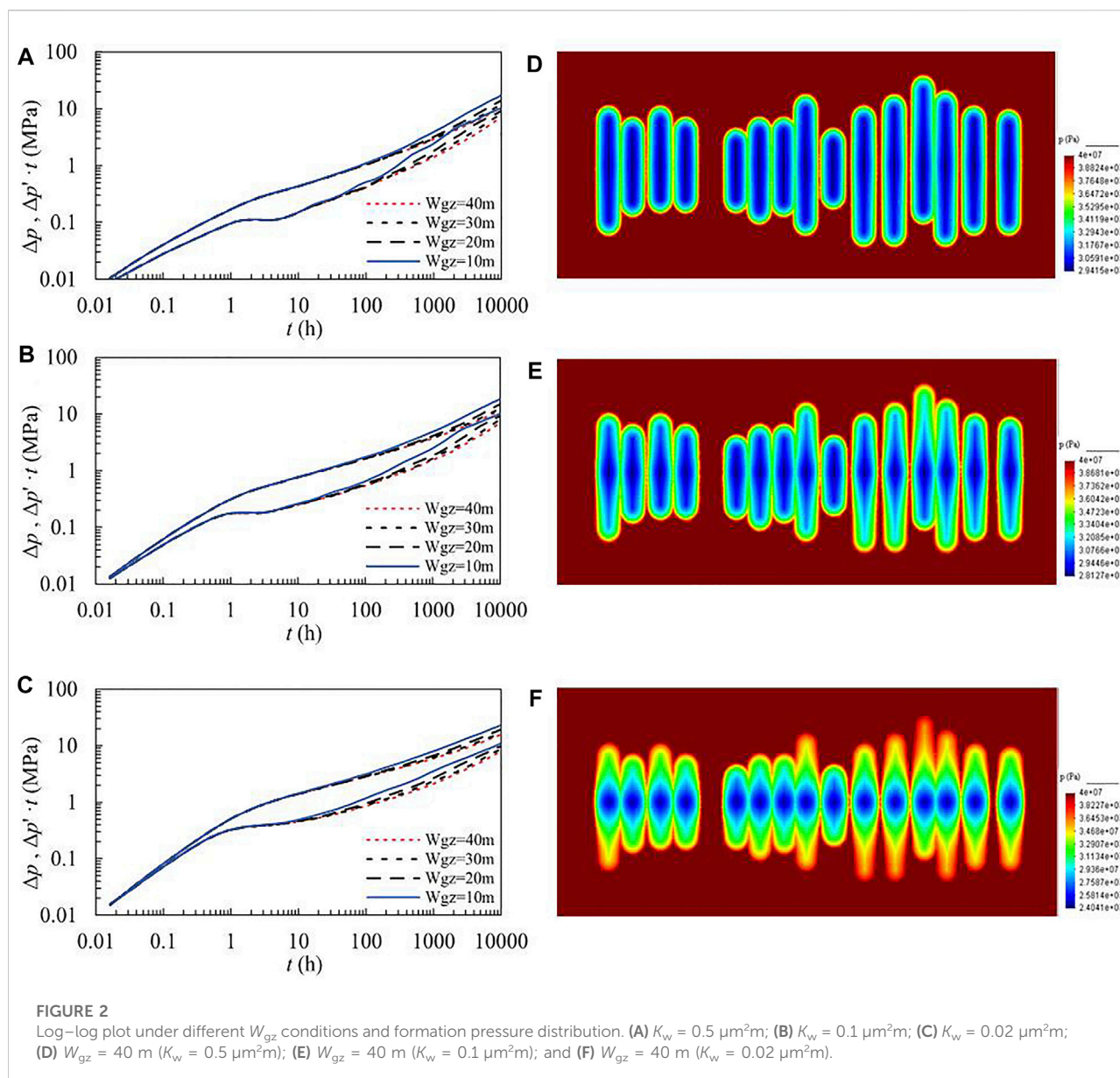
Basic parameters

The tight oil reservoir of Lucaogou Formation in Jimusar Sag of Changji Oilfield has an average porosity of 9.17%, an average permeability of $0.15 \times 10^{-3}\mu\text{m}^2$, and more than 70% permeability of the cores is less than $0.1 \times 10^{-3}\mu\text{m}^2$. The reservoir has the characteristics of low porosity and ultralow

stimulation effect, and the smaller is the distance from the fracture surface, the better is the stimulation effect. Two parameters can be used to characterize the stimulated area: the width and permeability. The maximum permeability of the stimulated area is at the fracture surface and assuming an exponential change in the direction perpendicular to the fracture surface, the following formula is used:

$$K_{gz} = \left(\frac{K}{K_{mf}} \right)^{\left(\frac{x}{W_{gz}} \right)^2} \cdot K_{mf}.$$

In addition, due to the improvement of formation permeability in the stimulated area, the fluid PTPG should

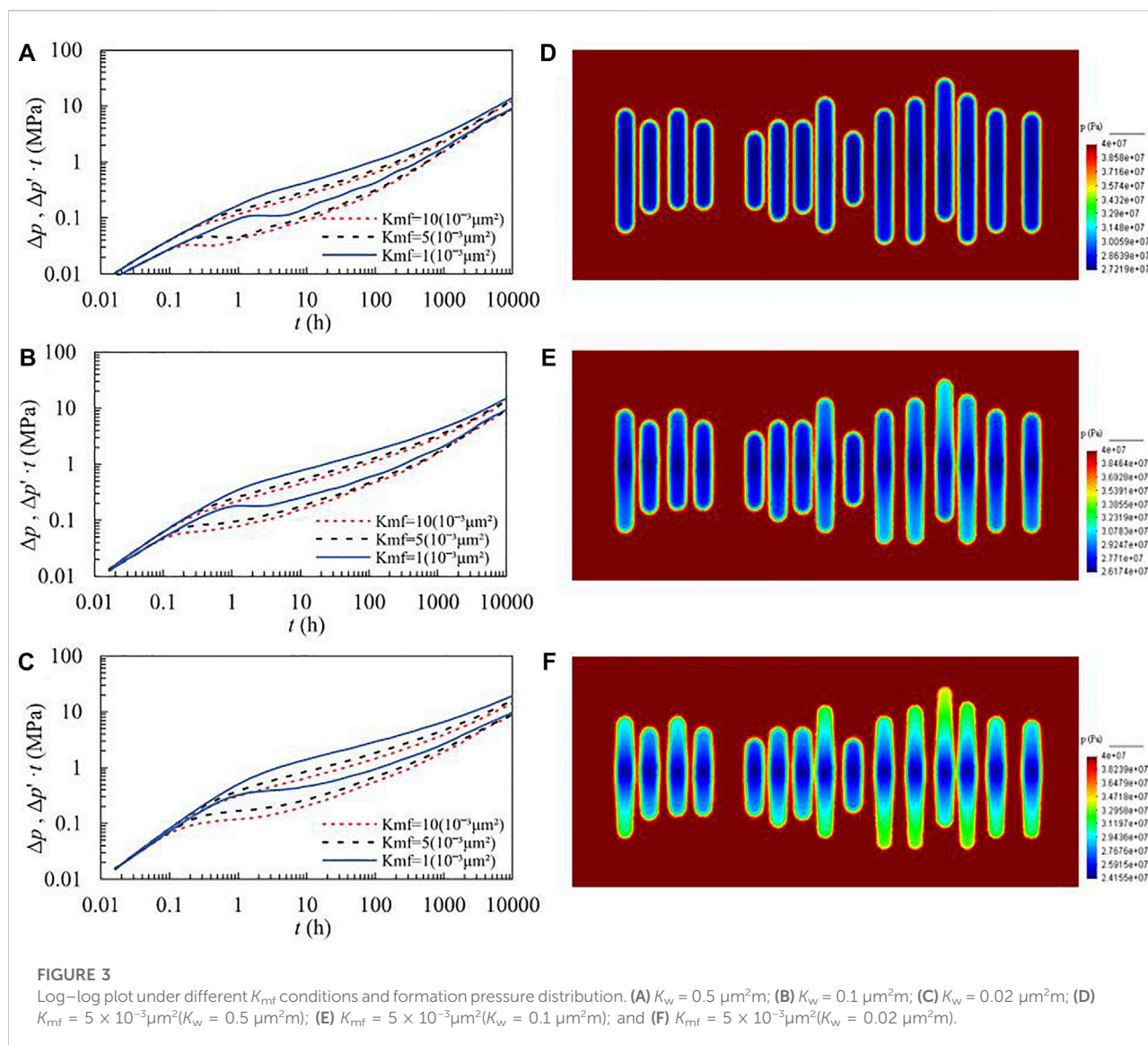


also be reduced, and it can be reset according to permeability. The width of the stimulated area is 40 m, the matrix permeability at the fracture surface is $5 \times 10^{-3} \mu m^2$, and PTPG is calculated according to the empirical formula $G = 0.0828K^{-0.66}$, which are obtained from laboratory experiments. The permeability distribution of the stimulated area is shown in Figure 1B. The permeability ranges from 0.043×10^{-3} to $5 \times 10^{-3} \mu m^2$, and PTPG ranges from 0.6606 to 0.0286 MPa/m. The method established in this article has the advantage of being able to characterize the stimulated area parameters in detail, the disadvantage is that the unstructured grid is used, the number of grids and computational workload are large, so only a two-dimensional model can be used for numerical calculation.

Results and discussion

Effect of stimulated area width on pressure transient response

The stimulated area width W_{gz} designs four cases: 10, 20, 30, and 40 m, and fracture conductivity K_w designs three cases: 0.5, 0.1, and $0.02 \mu m^2 m$. The permeability of the fracture surface is set to $1.0 \times 10^{-3} \mu m^2$. The pressure transient response curves of the four stimulated area width cases are shown in Figures 2A–C. The smaller the width of the stimulated area, the more obvious the upturning feature of the curve. The larger the width of the stimulated area, the more obvious the linear flow characteristics



of the fracture. The lower the fracture conductivity, the smaller the influence of the width of the stimulated area on the pressure response curve, and the more obvious the bilinear flow characteristics. The higher the fracture conductivity, the smaller the distance between the pressure curve and the derivative curve, and the more obvious the linear flow characteristics. The width of stimulated area is 40 m, and the pressure distributions (10000 h) of the three fracture conductivity schemes are shown in Figures 2D–F. It can be seen from the comparison that the higher is the fracture conductivity (Figure 2D), the larger is the range of the low-pressure area, the effect of stimulated area is stronger, and the low-pressure area near the fracture is distributed along the fracture. The lower the fracture conductivity (Figure 2F), the effect of the stimulated area is weaker, and the low-pressure area is mainly near the bottom hole. Combining the pressure response

curve and the pressure distribution map, it can be seen that the higher is the fracture conductivity, the higher is the bottom-hole flow pressure, the earlier the linear flow appears in the pressure response curve, and the low-pressure area distribute along the fracture and has a larger range.

Effect of stimulated area permeability on pressure transient response

The permeability at fracture surface K_{gz} designs three cases: 1.0×10^{-3} , 5×10^{-3} , and $10 \times 10^{-3} \mu\text{m}^2$, and fracture conductivity K_w designs three cases: 0.5, 0.1, and $0.02 \mu\text{m}^2\text{m}$. The pressure transient response curves of the three stimulated area permeability cases are shown in Figures 3A–C. The effect of stimulated area permeability on the pressure response curve is

mainly in the mid-term. The greater the stimulated area permeability, the stronger the supply capacity to fractures, and the derivative curve tends to be flat. From the comparison of different fracture conductivities, the lower is the conductivity, the less obvious is the effect of the stimulated area width. This is because the fracture conductivity is very low, and the effect of the stimulated area cannot be fully exerted (Figures 3D–F).

Conclusion

Applying the basic principle of finite element, according to the characteristics of tight oil reservoirs, a mathematical model of oil–water two-phase numerical well test is established considering the PTPG. Benefiting from the flexibility of finite element meshing, the DFM is used to describe artificial fractures for MFHW, which can achieve a reasonable characterization of the artificial fracture system.

A characterization method of stimulated area parameters changing with the spatial location is established. The stimulated area parameters of MFHW are described by the width, the permeability, and the PTPG that vary with the spatial position in the stimulated area. Based on the relationship between permeability and PTPG, an innovative detailed characterization of stimulated area can be achieved.

Both the width and the permeability of stimulated area have a great influence on the pressure response of the fracturing horizontal well, but their influence is controlled by the fracture conductivity. Very low fracture conductivity makes it difficult to obtain a good development effect even if there is a large stimulated area. Therefore, when fracturing, it is necessary to obtain a large SRV, more important thing is to ensure that the fractures have high conductivity, so as to achieve better development results.

Data availability statement

The original contributions presented in the study are included in the article/Supplementary Material; further inquiries can be directed to the corresponding authors.

References

- Brown, M., Ozkan, E., Raghavan, R., and Kazemi, H. (2011). Practical solutions for pressure-transient responses of fractured horizontal wells in unconventional shale reservoirs. *SPE Reserv. Eval. Eng.* 14 (06), 663–676. doi:10.2118/125043-PA
- Chen, P., Hu, C., Zou, P., Lin, L., Lu, S., and Gao, X. (2021). Pressure response of a horizontal well in tight oil reservoirs with stimulated reservoir volume. *Lithosphere* 2021 (1), 5383603. doi:10.2113/2021/5383603
- Chen, P., Jiang, S., Chen, Y., and Zhang, K. (2018). Pressure response and production performance of volumetric fracturing horizontal well in shale gas reservoir based on boundary element method. *Eng. Analysis Bound. Elem.* 87, 66–77. doi:10.1016/j.enganabound.2017.11.013

Author contributions

HW, ZL, and ZZ contributed to conception and design of the study. ZS and YC organized the database. HW, TL, ZS, YC, and YZ performed the numeral calculations and statistical analysis. HW, TL, ZS, and YZ wrote sections of the manuscript. All authors contributed to manuscript revision, read, and approved the submitted version.

Funding

This work is supported by the Daqing guiding science and technology plan project (No. zd-2021-51).

Conflict of interest

Authors HW, ZL, and ZZ were employed by Northeast Petroleum University. Authors CW, YZ, and YC were employed by the company Daqing Oilfield Co., Ltd.

The remaining authors declare that the research was conducted in the absence of any commercial or financial relationships that could be construed as a potential conflict of interest.

Publisher's note

All claims expressed in this article are solely those of the authors and do not necessarily represent those of their affiliated organizations, or those of the publisher, the editors, and the reviewers. Any product that may be evaluated in this article, or claim that may be made by its manufacturer, is not guaranteed or endorsed by the publisher.

Supplementary material

The Supplementary Material for this article can be found online at: <https://www.frontiersin.org/articles/10.3389/fenrg.2022.987098/full#supplementary-material>

- Fuentes-Cruz, G., Gildin, E., and Valkó, P. P. (2014a). Analyzing production data from hydraulically fractured wells: The concept of induced permeability field. *SPE Reserv. Eval. Eng.* 17 (02), 220–232. doi:10.2118/163843-pa

- Fuentes-Cruz, G., Gildin, E., and Valkó, P. P. (2014b). "On the analysis of production data: Practical approaches for hydraulically fractured wells in unconventional reservoirs," in *SPE hydraulic fracturing technology conference*. doi:10.2118/168608-MS

- He, Y., Xu, Y., Tang, Y., Qiao, Y., Yu, W., and Sepehrnoori, K. (2022). Multi-phase rate transient behaviors of the multi-fractured horizontal well with complex fracture networks. *J. Energy Resour. Technol.* 144 (4), 043006. doi:10.1115/1.4053247

- Hu, Y., Zhang, X., Cheng, Z., Ding, W., Qu, L., Su, P., et al. (2021). A novel radial-composite model of pressure transient analysis for multistage fracturing horizontal wells with stimulated reservoir volume. *Geofluids* 2021, 1–14. doi:10.1155/2021/6685820
- Li, Z., Wu, X., Han, G., Zhang, L., Zhao, R., and Shi, S. (2021). A semi-analytical pressure model of horizontal well with complex networks in heterogeneous reservoirs. *J. Petroleum Sci. Eng.* 202, 108511. doi:10.1016/j.petrol.2021.108511
- Liu, H., Zhao, X., Tang, X., Peng, B., Zou, J., and Zhang, X. (2020). A Discrete fracture-matrix model for pressure transient analysis in multistage fractured horizontal wells with discretely distributed natural fractures. *J. Petroleum Sci. Eng.* 192, 107275. doi:10.1016/j.petrol.2020.107275
- Prada, A., and Civan, F. (1999). Modification of Darcy's law for the threshold pressure gradient. *J. Petroleum Sci. Eng.* 22 (4), 237–240. doi:10.1016/s0920-4105(98)00083-7
- Stalgorova, E., and Mattar, L. (2012a). "Practical analytical model to simulate production of horizontal wells with branch fractures," in Paper presented at the SPE Canadian unconventional resources conference, October 30–November 1, 2012. Paper Number: SPE-162515-MS. (Society of Petroleum Engineers (SPE)). doi:10.2118/162515-MS
- Stalgorova, E., and Mattar, L. (2012b). Analytical model for unconventional multifractured composite systems. *SPE* 162516, 246–256. doi:10.2118/162516-PA
- Wang, J., Jia, A., and Wei, Y. (2016). A semi-analytical solution for multiple-trilinear-flow model with asymmetry configuration in multifractured horizontal well. *J. Nat. Gas Sci. Eng.* 30, 515–530. doi:10.1016/j.jngse.2015.12.013
- Wang, X., and Sheng, J. J. (2017). Effect of low-velocity non-Darcy flow on well production performance in shale and tight oil reservoirs. *Fuel* 190, 41–46. doi:10.1016/j.fuel.2016.11.040
- Xu, Y., Cavalcante Filho, J. S., Yu, W., and Sepehrnoori, K. (2017). Discrete-fracture modeling of complex hydraulic-fracture geometries in reservoir simulators. *SPE Reserv. Eval. Eng.* 20 (02), 403–422. doi:10.2118/183647-PA
- Zeng, B., Cheng, L., and Hao, F. (2010). "Experiment and mechanism analysis on threshold pressure gradient with different fluids," in Paper presented at the Nigeria annual international conference and exhibition, July 31–August 7, 2010. Paper Number: SPE-140678-MS. (Society of Petroleum Engineers (SPE)). doi:10.2118/140678-MS
- Zhang, Y., and Yang, D. (2021). Modeling transient pressure behaviour of a multi-fractured horizontal well in a reservoir with an arbitrary boundary and different fracture networks by considering stress-sensitive effect. *J. Hydrology* 600, 126552. doi:10.1016/j.jhydrol.2021.126552
- Zhao, Y. L., Zhang, L. H., Luo, J. X., and Zhang, B. N. (2014). Performance of fractured horizontal well with stimulated reservoir volume in unconventional gas reservoir. *J. Hydrology* 512, 447–456. doi:10.1016/j.jhydrol.2014.03.026

Glossary

Nomenclature

ϕ = porosity, fraction
 S_o = oil saturation, fraction
 S_w = water saturation, fraction
 t = time, day
 K = permeability, $10^{-3}\mu\text{m}^2$
 K_{gz} = permeability of stimulated area, $10^{-3}\mu\text{m}^2$
 K_{mf} = permeability of fracture surface, $10^{-3}\mu\text{m}^2$
 K_{ro} = oil-phase relative permeability, fraction
 K_{rw} = water-phase relative permeability, fraction
 μ_o = oil-phase viscosity, mPa·s
 μ_w = water-phase viscosity, mPa·s
 p_o = oil-phase pressure, MPa
 p_c = capillary pressure, MPa
 p_{wb} = wellface pressure, MPa
 p_{wf} = bottom hole flowing pressure, MPa
 Δp_s = additional pressure drop, MPa
 q_b = sand face flow rate, m^3/day
 q = well flow rate, m^3/day
 h = reservoir thickness, m
 C = wellbore storage coefficient, m^3/MPa
 S = skin factor

B = volume factor
 G = threshold pressure gradient, MPa/m
 C_t = comprehensive compressibility, 10^{-4} 1/MPa
 C_f = rock compressibility, 10^{-4} 1/MPa
 C_o = oil-phase compressibility, 10^{-4} 1/MPa
 C_w = water-phase compressibility, 10^{-4} 1/MPa
 λ = oil–water two-phase fluidity
 λ_o = oil-phase relative fluidity
 λ_w = water-phase relative fluidity
 v_t = total seepage velocity, m/s
 A = seepage area, m^2
 ∂ = differential operator
 V = domain
 Γ = boundary
 ∇ = Hamiltonian operator

Superscripts and subscripts

fo = oil-phase of fracture system
 fw = water-phase of fracture system
 fc = fracture capillary pressure
 $'$ = derivative
 n = previous time step



OPEN ACCESS

EDITED BY

Debin Kong,
University of Science and Technology
Beijing, China

REVIEWED BY

Hongjian Zhu,
Yanshan University, China
Yan Peng,
China University of Petroleum, Beijing,
China
Zhengdong Lei,
Research Institute of Petroleum
Exploration and Development (RIPED),
China

*CORRESPONDENCE

Hucheng Deng,
denghucheng@cdut.cn

SPECIALTY SECTION

This article was submitted to Advanced
Clean Fuel Technologies,
a section of the journal
Frontiers in Energy Research

RECEIVED 13 September 2022
ACCEPTED 29 September 2022
PUBLISHED 10 January 2023

CITATION

Li R, Deng H, Fu M, Hu L, Xie X, Zhang L
and Guo X (2023), Identification method
of thief zones in carbonate reservoirs
based on the combination of static and
dynamic data: A case study from the
Cretaceous Mishrif Formation in the H
oilfield, Iraq.
Front. Energy Res. 10:1043231.
doi: 10.3389/fenrg.2022.1043231

COPYRIGHT

© 2023 Li, Deng, Fu, Hu, Xie, Zhang and
Guo. This is an open-access article
distributed under the terms of the
[Creative Commons Attribution License
\(CC BY\)](https://creativecommons.org/licenses/by/4.0/). The use, distribution or
reproduction in other forums is
permitted, provided the original
author(s) and the copyright owner(s) are
credited and that the original
publication in this journal is cited, in
accordance with accepted academic
practice. No use, distribution or
reproduction is permitted which does
not comply with these terms.

Identification method of thief zones in carbonate reservoirs based on the combination of static and dynamic data: A case study from the Cretaceous Mishrif Formation in the H oilfield, Iraq

Ruixue Li^{1,2,3}, Hucheng Deng^{1,3*}, Meiyang Fu^{1,3}, Lanxiao Hu^{1,3},
Xinhui Xie^{1,3}, Liying Zhang¹ and Xiaobo Guo^{1,4}

¹College of Energy, Chengdu University of Technology, Chengdu, Sichuan, China, ²Engineering Research Center of Development and Management for Low to Ultra-Low Permeability Oil and Gas Reservoirs in West China, Ministry of Education, Xi'an Shiyou University, Xi'an, Shaanxi, China, ³State Key Laboratory of Oil and Gas Reservoir Geology and Exploitation (Chengdu University of Technology), Chengdu, Sichuan, China, ⁴Exploration and Development Research Institute of Daqing Oilfield Company Ltd., Daqing, Heilongjiang, China

Carbonate reservoirs usually have a strong heterogeneity. The zones with relatively high permeability will form a channel through which fluids can easily flow. These channels are called thief zones. Thief zones have notable effects on oil or gas production, for example, high oil recovery rates at the early stage of the exploitation or an early water breakthrough during the later stage of water flooding development. Therefore, it is essential to have a precise identification of thief zones in carbonate reservoirs. In this research study, a simple approach to identify thief zones based on reservoir permeability gathered from well logging is developed. The thief zones are first identified at wells based on the lower limit value of the thief-zone permeability. This value is determined based on the dynamic production data, indicating that the thief zones identified by applying this criterion can reflect the product characteristics. Then, a zonal inter-well recognition method is adopted to identify the connectivity and distributions of thief zones in the regions far away from the well. This method is applied to identify thief zones for the Cretaceous Mishrif Formation in the H oilfield, Iraq. The reliability of the identification results is tested by the well-group injection test. The distributions of thief zones in the study region are discussed. In the study region, 12 members developed thief zones, while two members (i.e., MC1-3 and MC2-2) did not develop thief zones. Specifically, there are five members having a high level of thief-zone development. They are MB1-2C, MB2-1, MB2-2, MC2-3, and MC3-2. Comparing the distribution of thief zones with that of sedimentary microfacies, it is concluded that the thief-zone development is mainly controlled by the sedimentary microfacies and tends to occur in high-energy shoals.

KEYWORDS

thief zone, production data, carbonate reservoir, Mishrif Formation, Iraq

Introduction

Carbonate reservoirs play an essential role in oil and gas recovery, especially in the Middle East and Middle Asia (Liu et al., 2016). Generally, there is a strong heterogeneity in carbonate reservoirs due to the comprehensive impacts of tectonic movement and the leaching effect (Ghafoori et al., 2009; He et al., 2014; Al-Ali et al., 2019). During oil and gas recovery, the zones with relatively high permeability will form low-resistivity seepage channels of fluids, that is, the so-called thief zones (Fu et al., 2019). Thief zones will have high oil recovery rates at the early stage of the exploitation, while they will result in an early water breakthrough and, thereby, lead to a low sweep efficiency at the later stage of water flooding development (Li et al., 2015; Kong et al., 2021). Therefore, it is crucial to identify the thief zones in carbonate reservoirs.

Many methods have been developed to identify thief zones based on analysis of various kinds of data gathered from oilfields, such as core data, well logging data, tracer test data, and production data. The core data (such as permeability, porosity, and pore throat size distribution) can be used to establish the pore structures, therefore providing the basis for the thief-zone identification (He and Hua., 1998; Liao et al., 2001; He et al., 2002). The tracer tests provide an intuitive way of the flow directions. Several researchers analyzed tracer test data to identify the thief zone and obtained relatively precise identification results (Batycky et al., 2008; Izgec and Kabir, 2009; Wang et al., 2011). However, these two methods are both expensive and lack adequate field data. Moreover, the tracer test is time-consuming.

Compared with the core and tracer test data, the well logging and production data are more abundant and can be easily obtained. Therefore, many methods have been developed based on well logging data and production data. Wang et al. (2002) identified thief zones by applying water-injection profile logging data. Al-Dhafeeri and Nasr-El-Din. (2007) adopted both the core data and production logging data to identify thief zones. Li et al. (2008) identified thief zones by using a method combining the high-resolution image logging data with the data collected from the production logging test (PLT) and nuclear magnetic resonance (NMR). Chen et al. (2008) applied the data gathered from PLTs to identify thief zones and provided the distributions of different thief-zone types. Feng et al. (2010) quantitatively identified thief zones between wells using the well test method. John et al. (2013) developed a thief-zone identification method which is a comprehensive analysis of the results obtained by distributed temperature sensing (DTS) technology, PLTs, and water flow logging (WFL). Wei et al. (2019) proposed an index to describe the relative contribution of a certain layer based on the data gathered

from PLT. One disadvantage of this kind of method is that the data collected from well logging can only describe the thief zones near well regions (Fu et al., 2019).

In this research study, a simple approach to identify thief zones based on the reservoir permeability obtained from well logging is provided. The lower limit values of the thief-zone permeability in each member are determined based on the dynamic production data. This indicates that the thief zones identified by applying this criterion can reflect the production characteristics. In this identification method, the lower limit values of the thief-zone permeability are first applied to the identified thief zones at each single well. Then, a zonal inter-well recognition method is adopted to carefully capture the connectivity and distributions of thief zones in the regions far away from the well. This identification approach is adopted to identify thief zones for the Cretaceous Mishrif Formation in the H oilfield, Iraq. The reliability of this approach is tested based on a well-group injection test. The distributions of thief zones for the Cretaceous Mishrif Formation in the H oilfield are discussed in this study.

Geological setting

Figure 1 shows the geographical location of the H oilfield. As shown in Figure 1, the H oilfield is approximately 400 km southeast of Baghdad, located in Maysan province in southeastern Iraq. This oilfield is in the foredeep belt of the Mesopotamian basin (Fouad, 2010; Fouad and Sissakian, 2011), which is a wide and gentle anticline with a length and width of about 31 km and 10 km, respectively. The long axis of this anticline is in the NW-SE trending. The H oilfield is a supergiant oilfield. In this oilfield, over 80% of the oil is produced from the limestone of the Lower Cretaceous Sadi Formation and Middle Cretaceous Mishrif Formation. The Mishrif Formation is the most important production zone in the study region with a thickness of around 400 m.

Figure 2 shows the stratigraphic column of Cretaceous in the H oilfield. Shelf carbonate developed in the H oilfield (Aqrawi et al., 1998; Wang et al., 2016). The sedimentary facies developing in most areas is an open platform, while a few areas developed the restricted platform and platform edge (Aqrawi et al., 1998; Wang et al., 2016). Based on the different sedimentary hydrodynamic conditions, the sedimentary microfacies in the study region can be divided into high-energy shoals (such as mussel clastic shoal, algal mound, and intraclastic shoal), low-energy shoals (such as bioclastic shoal and shallow open sea), non-clastic facies (such as subtidal flats and marsh), and tidal channels (Zhang et al., 2021). The Mishrif Formation belongs to the Middle Cretaceous

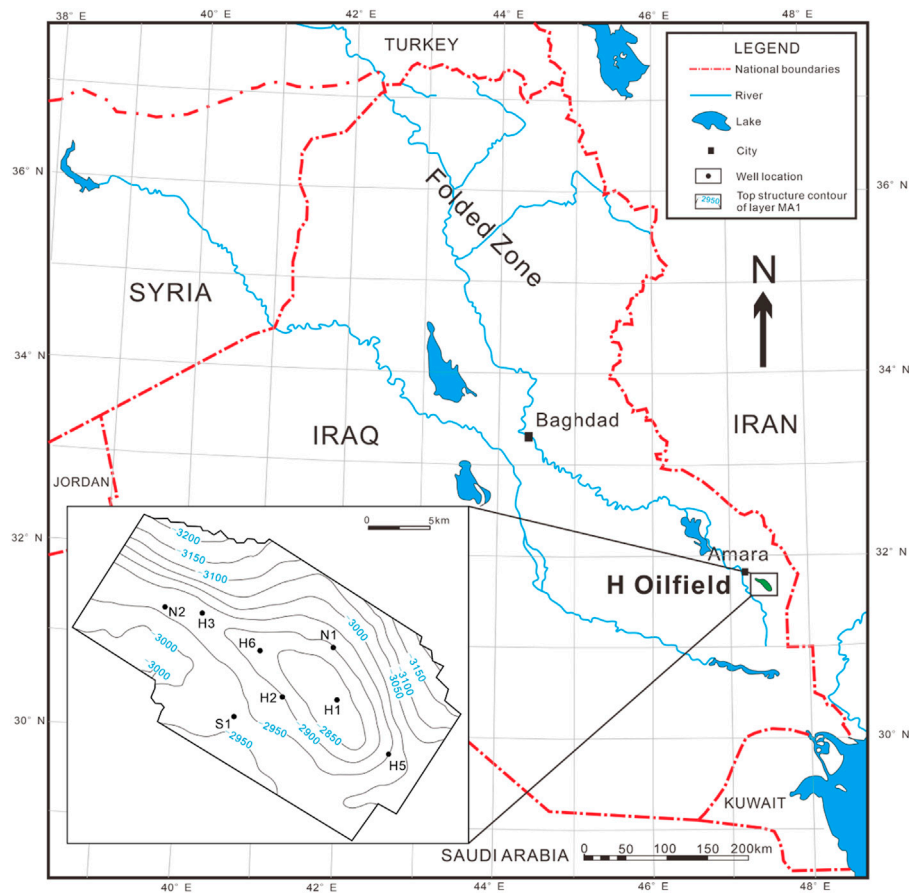


FIGURE 1
Geographical location of the H oilfield (after Fouad, 2015).

deposit. A regional unconformity forms the top of the Mishrif Formation (Wang et al., 2016; Bromhead et al., 2022). The Mishrif Formation in the H oilfield can be further subdivided into 18 members based on the characteristics of lithological variation. The members from top to bottom are MA1, MA2, MB1-1, MB1-2A, MB1-2B, MB1-2C, MB2-1, MB2-2, MB2-3, MC1-1, MC1-2, MC1-3, MC1-4, MC2-1, MC2-2, MC2-3, MC3-1, and MC3-2 (Wang, 2016). Among these members, MA1, MB1-1, MC2-1, and MC3-1 are interlayers.

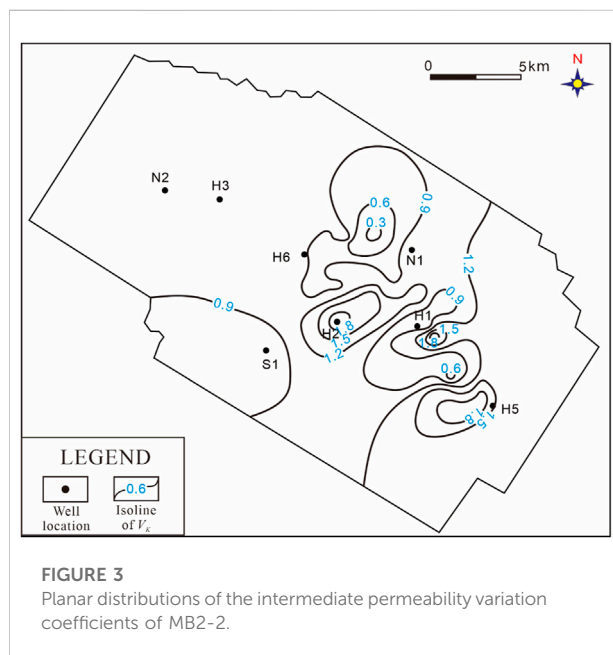
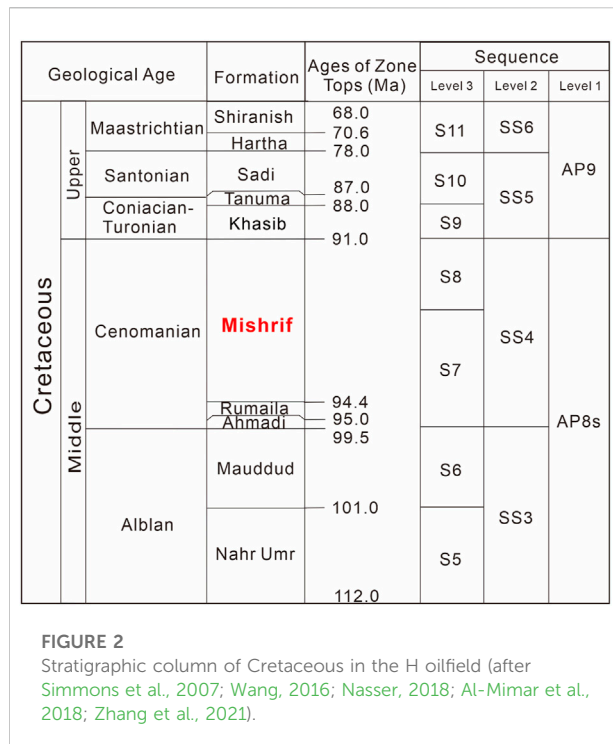
The high reservoir heterogeneity of the Mishrif Formation in the H oilfield is usually caused by the comprehensive influence of the sedimentary environment, diagenesis, tectonics, etc. (Ghafoori et al., 2009; He et al., 2014; Al-Ali et al., 2019). There are various lithofacies (with different particle types, particle contents, pore structures, and physical properties) that develop when sedimentary environments change. Sometimes, the diagenesis leads to the dissolution of unstable minerals, which increases the limestone permeability. Figure 3 shows the planar distributions of the intermediate permeability variation

coefficients of MB2-2. The permeability variation coefficients (V_k) can be calculated using the following equation.

$$V_k = \frac{\sqrt{\sum_{i=1}^n (K_i - \bar{K})^2 / n}}{\bar{K}}, \quad (1)$$

where K_i and \bar{K} represent the permeability of the i th test point and the average permeability of the study region, respectively; n represents the number of the test points. As shown in Figure 3, the variation coefficients in most regions are larger than 0.9, indicating that there is a strong intermediate heterogeneity of MB2-2 (Li et al., 2021).

The strong heterogeneity may cause the oil or the injected water to mainly flow through the zones with high permeability and, thereby, form thief zones. The existence of thief zones will lead to notable contradictions in the production data. Figure 4 shows the distribution of liquid products with the change in the cumulative thickness of the tested zones. It is to be noted that a tested zone usually corresponds to a perforated



interval. In this figure, the flow profiles of 86 zones gathered from 14 tested wells are counted. Then, these data are ranked from the smallest to the largest based on their liquid production yield per meter. We defined that the zone with low liquid production is the zone whose liquid production yield per meter is smaller than the average liquid production

yield per meter of all tested zones, while the zone with high liquid production is the zone whose liquid production yield per meter is larger than the average value. As shown in Figure 4, it can be found that the zones with low liquid production, whose cumulative thickness occupies 85.8% of the total thickness, only contribute 30.7% of the total liquid production. While the zones with high liquid production, whose cumulative thickness is only 14.2% of the total thickness, contribute 69.3% of the total liquid production. This indicates that thief zones exist in the study region and have a notable effect on oil production, making it necessary to identify thief zones in this region.

Methodology of determining the criteria of identifying thief zones

Static permeability, which can be easily obtained from well logging, is applied to identify thief zones in this study. The determination of the lower limit values of thief-zone permeability is based on the change of the oil productions of different perforated intervals. Since most wells in our study region have several perforated intervals, the production data collected from these wells are usually the total oil produced from all the perforated intervals. Hence, the layering production split should be first adopted to calculate the oil production from a single perforated interval. In our study region, there are 104 wells with conventional logs, including six cored wells. The permeability data used in this study have been corrected based on core data. The production dynamic data are available for 58 wells, while the PLT data are available for 13 wells.

Production split for multilayer production well

In this study, the production capacity of a given well is depicted by the average monthly oil production yield per meter. The formation coefficient method (KH method) (Zhao et al., 2010; Zheng et al., 2011) is applied in this study. The KH method is one of the most used production split methods in the oilfield. In this method, the oil production can be split only based on the reservoir permeability and effective thickness. First, the production split coefficient is calculated using the following equation (Zhao et al., 2010; Zheng, et al., 2011):

$$M_i = \frac{\bar{K}_i H_i}{\sum_{j=1}^m \bar{K}_j H_j} \quad (2)$$

where M_i represents the production split coefficient used in the KH method; m represents the number of layers; H_i and H_j

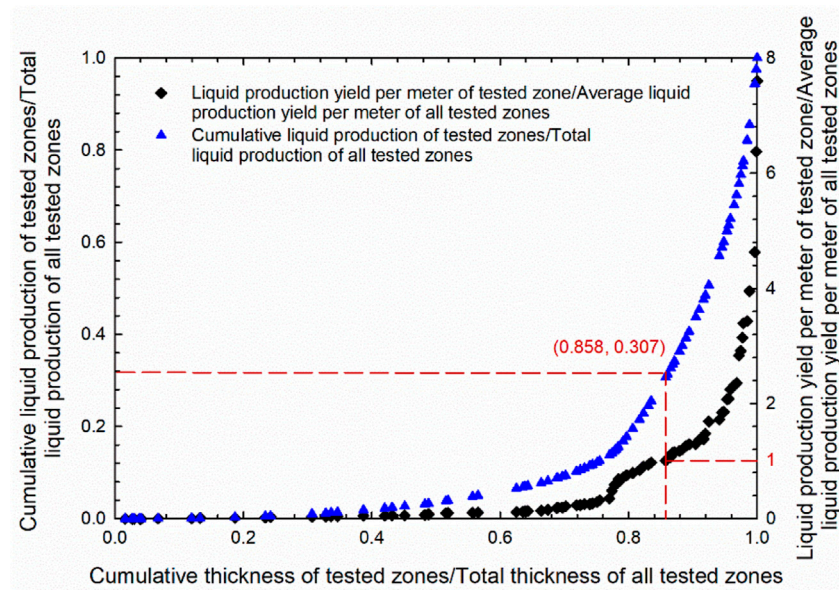


FIGURE 4

Distribution of liquid production with the change of the cumulative thickness of the tested zones (number of tested zones = 86).

represent the effective thickness of the i th layer and j th layer, respectively; \bar{K}_i and \bar{K}_j represent the average permeability of the i th layer and j th layer, respectively. It is to be noted that \bar{K}_i and \bar{K}_j are the thickness-weighted mean and can be calculated using the permeability collected from well logging. Then, the average monthly oil production yield per meter of a single layer can be calculated as follows:

$$q_{oi} = q_o M_i, \quad (3)$$

where q_o and q_{oi} represent the average monthly oil production yield per meter of a well and the i th layer, respectively. As can be seen in Eqs 2, 3, in the KH method, the oil production is split only based on the reservoir permeability and effective thickness. However, the fluid flow in the reservoir is influenced by many factors (such as permeability, relative permeability, fluid phase, pressure, and wettability). If permeability is the main controlling factor of fluid flow in our study region, the KH method can be applied in this region to roughly predict the oil production from a single layer. Therefore, to test if the KH method can be used to roughly predict the oil production from a single layer in our study region, we compared the calculated production split results with the data obtained by PLT for 13 wells. The detailed comparison results are shown by Li et al. (2021). The maximum, minimum, and average correlation coefficients for these 13 wells are 0.98, 0.60, and 0.80, respectively. This indicates that these two sets of data have a good agreement, indicating that the KH method is applicable in our study region.

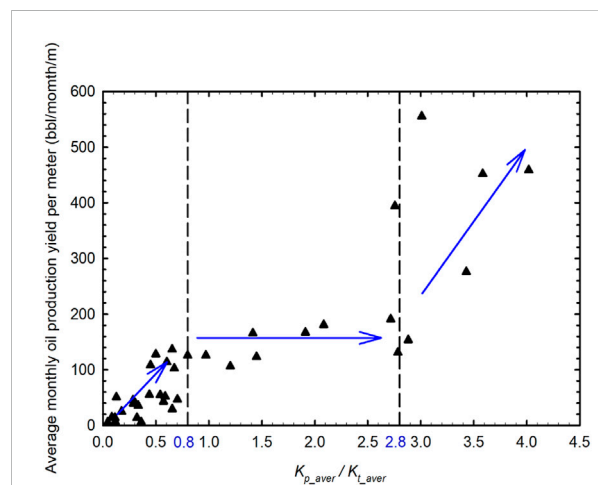


FIGURE 5

Variations of the average monthly oil production yield per meter of each perforated interval with the change of K_{p_aver}/K_{L_aver} .

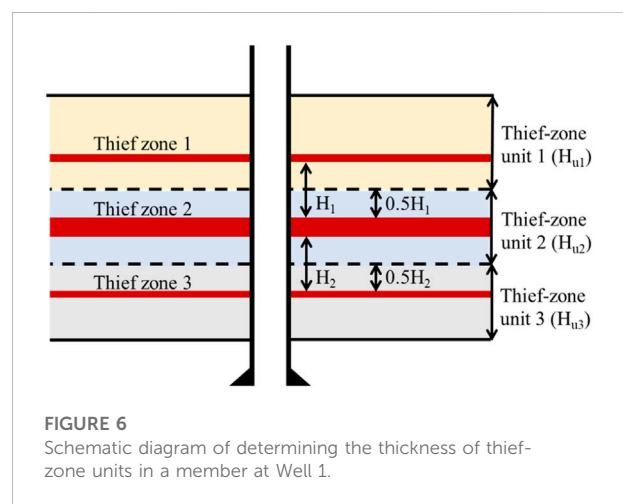
Lower limit values of thief-zone permeability

It is a prerequisite to know the lower limit values of thief-zone permeability in order to identify thief zones based on the reservoir permeability. Since there is a large discrepancy among the average permeability values of

TABLE 1 Lower limit values of the thief-zone permeability of 14 members in the Mishrif Formation (except the four interlayers).

Member	Lower limit value of the thief-zone permeability (mD)	Member	Lower limit value of the thief-zone permeability (mD)
MA2	12.29	MC1-1	287.76
MB1-2A	22.79	MC1-2	48.58
MB1-2B	20.08	MC1-3	21.28
MB1-2C	21.87	MC1-4	122.98
MB2-1	120.29	MC2-2	47.52
MB2-2	148.12	MC2-3	176.48
MB2-3	348.71	MC3-2	172.20

different members, the lower limit values of thief-zone permeability in each member should be different. In this study, different lower limit values of thief-zone permeability are provided for different members, which are determined based on the average permeability values of the corresponding members. Figure 5 shows the variations of the average monthly oil production yield per meter of each perforated interval with the change of the average permeability of the corresponding perforated interval (K_{p_aver}) dividing the average permeability of all the perforated intervals (K_{t_aver}). It is to be noted that the average monthly oil production yield per meter of each perforated interval is calculated by the KH method as previously mentioned. This parameter represents the oil production capability of each interval, while K_{p_aver}/K_{t_aver} represents the permeability heterogeneity among different intervals. The static and dynamic data gathered from 13 wells in the H oilfield are adopted to generate this figure. As can be seen in Figure 5, in low-permeability intervals ($K_{p_aver}/K_{t_aver} < 0.8$), the permeability controls the oil production capacity. Therefore, the oil production increases as K_{p_aver}/K_{t_aver} increases. As permeability increases ($0.8 \leq K_{p_aver}/K_{t_aver} \leq 2.8$), oil can easily pass through the reservoir, thereby leading to a reduced influence of permeability on oil production capacity. In this region, the oil production does not have an obvious increasing tendency as K_{p_aver}/K_{t_aver} increases. However, when $K_{p_aver}/K_{t_aver} < 2.8$, the permeability again controls the oil production, resulting in a rapid increase in the oil production as the value of K_{p_aver}/K_{t_aver} increases. Based on the relationship between the oil production capacity of an interval and permeability heterogeneity among different intervals, the lower limit value of the thief-zone permeability is defined as 2.8 times the average permeability of its corresponding member. Table 1 lists the lower limit values of the thief-zone permeability of 14 members in the Mishrif Formation (except the four interlayers).



Identification and verification of thief zones

Identification of thief zones

The identification of thief zones can be divided into three procedures. First, based on the lower limit values of the thief-zone permeability of the 14 members, the true vertical depth (TVD) and thickness of thief zones in all the 14 members can be recognized at a given well based on the well logging data. In this research study, thief zones are identified at 104 wells in the H oilfield. Second, TVDs and the thickness of thief zones among neighboring wells are compared to determine the connectivity of thief zones. Lastly, the planar distributions of thief zones in each member can be generated. Since there may be several disconnected thief zones with different TVDs at a well in the same member, it is required to divide a member into several units with different TVDs. The planar distributions of thief zones should be separately generated for each thief-zone unit.

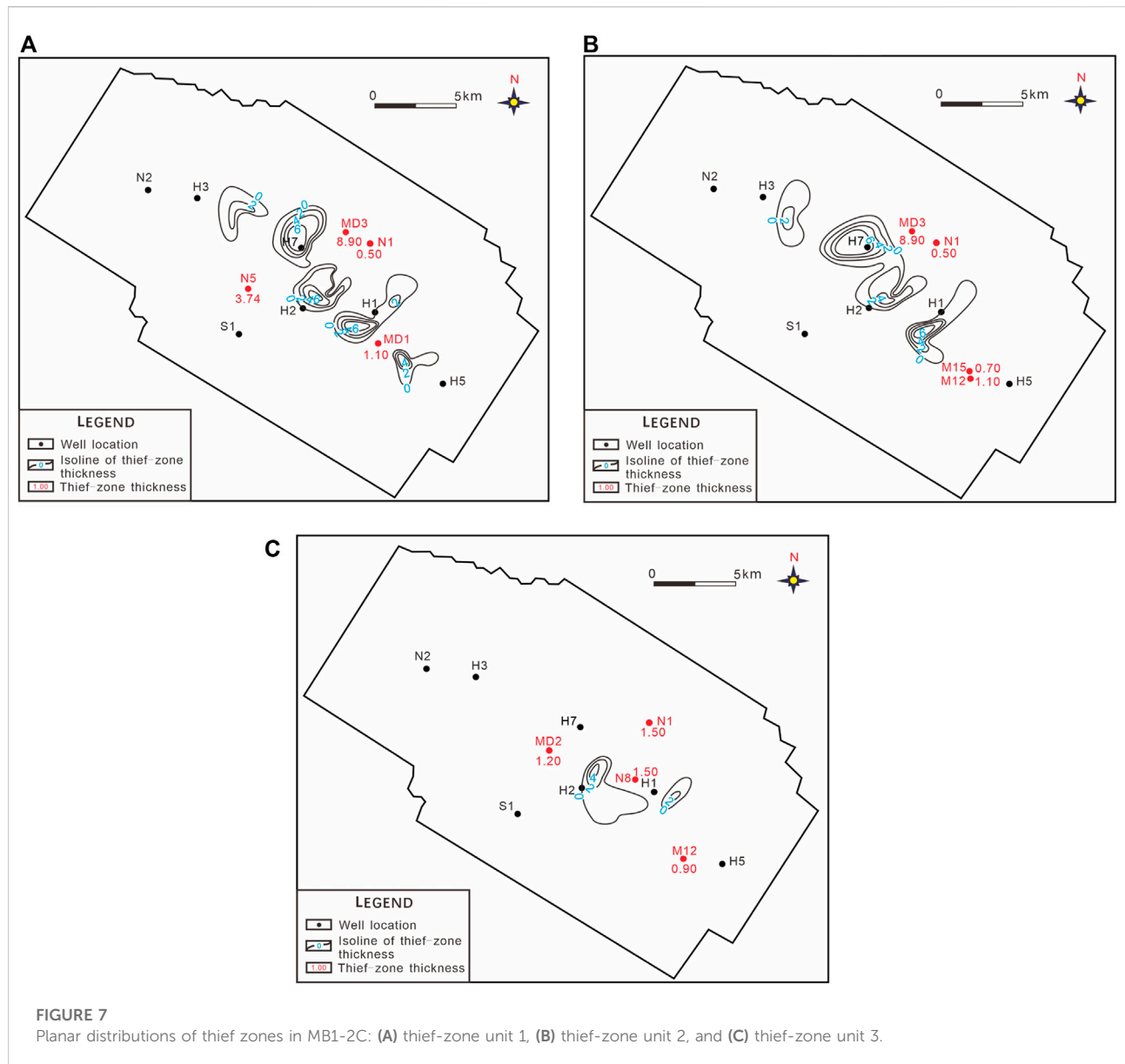
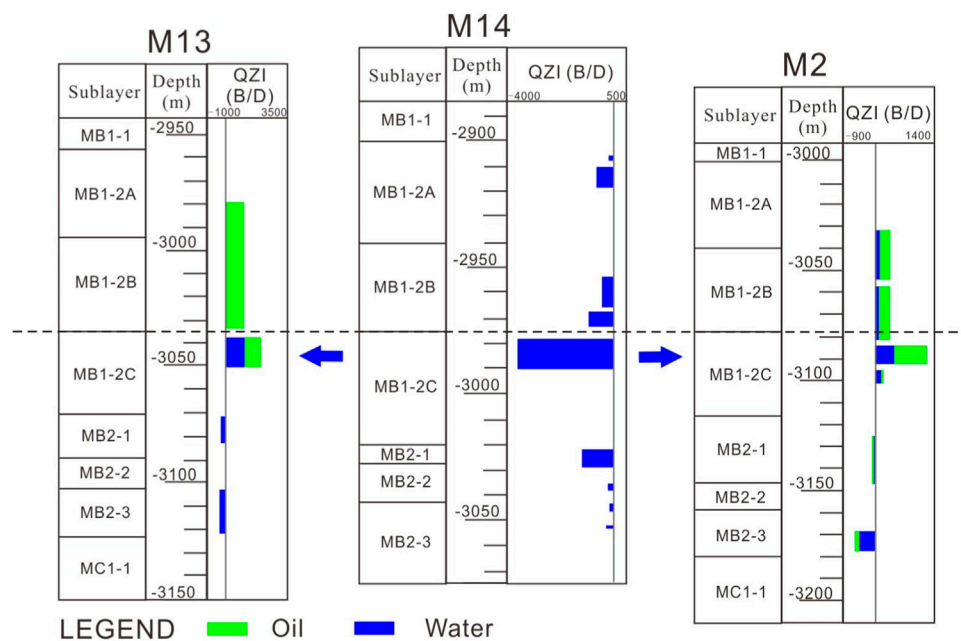


FIGURE 7

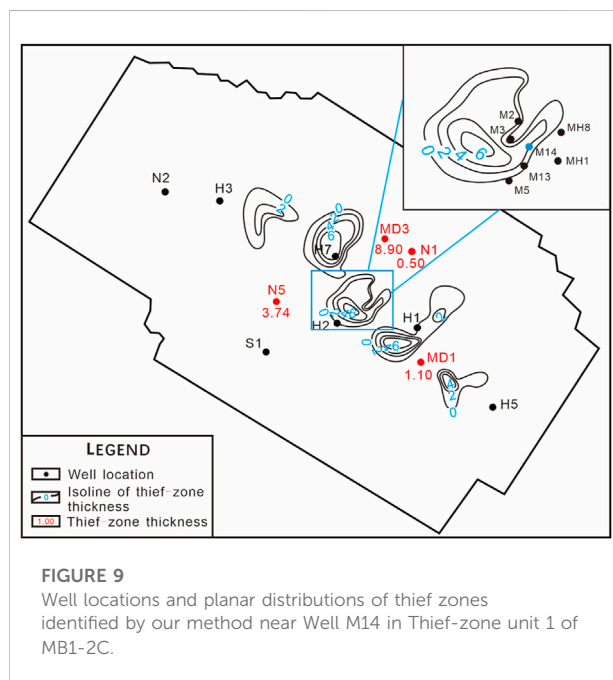
Planar distributions of thief zones in MB1-2C: (A) thief-zone unit 1, (B) thief-zone unit 2, and (C) thief-zone unit 3.

The member MB1-2C is taken as an example to show the detailed method of determining the TVDs of each thief-zone unit. First, we obtained the largest number of thief zones among all 104 wells, which is three. Figure 6 shows the schematic diagram of determining the thickness of thief-zone units in MB1-2C at the well which has the largest number of thief zones (named Well 1). As shown in Figure 6, the zone between two thief zones is evenly divided into two parts, which separately belong to two neighboring thief-zone units. The thief-zone units in a member are numbered from top to bottom. For other wells, the thickness of the three thief-zone units will be the total thickness of MB1-2C multiplied by the proportions of the thickness of the three thief-zone units at Well 1.

Figure 7 shows the planar distributions of thief zones in MB1-2C. As shown in Figure 7, there are overlaps of the thief zones in different thief-zone units at the same well location. Therefore, it is necessary to divide the member into several thief-zone units in order to clearly characterize the planar distributions of thief zones. Figure 7 mainly describes the large-scale thief zones, which cover three or more wells. The thief zones which cover less than three wells, that is, the small-scale thief zones or thief zones without enough wells to determine their boundaries, are marked with red points and their thickness at each well instead of providing their boundaries. The small-scale thief zones are regarded as having less effect on oil production, while the description of thief zones without enough wells to determine their boundaries can be completed when more information is collected.

**FIGURE 8**

Downhole flow profile at wells M2 and M13 after injecting water from Well M14 (note: QZI represents the downhole zonal inflow rate).

**FIGURE 9**

Well locations and planar distributions of thief zones identified by our method near Well M14 in Thief-zone unit 1 of MB1-2C.

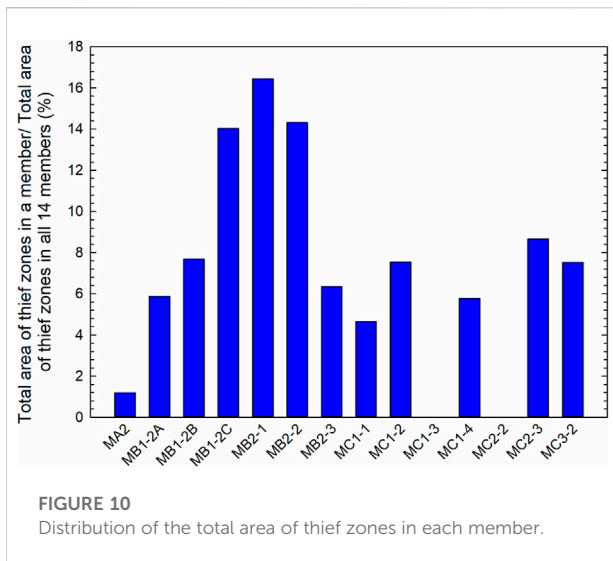
the newly developed criteria. In the well-group injection test, water is injected from Well M14. The downhole flow profiles and salinity of the neighboring six wells (i.e., M2, M3, M5, M13, MH1, and MH8) are monitored. The test results show that the water first appears at wells M13 and M2 within three and six months, respectively. Figure 8 shows the downhole flow profile at wells M13 and M2 after injecting water from Well M14. The salinity test shows that the water produced from wells M13 and M2 is indeed from the injected Well M14. As shown in this figure, the water first appears in MB1-2C at these two wells. This indicates that there are connected thief zones in MB1-2C between wells M14 and M13 and between wells M14 and M2. Whereas there is no thief zone between Well M14 and the other four wells in MB1-2C. Based on the TVDs of the water-breaking zone, this thief zone belongs to the Thief-zone unit 1 in MB1-2C. Figure 9 provides the well locations and planar distributions of thief zones identified by our method near Well M14 in Thief-zone unit 1 of MB1-2C. As shown in Figure 9, there is a thief zone among wells M2, M13, and M14. Meanwhile, there is no thief zone between Well M14 and the other four wells. This demonstrates that the developed criteria for identifying thief zones are reliable.

Verification of thief zones

The results obtained by the well-group injection test are adopted to verify the reliability of the thief zones identified by

Results and discussion

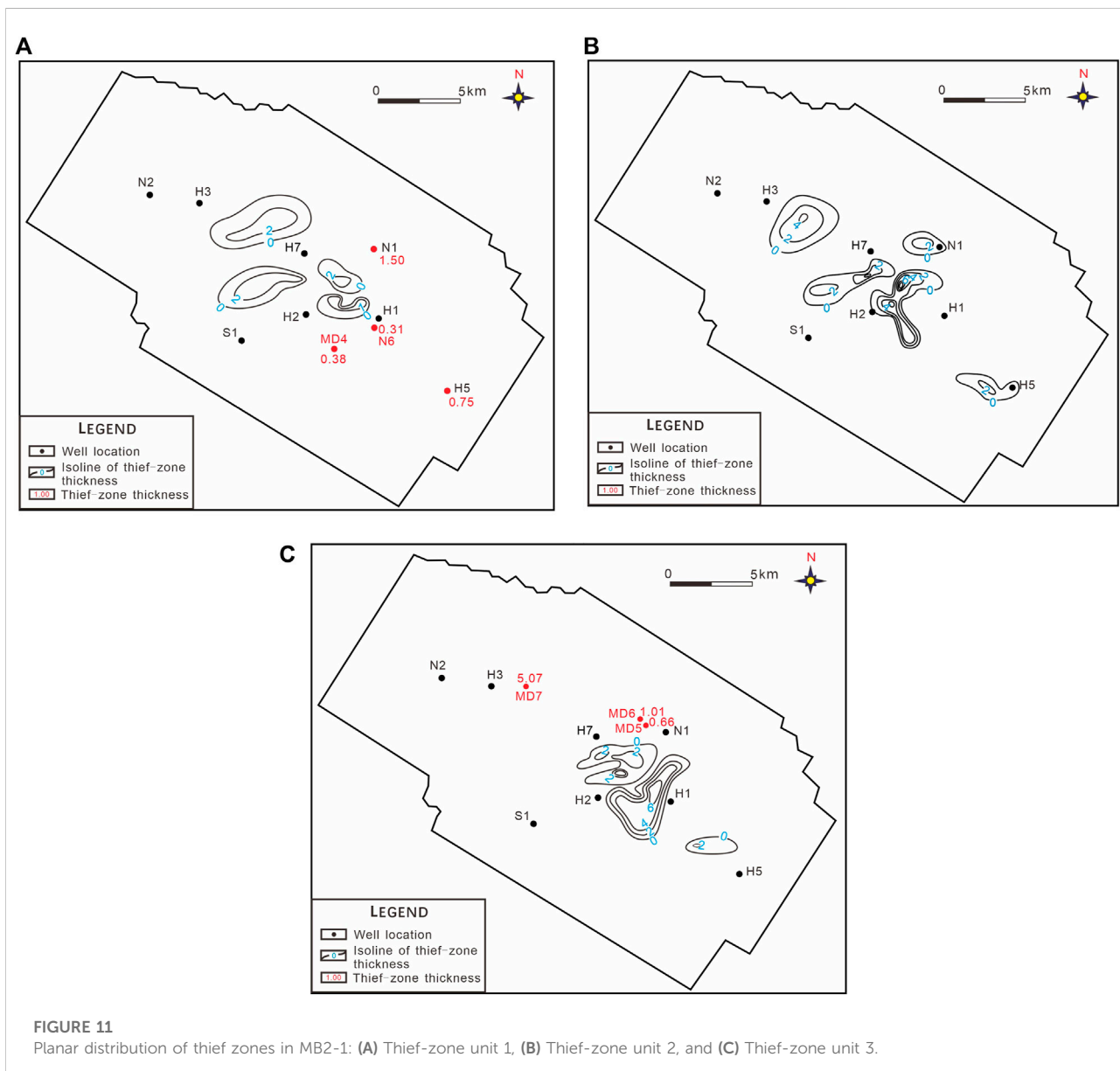
As mentioned in Section 4, the planar distributions of thief zones in 14 members are generated. The thickness of thief zones

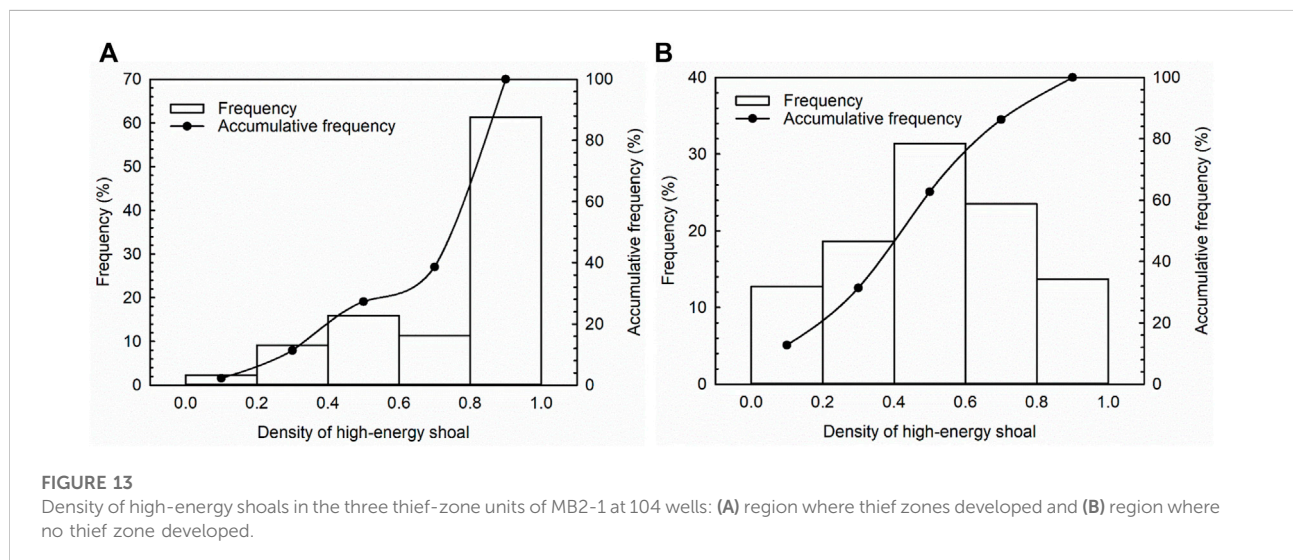
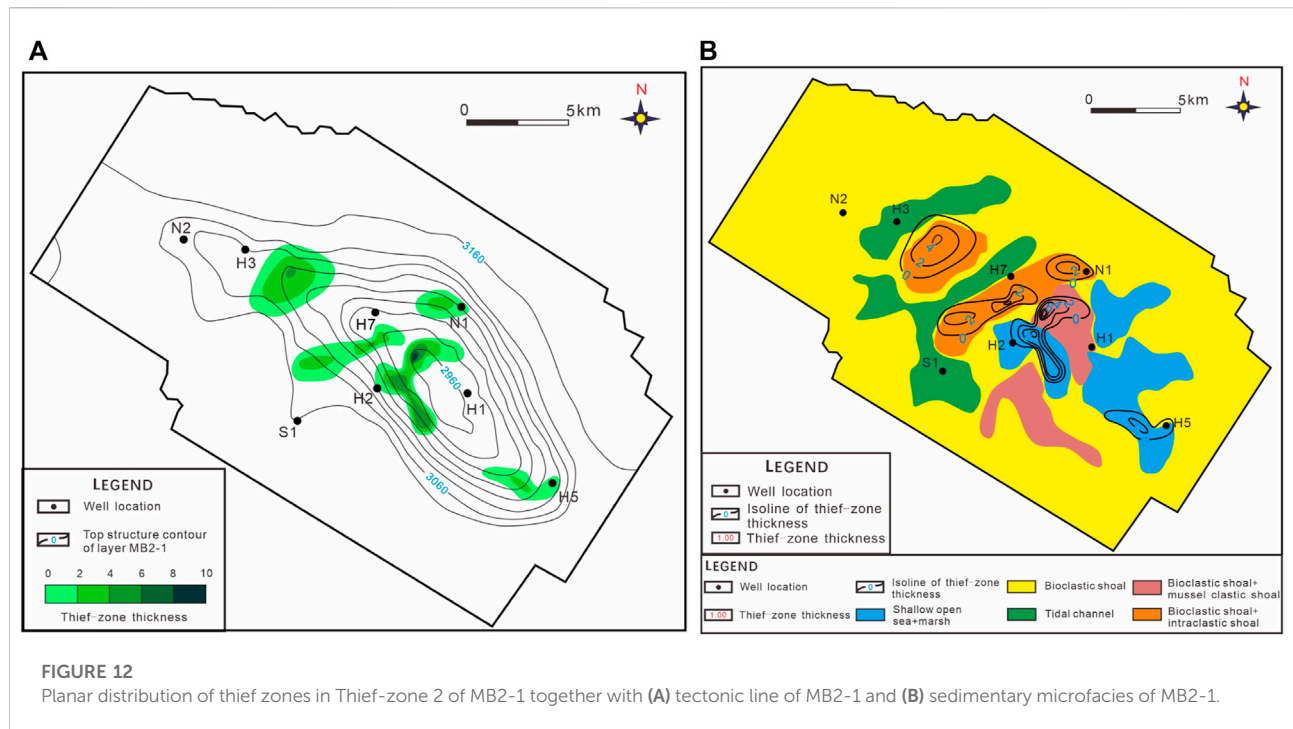


varies a lot, with the largest value of 18.2 m at the tested wells. The thickness of thief zones mainly falls in the range of 1 m–8 m, which is relatively thin compared with the thickness of a member. The vertical distributions, planar distributions, and connectivity of thief zones for the Mishrif Formation in the H oilfield are discussed in this section.

Vertical distributions of thief zones

Figure 10 depicts the distribution of the total area of thief zones in each member. It is to be noted that the total area of thief zones is the summation of the area inside the zero isoline of thief zone thickness. As shown in Figure 10, thief zones developed in 12 members, especially in MB1-2C, MB2-1, and MB2-2. While no thief zone developed in MC1-3 and MC2-2. Comparing with the distributions of sedimentary microfacies in these members, it





can be found that thief zones tended to appear in the members developed in high-energy shoals, while the two members with no thief zone mainly developed shallow open sea and subtidal flats. This demonstrated that the distributions of sedimentary microfacies have a notable effect on the development of thief zones.

Planar distributions of thief zones

Figure 11 shows the planar distribution of thief zones in MB2-1. As shown in Figures 7, 11, the thief zones mainly developed in the center of the study region and extended along the short axis. Figures 12A,B show the planar

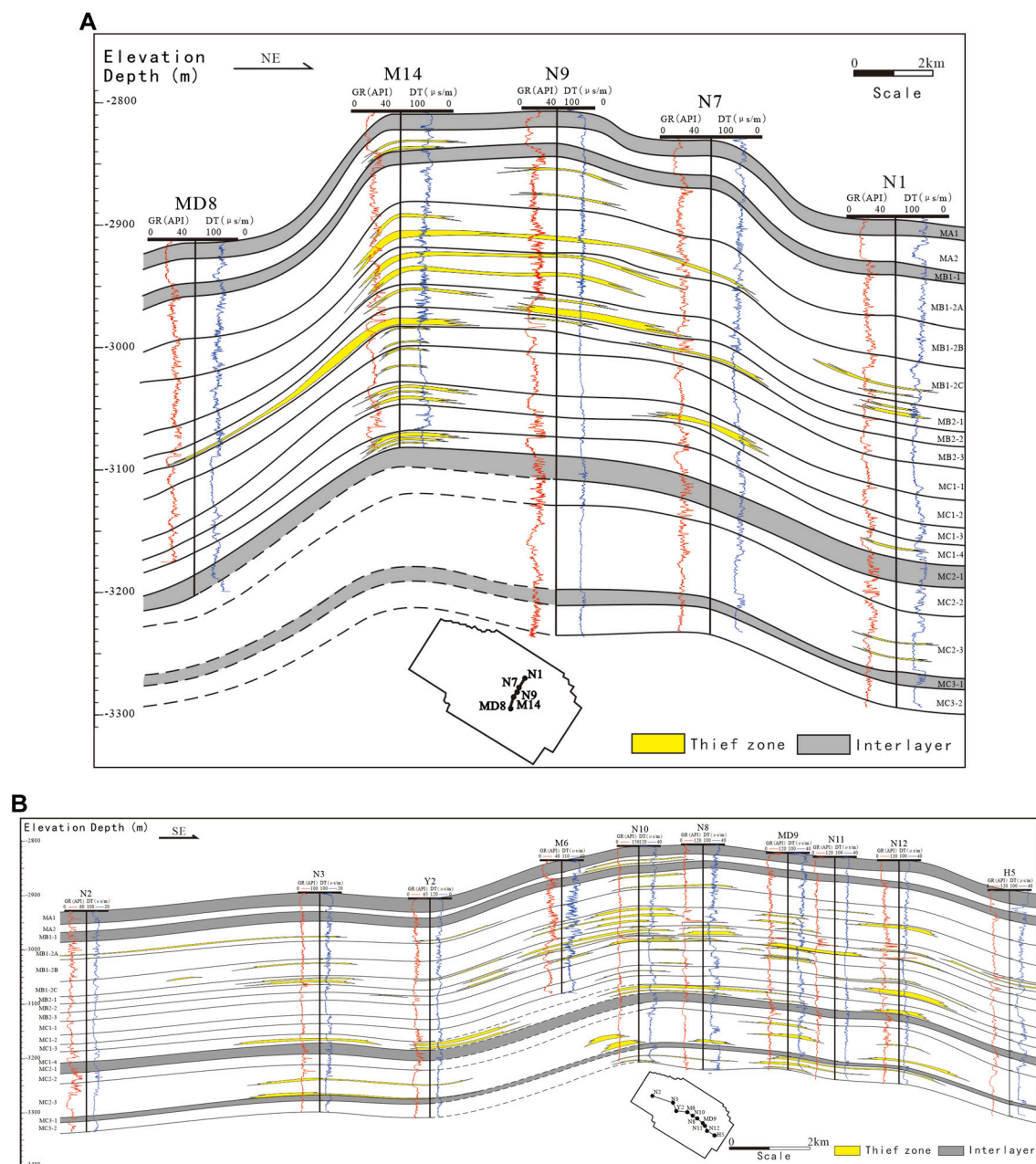


FIGURE 14

Well profile with the description of thief zones: (A) along the short axis (SW-NE trending) and (B) along the long axis (NW-SE trending).

distribution of thief zones in Thief-zone 2 of MB2-1 together with the tectonic line of MB2-1 and the planar distributions of sedimentary microfacies of MB2-1. As shown in these two figures, it can be concluded that the distributions of sedimentary microfacies have great contributions to the development of thief zones, while tectonism has less effect on the development of thief zones. Moreover, most of the thief zones developed in the high-energy shoals, such as algal mound, mussel clastic shoal, and intraclastic shoal.

Since the sedimentary microfacies shown in Figure 13 is the dominant sedimentary microfacies in MB2-1, it may show discrepancies when describing the distribution of the high-energy shoals in the three thief-zone units of MB2-1. Hence, the density of high-energy shoal in the three thief-zone units of MB2-1 at 104 wells can be calculated. The density of a high-energy shoal is defined by the following equation:

$$\text{High-energy shoal density} = \frac{\text{Total thickness of high-energy shoal in a given thief-zone unit}}{\text{Total thickness of the given thief-zone unit}} \quad (4)$$

As can be seen in this equation, the values of the density of high-energy shoal fall in the range of 0–1. As the thickness of the high-energy shoal increases, the density of the high-energy shoal increases. Figure 13 summarizes the density of high-energy shoals in the three thief-zone units of MB2-1 at 104 wells. Figures 13A,B show the density of high-energy shoals in the regions where thief zones developed and where no thief zone developed, respectively. As can be seen in these figures, 61.4% of the density of high-energy shoals is larger than 0.8 in the region where thief zones developed, while 86.3% of the density of high-energy shoals is smaller than 0.8 in the region where no thief zone developed. This indicates that the thief zones tended to develop in the region where high-energy shoals developed.

Description of the connectivity of thief zones

Figures 14A,B describe the well profile with the description of thief zones along the short axis (SW-NE trending) and the long axis (NW-SE trending), respectively. As shown in Figure 14A, thief zones have good connectivity in MB1-2B, MB1-2C, and MB2-1. The thief zones with good connectivity mainly developed in the center of the oilfield, while several small-scale thief zones developed at the edge of the oilfield. In Figure 14B, it can be found that thief zones in MB1-2B, MB1-2C, MB2-1, MC1-4, and MC2-3 have relatively good connectivity. Moreover, thief zones in the SE region have a better connectivity than those in the NW region.

Conclusion

In this research study, a simple approach to identify thief zones based on reservoir permeability obtained from well logging is developed. The lower limit values of the thief-zone permeability in each member are determined based on the dynamic production data, indicating that the thief zones identified by applying this criterion can reflect the production characteristics. After identifying the thief zones in each single well based on the newly developed criterion, the connectivity and distributions of thief zones in the regions far away from the well can be determined. To do this, a zonal inter-well recognition method is adopted in this research. This method is applied to identify thief zones for the Cretaceous Mishrif Formation in the H oilfield, Iraq. The results of the tracer test prove that this identification method is reliable. The distributions of thief zones for the Cretaceous Mishrif Formation in the H oilfield are discussed in this study. There are 12 members that develop thief zones, while two members (i.e., MC1-3 and MC2-2) do not develop thief zones. There are five members who have a high level of thief-zone development. They are MB1-2C, MB2-1, MB2-2, MC2-3, and MC3-2. The thief zones with good connectivity mainly developed in the center of the oilfield. Thief zones in the SE region have a better

connectivity than those in the NW region. Moreover, the thief-zone development is mainly controlled by the sedimentary microfacies. Thief zones tend to develop in high-energy shoals.

Data availability statement

The original contributions presented in the study are included in the article/Supplementary Material; further inquiries can be directed to the corresponding author.

Author contributions

RL: Methodology, funding acquisition, and writing—original draft; HD: Conceptualization, supervision, and funding acquisition; MF: Supervision; LH: Writing—review and editing; XX: Investigation; LZ: Validation; XG: Resources.

Funding

This study was supported by the project from the Exploration and Development Research Institute of Daqing Oilfield Company Ltd. (China) (Grant No. DQYT-1201002-2019-JS-71). The authors are grateful for the Open Fund of Engineering Research Center of Development and Management for Low to Ultra-Low Permeability Oil and Gas Reservoirs in West China, Ministry of Education, Xi'an Shiyou University to the first author (RL) (Grant No. KFJJ-XB-2020-2).

Conflict of interest

XG was employed by Exploration and Development Research Institute of Daqing Oilfield Company Ltd.

The remaining authors declare that the research was conducted in the absence of any commercial or financial relationships that could be construed as a potential conflict of interest.

The authors declare that this study received funding from Exploration and Development Research Institute of Daqing Oilfield Company Ltd. The funder had the following involvement in the study: collection of partial data.

Publisher's note

All claims expressed in this article are solely those of the authors and do not necessarily represent those of their affiliated organizations, or those of the publisher, the editors, and the reviewers. Any product that may be evaluated in this article, or claim that may be made by its manufacturer, is not guaranteed or endorsed by the publisher.

References

- Al-Ali, A., Stephen, K., and Shams, A. (2019). "Improved carbonate reservoir characterization: A case study from a supergiant field in southern of Iraq," in SPE Middle East Oil and Gas Show and Conference, Manama, Bahrain, 18–21 March.
- Al-Dhafeeri, A. M., and Nasr-El-Din, H. A. (2007). Characteristics of high-permeability zones using core analysis, and production logging data. *J. Pet. Sci. Eng.* 55, 18–36. doi:10.1016/j.petrol.2006.04.019
- Al-Mimar, H. S., Awadh, S. M., Al-Yaseri, A. A., and Yaseen, Z. M. (2018). Sedimentary units-layering system and depositional model of the carbonate Mishrif reservoir in Rumaila oilfield, Southern Iraq. *Model. Earth. Syst. Env.* 4, 1449–1465.
- Aqrabi, A. A. M., Thehni, G. A., Sherwani, G. H., and Kareem, B. M. A. (1998). Mid-Cretaceous rudist-bearing carbonates of the Mishrif formation: An important reservoir sequence in the mesopotamian basin, Iraq. *J. Pet. Geol.* 21 (1), 57–82. doi:10.1111/j.1747-5457.1998.tb00646.x
- Batycky, R. P., Thiele, M. R., Baker, R. O., and Chung, S. (2008). Revisiting reservoir flood-surveillance methods using streamlines. *SPE Reserv. Eval. Eng.* 11, 387–394. doi:10.2118/95402-pa
- Bromhead, A., van Buchem, F. S., Simmons, M. D., and Davies, R. B. (2022). Sequence stratigraphy, palaeogeography and petroleum plays of the cenomanian – turonian succession of the arabian plate: AN updated synthesis. *J. Petroleum Geol.* 45 (2), 119–161. doi:10.1111/jpg.12810
- Chen, Q., Gerritsen, M. Q., and Kovscek, A. R. (2008). Effects of reservoir heterogeneities on the steam assisted gravity drainage process. *SPE Reserv. Eval. Eng.* 11, 921–932. doi:10.2118/109873-pa
- Feng, Q., Wang, S., Gao, G. Q., and Li, C. Y. (2010). A new approach to thief zone identification based on interference test. *J. Pet. Sci. Eng.* 75, 13–18. doi:10.1016/j.petrol.2010.10.005
- Fouad, S. F., and Sissakian, V. K. (2011). Tectonic and structural evolution of the mesopotamia plain. *Iraqi Bull. Geol. Min.* 4, 33–46.
- Fouad, S. F. (2010). Tectonic and structural evolution of the mesopotamia foredeep, Iraq. *Iraqi Bull. Geol. Min.* 6 (2), 41–53.
- Fouad, S. F. (2015). Tectonic map of Iraq, scale 1: 1000 000, 2012. *Iraqi Bull. Geol. Min.* 11 (1), 1–7.
- Fu, C., Guo, T., Liu, C., Wang, Y., and Huang, B. (2019). Identification of the thief zone using a support vector machine method. *Processes* 7 (6), 373. doi:10.3390/pr7060373
- Ghafoori, M. R., Roostaiean, M., and Sajjadian, V. A. (2009). Secondary porosity: A key parameter controlling the hydrocarbon production in heterogeneous carbonate reservoirs (case study). *Petrophysics* 50 (1), 67–78.
- He, C. Z., and Hua, M. Q. (1998). Fractal geometry description of reservoir pore structure. *Oil Gas. Geol.* 1, 17–25.
- He, L., Zhao, L., Li, J., Ma, J., Lui, R., Wang, S., et al. (2014). Complex relationship between porosity and permeability of carbonate reservoirs and its controlling factors: A case study of platform facies in pre-caspian basin. *Petroleum Explor. Dev.* 41 (2), 225–234. doi:10.1016/s1876-3804(14)60026-4
- He, Y., Yang, C. M., Ying, J., and Yan, J. H. (2002). A new method for measuring the quantitative pore throat volume. *J. Southwest Pet. Inst.* 3, 5–7.
- Izgec, B., and Kabir, S. (2009). Identification and characterization of high-conductive layers in waterfloods. *SPE Reserv. Eval. Eng.* 14, 113–119. doi:10.2118/123930-pa
- John, D., Hans, V. D., Maersk, O., and Arve, O. N. (2013). "Interwell communication as a means to detect a thief zone using DTS in a Danish Offshore well," in Proceedings of the SPE Offshore Technology Conference, Houston, TX, USA, 6–9 May.
- Kong, D., Lian, P., Zheng, R., and Li, Y. (2021). Performance demonstration of gas-assisted gravity drainage in a heterogeneous reservoir using a 3D scaled model. *RSC Adv.* 11, 30610–30622. doi:10.1039/d1ra03859a
- Li, G. J., Liang, J., and Li, W. (2008). A study on the method to identify large pore paths using well logging data. *Oil Gas. Field Surf. Eng.* 9, 11–12.
- Li, D., Yang, J., and Lu, D. (2015). Thief zone identification based on transient pressure analysis: A field case study. *J. Pet. Explor. Prod. Te.* 6 (1), 63–72. doi:10.1007/s13202-015-0168-8
- Li, R., Chen, Q., Deng, H., Fu, M., Hu, L., Xie, X., et al. (2021). Quantitative evaluation of the carbonate reservoir heterogeneity based on production dynamic data: A case study from cretaceous Mishrif Formation in halfaya oilfield, Iraq. *J. Pet. Sci. Eng.* 206, 109007. doi:10.1016/j.petrol.2021.109007
- Liao, M. G., Li, S. L., and Tan, D. H. (2001). Relationship between permeability and mercury injection parameters curve for sandstone reservoir. *J. Southwest Pet. Inst.* 4, 5–8.
- Liu, L., Zheng, X., He, E., Liu, F., and Luo, H. (2016). "Findings and challenges of high permeability zone on water injection pilots in Iraqi carbonate reservoirs," in Abu Dhabi International Petroleum Exhibition & Conference, Abu Dhabi, UAE, 7–10 November (Society of Petroleum Engineers).
- Nasser, M. E. (2018). Stratigraphic sequence and basin development of the Mishrif Formation in selected oil fields in the Mesopotamian zone, Southeastern Iraq. *IJAERS* 5, 45–53. doi:10.22161/ijaers.5.5.6
- Simmons, M. D., Sharland, P. R., Casey, D. M., Davies, R. B., and Sutcliffe, O. E. (2007). Arabian Plate sequence stratigraphy: Potential implications for global chronostratigraphy. *GeoArabia* 12 (4), 101–130. doi:10.2113/geoarabia1204101
- Wang, J., Guo, R., Zhao, L., Li, W., Zhou, W., and Duan, T. (2016). Geological features of grain bank reservoirs and the main controlling factors: A case study on cretaceous Mishrif formation, H oilfield, Iraq. *Pet. Explor. Dev.* 43 (03), 367–377.
- Wang, X., Xia, Z. J., Zhang, H. W., Liu, X. P., Li, X. Q., and Zhang, L. J. (2002). Using injection profile log data to distinguish macropore formation. *Well Logging Technol.* 26, 162–164.
- Wang, Y. (2016). *Carbonate reservoir genesis and distribution of cretaceous Mishrif formation in halfaya oil field Iraq*. China, Sichuan: Chengdu University of Technology.
- Wang, Y. Q., Chen, F. H., Gu, H. J., Zhou, H. Z., Nie, Z. R., Liu, F. K., et al. (2011). Using tracer to study interwell water flow predominant channel. *Xinjiang Pet. Geol.* 32, 512–514.
- Wei, C., Zheng, J., Ouyang, X., Ding, Y., Ding, M., Lin, S., et al. (2019). "Thief zone characterization and its impact on well performance based on surveillance data, experimental data and theoretical analysis for a carbonate reservoir," in SPE Reservoir Characterization and Simulation Conference and Exhibition, Abu Dhabi, UAE, 17–19 September.
- Zhang, L., Li, R., Deng, H., Fu, M., Hu, L., Guo, X., et al. (2021). Identification, distribution characteristics, and effects on production of interlayers in carbonate reservoirs: A case study from the cretaceous Mishrif formation in halfaya oilfield, Iraq. *J. Pet. Sci. Eng.* 202, 108571. doi:10.1016/j.petrol.2021.108571
- Zhao, J., Zhang, S., and Qi, C. (2010). The methods of split and using these methods with an example. *Inn. Mong. Petrochem. Ind.* 3, 29–31.
- Zheng, A. L., Liu, D. H., and Shao, Y. L. (2011). Oil sand potential and development measures for complex fault-block reservoir. *Special Oil Gas Reservoirs* 18 (1), 93–95.

Nomenclature

H_i effective thickness of the i th layer

H_j effective thickness of the j th layer

K_i permeability of the i th test point

\bar{K} average permeability of the study region

\bar{K}_i average permeability of the i th layer

\bar{K}_j average permeability of the j th layer

K_{p_aver} average permeability of the corresponding perforated interval

K_{t_aver} average permeability of all the perforated intervals

m number of layers

M_i production split coefficient used in the KH method

q_o unit oil production of a well

q_{oi} unit oil production of the i th layer



OPEN ACCESS

EDITED BY

Jiafei Zhao,
Dalian University of Technology, China

REVIEWED BY

Qingyang Lin,
Zhejiang University, China
Jinze Xu,
University of Calgary, Canada

*CORRESPONDENCE

Xiukun Wang,
xiukunwang@cup.edu.cn

SPECIALTY SECTION

This article was submitted to Advanced
Clean Fuel Technologies,
a section of the journal
Frontiers in Energy Research

RECEIVED 26 September 2022

ACCEPTED 07 November 2022

PUBLISHED 17 January 2023

CITATION

Mu C, Hua H and Wang X (2023),
Characterization of pore structure and
reservoir properties of tight sandstone
with CTS, SEM, and HPMI: A case study
of the tight oil reservoir in fuyu oil layers
of Sanzhao Sag, Songliao basin,
NE China.

Front. Energy Res. 10:1053919.
doi: 10.3389/fenrg.2022.1053919

COPYRIGHT

© 2023 Mu, Hua and Wang. This is an
open-access article distributed under
the terms of the [Creative Commons
Attribution License \(CC BY\)](#). The use,
distribution or reproduction in other
forums is permitted, provided the
original author(s) and the copyright
owner(s) are credited and that the
original publication in this journal is
cited, in accordance with accepted
academic practice. No use, distribution
or reproduction is permitted which does
not comply with these terms.

Characterization of pore structure and reservoir properties of tight sandstone with CTS, SEM, and HPMI: A case study of the tight oil reservoir in fuyu oil layers of Sanzhao Sag, Songliao basin, NE China

Changhe Mu¹, Haojie Hua² and Xiukun Wang^{2*}

¹Exploration Utility Department of CNPC Daqing Oilfield Co., Ltd., Daqing, Heilongjiang, China, ²State Key Laboratory of Petroleum Resources and Prospecting, China University of Petroleum, Beijing, China

Quantitative characterization of the pore throat structures and reservoir properties of the tight sandstone in Fuyu oil layers of Sanzhao Sag, Songliao Basin, NE China was carried out using cast thin section (CTS), scanning electron microscopy (SEM) and high-pressure mercury intrusion (HPMI) combined with fractal theory. cast thin section and scanning electron microscopy describe the composition, pore filling, cementation, and connectivity of tight sandstones. Six different fractal models, i.e. 2D capillary model, 3D spherical model, 3D capillary model, geometric model, thermodynamic model, and wetting phase model are used to calculate the fractal dimension of pore size distribution using capillary pressure data of high-pressure mercury intrusion, and their correlations with reservoir properties were analyzed. The images of CTS and SEM show that the main lithology of this oil reservoir is tight sandstone, and the pore types are mainly intergranular dissolved pores and intragranular dissolved pores, with uneven pore distribution and poor connectivity. The study of the HPMI data shows that the throat sorting coefficient is the main influencing factor of tight sandstone permeability. The fractal dimensions calculated from the HPMI capillary pressure data using the 3D capillary model and the wetting phase fractal model have the strongest correlations with the reservoir properties compared with the other fractal model. As the fractal dimension increases, the pore throat structures become more heterogeneous and reservoir properties become poorer. For the wetting phase fractal model, the calculated fractal dimension is positively correlated with the heterogeneity of the pore throat structure of tight sandstone, which is contrary to the fractal theory and is not suitable for analyzing pore throat structures. The fractal dimensions calculated from the thermodynamic model have no obvious correlations with reservoir properties and cannot quantitatively characterize the heterogeneity of tight sandstone.

KEYWORDS

tight sandstone, pore structure, fractal porous media, permeability, high-pressure mercury intrusion

1 Introduction

The resource reserves of tight oil are abundant but the effective development of tight oil reservoir is difficult that is due to ultralow porosity and permeability of reservoir formation. The permeability of the tight oil reservoir with overburden pressure is generally lower than 0.1 mD, porosity is less than 10% as usual, and pore throat diameter is typically less than 1 μm (Jia et al., 2012). The apparent permeability of tight oil reservoir decreases with the decreasing pore diameters (Xu et al., 2019). There are approximately 66 basins worldwide buried with tight oil. Currently, the geological resource reserves of the main basins in China are 10.67–11.15 billion tons (Jia et al., 2012). In China, the tight oil reserves are mainly distributed in Ordos, Junggar, and Songliao basins, and the confirmed tight oil reserves are more than 600 million tons (Jia et al., 2012). However, the ultimate oil recovery factor of the tight oil reservoir is generally low (Sheng, 2015), and the characterization of pore throat structures and reservoir formation properties are significant to developing tight oil reservoirs.

Fractal geometry theory refers to phenomena in which an object exhibits similarity to the whole at each of its own scales, and widely exists in nature (Mandelbrot and Mandelbrot, 1982). Mandelbrot (Mandelbrot and Mandelbrot, 1982) firstly proposed the fractal theory in the 1980s. Compared with traditional Euclidean geometry, fractal geometry can more accurately analyze and describe the complex pore structure. The fractal theory has been widely used in the analysis and research of pore throat characteristics, and the physical properties of reservoir formations are negatively correlated with fractal dimensions (Wang et al., 2018a; Wang et al., 2018b; Wang et al., 2019; Wang et al., 2021). The larger the fractal dimension, the more complex the pore throat characteristics of reservoir formations (Shi et al., 2018). With the development of pore throat structure description technology, many methods are applied to the description and analysis of pore throat characteristics in tight oil reservoirs, such as HPMT, constant-rate mercury injection, CT scanning, SEM, CTS, etc. As we all know, HPMT is widely used to analyze pore throat structures. The constant-rate mercury injection method can inject mercury into pore space at

TABLE 1 The basic information about the cores.

Well No.	No.	Depth	ϕ	K	Structure coefficient	Throat sorting coefficient	\bar{p}	p_{50}	r_{50}	r_{\max}	Displacement pressure
		(m)	(%)	(mD)			(μm)	(MPa)	(μm)	(μm)	(MPa)
Z602-9	YG09-297	1774.00	13.1	0.49	2.454	2.927	0.271	4.527	0.165	1.057	0.696
Z602-10	YG09-368	1877.40	12.3	0.73	6.793	3.326	0.568	4.134	0.180	2.086	0.352
ZF59-45	YG09-208	1804.60	6.5	0.09	0.831	1.681	0.096	11.088	0.068	0.353	2.081
	YG09-209	1851.00	10.5	0.52	5.428	3.201	0.464	3.789	0.203	1.528	0.481
	YG09-210	1855.80	10.3	0.23	2.207	2.668	0.199	5.645	0.131	0.532	1.382
ZF81-49	YG09-207	1792.00	12.4	0.62	1.101	2.737	0.21	7.171	0.104	0.703	1.046
ZF86-54	YG09-363	1731.40	10.5	0.12	1.221	2.356	0.047	16.199	0.047	0.354	2.074
	YG09-364	1839.40	11.4	0.35	8.621	3.188	0.46	3.609	0.213	1.528	0.481
ZF59-51	1	1774.00	4.514	0.00078	0.354	0.007	0.011	63.478	0.012	0.0534	13.780
	3	1784.76	6.532	0.0115	1.911	0.106	0.098	9.16	0.080	1.0815	0.68
	5	1796.00	7.586	0.00083	15.852	0.075	0.071	15.917	0.046	0.5407	1.36
	7	1834.15	2.7	0.00042	0.304	0.005	0.008	96.36	0.008	0.0356	20.66
	8	1834.60	9.263	0.0007	0.973	0.008	0.011	69.4	0.011	0.0667	11.03
	9	1834.72	15.389	0.68	6.408	0.997	0.893	1.758	0.418	5.2529	0.14
	11	1839.18	12.465	0.35	1.105	0.327	0.327	2.705	0.272	1.5647	0.47
	13	1839.85	11.336	0.11	1.798	0.237	0.241	4.401	0.167	2.7237	0.27
	15	1840.40	5.746	0.0013	0.633	0.017	0.018	49.93	0.015	1.5647	0.47
Z102	8	1955.85	9.485	0.016	2.519	0.115	0.104	10.411	0.071	0.1340	5.49
Sample 5	-	-	13.621	0.2	2.147	0.315	0.256	6.635	0.111	1.0815	0.68

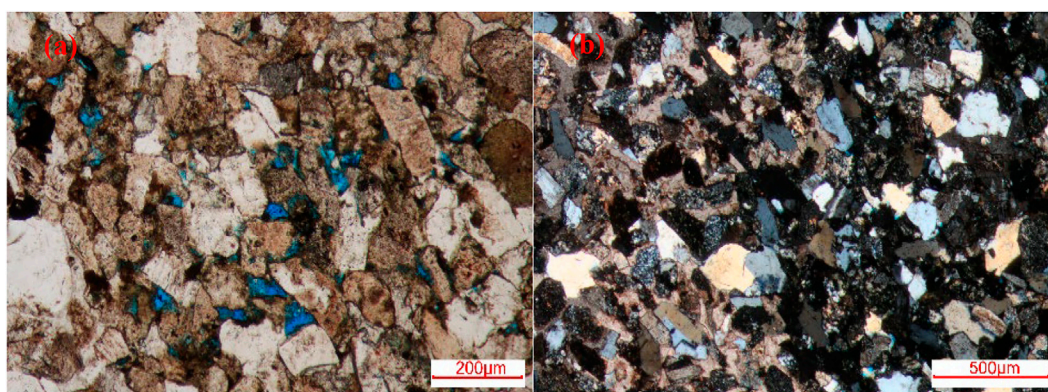


FIGURE 1

CTS image of No. 3 core of Zhoufu 59–51 well (A) The pore system is dominated by intergranular solvable pores with single-polarized light image (B) Gray-bearing medium fine-grained feldspar debris sandstone with orthogonal polarization image.

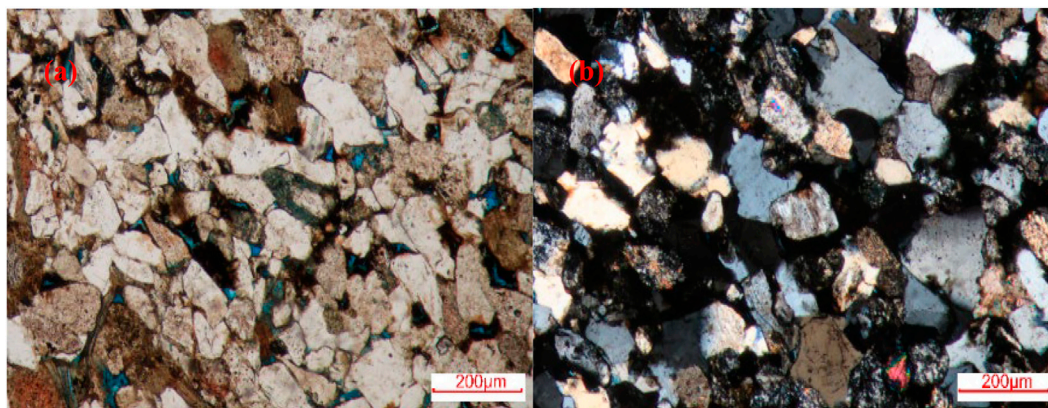


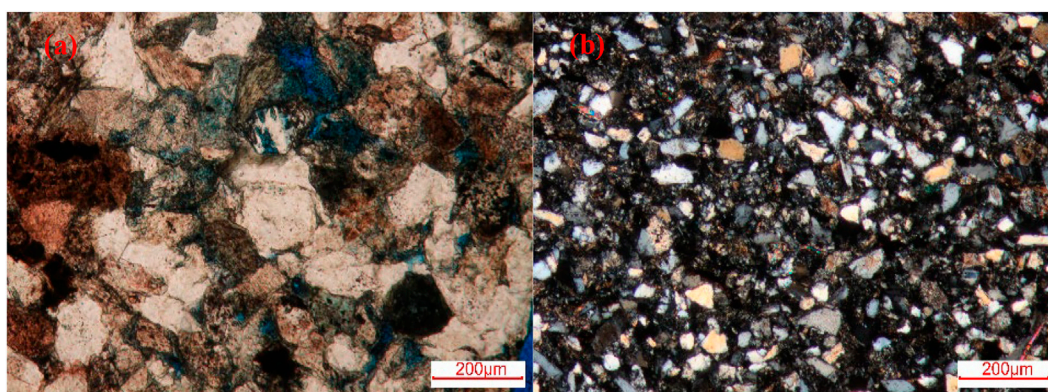
FIGURE 2

CTS image of No. 5 core of Zhoufu 59–51 well (A) The pore system is dominated by intergranular and intragranular solvable pores, single-polarized light image (B) Medium and fine-grained feldspar debris sandstone, orthogonal polarization image.

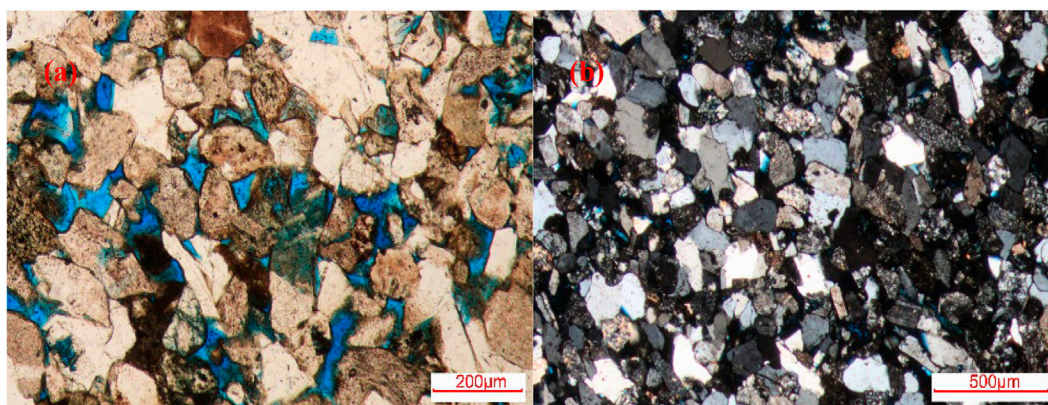
constant and low rates, and it can give a more detailed description of the core pore throat structure than conventional mercury intrusion methods (He et al., 2011; Li et al., 2012; Chen et al., 2013). However, it is hard to quantitatively characterize the pore throat structure with a pore size less than $0.12\mu\text{m}$ in ultra-low permeability tight reservoir (Zhang et al., 2021). CT scanning can build a 3D digital rock without damaging the core and has been widely used to describe the characteristics of pore throat (Knackstedt et al., 2007; Arzilli et al., 2016). The CTS refers to injecting colored liquid gel into the pore space of core samples and making cores into thin sections after gel solidification. It has the advantages of simple and easy experiments, low requirements, and a short experimental cycle, while CTS cannot directly

describe the pore throat characteristics in characterizing dense cores. Similar to CT scanning and CTS, the pore throat characteristics and composition can also be obtained from SEM images. The structural characteristics of different pore throats can be comprehensively studied with HPMT, X-CT, SEM, and other methods (Wang et al., 2018a), (Gutierrez and Jose, 2006; Martínez et al., 2010; Jouini et al., 2011).

Based on HPMT, CTS, and SEM tests, the pore throat characteristics of tight sandstones in Fuyu oil layers of Sanzhao Sag, Songliao Basin, NE China were characterized and analyzed by six fractal models, and the main influencing factors of permeability in other physical properties are analyzed as well. The pore throat and composition of tight sandstone are characterized and explored through CTS and SEM images, and the fractal dimensions of six

**FIGURE 3**

CTS image of No. 9 core of Zhoufu 59–51 well. (A) The pore system is dominated by intergranular and intragranular solvable pores, single-polarized light image (B) very fine-grained feldspar chip sandstone contains mud, orthogonal polarization image.

**FIGURE 4**

CTS of core 11 of Zhoufu 59–51 well. (A) The pore system is dominated by intergranular and intragranular solvable pores, single-polarized light image (B) Fine medium-grained feldspar debris sandstone, orthogonal polarization image.

different fractal models are calculated from HPMT capillary pressure data. The applicability of using fractal dimensions calculated from different models to characterize the pore throat characteristics and the correlation between fractal dimensions and reservoir physical parameters were analyzed.

2 Core samples

In this experiment, 19 low-permeability core samples were taken from the K1q4 layer from 1731.4m to 1955.85 m in the Songliao Basin and tested for HPMT. The porosity of the sample cores ranged from 2.7% to 15.389%, and the permeability was between 0.00042 mD and 0.73 mD. The basic information about the cores is shown in Table 1.

2.1 Core analysis

The distribution of clay minerals in the reservoir is anisotropic, seriously affecting oil generation, reserves, flow, exploration, and development of oil and gas reservoirs. Core SEM images and thin section images can reflect the effect of clay mineral particle morphology and pore development.

2.1.1 Analysis of CTS images

The CTS images of core 3 of well Zhoufu 59–51 are shown in Figure 1, and the particles are in a medium fine grain structure. The intermediate basic rock debris is mainly andesite, and the metamorphic rock debris is mainly composed of quartzite and phyllite. Argillaceous matrix is

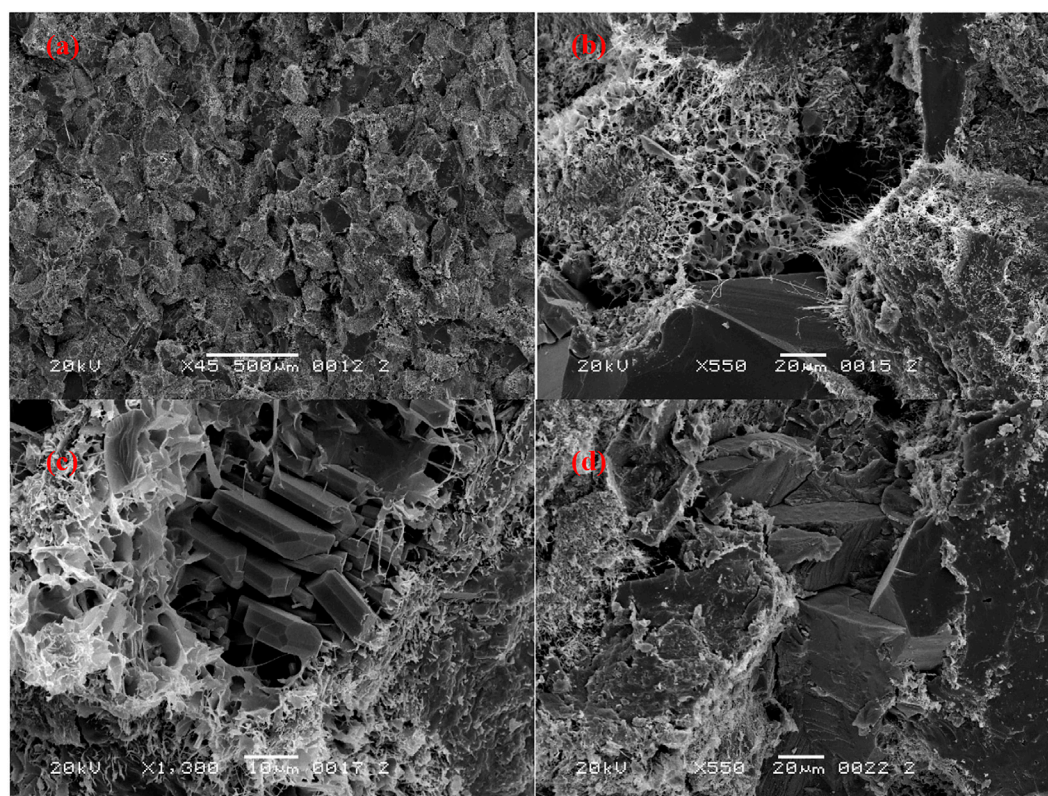


FIGURE 5
SEM image of No. 3 core of Zhoufu 59–51 well.

filled with intergranular, and anhydrite and calcite are filled in pores and replaced particles, and pyrite is distributed in patches. It can be seen that the pores are unevenly distributed, and it is mainly intergranular dissolved pores with poor connectivity.

Figure 2 is a thin section photo of the cast body of No. 5 core of Zhoufu 59–51 well, and the particles are in a medium fine grain structure. Sedimentary debris is mainly micrite limestone, and metamorphic debris is mainly phyllite and quartzite. Argillaceous matrix is distributed among intergranular, and calcite and anhydrite fill pores and replace grains. Common quartz secondary enlargement can be seen, and pyrite shows a patchy distribution. Intergranular and intragranular dissolved pores are developed with poor connectivity.

Core 9 of well Zhoufu 59–51 is shown in Figure 3, and the particles are of acceptable to excellent structure. The rock debris is mainly acid extrusive rocks. The argillaceous matrix is distributed among intergranular, and a small amount of calcite fills the pores and replaces the grains. Illite is distributed at the edge of grains, and pyrite is distributed in patches. There are a few inter-granular and intra-granular dissolved pores with poor connectivity.

According to Figure 4, it can be seen that the core of well Zhoufu 59–51 No. 11 is fine and medium grinding a small number of excellent particles. The intermediate bare cuttings are mainly andesite, and the metamorphic mainly consists of phyllite and quartzite. Argillaceous matrix is distributed among grains, and anhydrite is used to fill pores and replace grains. It can be also seen common quartz secondary enlargement. The pores are mainly intragranular dissolved pores and intergranular dissolved pores with poor connectivity.

2.1.2 Analysis of SEM images

Figure 5 is the scanning electron microscope image of No. 3 fine sandstone core of Zhoufu 59–51 well. It can be seen that the overall structure of the rock is relatively loose, the quartz crystal particles are secondarily enlarged and tend to be self-shaped, the secondary quartz crystals and hairy illite aggregates are attached to the particle surface, and the secondary albite crystals, hairy illite aggregates, calcite crystals, and honeycomb-like illite smectite are filled in the inter-granular pores. And residual intergranular pores can be seen.

Figure 6 shows the scanning electron microscope image of the No. 5 siltstone core of Zhoufu 59–51 well. It can be seen that

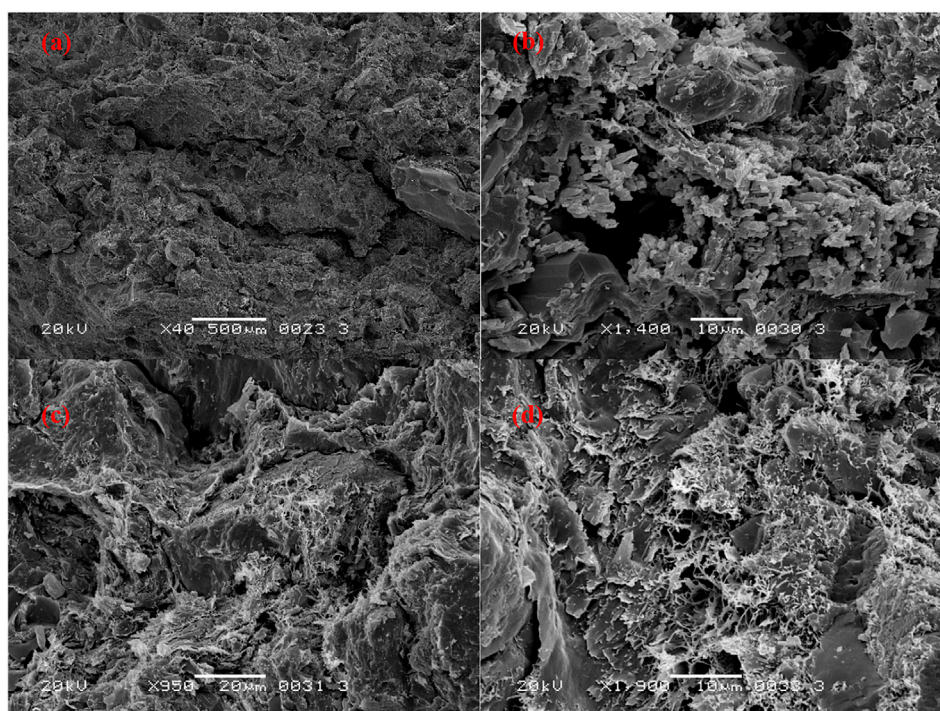


FIGURE 6
SEM image of core 5 of Zhoufu 59–51 well.

the overall structure of the rock is relatively loose, and the arrangement of clastic particles is slightly directional. Flake-like and hairy illite aggregates are filled in clastic particles and intergranular pores. Intergranular micro-fractures are developed. The clastic particles are in mosaic contact, and inter-granular dissolution pores are found. Feldspar particles are broken and hetero-basic by dissolution, and hairy illite aggregates are mixed with hetero-base. Dissolution micro-pores are developed, and secondary albite crystals are found in dissolution pores.

Figure 7 is the scanning electron microscope image of No. 9 fine sandstone core of well Zhoufu 59–51. It can be seen that the overall structure of the rock is loose. Secondary quartz crystals and leaf-like chlorite aggregates with a film structure are attached to the surface of clastic particles and filled in clastic particles. Residual intergranular pores and fissures are developed. The lamellar chlorite aggregate and asphaltene are filled in the intergranular pores, and the chlorite aggregate is mixed with quartz crystals.

Figure 8 is a scanning electron microscope image of the core of No. 11 siltstone in Zhoufu 59–51 well. It can be seen that the overall structure of the rock is loose, some flake-like and hairy illite aggregates and leaf-like chlorite aggregates with thin film structures are attached to the surface of debris particles. And secondary quartz crystals, asphaltene, and leaf-like chlorite aggregates are filled in the pores of debris particles and particles, which can be seen developed intergranular pores. Feldspar particles

are dissolved and broken along the cleavage with heterogeneity, and micro-dissolved pores are set in the particles.

3 Calculation of fractal dimension with HPMI data

According to the fractal theory, porous media have a fractal structure with a power rate relationship between scale ε and the number $N(\varepsilon)$:

$$N(\varepsilon) \propto \varepsilon^{-D_f} \quad (1)$$

Where D_f is fractal dimension.

3.1 Method I-2D capillary model

Assuming that the pore space is made up of capillary tube with the same length l under different radius r (Purcell, 1949), then:

$$N(>r) = \int_r^{r_{\max}} n(r) dr = \int_r^{r_{\max}} \frac{\Delta V_{Hg}(r)}{\pi r^2 l} dr \quad (2)$$

Where r is the pore radius, μm , $N(r)$ is the total number of pores with pore radius less than r , $n(r)$ is the number of pores at the

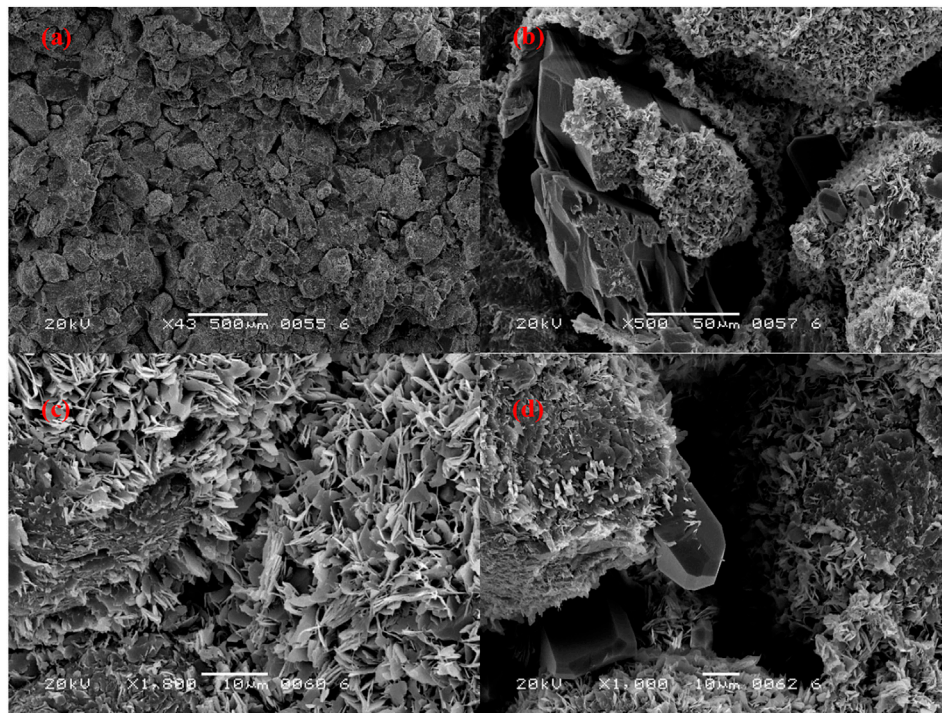


FIGURE 7
SEM image of No. 9 core of Zhoufu 59–51 well.

radius of r , $\Delta V_{Hg}(r)$ is the volume of mercury intake at the radius of r , cm^3 , l is the length of the rock sample, cm .

When the pore diameter in the reservoir is greater than r , the total number of pores is $N(r)$, and the logarithm of radius r and pore number $N(r)$ is a linear relationship (Katz and Thompson, 1985):

$$\lg N(r) \propto -D_f \lg r \quad (3)$$

Then D_f is the fractal dimension calculated by this method. It represents the fractal dimension of the cross-section of the rock sample and equals the opposite slope of the $N(r)$ - r in the logarithm plot.

3.2 Method II- 3D sphere model

If the pore space is made up of spheres with different radii, then:

$$N(>r) = \int_{r_{\max}}^r n(r) dr = \int_{r_{\max}}^r \frac{\Delta V_{Hg}(r)}{\frac{4}{3}\pi r^3} dr \quad (4)$$

D_{f2} , the fractal dimension obtained by this method, reflects the 3D distribution characteristics of rock pore space, and equals the opposite slope of the $N(r)$ - r curve in the logarithm plot.

3.3 Method III-3D capillary model

Assuming that the radius of the rock sample is r , the ratio of the total mercury injection volume $V_{Hg}(r)$ under this radius to the total volume of the core under this radius is the 3D capillary model, namely:

$$N(>r) = \frac{V_{Hg}(r)}{\pi r^2 l} \quad (5)$$

where D_{f3} is the fractal dimension calculated by this method, is opposite to the slope of $N(r)$ - r curve in the double logarithm plot. The fractal dimension calculated with this method can reflect the fractal characteristics of pore space in 3D space.

The saturation of mercury is:

$$S_{Hg} = \frac{V_{Hg}}{V_p} \quad (6)$$

where V_p is the pore volume of the whole core system, cm^3 , S_{Hg} is the saturation of mercury content, %.

Combining Eqs. 3, 5, 6, it can be seen that there is a power-law relationship between mercury saturation and capillary pressure, namely:

$$S_{Hg} \propto P_c^{-(2-D_f)} \quad (7)$$

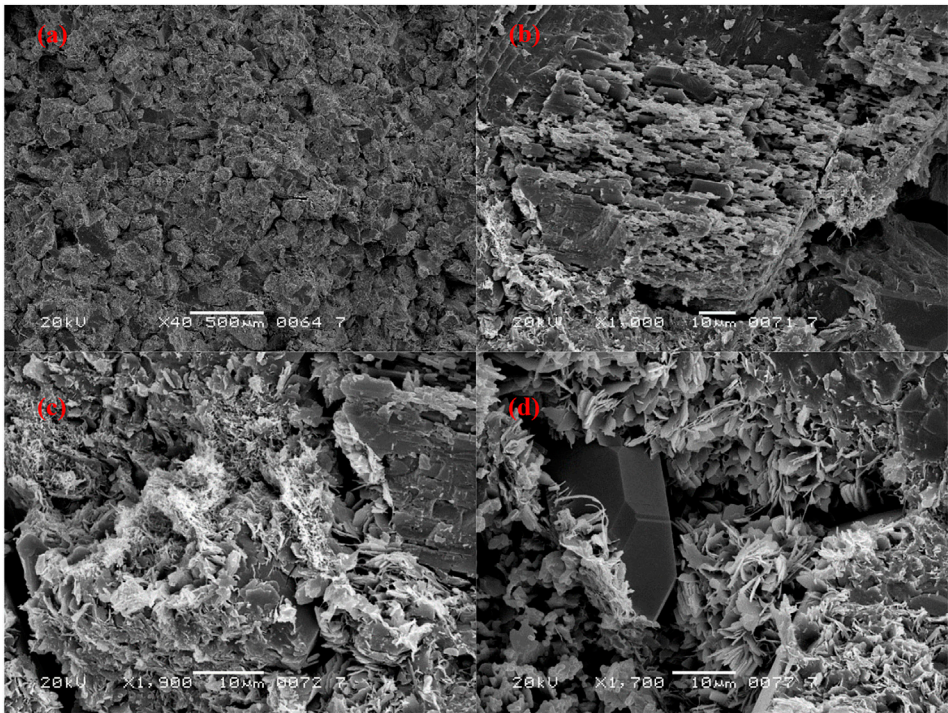


FIGURE 8
SEM image of core 11 of Zhoufu 59–51 well.

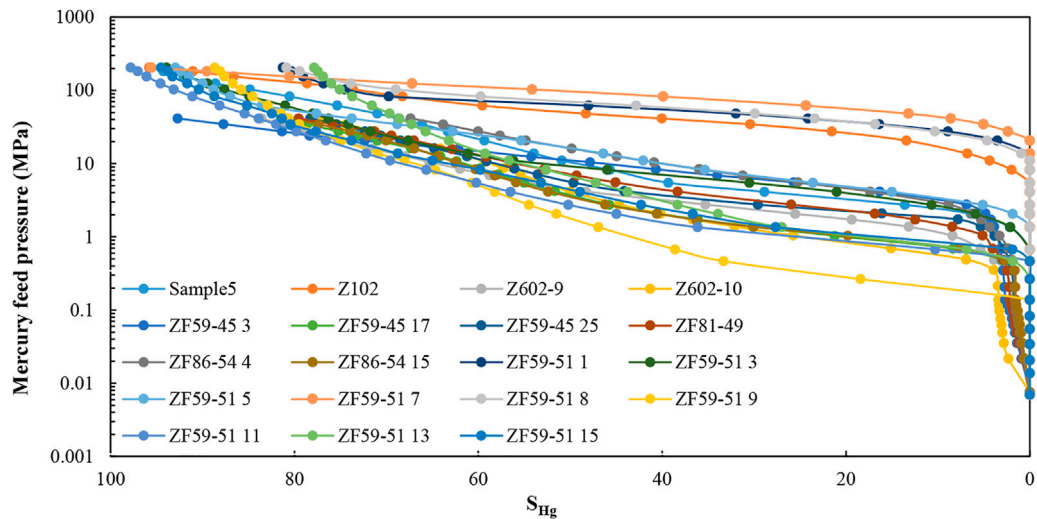


FIGURE 9
Mercury injection curve of corethe.

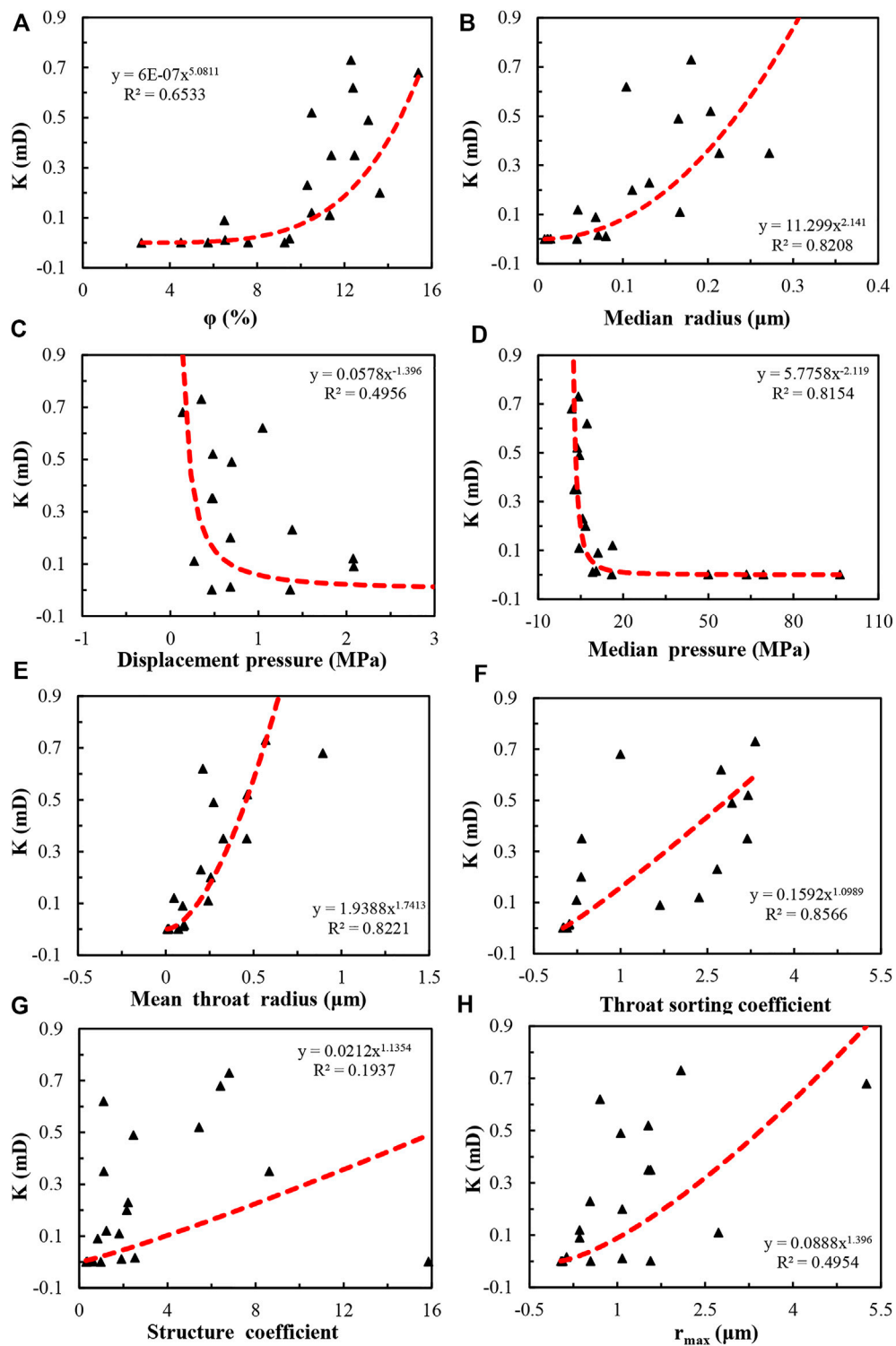


FIGURE 10
Correlations between permeability and pore structure parameters.

TABLE 2 Fractal dimension values calculated by different models.

Well No.act	No.	Method I	Method II	Method III	Method IV	Method V	Method VI
		D_{f1}	D_{f2}	D_{f3}	D_{f4}	D_{f5}	D_{f6}
Z602-9	YG09-297	2.123	3.039	2.609	2.641	2.745	2.549
Z602-10	YG09-368	1.823	2.783	2.478	2.833	2.799	2.705
ZF59-45	YG09-208	2.175	3.057	2.955	2.980	2.955	2.202
	YG09-209	1.767	2.729	2.520	2.828	2.724	2.654
	YG09-210	1.730	2.641	2.659	2.596	2.718	2.578
ZF81-49	YG09-207	1.786	2.724	2.580	2.839	2.734	2.581
ZF86-54	YG09-363	1.955	2.843	2.750	2.837	2.825	2.637
	YG09-364	1.733	2.693	2.531	2.792	2.704	2.663
ZF59-51	1	2.405	3.133	3.231	1.019	2.685	2.158
	3	1.680	2.619	2.580	2.598	2.657	2.442
	5	1.686	2.577	2.642	2.518	2.672	2.384
	7	3.308	4.179	3.776	2.905	2.827	1.670
	8	2.270	3.062	3.442	1.931	2.765	2.292
	9	1.730	2.690	2.177	2.753	2.657	2.700
	11	1.740	2.730	2.251	2.751	2.629	2.416
	13	—	2.628	2.388	2.680	2.638	2.751
	15	1.681	2.636	2.375	2.703	2.638	2.504
Z102	8	2.065	2.950	3.121	2.761	2.779	2.154
Sample 5	-	1.881	2.843	2.540	2.920	2.699	2.453

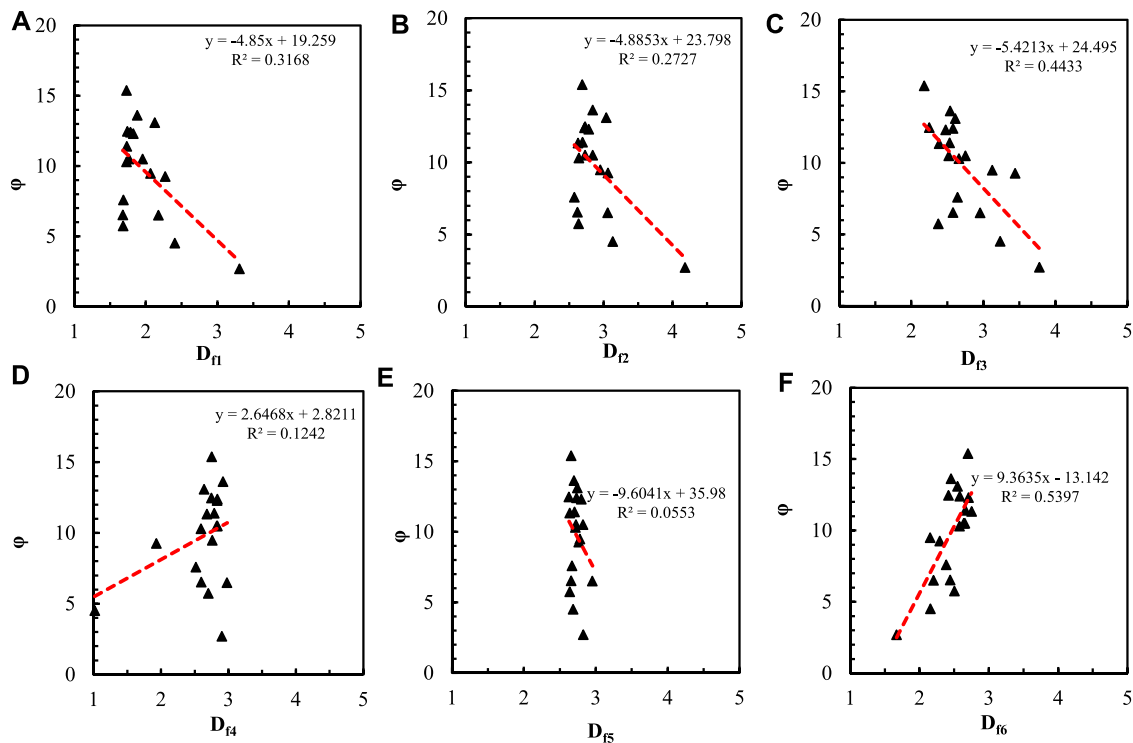


FIGURE 11 Relationship between porosity and fractal dimension calculated by six methods.

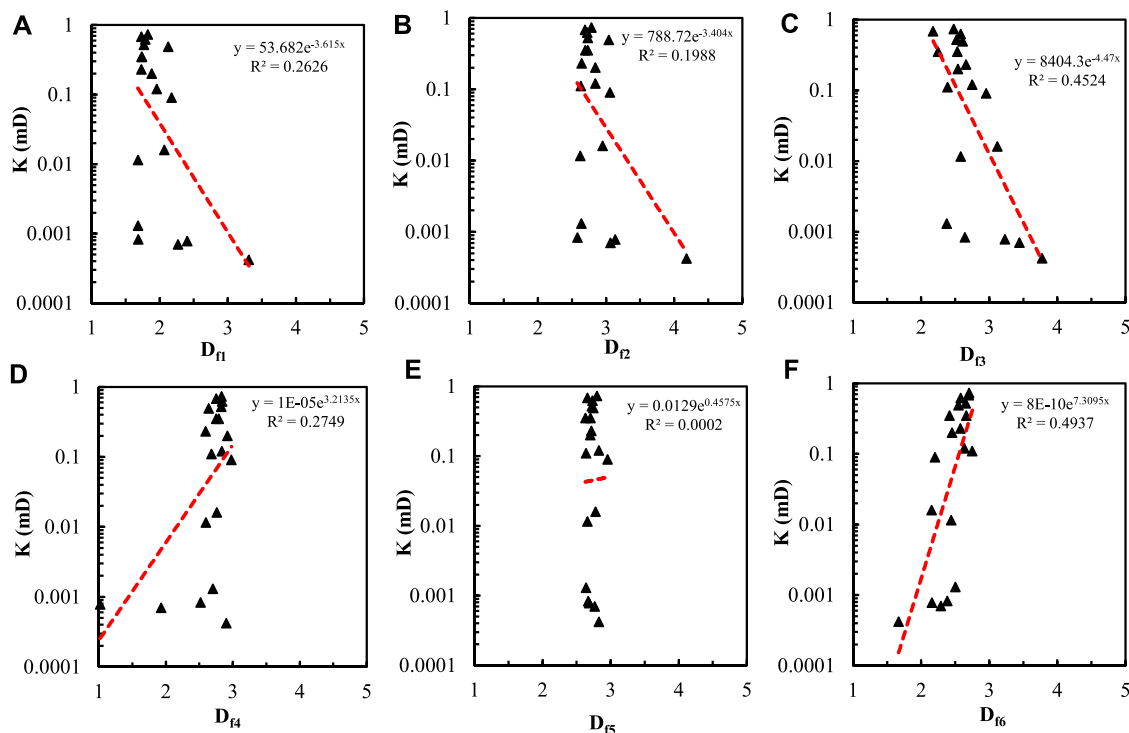


FIGURE 12
Relationship between permeability and fractal dimension calculated by six methods.

where P_c is capillary pressure, MPa. According to the formula, it is easy to see that the slope of S_{Hg} - P_c logarithmic curve plus 2 is the fractal dimension obtained by this method.

3.4 Method IV- geometric model

Assume that the pore radius r is a function of V_r derivative concerning r , then:

$$-\frac{dV_r}{dr} \propto r^{2-D_f} \quad (8)$$

Combining (7) and (8) to obtain:

$$-\frac{dS_{Hg}}{dp_c} \propto p_c^{-(4-D_f)} \quad (9)$$

From this formula, it can be seen that the slope of the $\frac{dS_{Hg}}{dp_c}$ - p_c curve in double logarithm plus 4 equals D_{f4} .

3.5 Method V- thermodynamic model

When mercury intrudes into pore space, the surface energy is directly proportional to the amount of mercury intrusion,

therefore there is a certain correlation between the number of pores and surface energy of mercury intrusion into rocks (Zhang and Li, 1995):

$$\ln(W_n) = C + \ln(Q_n) \quad (10)$$

$$Q_n = r_n^{2-D} V_n^{D/3} \quad (11)$$

$$W_n = \sum_{i=1}^n \bar{P}_i \Delta V_i \quad (12)$$

where W_n is cumulative increase in surface energy during mercury intrusion, KJ, \bar{P}_i is the average pressure, MPa, ΔV_i is the intruded mercury volume in the pressure interval, cm^3 .

Combined with Eqs. 10–12, the following equation can be changed into (Zhang et al., 2006):

$$\ln(W_n/r_n^2) = C + D_f \times \ln(V_n^{1/3}/r_n) \quad (13)$$

D_{f5} is the fractal dimension calculated by this method, which represents the roughness of the pore face, then the slope of the graph $\ln(W_n/r_n^2)$ - $\ln(V_n^{1/3}/r_n)$ is opposite to D_{f5} .

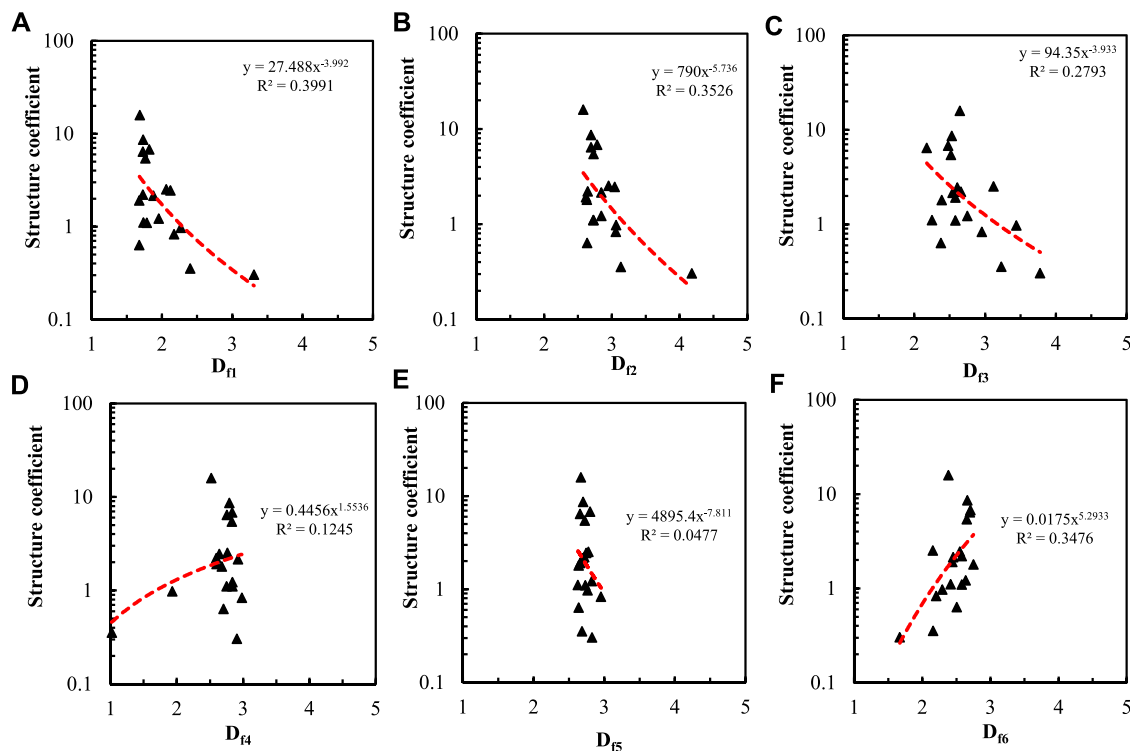


FIGURE 13

Relationship between structure coefficient and fractal dimension calculated by six methods.

3.6 Method VI- wetting phase model

When the minimum pore radius r_{min} is far less than r_{max} , the wetting phase saturation can be expressed with capillary pressure and fractal dimension as (Wang and Cheng, 2020):

$$S_w = \left(\frac{P_c}{P_{cmin}} \right)^{D_f-3} \quad (14)$$

where P_{min} is the displacement pressure. The fractal dimension calculated with this method can be noted with D_{f6} . As mercury is in the non-wetting phase, and it can be estimated by $S_w = 1 - S_{Hg}$. Therefore, the fractal dimension can be derived from the slope of $S_w - P_c$ in double logarithm plot.

3.7 Relationship between permeability and pore structure parameters

The capillary pressure of HPMT of 19 tight sandstone core samples is shown in Figure 9, and the calculated parameters of pore structures are shown in Table 1.

In this paper, permeability and porosity are derived from core measurements. And obtain values of physical parameters such as median radius, displacement pressure, average throat radius, median pressure, throat sorting coefficient, structure coefficient, and maximum radius from HPMT data. Moreover, the correlation curve between permeability and physical parameters are drawn to select main relevant parameters of permeability. The correlations between the different pore structure parameters and core permeability of 19 cores are shown in Figure 10. From the figure, it can be seen that the permeability is related to each physical parameter as a power. And the index of median pressure and the index of displacement pressure are negative which is caused by an inverse relationship between pressure and the radius of the pore throat. According to the comparison, the throat sorting coefficient has the strongest correlations with permeability, with a correlation coefficient of 0.8566. The median pressure, median radius and average throat radius have slightly poor correlations with permeability, and the corresponding correlation coefficients are 0.8154, 0.8208 and 0.8221 respectively. The porosity has a relatively poorer correlation with core permeability, and the correlation coefficients is 0.6533, respectively. The correlation between structure coefficient

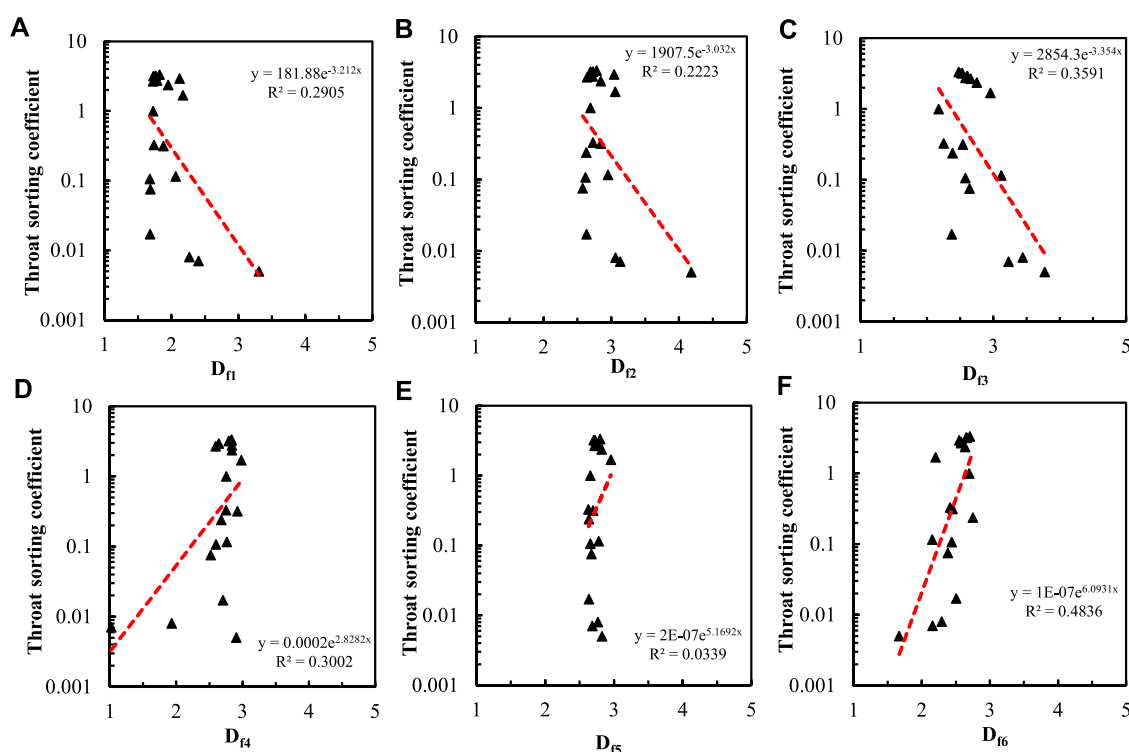


FIGURE 14
Relationship between throat sorting coefficient and fractal dimension calculated by six methods.

and permeability is the worst, and the correlation coefficient is only 0.1937.

4 The correlation between fractal dimension and reservoir properties

According to the above six fractal models, the fractal dimension of each model is calculated, as shown in Table 2. The fractal dimensions calculated by the models I to VI are respectively recorded as D_{f1} , D_{f2} , D_{f3} , D_{f4} , D_{f5} , and D_{f6} . The fractal dimension calculated by method I is mainly between 1 and 3. The fractal dimension calculated by method II and method III is mainly between 2 and 4. The fractal dimensions calculated by method IV and method V are primarily distributed in the range of 2–3. Meanwhile, the difference between the fractal dimensions calculated by method V is small, mainly in the range of 2.6–3. However, due to the special conditions of ultra-low permeability and low porosity of the core 7 of Zhoufu 59–51 well, the fractal dimensions calculated by the 2D capillary model and 3D sphere model are not in this range.

Figure 11 shows the relationship between porosity and fractal dimension calculated by six methods, respectively. It

can be seen that the fractal dimension calculated by the 3D capillary model and wetted phase model has a strong correlation with porosity, and the wetting phase model has the strongest correlation, with a correlation coefficient of 0.5397. The 3D capillary model is slightly worse than the 2D capillary model. The correlation between porosity and fractal dimension calculated by the 3D spherical model and geometric model was poorer and the correlation coefficient was 0.2727 and 0.1242, respectively. The correlation between the fractal dimension calculated by the thermodynamic model and porosity was the poorest, and the correlation coefficient was only 0.0553.

Figure 12 shows the relationship between permeability and fractal dimensions calculated by the six methods. Compared with porosity, the correlation between fractal dimensions and core permeability is poorer. The correlation between the wetting phase model and the 3D capillary model is slightly stronger than other methods, and the correlation coefficients are 0.4937 and 0.4524, respectively. According to the analysis, the fractal dimensions from the remaining four fractal models have no obvious correlation with permeability, and the correlation coefficients are all below 0.3. The fractal dimension calculated by the thermodynamic model has the poorest

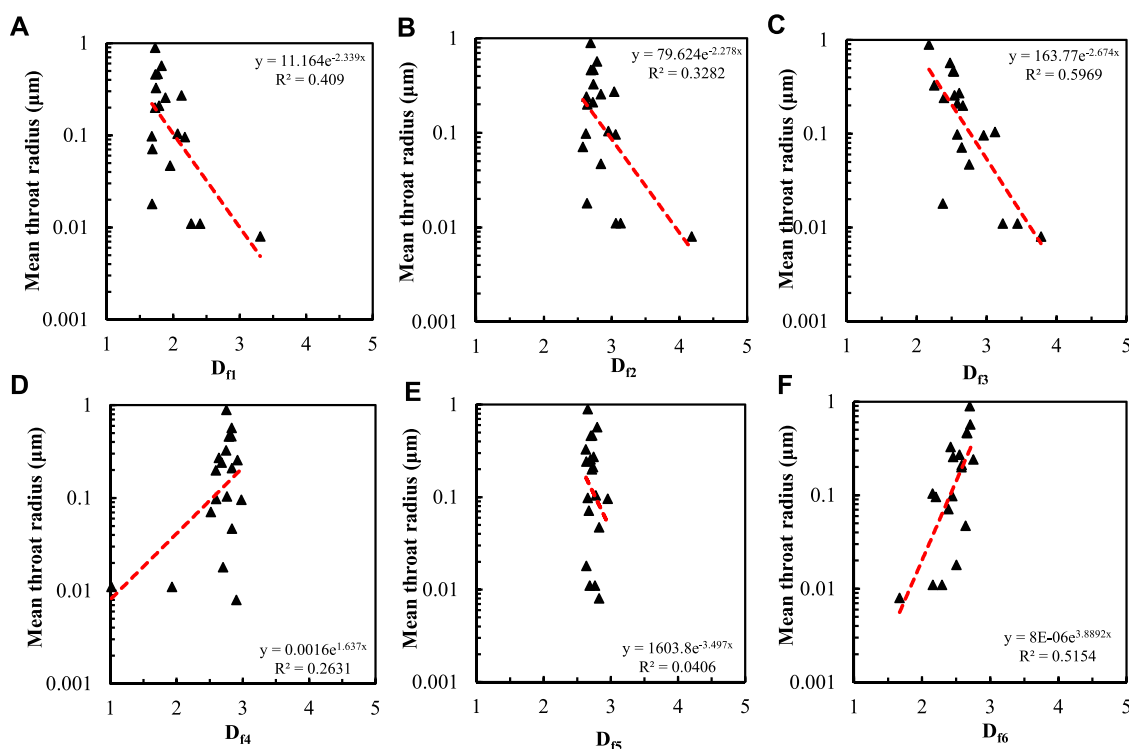


FIGURE 15
Relationship between average throat radius and fractal dimension calculated by six methods.

correlation with permeability, and the correlation coefficient is only 0.0002.

Figure 13 shows the relationship between the structure coefficient and fractal dimensions calculated from six models. It can be seen that the fractal dimensions calculated from the 2D capillary tube model, the 3D sphere model, and the wetting phase model have slightly stronger than that of other fractal dimensions. The fractal dimension calculated by the 2D capillary model has the strongest correlation with the structure coefficient, with a correlation coefficient of 0.3991. The correlation coefficients of D_{f2} and D_{f6} are 0.3526 and 0.3476 respectively. The correlation between other fractal dimensions and structure coefficient is poor, and the determination coefficient is below 0.3. The fractal dimension calculated by the thermodynamic model has the poorest correlation with the structure coefficient, and the determination coefficient is only 0.0477.

Figure 14 shows the relationship between the sorting coefficient of pore throats and fractal dimension calculated by six methods. It can be seen that the fractal dimension D_{f6} calculated by the wetting phase model has the strongest correlation with the sorting coefficient of pore throats, and the correlation coefficient is 0.4836. The fractal dimensions obtained by the 3D capillary model and geometric model have

a slightly poor correlation with the sorting coefficient of pore throats, and the correlation coefficients are 0.3591 and 0.3002 respectively. The correlation between other fractal dimensions and the sorting coefficient of pore throats is poor, and the determination coefficient is lower than 0.3. The fractal dimension calculated by the thermodynamic model has the poorest correlation with the sorting coefficient of pore throats, and the determination coefficient is only 0.0339.

Figure 15 shows the relationship between the average pore throat radius and the fractal dimension calculated by six methods. The fractal dimension D_{f3} derived from the 3D capillary model and the fractal dimension D_{f6} from the wetting phase model have the strongly correlated with the mean throat radius relationship, and the correlation coefficients are 0.5969 and 0.5154, respectively. D_{f1} and D_{f2} have a slightly poor correlation with the average throat radius. The determination coefficients are 0.409 and 0.3282, respectively. The fractal dimension obtained from the remaining fractal method has a poor correlation with the average pore throat radius. The correlation between the fractal dimension D_{f5} calculated by the thermodynamic model and the average pore throat radius is the poorest, and the determination coefficient is only 0.0406.

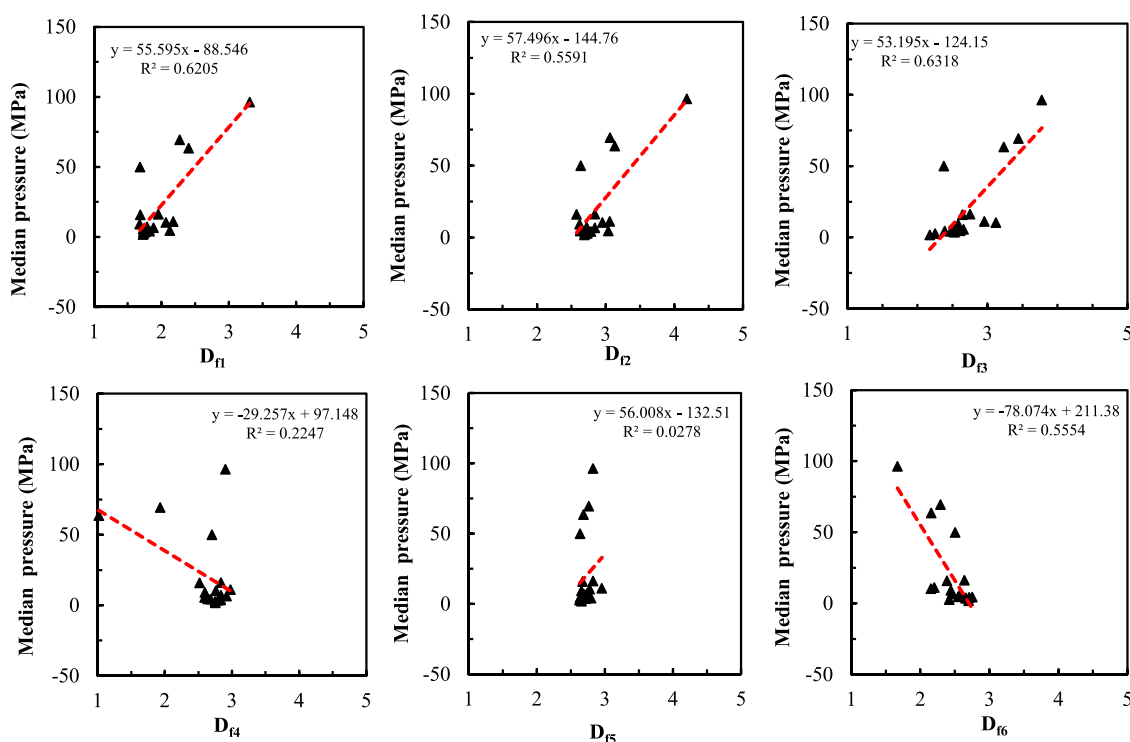


FIGURE 16
Relationship between median pressure and fractal dimension calculated by six.

The relationship between the median capillary pressure and the fractal dimension calculated by the six methods is shown in Figure 16. It can be seen that the fractal dimension D_{f3} calculated by the 3D capillary model and the fractal dimension D_{f1} calculated by the 2D capillary model has the strongest correlations with the capillary median pressure. The correlation coefficients are 0.6318 and 0.6205 respectively. The correlation between D_{f2} and D_{f6} and the median capillary pressure is slightly poor, and the determination coefficients are 0.5591 and 0.5554, respectively. The correlation between the other two fractal dimensions D_{f4} and D_{f5} and the median capillary pressure is poor. The correlation between the fractal dimension calculated by the thermodynamic model and the median capillary pressure is the poorest, and the determination coefficient is only 0.0278.

Figure 17 shows the relationship between the maximum pore throat radius and the fractal dimension calculated by the six methods. It can be seen that the fractal dimension D_{f3} calculated by the 3D capillary model has the strongest correlation with the maximum pore throat radius, with a correlation coefficient of 0.9317. The fractal dimensions D_{f6} , D_{f1} , and D_{f2} have a slightly poor correlation with the maximum pore throat radius, with correlation coefficients

of 0.6992, 0.6313, and 0.5239 respectively. The remaining two fractal dimensions are poorly correlated with the maximum pore throat radius, with correlation coefficients below 0.3.

To sum up, the fractal dimension calculated by the wetting phase model and the 3D capillary model can well characterize the reservoir properties. However, the fractal dimension of the wetting phase model essentially should be calculated by using the saturation of the wetting phase and its corresponding intrusion pressure data. Utilizing the equation $S_w = 1 - S_{Hg}$ to calculate the saturation of the wetting phase leads to results that contradict the fractal theory. This is because the method makes an inverse relationship between the wetting and non-wetting phases. According to Figure 12, median pressure and fractal dimension show a positive correlation. From $P_c = \frac{2\delta \cos \theta}{r}$, it can be seen that the capillary pressure is inversely related to the pore radius. Therefore, the fractal dimension is negatively correlated with the uniformity of pore throat distribution. Except for the wetting phase model, every fractal model has a negative relationship between fractal dimension and reservoir properties. That is, the smaller the fractal dimension value, the more homogeneous the corresponding rock surface is and the more uniform the pore throat distribution is.

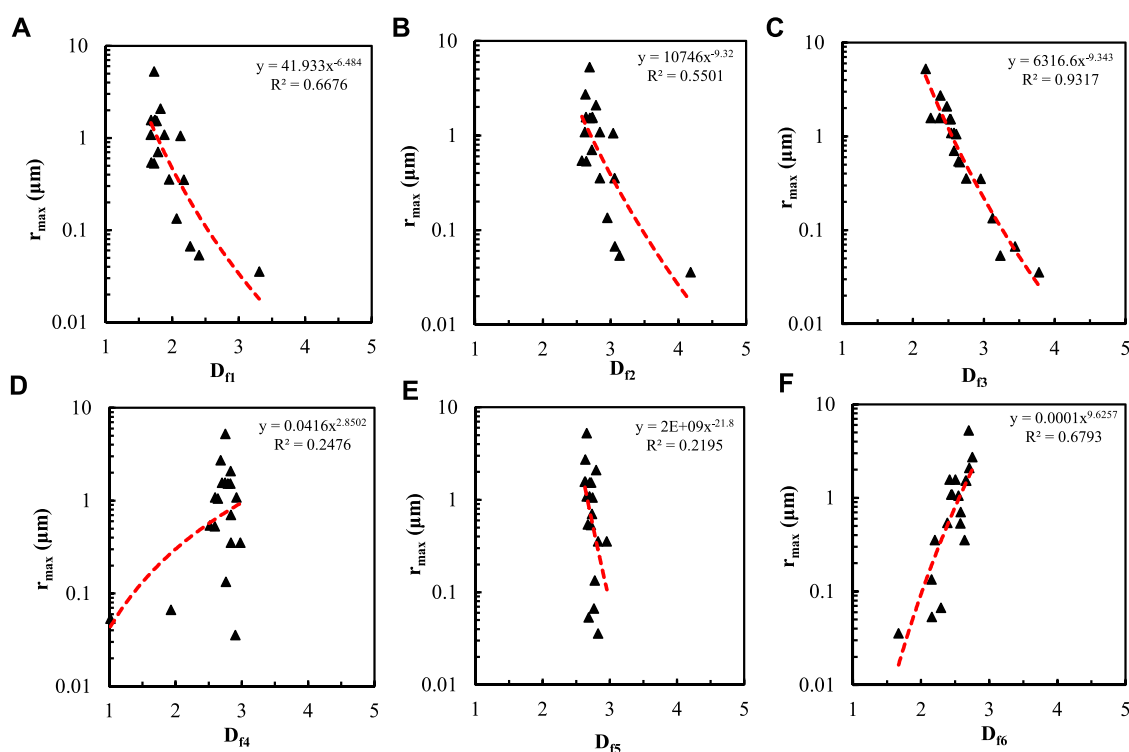


FIGURE 17

Relationship between maximum pore radius and fractal dimension calculated by six methods.

5 Conclusion

The pore fillings and composition of rock samples are analyzed through the CTS image and SEM image of tight sandstone rock samples obtained from Fuyu oil layers of Sanzhao Sag, Songliao Basin, NE China. And the connectivity of the rock samples is qualitatively characterized. Based on the data of HPMI, 6 kinds of fractal models are utilized for quantitative analysis of the samples' heterogeneity. And the best model was filtered by comparing. Combining the fractal models with the CTS image and SEM image, the reservoir properties of Daqing Oilfield are Qualitative and quantitative evaluated.

CTS and SEM images show that the lithology of the tight oil reservoir in the Fuyu oil layers of Sanzhao Sag, Songliao Basin are all sandstones, and the pore types are mainly inter-granular and intra-granular pores, with uneven distribution of pores and poor connectivity. The tight sandstone is mainly pore cemented and filled with muddy miscellaneous bases, calcite, and other cemented materials. Illite or chlorite is commonly found attached to the grain surface and filled between the grains.

HPMI tests show that the tight sandstone permeability is strongly correlated with the throat sorting coefficient. The fractal dimensions obtained from the 3D capillary model and wetting phase model have a strong correlation with the reservoir physical

properties, but the trend between the fractal dimension and reservoir properties are opposite to each other. The fractal dimension obtained from the 3D capillary model is more suitable for analyzing the reservoir properties, and there is a negative correlation between the fractal dimension and reservoir physical parameters. That is, the larger the fractal dimension, the worse the reservoir physical properties. The fractal dimension calculated by the thermodynamic model has no obvious correlation with reservoir properties, and it is not possible to quantitatively analyze the reservoir properties by the thermodynamic model method.

Data availability statement

The raw data supporting the conclusions of this article will be made available by the authors, without undue reservation.

Author contributions

CM and HH did the experiments and correlation model under the help of XW.

Funding

This work is funded by the Beijing Municipal Natural Science Foundation (No. 2214077) and National Natural Science Foundation (No. 52204060).

Conflict of interest

Author CM was employed by Exploration Utility Department of CNPC Daqing Oilfield Co., Ltd.

The remaining authors declare that the research was conducted in the absence of any commercial or financial

relationships that could be construed as a potential conflict of interest.

Publisher's note

All claims expressed in this article are solely those of the authors and do not necessarily represent those of their affiliated organizations, or those of the publisher, the editors and the reviewers. Any product that may be evaluated in this article, or claim that may be made by its manufacturer, is not guaranteed or endorsed by the publisher.

References

- Arzilli, F., Ciloni, A., Mancini, L., and Tondi, E. (2016). Using synchrotron X-ray microtomography to characterize the pore network of reservoir rocks: A case study on carbonates. *Adv. Water Resour.* 95, 254–263. doi:10.1016/j.advwatres.2015.07.016
- Chen, P. L., Wang, S., Wang, D., Jia, X., and Qian, H. (2013). Comparing the constant-speed mercury injection technique with the conventional mercury injection technique. *Xinjiang Geol.* 31, 139–141.
- Gutierrez, C. G., and Jose, F. S. (2006). *Geophysical research abstracts*. Munich, Germany: European Geosciences Union, 11094.
- He, S., Jiao, C., Wang, J., Luo, F., and Zou, L. (2011). Discussion on the differences between constant-speed mercury injection and conventional mercury injection techniques. *Duankuai Youqitian (Fault-Block Oil Gas Field)* 18, 235–237.
- Jia, C., Zou, C., Li, J., and Li, D. (2012). Assessment criteria, main types, basic features and resource prospects of the tight oil in China. *Acta Pet. Sin.* 33, 343. doi:10.1016/s2096-2495(17)30026-1
- Jouini, M. S., Vega, S., and Mokhtar, E. A. (2011). Multiscale characterization of pore spaces using multifractals analysis of scanning electronic microscopy images of carbonates. *Nonlinear process. geophys.* 18, 941–953. doi:10.5194/npg-18-941-2011
- Katz, A. J., and Thompson, A. H. (1985). Fractal sandstone pores: Implications for conductivity and pore formation. *Phys. Rev. Lett.* 54, 1325–1328. doi:10.1103/physrevlett.54.1325
- Knackstedt, M. A., Sok, R., Adrian, S., and Arns, C. H. 3D Pore Scale Characterisation of Carbonate Core: Relating pore types and interconnectivity to petrophysical and multiphase flow properties International Petroleum Technology Conference, 2007. doi:10.2523/iptc-11775-ms
- Li, W. C., Zhang, Y. M., Wang, F., Zhu, J., and Ye, B. (2012). Application of constant-rate mercury penetration technique to study of pore throat characteristics of tight reservoir: A case study from the upper triassic yanchang formation in Ordos basin. *Lithol. Reserv.* 24, 60–65.
- Mandelbrot, B. B., and Mandelbrot, B. B. (1982). *The fractal geometry of nature*. New York: W. H. Freeman.
- Martínez, F. S. J., Martín, M. A., Caniego, F. J., Tuller, M., Guber, A., Pachepsky, Y., et al. (2010). Multifractal analysis of discretized X-ray CT images for the characterization of soil macropore structures. *Geoderma* 156, 32–42. doi:10.1016/j.geoderma.2010.01.004
- Purcell, W. R. (1949). Capillary pressures-their measurement using mercury and the calculation of permeability therefrom. *J. Petroleum Technol.* 1, 39–48. doi:10.2118/949039-g
- Sheng, J. J. (2015). Increase liquid oil production by huff-n-puff of produced gas in shale gas condensate reservoirs. *J. Unconv. Oil Gas Resour.* 11, 19–26. doi:10.1016/j.juogr.2015.04.004
- Shi, Y., Yassin, M. R., and Dehghanpour, H. (2018). A modified model for spontaneous imbibition of wetting phase into fractal porous media. *Colloids Surfaces A Physicochem. Eng. Aspects* 543, 64–75. doi:10.1016/j.colsurfa.2017.12.052
- Wang, F., and Cheng, H. (2020). Characterization of pore structure and petrophysical properties of tight sandstone of yanchang formation, Ordos basin. *J. Jilin Univ. (Earth Sci. Ed.)* 50, 721–731.
- Wang, F., Lian, P., Jiao, L., Liu, Z., Zhao, J., and Gao, J. (2018). Fractal analysis of microscale and nanoscale pore structures in carbonates using high-pressure mercury intrusion. *Geofluids* 2018, 1–15. doi:10.1155/2018/4023150
- Wang, F., Yang, K., and Cai, J. (2018). Fractal characterization of tight oil reservoir pore structure using nuclear magnetic resonance and mercury intrusion porosimetry. *Fractals* 26, 1840017. doi:10.1142/s0218348x18400170
- Wang, F., Yang, K., You, J., and Lei, X. (2019). Analysis of pore size distribution and fractal dimension in tight sandstone with mercury intrusion porosimetry. *Results Phys.* 13, 102283. doi:10.1016/j.rinp.2019.102283
- Wang, F., Zeng, F., Wang, L., Hou, X., Cheng, H., and Gao, J. (2021). Fractal analysis of tight sandstone petrophysical properties in unconventional oil reservoirs with NMR and rate-controlled porosimetry. *Energy fuels* 35, 3753–3765. doi:10.1021/acs.energyfuels.0c03394
- Xu, J., Chen, Z., Wu, K., Li, R., Liu, X., and Zhan, J. (2019). On the flow regime model for fast estimation of tight sandstone gas apparent permeability in high-pressure reservoirs. *Energy Sources Part A Recovery Util. Environ. Eff.* 2019, 1–12. doi:10.1080/15567036.2019.1687625
- Zhang, B., and Li, S. (1995). Determination of the surface fractal dimension for porous media by mercury porosimetry. *Ind. Eng. Chem. Res.* 34, 1383–1386. doi:10.1021/ie00043a044
- Zhang, B., Liu, W., and Liu, X. (2006). Scale-dependent nature of the surface fractal dimension for bi- and multi-disperse porous solids by mercury porosimetry. *Appl. Surf. Sci.* 253, 1349–1355. doi:10.1016/j.apsusc.2006.02.009
- Zhang, W. K., Shi, Z. J., Tian, Y. M., Xie, D., and Li, W. J. (2021). The combination of high-pressure mercury injection and rate-controlled mercury injection to characterize the pore-throat structure in tight sandstone reservoirs. *Fault-Block Oil Gas. Field* 28, 14–20.



OPEN ACCESS

EDITED BY

Fuyong Wang,
China University of Petroleum, Beijing,
China

REVIEWED BY

Wenchao Liu,
University of Science and Technology
Beijing, China
Junjian Li,
China University of Petroleum, Beijing,
China

*CORRESPONDENCE

Detang Lu,
✉ dtlu@ustc.edu.cn

SPECIALTY SECTION

This article was submitted to Advanced
Clean Fuel Technologies,
a section of the journal
Frontiers in Energy Research

RECEIVED 23 November 2022

ACCEPTED 18 January 2023

PUBLISHED 26 January 2023

CITATION

Sun G, Li P, Du D, Song T and Lu D (2023),
Numerical simulation of in-depth profile
control for dispersed particle gel in
heterogeneous reservoirs.
Front. Energy Res. 11:1106191.
doi: 10.3389/fenrg.2023.1106191

COPYRIGHT

© 2023 Sun, Li, Du, Song and Lu. This is an
open-access article distributed under the
terms of the [Creative Commons
Attribution License \(CC BY\)](#). The use,
distribution or reproduction in other
forums is permitted, provided the original
author(s) and the copyright owner(s) are
credited and that the original publication in
this journal is cited, in accordance with
accepted academic practice. No use,
distribution or reproduction is permitted
which does not comply with these terms.

Numerical simulation of in-depth profile control for dispersed particle gel in heterogeneous reservoirs

Gang Sun¹, Peichao Li², Dongyuan Du³, Ting Song³ and Detang Lu^{1*}

¹Department of Modern Mechanics, University of Science and Technology of China, Hefei, China, ²School of Mechanical and Automotive Engineering, Shanghai University of Engineering Science, Shanghai, China, ³Shengli Oilfield Kangbei Petroleum Engineering Equipment Co., Ltd., Dongying, China

Introduction: As a new agent of enhancing oil recovery, the dispersed particle gel (DPG) has been gradually used for in-depth profile control in mature oilfields. Many researchers investigated the preparation, profile control mechanism and application of DPG based on a series of laboratory experiments. However, few numerical studies have been carried out on profile control mechanism of DPG.

Methods: This paper proposes a novel mathematical model to proceed numerical simulation of profile control for DPG, considering DPG particles adsorption and weak shear thinning effects. The numerical codes are verified by the UTCHEM simulator.

Results and discussion: The effects of the DPG viscosity, the DPG concentration, the water saturation of high permeable regions and the permeability ratio between high and low permeable regions on decreasing the water-cut of producing well are studied. Simultaneously, this paper also investigates the influence of different mobility ratios between high and low permeable regions on water shutoff of DPG. The numerical simulation results show that the effects of DPG profile control become better as the DPG solution viscosity, the suspension concentration and the permeability ratio increase. But the increased water saturation of high permeable regions is not helpful to improve oil recovery. Water plugging effect of DPG becomes worse with increasing mobility ratio between different regions. According to comparison results between DPG profile control and polymer flooding, it is found that DPG profile control is more suitable for heterogeneous reservoirs. These findings are of benefit to guide the efficient field application of DPG profile control in heterogeneous reservoirs.

KEYWORDS

dispersed particle gel, in-depth profile control, numerical simulation, heterogeneous reservoirs, a new agent

1 Introduction

At present, the major oil fields in China have come into high water-cut period after long-term water flooding exploitation. The water content of production wells in mature oil fields is generally above 90%. The injected water can easily reach production wells along channels or fractures in high permeable zones, making it more and more difficult to increase production by water injection (Ju et al., 2008; Deolarte et al., 2009; Li et al., 2016). As a result, there is a lot of residual oil in low permeable zones which cannot be displaced out by continued water flooding. According to statistics, conventional water flooding usually produces only one-third to two-fifths of the oil in geological reserves (Ji et al., 2012).

The main means of decreasing water production in mature oil fields is to improve oil recovery by replacing water flooding with new oil field development techniques, such as chemical flooding (Al-Muntasheri et al., 2007; Dai et al., 2014a; Dabiri and Honarvar, 2020). Enlarging swept volume and increasing displacement efficiency are two key approaches to enhance oil recovery by chemical flooding. Compared with increasing displacement efficiency, expanding swept volume is a better choice on the basis of field practice of oil fields in heterogeneous reservoirs. In order to decrease water-cut by means of expanding swept volume, various chemical methods were adopted, including conventional polymer flooding, foam flooding (Moosavi et al., 2019), *in situ* gel systems and particles gel systems (Moradi-Araghi, 2000; Perez et al., 2001; Wassmuth et al., 2007; Beverte, 2014). However, polymer flooding is unsuitable especially in highly heterogeneous reservoirs by reason of bad water shutoff effect and weak conformance control capacity. The foam flooding is difficult to sustain for a long time because of its very short timeliness. In order to obtain good foam flooding effect, stable and continuous nitrogen or air resources are required, which increases the cost of profile control treatments. *In situ* gel systems are easily affected by shear rate, extreme formation conditions and some other factors (Seright et al., 2003; McCool et al., 2009). Meanwhile, these gel systems have inherent drawbacks, such as uncontrollable swollen gel strength, uncontrollable gelation time and dilution caused by contact with formation fluids.

In order to overcome the above-mentioned problems, particles gel systems had been popularized and applied. Among them, micro gel (Chauveteau et al., 2001; Bybee, 2005; Zaitoun et al., 2007), preformed particle gel (Bai et al., 2007a; Bai et al., 2007b; Wang et al., 2013) and dispersed particle gel (Dai et al., 2012) are the most commonly used for profile control and water shutoff. The micro gel is not suitable for large-scale oilfield production due to lower displacement efficiency and higher cost. The particle size of preformed particle gel is mainly millimeter scale, making it more difficult to inject PPG particles into low permeable reservoirs, which limits the range of PPG application. Compared with first two particles gel systems, the dispersed particle gel (DPG) has the advantages of easy injection, easy preparation and meeting the needs of large-scale industrial production. As a new profile control agent for water shutoff treatments and enhancing oil recovery, previous studies are mainly focused on DPG particles preparation (You et al., 2011; Dai et al., 2012; Zhao et al., 2013), DPG profile control mechanism (Zhao et al., 2014; Liu et al., 2016) and experiments to explore the properties of DPG (You et al., 2013; You et al., 2014; Dai et al., 2017). It rarely involves numerical simulation of DPG conformance control. Based on experimental results of DPG physical properties, this paper proposes a novel mathematical model considering DPG particles adsorption and weak shear thinning. First, we investigate the influences of the DPG viscosity, the DPG concentration, the water saturation of high permeable regions and the permeability ratio between different regions on improving oil recovery by numerical simulation. Second, the effects of different mobility ratios of flowing through the high and low permeable regions on water plugging in the high permeable zones are studied. Finally, the differences of decreasing water-cut between polymer flooding and DPG flooding are compared. These numerical simulation results can ultimately

provide scientific basis and technical support for DPG formulation design and field application.

2 Preparation of DPG particles

2.1 Typical morphology of DPG particles

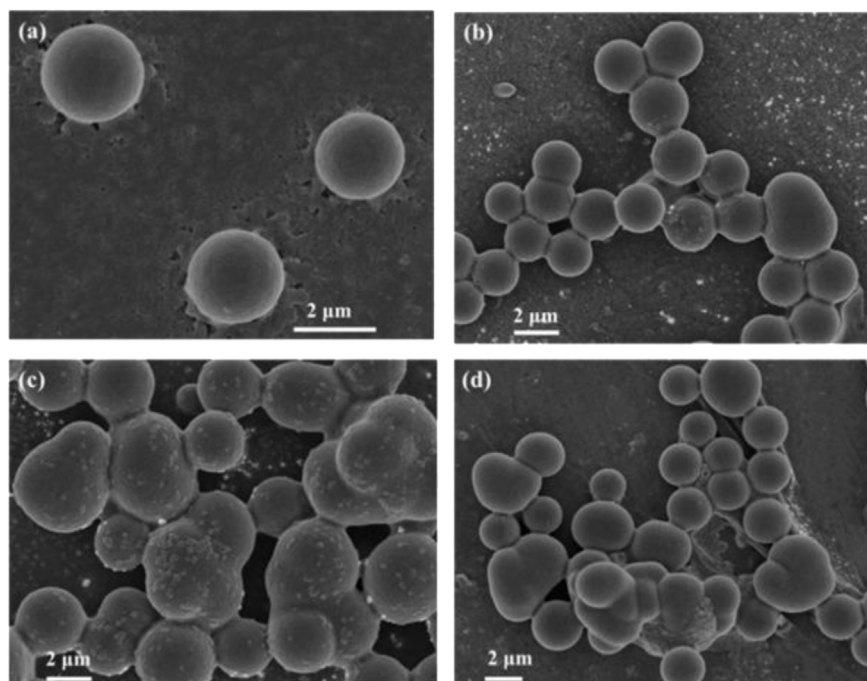
DPG is prepared with polymer and cross-linker, which can swell up to 30 times its beginning size in brine. DPG is a particle system formed by the mechanical shearing of the dried gel on the ground. Swollen gel strength and particle size are controllable, overcoming some distinct drawbacks of *in situ* gel systems. And as a new profile control agent, DPG is environmentally friendly, and not sensitive to reservoir minerals and formation brine (Dai et al., 2014b). With mechanical shearing for 6 min, the DPG particles are prepared on the shearing equipment. The microstructure of prepared DPG particles is observed by scanning electron microscope (SEM), which is shown in Figure 1.

It can be seen from Figure 1 that the DPG solution is composed of regular pseudo spheres particles. When the DPG solution is prepared with high salinity produced water and aged at 90°C for 5 days, 10 days, and 15 days respectively, SEM is used to study the microscopic morphology of DPG particles. Figure 1 reveals the microscopic morphology of DPG particles before and after aging at high temperature. Scanning electron micrographs show that the DPG solution is uniformly distributed as a single particle before aging, and single DPG particle size is mainly dispersed between 1.8 and 2.2 μm . After 5 days aging under high salinity and temperature conditions, the size of the individual particle begins to be bigger and the shape tends to be irregular, and the expansion of DPG particles is limited, which enables the particles to maintain a high strength; when the DPG is further aging, the particles aggregates with each other, forming larger DPG particle aggregates. After aging for 30 days, the aggregates size can be up to 20 μm . When the DPG begins to age at high temperature, the presence of electrolytes and high temperature accelerates particles aggregation. Because the surface of DPG particles is negatively charged, and high salinity water contains a high concentration of ions, there will be more ions in the adsorption layer so as to reduce or even completely neutralize the charge on the DPG particles surface, which decreases mutual repulsive force between particles. This is the main reason for the increase of particle size.

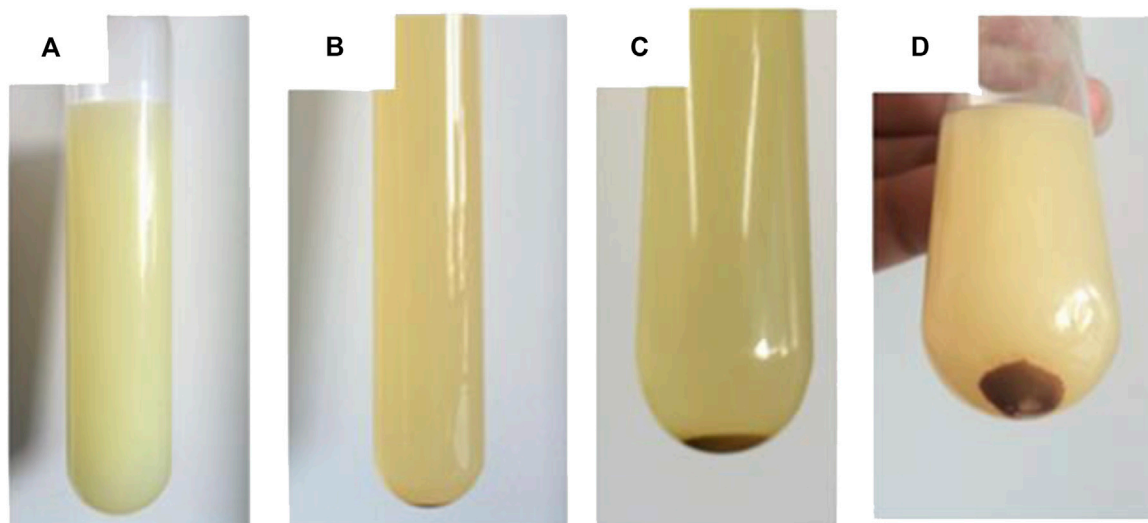
The macroscopic pictures of DPG solution before and after aging are showed in Figure 2. As we can see, no degradation or dehydration occurs in the DPG solution after ageing in Figure 2, which shows DPG good temperature and salt resistance. These properties of DPG are beneficial to the effective profile control of high permeable zones. When pore throat radius is small, a single particle can swell to implement water shutoff; when pore throat radius is large, multiple particles will form a larger particle aggregation and achieve conformance control of high water-cut reservoir.

2.2 Properties of DPG viscosity

Figure 3A points out that the viscosity of the gel system increases as the DPG concentration increases. This is because the DPG particles will clump together when the number of DPG particles increases, and free movement of particles becomes difficult with the increase of

**FIGURE 1**

Microscopic morphology of DPG: (A) Initial state; (B) aging for 5 days; (C) aging for 15 days; (D) aging for 30 days.

**FIGURE 2**

Macroscopic morphology of DPG: (A) Initial state; (B) aging for 5 days; (C) aging for 15 days; (D) aging for 30 days.

interaction force between particles, resulting in a big increase in the viscosity of the gel system. But the increase in polymer viscosity is mainly due to the random entanglement of groups of the polymer. Bond strength between polymer groups is very weak. Therefore, the viscosity of polymer solution at the same concentration is lower than that of DPG.

Conventional polymer used for enhancing oil recovery is affected by shear of ground injection equipment and underground percolation.

As shown in Figure 3B, the viscosity of polymer can be reduced by more than 50% after 20 min of ground equipment shearing. So the shear thinning effect should be considered in the numerical simulation model of polymer flooding. In other words, the shear resistance of polymer is poor, and most injected water easily reaches production wells along high permeable regions when implementing polymer flooding in heterogeneous reservoirs. In view of shear thinning, the shear resistance of DPG is investigated by comparing with polymer. At

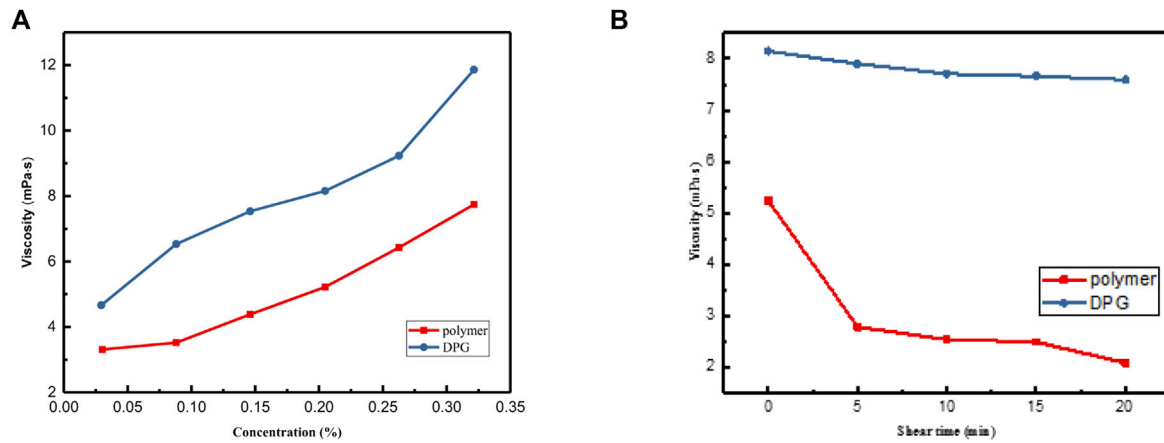


FIGURE 3

The comparison of polymer and DPG: (A) viscosity-concentration curve; (B) viscosity versus shear time.

room temperature, shearing equipment is respectively used to DPG particles and conventional polymer shear at 1,000 rpm for 5 min, 10 min, 15 min, and 20 min. The corresponding viscosity is measured at 30°C, and both of them have a mass concentration of 0.2%. Figure 3B illustrates that the viscosity of polymer decreases sharply with the increase of shear time, however the viscosity of DPG decreases slightly with increasing shear time. DPG solution is a stable system formed by the high viscoelasticity body gels with high-speed mechanical shear, which can still maintain effective viscosity after a period of shearing. So it is necessary to take shear resistance effect into account and it can be approximated that the viscosity of DPG is constant, when the mathematical model of DPG profile control is proposed.

3 Mathematical model

3.1 Model assumptions

For simplicity DPG in conformance control, the main assumptions are as follows: 1) The process of DPG profile control is isothermal and energy exchange is negligible in the reservoirs; 2) the extended Darcy's law applies when fluid flows through porous medium; 3) the fluid underground only contains two phases: The water phase and the oil phase, and the water phase contains three components: pure water, DPG particles and salt; 4) the process of DPG particles adsorption is irreversible; 5) no chemical reaction takes place; 6) diffusion and dispersion for DPG particles are negligible.

3.2 Governing equations

Using the above assumptions, mass balance equations are given for each component. Considering the physicochemical phenomena including weak shear thinning effect, permeability reduction, DPG particles adsorption and dead pore volume, the basic equations of the DPG profile control model are as follows:

Continuity equation for oil component:

$$\nabla \cdot \left[\frac{KK_{ro}}{\mu_o B_o} (\nabla p_o - \gamma_o \nabla D) \right] + q_o = \frac{\partial}{\partial t} \left[\frac{\phi S_o}{B_o} \right] \quad (1)$$

Continuity equation for water component:

$$\nabla \cdot \left[\frac{KK_{rw}}{\mu_w B_w} (\nabla p_w - \gamma_w \nabla D) \right] + q_w = \frac{\partial}{\partial t} \left[\frac{\phi S_w}{B_w} \right] \quad (2)$$

Continuity equation for DPG particles component:

$$\nabla \cdot \left[\frac{KK_{rw}}{R_k \mu_w B_w} (\nabla p_w - \gamma_w \nabla D) C_m \right] + q_m = \frac{\partial}{\partial t} \left[\frac{\phi (S_w C_m + C_{m,ads})}{B_w} \right] \quad (3)$$

Well flow equations for multiphase flow:

$$q_{sc,l} = \frac{2\pi K K_{rl}}{\mu_l B_l [\ln(r_e/r_w) + s]} (p_e - p_{wf}) \quad (4)$$

where p is the pressure, Pa; K is the absolute permeability, m^2 ; K_r is the relative permeability, dimensionless; C_m is the concentration of DPG particles in the water phase, kg/m^3 ; $C_{m,ads}$ is the concentration of DPG adsorbing on pore throat surface, kg/m^3 ; γ is the gravity factor, N/m^3 ; μ is the viscosity, Pa.s; D is the depth, m; q is the flow rate, m^3/s ; t is the time, s; ϕ is the porosity, dimensionless; B is the formation volume factor, dimensionless; r_w is the wellbore radius, m; r_e is the effective radius, m; s is the skin factor, dimensionless; subscript l represents the liquid phase, $l = o, w$, o represents oil, w represents water; subscript m is the DPG component.

3.3 Auxiliary equations

Constrained condition of saturation:

$$s_o + s_w = 1 \quad (5)$$

Constrained condition of capillary force:

$$p_{cow} = p_o - p_w = p_c(S_w, \sigma_{wo}) \quad (6)$$

Based on the capillary force function (J function), the capillary force (Qin and Li, 2003):

$$p_{cow} = J(s_w) \sigma_{wo} \cos \theta \sqrt{\frac{\phi}{k}} \quad (7)$$

where p_{cow} is the capillary pressure between water and oil, Pa; $J(s_w)$ is the Leverett J-function; σ_{wo} is interface tension between water and oil, N/m; θ is the wetting angle.

3.4 Adsorption term treatment of DPG particles

DPG particles flowing through the reservoir can interact with the rock surface, which causes DPG particles to bind to the surface of the rock, reducing DPG concentration in the aqueous phase. In the process of numerical simulation, empirical formula calculation and data table interpolation are given to determine the DPG adsorption concentration.

(1) Formula method:

The amount of DPG particles adsorption on rock surface can be calculated by Langmuir adsorption isotherm.

$$C_{m,ads} = \min \left(C_{m,ads}^{\max}, \frac{a_p C_m}{1 + b_p C_m} \right) \quad (8)$$

where $C_{m,ads}$ is the absorption concentration of DPG particles, kg/m³; $C_{m,ads}^{\max}$ is the maximum saturation adsorption concentration of DPG particles, kg/m³; a_p and b_p are the coefficients changing with ion concentration, obtained by fitting the experimental data, dimensionless.

(2) Data table interpolation method:

According to the relationship between DPG concentration and its adsorption concentration at a certain salt concentration in related experiments, DPG adsorption concentration is attained by interpolating DPG concentration.

For both of these methods, this paper assumes that DPG particles adsorption is an irreversible process. The following steps are adopted in the actual calculation: (1) Determine the maximum adsorption concentration of DPG, which is usually given by experiments; (2) the adsorption concentration of DPG in the current time step was calculated by Langmuir isothermal adsorption equation; (3) update DPG particles adsorption concentration if it is greater than the adsorption concentration of the previous time step, the adsorption concentration remains unchanged if the adsorption concentration is less than that of the previous time step.

3.5 Discretization and linearization of governing equations

PEBI grid has the following advantages: Flexible grid division, any grid points can be arranged in place, without considering other grid points; Easy to change the shape and size of the grid, suitable for describing complex geological boundaries, tectonic faults, pinch-outs, etc. Compared with regular grid, the grid orientation effect can be reduced. The near-well area can be locally encrypted and the coarse and fine mesh is smooth, which is suitable for describing the radial flow in the near-well area. So PEBI mesh is used for division instead of corner point grid in this paper. The governing equations are discretized by finite

volume method, linearized by Taylor expansion and time term conservation form expansion, and the coefficient matrix of the equations is obtained. Finally, GMRES solver is used to solve the coefficient matrix. Since GMRES algorithm is a mature solution technique for solving large sparse matrices, this section focuses on the discretization and full implicit linearization of equations (Zha et al., 2018).

Here, we take Eq. 3 as an example and its discrete scheme is given:

$$\begin{aligned} \sum_j [T_{ij,w} C_m (\Delta p_w - \gamma_w \Delta Z)]^{n+1} &= C_{mm} \delta p + C_{mw} \delta S_w \\ &+ C_{mc} \delta C_m \\ &+ C_{ma} \delta C_{m,ads} + q_{wsc}^{n+1} \end{aligned} \quad (9)$$

In Eq. 9, the coefficients of the terms are shown below:

$$\begin{aligned} T_{ij,w} &= \left(\frac{KK_{rw}}{\mu_w B_w R_k} \right)_{ij} \cdot \frac{w_{ij}}{d_{ij}}, \\ C_{mm} &= \frac{V_i}{\Delta t} \left[\frac{1}{B_w} \frac{\partial \phi_m}{\partial p} (C_m^n S_w^n + C_{m,ads}^n) \right. \\ &\quad \left. + \phi_m^{n+1} \frac{\partial (1/B_w)}{\partial p} (C_m^n S_w^n + C_{m,ads}^n) \right], \\ C_{mw} &= \frac{V_i}{\Delta t} \left(\frac{\phi_m C_m}{B_w} \right)^{n+1}, C_{mc} \\ &= S_w^n \frac{V_i}{\Delta t} \left(\frac{\phi_m}{B_w} \right)^{n+1}, C_{ma} = \frac{V_i}{\Delta t} \left(\frac{\phi_m}{B_w} \right)^{n+1}. \end{aligned}$$

where w_{ij} is the area of interface between adjacent grids, m²; d_{ij} is the distance between the center points of adjacent grids, m; V_i is the volume of grid i , m³; n is the time step.

Fully implicit linearization of Eq. 9 is as follows:

$$\begin{aligned} \sum_j \left[T_{ij,w}^v (\delta p_j - \delta p_i + p_j^v - p_i^v - \gamma_w \Delta Z) + \left(\frac{\partial T_{ij,w} C_m}{\partial p} \right)_+^v \delta p_+ (p_j^v - p_i^v - \gamma_w \Delta Z) \right. \\ \left. + \left(\frac{\partial T_{ij,w} C_m}{\partial C_m} \right)_+^v \delta C_{m+} (p_j^v - p_i^v - \gamma_w \Delta Z) \right] \\ = C_{mm}^{v+1} (\delta p + p^v - p^n) + C_{mw}^{v+1} (\delta S_w + S_w - S_w^n) + C_{mc} (\delta C_m + C_m^v - C_m^n) \\ + C_{ma} (\delta C_{m,ads} + C_{m,ads}^v - C_{m,ads}^n) + q_{wsc}^{n+1} \end{aligned} \quad (10)$$

where v is the iterative step, the subscript $+$ is the upstream grid.

4 Verification of the model

In view of no commercial software and field data available for verification, the mathematical model for profile control of DPG is simplified without considering the shear resistance and variable viscosity after aging. The numerical results by using this simulator are compared with those of UTCHEM simulator (Kazemi Nia Korrani et al., 2015). The reservoir is a 150 m × 150 m × 10 m rectangular area with a closed boundary. There is a production well and an injection well in the area, and the distance between them is 130.5 m. The rectangular grid with 13 rows and 13 columns is adopted in UTCHEM simulator. The simulation time is 2,000 days, and the total injected pore volume is 4 PV. The injection well firstly injects water for 100 days, then injects the DPG solution for 400 days and finally injects water for 1,500 days at a constant rate of 90 m³/d, and the concentration of DPG is 20 kg/m³, and the production well lasts 2,000 days with a constant rate of

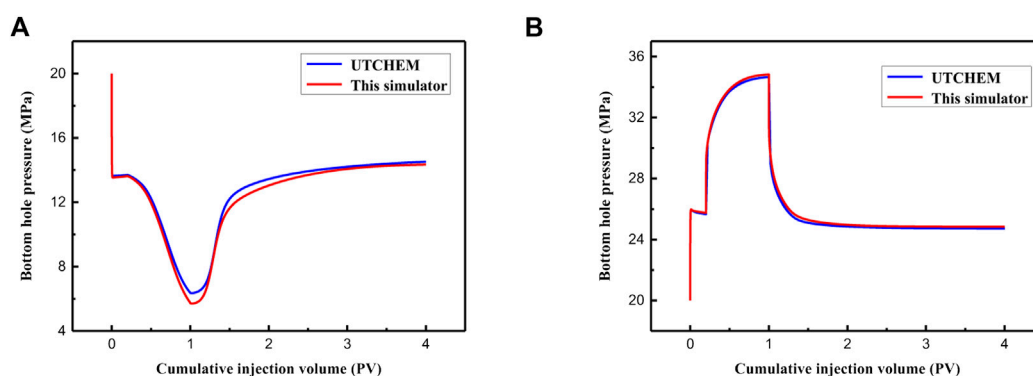


FIGURE 4
Flowing bottom hole pressure comparison: (A) Production wells; (B) injection wells.

TABLE 1 Reservoir and fluid property parameters.

Parameter	Value
Initial formation pressure, MPa	20
Formation thickness, m	10
Horizontal permeability, μm^2	0.2
Porosity	0.2
Rock compressibility, 1/MPa	0.00015
Initial water saturation	0.6
Initial DPG concentration	0
Wellbore radius, m	0.1
Viscosity of oil, Pa-s	0.004
Viscosity of water, Pa-s	0.001
Oil phase compressibility, 1/MPa	0.006
Water phase compressibility, 1/MPa	0.002

90 m^3/d at surface condition. Formation parameters for numerical simulation are listed in Table 1. Figure 4A shows that flowing bottom hole pressure of production well decreases first and then increases to reach a stable value as the volume of the injected displacement fluid increases. This is because the fluid around production well is extracted from the ground first and then the balance between injection and production is reached. It can be seen from Figure 4B that flowing bottom hole pressure of injection well increases first and then decreases to reach a stable value with the increase of the volume of the injected displacement fluid. This is due to the displacement fluid being injected into the formation and reaching an injection-production balance as it breaks through into the producing well. As shown in Figure 4A, the difference of bottom hole pressure of production wells is relatively large, which is because the bottom pressure of DPG profile control is very sensitive to the change of DPG concentration, and a small difference in DPG concentration may also lead to a big difference in pressure calculation results. The comparison results indicate that the numerical results of two simulators are similar, so the correctness of DPG profile control simulation is verified.

5 Results and discussion

5.1 Sensitivity analysis

The viscosity and concentration relationship of DPG is the key factor affecting water plugging in high permeability areas. The application of DPG can be limited by the relevant parameters of high water-containing heterogeneous layers such as water saturation and permeability ratio. In order to investigate the influences of DPG properties and reservoir conditions on water-cut reduction, a PEBI grid system ($500 \times 500 \times 5.9 \text{ m}$) is established. In the basic simulation case, there is an injection well and four production wells in the reservoir, as shown in Figure 5. The injection rates respectively are 72 m^3/d for 6 days, 48 m^3/d for 3 days, 0 m^3/d for 7 days and 60 m^3/d for 720 days; the production rates separately are 18 m^3/d for 6 days, 12 m^3/d for 3 days, 0 m^3/d for 7 days and 15 m^3/d for 720 days, every producing well produces same quantitative liquid. The DPG concentration is 1.6 kg/m^3 , the absolute permeability of high permeable layer is 4145 μm^2 , and the permeability ratio between high and low permeable regions is 8.4. The main numerical simulation parameters for sensitivity analysis are listed in Table 2.

5.1.1 DPG solution viscosity

The viscosity of DPG is an important property that determines whether it is suitable for decreasing water-cut in the process of DPG profile control. Therefore, it is necessary to investigate the impacts of the viscosity of DPG on increasing oil recovery by means of numerical simulation. In this section, a numerical example is used to study the influences of viscosity of DPG on conformance control. When the DPG viscosity is adjusted to 1, 2, 3, and 5 times that of conventional polymer at the same concentration, the water-cut of producing well 2 and the bottom hole pressure of the injection well varies.

It can be seen from Figure 6B that DPG profile control can reduce the water-cut of producing well 2 and improve oil recovery. As the viscosity of DPG increases, both the width and depth of water-cut funnel plots increase. Simultaneously, cumulative oil production of producing well 2 also increases when the viscosity of DPG increases in Figure 7. If the viscosity of DPG is too high, the bottom hole pressure of the injection well will exceed formation pressure allowable as shown in Figure 6A. In fact, bottom hole pressure of the injection well can't be very high and DPG can be easily injected into the reservoir because of

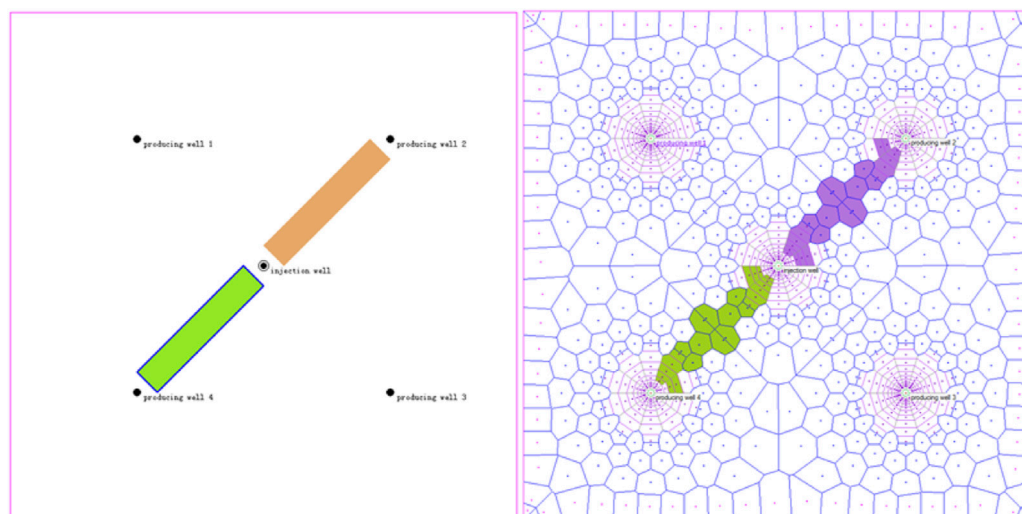


FIGURE 5
Well position and mesh generation.

TABLE 2 Reservoir and fluid property parameters.

Parameter	Value
Initial formation pressure, MPa	20
Formation thickness, m	5.9
Horizontal permeability in high permeable region, μm^2	0.4145
Horizontal permeability in low permeable region, μm^2	0.0493
Porosity	0.1665
Rock compressibility, 1/MPa	0.00015
Initial water saturation of high permeable region	0.8
Initial water saturation of low permeable region	0.5
Initial DPG concentration	0
Wellbore radius, m	0.1
Viscosity of oil, Pa-s	0.0067
Viscosity of water, Pa-s	0.00061
Oil phase compressibility, 1/MPa	0.00084
Water phase compressibility, 1/MPa	0.000449

artificial fractures or channels caused by water flooding for a long time in the reservoirs. In conclusion, considering the profile control effect and the cost of DPG, the viscosity of DPG is better to be about 2 times that of the conventional polymer.

5.1.2 DPG concentration

After a long time water flooding, a 432 cubic DPG solution is injected with the concentration of 0.5, 1.0, 1.6, 3.0 and 5.0 kg/m^3 , and then switch to water flooding for 3 days, afterwards shut down the wells for 7 days. After 15 days of DPG profile control, the reservoir begins to inject water for 720 days, the numerical results are shown in

Figure 8. It can be seen that both the width and depth of water-cut funnel increase with the increase of DPG concentration in Figure 8A. This is because that when the DPG concentration is lower, there is a smaller quantity of particles adsorbing on rock surface, and the permeability of high permeable regions decreases less, so the injected water can still channel into the producing well along the high permeable regions. The remaining oil in the low permeable regions has not been displaced out. As the DPG concentration increases, adsorption quantity in the high permeable regions increases, which improves formation heterogeneity in this way. Then, a mass of remaining oil in low permeable regions is displaced out by the sustained injection water. This is evident from Figure 8B that cumulative oil production will increase with the increase of DPG concentration.

5.1.3 Water saturation

After water flooding for a long period of time, a 432 cubic DPG solution is injected with water saturation of 0.6, 0.7, 0.8 and 0.9 in high permeable regions, and then switch to water flooding for 3 days, afterwards shut down the wells for 7 days, and the water saturation of low permeable regions keeps constant. After 15 days of DPG profile control, the reservoir begins to be injected with water for 720 days, the results are shown in Figure 9. It can be seen that both the width and depth of water-cut funnel increase, as the water saturation of high permeable regions decreases in Figure 9A. This is because the amount of DPG particles adsorbing on the rock surface decreases when water saturation increases in the high permeable regions. So the later injected water can easily channel into the producing well along the high permeable regions, which results in that the remaining oil in the low permeable regions cannot be displaced out. When the water saturation in the high permeable areas is more than 0.8, water cut funnel curve changes little and the effect of water shutoff is not obvious. As shown in Figure 9B, cumulative oil production decreases rapidly and eventually comes close to be stable with increasing water saturation in high permeable areas.

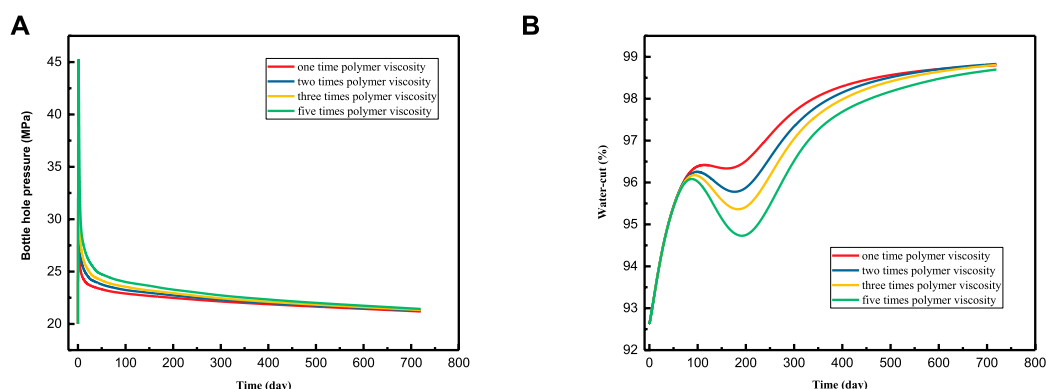


FIGURE 6

The comparison under different DPG viscosity: (A) Bottom hole pressure of injection well; (B) water-cut of production well 2.

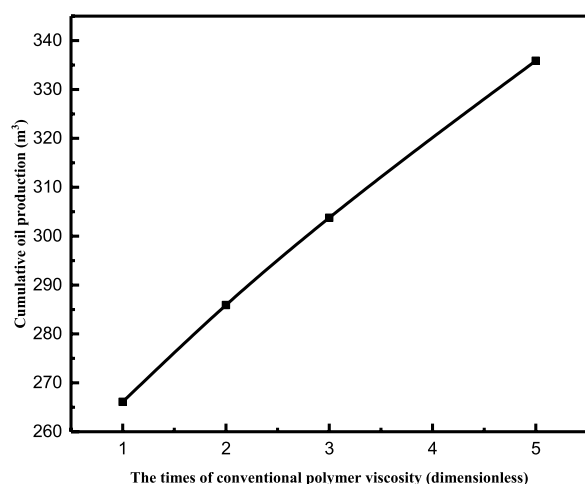


FIGURE 7

Cumulative oil production of producing well two under different DPG viscosity.

5.1.4 Permeability ratio between high and low permeable regions

First of all, we establish a series of geological models with the permeability ratio of 5, 10, 15, 20, 25 and 30 between high and low permeable regions. After a long time water flooding, a 432 cubic DPG solution is injected with the concentration of 1.6 kg/m³. After the implementation of profile control treatment, the reservoir begins to be injected with water for 240 days. Figure 10A indicates that the water-cut funnel is not obviously found, when the permeability ratio between high and low permeable regions is no more than 5; as the permeability ratio increases continuously, the water-cut funnel turns to be obvious and its depth and width increases gradually; after the permeability ratio reaches 15, the width of water-cut funnel increases slightly as permeability ratio increases. This is because that when the permeability ratio is small, the pore throat size makes a small difference between high and low permeable regions. The DPG particles can enter into different permeable regions at the same time, and the heterogeneity of

the reservoir is not well improved. Hence the DPG profile control is not suitable for reservoirs with poor heterogeneity. When the permeability ratio further increases, the difference of the pore throat size between high and low permeable regions gets bigger, and the DPG particles are easier to access to high permeable regions, which results in more particles adsorbing on pore throat surface or retention in the pore throat. As may be seen from Figure 10B, cumulative oil production increases with the increase of permeability ratio between high and low permeable areas. The cumulative oil production tends to be stable when the permeability ratio is more than 25. Because of the limit of maximum adsorption concentration, some extra DPG particles will enter into low permeable regions, which affects enhancing oil recovery. Therefore, it is very important to decide whether or not to implement DPG profile control in consideration of the actual conditions of the reservoirs.

5.2 The influence of the mobility ratio on water shutoff

In addition to the above DPG solution viscosity, DPG concentration, water saturation of high permeable regions and permeability ratio between high and low permeable regions, there are other factors affecting the water shutoff effect of DPG profile control. In order to further understand the water plugging principle of DPG, the following numerical simulation examples are given.

In this section, a 500 × 500 × 5.9 m single-layer heterogeneous reservoir is studied. The green and brown areas are high permeable areas and the other white areas are low permeable areas. There is a five-point well pattern with one injection well and four producing wells, and the brown high permeable zone is closer to the injection well, as shown in the Figure 11 below. The injection well is firstly injected with the DPG for 6 days and then the water for 3 days at a constant rate of 72 m³/d, and the concentration of DPG is 1.6 kg/m³, and the four production wells last 9 days with a constant rate of 18 m³/d at surface condition. The main numerical simulation parameters are the same as the sensitivity analysis example.

In order to reveal effective factors of water shutoff, the mobility ratio between the high and low permeability zones is adjusted in the process of numerical simulation. The following Figure 12 show the

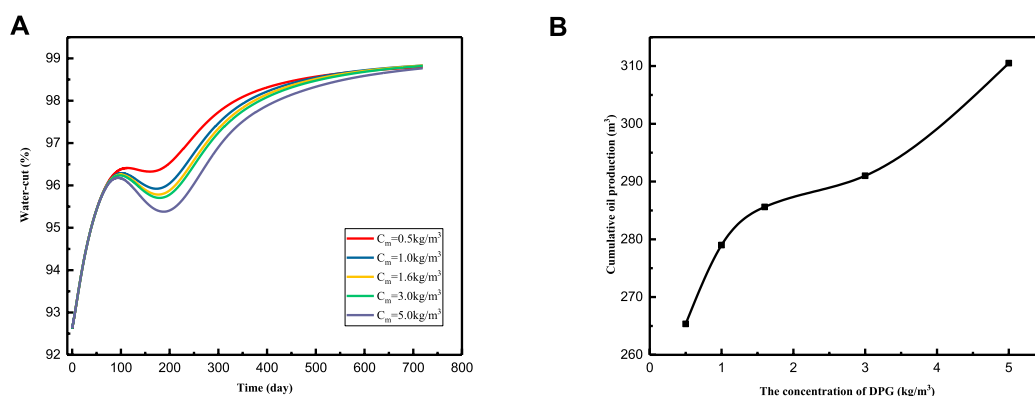


FIGURE 8

The comparison under different DPG concentrations: (A) Water-cut of producing well 2; (B) cumulative oil production of producing well 2.

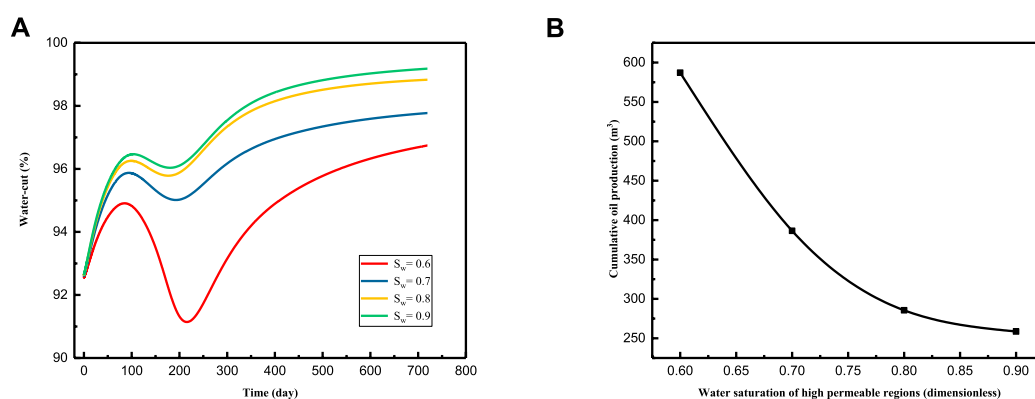


FIGURE 9

The comparison under different water saturation: (A) Water-cut of production well 2; (B) cumulative oil production of producing well 2.

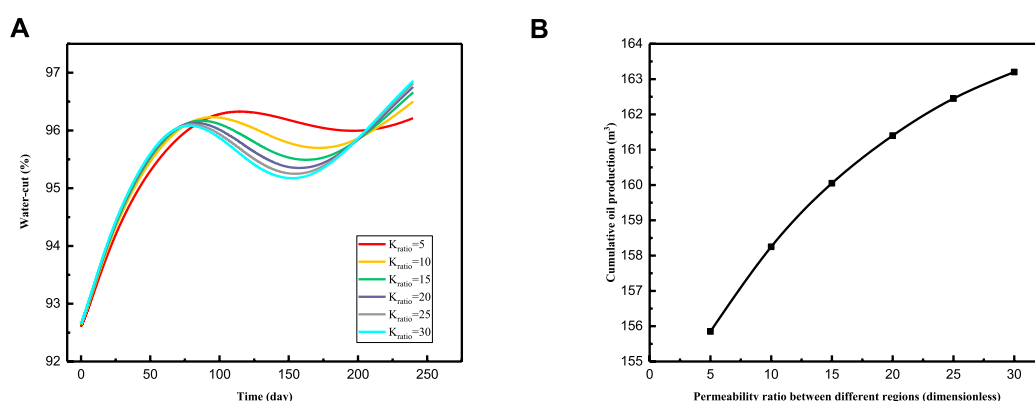


FIGURE 10

The comparison under different permeability ratios: (A) Water-cut of production well 2; (B) cumulative oil production of production well 2.

distribution of DPG concentration after profile control for 9 days when the mobility ratios are 24 and 84 respectively. As can be seen from the figures below, the DPG concentration closer to the injection well in the high permeability zones is lower than that

in other high permeability zones, so the injected water is easier break through the DPG sealing zones closer to the injection well. When the mobility ratio is relatively high, it is more unfavorable to water plugging, as shown in Figure 12B.

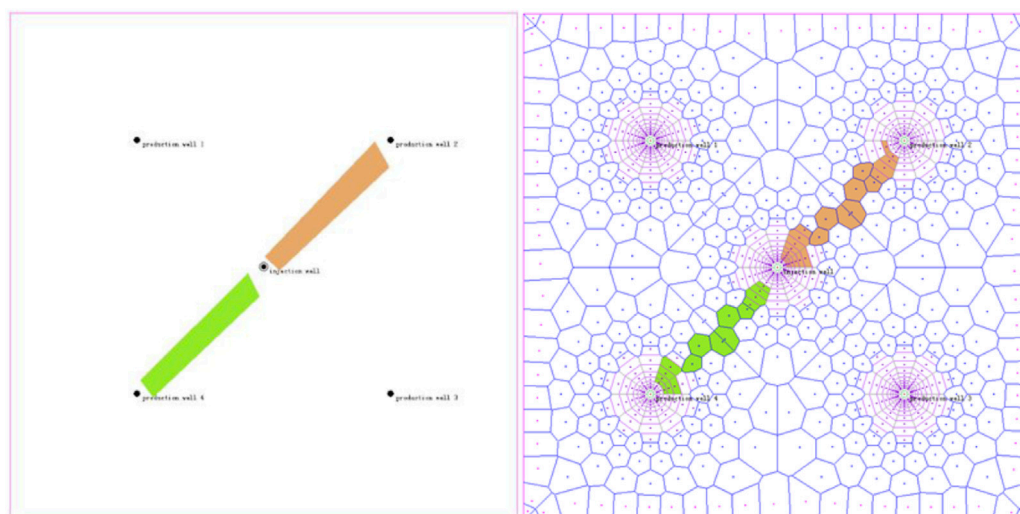


FIGURE 11
Well position chart and mesh generation.

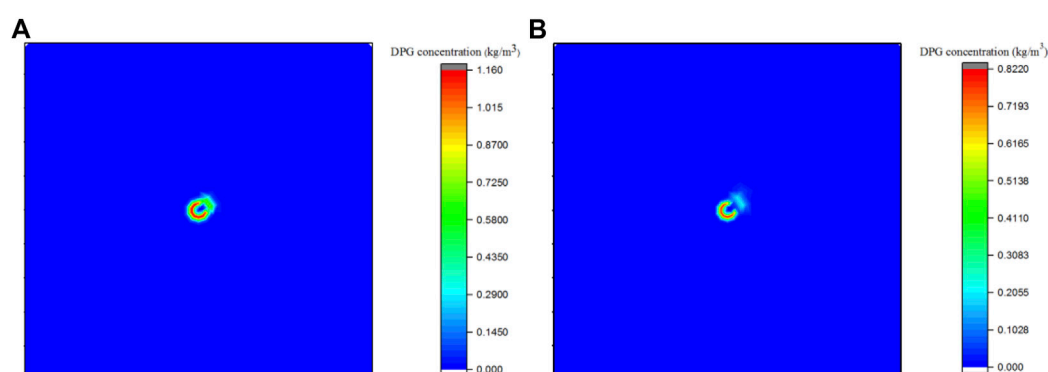


FIGURE 12
The distribution of DPG concentration comparison after 9 days: (A) When the mobility ratio is 24; (B) when the mobility ratio is 84.

5.3 Comparison between DPG profile control and polymer flooding

After a long time water flooding in mature oil fields, the reservoir has high permeable channels or fractures, and the injected water can easily enter into the producing well along high permeable regions, if we continue to apply water flooding treatment. In order to displace out remaining oil in low permeable regions, polymer flooding has been widely used in high water-cut oil fields. Polymer flooding does not significantly increase oil production when the permeability ratio of high permeability zones to low permeability zones increases. But the effect of DPG profile control becomes better, as the permeability ratio between high and low permeable regions increases. In order to clarify the difference between DPG profile control and polymer flooding in heterogeneous reservoirs, a series of geological models with the permeability ratios of 5, 10, 15, and 20 between high and low permeable regions are investigated. A 432 cubic DPG solution is

injected with the concentration of 1.6 kg/m^3 , and then switch to water flooding for 3 days, afterwards shut down the wells for 7 days. After 15 days of DPG profile control, the reservoir begins to be injected with water for 240 days. The following operation of polymer flooding is the same as that of DPG profile control except displacement fluid, the comparison results are seen in Figure 13. From Figure 13A, the water-cut reduction effect of polymer flooding becomes worse, when the permeability ratio between high and low permeable regions increases. This is because that polymer is easier to channel into the production well along the high permeable zones, leading to less oil displaced out in low permeable areas, as the permeability ratio increases. In comparison with polymer flooding, there is more obvious water-cut reduction funnel for DPG profile control with the increase of permeability ratio. This is because polymer flooding cannot effectively plug water in high water cut areas when the permeability ratio increases. Cumulative oil production for polymer flooding will decrease by degrees as permeability ratio

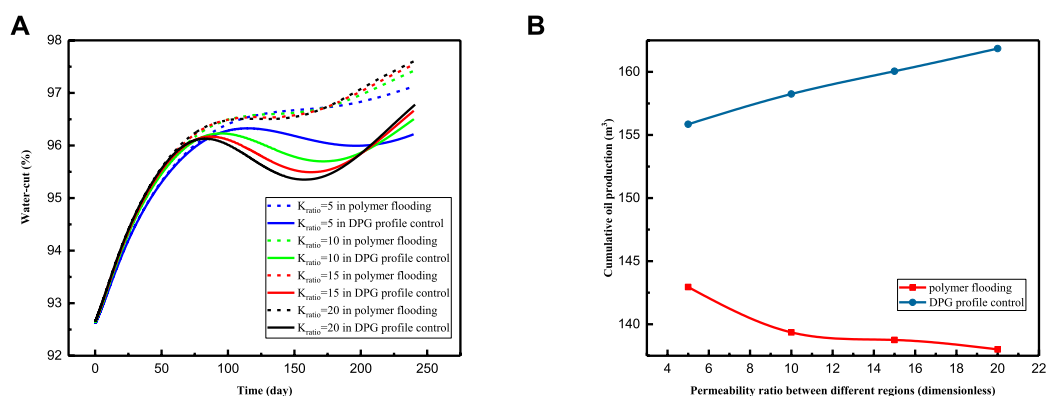


FIGURE 13

The comparison between polymer flooding and DPG profile control: (A) Water-cut comparison of production well 2; (B) cumulative oil production comparison of producing well.

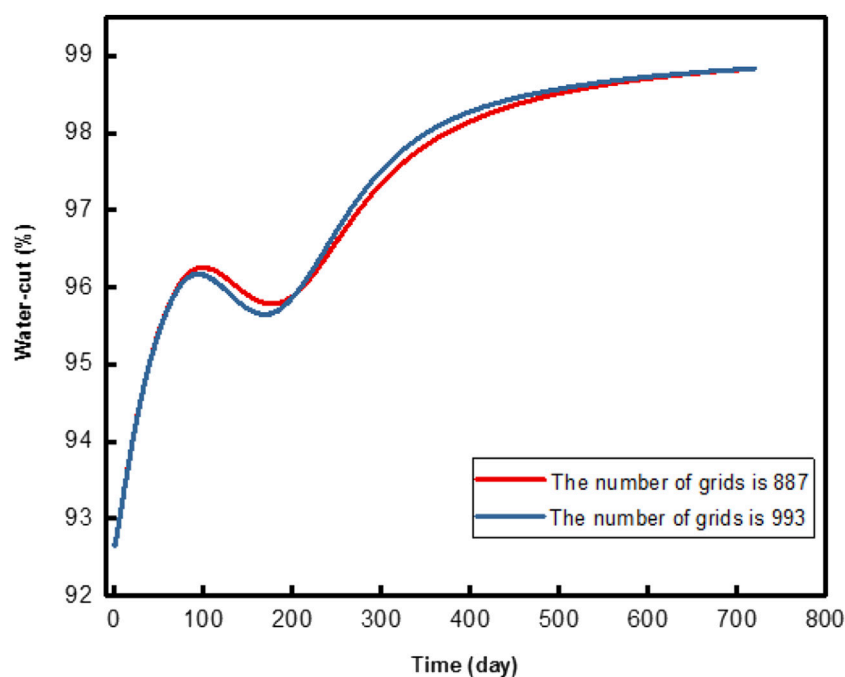


FIGURE 14

Water-cut of producing well 2 under different number of grids.

between high and low permeable areas increases. However, DPG profile control comes to the opposite conclusion in Figure 13B. So the DPG profile control is more suitable for heterogeneous reservoirs than polymer flooding.

5.4 The stability of the numerical simulation

The stability of the numerical simulation largely independent on the grids is very important. Therefore, it is necessary to investigate the impacts of the number of grids on numerical simulation results. After

a long period of water flooding, a 432 cubic DPG solution is injected with water saturation of .8 in high permeable regions, and then switch to water flooding for 3 days, afterwards shut down the wells for 7 days, and the main numerical simulation parameters are the same as the sensitivity analysis example except for the number of grids. After 15 days of DPG profile control, the reservoir begins to be injected with water for 720 days, the results are shown in Figure 14. It can be seen from Figure 14 that the difference of calculated water cut in production well near high permeability areas under different grid numbers is in the range of permitted errors and does not affect the actual numerical simulation results.

6 Conclusion

This paper proposes a mathematical model of two-phase and three-component DPG conformance control considering DPG particles adsorbing on pore throat surface and weak shear thinning effect when entering into the reservoirs. The finite volume method based on unstructured PEBI grid is used to discretize the related equations, which are solved by fully implicit iteration technique. The viscosity of DPG, the concentration of DPG, the water saturation of high permeable regions, the permeability ratio between different regions and the mobility ratio between the high and low permeability zones are the key parameters which have significant impacts on profile control of DPG. Based on the numerical results, the main conclusions are summarized as follows:

- (1) As DPG solution viscosity, DPG concentration and the permeability ratio between high and low permeable regions increase, both the width and depth of water-cut funnel increase and the effect of profile control becomes better. However, both the width and depth of water-cut funnel decrease with the increase of water saturation in high permeable regions.
- (2) Considering injection well pressure, water-cut of producing well and cost of production, the effect of profile control is best when the viscosity of DPG is two times the viscosity of conventional polymer.
- (3) In this case, the appropriate DPG concentration is 1.6 kg/m^3 , DPG profile control treatment is more suitable for highly heterogeneous reservoirs than polymer flooding. And the permeability ratio between high and low permeable regions should not exceed 25 in heterogeneous reservoirs when implementing DPG profile control.
- (4) The mobility ratio between the high and low permeability zones has great influence on the water shutoff effect of DPG. As the mobility ratio increases, it is more unfavorable to water plugging in the high permeable regions.

References

- Al-Muntasheri, G. A., Nasr-El-Din, H. A., and Hussein, I. A. (2007). A rheological investigation of a high temperature organic gel used for water shut-off treatments. *J. Petroleum Sci. Eng.* 59 (1), 73–83. doi:10.1016/j.petrol.2007.02.010
- Bai, B., Li, L., Liu, Y., Liu, H., Wang, Z., and You, C. (2007a). Preformed particle gel for conformance control: Factors affecting its properties and applications. *SPE Reserv. Eval. Eng.* 10 (4), 415–422. doi:10.2118/89389-pa
- Bai, B., Liu, Y., Coste, J.-P., and Li, L. (2007b). Preformed particle gel for conformance control: Transport mechanism through porous media. *SPE Reserv. Eval. Eng.* 10 (2), 176–184. doi:10.2118/89468-pa
- Beverte, I. (2014). Determination of highly porous plastic foam structural characteristics by processing light microscopy images data. *J. Appl. Polym. Sci.* 131 (4), 39477. doi:10.1002/app.39477
- Bybee, K. (2005). Rheology and transport in porous media of new water-shutoff/conformance-control microgels. *J. Petroleum Technol.* 57 (11), 71–72. doi:10.2118/1105-0071-jpt
- Chauveteau, G., Omari, A., Tabary, R., Renard, M., Veerapen, J., and Rose, J. (2001). "New size-controlled microgels for oil production," in Proceeding of the SPE International Symposium on Oilfield Chemistry, Houston, Texas, USA, February 2001.
- Dabiri, A., and Honarvar, B. (2020). Synergic impacts of two non-ionic natural surfactants and low salinity water on interfacial tension reduction, wettability alteration and oil recovery: Experimental study on oil wet carbonate core samples. *Nat. Resour. Res.* 29 (6), 4003–4016. doi:10.1007/s11053-020-09657-9
- Dai, C., Zhao, G., Zhao, M., and You, Q. (2012). Preparation of dispersed particle gel (DPG) through a simple high speed shearing method. *Molecules* 17 (12), 14484–14489. doi:10.3390/molecules171214484
- Dai, C., Zhao, G., You, Q., and Zhao, M. (2014b). A study on environment-friendly polymer gel for water shut-off treatments in low-temperature reservoirs. *J. Appl. Polym. Sci.* 131 (8), 40154. doi:10.1002/app.40154
- Dai, C., Zhao, G., You, Q., and Zhao, M. (2014a). The investigation of a new moderate water shutoff agent: Cationic polymer and anionic polymer. *J. Appl. Polym. Sci.* 131 (3), 39462. doi:10.1002/app.39462
- Dai, C., Liu, Y., Zou, C., You, Q., Yang, S., Zhao, M., et al. (2017). Investigation on matching relationship between dispersed particle gel (DPG) and reservoir pore-throats for in-depth profile control. *Fuel* 207, 109–120. doi:10.1016/j.fuel.2017.06.076
- Deolarte, C., Vasquez, J., Soriano, J., and Santillan, A. (2009). Successful combination of an organically crosslinked polymer system and a rigid-setting material for conformance control in Mexico. *SPE Prod. Operations* 24 (4), 522–529. doi:10.2118/112411-pa
- Ji, S., Tian, C., Shi, C., Ye, J., Zhang, Z., and Fu, X. (2012). New understanding on water-oil displacement efficiency in a high water-cut stage. *Petroleum Explor. Dev.* 39 (3), 362–370. doi:10.1016/s1876-3804(12)60052-4
- Ju, B., Qiu, X., Dai, S., Fan, T., Wu, H., and Wang, X. (2008). A study to prevent bottom water from coning in heavy-oil reservoirs: Design and simulation approaches. *J. Energy Resour. Technol.* 130 (3), 033102. doi:10.1115/1.2955560

Data availability statement

The original contributions presented in the study are included in the article/supplementary material, further inquiries can be directed to the corresponding author.

Author contributions

GS, derived the mathematical model, performed the calculation analysis, drafted and revised the manuscript; PL, revised the manuscript; DD and TS, participated the discussions; DL, contributed to the new idea of the study and approved the submission.

Funding

This work was supported by the National Science and Technology Major Project of China (Grant No. 2017ZX05009005-002).

Conflict of interest

DD and TS were employed by the company of Shengli Oilfield Kangbei Petroleum Engineering Equipment Co., Ltd.

The remaining authors declare that the research was conducted in the absence of any commercial or financial relationships that could be construed as a potential conflict of interest.

Publisher's note

All claims expressed in this article are solely those of the authors and do not necessarily represent those of their affiliated organizations, or those of the publisher, the editors and the reviewers. Any product that may be evaluated in this article, or claim that may be made by its manufacturer, is not guaranteed or endorsed by the publisher.

- Kazemi Nia Korrani, A., Sepehrnoori, K., and Delshad, M. (2015). Coupling IPHreeeq with UTCHEM to model reactive flow and transport. *Comput. Geosciences* 82, 152–169. doi:10.1016/j.cageo.2015.06.004
- Li, D., Zha, W., Liu, S., Wang, L., and Lu, D. (2016). Pressure transient analysis of low permeability reservoir with pseudo threshold pressure gradient. *J. Petroleum Sci. Eng.* 147, 308–316. doi:10.1016/j.petrol.2016.05.036
- Liu, Y., Dai, C., Wang, K., Zhao, M., Gao, M., Yang, Z., et al. (2016). Investigation on preparation and profile control mechanisms of the dispersed particle gels (DPG) formed from phenol-formaldehyde cross-linked polymer gel. *Industrial Eng. Chem. Res.* 55 (22), 6284–6292. doi:10.1021/acs.iecr.6b00055
- McCool, C. S., Li, X., and Wilhite, G. P. (2009). Flow of a polyacrylamide/chromium acetate system in a long conduit. *SPE J.* 14 (1), 54–66. doi:10.2118/106059-pa
- Moosavi, S. R., Wood, D. A., Ahmadi, M. A., and Choubineh, A. (2019). ANN-based prediction of laboratory-scale performance of CO₂-foam flooding for improving oil recovery. *Nat. Resour. Res.* 28 (4), 1619–1637. doi:10.1007/s11053-019-09459-8
- Moradi-Araghi, A. (2000). A review of thermally stable gels for fluid diversion in petroleum production. *J. Petroleum Sci. Eng.* 26 (1), 1–10. doi:10.1016/s0920-4105(00)00015-2
- Perez, D., Fragachan, F. E., Barrera, A. R., and Feraud, J. P. (2001). Applications of polymer gel for establishing zonal isolations and water shutoff in carbonate formations. *SPE Drill. Complet.* 16 (3), 182–189. doi:10.2118/73196-pa
- Qin, J. S., and Li, A. F. (2003). *Physical properties of petroleum reservoir*. Qingdao: China University of Petroleum Press. (in Chinese).
- Seright, R. S., Lane, R. H., and Sydansk, R. D. (2003). A strategy for attacking excess water production. *SPE Prod. Facil.* 18 (3), 158–169. doi:10.2118/84966-pa
- Wang, J., Liu, H., Wang, Z., Xu, J., and Yuan, D. (2013). Numerical simulation of preformed particle gel flooding for enhancing oil recovery. *J. Petroleum Sci. Eng.* 112, 248–257. doi:10.1016/j.petrol.2013.11.011
- Wassmuth, F. R., Arnold, W., Green, K., and Cameron, N., 2007. Polymer flood application to improve heavy oil recovery at East Bodo. In: Proceeding of the Canadian International Petroleum Conference, Calgary, Alberta, Canada, June 2007.
- You, Q., Tang, Y., Dai, C., Shuler, P., Lu, Z., and Zhao, F., 2011. Research on a new profile control agent: Dispersed particle gel. In: Proceeding of the SPE Enhanced Oil Recovery Conference, Kuala Lumpur, Malaysia, July 2011.
- You, Q., Dai, C., Tang, Y., Guan, P., Zhao, G., and Zhao, F. (2013). Study on performance evaluation of dispersed particle gel for improved oil recovery. *J. Energy Resour. Technol.* 135 (4), 042903. doi:10.1115/1.4024119
- You, Q., Tang, Y., Dai, C., Zhao, M., and Zhao, F. (2014). A study on the morphology of a dispersed particle gel used as a profile control agent for improved oil recovery. *J. Chem.* 2014, 1–9. doi:10.1155/2014/150256
- Zaitoun, A., Tabary, R., Rousseau, D., Pichery, T. R., Nouyoux, S., Mallo, P., et al. 2007. Using microgels to shut off water in a gas storage well. In: Proceeding of the International Symposium on Oilfield Chemistry, Houston, Texas, USA, February-March 2007.
- Zha, W., Li, D., Lu, Z., and Jia, B. (2018). An equivalent single-phase flow for oil-water two-phase flow and its potential application in well test. *Adv. Geo-Energy Res.* 2 (2), 218–227. doi:10.26804/ager.2018.02.09
- Zhao, G., Dai, C., Zhao, M., You, Q., and Chen, A. (2013). Investigation of preparation and mechanisms of a dispersed particle gel formed from a polymer gel at room temperature. *Plos One* 8 (12), e82651. doi:10.1371/journal.pone.0082651
- Zhao, G., Dai, C., and Zhao, M. (2014). Investigation of the profile control mechanisms of dispersed particle gel. *Plos One* 9 (6), e100471. doi:10.1371/journal.pone.0100471



OPEN ACCESS

EDITED BY

Debin Kong,
University of Science and Technology
Beijing, China

REVIEWED BY

Daobing Wang,
Beijing Institute of Petrochemical
Technology, China
Chiyu Xie,
University of Science and Technology
Beijing, China
Dongjin Xu,
Yangtze University, China

*CORRESPONDENCE

Mingchuan Wang,
✉ wangmc.syky@sinopec.com

SPECIALTY SECTION

This article was submitted to Advanced
Clean Fuel Technologies,
a section of the journal
Frontiers in Energy Research

RECEIVED 02 January 2023

ACCEPTED 20 January 2023

PUBLISHED 13 February 2023

CITATION

Wang M, Wang R, Yuan S and Zhou F
(2023), A pore-scale study on the
dynamics of spontaneous imbibition for
heterogeneous sandstone gas reservoirs.
Front. Energy Res. 11:1135903.
doi: 10.3389/fenrg.2023.1135903

COPYRIGHT

© 2023 Wang, Wang, Yuan and Zhou. This
is an open-access article distributed under
the terms of the [Creative Commons
Attribution License \(CC BY\)](#). The use,
distribution or reproduction in other
forums is permitted, provided the original
author(s) and the copyright owner(s) are
credited and that the original publication in
this journal is cited, in accordance with
accepted academic practice. No use,
distribution or reproduction is permitted
which does not comply with these terms.

A pore-scale study on the dynamics of spontaneous imbibition for heterogeneous sandstone gas reservoirs

Mingchuan Wang^{1*}, Ran Wang¹, Shuai Yuan² and Fujian Zhou²

¹Petroleum Exploration and Production Research Institute, SINOPEC, Beijing, China, ²State Key Laboratory of Petroleum Resources and Prospecting, China University of Petroleum-Beijing, Beijing, China

The underlying mechanism for spontaneous imbibition in a water–gas system plays a significant role in hydraulic fracturing in sandstone gas reservoirs. The objective of this study is to characterize the heterogeneity of low-permeability sandstones and investigate their effect on spontaneous imbibition from the perspective of the pore scale. We selected different cores with various pore structures and heterogeneity to evaluate their impact on the dynamics of spontaneous imbibition. The heterogeneities of the cores are contributed from the clay mineral distribution and are characterized through CT scans. The results show that clay minerals have higher CT numbers than the core matrix and that micropores are predominantly distributed in clay particles rather than in the core matrix. Additionally, the water imbibition rate of micropores is larger than that of the macropores, and when the porosities are similar, the water imbibition rate is increased with decreasing permeability. Moreover, the results of 1D frequency scans show that the distribution of water at different locations in the core is governed by the distribution of clay particles. These findings can help us further understand the distribution of fracturing fluids in the heterogeneous low-permeability sandstone reservoirs.

KEYWORDS

spontaneous imbibition, heterogeneous sandstone, hydraulic fracturing, pore structure, sandstone gas reservoir

1 Introduction

Hydraulic fracturing is the most essential technology for the development of low-permeability sandstone gas reservoirs. Complex artificial fracture networks are generated by injecting large amounts of fracturing fluid into the formation at extremely high pressures. The fracturing fluid is spontaneously imbibed into the matrix pores during fracture propagation. However, the flow back efficiencies of low-permeability sandstone gas reservoirs are generally lower than 50% (Alkough and Wattenbarger, 2013). The flow back fluid mainly contributes to the fracture rather than the matrix pores. This results from the fracturing fluid imbibition which are promoted by the high capillary pressure in matrix pores, and the capillary pressure can also prevent the outflow of fracturing fluids from matrix pores. In addition, the residual fracturing fluid can lead to severe formation damage by reducing the relative gas permeability and forming aqueous phase trapping. Therefore, it is important to clarify the water distribution and spontaneous imbibition mechanism in low-permeability sandstone gas reservoirs. Numerous studies have been performed to investigate the spontaneous imbibition in the gas–water system from different perspectives, including the boundary conditions (Yang et al., 2016), permeability differences (Meng et al., 2015), initial water saturations (Li and Horne, 2001), and water block damages (Zhou et al., 2016; Zhang et al., 2019). Additionally, computed tomography (CT) scans, nuclear magnetic resonance (NMR) scans, and microfluidic models are selected as new methods to monitor the spontaneous imbibition (Bao et al., 2017; Liang

TABLE 1 Properties of the core samples.

No.	Length (mm)	Diameter (mm)	Permeability (mD)	Porosity (%)	Dry weight (g)	Depth (m)	Description
1	51.67	49.14	0.011	12.8	227.62	2,163	Mixed-layer sandstone (MLS)
2	40.26	50.05	0.288	13.9	174.23	2,168	Matrix sandstone (MS)
3	42.87	49.89	1.965	15.4	185.70	2,180	Clay-particle sandstone (CPS)

et al., 2017; Liu et al., 2017; Shen et al., 2017; Liang et al., 2018; Yuan S. et al., 2019; Liang et al., 2020). Through these microstructure characterization techniques, the water distribution in different pores can be quantified and analyzed, and thus, it can clarify the effects of different factors on spontaneous imbibition. The water distribution and flow morphology during spontaneous imbibition in cores have been depicted based on CT scans and NMR scans (Standnes, 2003; Mirzaei et al., 2016; Akbarabadi et al., 2017). Li and Horne (2001) characterized the process of spontaneous water imbibition into gas-saturated rocks, and they demonstrated a linear relationship between the imbibition rate and the gas recovery by water imbibition. They also found that the imbibition rate and the ultimate gas recovery are decreased with the initial water saturation. Dutta et al. (2014) investigated the spontaneous imbibition in the low-permeability Berea sandstones by using CT scans. They show that the water saturation distribution along the length of the rock sample is changed with imbibition time, and they indicate that the heterogeneity of these samples plays an important role in the spreading and final saturation of the imbibition front. There is a linear relationship between the imbibed volume and the square root of imbibition time, but during the later period of imbibition, the imbibed water volume is not proportional to the square root of imbibition time (Washburn, 1921; Handy, 1960; Li and Horne, 2001).

The previous studies mostly focused on the spontaneous imbibition in homogenous core samples. There are a few studies to comprehensively consider the difference in the pore structure caused by heterogeneity of cores and its effects on the spontaneous imbibition. Also, the water distribution in heterogeneous cores and the effects of clay mineral distribution on the heterogeneity of spontaneous imbibition are still not clear.

In this study, three core samples with different clay mineral distribution patterns are selected to investigate the spontaneous imbibition in the heterogeneous sandstones. The clay mineral distribution and heterogeneity of core samples are characterized through CT scans. NMR scans are used to monitor the changes of water distribution in different pores. The relationship between the clay mineral distribution and water saturation is established based on the results of CT scans and NMR scans. This study has a great significance in further understanding the water distribution in the formation matrix and the mechanism of spontaneous imbibition in tight gas reservoirs.

2 Methodology

2.1 Experimental materials

Three core samples were obtained from the same well in a low-permeable sandstone gas reservoir in the Ordos Basin of the Changqing Field in China. These core samples were carefully drilled from the different depths. The basic properties of the core

samples were analyzed using the Chinese petroleum industry standard (Table 1). All core samples were completely cleaned using the Soxhlet extraction device with petroleum ether and methanol. The mineral compositions of core samples are listed in Table 2. The core samples mainly consist of quartz and feldspar, and the main clay minerals are illite, kaolinite, and chlorite. According to the different distribution patterns of the clay mineral, the three core samples are distinguished and called the mixed-layer sandstone (MLS), matrix sandstone (MS), and clay-particle sandstone (CPS). The pictures of the core samples from different views are shown in Figure 1. To avoid permeability damage from clay swelling, 2 wt% KCl was selected as the aqueous phase to perform the spontaneous imbibition experiments in this study. Before conducting experiments, all core samples were dried at the temperature of 105°C until their weights were constant. The contact angles of core samples were measured using the sessile drop method. Also, the contact angles range from 10° to 20°, which indicates that the core samples are all strongly water-wet.

2.2 CT scans

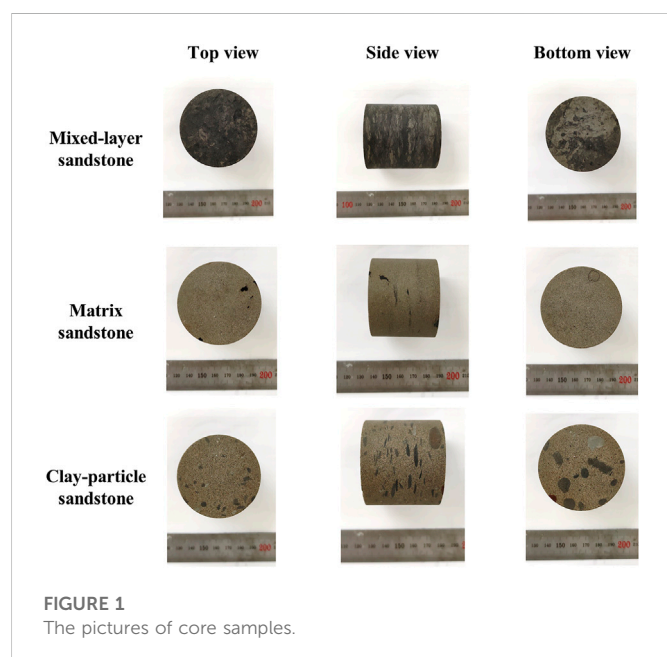
A CT scan is an effective method to investigate the mineral distributions and internal structures of the core samples. Due to the density difference, the CT number is different for different minerals. Therefore, a GE Brivo 385 CT scanner is used to characterize the heterogeneity due to clay mineral distribution. Helical scans are set on 120 kV and 140 mA with a rotation time of 1 s and a slice thickness of 0.625 mm. Then, these data were analyzed using Avizo 2019 software. The data processing procedures mainly include the following steps: 1) Data of CT scans are loaded through Avizo software; 2) the interactive threshold module is selected to separate the clay minerals and core matrix with appropriate threshold value; 3) the label analysis module is selected to analyze the properties of clay minerals, including space coordinates, areas, and volumes; 4) the volume-rendering module is used to display the clay mineral distribution in the 3D view.

2.3 NMR scans

NMR relaxation is a rapid and non-destructive tool to study the water distribution in the porous medium. The water-molecule relaxation time (T_2) in the magnetic field can be divided into bulk relaxation time ($T_{2,bulk}$), surface relaxation time ($T_{2,surface}$), and diffusion relaxation time ($T_{2,diffusion}$) as the water molecules in the porous media are confined in the pores due to the capillary and adsorptive force. This will result in less contributions of $T_{2,bulk}$ and $T_{2,diffusion}$ to T_2 . Therefore, T_2 of water molecules can be described by Eq. 1:

TABLE 2 Mineral compositions of the core samples.

No.	Quartz (%)	Feldspar (%)	Siderite (%)	Anhydrite (%)	Dolomite (g)	Clay minerals (%)
1	47.9	14.9	0.8	—	3.2	33.2
2	63.6	20.1	0.8	2.6	—	12.9
3	63.1	18.9	—	—	—	18.0

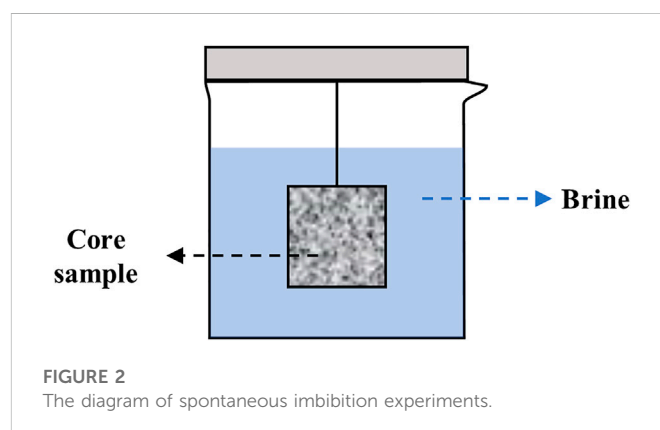


$$\frac{1}{T_2} = \frac{1}{T_{2,surface}} + \frac{1}{T_{2,bulk}} + \frac{1}{T_{2,diffusion}} \approx \rho \frac{S}{V}, \quad (1)$$

where S (μm^2) and V (μm^3) are the pore surface area and pore volume, respectively, and ρ ($\mu\text{m/s}$) is the surface relaxivity (Lai et al., 2016). For a specific core, its surface reflectivity can be assumed to be constant. Therefore, T_2 can be converted into the pore radius using the following equation:

$$T_2 = \frac{1}{\rho F_s} r = Cr, \quad (2)$$

where F_s is a function of the dimensionless shape factor of a pore, which is equal to S/V ; C is the constant conversion coefficient ($\text{ms}/\mu\text{m}$). On the basis of Eqs 1, 2, it is found that T_2 has a linear relationship with the pore radius (Wei et al., 2020). Therefore, the T_2 value is increased with the pore radius. To obtain the water distribution along the length of cores, 1D frequency scanning is selected by collecting and calculating the signals in different positions. The T_2 distributions and 1D frequency scans of different core samples are measured using a MacroMR12-150H-I NMR spectrometer (NIUMAG, Shanghai, China). The T_2 measurements are conducted based on the Carr–Purcell–Meiboom–Gill (CPMG) sequence, and 1D frequency scans are conducted by using the GR-HSE sequence



(Liu and Sheng 2020). The water saturations of different positions are calculated with Eq. 2

$$S_w = \frac{\sum A_{im}}{\sum A_w}, \quad (3)$$

where S_w is the water saturation of a certain length of cores; A_{im} is the amplitude of spontaneous imbibition experiments at a certain position; and A_w , the amplitude of the water-saturated condition at a certain position. All measurements are conducted at an ambient temperature (25°C). The field frequency is 12.448 MHz. The magnetic field intensity is 0.3T. The polarization times, scanning times, and echo numbers for T_2 scans and 1D frequency scans are 3,000 ms, 16, and 18,000, respectively. The echo spacings for T_2 scans and 1D frequency scans are 0.2 ms and 1.2 ms, respectively.

2.4 Spontaneous imbibition experiments

The spontaneous imbibition experiments are performed through the following steps: 1) After drying them to a constant weight, the core samples are weighted to obtain their dry weight. 2) The core samples are immersed in brine as shown in Figure 2. The boundary condition is considered an all-face open (AFO) condition. 3) The core samples are taken out from brine at a certain time interval and the NMR scans are conducted, including T_2 scans and 1D frequency scans. In addition, the current weights of core samples are recorded. The spontaneous imbibition experiments are completed until the peak areas of T_2 spectra and the weights of the core samples have changed by less than 1%. To obtain the T_2 spectra of the core samples saturated with brine, the core samples are dried and vacuum saturated with brine under a pressure of 10 MPa for 48 h after the spontaneous imbibition experiments are completed. Then, the same scanning sequence and procedures are performed again.

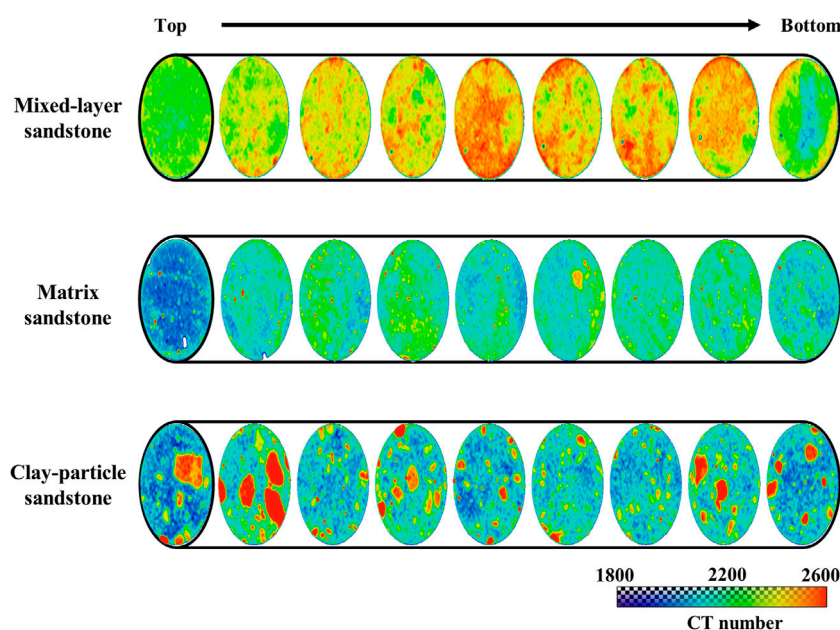


FIGURE 3
CT scanning slices in different positions for different cores.

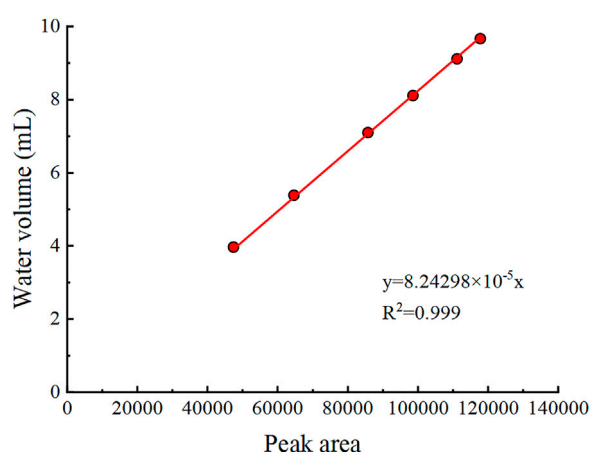


FIGURE 4
Standard curve between peak area and water volume.

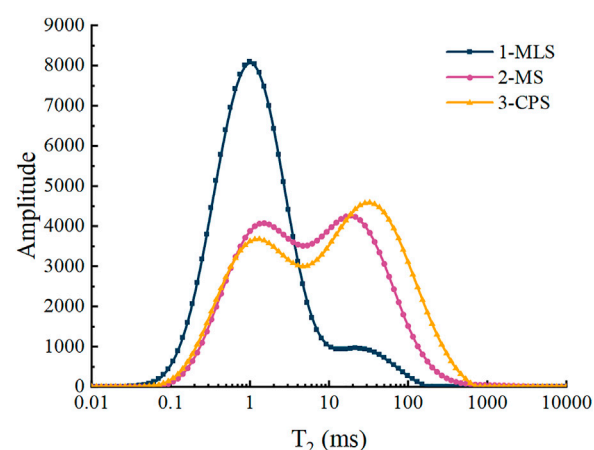


FIGURE 5
 T_2 spectrums for water-saturated cores.

3 Results and discussion

3.1 Heterogeneity characterization

The CT scanning images along the core samples are shown in Figure 3. The slice interval of CT scans for MLS, MS, and CPS are 6.459 mm, 5.033 mm, and 5.359 mm, respectively. There are notable differences among different the core samples. For the mixed-layer sandstone, there is a large area of high CT number in each scanning slice, which corresponds with the area of high clay-mineral content. The clay minerals are associated with other minerals such as quartz, feldspar, and dolomite, and this leads to high CT numbers in these areas. Additionally, the mixed-layer regions have CT numbers

ranging from 2,300 to 2,600. This indicates that the distribution of clay minerals in MLS is not uniform, and this may have effects on the heterogeneity of spontaneous imbibition in different positions of this core. For the matrix sandstone, there are a few areas of high CT number. The small red areas in some slices are probably some clay particles formed by the aggregation of clay minerals. This is consistent with the lower clay mineral content of the matrix sandstone. The result of CT scanning shows that the matrix sandstone is more homogeneous along the length of the core than the mixed-layer sandstone. The CT number of MS ranges from 1,800 to 2,300. For the clay-particle sandstone, which has more evident differences between clay particles and matrix in each scanning slice, it is notable that the clay particles in these core

TABLE 3 Pore volumes and proportions for different core samples.

Core name	Micropore volume (mL)	Macropore volume (mL)	Micropore proportion (%)	Macropore proportion (%)
1-MLS	11.5	1.0	92.2	7.8
2-MS	7.1	4.4	61.6	38.4
3-CPS	6.8	6.2	52.2	47.8

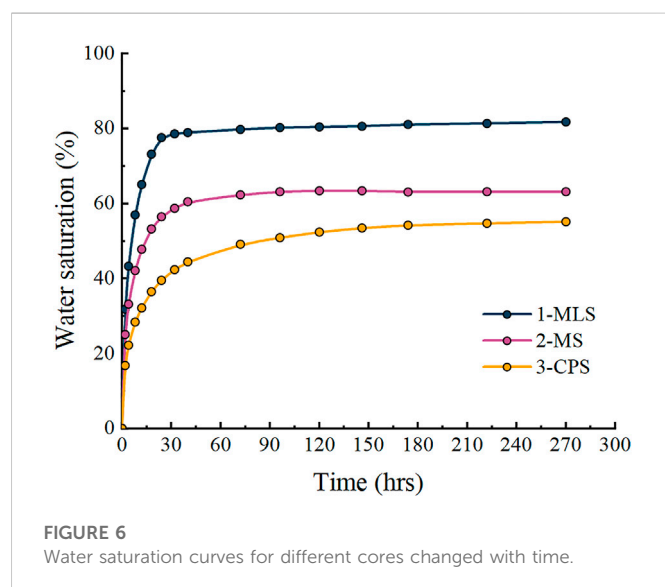


FIGURE 6

Water saturation curves for different cores changed with time.

samples are separated from the core matrix. Also, the CT numbers of clay particles and core matrix range from 2,300 to 2,600 and 1,800 to 2,300, respectively, which is consistent with the ranges of the CT numbers in MLS and MS. Additionally, the heterogeneity of CPS is more severe than MLS and MS. Finally, the sequence of core heterogeneity is CPS > MLS > MS. The different distribution patterns of the clay minerals may affect the pore structures of the core samples and thus the spontaneous imbibition performances along the length of the core samples.

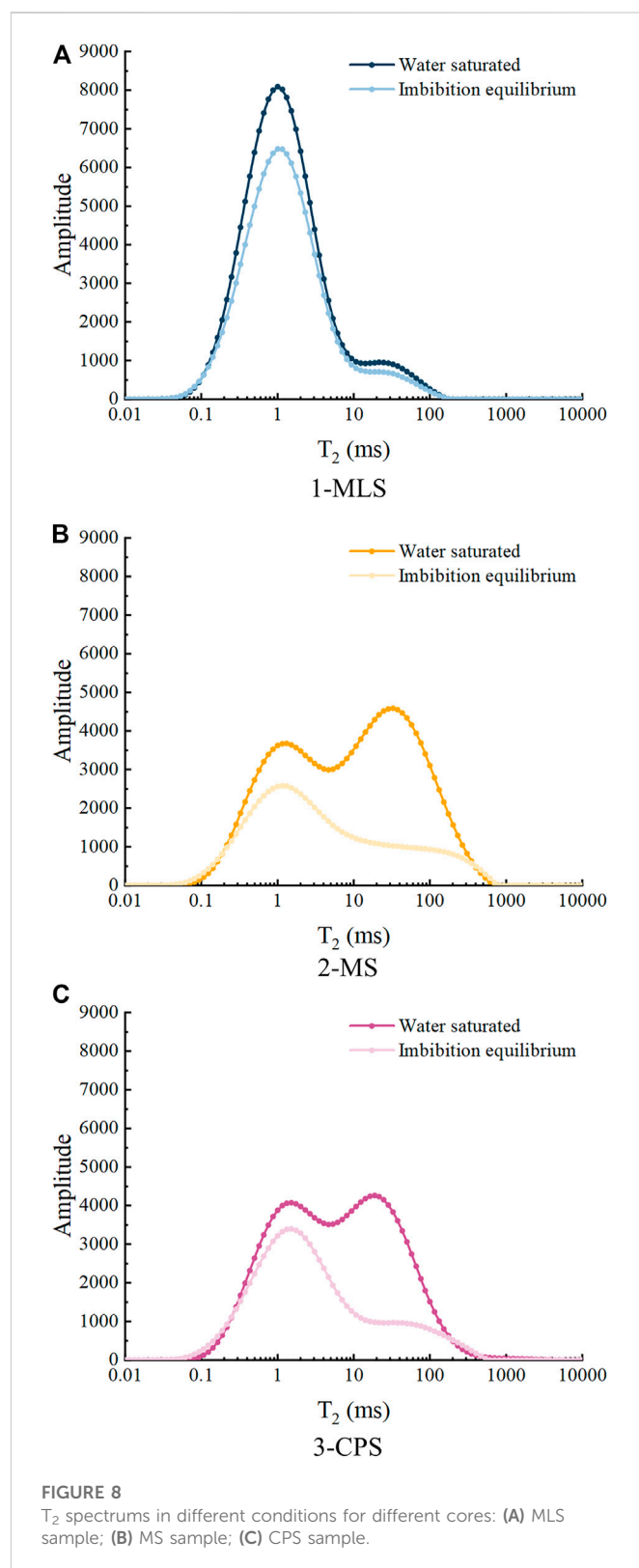
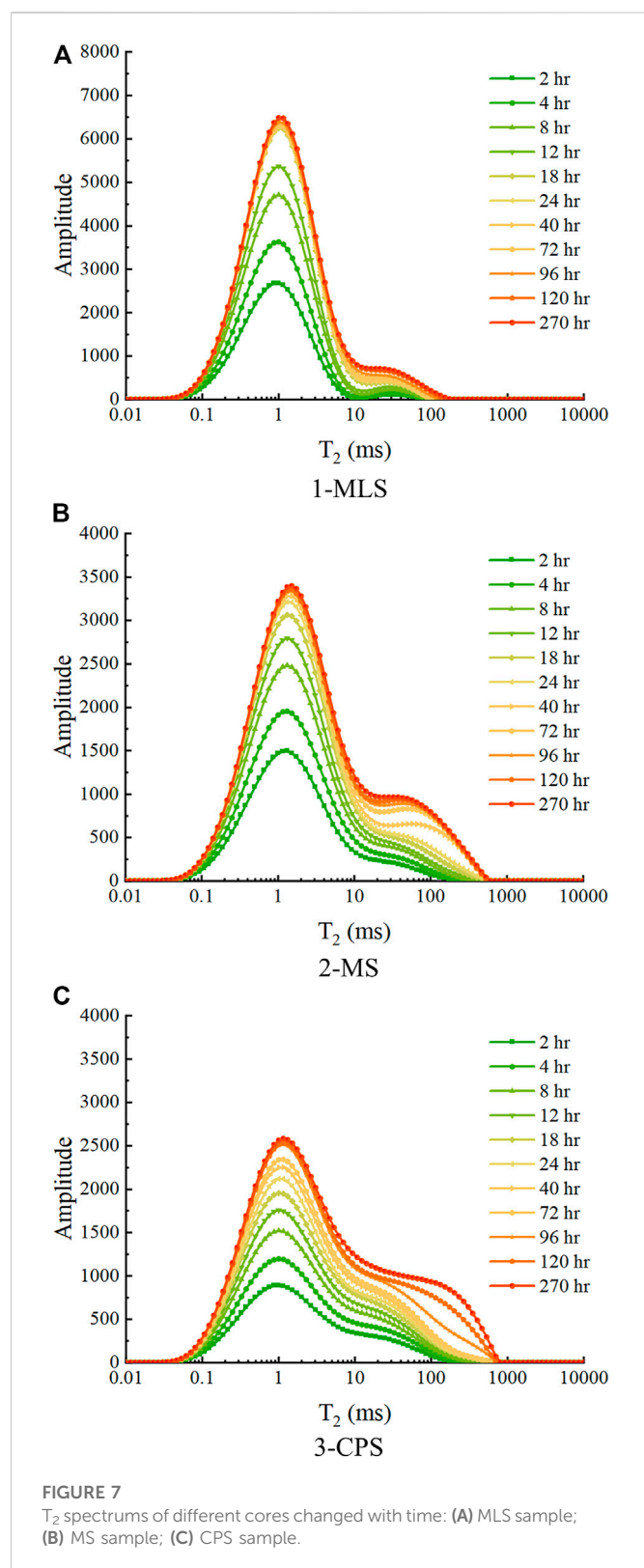
3.2 Pore structure analysis

To correlate the water volume and peak area of the T_2 spectrum, the weight differences and peak area differences in the spontaneous imbibition experiments are used to generate a standard curve. As shown in Figure 4, the water volumes in the core samples and the peak areas of the T_2 spectra have a good linear relationship. This demonstrates that the water distribution in different pores can be reflected through the T_2 spectra and the water volumes can be calculated through the fitting equation. Figure 5 shows the T_2 spectra of the core samples saturated with brine, and they can also represent the pore structure of the core samples due to the correlation between T_2 and the pore radius. It is found that the T_2 spectrum of MLS mainly has one peak of 1.0 ms, and the T_2 spectra of MS and CPS both have two peaks. The first peaks of these two samples are the same as that in MLS. The second peaks of MS and CPS are 18.74 ms and 32.75 ms, respectively. Therefore, the pores of the core samples can be divided into two types using the T_2 spectra: micropores (1–10 ms) and

macropores (10–1,000 ms). Additionally, this indicated that the pore structure of MLS mainly consists of micropores, and the MLS and CPS have both micropores and macropores. The pore volumes and proportions of micropores and macropores for the core samples are listed in Table 3. The proportion of macropores in CPS is larger than that of MS. In addition, CPS also has more macropores than MS. The results of the T_2 spectra for different core samples are correlated with the core permeabilities. Also, the permeability of the core sample is increased with the proportion of macropores.

3.3 Spontaneous imbibition experiments

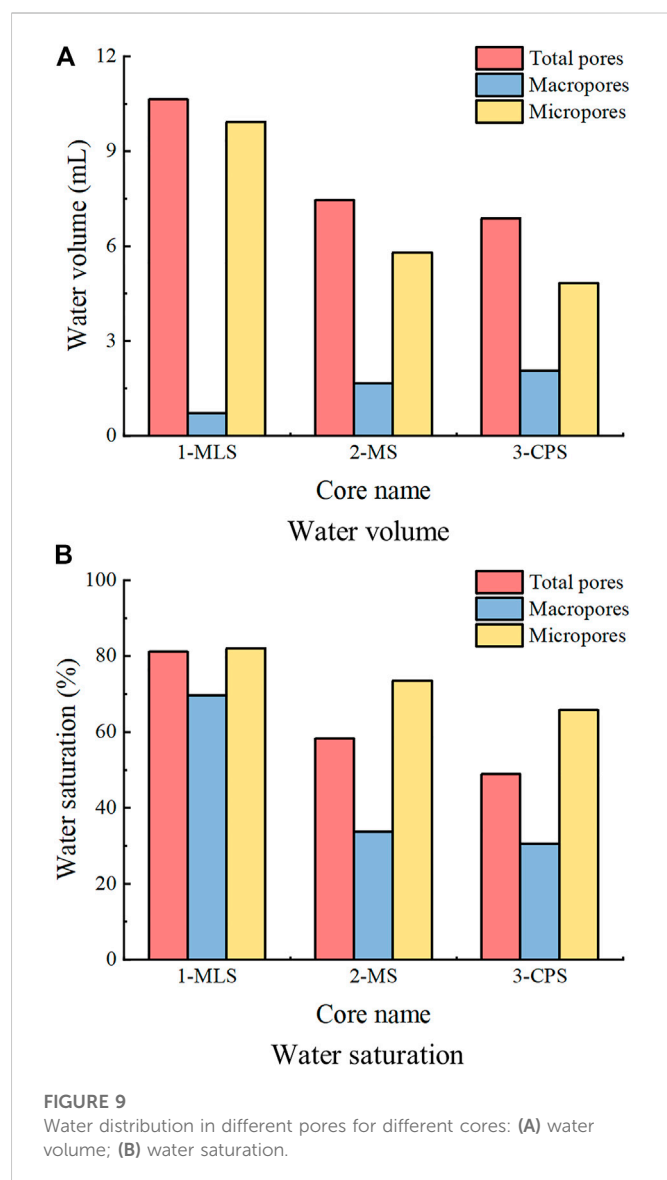
The water saturation curves of the core samples are obtained using the weight differences at different times. In Figure 6, the water saturations of the core samples are rapidly increased in the early period and gradually reach plateaus. It is found that MLS has the highest water saturation of 81.8%, and the final water saturations of MS and CPS are 63.1% and 55.2%, respectively. Additionally, the sequence of time to reach imbibition equilibrium is CPS (222 h) > MS (96 h) > MLS (32 h). This indicates that higher clay mineral content of the core sample can make water imbibition faster. However, the results show that the final water saturations of the core samples decrease with core permeability. To further investigate the imbibition characteristics in different pores of the core samples, the changes of the T_2 spectra for different cores are shown in Figure 7. It is found that the amplitudes of micropores in MLS gradually increase with time and reach equilibrium at around 24 h, as shown in Figure 7A. After that, the difference in the T_2 spectra mainly results from the macropores. In Figure 7B, it is evident that the water mostly is imbibed into micropores rather than macropores, and the amplitudes of micropores increase more rapidly than those of macropores. The same tendency of amplitude changes is found in the case of CPS (Figure 7C). The amplitude of micropores in MS is larger than that of CPS, but the amplitude of macropores in MS is smaller than that of CPS. This probably results from the different pore structures of the two cores. CPS has a larger proportion of macropores but a smaller proportion of micropores than MS, which indicates the pore structures of core samples can dominate the spontaneous imbibition in different pores. Furthermore, there is a similar trend for these core samples that indicates that the imbibition rate of micropores is larger than that of macropores. For the homogenous cores, a larger pore size means a higher permeability and thus a higher imbibition rate (Washburn, 1921; Meng et al., 2017; Abd et al., 2019). However, there is crossflow between micropores and macropores due to the capillary pressure difference. Also, this can lead to the driven forces in micropores being larger than macropores, and thus, the imbibition fronts in micropores move faster than macropores (Dong et al., 2006; Li et al., 2019). A similar phenomenon is also observed in coals (Yuan X. et al., 2019) and low-permeability sandstones (Chen et al., 2018).



3.4 Water distributions in different pores

To investigate the water saturation of different core samples, the comparisons of the T_2 spectra when the cores are saturated with brine and reach imbibition equilibrium are shown in Figure 8. It is found

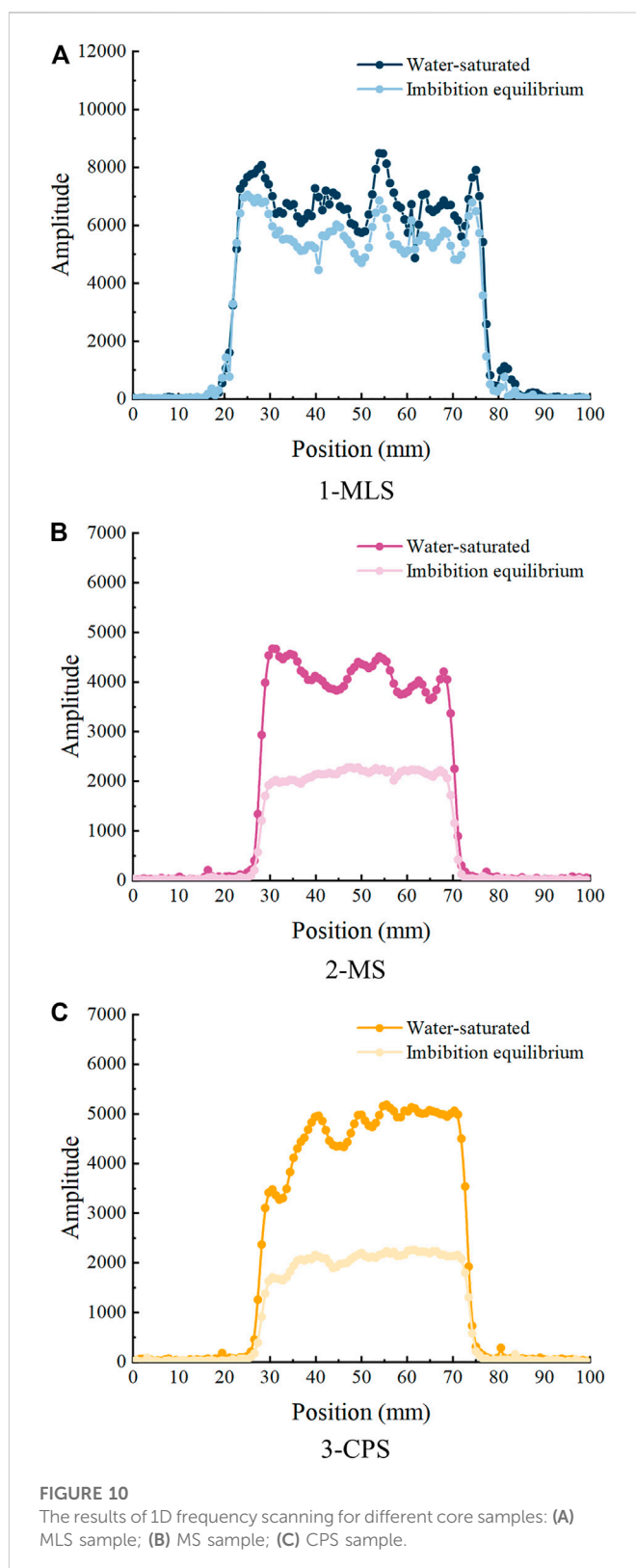
that water saturation of micropores is much higher than that of macropores. The water saturation and water volumes in different pores are summarized in Figure 9. The sequence of water volumes in micropores is $MLS > MS > CPS$, which is consistent with the trend of clay mineral contents and micropore proportions. The sequence of



water volume in macropores is $CPS > MS > MLS$, which is consistent with the trend of macropore proportions. This demonstrates that the differences in spontaneous imbibition mainly resulted from the differences of the pore structure. However, the water saturations in micropores and macropores have the same sequence: $MLS > MS > CPS$. The water saturation of micropores is increased with the increase in the micropore proportion. This indicates that the water volume of macropores for CPS is larger than that of MS, but the water saturation of macropores is still smaller than that of MS. This also demonstrates that the spontaneous imbibition is dominated by the micropores and the water saturation of different pores is increased with the micropore proportions.

3.5 Effects of heterogeneity on spontaneous imbibition

To further understand the effects of the clay mineral distribution during spontaneous imbibition, the results of 1D frequency scanning are shown in Figure 10. For the mixed-layer sandstone, the amplitudes



in different positions vary with the mixed-layer area, and the positions of high amplitude correspond with the positions that have high mixed-layer areas. For the matrix sandstone, the amplitudes of the water-saturated condition are more uniform than those in the mixed-layer sandstone. Also, the amplitudes of the imbibition equilibrium condition are much more uniform than those of MS. For the clay-

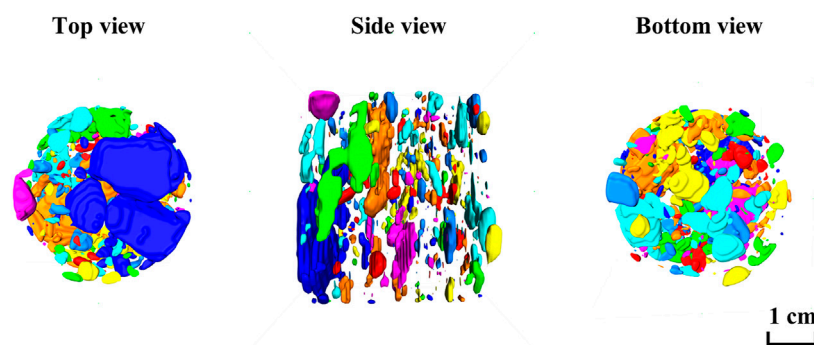


FIGURE 11
The clay particle distribution of CPS in 3D view.

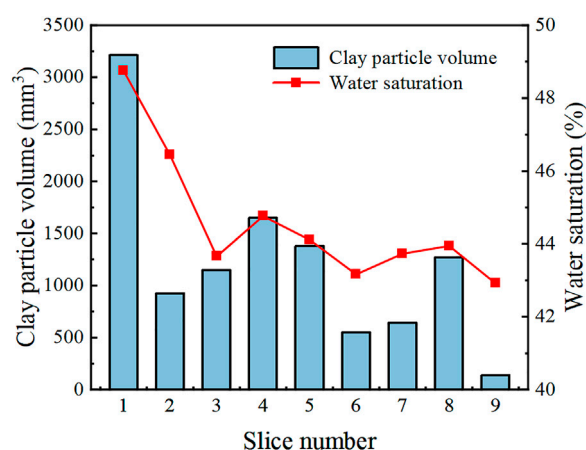


FIGURE 12
The water saturations and clay particle volumes at different position of CPS.

particle sandstone, the amplitudes of different positions are mainly controlled by the positions of the clay particles. The clay particle positions are shown in Figure 11 from different perspectives. The colors of clay particles are generated from the label analysis module, and the different colors are used to distinguish the clay particles in different positions. It is evident that the clay particles are not uniformly distributed along the length of the core sample. Due to the significant difference between the clay particles and core matrix in CPS, the relationship between water saturations and clay particle volumes in the different positions are illustrated in Figure 12. There is the same tendency for water saturations and clay particle volumes changing with the positions. A high clay particle volume can lead to high water saturation, which demonstrated that the heterogeneity of the core samples can affect the water distribution. Also, water is mainly distributed in the clay minerals. These results have a good correlation with the changes of the T_2 spectra.

4 Conclusion

In this study, three kinds of heterogeneous sandstone cores are used to characterize the heterogeneity through CT scans and

investigate the effects of the clay mineral distribution on spontaneous imbibition. The water distribution at different pores and positions of core samples are characterized and quantified through T_2 scans and 1D frequency scans. The conclusion can be drawn as follows:

- (1) The CT number of the clay minerals is higher than the core matrix; therefore, the clay mineral distribution can be characterized through CT scans. The sequence of heterogeneity of the core sample is CPS > MLS > MS. The different pore structures of core samples are related to the clay mineral distribution patterns, and the micropore proportion is increased with clay mineral content.
- (2) The water saturation of the core samples is increased with the clay mineral content. The sequence of water saturation is MLS > MS > CPS. Water is mainly imbibed in the micropores, and this leads to a higher imbibition rate of micropores than that of macropores. The water saturations of different pores are increased with the corresponding pore proportions. This mainly results from the crossflow between micropores and macropores due to the capillary difference.
- (3) The clay mineral distribution along the length of the core samples affects the water distribution. For CPS, the water saturation is correlated with the clay particle volume in different positions. This is because the micropores are mainly contributed by clay minerals. Also, this indicates that the water distribution is dominated by the clay mineral distribution in the heterogeneous sandstone.

Data availability statement

The original contributions presented in the study are included in the article/Supplementary Material; further inquiries can be directed to the corresponding authors.

Author contributions

MW: Experiments, Investigation, Writing original draft, Supervision. RW: Methodology, Writing reviewing & editing.

SY: Experiments, Writing reviewing & editing. FZ: Methodology, Writing reviewing & editing.

Funding

This work is financially supported by Sinopec Fundamental Prospective Research Project (Grant number: P22205).

Conflict of interest

MW and RW were employed by SINOPEC.

References

- Abd, A. S., Elhafyan, E., Siddiqui, A. R., Alnoush, W., Blunt, M. J., and Alyafei, N. (2019). A review of the phenomenon of counter-current spontaneous imbibition: Analysis and data interpretation. *J. Petroleum Sci. Eng.* 180, 456–470. doi:10.1016/j.petrol.2019.05.066
- Akbarabadi, M., Saraji, S., Piri, M., Georgi, D., and Delshad, M. (2017). Nano-scale experimental investigation of *in-situ* wettability and spontaneous imbibition in ultra-tight reservoir rocks. *Adv. Water Resour.* 107, 160–179. doi:10.1016/j.advwatres.2017.06.004
- Alkough, A., and Wattenbarger, R. A. (2013). “New advances in shale reservoir analysis using flow back data,” in SPE Eastern Regional Meeting, Pennsylvania, USA, August 20–22, 2013. doi:10.2118/165721-MS
- Bao, B., Riordon, J., Mostowfi, F., and Sinton, D. (2017). Microfluidic and nanofluidic phase behaviour characterization for industrial CO₂, oil and gas. *Lab a Chip* 17 (16), 2740–2759. doi:10.1039/C7LC00301C
- Chen, M., Dai, J., Liu, X., Qin, M., Pei, Y., and Wang, Z. (2018). Differences in the fluid characteristics between spontaneous imbibition and drainage in tight sandstone cores from nuclear magnetic resonance. *Energy & Fuels* 32 (10), 10333–10343. doi:10.1021/acs.energyfuels.8b01396
- Dong, M., Dullien, F. A. L., Dai, L., and Li, D. (2006). Immiscible displacement in the interacting capillary bundle model Part II. Applications of model and comparison of interacting and non-interacting capillary bundle models. *Transp. Porous Media* 63 (2), 289–304. doi:10.1007/s11242-005-6530-4
- Dutta, R., Lee, C.-H., Odumabo, S., Peng, Y., Walker, S. C., Karpyn, Z. T., et al. (2014). Experimental investigation of fracturing-fluid migration caused by spontaneous imbibition in fractured low-permeability sands. *SPE Reserv. Eval. Eng.* 17 (01), 74–81. doi:10.2118/154939-PA
- Handy, L. L. 1960. Determination of effective capillary pressures for porous media from imbibition data, January. Available at: https://www.onepetro.org/general/SPE-1361-G?sort=&start=0&q=Determination+of+Effective+Capillary+Pressures+for+Porous+Media+From+Imbibition+Data&from_year=&peer_reviewed=&published_between=&fromSearchResults=true&to_year=&rows=10.
- Lai, J., Wang, G., Fan, Z., Chen, J., Wang, S., Zhou, Z., et al. (2016). Insight into the pore structure of tight sandstones using NMR and HPMT measurements. *Energy & Fuels* 30 (12), 10200–10214. doi:10.1021/acs.energyfuels.6b01982
- Li, K., and Horne, R. N. (2001). Characterization of spontaneous water imbibition into gas-saturated rocks. *SPE J.* 6 (04), 375–384. doi:10.2118/74703-PA
- Li, Y., Li, H., Chen, S., Ma, Q., and Chang, L. (2019). Two-phase fluid flow characterizations in a tight rock: A fractal bundle of the capillary tube model. *Industrial Eng. Chem. Res.* 58 (45), 20806–20814. doi:10.1021/acs.iecr.9b04328
- Liang, T., Longoria, R. A., Lu, J., Nguyen, Q. P., and DiCarlo, D. A. (2017). Enhancing hydrocarbon permeability after hydraulic fracturing: Laboratory evaluations of shut-ins and surfactant additives. *SPE J.* 22 (041), 1011–1023. doi:10.2118/175101-PA
- Liang, T., Luo, X., Nguyen, Q., and DiCarlo, D. (2018). Computed-tomography measurements of water block in low-permeability rocks: Scaling and remedying production impairment. *SPE J.* 23 (03), 762–771. doi:10.2118/189445-PA
- Liang, X., Zhou, F., Liang, T., Wang, C., Wang, J., and Yuan, S. (2020). Impacts of low harm fracturing fluid on fossil hydrogen Energy production in tight reservoirs. *Int. J. Hydrogen Energy* 45 (41), 21195–21204. doi:10.1016/j.ijhydene.2020.06.011
- Liu, J., and Sheng, J. J. (2020). Investigation of countercurrent imbibition in oil-wet tight cores using NMR technology. *SPE J.* 25, 2601–2614. doi:10.2118/201099-PA
- Liu, Y., Leung, J. Y., Chalaturnyk, R., and Virues, C. J. J. (2017). “Fracturing fluid distribution in shale gas reservoirs due to fracture closure, proppant distribution and gravity segregation,” in SPE Unconventional Resources Conference, Alberta, Canada, February 15–16, 2017. doi:10.2118/185043-MS
- Meng, M., Ge, H., Ji, W., Wang, X., and Chen, L. (2015). Investigation on the variation of shale permeability with spontaneous imbibition time: Sandstones and volcanic rocks as comparative study. *J. Nat. Gas Sci. Eng.* 27, 1546–1554. doi:10.1016/j.jngse.2015.10.019
- Meng, Q., Liu, H., and Wang, J. (2017). A critical review on fundamental mechanisms of spontaneous imbibition and the impact of boundary condition, FLuid viscosity and wettability. *Adv. Geo-Energy Res.* 1 (1), 1–17. doi:10.26804/ager.2017.01.01
- Mirzaei, M., DiCarlo, D. A., and Pope, G. A. (2016). Visualization and analysis of surfactant imbibition into oil-wet fractured cores. *SPE J.* 21 (01), 101–111. doi:10.2118/166129-PA
- Shen, Y., Ge, H., Su, S., Liu, D., Yang, Z., and Liu, J. (2017). Imbibition characteristic of shale gas formation and water-block removal capability. *Sci. SINICA Phys. Mech. Astronomica* 47 (11), 114609. doi:10.1360/sspma2016-00538
- Standnes, D. (2003). Experimental study of the impact of boundary conditions on oil recovery by Co-current and counter-current spontaneous imbibition. *Energy & Fuels - ENERG FUEL* 18, 271–282. doi:10.1021/ef030142p
- Washburn, E. W. (1921). The dynamics of capillary flow. *Phys. Rev.* 17 (3), 273–283. doi:10.1103/PhysRev.17.273
- Wei, B., Gao, K., Song, T., Zhang, X., Pu, W., Xu, X., et al. (2020). Nuclear-magnetic-resonance monitoring of mass exchange in a low-permeability matrix/fracture model during CO₂ cyclic injection: A mechanistic study. *SPE J.* 25 (01), 440–450. doi:10.2118/199345-PA
- Yang, L., Liu, D., Ge, H., Shen, Y., Li, C., and Zhang, K. (2016). “Experimental investigation on the effects of flow resistance on the fracturing fluids imbibition into gas shale,” in SPE Asia Pacific Hydraulic Fracturing Conference, Beijing, China, August 24–26, 2016. doi:10.2118/181825-MS
- Yuan, S., Liang, T., Zhou, F., Liang, X., Yu, F., and Li, J. (2019). “A microfluidic study of wettability alteration rate on enhanced oil recovery in oil-wet porous media,” in Abu Dhabi International Petroleum Exhibition & Conference, Abu Dhabi, UAE, November 11–14, 2019.
- Yuan, X., Yao, Y., Liu, D., and Pan, Z. (2019). Spontaneous imbibition in coal: Experimental and model analysis. *J. Nat. Gas Sci. Eng.* 67, 108–121. doi:10.1016/j.jngse.2019.04.016
- Zhang, L., Zhou, F., Zhang, S., Wang, Y., Wang, J., and Wang, J. (2019). Investigation of water-sensitivity damage for tight low-permeability sandstone reservoirs. *ACS Omega* 4 (6), 11197–11204. doi:10.1021/acsomega.9b01286
- Zhou, Z., Abass, H., Li, X., and Teklu, T. (2016). Experimental investigation of the effect of imbibition on shale permeability during hydraulic fracturing. *J. Nat. Gas Sci. Eng.* 29, 413–430. doi:10.1016/j.jngse.2016.01.023

Publisher's note

All claims expressed in this article are solely those of the authors and do not necessarily represent those of their affiliated organizations, or those of the publisher, the editors, and the reviewers. Any product that may be evaluated in this article, or claim that may be made by its manufacturer, is not guaranteed or endorsed by the publisher.

Nomenclature

S pore surface area, μm^2

V pore surface area, μm^3

ρ surface relaxivity, $\mu\text{m/s}$

C constant conversion coefficient, $\text{ms}/\mu\text{m}$

S_w water saturation of a certain length of cores, %

A_{im} the amplitude of spontaneous imbibition experiments at a certain position

A_w the amplitude of water-saturated condition at a certain position



OPEN ACCESS

EDITED BY

Debin Kong,
University of Science and Technology
Beijing, China

REVIEWED BY

Wendong Wang,
China University of Petroleum, Huadong,
China
Ruixue Li,
Chengdu University of Technology, China

*CORRESPONDENCE

Hou Yanan,
✉ houyn2@cnoc.com.cn

SPECIALTY SECTION

This article was submitted to Advanced
Clean Fuel Technologies,
a section of the journal
Frontiers in Energy Research

RECEIVED 02 January 2023

ACCEPTED 20 January 2023

PUBLISHED 16 February 2023

CITATION

Yishan L, Lin Z, An S, Yanan H, Yuqi L,
Changbing T, Xiaohu D and Zhengdong L
(2023), Study on gas injection
development effect of tight reservoir
based on fluid occurrence state.
Front. Energy Res. 11:1136020.
doi: 10.3389/fenrg.2023.1136020

COPYRIGHT

© 2023 Yishan, Lin, An, Yanan, Yuqi,
Changbing, Xiaohu and Zhengdong. This is
an open-access article distributed under
the terms of the [Creative Commons
Attribution License \(CC BY\)](https://creativecommons.org/licenses/by/4.0/). The use,
distribution or reproduction in other
forums is permitted, provided the original
author(s) and the copyright owner(s) are
credited and that the original publication in
this journal is cited, in accordance with
accepted academic practice. No use,
distribution or reproduction is permitted
which does not comply with these terms.

Study on gas injection development effect of tight reservoir based on fluid occurrence state

Liu Yishan¹, Zu Lin², Sheng An^{2,3}, Hou Yanan^{4*}, Liu Yuqi¹,
Tian Changbing¹, Dong Xiaohu⁵ and Lei Zhengdong¹

¹Research Institute of Petroleum Exploration and Development, PetroChina, Beijing, China, ²Research Institute of Exploration and Development of Daqing Oilfield Company Ltd., PetroChina, Daqing, Heilongjiang, China, ³NO 2 Oil Production Plant Daqing Oilfield Company, PetroChina, Daqing, Heilongjiang, China, ⁴CNOOC Research Institute Ltd., Beijing, China, ⁵State Key Laboratory of Petroleum Resources and Prospecting, China University of Petroleum, Beijing, China

Based on the tight oil reservoir conditions of Lucaogou Formation in Jimusar Sag, Xinjiang, this paper conducts a full-scale characterization experiment of pore structure and designs the optimization numerical simulation of the development scheme based on the geological model combination with the fluid occurrence state. A comparative study on the development methods of tight reservoirs shows that the enhanced oil recovery effect of CO₂ flooding is obviously better than that of CH₄ flooding and water flooding. When the production bottom hole pressure is lower than the formation fluid saturation pressure, changing the production bottom hole pressure has little impact on the productivity of CO₂ flooding in tight reservoirs. The recovery factor increases with the increase of injection rate, but when the injection rate is higher than 15,000 m³/d, the increase of oil recovery and the oil change rate decrease obviously; The complex fractures near the well can help to increase the swept volume of CO₂ flooding, while the complex fractures far away from the well will cause channeling, which is not conducive to production. Combined with the occurrence state of the fluid, it is obtained that in the process of CO₂ displacement, when the adsorption is considered, when the adsorption components are the same, with the increase of the adsorption capacity, the recovery factor decreases; When the adsorption capacity is constant, the higher the proportion of heavy components is, the lower the recovery factor is; With the increase of adsorption capacity, the permeability decreases more. The fluid occurrence state in tight oil reservoirs is very different from that in conventional reservoirs, and the adsorption phase accounts for a larger proportion, which seriously affects the flow capacity of the fluid during the development process. However, conventional numerical simulation rarely considers the influence of fluid occurrence state.

KEYWORDS

tight oil reservoirs, occurrence state, gas injection development, numerical simulation, development effect

1 Introduction

The main difference between tight reservoir and conventional reservoir is that it is generally tight, resulting in poor physical properties. The specific performance is as follows: low matrix permeability, large variation range of reservoir porosity, complex pore throat structure, micro nano scale reservoir units and flow channels in the reservoir, and strong

heterogeneity (Hu et al., 2010; Jarvie, 2010; Clarkson and Pedersen, 2011). At present, the production of tight oil requires targeted use of technologies such as manual transformation, massive drilling, multi branch wells or horizontal wells. The overall idea is to “artificially construct an oil flow channel with high conductivity and rely on the reservoir’s own energy for exploitation”, which can achieve high production in a short time, but cannot achieve stable production (Li and Zhang, 2011). Scholars have defined tight oil reservoirs according to permeability characteristics after long-term field investigation and experimental exploration: overburden permeability is less than $0.1 \mu\text{m}^2 \times 10^{-3} \mu\text{m}^2$ of tight sandstone, tight carbonate rock or mixed rock (Andrews, 2012; Jarvie, 2012; Liang et al., 2012). The depletion development capacity is extremely weak, and there is no possibility of high and stable production without artificial reservoir reconstruction (Kong et al., 2019). However, after fracturing, horizontal wells and other measures, the productivity has been improved to a certain extent (Jia et al., 2012; Tong, 2012; Hou et al., 2021). North America has made a double breakthrough in technology and production, enabling tight reservoirs to replace conventional reservoirs as the main source of oil resources (Lu et al., 2012; Montgomery and O’sullivan, 2017; Hou et al., 2022).

China is rich in tight oil resources (Li et al., 2020). In recent years, many tight oil reservoirs have been put into production, which can effectively supplement China’s oil resources. Taking Yanchang Formation of Ordos Basin as a typical representative (Zou et al., 2012; IEA, 2016), the first industrialized tight oil production area in China has been built (BP, 2016; Zhang et al., 2015). Tight oil in China reservoirs is characterized by deep burial depth, poor physical properties, micro nano scale pores, strong heterogeneity, poor fluid physical properties, and difficulty in producing (Tian et al., 2014; Shi et al., 2015; Yang et al., 2016). Before industrial production can be formed, a lot of research work needs to be carried out to solve problems such as fluid flow and reservoir reconstruction, and the goal of achieving high and stable production is a challenge (Du et al., 2014).

The Lucaogou Formation in Jimusar, Xinjiang, is a tight oil source reservoir with high organic carbon content, strong hydrocarbon generation capacity, stable distribution, and relatively concentrated vertical and wide horizontal distribution of tight oil desserts. The reservoir space is dominated by intergranular and intragranular dissolved pores. Microfractures are underdeveloped and only a small amount of them is developed in carbonate rocks. High pressure mercury injection data show that the reservoir is developed with nano pore throat, and the pore throat structure of the upper dessert body is superior to that of the lower dessert body. Dessert has good oil content and high saturation. The oil saturation is between 70% and 95%. The fluid property is poor. The density of the top “dessert” crude oil is 0.882 g/cm^3 , and the viscosity at 50°C is $50.27 \text{ mPa}\cdot\text{s}$. Studying the specific occurrence state of fluid in micro nano scale pores is the basis for its exploitation and can propose effective exploitation methods. The pore structure of tight reservoir is dense, usually micro nano level. The fluid adsorption layer formed due to adsorption will account for a large proportion and will also affect the effective diameter of pores. It is important to describe the fluid occurrence mechanism accurately and comprehensively. The occurrence state of tight oil will be comprehensively affected by temperature, pressure, pore

size, pore mineral composition, fluid composition and other factors (Liu et al., 2020). For unconventional reservoirs such as tight oil, the occurrence state of fluid in reservoirs is quite different from that of conventional oil and gas reservoirs (Kong et al., 2021). At present, the occurrence state of pore fluid in tight oil reservoirs of Lucaogou Formation in Jimusar Sag, Xinjiang is unclear, the description of the availability of pore fluid is not accurate, and the development effect is not ideal.

At present, the effective development mode for tight reservoirs is depletion after fracturing and gas injection development. Therefore, this study combines the research results of fluid occurrence state and fluid availability, designs a targeted development plan and conducts numerical simulation research. By comparing and analyzing the effects of different development methods, bottom hole pressure, injection rate, occurrence state and fracture distribution on the development effect, the effective development methods for tight reservoirs are determined.

This study takes the Lucaogou Formation in Jimusar Sag as an example to carry out the feasibility of CO_2 injection in typical work areas to improve the recovery rate and optimize the injection production and construction parameters to maximize the productivity. In this paper, a real reservoir geological model is established, and the effects of different development methods, production systems, oil occurrence state such as absorption and engineering factors on productivity are compared and discussed in combination with the actual situation, and the development parameters are optimized.

2 Reservoir geology and model establishment

First, based on the reservoir data of Lucaogou Formation in Jimusar Depression, Xinjiang, $42 \text{ (I)} \times 39 \text{ (J)} \times 8 \text{ (K)}$, the top depth is 3,144.3 m. The fourth layer in the K direction adopts the reverse five-point method to arrange wells and establish the horizontal well in the J direction. By default, the length of the horizontal section of the injection well is 475 m, the length of the horizontal section of the production well is 275 m, the interval between the major fractures is 70 m, and which is 50 m in secondary fractures. There are six major fractures in the injection well, four major fractures in each production well, and four secondary fractures in each major fracture. To form an effective flow in the formation, the secondary fractures at the corresponding positions are interconnected. The formation and fracture parameters are shown in Table 1, and the geological model is shown in Figure 1.

3 Establishment of numerical model and optimization of development mode

3.1 Establishment of numerical model

Carry out relative permeability test experiment with tight cores in the target block, obtain oil-water two-phase relative permeability curve and gas-liquid relative permeability curve, and apply the relative permeability curve to the numerical model, as shown in Figure 2. Crude oil composition is shown in Table 2.

TABLE 1 Formation and fracture parameters.

Formation parameters	Value	Fracture parameters	Value
Porosity	0.02–0.16	Fracture spacing/m	Major:70; Secondary:50
Permeability/ $10^{-3} \mu\text{m}^2$	0.001–0.26	Number of major fractures	Injection:6; Production:4
Initial oil saturation	0.8	Half-length of fracture/m	125
Temperature/ $^{\circ}\text{C}$	71.6	Width of fracture/m	0.0038
Formation pressure/kPa	40,000	Effective fracture permeability/ $10^{-3} \mu\text{m}^2$	199.36

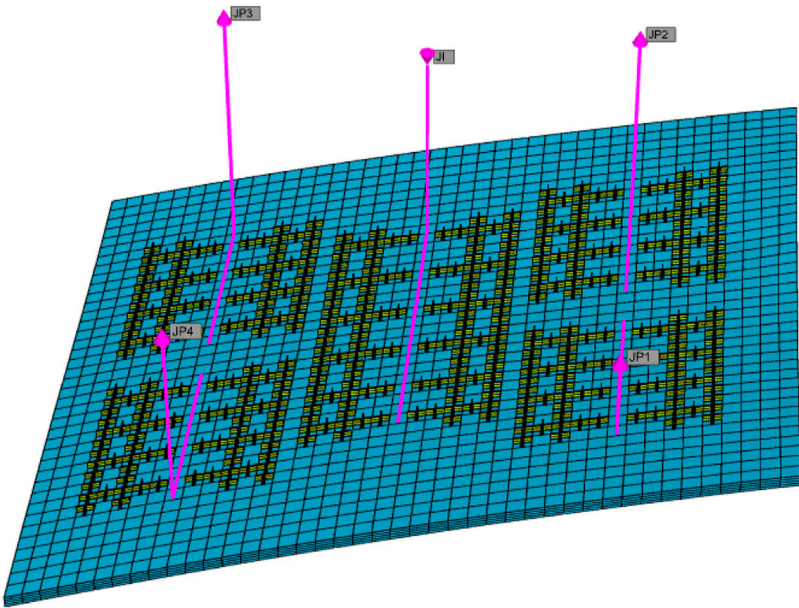


FIGURE 1 Geological model of target reservoir and distribution of fractures.

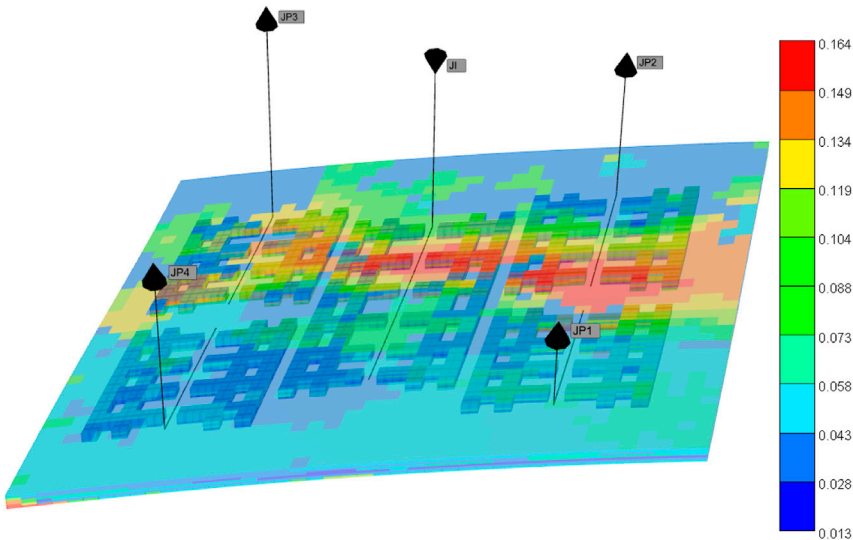


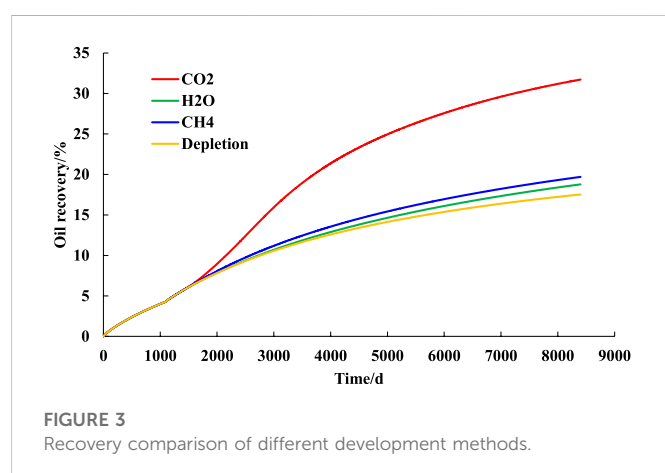
FIGURE 2 Porosity distribution map of target reservoir.

TABLE 2 Oil component parameters.

Components	Critical pressure/bar	Critical temperature/K	Eccentricity factor
CO ₂	72.80	304.20	0.22
C1	45.24	189.67	0.01
IC4	43.49	412.47	0.15
FC7	37.69	556.92	0.25
FC12	31.04	667.52	0.33
FC19	19.29	673.76	0.57
FC30	15.38	792.40	0.9422

TABLE 3 Injection mode comparison scheme design.

Development mode	Depletion development		Displacement development				
	Time	Production bottom hole pressure	Time	Injection bottom hole pressure	Production bottom hole pressure	Injection rate	
	/a	/kPa	/a	/kPa	/kPa	/m ³ /d	
Water flooding	3	20,000	20	50,000	8,000	60	
CH ₄ flooding				50,000		15,000	
CO ₂ flooding				50,000		15,000	
Depletion				/		/	



3.2 Feasibility analysis of development mode

Based on depletion development, this section has carried out water flooding, CO₂ flooding and CH₄ flooding, respectively. Simulation scheme is shown in Table 3. Compare and analyze the enhanced oil recovery range of each means and the composition of the fluid at the outlet end and discuss its applicability from the mechanism. The CMG numerical simulation software component model GEM module is used for this section and subsequent numerical simulation.

The reason why the production bottom hole pressure in the depletion stage in the simulation scheme is set as 2×10^4 kPa is that, considering that the real crude oil of the target reservoir contains a lot of dissolved gas, the production bottom hole pressure needs to be maintained at a high level in

order to ensure that the formation fluid still has good fluidity after depletion development. CH₄ and CO₂ injection rate is set to $1.5 \text{ m}^3/\text{d} \times 10^4 \text{ m}^3/\text{d}$ underground conditions. However, CH₄ and CO₂ have strong compressibility, and the injection amount converted according to the formation conditions is about $60 \text{ m}^3/\text{d}$. However, the compressibility of displacement medium water can be ignored, so the injection rate of water flooding is set as $60 \text{ m}^3/\text{d}$.

The enhanced oil recovery (Figure 3) and remaining oil saturation distribution (Figure 4) obtained by different development methods are compared and analyzed. It can be seen from Figure 3 that the enhanced oil recovery of CO₂ flooding is much higher than that of water flooding and CH₄ flooding. The enhanced oil recovery of CO₂ flooding is 26.86%, that of CH₄ flooding is 14.84%, that of water flooding is 13.92%, and that of pure depletion development is 13.25% after three years. At the initial stage of CO₂ flooding, it can be found that the recovery factor has been significantly improved, and then the growth rate has decreased slowly. It can be seen from Figure 4 that CO₂ flooding and CH₄ flooding can effectively form a displacement channel to effectively use the crude oil within the well control range, while the water flooding has poor injectivity, and the oil saturation near the production well has not decreased, only relying on depletion development near the production well to maintain productivity.

4 Productivity sensitivity analysis of tight reservoirs

The development mode of five wells depletion + intermediate wells gas injection displacement is adopted, and the basic model parameters are formulated according to the domestic and foreign oilfield

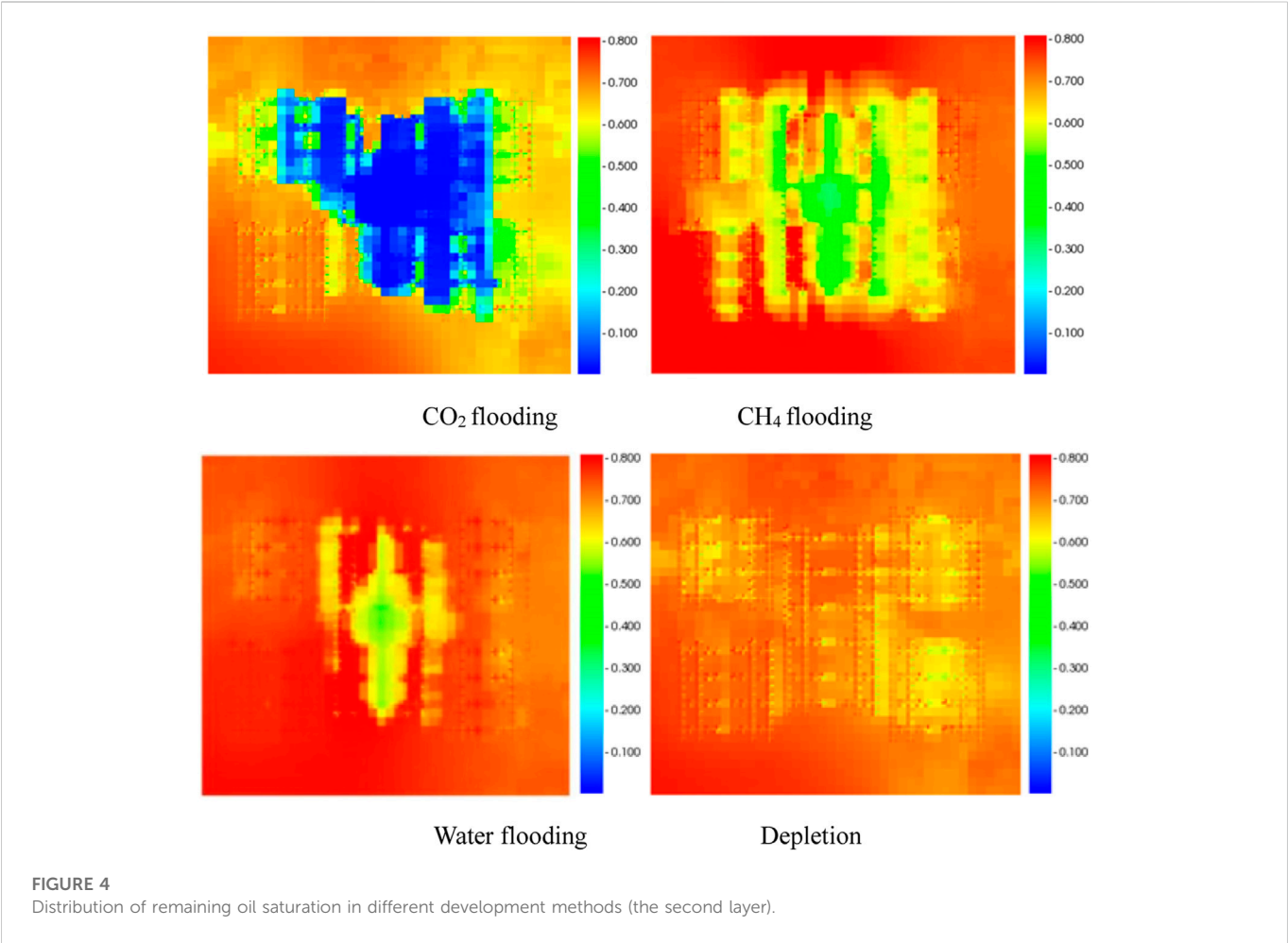


TABLE 4 Bottom hole pressure comparison scheme design.

Optimization parameters	Value range of each parameter				
Production bottom hole pressure/kPa	4,000	8,000	12,000	16,000	20,000
Injection rate/m ³ /d	5,000	8,000	10,000	15,000	20,000

development experience. As shown in Table 4, the value ranges of different parameters are designed and different fracture distribution schemes of no fracture, no secondary fracture, one secondary fracture (in the middle of the main fracture), one secondary fracture (at the edge of the main fracture) and two secondary fractures are simulated to compare the effects of the location of the main fracture, secondary fracture and secondary fracture on the recovery and residual oil saturation. The fracture design scheme is shown in Table 5, and the fracture distribution is shown in Figure 5.

4.1 Analysis of bottom hole pressure influence

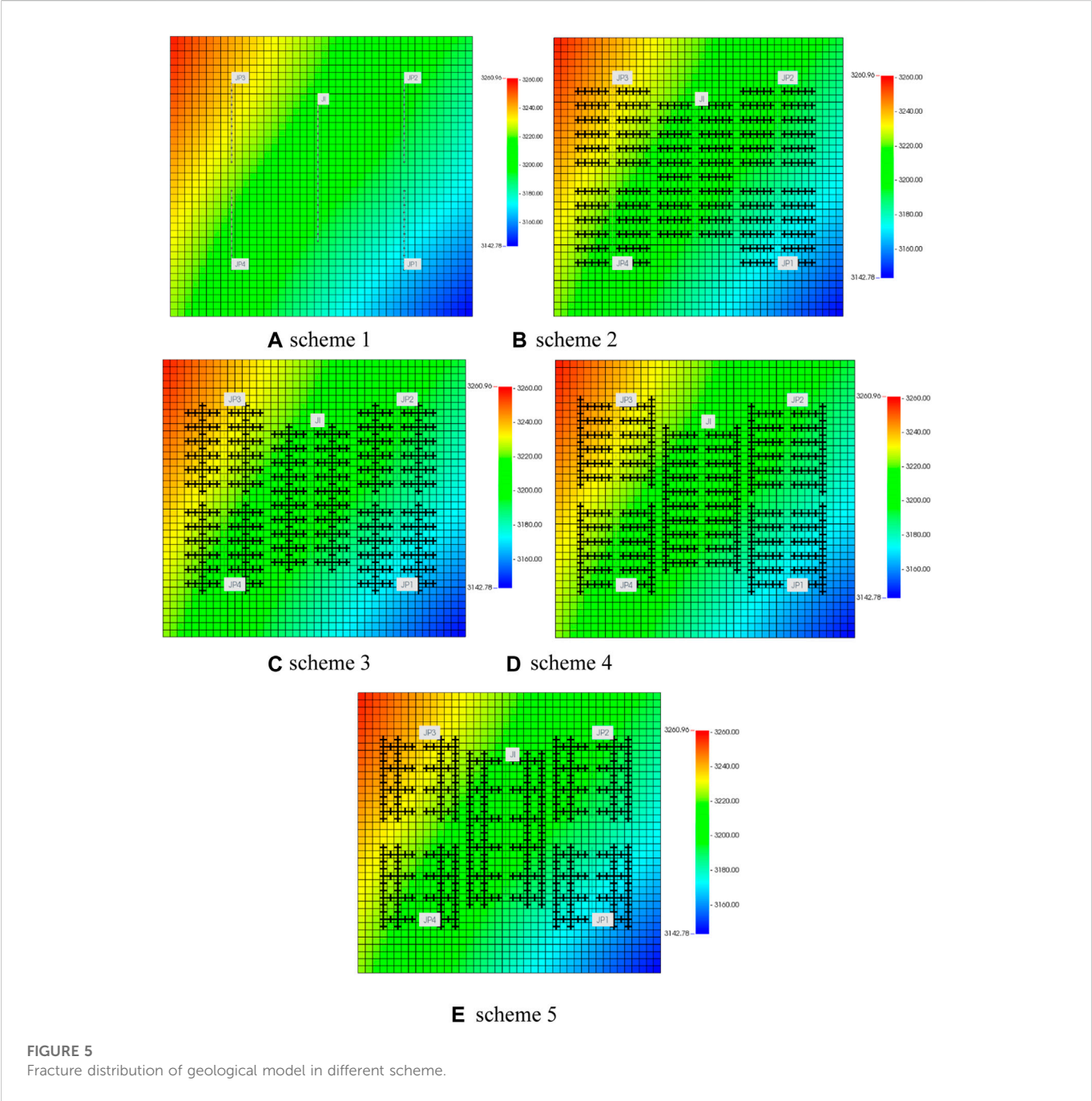
The influence of bottom hole pressure of production wells on productivity is compared and analyzed, and the results are shown in Figure 6. It can be seen from the figure that during the development process, with the development, the production bottom hole

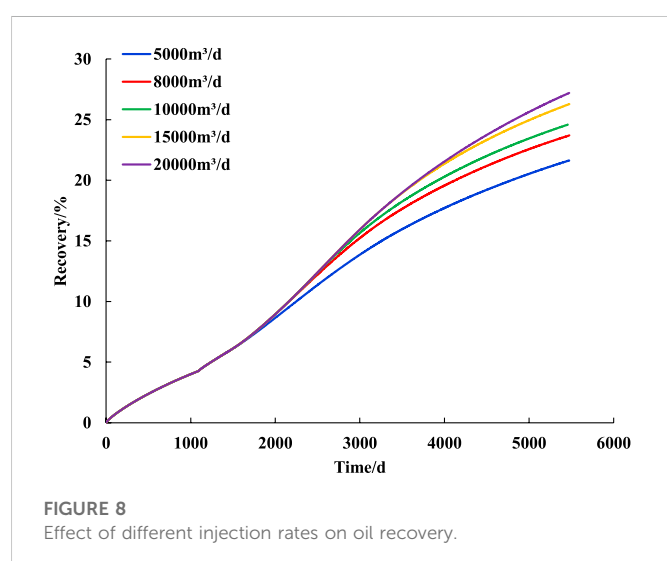
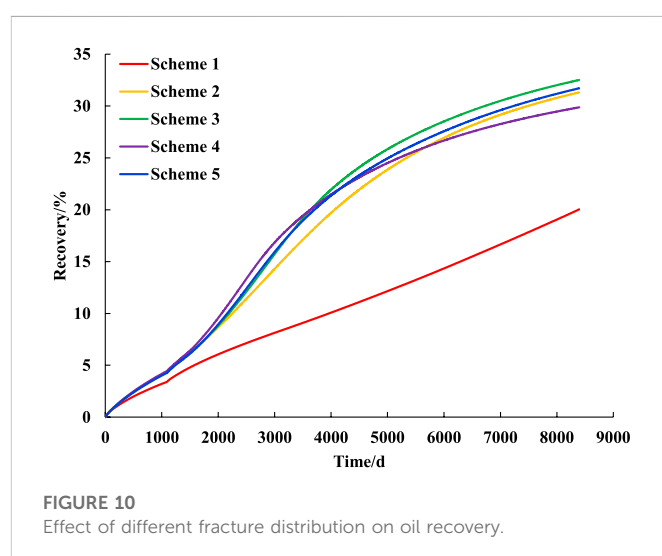
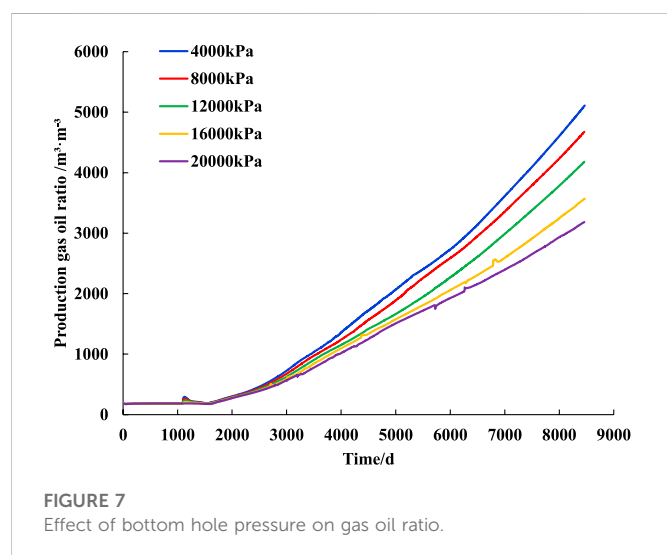
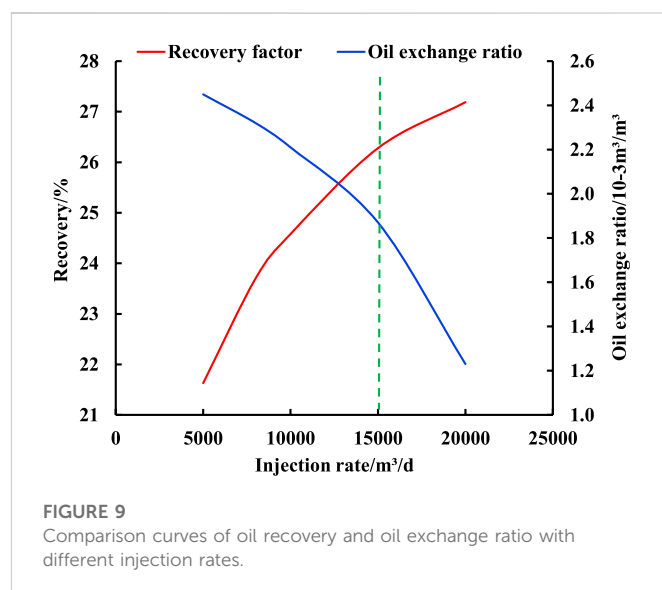
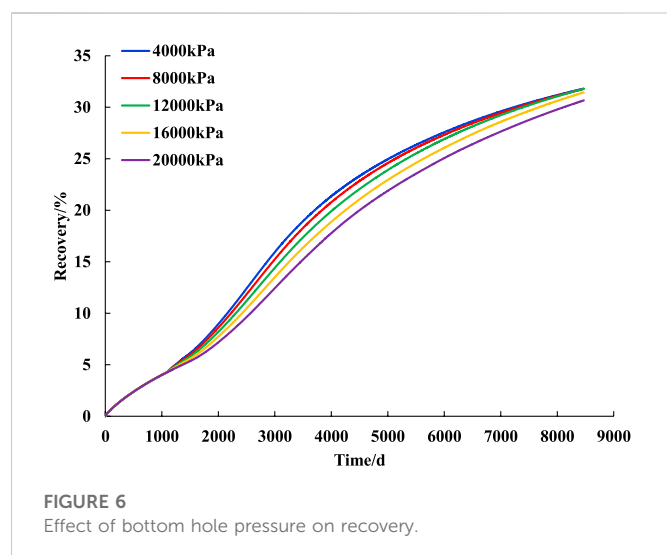
pressure will affect the productivity. In the first 12 years of CO₂ injection, the lower the production bottom hole pressure, the greater the production pressure difference, and the higher the recovery factor. After 15 years of production, the production difference caused by the production pressure difference gradually decreases. At the end of production, the final recovery factors of the schemes with the production bottom hole pressure of 0.4 × 10⁴ kPa, 0.8 × 10⁴ kPa and 1.2 × 10⁴ kPa are very close, it is also higher than the development plan with the production well bottom pressure of 1.6 × 10⁴ kPa. When the production well bottom pressure is 2 × 10⁴ kPa, the recovery factor is the lowest.

The reason why the impact of production pressure difference on productivity increases first and then decreases is that the crude oil in the target block contains a large amount of dissolved gas. At the initial stage of development, the formation pressure decreases slowly, the fluid phase does not change, and no dissolved gas is separated. With the development, the formation pressure

TABLE 5 Fracture parameter design.

Simulation scheme	Fracture spacing/m		Number of fractures		Half-length of fracture/m		Width of fracture/m	Effective fracture permeability
	Major	Secondary	Major	Secondary	/10 ⁻³ μm ²	Secondary		
1	/	/	/	/	/	/	/	/
2	50	/	10;6	/	125	/	0.0038	199.36
3	50	/	10;6	1	125	25		
4	50	/	10;6	1	125	25		
5	100	50	6;4	2	125	25		





gradually decreases and is lower than the bubble point pressure (the bubble point pressure of the crude oil measured by the high temperature and high pressure PVT experiment at the formation

temperature is 15.3 MPa, and the minimum miscible pressure of the crude oil and CO₂ calculated by the WINPROP component simulator is 18.75 MPa) [Peng and Robinson, 1976](#), resulting in the release of dissolved gas, volume expansion, and the formation of dissolved gas flooding, thus making up for the lack of production pressure difference. However, when the production bottom hole pressure is 15.3 MPa higher than the bubble point pressure, such as 16 MPa and 20 MPa in the production plan, the dissolved gas cannot be separated and the dissolved gas flooding cannot be formed, so the final production capacity is lower than the other three plans. To screen more suitable bottom hole pressure of production wells, the production gasoline ratios of the three schemes are analyzed and compared, and the results are shown in [Figure 7](#). It can be found that with the decrease of bottom hole pressure of production wells, the production gasoline ratio will increase. With the increase of production pressure difference, crude oil will be degassed seriously, which is not conducive to production. Therefore, in combination with oil production rate and gas oil ratio, 8000 kPa is selected as the best production well

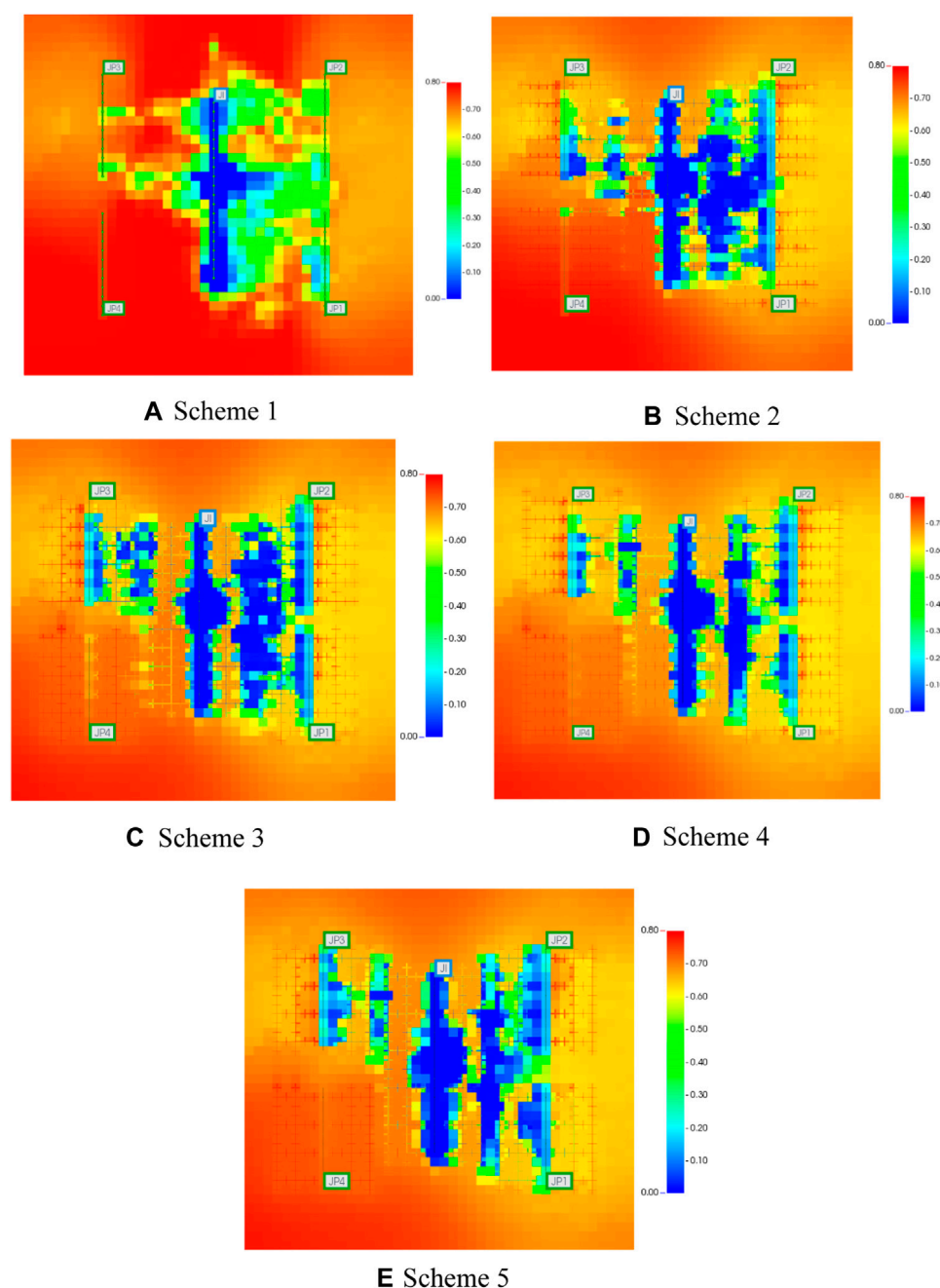


FIGURE 11
Distribution of remaining oil saturation with fracture distribution in different scheme.

bottom hole pressure, which can not only consider efficiency, but also maintain a certain degree of stable production.

4.2 Analysis of injection rate

In the production process, due to the strong heterogeneity of tight reservoirs, it is not the more injection, the more production. There is a reasonable injection volume, which makes the injection and output have the best economic benefits. Therefore, this section compares and evaluates the injection volume of CO₂ and optimizes the injection volume according to the proportion of injection and production.

The influence of different injection rates on productivity is analyzed and compared. The results are shown in Figure 8. It can be seen from the figure that in the early stage of displacement development, the injection rate has little impact on productivity. When the displacement development exceeds 3 years, the recovery factor increases with the increase of injection rate. When the injection rate increases from $0.5 \text{ m}^3/\text{d} \times 10^4 \text{ m}^3/\text{d}$ to $1 \text{ m}^3/\text{d} \times 10^4 \text{ m}^3/\text{d}$, the recovery factor changes in the early and middle stages, while when the injection rate increases from $1 \text{ m}^3/\text{d} \times 10^4 \text{ m}^3/\text{d}$ to $2 \text{ m}^3/\text{d} \times 10^4 \text{ m}^3/\text{d}$, the recovery factor is different in the late stage of development. Therefore, the greater the injection amount, the later the effective period. This is because the greater the injection amount will produce

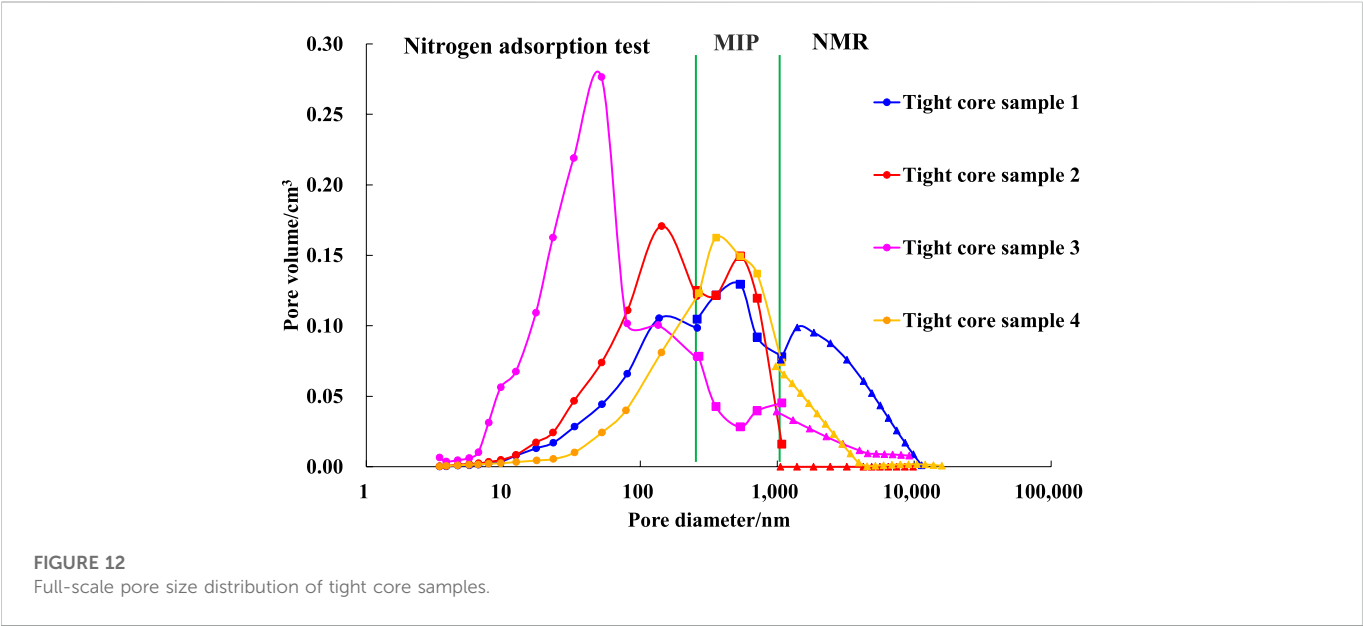


TABLE 6 Comparison scheme design considering adsorption.

Displacement mode	Time	Production BHP	Injection rate	Adsorption component	Adsorption capacity/mol%
	/a	/kPa	/m³/d		
CO ₂ flooding	10	8,000	5,000	None	/
				C19	5
				C19	8
				C19	10
				C19	15
				C30	3
				C30	5
				C19 + C30	1 + 4
				C19 + C30	2 + 3
				C19 + C30	3 + 2
				C19 + C30	4 + 1

higher injection pressure. However, in the early stage of development, when the oil saturation is high, CO₂ cannot effectively enter the formation, so it can only supplement the formation energy. With the development, the oil saturation decreases, the gas saturation of CO₂ in the formation gradually increases, and the crude oil and CO₂ are more in contact, at this time, the high oil carrying capacity of CO₂ is reflected. On the contrary, with the decrease of oil saturation in the middle and later stages of development, the formation energy cannot be supplemented. The contact area between CO₂ and crude oil is smaller than the large injection volume, and the recovery factor is significantly reduced.

According to the above results, it can be found that the greater the injection rate is, the higher the recovery factor is and the longer the high yield is maintained. However, it can be found that there is a difference between the enhanced oil recovery when the injection volume is increased from 1 m³/d × 10⁴ m³/d to 1.5 m³/d × 10⁴ m³/d

and the enhanced oil recovery when the injection volume is increased from 1.5 m³/d × 10⁴ m³/d to 2 m³/d × 10⁴ m³/d. Therefore, by comparing the oil exchange ratio, the oil exchange ratio is defined as the ratio of the cumulative oil production volume to the cumulative gas injection volume to screen the best injection volume.

It can be seen from Figure 9 that with the increase of injection volume, the recovery factor increases and the oil exchange ratio decreases, which means that the CO₂ required to obtain unit crude oil increases with the increase of injection volume and the recovery cost increases, but more crude oil can be obtained correspondingly. From the curve in the figure, it can be found that when the injection volume increases to 1.5 m³/d × 10⁴ m³/d, the recovery factor increases slowly, and the oil exchange ratio decreases rapidly. Combined with the matching degree of recovery factor and oil exchange ratio, select 1.5 m³/d × 10⁴ m³/d as the best injection rate.

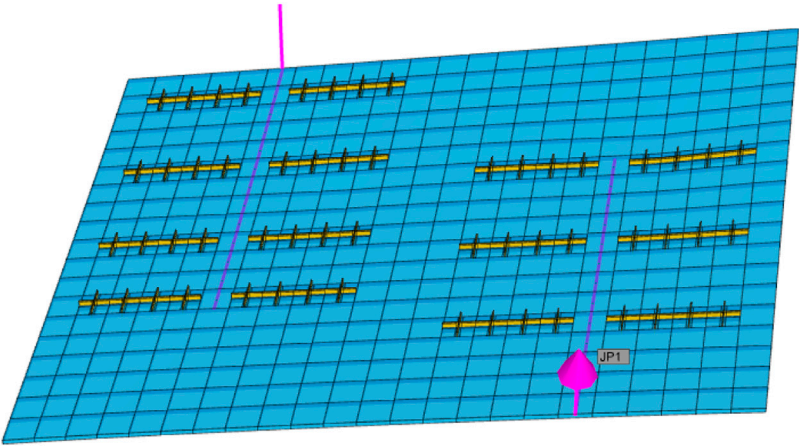


FIGURE 13
Part of geological model and distribution of fracture.

TABLE 7 Geological and fracture parameters.

Formation parameters	Value	Fracture parameters	Value
Porosity	0.076–0.1542	Fracture spacing/m	75
Permeability/ $10^{-3} \mu\text{m}^2$	0.027–0.2556	Number of major fractures	Inj:4; Pro:3
Initial oil saturation	0.8	Half-length of fracture/m	100
Temperature/ $^{\circ}\text{C}$	71.6	Width of fracture/m	0.0038
Formation pressure/kPa	40,000	Effective fracture permeability/ $10^{-3} \mu\text{m}^2$	199.36

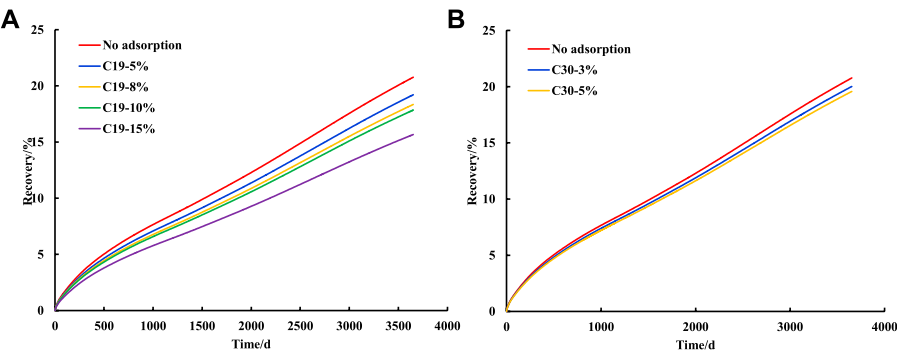


FIGURE 14
Effect of different adsorption capacity of single component on oil recovery (a.C19, b.C30).

4.3 Analysis of fractures

This section makes a comparative study on the distribution design of fractures. Artificial fractures are needed to form oil flow channels. This section makes a comparative analysis on the number and length of main fractures and the impact of secondary fractures on productivity.

Combined with the occurrence state of the fluid, it is obtained that in the process of CO₂ displacement, the recovery factor decreases with the increase of the adsorption capacity, when the adsorption

components are the same. The influence of different fracture distributions on oil recovery is compared and analyzed, and the results are shown in Figure 10. It can be found that the ultimate recovery factor of different fracture distributions from high to low is one secondary fracture (middle) > 2 secondary fractures > no secondary fractures > 1 secondary fracture (edge) > no fractures. The result is not as expected: The more secondary fractures, the better. This is because compared with the reservoir matrix, the fractures are high conductivity channels. Excessive infilling fractures will cause the

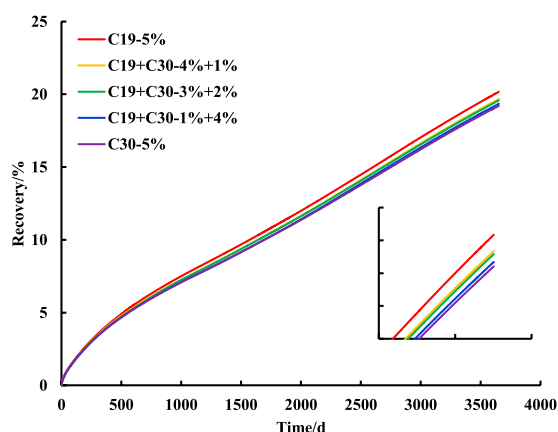


FIGURE 15

Effect of different components with the same adsorption capacity on oil recovery.

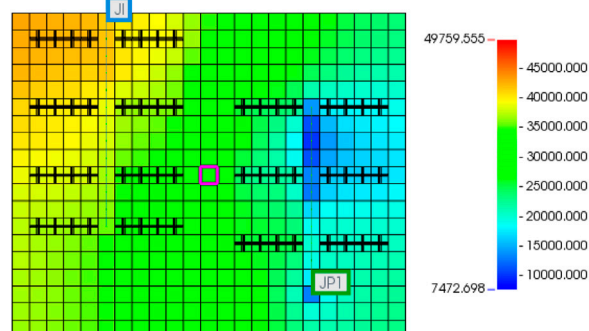


FIGURE 16

Model position of comparison grid.

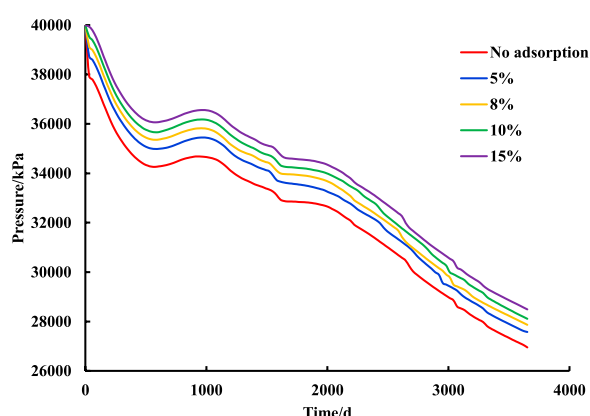


FIGURE 17

Influence of different adsorption capacity on grid pressure.

formation of high permeability channels between injection and production wells, which is not conducive to the further spread of displacement phases. According to the experiment results, the effective permeability of the fracture is 200 mD, which is a high conductivity

channel for CO_2 because of its high flow ability, excessive infilling fractures will cause the connection of the fracture which make the CO_2 flow in the fractures but not motivate the oil in the matrix. Therefore, the key to improve the recovery of tight reservoirs through fracturing is to conduct complex volume fracturing in the near well zone, while the fracturing effect in the far well zone is not ideal. By comparing the effect of fracture distribution on oil production rate, the existence of fractures has greatly improved the oil production rate in the short term. When the development time is long, the oil production rate of the non-fracture scheme is relatively higher, because fractures will induce the directional migration of displacement phase, so that the swept volume of the non-fracture scheme will be smaller, but more efficient. Combined with Figure 11, it can be found that Scheme 3 has the largest swept volume.

5 Influence of oil occurrence state on production

5.1 Reservoir fluid occurrence characteristics

According to the previous research, reservoir fluids can be divided into three categories according to their occurrence state: body phase available crude oil, movable adsorption phase and immovable adsorption phase (Liu et al., 2021). This section makes a comparative analysis on the productivity considering adsorption.

Firstly, low-temperature liquid nitrogen adsorption experiment, high-pressure mercury intrusion porosimetry (MIP) and nuclear magnetic resonance experiment (NMR) were carried out, the obtained pore sizes were combined. According to the experimental principle of various test methods, the liquid nitrogen adsorption test was selected to obtain the interval with pore size less than 270 nm, the high-pressure mercury intrusion test was used to obtain the interval with pore size of 270 nm–1000 nm and the nuclear magnetic resonance test was used to obtain the interval with pore size greater than 1000 nm, as shown in Figure 12. To unify the standard, all experimental data are converted into cylindrical core with a diameter of 25 mm and a length of 20 mm, with a mass of about 10 g.

According to the integration results, it can be obtained that the size distribution of compact core is within the range of 6.5 nm–19.2 μm , in which nano scale pores are dominant, while a small number of micro scale pores exist.

5.2 Simulation scheme design

According to the theoretical simulation of Dong et al. (2021). Based on the theoretical calculation of the matching relationship between adsorption capacity and pore size, it is preliminarily determined that the adsorption capacity is 3%–15%, and the oil recovery and reservoir physical property changes are compared. The specific simulation scheme is shown in Table 6.

Due to the consideration of adsorption, the amount of simulation calculation is greatly increased, so part of the geological model grid is intercepted, and the model size is 23 (I) \times 19 (J) \times 4 (K), the top depth is 3214 m. A single injection-production horizontal well group is established. The geological model is shown in Figure 13 and the physical properties of the model are shown in Table 7.

5.3 Production conditions considering occurrence state

The effects of different adsorption capacity of single component on oil recovery (Figure 14) and the effects of the same adsorption capacity and different components on oil recovery (Figure 15) were analyzed respectively. The adsorption capacity is the mole fraction of the adsorption phase.

It can be seen from Figure 14 that with the increase of adsorption capacity, the recovery factor shows a downward trend. For C19 component, the recovery factor without adsorption is 20.78%; When the adsorption capacity is 5%, the recovery rate is 19.54%; When the adsorption capacity is 8%, the recovery rate is 18.34%; When the adsorption capacity is 10%, the recovery rate is 17.85%; The recovery rate is 15.67% when the adsorption capacity is 15%. At the same time, with the increase of adsorption capacity, the decline of oil recovery increases. Compared with no adsorption capacity, the adsorption capacity of 5% decreases the oil recovery by 1.24%; Compared with 5% adsorption, 10% adsorption decreased the recovery by 1.69%; Compared with 10% adsorption, 15% adsorption decreased the oil recovery by 2.18%. For C30 component, when the adsorption capacity is 3%, the recovery factor is 20.02%; When the adsorption capacity is 5%, the recovery factor is 19.58%.

It can be seen from Figure 15 that when the adsorption amount is the same, which is 5%. The more the heavy components are, the lower the recovery factor is. When the adsorption components are all C19, the recovery factor is 19.54%; The recovery factor is 18.77% when C19 accounts for 4% and C30 accounts for 1%; When C19 accounts for 3% and C30 accounts for 2%, the recovery factor is 18.66%; When C19 accounts for 1% and C30 accounts for 4%, the recovery factor is 18.33%; When all are C30, the recovery factor is 18.20%. According to the previous research results, the light components can be extracted by CO₂ to further improve oil recovery, while the heavy components will be adsorbed on the pore surface and are difficult to use.

For the same grid on the mainstream channel at the same development time, the physical property analysis is carried out. The grid is selected as the second layer grid (12, 10, 2) (Figure 16). The physical property compared is the grid pressure (Figure 17).

It can be seen from Figure 17 that with the increase of adsorption capacity, the pressure of the grid will also increase, indicating that the lower the permeability of the grid, the lower the effective pore size will be combined with the adsorption phase, which will result in the decrease of the permeability (Lei et al., 2020). Therefore, in the numerical simulation of unconventional tight oil, it is necessary to consider the reduction of effective permeability caused by adsorption, otherwise the simulation result will be higher than the actual value.

6 Conclusion

Conventional numerical simulation of different fractures rarely considers the influence of fluid occurrence state. The experiment shows that there are two parts of fluid in nano-porous: adsorption phase and bulk phase. This paper considers the influence of occurrence state on reservoir physical properties and fluid flow ability in numerical simulation for the first time.

- 1) The enhanced oil recovery effect of CO₂ flooding is obviously better than that of CH₄ flooding and water flooding, which are 26.86%, 14.84% and 13.92% respectively. The content of light components in CO₂ flooding production fluid is higher than the average content of formation crude oil, which can effectively extract the light components in crude oil.
- 2) When the production bottom hole pressure is lower than the formation fluid saturation pressure, changing the production bottom hole pressure has little impact on the productivity of CO₂ flooding in tight reservoirs. When it is higher than the formation fluid saturation pressure, the productivity decreases with the increase of the production bottom hole pressure, and the optimal production bottom hole pressure is 8,000 kPa.
- 3) The recovery factor increases with the increase of injection rate, but when the injection rate is higher than 1.5 m³/d × 10⁴ m³/d, the increase of oil recovery rate is significantly slowed down, and the oil change rate is significantly reduced. According to the extent of enhanced oil recovery rate and the economic benefits of oil change rate × 10⁴ m³/d is the optimal CO₂ injection amount.
- 4) The complex fractures in the near well zone help to improve the swept volume of CO₂ flooding, while the complex fractures in the far well zone will cause gas channeling, which is not conducive to production.
- 5) When adsorption is considered, the recovery factor decreases with the increase of adsorption capacity; When the adsorption capacity is fixed, the recovery efficiency of the adsorbed heavy component is lower than that of the adsorbed light component. The adsorption can cause the permeability to decrease. With the increase of the adsorption amount, the permeability decreases.

Data availability statement

The original contributions presented in the study are included in the article/supplementary material, further inquiries can be directed to the corresponding author.

Author contributions

LY and ZL designed the research and write the manuscript; HY performed the research; SA and LY collected the data; DX analyzed data; TC and LZ contributed to the paper revisions. All authors have read and agreed to the published version of the manuscript.

Funding

This work was supported by the Chinese National Natural Science Foundation (No. 51774256), Chinese National Natural Science Foundation (No. 52004303) and Beijing Natural Science Foundation (3212020). This work was also done at the Beijing key laboratory of unconventional natural gas geological evaluation and development engineering.

Conflict of interest

LY, LYU, TC and LZ were employed by Research Institute of Petroleum Exploration and Development, PetroChina. ZL and SA

were employed by Daqing Oilfield Company Ltd., PetroChina. SA was employed by NO 2 Oil Production Plant Daqing Oilfield Company, PetroChina. HY was employed by CNOOC Research Institute Ltd.

The remaining authors declare that the research was conducted in the absence of any commercial or financial relationships that could be construed as a potential conflict of interest.

References

- Andrews, T. (2012). *Experiences in alberta's tight oil plays: Devonian to the cretaceous. Shale gas and oil symposium*. Calgary: EIA.
- Bob, D. (2016). *BP statistical review of world energy [EB/OL]*. Energy economics, London.
- Clarkson, C., and Pedersen, P. (2011). "Production analysis of Western Canadian unconventional light oil plays," in *Canadian unconventional resources conference* (Calgary, Alberta, Canada: SPE).
- Dong, X. H., Chen, Z. X., and Liu, H. Q. (2021). Mathematical modeling for occurrence state of hydrocarbon in micro/nano-scale pores (in Chinese). *J. China Univ. Petroleum (Edition)*. *Nat. Sci.* 45 (02), 87–95. doi:10.3969/j.issn.1673-5005.2021.02.010
- Du, J. H., Liu, H., and Ma, D. S. (2014). Discussion on effective development techniques for continental tight oil in China (in Chinese). *PETROLEUM Explor. Dev.* 41 (2), 198–205. doi:10.1016/S1876-3804(14)60025-2
- Hou, Y. N., Peng, Y., Chen, Z. X., Liu, Y., and Tian, Y. (2022). Investigating heterogeneous distribution of fluid pressure in hydraulic fractures during pulsating hydraulic fracturing. *J. Petroleum Sci. Eng.* 209, 109823. doi:10.1016/j.petrol.2021.109823
- Hou, Y. N., Peng, Y., Chen, Z. X., Liu, Y., Zhang, G., Ma, Z., et al. (2021). Investigation on the controlling factors of pressure wave propagation behavior induced by pulsating hydraulic fracturing. *SPE J.* 26, 2716–2735. doi:10.2118/205384-pa
- Hu, W. R., Zhai, G. M., and Li, J. M. (2010). Potential and development of unconventional hydrocarbon resources in China (in Chinese). *Strategic Study CAE* 12 (5), 25–29.
- IEA (2016). *World energy outlook 2016*. IEA, Paris. Available at: <https://www.iea.org/reports/world-energy-outlook-2016>.
- Jarvie, D. (2012). "Shale resource systems for oil and gas: part2-shale-oil resource systems," in *Shale Reservoirs-Giant Resources for the 21st century*. 97, 89–119. doi:10.1306/M971332
- Jarvie, D. (2010). *Unconventional oil petroleum systems: Shales and shale hybrids*. Calgary, Alberta: AAPG Conference and ExhibitionCanada, 12–15.
- Jia, C. Z., Zou, C. N., and Li, J. Z. (2012). Assessment criteria, main types, basic features and resource prospects of the tight oil in China (in Chinese). *Acta Pet. Sin.* 33 (3), 343–350. doi:10.1016/0031-9384(73)90235-7
- Kong, D. B., Gao, Y. B., Sarma, H., Li, Y., Guo, H., and Zhu, W. (2021). Experimental investigation of immiscible water-alternating-gas injection in ultra-high water-cut stage reservoir. *Adv. Geo-Energy Res.* 5 (2), 139–152. doi:10.46690/ager.2021.02.04
- Kong, D. B., Li, Y. Q., Yu, M., Ma, R., Guo, H., Peng, Y., et al. (2019). Experimental investigation on block and transport characteristics of foam in porous media for enhanced oil recovery processes. *Colloids Surfaces A Physicochem. Eng. Aspects* 570, 22–31. doi:10.1016/j.colsurfa.2019.02.067
- Lei, Z. D., Lai, L. B., Sun, Z., and Wu, K. (2020). Comprehensive model for oil transport behavior in nanopores: Interactions between oil and pore surface. *Industrial Eng. Chem. Res.* 59 (46), 20527–20538. doi:10.1021/acs.iecr.0c04025
- Li, X., Li, C. L., and Li, B. (2020). Response laws of rock electrical property and saturation evaluation method of tight sandstone (in Chinese). *PETROLEUM Explor. Dev.* 47 (01), 202–212. doi:10.1016/S1876-3804(20)60020-9
- Li, Y. X., and Zhang, J. C. (2011). Types of unconventional oil and gas resources in China and their development potential (in Chinese). *Int. Pet. Econ.* 34 (3), 61–67. doi:10.3969/j.issn.1004-7298.2011.03.011
- Liang, S. J., Huang, Z. L., and Liu, B. (2012). Formation mechanism and enrichment conditions of Lucaogou Formation shale oil from Malang sag, Santang hu Basin (in Chinese). *Acta Pet. Sin.* 33 (4), 588–594. doi:10.7623/syxb201204007
- Liu, Y. S., Dong, X. H., Chen, Z. X., Hou, Y., Luo, Q., and Chen, S. (2020). Pore-scale movability evaluation for tight oil enhanced oil recovery methods based on miniature core test and digital core construction. *Industrial Eng. Chem. Res.* 60 (6), 2625–2633. doi:10.1021/acs.iecr.0c04256
- Liu, Y. S., Dong, X. H., Chen, Z. X., Hou, Y., Luo, Q., and Chen, Y. (2021). A novel experimental investigation on the occurrence state of fluids in microscale pores of tight reservoirs. *J. Pet. Sci. Eng.* 196, 107656. doi:10.1016/j.petrol.2020.107656
- Lu, S. F., Huang, W. B., and Chen, F. W. (2012). Classification and evaluation criteria of shale oil and gas resources: Discussion and application (in Chinese). *PETROLEUM Explor. Dev.* 39 (2), 249–256. doi:10.1016/S1876-3804(12)60042-1
- Montgomery, J. B., and O'sullivan, F. M. (2017). Spatial variability of tight oil well productivity and the impact of technology. *Appl. Energy* 195, 344–355. doi:10.1016/j.apenergy.2017.03.038
- Peng, D. Y., and Robinson, D. B. (1976). A new two-constant equation of state. *Ind. Eng. Chem. Fundam.* 15, 59–64. doi:10.1021/i160057a011
- Shi, L. Z., Wang, Z. Z., and Zhang, G. (2015). Distribution and formation of tight oil in Qijia area, Songliao Basin, NE China (in Chinese). *PETROLEUM Explor. Dev.* 42 (1), 44–50. doi:10.1016/S1876-3804(15)60005-2
- Tian, J. C., Liu, W. W., and Wang, F. (2014). Heterogeneity of the paleozoic tight sandstone reservoirs in gaoqiao area of Ordos Basin (in Chinese). *Oil Gas Geol.* 35 (2), 183–189. doi:10.11743/ogg20140202
- Tong, X. G. (2012). Genesis and distribution of unconventional oil (in Chinese). *Acta Pet. Sin.* 3 (S1), 20–26. doi:10.7623/syxb2012S1004
- Yang, Z. F., Zeng, J. H., and Feng, X. (2016). Small-scaled heterogeneity of tight sandstone reservoirs and oil accumulation characteristics (in Chinese). *J. China Univ. Min. Technol.* 45 (01), 1–9. doi:10.13247/j.cnki.jcmt.000402
- Zhang, G. Y., Wang, Z. Z., and Guo, X. G. (2015). Characteristics and 'sweet spot' prediction of dolomitic tight oil reservoirs of the Fengcheng Formation in Wuxia area, Junggar Basin (in Chinese). *Oil Gas Geol.* 36 (2), 219–229. doi:10.11743/ogg20150206
- Zou, C. N., Yang, Z., and Tao, S. Z. (2012). Nano-hydrocarbon and the accumulation in coexisting source and reservoir (in Chinese). *PETROLEUM Explor. Dev.* 39 (1), 13–26. doi:10.1016/S1876-3804(12)60011-1

Publisher's note

All claims expressed in this article are solely those of the authors and do not necessarily represent those of their affiliated organizations, or those of the publisher, the editors and the reviewers. Any product that may be evaluated in this article, or claim that may be made by its manufacturer, is not guaranteed or endorsed by the publisher.

Frontiers in Energy Research

Advances and innovation in sustainable, reliable
and affordable energy

Explores sustainable and environmental
developments in energy. It focuses on
technological advances supporting Sustainable
Development Goal 7: access to affordable,
reliable, sustainable and modern energy for all.

Discover the latest Research Topics

[See more →](#)

Frontiers

Avenue du Tribunal-Fédéral 34
1005 Lausanne, Switzerland
frontiersin.org

Contact us

+41 (0)21 510 17 00
frontiersin.org/about/contact



Frontiers in Energy Research

